

# **Elements of 3D Seismology**

*second edition*

**Christopher L. Liner  
Department of Geosciences  
University of Tulsa**



## **Disclaimer**

The recommendations, advice, descriptions, and the methods in this book are presented solely for educational purposes. The author and publisher assume no liability whatsoever for any loss or damage that results from the use of any of the material in this book. Use of the material in this book is solely at the risk of the user.

Copyright ©2004 by  
PennWell Corporation  
1421 S. Sheridan Road/P.O. Box 1260  
Tulsa, Oklahoma 74101

800.752.9764  
+1.918.831.9421  
[sales@pennwell.com](mailto:sales@pennwell.com)  
[www.pennwellbooks.com](http://www.pennwellbooks.com)  
[www.pennwell.com](http://www.pennwell.com)

Managing Editor: Marla Patterson  
Production Editor: Sue Rhodes Dodd  
Cover Design: Matt Berkenbile  
Book Design: Robin Remaley

Library of Congress Cataloging-in-Publication Data

Liner, Christopher L.  
Elements of 3D seismology / by Christopher L. Liner.-- 2nd ed.  
p. cm.  
Rev. ed. of: Elements of 3-D seismology. c1999.  
Includes bibliographical references and index.  
ISBN 1-59370-015-6  
ISBN 978-1-59370-015-7  
1. Seismic reflection method. I. Title: 3D seismology. II. Liner, Christopher L.  
Elements of 3-D seismology. III. Title.

TN269.84.L56 2004  
622'.1592--dc22

2004009833

All rights reserved. No part of this book may be reproduced, stored in a retrieval system, or transcribed in any form or by any means, electronic or mechanical including photocopying or recording, without the prior permission of the publisher.

Printed in the United States of America.

2 3 4 5 6 12 11 10 09 08

# Introduction

## Scope

This book is related to surface petroleum seismology, meaning those acquisition techniques involving sources and receivers at the earth surface. This represents the vast majority of seismic effort worldwide and includes data gathered by receivers on the seafloor. Downhole methods such as vertical seismic profiling and crosswell seismic are only discussed as they relate to surface seismic data.

## A brief history of seismology

Earthquakes have affected human societies from the earliest times. The occurrence of earthquakes were recorded by civilizations around the world, including China, Egypt, Babylonia and other societies of the ancient near east, and Greece. The first attempts at explaining the causes of earthquakes are found in the fragmentary literature of the Greek pre-Socratic philosophers [114] from 580 BCE onward.

Little of value on this subject was added after the third century BCE. Earthquake theories of the ancient world are diverse but nowhere show an appreciation of faulting and wave motion as the cause of earthquakes. Perhaps the closest is Metrodorus of Chios (fourth century): “When someone sings into a large jar, his voice vibrates and runs through the whole jar...” But only by abuse of a modern vantage point does an elastic wave theory of earthquakes emerge out of this passage or any of the ancient works.

The great earthquake of Lisbon in 1755 began a modern march toward seismic understanding that continues today. A major cultural center of Europe was destroyed, and many thousands were killed from the earthquake, tsunami,

## Elements of 3D Seismology

and aftershocks. Include the death toll from fire and disease, and perhaps half of the population was lost within a month. This event has been said to be “the slap that started the infant science of seismology breathing.”

The equations of motion for an elastic medium were published by Navier in 1821. Poisson showed in 1828 that the equations of motion implied two kinds of elastic waves now called P- and S-waves. Between 1830 and 1860, many of the world’s top physicists developed elastic wave theory as a possible mathematical foundation of light. Maxwell’s equations ended this quest in 1861, but the theoretical results were of direct use later in seismology.

Notable in this period is a brilliant 1849 memoir by Stokes, *Dynamical Theory of Diffraction*. The foundations of elastic wave theory were completed by Rayleigh (1885) describing the surface wave that bears his name, Knott (1899), and Zoeppritz (1919) on elastic reflection coefficients. Finally, Lamb (1904) solved the general problem of elastic waves emitted by a point source on the surface of an elastic self-gravitating sphere.

Modern observational seismology began with the Milne seismograph built in 1880. Instrumentation improved parallel to industrial and electronic progress until portable seismographs were possible.

The first modern reflection seismic experiments were conducted in the United States by Fessenden in 1913, and he received a patent for “Method and Apparatus for Locating Ore Bodies” in 1917. However, the first known reference to a reflection seismic experiment is described by the Greek historian Herodotus writing in about 445–430 BCE. Recounting an event of 580 BCE, he writes:

*Then the Persians besieged Barce for nine months, digging mines leading to the walls, and making violent assaults. As for the mines, a smith discovered them by the means of a brazen shield, and this is how he found them: Carrying the shield round the inner side of the walls he smote it against the ground of the city; all other places where he smote it returned but a dull sound, but where the mines were the bronze of the shield rang clear. Here the Barcaeans made a counter-mine and slew those Persians who were digging the earth. Thus the mines were discovered and the assaults were beaten off by the townsmen.*

In modern terms, we would say the smith used his shield to perform a seismic tunnel detection experiment. While this application of reflection seismology had no influence on later developments in the science, it does predate Fessenden by about 2500 years.

The progress of reflection seismology from Fessenden’s time to the advent of CDP shooting in 1956 can be found elsewhere [101], and highlights of progress in the period 1956–2003 are given in Table I–1. Like any such list, this one is subjective, but it does capture the sense of progress over the last 40 years.

**Table I-1 Selected advances in petroleum seismology 1956–2003**

1956	Common midpoint shooting	Acquisition
1958	Synthetic seismogram	Interpretation
1960	Vibroseis	Acquisition
1962	Marine air gun	Acquisition
1967	Digital seismic processing	Processing
1968	Digital migration	Processing
1971	Seismic stratigraphy	Interpretation
1972	3D shooting	Acquisition
1974	Vertical seismic profile	Acquisition
1978	2D Poststack depth migration	Processing
1979	Residual statics	Processing
1979	Complex trace attributes; Impedance aversion	Interpretation
1980	2D prestack depth migration	Processing
1980	Bright spot analysis; Workstations	Interpretation
1981	3D migration velocity analysis; Slant stack	Processing
1984	DMO, 2D refl tomography, optimization	Processing
1985	3D Poststack Depth Migration	Processing
1985	Amplitude Variation with Offset AVO	Interpretation
1986	3D reflection tomography, FX deconvolution	Processing
1986	Ocean bottom cable; Crosswell	Acquisition
1989	4D seismic	Acquisition
1989	3D prestack depth migration; Neural networks	Processing
1989	Dip and azimuth attributes	Interpretation
1990	Subsalt imaging	Interpretation
1991	Vertical cable	Acquisition
1991	Turning wave migration; Wavelet transforms	Processing
1992	Seismic sequence stratigraphy	Interpretation
1994	Routine anisotropic processing	Processing
1994	4D flow parameters → seismic parameters	Interpretation
1995	Coherence; Fluid substitution; Wavelet transforms	Interpretation
1996	Impedance optimization; Attribute classification	Interpretation
1997	Spectral decomposition	Interpretation
1998	Seismic monitoring of hydraulic fracturing	Acquisition
1999	Least squares migration	Processing
2000	Overpressure from attributes	Interpretation
2001	Reservoir prediction with multiattribute transforms	Interpretation
2003	Generalized Hilbert transform; Spice	Interpretation

### Why 3D?

This is a book on 3D seismic with detours to 2D when this is adequate to convey a concept or technique. Seismic prospecting was almost exclusively 2D until the mid-1980s. In the 1970s when computing became common, 3D acquisition, processing, and interpretation advanced dramatically. Current worldwide seismic effort is dominated by 3D, and its dominance is growing.

What is the attraction of 3D? Since 3D seismic is now the default mode, it needs no special justification. But it is worth making a short list of benefits to remind us how 3D came to be the preferred technique.

A 3D seismic survey has many advantages over a 2D line or a dense grid of 2D lines. A 2D grid is considered dense if the line spacing is less than about 400 m.

The advantages of 3D include

1. true versus apparent structural dip
2. more and better stratigraphic information from time and horizon slices
3. optimum mapping of faults in map view
4. optimum lateral resolution
5. much better reduction of drilling risk

From a physics point of view, 3D is what we should have been doing all along.

### Getting started

Here are a few recurring ideas and concepts related to 3D seismology.

**Onion.** You can think of the knowledge required for working with 3D seismic as being built up of layers like an onion. At the core are 1D seismic ideas like wavelet, convolution, phase, and reflection coefficient. The next layer is 2D seismic where new concepts include offset and angular reflection. Next is 3D where we find azimuth, bins, the data volume, and ways to slice it. The outside layer is time-lapse 3D where new ideas include repeatability and seismic response to pore fluid changes.

**Quality.** The main job for seismic interpretation is to map structure, stratigraphy, and reservoir properties. In that order, each task requires increasing data quality. Quality is a nebulous thing determined at acquisition time by correct survey design and execution. Processing generally has less impact on quality but is still very important.

**Stack.** Prestack data is acquired in shot records, sorted into common-midpoint gathers, normal moveout corrected, and summed over offsets (stacked) to form the poststack interpretation volume.

**Volume.** On a regular cubic grid, 3D seismic data is a volume of data values. The size of this grid is  $(nt, nx, ny)$  which can be millions or billions of individual samples.

**Information.** Seismic data consists of (1) traveltimes, (2) amplitude, and (3) waveform information. Structure mapping involves only (1), stratigraphic information involves (1)–(3), and reservoir property prediction is based primarily on (2)–(3).

**Echo.** Seismic is an echolocation technique similar to sonar, radar, and medical ultrasound. A wave is emitted on the surface of a medium, it bounces around in the material, and part of it is reflected back to the surface. From the returned signal, we attempt to determine internal features of the medium.

**Edges.** If you go to an outcrop and look at the geology, you see rock units—sandstone, shale, and limestone. If you look at seismic data, you are seeing the edges of rock units. Seismic is, in effect, an edge detection technique that responds to acoustic impedance changes. Acoustic impedance is density multiplied by seismic P-wave velocity.

**Layers.** A key part of the interpretation process for 3D seismic data is event tracking. You can picture this by thinking of the 3D seismic data volume as a cube of vanilla ice cream with chocolate streaks. Tracking means we follow a streak into the cube to find its 3D shape. This is time structure mapping. We also keep track of how dark the chocolate is as we follow it. This is horizon amplitude mapping.

**Computer.** Available computer power is such that seismic imaging of a large 3D data set involves many approximations and shortcuts, and still can take several months.

**Risk.** In the search for petroleum, seismic imaging reduces risk of drilling dry holes and marginal wells and under or over estimating reserves. But no one finds oil with seismic data. It is found by drilling. Medical imaging is a suitable analogy to seismic imaging. Both are noninvasive, nondestructive, and reduce risk. Surgery repairs the problem, but in this day and age, who would undergo surgery without some kind of medical imaging first?

# Part I

*Waves:  
The Foundation of Seismology*

# 1

## General Properties of Waves

Reflection seismology is the science of examining the earth's interior through the analysis of mechanical waves. Seismic rays are bent, reflected, refracted, diffracted, and scattered. The emitted signal is weakened by these effects as well as geometric spreading and attenuation.

The waves are generated by controlled sources and travel through fluids, solids, and porous solids. In this chapter, we consider those properties of waves that do not depend on the kind of material supporting the wave propagation. For example, Snell's law is a general property of wave motion but differs in detail between reflection of acoustic and elastic waves. When considering a general property like Snell's law, in this chapter, we will discuss the scalar wave case.

When considered from this classification scheme (for that is what it is), all acoustic wave phenomena are also present in elastic wave propagation as well as a relatively small number of new, uniquely elastic effects. Similarly, the passage from elastic to poroelastic introduces just a few new ideas and observable effects.

This chapter emphasizes conceptual discussion and visualization of these concepts. Mathematics enters where necessary and useful, but not gratuitously.

### 1.1 Mechanical waves

Mechanical wave motion involves a disturbance propagating through a compressible or elastic medium thereby transferring energy from one region to another without transfer of mass [107]. The energy transport is via elastic properties of the material, whether elastic in the sense of fluids characterized by mass density and bulk modulus, or solids described by mass density and stiffness parameters. Such parameters form a numerical model of the material and a primary goal of reflection seismology is to estimate these parameters from observed seismic data.

## **Elements of 3D Seismology**

When considering a fluid or solid medium for wave propagation problems, we distinguish between the interior (or body) and the free surface. By free surface, we mean a boundary between the material and a vacuum, or at least a region with relatively small elastic parameters and/or density. For example, in many problems, the earth surface behaves very much like a free surface because bulk modulus and density of the lower atmosphere are orders of magnitude smaller than these parameters are in surface rocks.

Even the ocean/air interface is a good approximation to a free surface. In general, the body can be bounded on all sides by free surfaces, as would be the case in studying seismic waves in an entire planet. For the problems we will encounter, there will be one free surface representing the surface of the solid earth or ocean.

A broad distinction of mechanical waves is made between body and surface waves. Body waves are those that can propagate through the interior of a fluid or solid, while surface waves exist only in the vicinity of the free surface.

Sound is the only kind of mechanical body wave in a fluid. For an isotropic elastic solid, two kinds are possible, termed P and S. In an anisotropic solid, there are three possible mechanical waves. The technically correct designations are quasi P-wave (qP), quasi S-wave one (qS1), and quasi S-wave two (qS2). In practice, however, people quickly tire of saying “quasi” all the time and these waves are called P, S1, and S2. The shear waves travel at different speeds and are therefore also referred to as fast and slow S-waves, with S1 being the faster of the two. Finally, one additional kind of body wave is theoretically possible when the solid is porous. This new wave is called a Type II P-wave and only exists at frequencies well above surface seismic band of 10-100 Hz. However, this wave can play a role in sonic logs operating at 10 to 15 thousand Hertz, and especially in core measurements (one megahertz or higher).

### **1.2 Particle motion**

As a mechanical wave progresses, it is said to be propagating in a particular direction (the direction of energy transport). This wave causes the material to vibrate and the orientation of this vibration is called the direction of particle motion. Of fundamental importance are the relative directions of propagation and particle motion, (see Fig. 1.1).

In general, there are two kinds of pure waves—longitudinal and transverse. A longitudinal wave is one in which the particle motion is parallel to the propagation direction. Examples include sound and seismic P-waves. In a transverse wave, the particle motion is perpendicular to the propagation direction. A seismic S-wave is of this type.

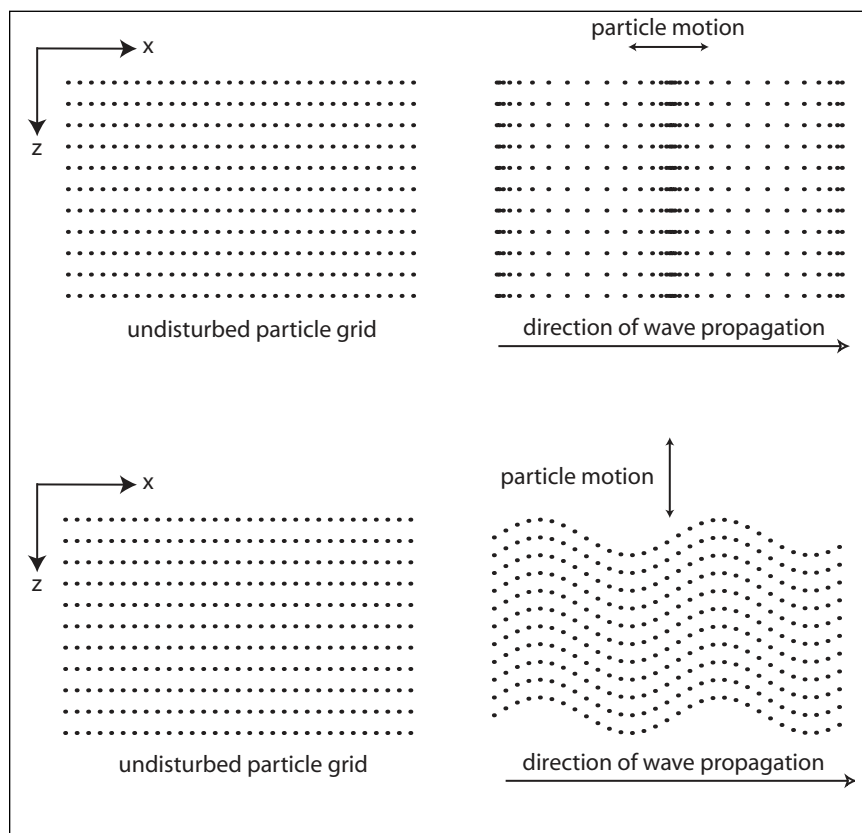


Fig. 1.1 Mechanical waves are distinguished by the vibration patterns they cause in the medium. By definition, a longitudinal wave (upper right) has particle motion parallel to the direction of propagation. In transverse wave motion (lower right), the particles vibrate perpendicular to the propagation direction.

Waves of a mixed type are possible, in which the particle motion is some combination of parallel and perpendicular vibration relative to the direction of propagation. Examples include surface gravity waves on water (prograde ellipse), Rayleigh wave (retrograde ellipse shallow to prograde ellipse deep), anisotropic P-waves, and near field elastic waves.

### 1.3 Polarization

Polarization is not possible for longitudinal wave motion but occurs in a transverse wave when particle motion is confined to one direction. In Figure 1.2

## Elements of 3D Seismology

we see a 3D view of a grid of points that lie in a plane (left plots). A transverse wave propagating in the  $x$ -direction can have particle motion in the  $y$ -direction (upper right) or the  $z$ -direction (lower right). These are pure mode transverse waves; a general transverse wave can have particle motion in any direction perpendicular to the propagation direction.

For seismic shear waves, it is common to distinguish a shear wave with horizontal polarization (SH) from one with vertical polarization (SV). Another example involves fast (S1) and slow (S2) shear waves associated with propagation in anisotropic rock.

### 1.4 Elastic properties

Whether the material under consideration is a fluid, solid, or porous solid, it is characterized by a certain number of elastic parameters. Mass density is a

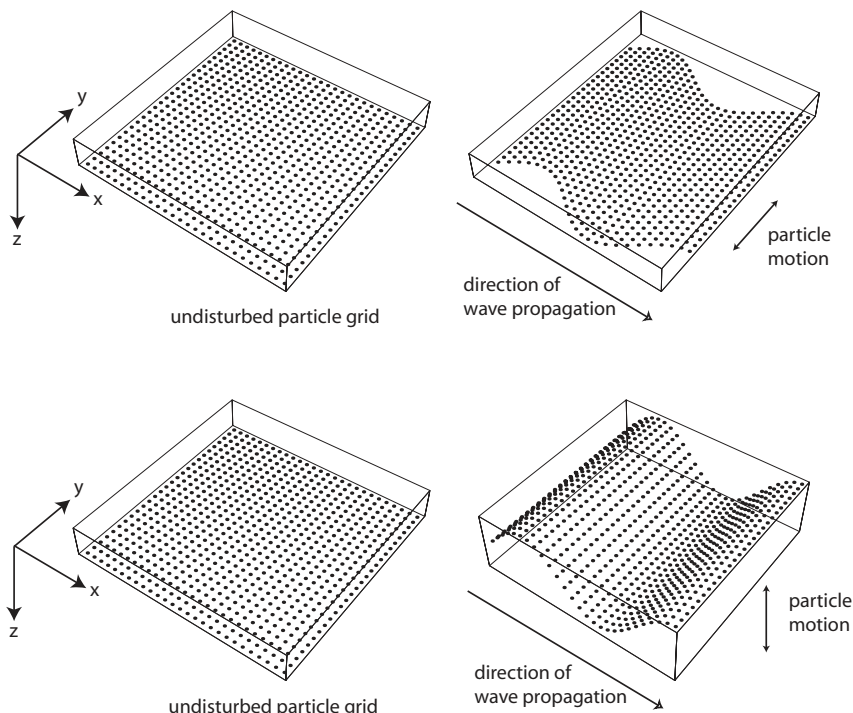


Fig. 1.2 Polarization is a property of transverse waves. A horizontally polarized wave (upper right) has particle motion confined to the horizontal plane. Vertical polarization occurs when the particles vibrate only in the vertical direction (lower right).

parameter universal to all media and is not generally counted among the elastic parameters. In a slight abuse of terminology, we use the term *elastic parameter* to describe the bulk modulus of a fluid even though a fluid is not an elastic solid. At any rate, the general scheme is enumerated this way: a fluid is characterized by one elastic parameter, an isotropic solid by two, and the simplest useful anisotropic solid by four. This kind of anisotropy is the representation most often used in petroleum seismic work, but a generally anisotropic material could have up to 21 elastic parameters.

## 1.5 Wavespeed

As a waveform travels through a solid or fluid, it is possible to track a particular feature and associate a speed with its movement. This is the phase velocity of the wave, and, as with any velocity, it has both magnitude and direction (that is to say, it is a vector). However, in seismic studies, the velocity referred to is seldom the vector velocity of a specific traveling wave, but the scalar wavespeed, which is a material parameter associated with a point in space. Clear understanding of this distinction avoids a vast amount of confusion. In accordance with standard practice, throughout this work we will use the terms *velocity* and *wavespeed* interchangeably.

In general terms, a wave propagating through a fluid or solid has a distinct velocity that depends on four quantities [77],

$$v(\underline{x}, \hat{n}, \lambda, A) \quad (1.1)$$

where  $\underline{x}$  is the observation point in 3D space,  $\hat{n}$  is a unit vector pointing in the direction of wave travel,  $\lambda$  is the wavelength, and  $A$  is the amplitude of the wave.

If wavespeed depends on the observation point, the material is said to be heterogeneous. This is the common case with seismic body waves since rock properties vary from point to point in the earth. For an acoustic wave example, consider the speed of sound in a lecture hall. Near a warm object, the sound speed is relatively high, while it is relatively low near a cool object.

One can imagine a 3D model of the sound speed in such a room on a regular cubic grid—hot colors (red, yellow) indicating high velocity and cool colors (blue, green) low ones. In much the same way, 3D velocity models of the earth are constructed for use in modeling and imaging of seismic data. But an earth velocity model might be a cube several kilometers on a side (see Fig. 1.3). As physical properties in the earth change the seismic wavespeed also varies. First order effects are increase of temperature and pressure with depth, and other factors include pore fluids, porosity, mineralogy, and fractures.

## Elements of 3D Seismology

If wavespeed depends on direction of travel, the medium is said to be anisotropic. Our acoustic example is no help here, since sound waves are isotropic, traveling at the same speed in any direction. This is also very nearly true for seismic waves in thick, uniform rock units. But anisotropy affects both P- and S-waves and is common in sedimentary rocks due to fine layering, fracturing, regional stress fields, and other causes. In layered rocks such as shale, it is not unusual for a horizontally traveling P-wave to go 20% faster than a vertical one. In practice P-wave anisotropy is often overshadowed by other velocity effects and therefore difficult to discern on its own.

In a basin under lateral tectonic stress, wavespeed will vary with compass direction of travel, and fractured rocks give rise to the interesting phenomena of shear wave splitting. This is the seismic equivalent of the splitting of light by the mineral calcite to create a double image of objects viewed through it. Shear wave anisotropic effects, while interesting, are not as important in petroleum seismology as P-wave effects simply because the great majority of work is done with P-wave data.

If the wavespeed depends on wavelength, the medium is said to be dispersive. This is commonly the case for seismic surface waves (Rayleigh wave) when the near surface is layered. Seismic body waves, both  $P$  and  $S$ , are only slightly dispersive until pressed into higher frequency bands associated with sonic logging or laboratory rock physics measurements. For dispersive waves, it is necessary to distinguish the speed at which a recognizable feature propagates (phase velocity) from the speed of energy transport (group velocity). By necessity, dispersion is associated with absorption, which is the conversion of wave energy into heat. Absorption is one of an entire class of mechanisms that cause seismic amplitude to decay with distance traveled, and it is challenging to isolate absorption from the others.

Finally, if the wavespeed depends on the amplitude of the wave, the medium is said to be nonlinear. This is not a consideration for seismic waves in the 10–100 Hz band typical of petroleum seismic data. However, as with dispersion, there are measurable effects at sonic frequencies and beyond [46].

In summary, for the vast majority of seismic work the P-wave velocity can be considered a function of position  $v(\underline{x}) = v(x,y,z)$  intertwined with anisotropy effects of up to 20%. Figure 1.3 shows a 2D velocity model with gray levels representing isotropic P-wavespeed. This particular model was created to study imaging algorithms, but models of similar complexity are derived from real data.

## 1.6 Display of wavefield data

When a receiver records data, a time series is created that consists of some number of consecutive measured values separated in time by a constant time

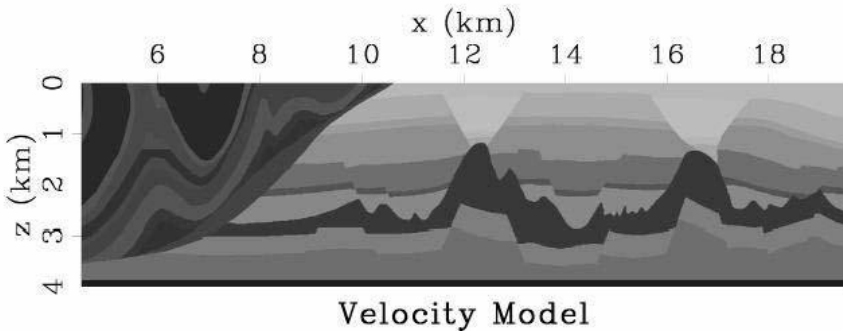


*Fig. 1.3 This 2D velocity model represents P-wavespeed in the Earth. Such models are used in seismic imaging and modeling. Light shades represent low velocity and dark shades high velocity. (Modified from [58]).*

sample rate. Whatever the actual measured quantity (particle velocity, pressure, etc.), it is usually referred to as amplitude data. A time series recorded by any kind of seismic receiver is called a trace and will generally consist of a few thousand samples with a time sample rate of 1, 2, or 4 ms (1 millisecond = 0.001 sec.). Many such traces taken together form a gather or section, which represents the measured wavefield or image created from it. The display of seismic wavefield data is generally in one of two forms, an image or a wiggle trace display. In the image display, gray levels or color values are associated with amplitudes.

A data panel consisting of 1000 traces with 500 samples per trace is shown in Figure 1.4. Even with 500,000 (500K) data samples, we clearly see seismic reflection events associated with the seafloor, faults, bed terminations, unconformity surfaces, and other geologic features. A wiggle trace display of this data at this scale would be unusable due to the data density (about 20K samples per square inch).

Figure 1.5 shows cascading levels of zoom for this same data panel. Note the distance bar on each plot for scale. Working down from the top, each data panel contains 500K, 100K, 50K, 25K, 5K, and 500 data samples. Even though all panels are physically the same size, the data density is different in each. When working with a lot of data (very high sample density), image displays are essential. For close work, the wiggle trace display is preferred as it allows the interpreter to analyze individual waveforms.

## 1.7 Waveform

Think of a sound wave moving from left to right and a magic camera that can take a picture of the pressure field. If we take a snapshot, the wave is frozen

## Elements of 3D Seismology

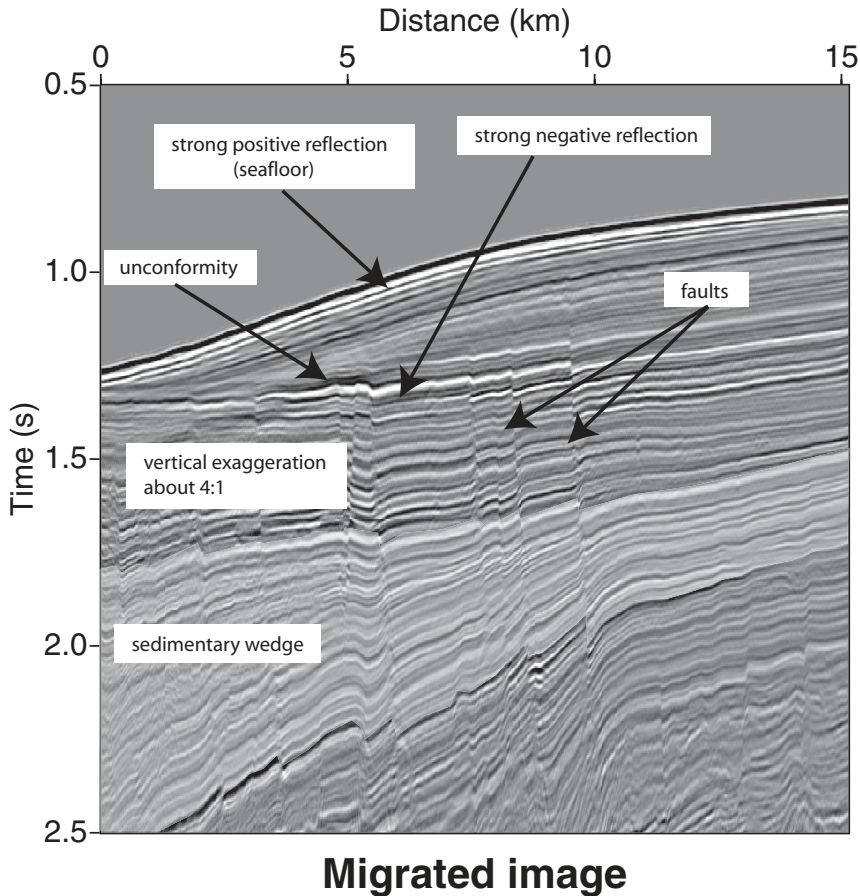


Fig. 1.4 Grayscale image of a data panel consisting of 1000 traces and 500 time samples per trace. Trace spacing is 15 m and the time sample rate is 4 ms. A sedimentary interval is highlighted to show thickening. This is offshore data from Southeast Asia.

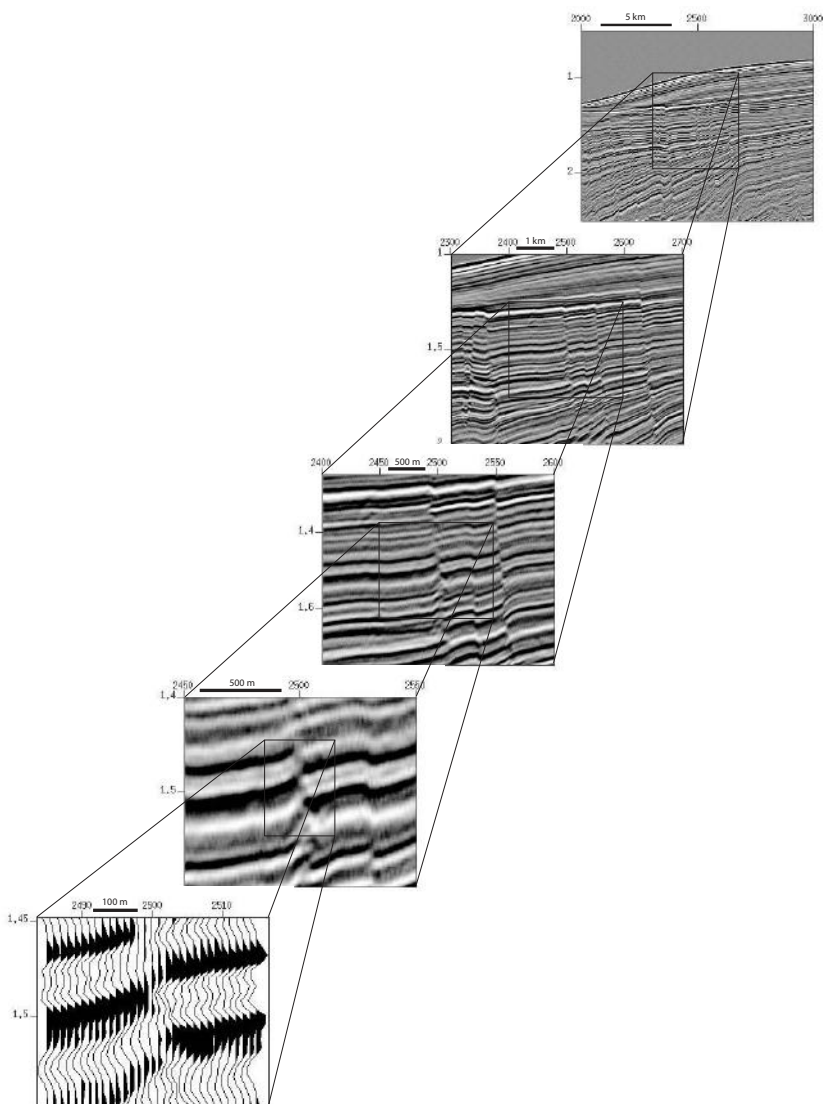


Fig. 1.5 The top image contains the same data as Figure 1.4 and each lower panel is a zoom view of the one up and to the right of it. When the zoom level gets in close enough a wiggle plot is useful to show waveform details. Note horizontal scale bar on each plot.

## Elements of 3D Seismology

at a particular instant in time. The pressure is now a function of  $x$  and will vary between high and low as indicated by shades of gray in Figure 1.6.

The variation may also be plotted as the line graph shown in Figure 1.7. Since the horizontal axis in this plot is distance, the peak-to-peak interval is the wavelength. The deflection of the wave from zero is the amplitude representing an observed physical quantity, in this case pressure. The distance between any two recurring features (peak, trough, downslope zero crossing<sup>1</sup>, etc.) is the wavelength.

Think now of a receiver (i.e., a microphone) fixed in space and measuring the passage of the same sound wave as a function of time. This is the typical case in acoustics and seismology. Figure 1.8 is the time series or trace for this case. Since the horizontal axis is now a time coordinate the peak-to-peak interval is the period of the wave,  $T$ , given in seconds. The frequency associated with this period is

$$f = \frac{1}{T} \quad (1.2)$$

where the units of frequency are Hertz whose dimensions are 1/sec.

These two views of the sound wave (fixed time and fixed space) are connected by the general relationship

$$v = f\lambda \quad (1.3)$$

where  $v$  is wavespeed,  $f$  is frequency, and  $\lambda$  is wavelength. Clearly, we can use this equation to find  $f = v/\lambda$  or  $\lambda = v/f$  as the situation requires.

The waves shown in Figures 1.7 and 1.8 are termed monochromatic, because they contain only one frequency or wavelength. In seismic data, we deal with a wavelet, or wave pulse, which contains many frequencies (Fig. 1.9) and is time-limited, meaning that it exists only for a finite time instead of oscillating forever like a sine wave. Since each frequency has its own period, we speak of the entire waveform as having a dominant period. The dominant frequency and dominant wavelength are then given by  $f_{dom}=1/T_{dom}$  and  $\lambda_{dom}=v/f_{dom}$  respectively. The particular waveform shown in Figure 1.9 is a sinc wavelet whose mathematical expression is

$$\text{sinc}(t, f) = \frac{\sin(2\pi ft)}{2\pi ft} \quad (1.4)$$

where  $f$  is the dominant frequency.

---

<sup>1</sup>This distinction is necessary because the distance between successive zero crossings is actually the half wavelength.

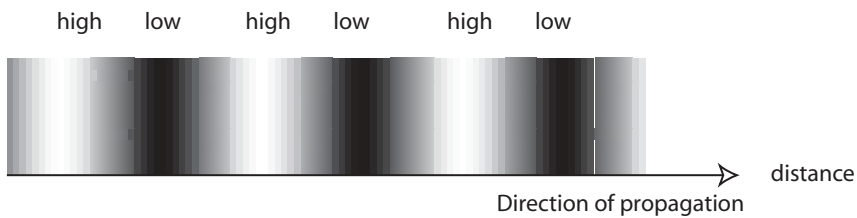


Fig. 1.6 A sound wave moving to the right at fixed time. Gray levels represent pressure.

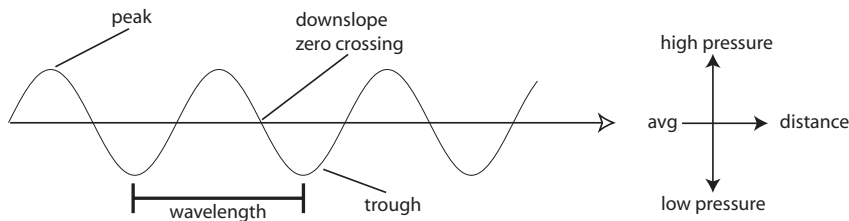


Fig. 1.7 Line graph of the sound wave in Figure 1.6.

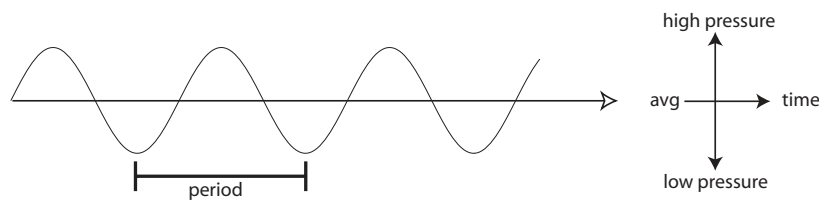


Fig. 1.8 Time trace measured by a fixed receiver.

## Elements of 3D Seismology

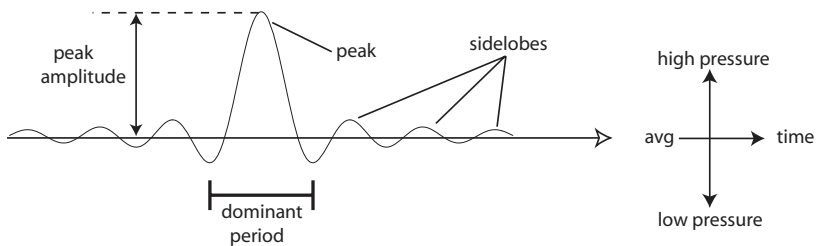


Fig. 1.9 A sinc wavelet contains many frequencies and therefore many periods. It is characterized by its dominant period.

If  $f_1$  and  $f_2$  are the minimum and maximum signal frequencies in a general wavelet, the dominant frequency is the average given by

$$f_{dom} = (f_1 + f_2)/2 \quad (1.5)$$

Another common definition of dominant frequency is the peak of the amplitude spectrum of a window in the seismic data. See appendix A for a discussion of the Fourier transform and associated topics such as the amplitude and phase spectrum. The bandwidth of the wavelet can be described in Hz or octaves

$$\begin{aligned} \text{Hz} &: f_2 - f_1 \\ \text{octaves} &: \ln_2(f_2/f_1) = \frac{\ln(f_2/f_1)}{\ln 2} \end{aligned} \quad (1.6)$$

The octave range is a measure of how dominant the central peak is relative to sidelobes. In order to achieve a strongly peaked waveform, the bandwidth should be at least 2.5 octaves. An easy way to estimate bandwidth in octaves comes from the fact that an octave is the doubling of frequency. For example, consider a 10–90 Hz wavelet. To estimate the octave bandwidth, begin at the lowest frequency and start doubling until the highest frequency is met or exceeded—10, 20, 40, 80, 160. This wavelet has a bandwidth of a little over three octaves as detailed calculation would confirm.

It is instructive to put this in the context of human hearing. The speed of sound in air is about 335 m/s and the range of human hearing is 20–20,000 Hz. This is the range for a healthy, young adult. Children can hear up to 25,000 Hz and most of the energy in speech is in the 300–3000 Hz range.

The octave bandwidth of normal adult hearing is

$$\frac{\ln(20\,000/20)}{\ln 2} = 9.97 \quad (1.7)$$

which is much better than the 2 or 3 we get in typical seismic data. This impressive range allows us to distinguish chirps arriving almost simultaneously and determine the source direction.

The calculations can be done by the reader, but the approximate range of sound wavelengths we can hear go from 17 m down to 2 cm. So what is it about the human body as a sound receiver that has a length scale of 17 m? These low frequency (long wavelength) sounds feel more like a whole-body vibration or buzzing than a true sound. Examples are boom cars (ultrabase stereo), power transformers ( $f=120$  Hz;  $\lambda=3$  m), and the buzz of a bee ( $f=20$  Hz;  $\lambda=17$  m). These sounds are received by the entire body, which on average is 2 m tall. So the lowest frequency that registers with you is one whose wavelength is about eight times your greatest dimension.

Now think about an elephant or a whale and the very low frequencies they must be able to hear. In fact, recent research in South Africa has shown that elephants communicate across great distances using sound that is far below the range of human hearing. Apparently that is the way they all know when to show up at the watering hole.

And what about the short wavelengths? What is there about our hearing apparatus which has a length scale of two centimeters? This is about the size of the small bones of the human inner ear. Small animals can hear much higher frequencies than we do. To cite one example, the big brown bat [168] responds to frequencies up to 100,000 Hz.

## 1.8 Impulse response

The simplest kind of source that can initiate wave propagation acts at one point in space and one point in time. This source is called a spike or delta function,  $\delta(\cdot)$ , and is discussed in appendix A. Such an impulsive point source located in a 3D medium at a point in space  $\underline{x}_0=(x_0, y_0, z_0)$  and acting at time  $t_0$ , symbolically  $\delta(\underline{x}-\underline{x}_0)\delta(t-t_0)$ , generates an outgoing wavefield that is called the impulse response of the medium. The impulse response may be analytic, if the medium is simple and the equations of motion are mathematically solved for the wavefield, or numerical, if the wavefield is simulated by computer.

A numerical impulse response for 2D acoustic waves is shown in Figure 1.10. The velocity model appears in each panel as layers in varying shades of gray, the darker layer colors being higher velocity. The source acted at time zero (not shown)

## Elements of 3D Seismology

at the precise center of the model ( $x,z)=(1250\text{ m}, 1250\text{ m})$ ). This source initiates a wavefield that is shown as a transparent overlay at progressively later times in each panel. So, the wavefield represents the time evolution of the impulse response. To be precise, the source was not actually a pure spike in this case but a waveform much like the one in Figure 1.9. However, considering the scale of the model and short duration of the source pulse, we can consider it a good approximation to the impulse response.

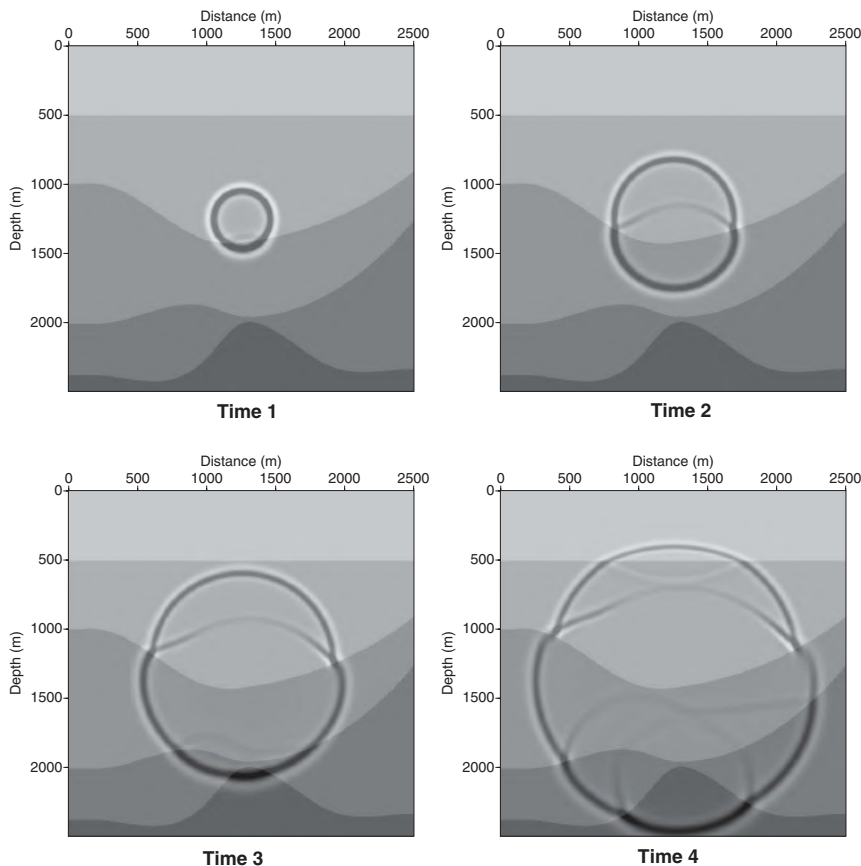


Fig. 1.10 A 2D acoustic wave simulation impulse response. A point source at the center of the model gives rise to a wavefield that propagates outward. The wavefield is shown at four successively later times and the layered velocity model is seen as a transparent overlay with darker shades indicating higher velocity.

The impulse response is a useful concept for modeling, processing, and imaging. In each case, it allows us to isolate the effect of a very simple stimulus before dealing with complicated, real world issues.

## 1.9 Reciprocity

As the wavefield in Figure 1.10 moves across any point in the model, we can imagine a receiver located there, which records its passage. We have a point source generating waves that are recorded by a point receiver. A powerful idea related to this situation is the reciprocity principle that in this case states:

*For any velocity model and source wavelet, the seismic trace recorded at point  $(x_1, y_1)$  due to a point source acting at  $(x_2, y_2)$  is identical to the trace recorded at point  $(x_2, y_2)$  due to a point source acting at  $(x_1, y_1)$ .*

In other words, if we swap the location of the source and receiver, the recorded trace does not change.

Reciprocity is not just a property of 2D acoustic waves, but extends to much more complicated situations [200]. The usefulness of reciprocity is that it forms the basis of many seismic imaging and inversion methods [5], including surface related marine multiple suppression algorithms [71]. In difficult situations, such as extended sources shooting into multicomponent receivers through anisotropic rocks [59], it is also the source of recurring controversy.

## 1.10 Source and receiver directivity

The point source discussed above is an idealization. If such a source did exist in a fluid, then waves generated by it would spread out with uniform strength in all directions. However, any real source has a finite size and does not radiate equally in all directions. This agrees with our common experience concerning sound. When speaking to someone, you face them, partially out of habit and courtesy, but mainly because it is easier for that person to hear what you are saying. Someone behind you might be closer, yet not hear what is being said. From a physics perspective, your voice exhibits a radiation pattern; it is emitting more power in some directions than in others.

Figure 1.11 illustrates this point with 2D waves. The fact is that any physical source used in petroleum seismology, from a marine air gun to a land vibrator, will exhibit 3D source directivity. You can imagine that a source radiation pattern will affect all subsequent evolution of the wavefield. If possible, this directivity will be processed out of the data to avoid interference with other effects that carry more useful information.

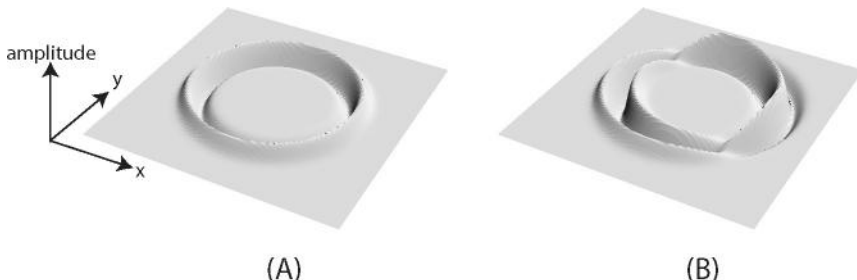


*Fig. 1.11 Snapshots of two wavefields. The source in each case was at the center of the grid. (A) Waves from a symmetric point source are emitted identically in all directions. (B) Actual sources behave more like this simulation. The power and emitted waveform vary with direction from the source forming a radiation pattern.*

Directivity is not just an issue with the source but also the receiver. Our analogy with sound still works here, since the ear is a very directional receiver. What we measure generally depends on the direction the wave is traveling relative to the directivity pattern of the receiver. This effect needs to be understood and removed to preserve accurate amplitude information.

It should be noted that source and receiver directivity are fundamentally different than anisotropy. The effects we have described exist in isotropic media, and more complicated versions would exist in anisotropic media.

### 1.11 Wavefront and rays

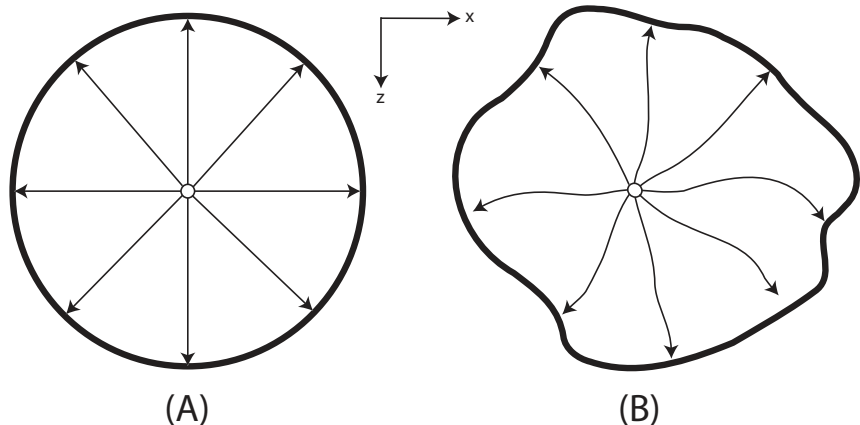
Just as we see the wavefront moving away from a stone tossed into quiet water, we see the wavefront when looking at a wavefield snapshot such as Figure 1.10. Another viewpoint is that the wavefield is characterized by rays, which connect the source point with the wavefront. These are equivalent ways of looking at the situation, and which one we choose depends on the problem being solved.

In the simplest case of a point source in a constant velocity medium, the wavefront is circular (2D) or spherical (3D) and all rays are straight. The rays radiate from the source to land perpendicular on the wavefront as shown in Figure 1.12A.

As the wavefield evolves with time, the rays lengthen and the wavefront moves progressively farther from the source as seen in Figure 1.10. But you will notice that the outermost wavefront in the later snapshots are clearly not circular. When velocity varies from one point to the next, it has the effect of bending the

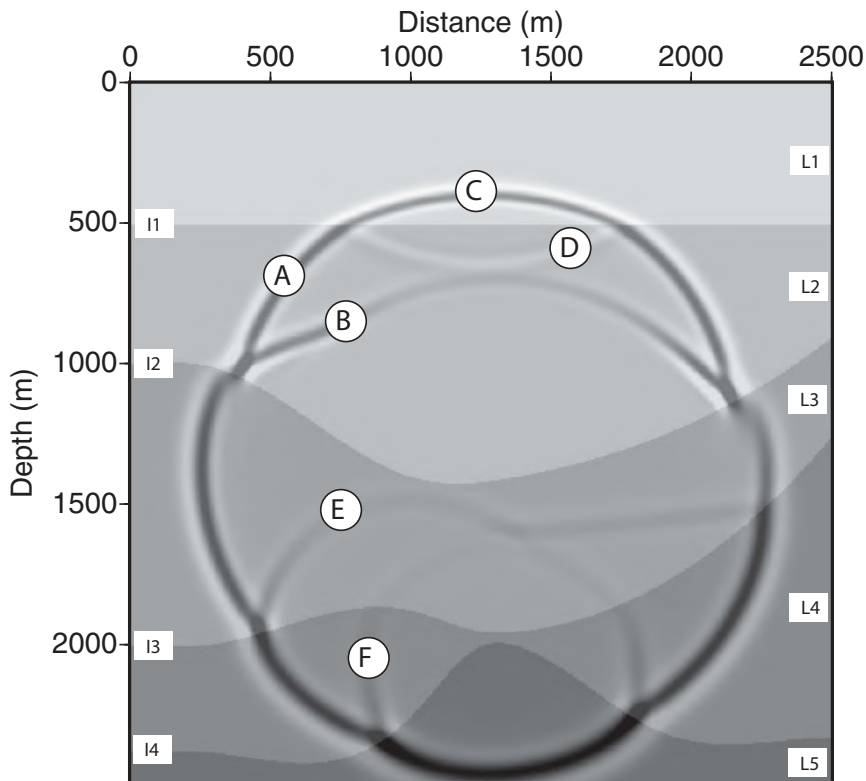
rays and deforming the wavefront. Specifically, the wavefront is pulled into high velocity zones and appears to accelerate away from the source in these regions, while rays bend away from high velocity zones and toward low velocity regions.

Figure 1.12B is a cartoon of this situation. Computing the precise raypaths and wavefront geometry for complex velocity models is a significant problem—one either uses ray theory to find the rays or wave equation methods to find the wavefronts. Figure 1.13 is the rather complicated wavefront of Figure 1.10 (Time 4). It is marked up to show velocity model layers ( $L_1, L_2, \dots$ ), interfaces ( $I_1, I_2, \dots$ ), and some wavefield events, including  $I_1$  downgoing reflection, wave transmitted through  $I_1, I_2$  reflection,  $I_4$  reflection, direct wave in  $L_2$ , and  $I_3$  reflection.



*Fig. 1.12 Rays (arrowhead lines) connect the source point (center circle) with the wavefront (heavy line). (A) In constant velocity media the rays are straight and the wavefront is a circle (2D) or sphere (3D). (B) When velocity varies in the medium, rays bend and wavefronts deform.*

While Figure 1.13 includes wavefield events, such as reflections, for really complicated velocity models just computing direct arrival raypaths is a difficult problem. Figure 1.14 shows first arrival rays [139] for one shot location in the Marmousi model [192], which has been used extensively to test and develop seismic imaging algorithms. The rays in this case are severely bent, cross each other, and leave holes where they have twisted around high velocity regions. Time along each ray increases away from the source and reflection events are not included. The wavefronts could be constructed by connecting the rays at some fixed time. You can



### Acoustic Wavefield Snapshot

Fig. 1.13 Detail of the Time 4 snapshot in Figure 1.10. Velocity model layers and interfaces are labeled as well as some wavefield events.

imagine that the wavefronts would become extremely distorted far from the source. Unless the medium is anisotropic, rays will always be perpendicular to wavefronts.

## 1.12 Huygens' principle

An important concept in wave propagation of any kind was given by Christiaan Huygens in 1678 and published [86] in 1690. It states [21]

*...every point of a wavefront may be considered as a center of a secondary disturbance which gives rise to spherical waves and the wavefront at any later instant may be regarded as the envelope of those wavelets.*

The precise meaning and mathematical details of this principle have occupied minds for centuries [9]. Born and Wolf [21] point out that, taken literally, the principle is incorrect because it would lead immediately to a secondary wavefront propagating back toward the source, as well as the one we observe moving farther

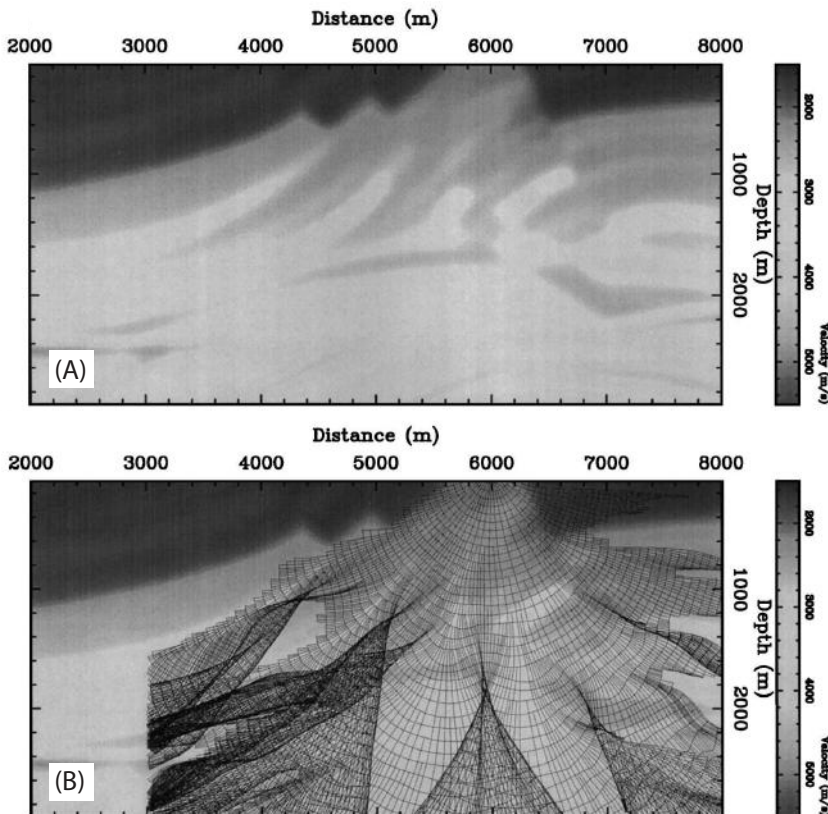


Fig. 1.14 (A) The Marmousi velocity model. (B) Direct arrival ray fan for a source located at 6000 m. Note intense folding of the ray field in response to strong velocity variations in the model. (Modified from [139]).

away as illustrated in Figure 1.15. The principle is saved, if the secondary sources have directivity patterns of such a nature that only the physical wave is generated by their summation [21]. This extended form is called the Huygens-Fresnel principle.

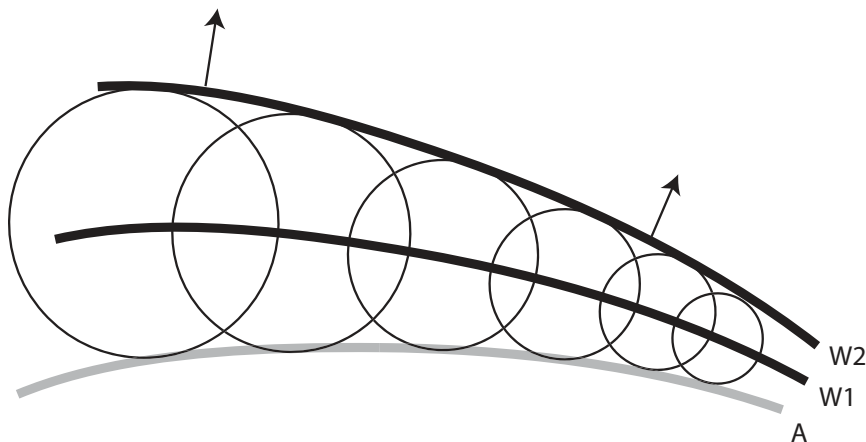


Fig. 1.15 Huygens' Principle. Each point on the upgoing wavefront  $W_1$  at time 1 is considered to be the center of a secondary spherical source (a circle here in 2D). After a small interval of time, each has a radius determined by the velocity at its center, and the envelope of these is the new wavefront  $W_2$  at time 2. The false wavefront  $A$  heading in the wrong direction is eliminated in an extended form of the principle (termed Huygens-Fresnel), where the amplitude emitted by each secondary source is directional.

While this fundamental principle underlies much of seismic wave propagation, its direct use in solving problems is rare [159].

### 1.13 Fermat's principle

We have seen that in variable velocity media wavefronts distort and rays bend. But why is this?

Think about two points in a complicated velocity model and imagine a source at one point shooting a ray into a receiver at the other point. Clearly there are an infinite number of ways to connect these points—a straight line, a parabolic curve, a general curve, etc. Along any path we care to choose, the traveltime can be calculated for each small step along that path by

$$dt = \frac{ds}{v(x, y, z)} \quad (1.8)$$

where  $dt$  is the traveltime over the short interval  $ds$ , and  $v(x, y, z)$  is the velocity in that small interval. The total traveltime along the path from source point ( $p_1$ ) to receiver point ( $p_2$ ) will therefore be

$$t = \int_{p_1}^{p_2} \frac{ds}{v(x, y, z)} \quad (1.9)$$

The problem is that for every path we choose to connect the fixed points ( $p_1, p_2$ ), we get a different traveltime. This is where Fermat's principle comes in. In its original 1662 form, [198] it says, "The actual path between two points taken by a beam of light is the one which is traversed in the least time." This is also called the principle of least time. It leads directly to Snell's law and ray equations [18] for determining raypath geometry in complex media.

It is comforting to know that when the velocity is constant, and the ray is therefore straight (say along the x direction), the equation above gives  $t=x/v$  as it should since time equals distance divided by speed.

## 1.14 Snell's law

In 1621, Willebrord Snell discovered the mathematical rule by which light bends as it passes from one material into another. Snell's law in some form is valid for all waves, but we will develop the idea here in the context of sound waves as this is the simplest case.

We consider two points, ( $p_1, p_2$ ), in a model with two velocities separated by a horizontal interface, Figure 1.16. In drawing (A) one path is shown connecting the points, but an infinite number of such paths could be drawn. A convenient way to distinguish any given path is by the horizontal distance,  $x_1$ , from  $p_1$  to the point where it strikes the interface. For any path, the traveltime between ( $p_1, p_2$ ) will be the sum of the distances traveled in each layer divided by the velocity of that layer,

$$t(x_1) = \frac{L_1(x_1)}{v_1} + \frac{L_2(x_1)}{v_2} \quad (1.10)$$

Armed with Fermat's principle, we know the actual path taken will be the one which takes the least time. As the distance  $x_1$  takes on different values, the intercept

## Elements of 3D Seismology

point moves and the traveltimes changes. Some of these times are longer and some shorter, but there is a unique time that is the smallest of all. This is a classic minimization problem in one variable and the solution is the value of  $x_1$  satisfying

$$\frac{\partial t(x_1)}{\partial x_1} = 0 \quad (1.11)$$

The result of solving this problem is a relationship between the incidence angle,  $\theta_1$ , and the transmission angle,  $\theta_2$ ,

$$\frac{\sin \theta_1}{v_1} = \frac{\sin \theta_2}{v_2} \quad (1.12)$$

as illustrated in Figure 1.16B. The vertical dashed line is termed the normal to the interface (i.e., it is perpendicular to the interface).

It is interesting to note that Aristotle (384–322 BCE) understood this law to be

$$\frac{\theta_1}{v_1} = \frac{\theta_2}{v_2} \quad (1.13)$$

which agrees with Snell's law in the small angle limit as  $\theta_1 \rightarrow 0$ .

When  $v_1 > v_2$  Snell's law says the transmission angle will be less than the incidence angle and the transmitted ray will bend toward the normal, (see Fig. 1.16D). From this case, we know that rays will bend into low velocity regions. If  $v_1 = v_2$ , it follows that  $\theta_1 = \theta_2$ , and the ray does not bend, (see Fig. 1.16C). Not very exciting, but true. Finally, if the velocity increases across the interface,  $v_1 < v_2$ , the transmission angle is greater than the incidence angle, and the transmitted wave bends away from the normal, (see Fig. 1.16B). It follows that rays bend away from high velocity regions.

If the interface is not horizontal, Snell's law still works because it is all relative to the normal to the interface. In fact, the model could be flipped upside down so that the incident wave is coming from below. In any case, we understand medium 1 in the formula refers to the incident side of the interface, and medium 2 is the transmission side. Also, Snell's law clearly extends to the 3D case, where the normal is associated with a plane separating  $v_1$  and  $v_2$ . If the interface is curved, the tangent plane is used. The geometry gets more complicated, but there is nothing fundamentally new. All of these facts conspire to give the complicated raypath behavior seen in large-scale models such as Figure 1.14.

Figure 1.17 shows both reflected and transmitted rays which, taken together, are termed scattered waves. Since both the incident and reflected rays travel with

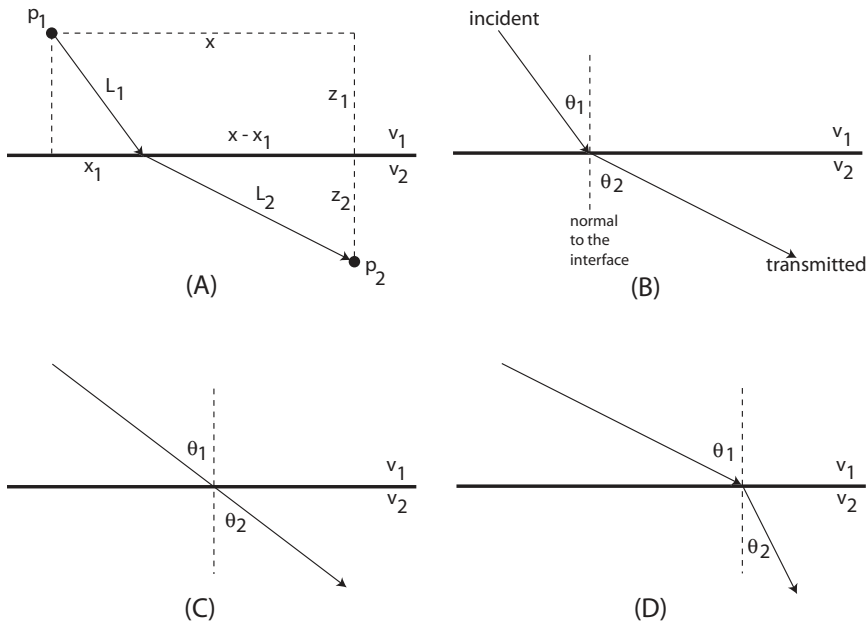


Fig. 1.16 Snell's Law. (A) Geometry of a raypath connecting two points across an interface separating regions of different wavespeed. (B) When  $v_1 < v_2$ , the transmitted wave is bent away from the normal. (C) When  $v_1 = v_2$ , the ray does not bend. (D) For  $v_1 > v_2$ , the ray bends toward the normal.

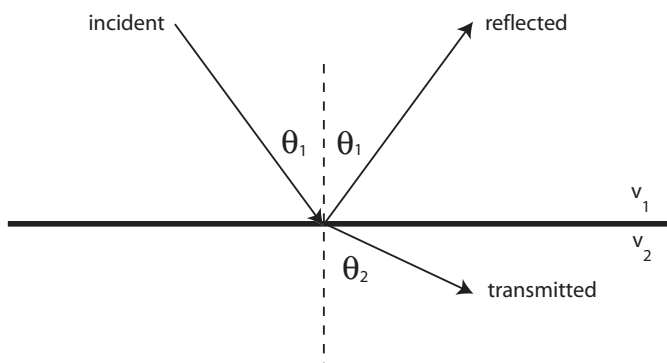


Fig. 1.17 Acoustic reflection and transmission geometry. The reflected and transmitted waves are collectively called scattered waves.

## Elements of 3D Seismology

speed  $v_1$ , Snell's law confirms the angle of incidence equals the angle of reflection. In the case we have been considering, it is assumed that either only one wave type exists, or if others exist, the incident wave does not excite them. More general cases will be dealt with later.

### 1.15 Critical angle

The example in Figure 1.16B shows the transmitted ray bending away from the normal when velocity increases across the interface. At some angle of incidence, this will cause the transmitted ray to run parallel to the interface, and this incidence angle is called the critical angle,  $\theta_c$ . If the transmission angle is 90 degrees, then Snell's law takes the form

$$\frac{\sin \theta_c}{v_1} = \frac{1}{v_2} \quad (1.14)$$

which can be solved for the critical angle

$$\theta_c = \sin^{-1} \left( \frac{v_1}{v_2} \right) \quad ; \quad v_1 < v_2 \quad (1.15)$$

To cite one example, sound waves traveling through air ( $v_1=335$  m/s) and passing into water ( $v_2=1500$  m/s) have a critical angle of about 13 degrees. This means that only sound striking the air-water interface at angles less than 13 degrees will be transmitted into the water.

### 1.16 Dimensional effects

**1.16.1 Waveform.** The real world is 3D, but seismic modeling is often done in 2D to save time and effort. The wavefield snapshots in Figure 1.10, for example, are 2D results. But a 2D point source is actually a 3D line source. In other words, the physics of the situation does not see a single source sitting in a 2D world, but a line of point sources stretching away into the third dimension.

Consider what happens when a 3D impulsive point source explodes in a constant velocity world. It generates a wavefront that spreads out in a spherical shell, and behind the wavefront it quickly goes still, because the source is no longer emitting any waves. This is not the case for a 2D impulsive point source. Behind the wavefront, there is always energy arriving from somewhere along the line source [3]. In effect, we need to add up the contributions from the infinite number of point sources along the  $y$ -axis to find the 2D result.

As a consequence, 3D wave modeling will propagate the actual waveform as emitted by the source, while 2D modeling will propagate the y-integral of the source waveform. The effect of this on an impulse would be the appearance of the spike stretching back toward the source in what is called a square-root-t tail. Figure 1.18 illustrates the significant difference this can represent for a more realistic emitted waveform. When very detailed modeling is used for stratigraphic or rock property investigations, this issue can sneak in and lead to confusion. This effect is sometimes corrected under the name of 2.5D wave equation modeling [110, 112].

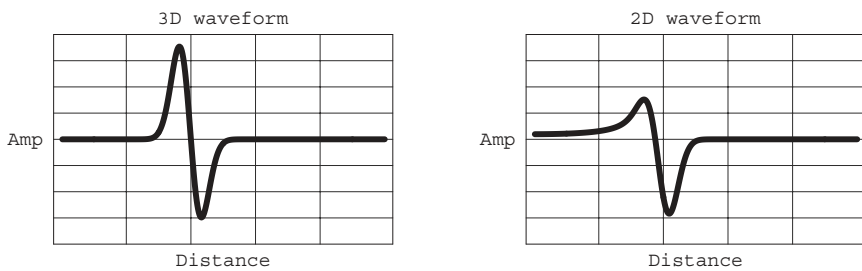


*Fig. 1.18 3D Seismic modeling propagates the actual source waveform while 2D modeling propagates the y-integral of that waveform. This can be confusing when comparing waveforms between modeled data and field data.*

**1.16.2 Energy density and geometric spreading.** A property of any wave is that it gets weaker with distance traveled. There are many reasons for this. Most are related to material properties, but geometric spreading is a general effect that is different for waves propagating in a 2D or a 3D world. Of course, we live and work in a 3D world, but waves associated with surfaces are often confined to those surfaces and thus spread out in 2D. So the 2D case is also relevant to us.

Consider an impulsive point source of waves in an infinite 3D medium. The source injects energy into the material for a brief period of time (say a few ms) then stops. This generates an outgoing wavefront that, if velocity is constant, will be spherical. At some short time after the source acted, all of the energy is concentrated on the surface of a small sphere. For this ideal case, the energy distributed over the sphere at any time represents the total energy injected by the source and is therefore a constant. The total energy,  $E_T$ , divided by the surface area,  $S$ , of the spherical wavefront is the energy density,  $E$ ,

$$E = \frac{E_T}{S} \quad (1.16)$$

## Elements of 3D Seismology

Since the surface area of a sphere is

$$S = 4\pi r^2 \quad (1.17)$$

the energy density as a function of distance,  $r$ , from the source is

$$E = \frac{E_T}{4\pi r^2} \propto \frac{1}{r^2} \quad (1.18)$$

where the last form hides all the constants to isolate the dependence on distance. This equation says that as the wavefield evolves the energy density decreases as  $1/r^2$ .

When we make measurements of sound or seismic waves, the observed quantity is not energy density, but the amplitude of pressure, particle displacement, or some other physical characteristic of the wave. The energy density [177] is proportional to the square of the measured amplitude

$$E(r) \propto A^2(r) \quad (1.19)$$

and it follows that

$$A(r) \propto \sqrt{E(r)} \quad (1.20)$$

Now consider the wavefront at two distances from the source,  $(r_0, r)$ , where  $r_0$  is some small nonzero reference distance. The amplitude ratio between measurements at  $r_0$  and  $r$  is

$$\frac{A_0}{A} = \sqrt{\frac{E_0}{E}} = \sqrt{\frac{r^2}{r_0^2}} = \frac{r}{r_0} \quad (1.21)$$

and solving this for the amplitude at  $r$ ,

$$A = \frac{A_0 r_0}{r} \propto \frac{1}{r} \quad (1.22)$$

This effect is termed either geometrical spreading, spherical spreading, or spherical divergence. The equation tells us that for 3D spherical waves the amplitude decay due solely to geometry is inversely proportional to distance traveled.

As an analogy, consider a bright red balloon. The reason it has such intense color is because the amount of pigment per unit surface area is high, something we can call the pigment density. Now inflate the balloon and notice the color. As the balloon expands, it changes from bright red, to red, to pink, to light pink. This occurs because the amount of red pigment in the balloon is constant, but the surface area is increasing, and therefore the pigment density is decreasing. In the same way, sound waves spreading in 3D become weaker as time progresses, because a fixed amount of energy is distributed over a spherical wavefront of increasing radius.

The wavefront radius depends on the velocity and time as

$$r = vt \quad (1.23)$$

which allows us to conclude

$$A \propto \frac{1}{t} \quad (1.24)$$

The 2D case follows the same line of argument with one essential difference; the energy for a 2D wave is not spread over the surface of a sphere but along the perimeter of a circle. This is because 2D wavefronts are expanding circles like surface waves in water. The analysis for the 2D case leads to geometric amplitude decay of

$$A_{2d} \propto \frac{1}{\sqrt{r}} = \frac{1}{\sqrt{t}} \quad (1.25)$$

The difference between  $1/r$  and  $1/\sqrt{r}$  amplitude decay is significant and grows more significant the farther you are from the source. Figure 1.19 illustrates this difference. In Figure 1.19A, a 2D wavefield is shown at five different times. Velocity is constant and each time corresponds to a circular wavefront progressively farther from the source and the peak amplitudes are seen slowly decaying. The 3D case, Figure 1.19B, is a horizontal slice through the spherical wavefield at the same time/distance values as Figure 1.19A. Note the more rapid loss of amplitude as expected from  $1/r$  decay.

## Elements of 3D Seismology

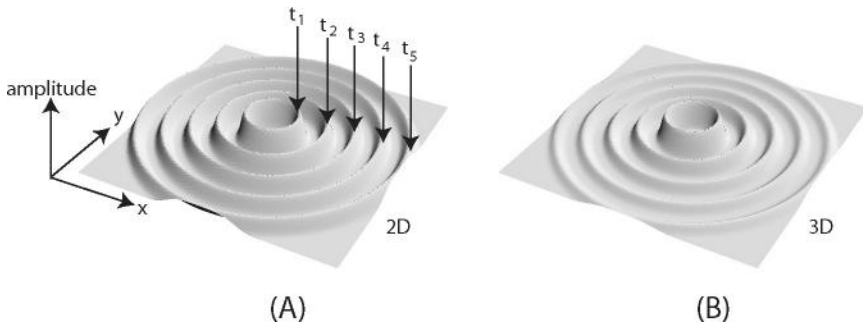


*Fig. 1.19 Geometric spreading. (A) The amplitude of 2D waves decays with distance as circular wavefronts spread out. (B) In 3D, the wavefronts are spherical and decay is more rapid, as seen in this 2D slice through a series of wavefronts.*

To show a numerical example, we need the concept of dB (decibels). This is a logarithmic unit for expressing ratios [165]. If  $D$  is the decimal ratio, then the dB measure is

$$dB = 10 \log_{10}(D) \quad (1.26)$$

which can be inverted to find the decimal ratio when the dB level is known,

$$D = 10^{dB/10} \quad (1.27)$$

Extending a calculation in Telford et al. [177], we consider 3D and 2D wave amplitudes at various distances from a source relative to a reference location,  $r_0$ , of 200 m. The dB loss due to geometrical spreading in 3D,  $L_{3D}$ , is

$$L_{3D} = 10 \log_{10} \left( \frac{A}{A_0} \right) = 10 \log_{10} \left( \frac{r_0}{r} \right) = 10 \log_{10} \left( \frac{200}{r} \right) \quad (1.28)$$

and for 2D the result is

$$L_{2D} = 10 \log_{10} \left( \frac{A}{A_0} \right) = 10 \log_{10} \left( \frac{r_0}{r} \right)^{1/2} = 5 \log_{10} \left( \frac{200}{r} \right) \quad (1.29)$$

Figure 1.20 plots this case in two ways. On the left are curves for 2D and 3D spreading losses as a function of distance from the source. For example, at 1500 m the 3D wave is 20 dB down from the measurement at 200 m. In decimal form, this result says the 3D wave at 1500 m has 1/100th of the amplitude measured 200 m from the source. At the same distance, the 2D wave is only 10 dB down and thus is 1/10th of the 200 m amplitude. In other words, the peak amplitude of the 2D wave at this distance is 10 times that of the 3D wave.

The right graph captures this information in another way by plotting the difference of 3D and 2D spreading loss. At 1500 m this difference is -10 dB showing again that the 2D wave has 10 times the amplitude of the 3D wave. Note that throughout this discussion, it has been assumed the 2D and 3D waves had equal peak amplitude 200 m from the source, an unlikely situation. However, if the peak amplitudes are unequal at the reference distance, they can be normalized, and the results would still hold.

The consequence of our geometric spreading analysis is to realize that 2D waves will decay much more slowly than 3D waves, and this fact is evident in seismic data. Seismic surface waves, which we consider noise, must be actively suppressed, or they will easily overpower weak reflection events which exhibit 3D decay.

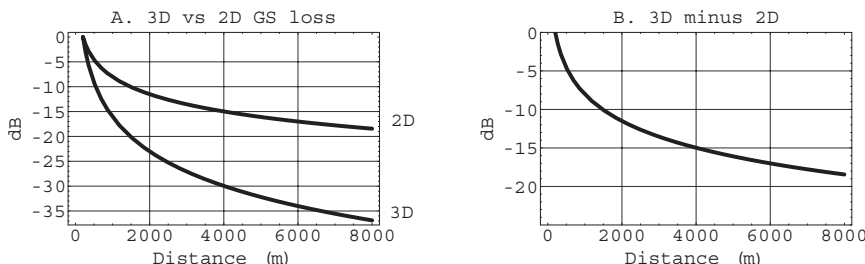


*Fig. 1.20 Geometric spreading. (A) Another way of expressing different decay rates in 2D and 3D is to use decibels (dB). This example shows amplitude spreading losses relative to a reference measurement 200 m from the source. (B) The difference between 3D and 2D geometric spreading loss expressed in dB as a function of distance.*

# 2

## Waves in Fluids

### 2.1 Why fluids?

The physical properties of earth materials controlling mechanical wave propagation are numerous. A short list would include mineralogy, lithology, porosity, pore fluid, fractures, density, and permeability, as well as large-scale structure and stratigraphy. All of these properties can and do vary from point to point in the earth.

To make progress in seismic simulation and processing, a mathematical model is used to approximate wave propagation and understand phenomena. This model can assume the earth is a fluid, a solid, or a porous solid. As with many other topics, we develop the theory of seismic waves in progression from the simplest useful setting to complex models that exhibit most wave effects seen in real data.

We will spend some time and effort to show how mechanical wave propagation in a fluid is characterized by two parameters and a wave equation. Why spend time discussing sound waves in fluids when this book is about seismology and the earth is a solid? One answer is that fluids are an important aspect of seismology—sound waves in air, the ocean, and pore fluids. After all, pore fluids are the prize we seek in applying seismology to petroleum exploration and production.

But another justification comes from seismic data itself, and the way it is manipulated to create images of the subsurface. The vast majority of seismic data simulation and processing assumes we are dealing with acoustic waves, even when the waves are passing through the solid earth. This is because most effects seen in real data can be explained by acoustic wave phenomena. Elastic behavior is included only when it cannot be avoided or yields fundamentally new kinds of information, as in amplitude versus offset (AVO) analysis, anisotropy, or mode conversion.

### 2.2 Parameters

Consider a liquid or gas, which stretches away infinitely in all directions. Two physical parameters are required to characterize this fluid, typically either density and bulk modulus ( $\rho, k$ ) or density and wavespeed ( $\rho, v$ ).

Acoustic media can support only one type of mechanical wave and that is sound. Since this wave can move through all parts of the fluid space, it is a body wave. There are other kinds of acoustic waves associated with a free surface (vacuum/fluid contact) and interfaces (fluid/fluid contact). The surface waves referred to here are not surface gravity waves, the familiar visible surface waves in water. Surface gravity waves exist because of the presence of gravity and are fundamentally different than sound, which would propagate through a fluid in a gravity-free environment.

A sound wave propagates by compressing and decompressing the fluid in such a way that a small volume of material will oscillate in the direction the wave is traveling. As we have seen, *longitudinal wave* is the general term for a mechanical wave whose particle motion is parallel to propagation. Other names for a sound wave are *compressional wave* and rarely, outside of seismology, *P-wave*.

Density has the standard meaning of mass per unit volume and is nearly always expressed in units of grams per cubic centimeter (g/cc). However, in some situations it is useful to express density in kilograms per cubic meter. As a sound wave propagates, the density will necessarily change as the wave compresses and decompresses the fluid. The density characterizing the medium is the undisturbed density that would be measured in the absence of any wave motion. Fluid densities of water (1.0 g/cc) and air (0.0013 g/cc) are only typical values. Accurate density calculations for even pure fluids can be quite complicated.

Wavespeed is the common notion of progress that a wave makes through time, such as the rate at which ripples spread out when a stone is tossed into still water. These surface gravity waves are very slow (about 3 m/s) compared to the unseen sound waves traveling in the water (1500 m/s) and or air (330 m/s). Again, these sound speeds are only typical numbers; precise values are complex functions of pressure, temperature, and other parameters.

Bulk modulus, also called incompressibility, is less familiar than density or wavespeed, but is easily understood from an experimental point of view. Imagine a small sphere of material immersed in a fluid (if the material itself is a fluid, then imagine it is contained in a flexible membrane). When the pressure in the confining fluid is changed, the volume of the sphere will also change. The bulk modulus is defined as the ratio (pressure change)/(volume change) multiplied by the original volume,

$$k = \frac{\Delta p}{\Delta V} V \quad (2.1)$$

An incompressible fluid (i.e., one that cannot be compressed at all) would have  $\Delta V=0$  and thus an infinite bulk modulus. Conversely, a small bulk modulus means the material is very compressible. These concepts work for both fluids and solids. For example, the bulk modulus of steel is about 80 times higher than the value for water showing that steel resists compression much more than water.

The three parameters ( $\rho, v, k$ ) are related through

$$k = \rho v^2 \quad (2.2)$$

which can be used to understand the units and typical numerical values of bulk modulus. For water, we can say that approximately  $\rho=1000 \text{ kg/m}^3$  and  $v=1500 \text{ m/s}$  giving a bulk modulus of  $k=2.25 \cdot 10^9 \text{ kg/(m s}^2)$ . This value would more commonly be given as 2250 mPa, where a megapascal (mPa) is one million pascals (1 pascal =  $1 \text{ kg/(m s}^2)$ ). For air at surface temperature and pressure, we have  $\rho=1.3 \text{ kg/m}^3$  and  $v=335 \text{ m/s}$  for a bulk modulus of  $k=0.15 \text{ mPa}$ . These bulk modulus values indicate that air is about 15 000 times more compressible than water (2250/0.15).

Another way to look at the ( $\rho, v, k$ ) relationship is

$$v = \sqrt{k/\rho} \quad (2.3)$$

This equation says that wavespeed increases when the material is very difficult to compress (large  $k$ ). One can think of such a material as very “springy,” recoiling vigorously when any attempt is made to compress it. This elastic property causes the waves to propagate quickly. On the other hand, the wave must induce vibrations in the material, and this process is impeded by higher density. Thus the wavespeed decreases as the density increases. For any kind of mechanical wave, the velocity will behave in this way, which can be summarized as

$$v = \sqrt{\frac{\text{elastic property}}{\text{inertial property}}} \quad (2.4)$$

where, in the fluid case, the elastic property is bulk modulus. For mechanical waves, the inertial property is always mass density.

## 2.3 Equation of motion

Imagine a ball attached to a very thin wire spring and located somewhere away from the earth's gravitational field. The position of the ball at rest is the zero point. When it is pulled and released, the ball moves vertically (let's say) and possesses two kinds of energy. Ignoring the mass of the spring itself, the kinetic energy at any instant of time depends on the mass,  $m$ , of the ball and its velocity,  $v$ , at that instant,

$$KE = \frac{1}{2} m v^2 \quad (2.5)$$

The potential energy at any instant is due to the mass of the ball, its displacement,  $x$ , from the zero point, and an elastic constant,  $k$ , describing the stiffness of the spring

$$PE = \frac{1}{2} k x^2 \quad (2.6)$$

A powerful way to think about the entire process of the ball starting from an initial displacement (say down), moving upward, passing through the zero point, slowing to a stop, then reversing direction, and so on, is to see it as an interplay of energy. The ball starts out with pure potential energy, which is gradually converted to pure kinetic energy as it passes through the zero point. As it slows down again, moving toward maximum displacement, the energy is then converted back from kinetic to potential.

Sound waves in a fluid also have kinetic and potential energy. We consider the fluid to exist in a three-dimensional world and label these directions

$$\underline{x} = (x_1, x_2, x_3) \quad (2.7)$$

equivalent to  $(x, y, z)$ . The symbol  $\underline{x}$  (a vector) is shorthand for the three-element list.

Consider what happens at a point to a small volume of the fluid as a wave passes. This point will vibrate around its rest position, and if the action were to be frozen, we would see the point has moved from the rest position. In general, the new location is the old location plus a displacement along each of the three axes. We label these displacements

$$\underline{u} = (u_1, u_2, u_3) \quad (2.8)$$

Since these displacements are only nonzero due to existence of the wavefield they are called *field variables*.

As the wave passes, the point moves and the displacements change with time. This motion represents the kinetic energy of the wave given by

$$KE = \frac{\rho}{2} \left( \frac{\partial u_1}{\partial t}^2 + \frac{\partial u_2}{\partial t}^2 + \frac{\partial u_3}{\partial t}^2 \right) \quad (2.9)$$

This expression is the generalization of  $mv^2/2$  to a three-dimensional fluid with density playing the role of mass in the ball-and-spring example.

As the wave passes, energy is transported through the medium, but there is no mass transfer, no net flow of fluid. This means that as the point volume we are considering oscillates around its rest position, it must do so by compressing and decompressing nearby fluid. But the material resists this and will be pushing back. This represents the potential energy of the wave and it is given by

$$PE = \frac{k}{2} \left( \frac{\partial u_1}{\partial x_1} + \frac{\partial u_2}{\partial x_2} + \frac{\partial u_3}{\partial x_3} \right)^2 \quad (2.10)$$

where  $k$  is bulk modulus. In this equation, we see the generalization of potential energy from the ball-and-spring example. The form of this equation shows the central role bulk modulus plays in acoustic wave propagation. The total energy in the wave is constant, but it is continuously being reallocated between kinetic and potential energy. Therefore, the total energy in the wave at any time is given by

$$E = KE + PE \quad (2.11)$$

Aside from the insight the energy equations give about the nature of wave propagation in a fluid, they also lead to a very general method of deriving the equation of motion. There are other ways to find equations of motion such as combining physical laws (Hooke's law + Newton's law) or geometrical analysis from first principles. A powerful advantage of the energy approach is the ability to incorporate multiphysics. For example, the previous discussion tacitly assumed the fluid was stationary except for vibrations induced by passage of the sound waves. But, if the fluid were flowing, this could be accounted for with another term in the kinetic energy equation.

We have also ignored that the fluid is in a gravitational field. But a sound wave propagating in the ocean on earth induces density fluctuations that will be

## Elements of 3D Seismology

associated with changes in gravitational potential energy. This effect could be accounted for by adding a new term in the PE equation [181]. Other possibilities include coupling of electromagnetic and mechanical waves through electrical and magnetic properties of the fluid.

In physics this approach of deriving equations of motion from energy relationships is termed Lagrangian mechanics. We show the steps in some detail for the fluid case because it is the simplest, but the method is general and also leads to equations of motion for elastic solids and porous elastic solids. There is comfort in knowing the approach is powerful enough to handle whatever comes along.

From the energy equations a quantity called the Lagrangian,  $L$ , can be formed from the difference of kinetic and potential energy

$$L = KE - PE \quad (2.12)$$

As the wavefield evolves, there is continuous interchange of kinetic and potential energy and this balance is captured in the Lagrangian function. Notice that  $L$  is a function of four coordinates

$$\text{coordinates : } t, \underline{x} \quad (2.13)$$

three field variables

$$\text{field variables : } u_1(t, \underline{x}), u_2(t, \underline{x}), u_3(t, \underline{x}) \quad (2.14)$$

and two parameters

$$\text{parameters : } k(\underline{x}), \rho(\underline{x}) \quad (2.15)$$

In general, the bulk modulus and density change from point to point and thus represent a model of the fluid through which the waves propagate.

By integrating the Lagrangian over all time and all space, we form what is called the action integral

$$I = \int \int \int \int L \, dt \, dx_1 \, dx_2 \, dx_3 \quad (2.16)$$

This mathematical representation of action was introduced by William Rowan Hamilton in 1833. But it has ancient roots, as Turnbull [185] has noted in writing about the third century Greek mathematician Hero of Alexandria:

*One of his most interesting theorems proves that, when light from an object is broken by reflection on mirrors, the path of the ray between object and eye is a minimum. This is an instance of a principle of least action, which was formally adopted for optics and dynamics by Hamilton in the last century, and which was has been incorporated in the work of Einstein.*

The modern form of this principle says that of all possible motions that could occur, the motion that will actually occur is such that the action as defined here will be a minimum [134]. So the challenge is to find the displacements as a function of space and time, which will minimize the action integral.

This is a problem in the calculus of variations [197], which gives a general recipe for its solution. The idea is that a certain differential equation, called the Euler-Lagrange equation, must hold if the action integral is to be minimized. In other words, the action integral will be a minimum only when the displacements satisfy the Euler-Lagrange differential equation. This equation takes on various forms depending on the number of dependent and independent variables in the function L [4]. For mechanical wave propagation in a three-dimensional world, we have seen the most general case has four independent variables (space coordinates and time) and three dependent variables (the displacements). The Euler-Lagrange equation for this case is

$$\frac{\partial L}{\partial u_i} - \sum_{j=1}^4 \frac{\partial}{\partial x_j} \frac{\partial L}{\partial d_{ij}} = 0 \quad ; \quad i = 1, 2, 3 \quad (2.17)$$

where  $j=4$  is understood to mean time (the fourth coordinate) and where

$$d_{ij} = \frac{\partial u_i}{\partial x_j} \quad (2.18)$$

The alert reader will realize that the Euler-Lagrange equation given here is actually three equations. If the discussion were limited to a two-dimensional world, there would only be two possible displacements and therefore two equations and one equation for a 1D world.

Although it is not easy to see in this condensed notation, if the energy function involves exponents no larger than two, the resulting equations of motion will be linear. However, higher order energy functions are possible, and

## Elements of 3D Seismology

this would lead to nonlinear equations of motion. These give rise to a variety of phenomena not seen in linear acoustics, including shock waves, finite-amplitude waves, interaction of sound with sound, radiation pressure, and streaming cavitation [14]. As already noted, the fundamental characteristic of a nonlinear wave is that its velocity depends on the amplitude of the wave itself. Nonlinear waves are an accelerating area of interest and research in seismology, but linear waves are still the basis of current practice.

When the Lagrangian,  $L$ , given above is inserted into the Euler-Lagrange equation, the result will be the three coupled partial differential equations given earlier. These are the equations of motion in displacement form. However, it is convenient to introduce the pressure defined by

$$p(t, \underline{x}) = -k \left( \frac{\partial u_1}{\partial x_1} + \frac{\partial u_2}{\partial x_2} + \frac{\partial u_3}{\partial x_3} \right) \quad (2.19)$$

which collapses the three equations on displacement to one on pressure

$$\begin{aligned} \sum_{j=1}^3 \frac{\partial}{\partial x_j} \frac{1}{\rho} \frac{\partial p}{\partial x_j} - \frac{1}{k} \frac{\partial^2 p}{\partial t^2} &= 0 \\ \nabla \cdot \left( \frac{1}{\rho} \nabla p \right) - \frac{1}{k} \frac{\partial^2 p}{\partial t^2} &= 0 \end{aligned} \quad (2.20)$$

where the last version is in vector form ( $\nabla \cdot$  = divergence operator,  $\nabla$  = gradient operator). This is the 3D variable density acoustic wave equation on pressure [68]. The familiar form of this equation is found when density is assumed constant

$$\nabla^2 p - \frac{1}{v^2} \frac{\partial^2 p}{\partial t^2} = \rho S \quad (2.21)$$

where the Laplacian operator is defined in Cartesian coordinates by

$$\nabla^2 = \frac{\partial^2}{\partial x_1^2} + \frac{\partial^2}{\partial x_2^2} + \frac{\partial^2}{\partial x_3^2} \quad (2.22)$$

and a general source term,  $S(t, x_1, x_2, x_3)$  has been added on the right side. This acoustic wave equation is valid for arbitrary 3D velocity variations and is the starting point for most seismic compressional wave modeling studies.

## 2.4 The big picture

A conceptual view of our journey toward the equation of motion is given in Figure 2.1. It is important to realize that the physics of a particular problem are completely specified by the kinetic and potential energy functions. Once these are specified and agreed upon, the rest is pure mathematics and not subject for debate. For relatively simple problems like wave propagation in a compressible fluid, there are many other ways to get at the equations of motion. But as the physics of the situation ramps up, the variational approach outlined here becomes increasingly indispensable. A prime example is M. A. Biot's [19, 20] mid-1950s work on wave propagation in porous solids. It is a classic variational formulation and nearly 50 years later is still the foundation of advanced research in this area.

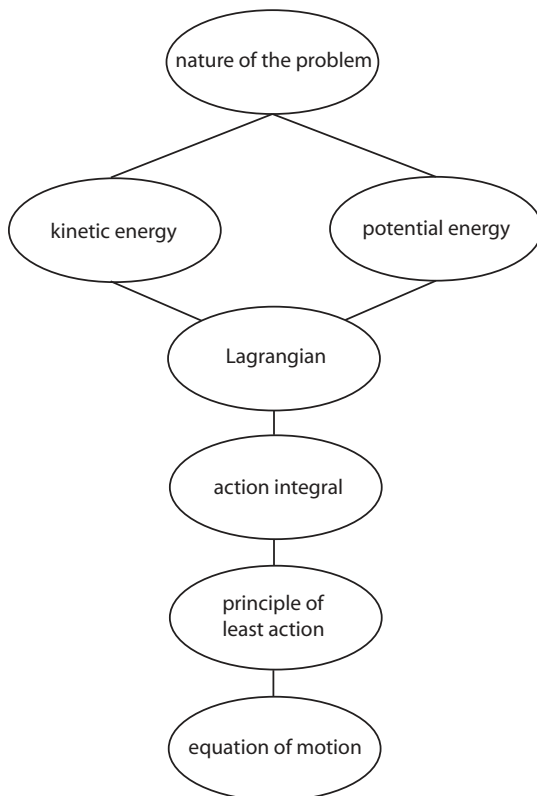


*Fig. 2.1 Conceptual diagram showing the variational approach for deriving equations of motion.*

## Elements of 3D Seismology

The equations of motion have twofold value. First, if parameters representing an earth model are known or assumed, the equation of motion can be solved for the field variables (displacement, pressure), as a function of time and space. This is termed modeling or simulation and is effectively running the equations in the same time direction as the natural phenomena.

Second, if the wavefield is known as a function of time and space, the equation of motion can be inverted to get information about the parameters (velocity and density). This is termed inversion or imaging. If the wavefield were known perfectly for all time and space, it would be possible to accurately compute the velocities and densities. However, seismic data acquisition is always limited to the surface of the earth, the ocean surface, the seafloor, or a few boreholes. This sets fundamental limits on the inversion process, and away from dense well control the best we are able to do is create an image of those locations in the earth where velocity and density change or jump significantly. These are the interfaces that give rise to seismic reflection events and our data processing methods attempt to reconstruct these discontinuities. Figure 2.2 is a summary of these concepts.

## 2.5 Velocity variation

Shown schematically in Figure 2.3 are special cases describing how velocity can vary in the earth. If geology is composed of essentially horizontal layers, then velocity varies only with depth as in Figure 2.3A. This is termed  $v(z)$  media and is a good approximation in some geologic settings.

If the velocity varies with depth and just one horizontal coordinate, then it is  $v(x,z)$  as seen in Figure 2.3B. Geologically this means that we are in an area with a dominant dip direction. There is no loss of generality in considering this to be the  $x$ -direction, since the surface coordinates can always be rotated to align with the dip direction.

The most general case of acoustic velocity variation is  $v(x,y,z)$  shown in Figure 2.3C. If a large enough volume of the earth is considered, this is nearly always the case with the simpler velocity models being only locally valid.

The velocity models shown in Figure 2.3 A-C are layer based or piecewise continuous. But in the earth, conditions such as temperature, pressure, porosity, and lithology change continuously in all directions. Continuous velocity variations are termed velocity gradients and are common to realistic earth models such as Figure 2.3D.

If the gradient is a constant, then the velocity function is termed “linear  $v(z)$ ”. In the linear  $v(z)$  model, the velocity is given by

$$v(z) = v_0 + k z \quad (2.23)$$

where  $v_0$  is the surface velocity,  $k$  is the velocity gradient, and  $z$  is depth. The velocity gradient has units of [m/s]/m or 1/s, which being independent of length units implies that  $k$  is numerically unchanged if velocity is expressed in m/s, km/s, or with any other length unit.

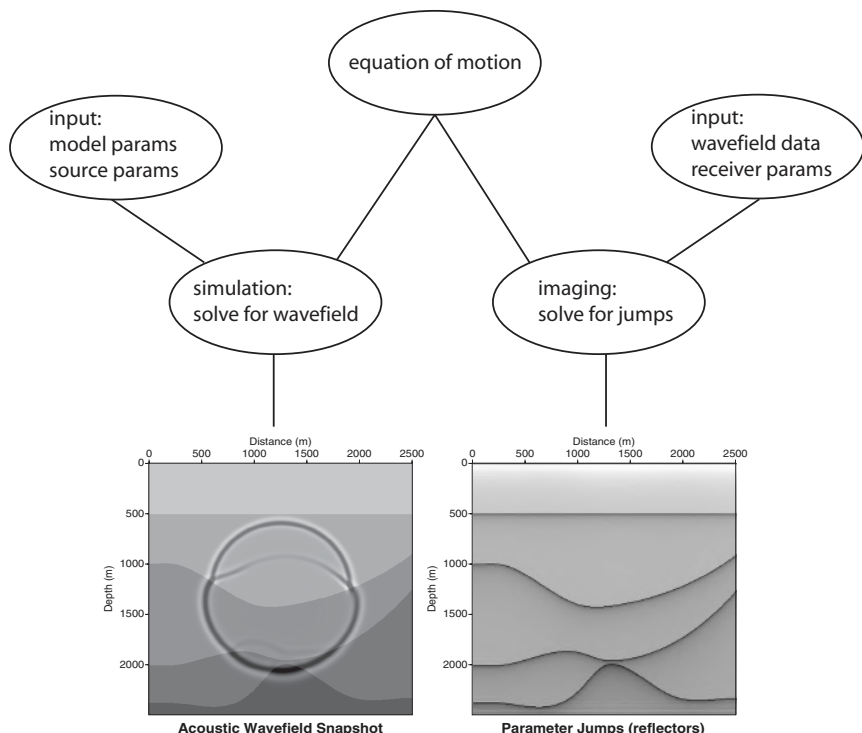


Fig. 2.2 Equations of motion can be solved to simulate wave propagation through an earth model or solved to image jumps in model parameters. The lower left image shows a wavefield frozen in time. The source was at the center of the model, and the velocities are shown as a transparent overlay for reference. The lower right plot is an image of parameter jumps, which correspond to layer boundaries. Because seismic data is only recorded on the surface of the earth, there is insufficient information to directly reconstruct the velocity model itself.

## Elements of 3D Seismology

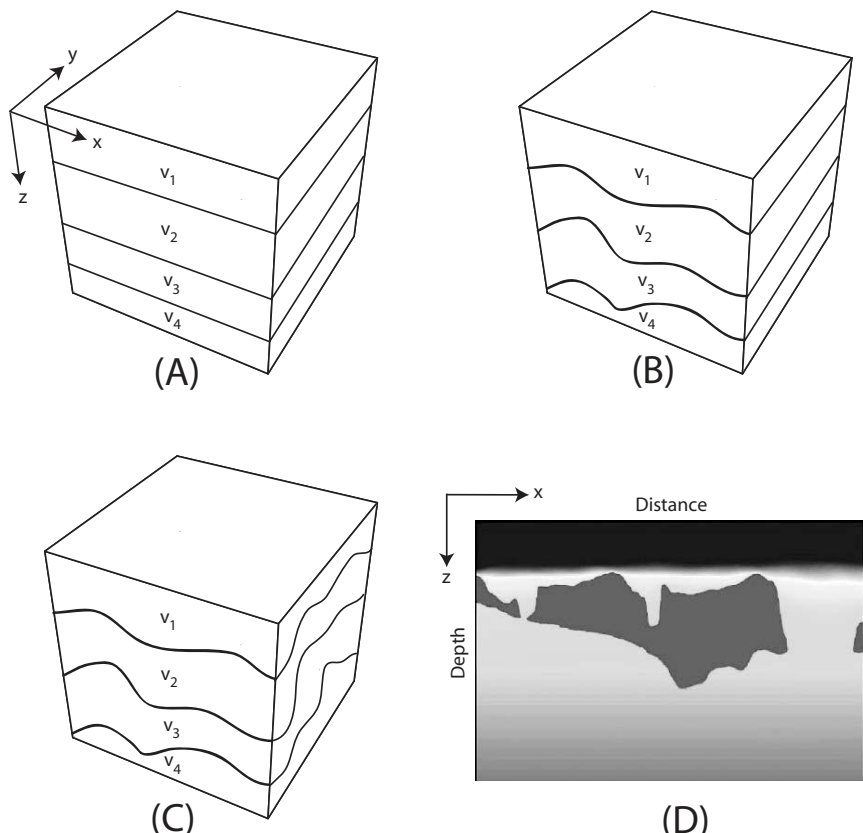


Fig. 2.3 Acoustic velocity model concepts. (A)  $v(z)$ , (B)  $v(x,z)$ , (C)  $v(x,y,z)$ . All of these are layered models which assume velocity is constant in each layer. (D) Continuous  $v(x,z)$  velocity model demonstrating a vertical velocity gradient and a floating salt body ((D) only modified from [70]).

Figure 2.4 shows three representative linear velocity functions. A gradient of 0.4 is often appropriate for soft clastic basins such as the Gulf of Mexico. Linear  $v(z)$  is a useful continuous velocity profile for designing 3D seismic surveys, streamlining certain data processing algorithms, and other applications. For example, Keho et al. [95] use linear  $v(z)$  to represent average velocity from surface for depth conversion and also use linear  $v(z)$  for interval velocity inside a specific formation. This kind of velocity model respects the first order effect of increasing velocity with depth due to increasing pressure and temperature. It also allows the existence of turning waves, which a constant velocity medium does not.

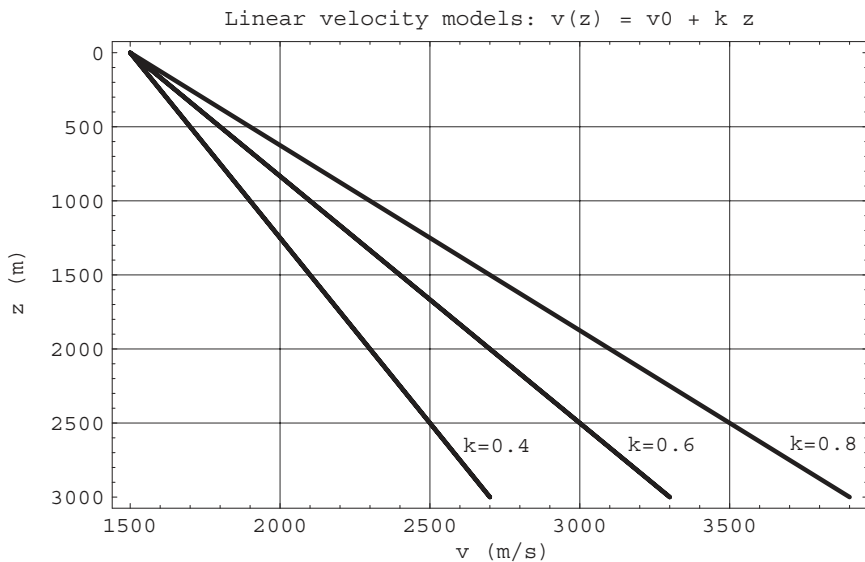


Fig. 2.4 Linear  $v(z)$  models can be useful in seismic survey design, some processing steps, and depth conversion. The parameter  $k$  is the velocity gradient.

## 2.6 What about density?

Velocity variation determines the traveltimes of waves, and thus the velocity model plays a central role in all stages of survey design, processing, and interpretation. By contrast, density only plays a role in traveltimes through Backus averaging, which is not commonly applied. In processing, density is of marginal importance unless true-amplitude inversion work is attempted, again a relatively rare situation. It does affect reflection amplitude through acoustic impedance and thus is important in seismic interpretation.

All this adds up to the fact that it is not common to construct volumetric density models. Of course, the actual density in the earth varies from point to point just as velocity does, and depending on local geology, could be represented by density models analogous to the velocity models described above.

## 2.7 Fine layering

In the discussion so far, we have considered velocity models with thick layers and velocity gradients. While these are both useful views, the reality of velocity in the earth is somewhere between the two. The primary source of direct velocity information is the sonic log, which gives a velocity value at intervals of about 0.3 m along the well bore, which we assume for now is vertical. The velocity

## Elements of 3D Seismology

measured by the sonic log is termed the interval velocity because it represents the sound speed averaged along a short interval of the well bore equal to the source-receiver spacing of 1–2 m. Figure 2.5A shows interval velocities from a sonic log in the Glenpool field of NE Oklahoma.

Sonic velocities almost always show layering on a very fine scale. The distinction between thick and thin layering is a relative one based on seismic wavelength. Since seismic waves have a dominant frequency of about 50 Hz and (for this particular velocity profile) travel through rocks with P-wave speeds of about 3500 m/s, the seismic wavelength is about 70 m. A quick glance at the interval velocity curve confirms that the layering is on a length scale much, much smaller than the wavelength. This kind of fine layering introduces three subtle but important effects. First, the medium becomes anisotropic [178], but this apparent anisotropy is indistinguishable from intrinsic anisotropy of elastic media and will therefore be discussed in relation to waves in solids.

A second effect is apparent attenuation and dispersion, which arise from an infinite coda of multiples, sometimes termed “friendly multiples” [137]. Again, this is indistinguishable from intrinsic attenuation present in porous solids and is discussed elsewhere.

The third effect relates to the velocities themselves. As long-wavelength seismic waves pass through a finely layered medium, the velocities as seen by the seismic waves are different from those seen on the fine scale by sonic logs [178]. Specifically, the seismic waves see an average velocity, and it is this average which plays a role in depth conversion and interpretation.

Two averages in standard use [165] are the root-mean-square average,  $v_{rms}$ , and the time- or depth-weighted average,  $v_{avg}$ . A third important form is the Backus[7] average,  $v_{bac}$ , which is more familiar to theorists than interpreters [178]. The equations describing these averages are

$$\begin{aligned} v_{rms}(j) &= \left( \frac{\sum v_i^2 t_i}{\sum t_i} \right)^{1/2} = \left( \frac{\sum z_i v_i}{\sum (z_i/v_i)} \right)^{1/2} \\ v_{avg}(j) &= \frac{\sum v_i t_i}{\sum t_i} = \frac{\sum z_i}{\sum (z_i/v_i)} \\ v_{bac}(j) &= \left( \frac{\sum z_i^2}{\sum \rho_i z_i \sum (z_i/v_i^2 \rho_i)} \right)^{1/2} \end{aligned} \quad (2.24)$$

In these expressions, the depth levels are mapped onto an integer counter (depth level 1, level 2, etc.), and all sums run from  $i=1$  to  $i=j$ . The interval (sonic) velocity at

the *i*th depth level is  $v_i$ , the density is  $\rho_i$ , the depth at that level is  $z_i$ , and the vertical traveltime to that level is  $t_i$ . All three of these averages are shown in relation to sonic interval velocities in Figure 2.5A and relative to each other in Figure 2.5B.

The use of such average velocity information is primarily in depth conversion. For example, imagine we want to calculate the vertical two-way traveltime from the top of the sonic log at 440 m to a depth of 700 m, a distance of 260 m. The time will be given by

$$t = \frac{2z}{v} \quad (2.25)$$

where  $z$  is the distance and  $v$  is some average velocity. Our three average velocities at the 700 m level are

$$\begin{aligned} v_{rms} &= 3885 \text{ m/s} \\ v_{avg} &= 3828 \\ v_{bac} &= 3775 \end{aligned} \quad (2.26)$$

and the corresponding 2-way times, in milliseconds, are

$$\begin{aligned} t_{rms} &= 587 \text{ ms} \\ t_{avg} &= 596 \\ t_{bac} &= 604 \end{aligned} \quad (2.27)$$

A difference of 20 ms can make or break a subtle structural interpretation. But which traveltime is correct? The Backus average is the correct answer to this problem, but it is often ignored as being unfamiliar, more complicated, and requiring density information.

The Backus average curve shown in Figure 2.5 was computed assuming constant density. Figure 2.6 shows the density log for this well and two Backus average velocity curves, one of which honors the density log, and another that ignores it. Notice that by using the density information, we have moved to yet lower average velocity values. The maximum percentage difference is 0.6%. The lesson here is that Backus averaging without density information is more accurate than either of the more commonly used averages.

Finally, we summarize that in the examples presented here, we find

$$v_{bac}(v_i, \rho_i) < v_{bac}(v_i) < v_{avg}(v_i) < v_{rms}(v_i) \quad (2.28)$$

## Elements of 3D Seismology

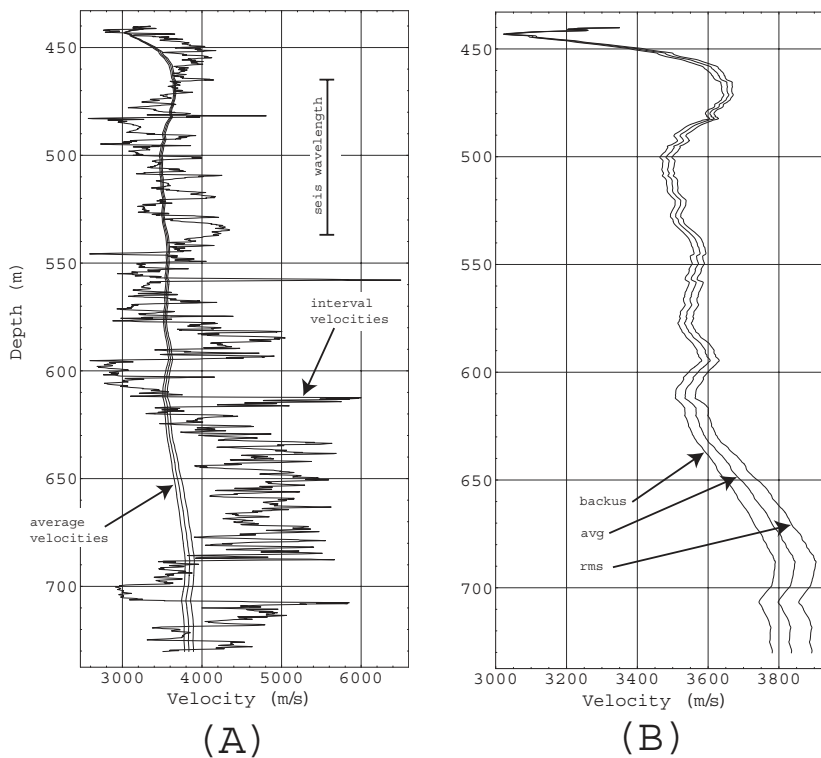


Fig. 2.5 Sonic velocities and three kinds of average velocity.

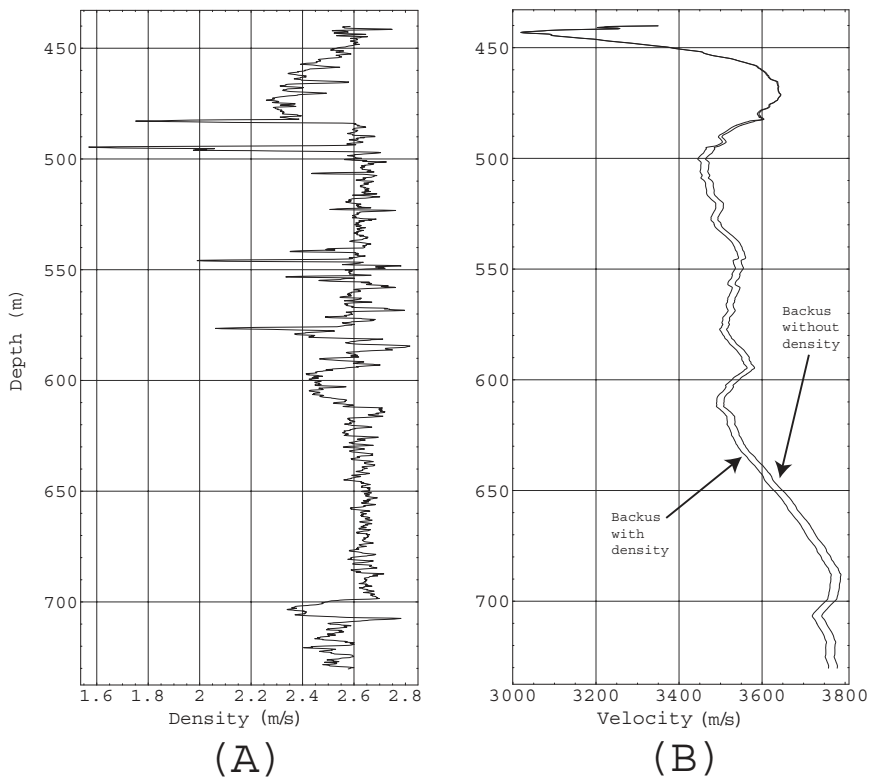


Fig. 2.6 (A) Density values for the well in Figure 2.5. (B) Backus average velocity curves computed with and without density information. The maximum difference is less than 1%.

# 3

## Understanding Seismic Events

The fundamental experiment in reflection seismology is a single source shooting into many receivers resulting in a collection of seismic traces showing certain events. In this chapter, we describe the different kinds of events likely to be seen in field data and attempt to understand them. By “understand,” we mean the ability to recognize events by their traveltimes, amplitude variations, and relationship to related events. Furthermore, we want to understand the subsurface conditions that give rise to these events.

### 3.1 Half space

Consider a source located at the surface of a constant velocity acoustic medium. This could represent an air gun firing in the ocean or be a good approximation for an explosive source on land, if we limit discussion to P-waves only. We will use the term P-wave and sound wave in this chapter without distinction. As shown in Figure 3.1, when the source acts, two wave types will be generated: a sound wave in the air with speed  $v_a$  and a direct P-wave with speed  $v_p$ . The term “direct” is used in relation to the P-waves to distinguish this arrival from reflections, diffractions, etc. A direct surface wave is not included here because that is an elastic effect, not present in the acoustic world under discussion.

Each wave will travel with characteristic speeds determined by physical properties of the media. These are acoustic body waves, which in this case just happen to be traveling along the surface of the earth. Figure 3.2 gives a different representation using wavefronts and rays. As we have seen, the constant velocity assumption implies straight rays and circular wavefronts.

In the real world a single source generates a wavefield that is measured by many receivers. Each receiver generates a seismic trace of ground motion a few seconds long. The entire collection of traces associated with one source is a shot

## Elements of 3D Seismology

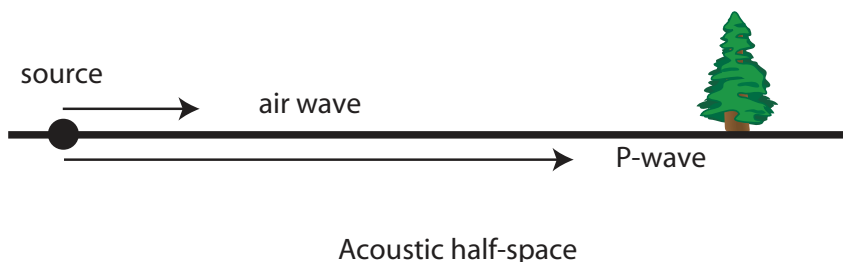


Fig. 3.1 Conceptual drawing of wave types generated by a source at the surface of an acoustic half-space.

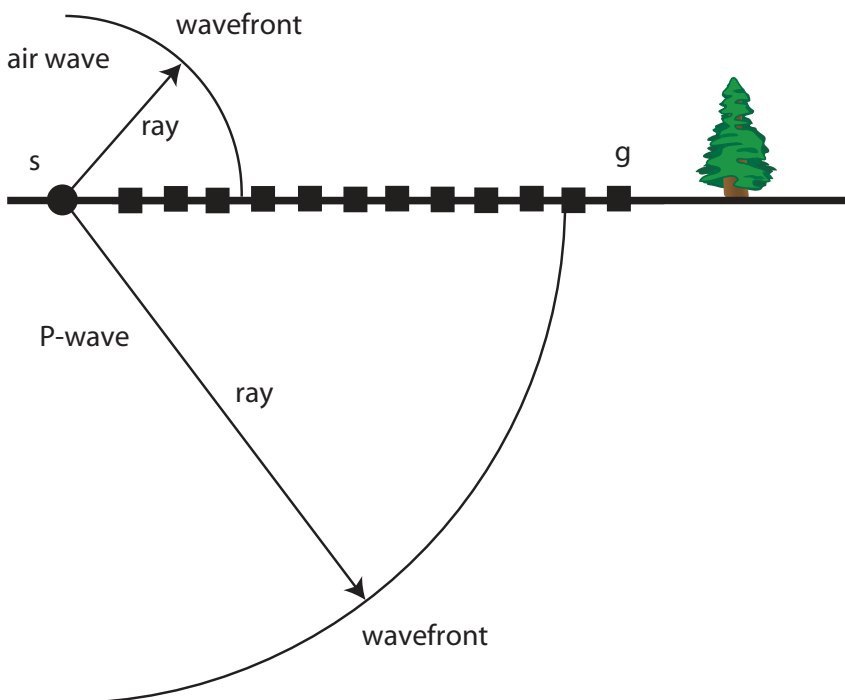


Fig. 3.2 Rays and wavefronts for a source at the surface of an acoustic half-space. The source is at s and each box is a receiver group location.

record (or shot profile, or common shot gather). A shot profile can be either off-end, with receivers all to one side of the source, or split spread, where the source is somewhere in the receiver spread. From these comments, it should be clear that the recording geometry of Figure 3.2 is off-end.

If the receiver spacing is constant along a line that projects back through the source, both waves shown in Figure 3.2 will be linear events on a shot profile. This is often the case in 2D data. Such a direct wave will have an arrival time given by

$$t(x) = \frac{x}{v} \quad (3.1)$$

where  $x$  is the source-receiver distance or offset. Figure 3.3 shows the traveltime geometry of a direct arrival. Using this equation in another way, we can estimate the velocity of any direct wave by laying off a right triangle with a segment of the direct arrival as hypotenuse

$$v = \frac{\Delta x}{\Delta t} \quad (3.2)$$

where examples of  $(\Delta t, \Delta x)$  are shown in the figure. Specifically using the dashed triangles we find for this synthetic example

$$\begin{aligned} v_{air} &= \frac{1000}{3} = 333 \text{ m/s} \\ v_p &= \frac{1000}{0.527} = 1897 \text{ m/s} \end{aligned} \quad (3.3)$$

which are close to the true values of  $v_{air}=335$  and  $v_p=2000$ .

The time slope of a direct arrival with velocity  $v$  is defined by

$$\phi \equiv \frac{\Delta t}{\Delta x} = \frac{1}{v_p} \quad (3.4)$$

which is also called the slowness. This equation says that slow direct waves correspond to steep slopes on a shot profile as confirmed by Figure 3.3. In appendix A, Figure A.7 shows how a linear event in  $(t, x)$  space, such as a direct arrival, maps to a straight line in  $(\omega, k)$  space with slope  $k/\omega=1/v$ .

## Elements of 3D Seismology

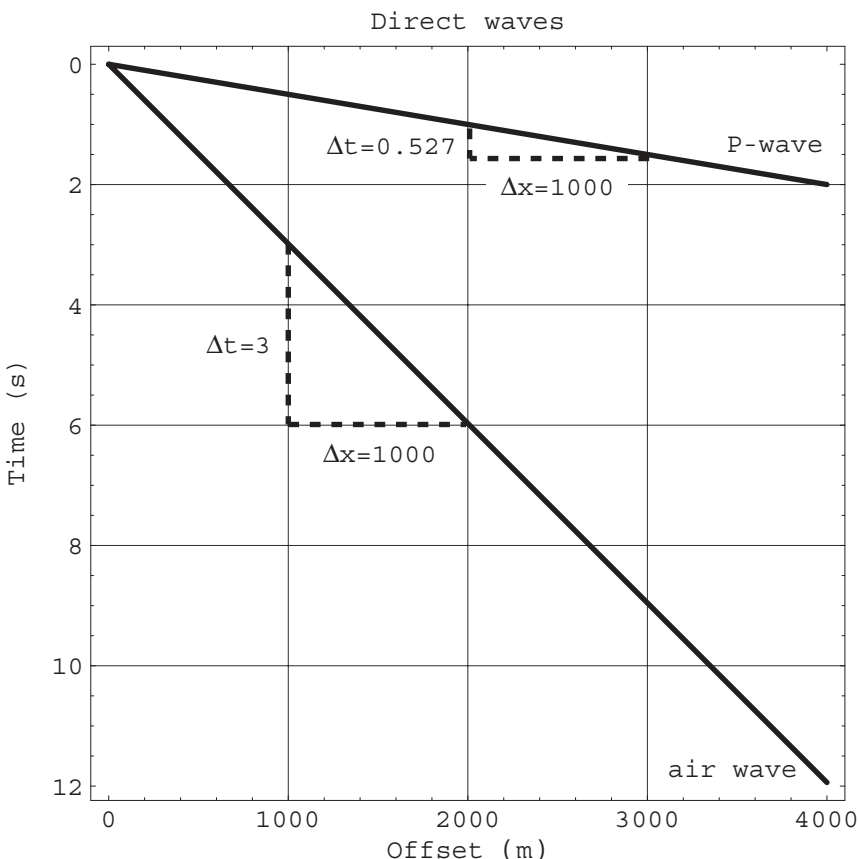


Fig. 3.3 Shot profile sketch showing direct air wave and P-wave arrivals. Time and distance measurements along the dashed lines allow the velocity of each direct arrival to be calculated.

**3.1.1 Uncertainty analysis applied to direct waves.** Why should the estimated direct arrival velocities for this example differ at all from the known values? They differ because the values of  $(\Delta t, \Delta x)$  were read from a plot with some amount of uncertainty. Considering the time scale, the line for each direct event is several milliseconds thick. Similarly, we cannot expect to pick an exact offset associated with an event in this plot. How do these measurement uncertainties affect our estimate of velocity?

---

<sup>1</sup>Obviously, we could draw this graph with a much thinner line and zoom in to get better numbers but that is not the point. The plot as drawn allows us to illustrate this approach to uncertainty analysis.

This question can be answered by using a standard, and very general, error analysis method involving the total differential. If  $g(x_1, x_2, \dots, x_n)$  is a general function of  $x_n$  independent variables, then the total differential of  $g$  is

$$\delta g(x_1, x_2, \dots, x_n) = \frac{\partial g}{\partial x_1} \delta x_1 + \frac{\partial g}{\partial x_2} \delta x_2 + \dots + \frac{\partial g}{\partial x_n} \delta x_n \quad (3.5)$$

where  $\delta x_i$  is the uncertainty in the variable  $x_i$  and the partial derivatives are to be evaluated using the estimated values of all variables.

For the direct arrival velocity equation we have

$$v(t, x) = \frac{x}{t} \quad (3.6)$$

where  $(t, x)$  can be measured from the source or be relative to an arbitrary point on the event. This case has two independent variables  $(t, x)$  and the total differential is

$$\delta v = \frac{1}{t} \delta x - \frac{x}{t^2} \delta t \quad (3.7)$$

Now consider again the air wave arrival of Figure 3.3. The line representing the air wave is about 90 ms thick in the vertical direction<sup>1</sup> and has a horizontal thickness of about 30 m. Using the same time and offset intervals as before, we have

$$\begin{aligned} (t, x) &= (3, 1000) \\ (\delta t, \delta x) &= (\pm 0.9, \pm 30) \end{aligned} \quad (3.8)$$

where the plus-minus symbols acknowledge the fact that our time and offset estimates could be too high or too low. These values give an uncertainty in the air wave velocity of

$$\delta v = \pm \frac{1}{3} 30 \mp \frac{1000}{3^2} .09 = \pm 20 \text{ m/s} \quad (3.9)$$

So our actual air wave velocity estimate is  $v_{air}=333\pm20$  m/s, which is consistent with the correct value of 335 m/s. While we have applied the uncertainty analysis method here to a very simple case, it is general enough to be useful in much more complicated settings.

## 3.2 Reflection

The first extension beyond a simple half-space is the introduction of a single layer. The base of this layer is an interface that will act as a reflector, and receivers at the surface of the earth will observe a reflection event. Notice the distinction between a reflector (an interface in the earth) and a reflection (an event on a seismic record).

**3.2.1 Traveltime.** Traveltime curves are fundamental to any understanding and discrimination of seismic events. We have already seen the traveltimes for a direct arrival on 2D data is linear, but reflections are not. The reflection geometry is shown in Figure 3.4A for a horizontal interface and a single source-receiver pair.

The shot,  $s$ , can be considered to emit rays in all directions including a unique one that strikes the interface at a reflection point,  $R$ , then travels upward to the receiver group,  $g$ . The surface location half way between source and receiver is the midpoint,  $m$ ; the source-receiver distance is the offset,  $x$ . Because the interface is parallel to the earth surface, the take-off angle (relative to the vertical direction) is equal to the incidence angle as measured as in the earlier discussion of Snell's law. The traveltimes as a function of offset,  $t(x)$ , can be determined from the total length of the raypath,  $2L$ , and the layer velocity,  $v$ ,

$$t(x) = \frac{\text{distance}}{\text{speed}} = \frac{2L}{v} = \frac{1}{v} \sqrt{x^2 + 4z^2} \quad (3.10)$$

where  $z$  is the vertical distance from the source to the interface. This can also be written in the form

$$\frac{t^2}{(4z/v)^2} - \frac{x^2}{(2z)^2} = 1 \quad (3.11)$$

which shows that the reflection time is a hyperbolic curve on a  $(t,x)$  plot. The reflection event on a 2D shot profile is thus said to exhibit hyperbolic moveout, also called normal moveout. Moveout is the general term for the time delay associated with any kind of event as offset increases. From the geometry, it is clear that the midpoint is directly above the reflection point for the horizontal reflector.

Figure 3.5 illustrates the traveltimes curves associated with direct waves and a reflection event for a case where the layer velocity is 2000 m/s. In Figure 3.5A, the reflector depth is 500 m, while in Figure 3.5B the reflector is at 1500 m depth. The time associated with the apex of the reflection hyperbola is the zero offset time given by

$$\lim_{x \rightarrow 0} t(x) = \frac{2z}{v} = t_0 \quad (3.12)$$

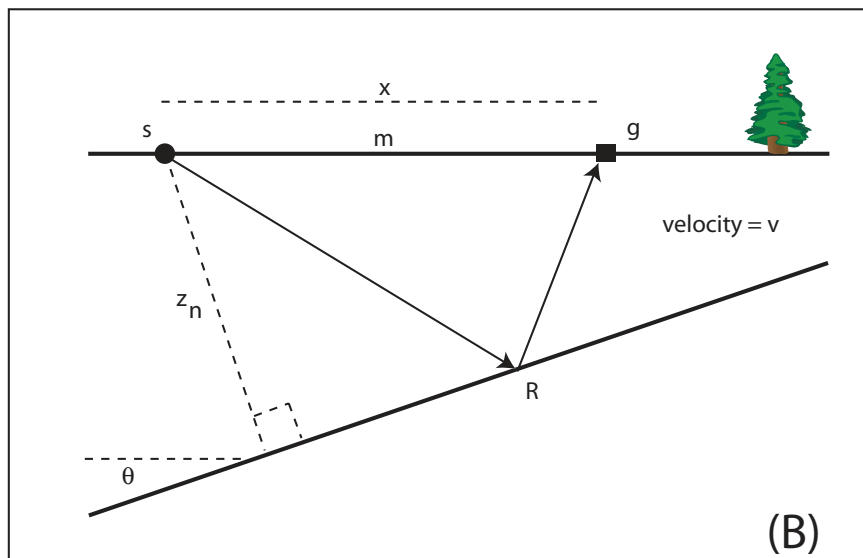
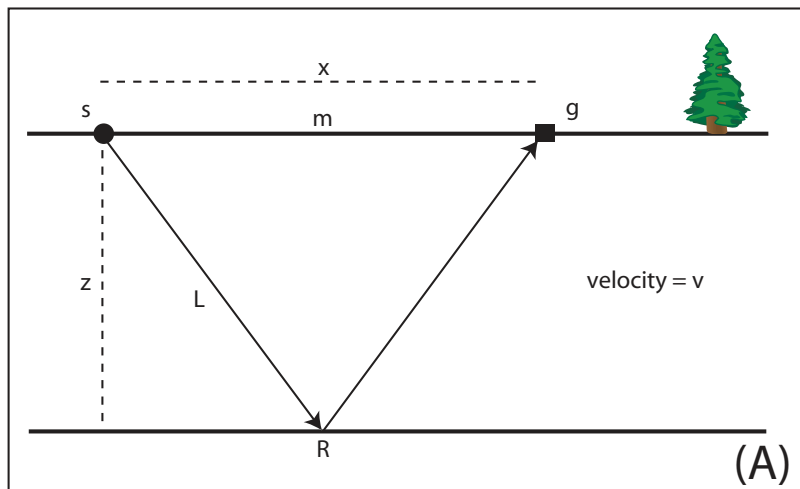


Fig. 3.4 Reflection geometry (A) for a horizontal interface, (B) for a dipping interface. The interface is also called the reflector.

## Elements of 3D Seismology

At large offsets, the direct arrival and reflection are asymptotic as seen in Figure 3.5A. For example, if you think about reflection from an interface a few meters deep as seen by receivers hundreds of meters from the source, it is clear that the difference in traveltimes between the direct arrival and reflection is very nearly zero. Mathematically this follows from taking the limit as offset becomes much greater than reflector depth. In this situation, the reflection arrival time becomes

$$\lim_{x \gg z} t(x) = \frac{x}{v} \sqrt{1 + 4(z/x)^2} \approx \frac{x}{v} \quad (3.13)$$

which is the direct arrival time equation seen earlier.

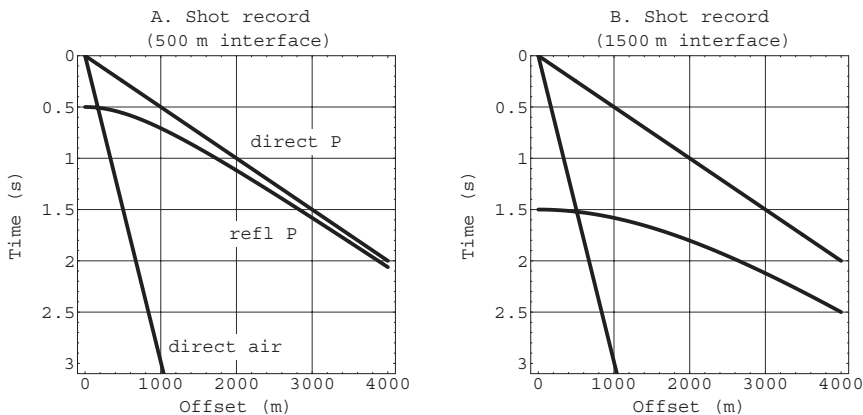
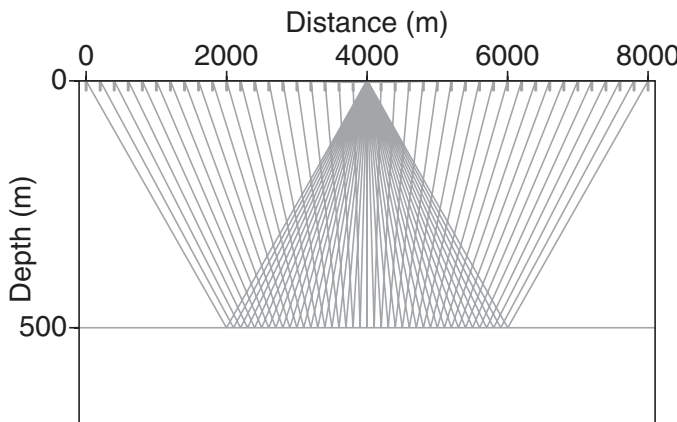
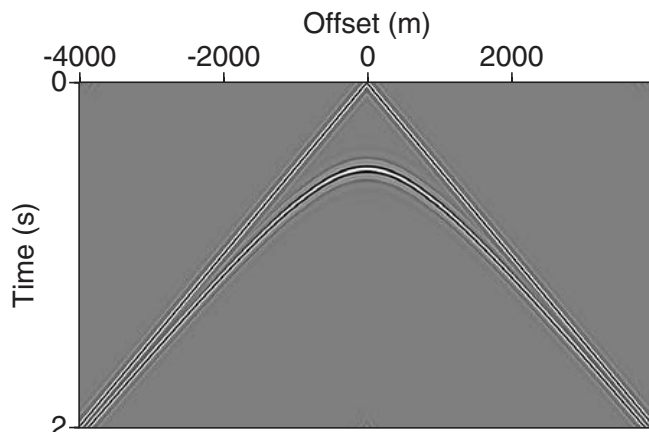


Fig. 3.5 Shot profile sketch showing direct air and P-waves and the reflected P-wave for a horizontal interface such as that shown in Figure 3.4A. The layer velocity is 2000 m/s. (A) 500 m reflector depth, (B) 1500 m reflector.

In Figure 3.6 the raypaths and shot record are shown for a horizontal interface. As before, the layer velocity is 2000 m/s. Notice the axis labels make the important distinction between generic horizontal distance in the raypath plot and offset in the shot record. The use of positive and negative offsets is useful in 2D but is superseded by the concept of azimuth in 3D shooting.



**A. Rays**



**B. Shot record**

Fig. 3.6 (A) Raypaths for a single source shooting into a symmetric spread of receivers over a horizontal reflector. (B) Shot record for this case showing apex of reflection hyperbola at zero offset and asymptotic behavior of reflection and direct P-wave at far offsets.

## Elements of 3D Seismology

For a 2D dipping interface, the reflection travelttime equation becomes

$$t(x) = \frac{1}{v} \sqrt{x^2 + 4z_n^2 - 4xz_n \sin\theta} \quad (3.14)$$

where  $z_n$  is the normal (perpendicular) distance from the shot location to the reflecting interface, and  $\theta$  is geological dip. This equation is sometimes seen with a positive sign on the last term under the square root, but the sign is merely a consequence of how one defines positive dip relative to positive offset.

Figure 3.4B illustrates the geometry of this case, including the fact that the midpoint (a surface coordinate) is no longer directly over the reflection point (a subsurface coordinate). Finding the reflection point requires knowledge of dip and velocity, whereas the midpoint is always known because the source and receiver locations are known. For this reason, many data processing procedures are referenced to the midpoint not the reflection point.

We can recognize dip in a shot record because it has the effect of shifting the reflection apex away from zero offset. Specifically, you can take the derivative of the above travelttime equation with respect to  $x$ , set that to zero, and solve for  $x$ . This gives the offset where travelttime is a minimum

$$x = 2 z_n \sin\theta \quad (3.15)$$

Figure 3.7 shows raypaths and the shot record for a split-spread seismic experiment over an interface dipping at 20 degrees. The first layer velocity is 2000 m/s, and normal distance from the source to the interface is 1500 m. These values lead us to expect the reflection curve to be a minimum at

$$x = 2 (1500) \sin(20^\circ) = 1026 \text{ m} \quad (3.16)$$

which is consistent with the raytracing results. The shape and placement of three reflection events with dips of 0, 10, and 20 degrees are shown in Figure 3.8.

Finally, the travelttime equation for a 3D dipping reflector as seen on a 2D shot profile is

$$t(x) = \frac{1}{v} \sqrt{x^2 + 4z_n^2 - 4xz_n \sin\theta \cos\phi} \quad (3.17)$$

where  $\phi$  is the map-view angle between the dip direction and the source-receiver azimuth. As with the 2D version, this equation has many forms in the literature, some of which differ from the one given here by using the normal distance from the midpoint rather than from the source [103].

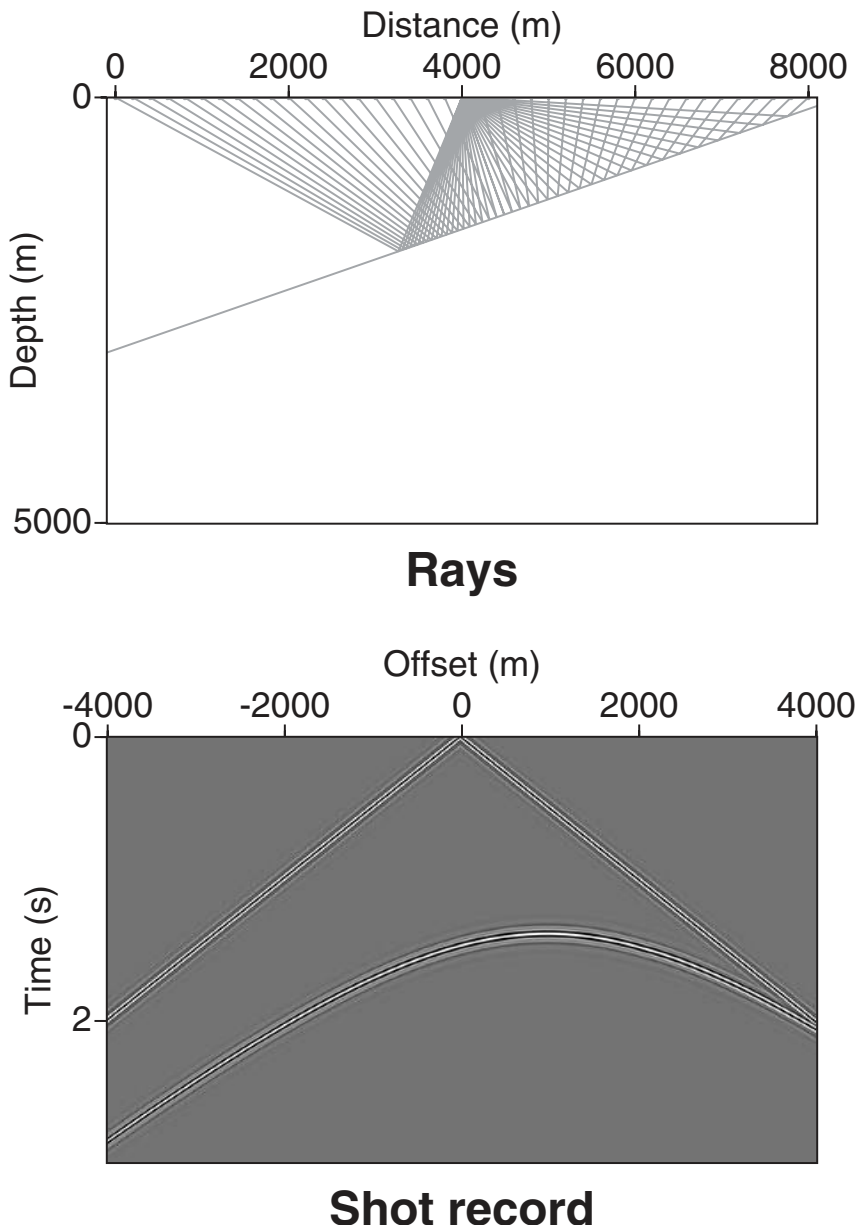
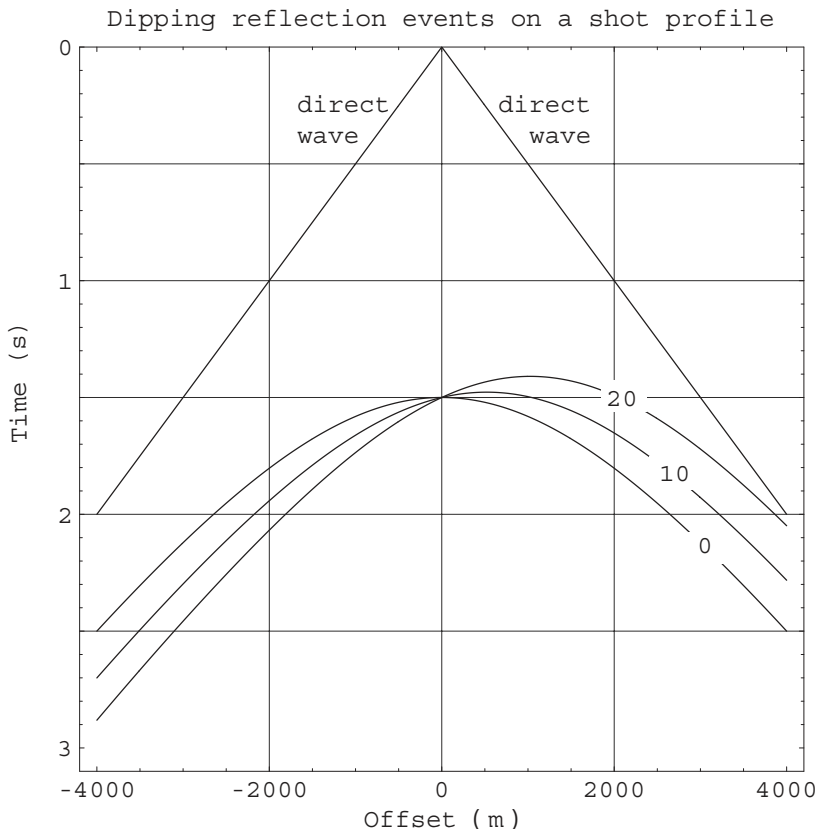


Fig. 3.7 Rays and shot profile for reflection from an interface dipping at 20 degrees. Velocity above the reflector is 2000 m/s and the normal distance from source to the interface is 1500 m. The effect of dip is to move the apex of the reflection event away from zero offset.

## Elements of 3D Seismology



*Fig. 3.8 Sketch of shot profile showing the effect of dip on reflection events. Velocity above the reflector is 2000 m/s and in all cases the normal distance from source to interface is 1500 m. The dip labels are in degrees and the 20 degree curve corresponds to the case in Figure 3.7.*

**3.2.2 Reflection coefficient.** As a wavefront moves through the earth, reflections arise from interfaces separating layers that differ in velocity or density. Specifically the pertinent combination of density and velocity is the acoustic impedance,

$$I = \rho v \quad (3.18)$$

This name comes from an analogy which can be made between 1D seismic simulation and certain kinds of electrical circuits. Note that impedance is a dimensional quantity with metric units of  $\text{kg}/(\text{m}^2 \text{ s})$ .

For a reflected wave, some important components of amplitude behavior are geometric spreading,  $1/r$ , attenuation,  $e^{-\alpha r}$ , and scaling by a reflection coefficient,  $R(\theta)$ , where  $\theta$  is the angle of incidence on the reflecting interface. If the initial amplitude generated by the source along a given ray is  $A_0$ , then the amplitude returned to the surface after reflection is

$$A \rightarrow \frac{A_0 R(\theta) e^{-\alpha r}}{r} \quad (3.19)$$

Most of the desired amplitude information is in the reflection coefficient, and we attempt to compensate for (i.e., remove) the other effects in processing.

**3.2.3 Normal incidence.** Consider an acoustic wave striking an interface in the earth as shown in Figure 3.9. We consider the incident wave to have unit amplitude immediately before striking the interface and assume it strikes at normal incidence. There are two boundary conditions to be satisfied.

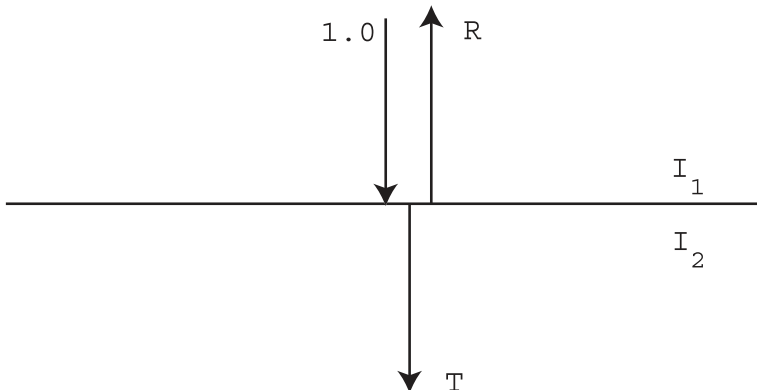


Fig. 3.9 Normal incidence coefficients of reflection,  $R$ , and transmission,  $T$ , are determined by boundary conditions at an interface between regions of different acoustic impedance,  $(I_1, I_2)$

## Elements of 3D Seismology

First, the pressure must be continuous across the interface at all times. The amplitude we measure is proportional to excess pressure induced by the wave; therefore, amplitude must also be continuous. Immediately prior to impact the incident wave amplitude is the total amplitude because scattering has not yet occurred. Just after scattering, the total amplitude is the sum of the reflected and transmitted wave amplitudes. Since the incident wave has unit amplitude, the continuity of pressure condition is

$$1 = R + T \quad (3.20)$$

The second boundary condition is conservation of energy. The energy of an acoustic wave is proportional to acoustic impedance times the square of the amplitude. Immediately before and after impact the energy,  $E$ , is given by

$$E = \begin{cases} I_1, & \text{before} \\ I_1 R^2 + I_2 T^2, & \text{after} \end{cases} \quad (3.21)$$

where we have used the fact that the pre-impact amplitude is one, whose square is also one. Thus the conservation of energy boundary condition leads to the equation

$$\begin{aligned} I_1 &= I_1 R^2 + I_2 T^2 \\ 1 &= R^2 + \frac{I_2}{I_1} T^2 \end{aligned} \quad (3.22)$$

Combining this with the first boundary condition equation yields two equations in two unknowns, which can be solved for the reflection and transmission coefficients

$$\begin{aligned} R_0 &= \frac{I_2 - I_1}{I_2 + I_1} = \frac{\rho_2 v_2 - \rho_1 v_1}{\rho_2 v_2 + \rho_1 v_1} \\ T_0 &= \frac{2I_1}{I_2 + I_1} = \frac{2\rho_1 v_1}{\rho_2 v_2 + \rho_1 v_1} \end{aligned} \quad (3.23)$$

where the subscripted zero signifies normal incidence. In a quantity such as  $I_1$  the subscript is relative to the direction the incident wave is traveling, 1 being the incident medium, and 2 being the transmission medium. It should not be assumed that medium 1 is always above medium 2, since the incident wave could be traveling at an angle, horizontally, or be upgoing.

These are the amplitude scattering coefficients in common use, but a related set of coefficients for energy or displacement can also be derived. We will always deal with amplitude coefficients unless otherwise stated.

There are some things to note about the normal incidence reflection coefficient. (1)  $R_0$  is a dimensionless quantity. This means we get a correct  $R_o$  even if velocities are in ft/s and densities are in g/cc. This drives some people crazy until they figure out it doesn't matter. For consistency we will use metric units here. (2)  $R_0$  depends on velocity and density contrast, and these depend in turn on important rock and fluid properties.

It is fair to say that rock and fluid property information lives in  $R_o$ . (3)  $R_0$  values range from  $-1$  to  $+1$ . (4) It is possible, and not that uncommon, to have  $\rho_1 v_1 = \rho_2 v_2$  even though  $\rho_1 = \rho_2$  and  $v_1 = v_2$ . This condition is called matched impedance and gives  $R_0 = 0$ . In this sense, an interface may be seismically invisible, even though velocities and densities change across it.

The normal incidence reflection coefficient is a powerful, unifying idea in reflection seismology. It is central to generation of synthetic seismograms, forms the basis of seismic amplitude interpretation, has the same form for acoustic and elastic media, and ties seismic data to important rock properties such as porosity and pore fluids.

The basic concepts of normal incidence reflection and transmission are important enough to illustrate with a few examples. Consider a marine seismic case involving four materials—air, water, a hard seafloor, and a soft seafloor. Medium parameters, symbols, and units are given in Table 3.1.

	Seafloor			
	Air	Water	Soft	Hard
Density ( $kg/m^3$ )	$\rho_a = 1.3$	$\rho_w = 1000$	$\rho_s = 2000$	$\rho_h = 2200$
velocity ( $m/s$ )	$v_a = 335$	$v_w = 1500$	$v_s = 2000$	$v_h = 3200$
Impedance ( $kg/(m^2 s)$ )	$I_a = 435.5$	$I_w = 1.5 \times 10^6$	$I_s = 4 \times 10^6$	$I_h = 7 \times 10^6$

Table 3.1 Representative parameters for marine seismic examples of normal incidence reflection and transmission.

## Elements of 3D Seismology

Consider first a wave in water striking a soft seafloor. The scattering coefficients will be

$$\begin{aligned} R_0 &= \frac{I_s - I_w}{I_s + I_w} = \frac{4 \times 10^6 - 1.5 \times 10^6}{4 \times 10^6 + 1.5 \times 10^6} = 0.45 \\ T_0 &= \frac{2I_w}{I_s + I_w} = \frac{2(1.5 \times 10^6)}{4 \times 10^6 + 1.5 \times 10^6} = 0.55 \end{aligned} \quad (3.24)$$

We see from this calculation that the continuity condition,  $1=R_0+T_0$ , is satisfied. We can also calculate how the energy has been partitioned among the reflected and transmitted wave,

$$\begin{aligned} E_R &= R_0^2 = 0.2 \\ E_T &= \frac{I_2}{I_1} T_0^2 = \frac{I_s}{I_w} T_0^2 = 0.8 \end{aligned} \quad (3.25)$$

This says that 80% of the incident energy has been transmitted through the seafloor to go on its way probing the earth, while 20% of the energy has been reflected back into the water column. This soft seafloor scenario is close to what happens in areas like the Gulf of Mexico, offshore west Africa, and other places in the world where silt and sand are currently being deposited on the ocean floor.

If the ocean floor is limestone or igneous rock, then our hard seafloor parameters are closer to reality. In this case we find

$$\begin{aligned} R_0 &= \frac{I_h - I_w}{I_h + I_w} = 0.65 \\ T_0 &= \frac{2I_w}{I_h + I_w} = 0.35 \\ E_R &= R_0^2 = 0.42 \\ E_T &= \frac{I_h}{I_w} T_0^2 = 0.58 \end{aligned} \quad (3.26)$$

This reflection coefficient is on the high end of those likely to be seen in routine seismic work. Only 58% of the incident energy makes it through the seafloor to be available for use in mapping the deeper subsurface. Considering a marine seismic crew costs over one million dollars per month, this is very expensive energy that bounces back from the seafloor.

What happens to that energy? It travels upward to the surface of the ocean. Since the wave is incident from below, medium 1 in this reflection problem is the water, and medium 2 is the air. The scattering quantities for this case are

$$\begin{aligned}
 R_0 &= \frac{I_a - I_w}{I_a + I_w} = -1 \\
 T_0 &= \frac{2I_w}{I_a + I_w} = 2 \\
 E_R &= 1 \\
 E_T &= \frac{I_a}{I_w} T_0^2 = 0
 \end{aligned} \tag{3.27}$$

where the values have been rounded off, but the first departure from the numbers shown is in the fifth or sixth decimal place. These results indicate the waves are reflected back down into the water at full strength, and virtually no energy propagates into the air (The transmission coefficient might be 2, but there is so little energy that a sensitive device just above the water would not detect the wave). The minus sign on the reflection coefficient means the reflected wavelet has reverse polarity relative to the incident wave.

Figure 3.10 shows the meaning of this phrase. The process of strong reflection from a hard seafloor, complete reflection with polarity reversal from the sea surface, and seafloor reflection again, is the origin of seafloor multiples that can be a serious problem in marine seismic data [140].

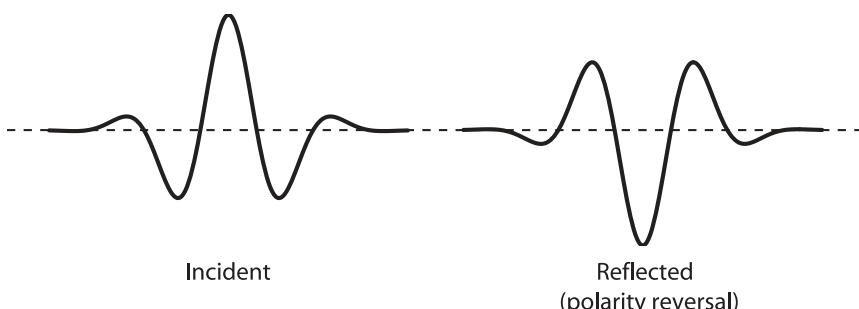


*Fig. 3.10 When an upgoing acoustic wave in water strikes the water/air surface, the reflection coefficient is  $-1$ . This means the reflected wave is unchanged, except that polarity is reversed relative to the incident wave. The horizontal axis is time increasing to the right.*

## Elements of 3D Seismology

**3.2.4 Angular reflection coefficient.** From Snell's law, we know the relationship between incidence, reflection, and transmission angles when a ray hits an interface at non-normal incidence. As with the normal incidence case, the boundary conditions lead to reflection and transmission coefficients, which are now a function of the incidence angle. The mathematical form and complexity of the angular reflection coefficient depend on the kind of media in contact, fluid-fluid, fluid-solid, free surface on fluid, etc.

The fluid-fluid angular reflection coefficient is given by

$$R(\theta) = \frac{I_2 \cos \theta - I_1 \sqrt{1 - \left(\frac{v_2 \sin \theta}{v_1}\right)^2}}{I_2 \cos \theta + I_1 \sqrt{1 - \left(\frac{v_2 \sin \theta}{v_1}\right)^2}} \quad (3.28)$$

where  $\theta$  is the angle of incidence. In the limit as the incidence angle approaches zero,  $\cos \theta=1$  and  $\sin \theta=0$ , and the angular acoustic reflection coefficient reduces to

$$\begin{aligned} \lim_{\theta \rightarrow 0} R(\theta) &= \frac{I_2 - I_1}{I_2 + I_1} \\ &= R_0 \end{aligned} \quad (3.29)$$

which is the zero-offset reflection coefficient derived earlier.

The behavior of  $R(\theta)$  for  $I_2 > I_1$  is shown in Figure 3.11. In both cases the impedance decreases across the interface, and in such cases the reflection coefficient can be expected to smoothly progress from the normal incidence reflection coefficient to near  $-1.0$  at 90 degrees. As with  $R_0$ , the effect of  $R(\theta)$  is to act as a multiplier on the incident wave.

Figure 3.11A shows a case with significant decrease in impedance. The waveform plots below the graph show the unit amplitude incident waveform (labeled "inc") and the result of scaling this waveform by  $R(\theta)$  for five values of incidence angle between 0 and 80 degrees. A case with less impedance contrast, Figure 3.11B, shows correspondingly less variation in reflection coefficient with incidence angle. In fact, the reflection amplitude is virtually unchanged until the incidence angle is near 60 degrees. The amplitude variation in Figure 3.11 would be difficult to detect on real traces, because the range of incidence angles likely to be encountered in field data is about 0–30 degrees.

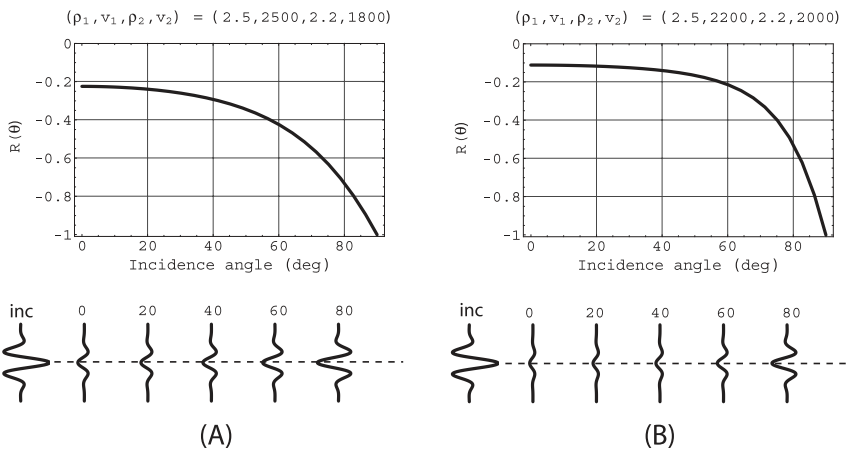


Figure 3.11 Angular acoustic reflection coefficient behavior as a function of incidence angle. In both cases velocity and density decrease across the interface. The incident waveform is labeled “inc,” and the other waveforms are the result of scaling by  $R(\theta)$  at the labeled incidence angles.

**3.2.5 Postcritical reflection.** The appearance of a square root in the angular reflection coefficient introduces the possibility of  $R(\theta)$  becoming complex. From the previous discussion of Snell’s law, we have already noted the existence of a critical angle given by

$$\theta_c = \sin^{-1} \left( \frac{v_1}{v_2} \right) \quad ; \quad v_1 < v_2 \quad (3.30)$$

Substituting this value of incidence angle into the square root term of  $R(\theta)$  gives

$$\sqrt{1 - \left( \frac{v_2 \sin \theta_c}{v_1} \right)^2} = \sqrt{1 - \left( \frac{v_2 (v_1/v_2)}{v_1} \right)^2} = 0 \quad (3.31)$$

For incident angle values less than critical, the quantity under the square root will be positive, at critical angle, it is zero, and beyond critical, it is negative. Once the square root argument goes negative, the reflection coefficient becomes a complex number.

## Elements of 3D Seismology

In Figure 3.12, we see a series of plots describing the reflection coefficient for a hard interface; in this case the velocity increases across the interface by about 40%. The parameters on either side of the interface are shown in the figure and the critical angle is 46 degrees. The region where incidence angle is less than critical is termed precritical, and those angles beyond  $\theta_c$  are postcritical or wide angle. Notice that the amplitude is 1.0 at critical angle and beyond. If the reflection coefficient is 1.0 then the transmission coefficient must be zero, since the boundary condition on amplitude at any incident angle is  $1=R(\theta)+T(\theta)$ . This means there is no amplitude, and therefore no energy, being transmitted into medium 2. This is a case of total internal reflection.

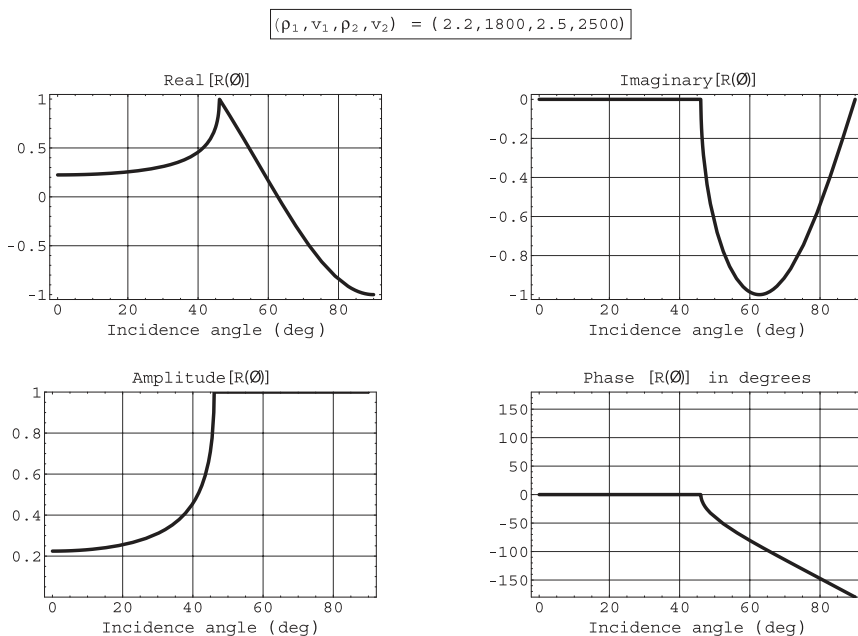


Figure 3.12 When velocity increases across the interface a critical angle is introduced (46 degrees in this example). For incident angles beyond critical, the reflection coefficient is a complex number, which can be represented in terms of real and imaginary parts or amplitude and phase.

A complex reflection coefficient when applied to the incident wave will introduce a phase shift,  $\theta_p$ , in the reflected wave given by

$$\theta_p = \tan^{-1} \left( \frac{\text{Im}[R(\theta)]}{\text{Re}[R(\theta)]} \right) \quad (3.32)$$

where  $(\text{Re}[ ], \text{Im}[ ])$  denote the real and imaginary parts, respectively. As shown in Figure 3.13, the phase shift has the effect of actually changing the waveform, not just scaling the peak amplitude up or down as a precritical reflection coefficient does. This is undesirable because this kind of waveform change could also represent interference patterns from a thin bed or other geological effects. This is one of several reasons that petroleum seismic data is usually acquired in such a way that reflections from horizons of interest are in the precritical region, even at the farthest offset in the data.

**3.2.6 Fresnel zone.** Most of the time we can get away with thinking about rays and reflection points. But a fundamental concept in seismology is that reflection does not actually arise from a single point on a reflector. It arises from an area called the Fresnel zone [106], which is also the lateral resolution limit of seismic data. By this we mean that two closely spaced objects in the subsurface, which fall inside the Fresnel zone, cannot be individually distinguished. This lateral resolution limit applies to unmigrated seismic data.

Think of the high frequencies in our data as being like a golf ball. Paint it red and bounce it off a clean sidewalk. How big is the paint mark? This is like the Fresnel zone. The ball bounced from a small area that is now red. Now consider the low frequencies in our data to be like a beach ball. Paint it blue, bounce it, and look at the spot it leaves. It is a big spot, because it interacted with a large area during the reflection process. The Fresnel zone for low frequency data can be very large.

Figure 3.14 shows a ray traveling down and back to a horizontal reflector. The symbol  $s/g$  is a coincident source and receiver location, and two wavefronts from the source are shown. In addition to the normal incidence (vertical) raypath, as the wavefront interacts with the reflecting surface, there are other rays not quite vertical,  $L$ , which constructively interfere with the normal ray to generate the total response. These rays do not obey Snell's law of reflection and carry progressively less amplitude as they deviate from the Snell path. They are termed nonspecular rays.

## Elements of 3D Seismology

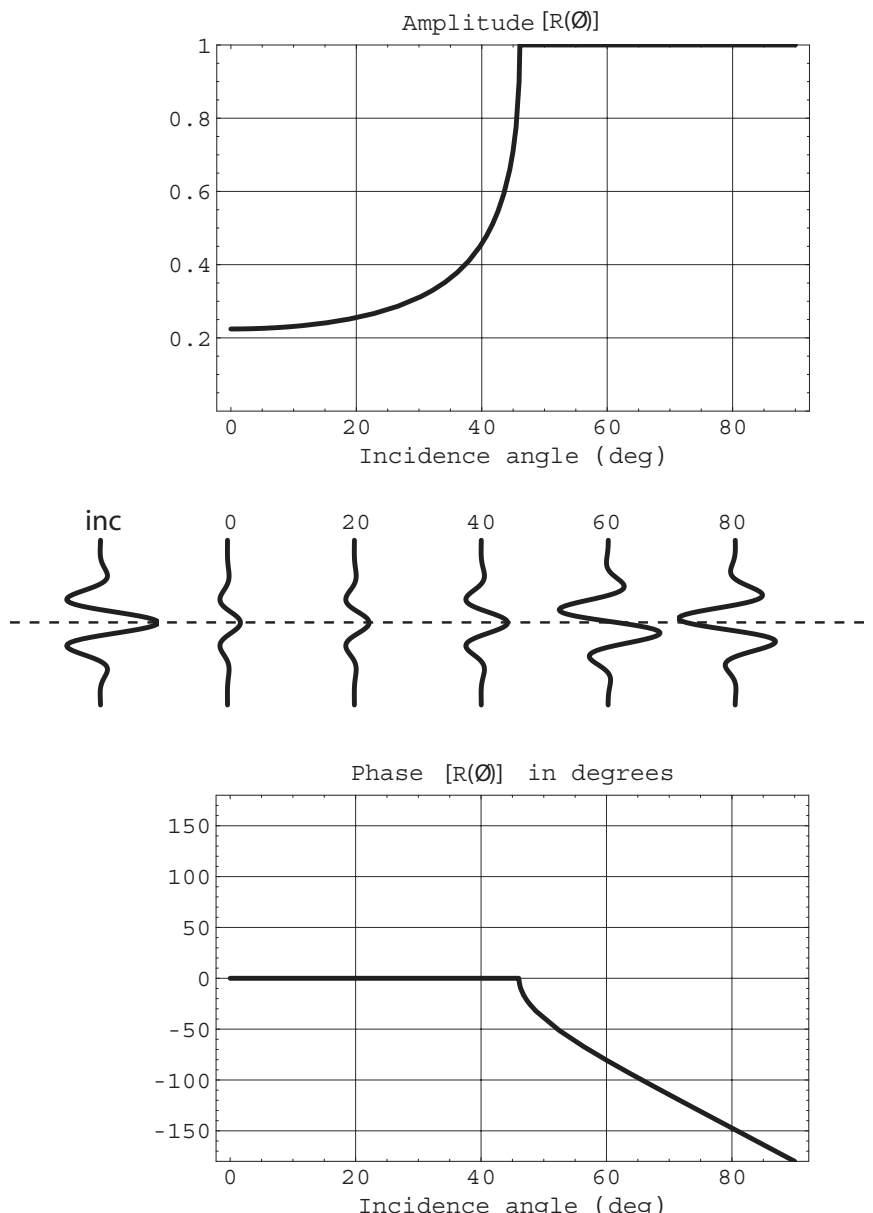


Fig. 3.13 Phase changes due to complex reflection coefficients cause reflected waveforms to differ in significant ways from the incident waveform (inc). This figure uses the same model parameters as Figure 3.12.

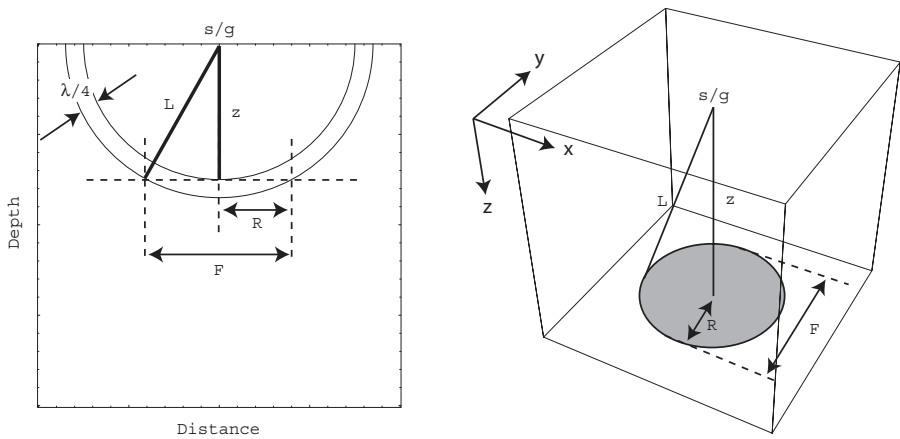


Fig. 3.14 Fresnel zone geometry in 2D and 3D for zero offset data and zero dip. Reflection occurs over an area not at a mathematical point. The size of the Fresnel zone (shaded) is a function of reflection time and frequency.

In defining the Fresnel zone, the extra distance the nonspecular ray travels is taken as  $\lambda/4$  on the way down and  $\lambda/4$  on the way back up for a total extra travel length of  $\lambda/2$ . This is a half-wavelength interference condition. From the geometry we find the Fresnel zone diameter,  $F$ , is given by

$$\begin{aligned}
 F &= v \sqrt{\frac{t_0}{f} + \frac{1}{4f^2}} \\
 &= v \sqrt{\frac{2z}{vf} + \frac{1}{4f^2}} \\
 &= \sqrt{2\lambda z + \lambda^2/(2v)^2}
 \end{aligned} \tag{3.33}$$

where  $v$  is the average velocity,  $t_0$  is the normal incidence reflection time,  $f$  is the dominant frequency, and  $z$  is the depth of the reflector.

## Elements of 3D Seismology

In most cases of seismic interest

$$t/f \gg 1/(4f^2) \quad (3.34)$$

and these expressions can be accurately approximated by various short forms

$$F \approx v \sqrt{\frac{t_0}{f}} = v \sqrt{\frac{2z}{v f}} = \sqrt{2\lambda z} \quad (3.35)$$

The Fresnel zone described here is also called the first Fresnel zone and is the leading term in a series [138] given by

$$F = \sqrt{2n\lambda z} \quad (3.36)$$

where  $n$  is an integer. The first Fresnel zone corresponds to  $n=1$ , the second to  $n=2$ , and so on. Since the dominant contribution to reflection energy comes from the first Fresnel zone, higher order zones are generally ignored in petroleum seismic applications, (see Table 3.2).

	Minimum	Maximum	Average
Frequency (Hz)	10	100	50
Velocity (m/s)	1500	6000	3000
Wavelength (m)	15	600	60
Target depth (m)	600	6000	3000
Fresnel zone diameter (m)	135	2700	600

Table 3.2 Typical parameters for Fresnel Zone calculations.

So far we have given the conventional view of a Fresnel zone and how its size is calculated. This approach is also found in optics [21] and acoustics [49] in the context of monochromatic (single frequency) fields. However, recent work on the Fresnel zone for broadband radiation offers a different perspective [32] and has been experimentally verified by terahertz time-domain spectroscopy [145]. This new approach is briefly outlined next.

Consider the Fresnel zone to be a circular reflecting disk, and a point source of spherical waves to be located some distance above the disk center. As before, we will take the source and receiver to be coincident. The emitted spherical wave will interact with the disk in accordance with a mathematical representation called the Kirchhoff diffraction integral, which is based on Huygens' principle.

The Kirchhoff theory states that every small surface element of the disk responds to the incident wave by acting as a secondary source of spherical waves, and the response at the receiver is the coherent sum of all these secondary waves. For a circular disk, the Kirchhoff integral reduces to a simple form. The measured field consists of two replicas of the source wavelet, one reflected from the center of the disk and another, inverted and appropriately scaled from the disk edge.

If the emitted wavelet is  $w(t)$ , then the reflection response,  $p(t, R)$ , from a disk of radius  $R$  will be

$$p(t, R) = w(t - t_0) - \frac{z^2}{L^2} w(t - t_L) \quad (3.37)$$

where the normal incidence reflection time,  $t_0$ , path length to the edge,  $L$ , and edge reflection time,  $t_L$ , are given by

$$\begin{aligned} t_0 &= 2z/v \\ L &= \sqrt{R^2 + z^2} \\ t_L &= 2L/v \end{aligned} \quad (3.38)$$

and the geometry of Figure 3.14 still applies.

The total energy,  $E(R)$ , of the reflected field is

$$E(R) = \int_0^\infty |p(t, R)|^2 dt \quad (3.39)$$

The Fresnel zone in this approach is defined as the disk diameter, that maximizes the received energy [145]. However, even for an analytic waveform, it is not known if a closed form expression for the Fresnel zone can be found for comparison with the conventional formula. We use a numerical example to illustrate the concept.

## Elements of 3D Seismology

A Ricker wavelet is convenient to use in this example because it has many known analytic properties [165]. Figure 3.15 shows a 20 Hz Ricker wavelet and its amplitude spectrum. Notice that although 20 Hz is the peak frequency, this is in fact a broad band pulse with significant amplitudes in the range 5–40 Hz. The phase spectrum is not shown because the phase for this wavelet is zero for all frequencies.

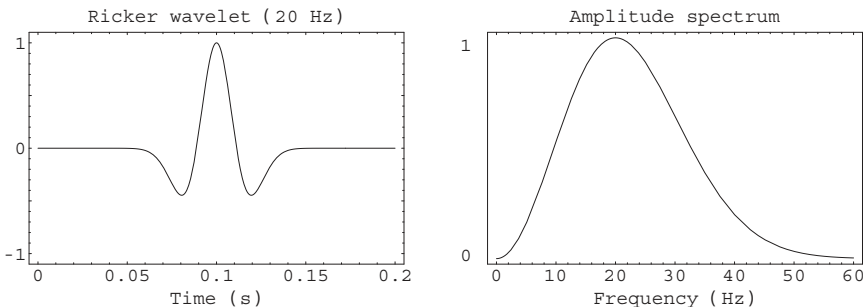


Fig. 3.15 A 20 Hz Ricker wavelet and its Fourier amplitude spectrum. The phase is zero at all frequencies.

We take the disk radius to be 300 m, depth 1500 m, and velocity 2000 m/s, which yield the following computed quantities  $(t_0, L, t_L) = (1.500 \text{ s}, 1530 \text{ m}, 1.530 \text{ s})$ . Figure 3.16 shows the reflected waveforms in this case. In (A) the reflection from the center of the disk is shown as a solid line, and the edge contribution is dashed; (B) shows the total response formed by summing the two wavelets. The total energy in (B) would be found by summing the squared amplitudes in this plot for all time points. As the disk progresses from zero radius to larger values, the total energy will fluctuate depending on the details of wavelet interference, with the maximum energy defining the Fresnel zone.

For 10 Hz and 20 Hz Ricker wavelets, the result of this energy calculation is shown in Figure 3.17. The horizontal axis is reflecting disk diameter (not radius). The 20 Hz peak energy value occurs at 510 m, compared to 548 m from the usual calculation (dashed line), a 7% reduction in predicted Fresnel zone diameter, which corresponds to a 14% reduction in the circular Fresnel zone area. The 10 Hz case in Figure 3.17 peaks at 720 m, again 7% smaller than the predicted value.

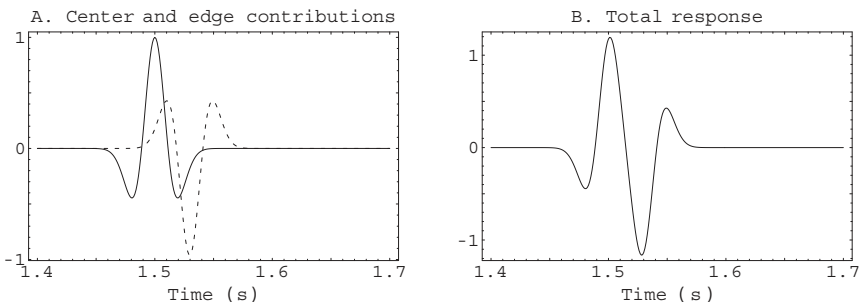


Fig. 3.16 (A) The response from a 300 m diameter Fresnel disk is composed of a reflected wavelet from the center (solid) and one from the disk edge (dashed). (B) The total response is the summation of both wavelets.

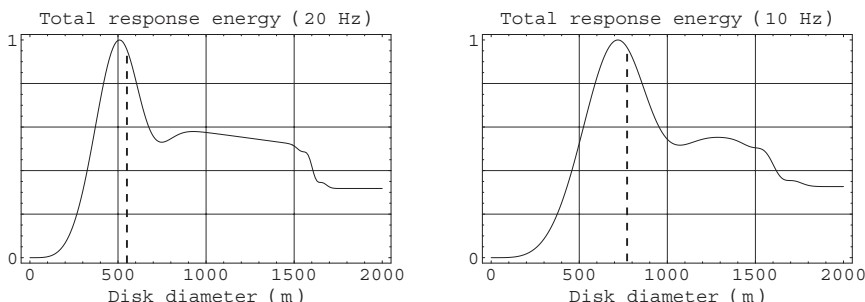


Fig. 3.17 Total reflection energy as a function of disk diameter shows a strong peak that is defined as the Fresnel zone. Results for a 20 Hz and 10 Hz Ricker wavelet are shown, and in each case the dashed line is the Fresnel zone diameter predicted by the traditional formula. Since unmigrated lateral resolution is determined by the area of the Fresnel zone, the energy method predicts somewhat better resolution.

Do these results depend on the wavelet? Figure 3.18 gives the result for a 20 Hz Gaussian-tapered cosine wavelet with 120-degree phase shift. This wavelet is more oscillatory and has longer duration than the Ricker wavelet, and we might suspect these features would diminish its resolving power (i.e., result in a larger Fresnel zone). This is confirmed by the fact that the Fresnel zone peak in this case is at 540 m compared to 510 m with the Ricker wavelet.

## Elements of 3D Seismology

Also noticeable in Figure 3.18B is a secondary peak at about 900 m representing the second Fresnel zone, another consequence of the multiple oscillations in the wavelet. Since each of these wavelets has a strongly peaked amplitude spectrum centered on 20 Hz, we conclude that the Fresnel zone is dependent on the wavelet not just the dominant frequency.

Admittedly, a distinction of 30 m in the Fresnel zone diameter might not seem dramatic. But considering the billions of dollars spent worldwide on seismic data each year [31], any improvement in resolution or our understanding of it is significant.

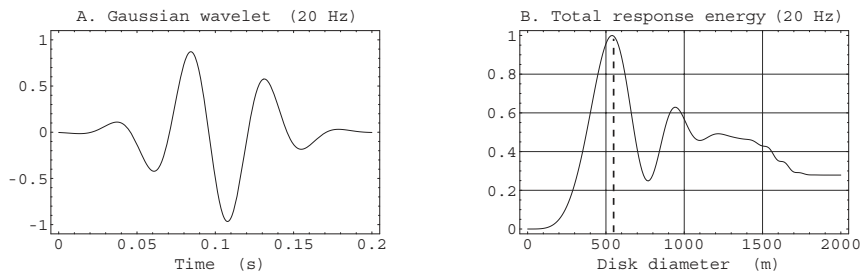


Fig. 3.18 (A) 20 Hz Gaussian Cosine Wavelet. (B) Disk reflection energy peaking at a Fresnel zone diameter of 540 m, with second Fresnel zone peak at 900 m. The dashed line is the Fresnel zone diameter predicted by the traditional formula.

### 3.3 Headwave

We have discussed direct and reflected arrivals, but when velocities increase across an interface a third arrival type is possible. This is called a headwave (also called a refraction, or rarely, a conical wave). The headwave arises when the incident ray strikes the interface at precisely the critical angle. From the horizontal interface geometry of Figure 3.4A, the distance,  $x_c$ , at which the incident angle equals the critical angle,  $\theta_c$ , is given by

$$x_c = 2 z \tan \theta_c = \frac{2z}{\sqrt{(v_2/v_1)^2 - 1}} \quad (3.40)$$

where the last form follows from the rules of trigonometry and the definition of the critical angle,

$$\theta_c = \sin^{-1} \left( \frac{v_1}{v_2} \right) \quad ; \quad v_1 < v_2 \quad (3.41)$$

This distance is called the critical distance or critical offset. Only receivers beyond the critical offset will see a headwave arrival and those will register an arrival time,  $t_h$ , of

$$t_h(x) = \frac{x}{v_2} + \frac{2 z \cos \theta_c}{v_1} \quad ; \quad x > x_c \quad (3.42)$$

where  $x$  is the offset. This expression shows that the headwave event is linear with slope  $1/v_2$ . Furthermore, the reflection hyperbola at the critical offset has the same traveltime and slope, meaning that the headwave and reflection event are tangent at the critical offset.

Figure 3.19 illustrates these concepts. In (A) the earth model is shown, consisting of an interface at 1500 m depth between velocities  $v_1=2000$  m/s and  $v_2=4000$  m/s, giving a critical angle of 30 degrees. Also shown in (A) are the headwave rays, which all share the same ray from the source and all emerge at the critical angle. The critical offset in this case is about 1800 m. Only the headwave event is shown in (B). This event exhibits the behavior we expect; it exists only at and beyond the critical offset and has linear moveout with slope of

$$\phi = \frac{1}{4000 \text{ m/s}} = 0.00025 \text{ s/m} \quad (3.43)$$

So, for example, between offsets 2000 m and 6000 m, we see the event time-delayed by about 1 sec (4000 m times 0.00025 s/m). Figures 3.19C and D show all rays and events including direct, reflected, and headwave. The reflection event in this case can be segmented into three regions, precritical reflection at offsets less than  $x_c$ , critical reflection at  $x_c$ , and post-critical or wide angle reflection beyond  $x_c$ . Notice that for some range of offsets near the source, the first arrival is the direct wave then beyond a certain offset the first arrival is the headwave. This crossover offset is

$$x_{co} = \frac{2 z \cos \theta_c}{1 - v_1/v_2} \quad (3.44)$$

or 5196 m in this case.

## Elements of 3D Seismology

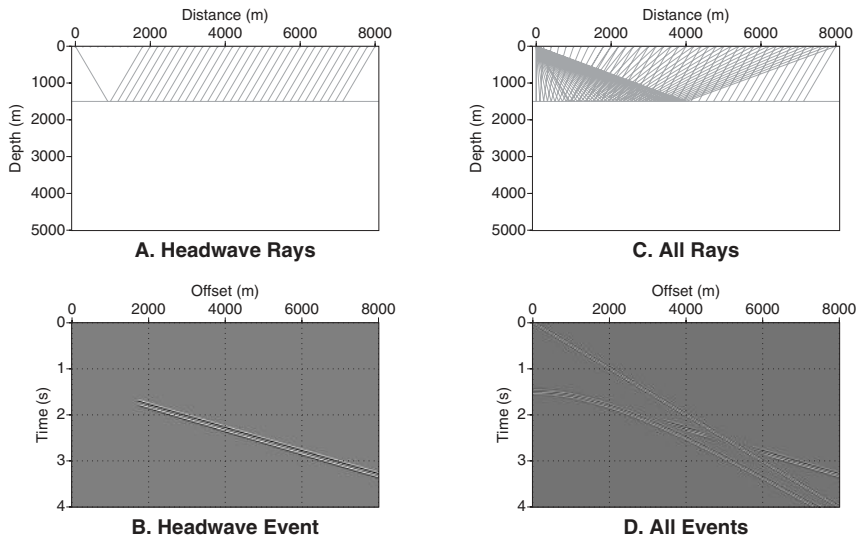


Fig. 3.19 When velocity increases across the interface a headwave event occurs in addition to direct and reflected arrivals.

The theory of the headwave is part of the problem of spherical wave reflection from a plane boundary, often called Lamb's problem from an important 1904 study by H. Lamb who developed an approximate solution. The exact solution was first published in 1939 by Cagniard [34] and reached a general audience only much later [3]. From this work, we know the headwave amplitude in the frequency domain is given asymptotically [3] by

$$A \sim \frac{g(\rho_1, v_1, \rho_2, v_2)}{i\omega x^{1/2} L^{3/2}} \quad (3.45)$$

where  $x$  is the offset, the distance the headwave travels in medium 2 is

$$L = x - z \tan\theta_c \quad (3.46)$$

and  $g()$  is a function of the material parameters on either side of the interface

$$g(\rho_1, v_1, \rho_2, v_2) = \frac{2\rho_1 v_1^2}{\rho_2 v_2 (1 - v_1^2/v_2^2)} \quad (3.47)$$

The factor of  $1/(i\omega)$  says that the headwave will be a time-integrated version of the wavelet. This has the effect of making the headwave wavelet appear 90-degree-phase shifted, smoother, and have a distinct tail. Furthermore, the distance dependence of the headwave amplitude is such that it is very weak compared to either the reflected or direct waves. To see this, consider a case where the offset is much greater than the depth of the refracting interface. The headwave amplitude then falls off with offset as

$$\lim_{x \gg z} \frac{1}{x^{1/2} L^{3/2}} = \frac{1}{x^{1/2} x^{3/2}} = \frac{1}{x^2} \quad (3.48)$$

whereas both direct and reflection events decay as  $1/x$  (since the offset in this case is also the radius from the source).

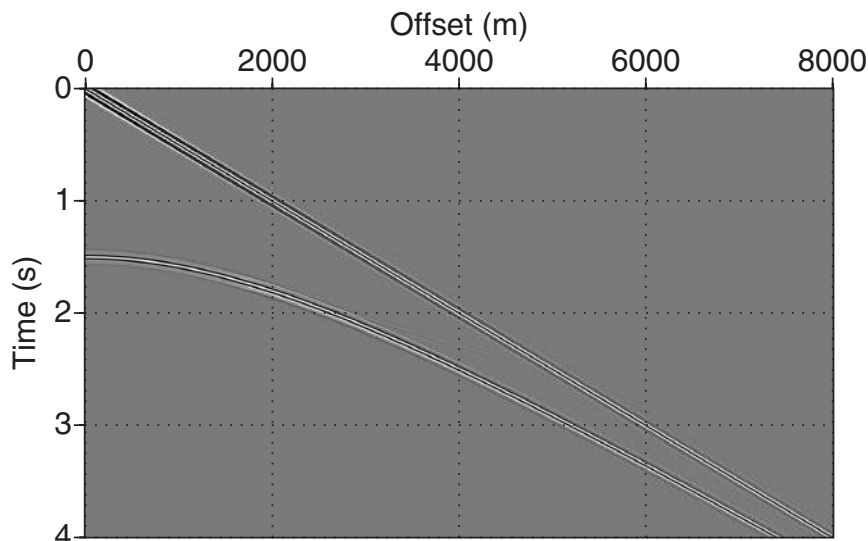
You might wonder at these results, considering the headwave appears quite strong on Figure 3.19D. The events of this figure are shown with a display gain for the purpose of making all events equally visible. But the fact that the headwave dims out on intersection with the direct arrival is a good clue that the plot is not true amplitude.

Figure 3.20 shows this shot record without any distorting display gain. The headwave is virtually invisible in relation to the direct and reflected waves, Figure 3.20A, and not much better when isolated against just the reflection, Figure 3.20B. This is a curious result considering that strong headwave events are often measured on land seismic data.

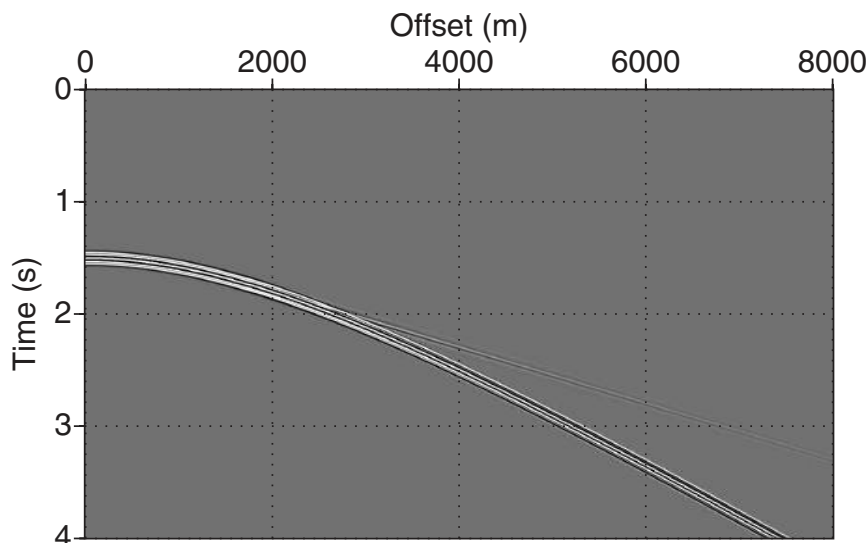
### 3.4 The point source: tying it all together

Lamb's problem was mentioned earlier as the theoretical framework for a point source of waves over a single plane interface. Many of the events we have discussed are present in this one simple problem as seen in the numerical simulation of Figure 3.21. The velocity above the interface is 1525 m/s and 2645 m/s below and density is constant. The shot record in this figure corresponds to measurements taken along the dotted line in the wavefield snapshot, and the source location is the black dot in the center of this line.

The data was created by 2D modeling, which preserves the relative amplitudes of all events, but we understand that geometric spreading and the propagated waveform exhibit 2D behavior. In the snapshot view, the headwave is seen as a tenuous linkage between the reflected wave and the transmitted wave. It is also clear that the headwave energy is associated with the horizontally traveling transmitted wave in the vicinity of the interface.

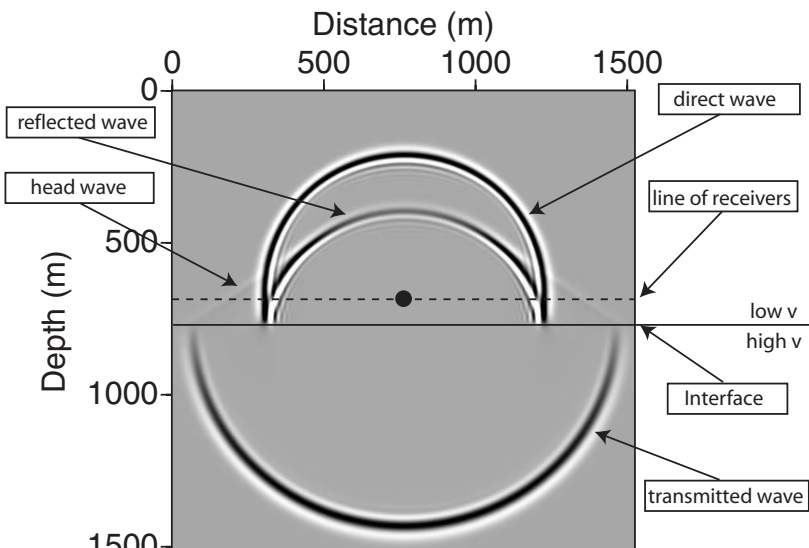
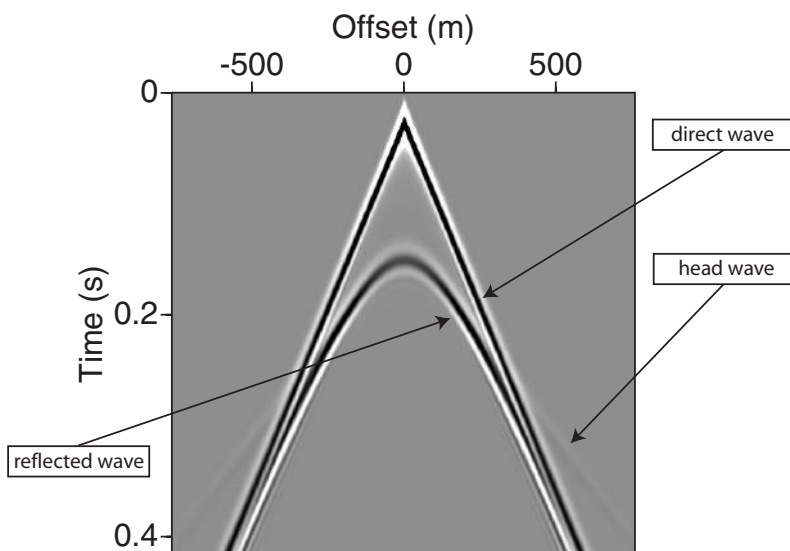


**A. All Events -- Relative Amplitude**



**B. Refl + Head -- Relative Amplitude**

Fig. 3.20 Relative amplitude plots of the data of Figure 3.19D showing how weak the headwave arrival is compared to the direct and reflected wave.

**Wavefield Snapshot****Shot Record**

*Fig. 3.21 Numerical simulation of a point source over a plane interface separating low velocity above and high velocity below. This simple problem binds together the concepts of direct, reflected, transmitted, and headwave. The relative amplitudes are correct in a 2D sense.*

For this reason, another name for a headwave is lateral wave. Notice the reflected wave polarity is the same as the direct wave (i.e., both are dark colors). This follows from  $I_2 > I_1$ , which gives a positive reflection coefficient. The case of velocity decrease across the interface, Figure 3.22, appears less complicated due to absence of the headwave. Also, note the reflection is opposite polarity to the direct wave, indicating a negative reflection coefficient.

A last view of this problem is seen in Figure 3.23. Here the wavefield for each model is shown evolving from the source and interacting with the layer boundary. The wavefield is displayed at intervals of 50 ms.

### 3.5 Diffraction

Diffraction events are commonly seen in seismic data, and along with reflections are the raw material migrated seismic images are built from. Geometry similar to that describing reflection from a horizontal interface can be applied to scattering from a point diffractor. You can think of a diffractor as a shiny ball that takes an incoming ray and sends out scattered rays in all directions.

Following Figure 3.24, we consider a point diffractor in the earth at  $(x_d, z_d)$ , a source point at  $(x_s, z_s)$ , and a receiver group with coordinates  $(x_g, z_g)$ . For constant velocity,  $v$ , the 3D travelttime equation is given by

$$\begin{aligned} L_1 &= \sqrt{(x_s - x_d)^2 + (y_s - y_d)^2 + (z_s - z_d)^2} \\ t_1 &= \frac{L_1}{v} \\ L_2 &= \sqrt{(x_g - x_d)^2 + (y_g - y_d)^2 + (z_g - z_d)^2} \\ t_2 &= \frac{L_2}{v} \\ t &= t_1 + t_2 \end{aligned} \tag{3.49}$$

where the  $y$ -coordinates of shot and receiver are  $(y_s, g_s)$ , respectively. Although not obvious, this double square-root travelttime equation describes a hyperbolic curve.

Figure 3.25 shows a raypath plot for the point diffractor and corresponding shot record travelttime curve. In this case, the diffractor is 1220 m deep and 1000 m laterally displaced from the source point (indicated by  $s$ ). There is one ray from the source to the diffracting point and one ray out from that point to each receiver. The first leg of the journey (shot to diffractor) is always the same, but the second leg (diffractor to receiver) varies with receiver location. Thus the receiver directly above the diffractor should have the minimum travelttime as verified in Figure 3.25.

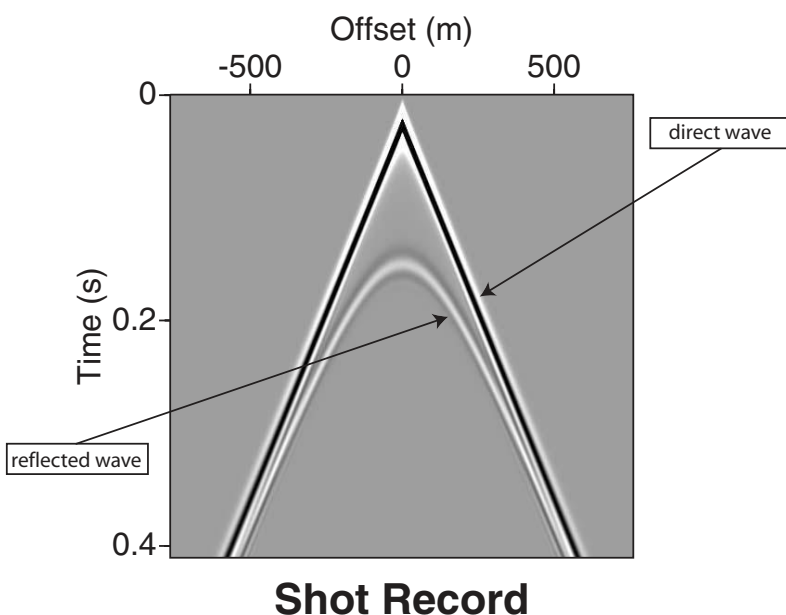
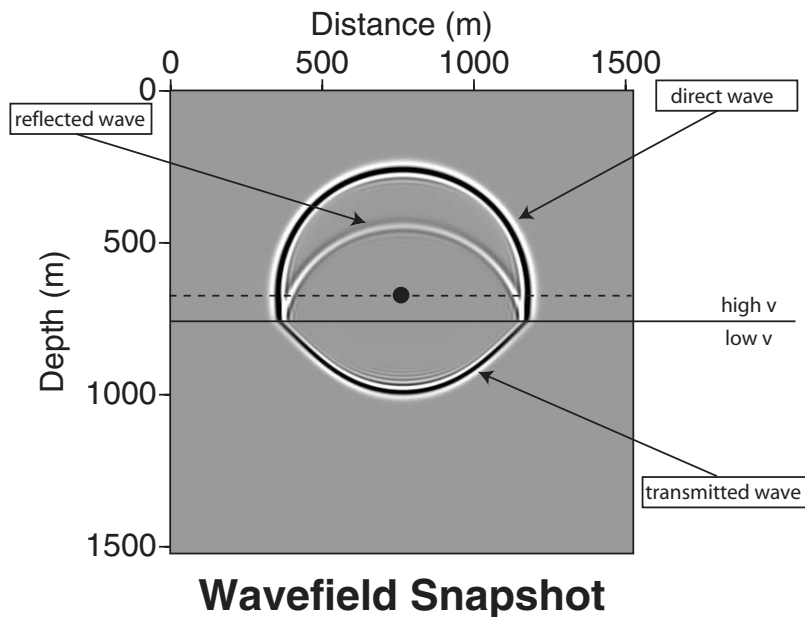


*Fig. 3.22 Simulation for the case of a velocity decrease across the interface. The headwave does not occur in this situation and the reflected wave has opposite polarity relative to the direct and transmitted waves.*

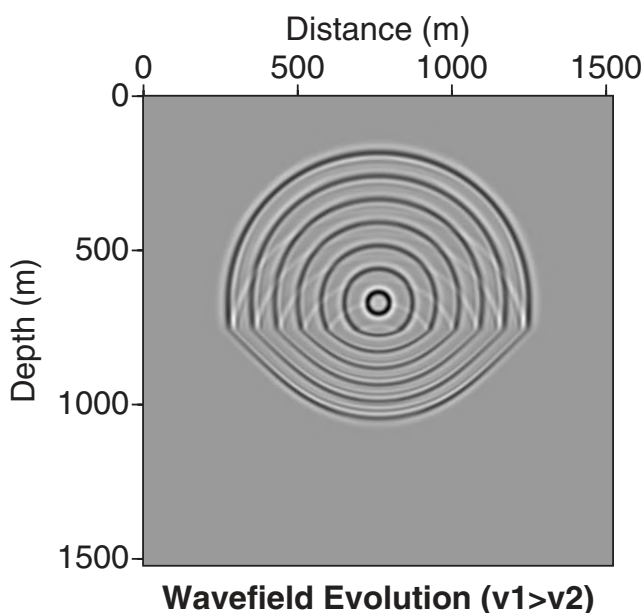
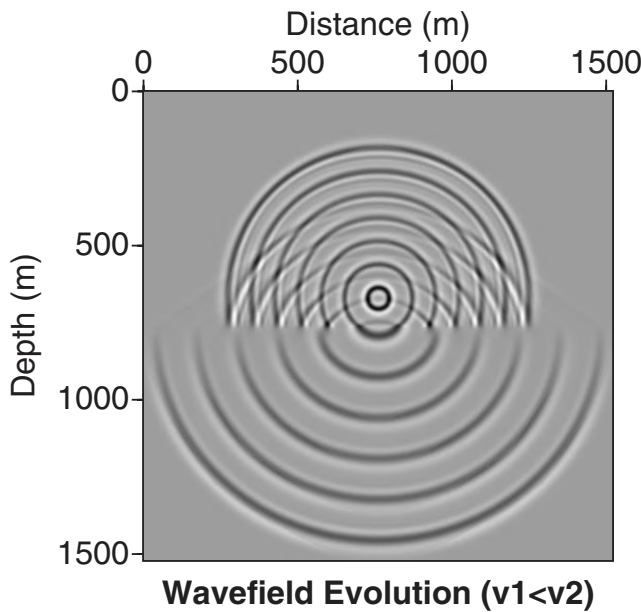


*Fig. 3.23 Time evolution of the wavefield for each case is visualized here by superimposed snapshots taken at 50 ms intervals.*

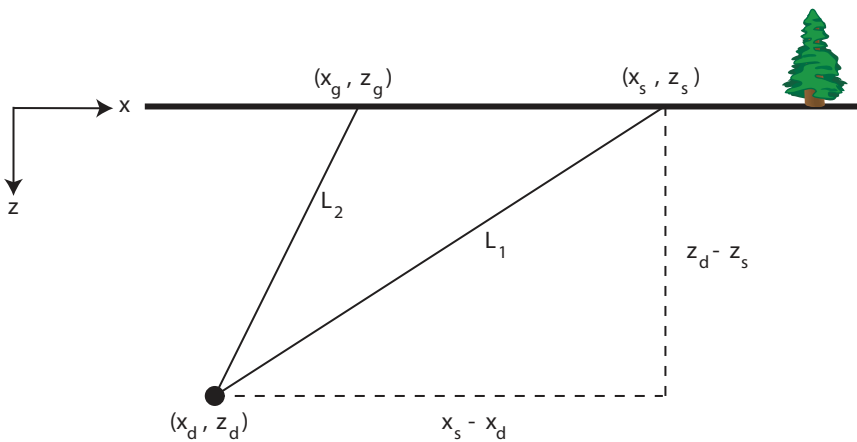


Fig. 3.24 2D Geometry for scattering from a point diffractor.

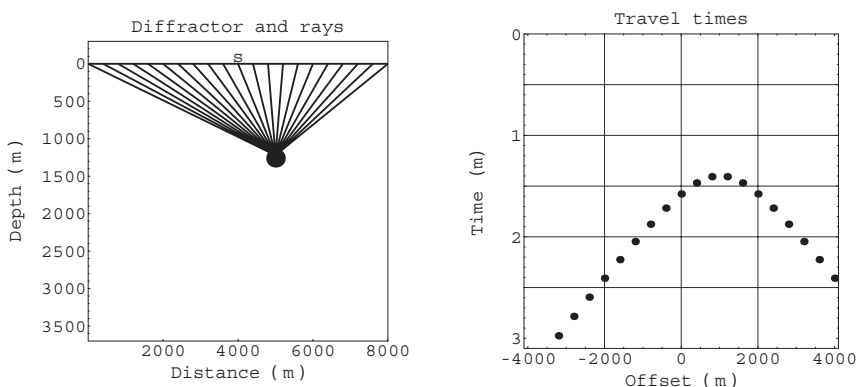


Fig. 3.25 Rays and traveltime curve for a point diffractor. Note vertical exaggeration in the earth model.

## Elements of 3D Seismology

You might wonder how we can distinguish reflection and diffraction events if they are both hyperbolic. Figure 3.26 shows two traveltime curves, one for the point diffractor discussed earlier, and another for reflection from a dipping bed. The dipping bed case has been adjusted so that the traveltime apex is coincident with the diffraction apex. We see the diffraction event is a narrower hyperbola, sometimes called the curve of maximum convexity.

These two curves will behave very differently under the action of seismic migration; the reflection curve will migrate to a dipping line segment, and the diffraction curve will migrate to a point. In a 3D shot record, the diffraction curve is a hyperbolic surface as shown in Figure 3.26B. In this case, the diffractor is directly beneath the shot point identified by the letter s. Claerbout [48] has examined the geometry of this surface in detail.

The point diffractor model might seem a useless curiosity except that something in the earth actually behaves this way. When a rock unit is laterally terminated due to a fault, the end of the bed acts like a point diffractor. Faults generate many diffractions, one for each bed that is broken. Also, the double-square-root equation for diffraction travelttime is at the heart of prestack migration theory [48].

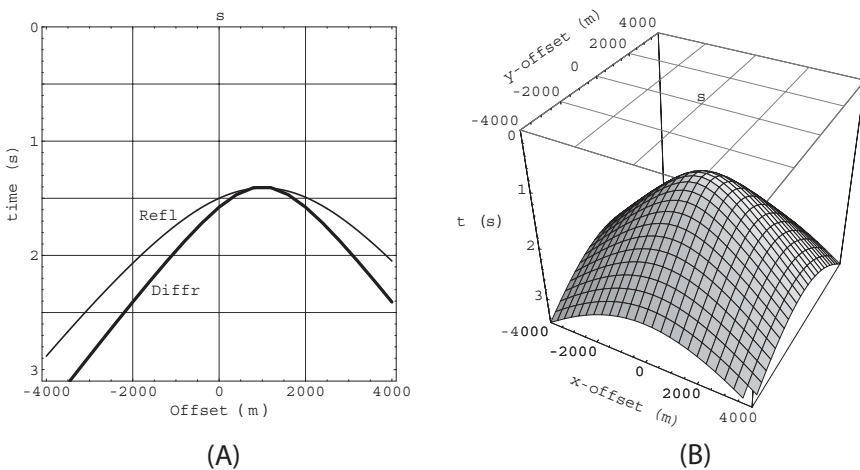


Fig. 3.26 (A) The traveltime curves for a point diffractor and dipping bed are both hyperbolic but not identical. (B) In 3D the point diffractor travelttime is a hyperbolic surface.

### 3.6 Ghost

It is often the case that the source or receiver is not actually located on the earth surface, but some depth into it. This is always true for marine shooting and common in land areas with near surface problems (thick weathering layer, glacial till, etc.).

Some energy from the source will necessarily go up to strike the free surface and reflect. This is termed a “ghost reflection,” an appropriate name since the direct downgoing pulse will be quickly followed by an inverted copy of itself.

Figure 3.27 illustrates the ghost using rays. In this example, the source is shooting into four receivers. Both source and receivers have a depth of 200 m, which is much deeper than actual practice, but serves to make the ghost rays easily visible without vertical exaggeration. A reflector exists at 5000 m depth.

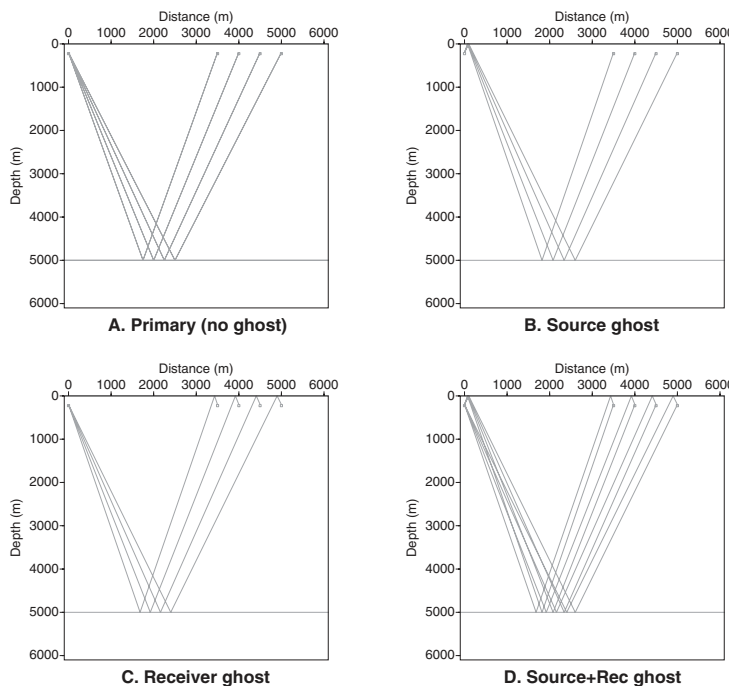


*Fig. 3.27 A ghost is a multiple reflection from a free surface such as the surface of the ocean. The reflection event we see will include the primary reflection and all combinations of ghost reflections.*

## Elements of 3D Seismology

Figure 3.27A shows reflection rays without ghost effects; travel is from source to reflection point to receiver. In Figure 3.27B the source ghost paths are shown and Figure 3.27C shows the receiver ghost paths. Whether the land or marine case is considered, the free surface reflection coefficient will be  $-1$ , and the individual source and receiver ghosts will be opposite sign to the primary pulse. What actually occurs is that four reflection events arrive in quick succession at the receiver.

To be specific, assume the surface layer is water ( $v = 1500$  m/s), the source/receiver depth is 6 m, all raypaths are vertical, and the reflection time is 1 sec. Figure 3.28A shows the four individual arrivals: the primary (trace 1, representing the actual source wavelet), a negative source ghost arrival (trace 2), a negative receiver ghost (trace 3), and a positive source+receiver ghost (trace 4). The source ghost and receiver ghost arrive with the same 8 ms time delay, (12 m divided by 1500 m/s), relative to the primary, while the double ghost has twice

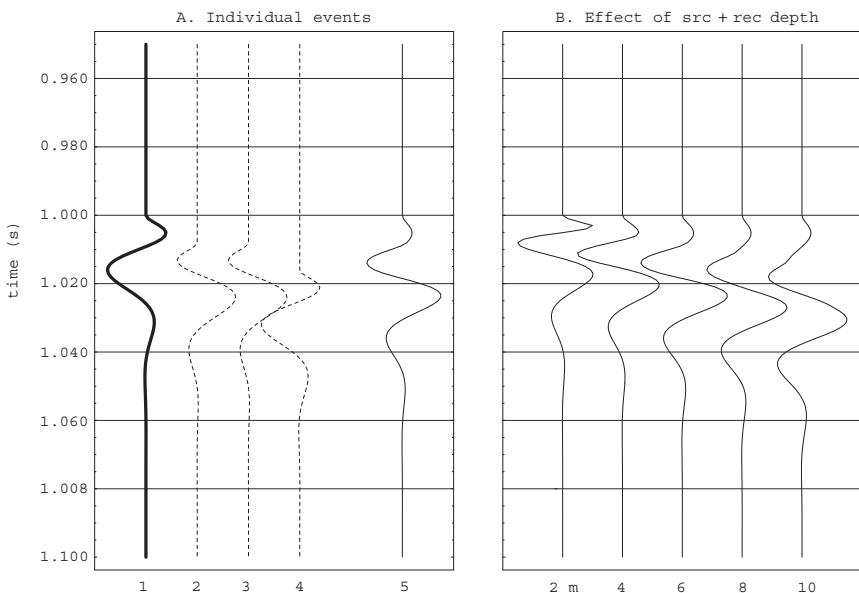


*Fig. 3.28 Details of the ghost effect for a water layer ( $v = 1500$  m/s) and reflection time of 1 sec. (A) For source and receiver at 6 m depth the individual arrivals are the primary (1), source ghost (2), receiver ghost (3), and source+rec ghost (4). The observed waveform (5) is the sum of (1)-(4). (B) The observed waveform varies significantly as acquisition depth changes from 2 m to 10 m.*

this delay. The recorded waveform (trace 5) is the sum of these individual events and is strongly influenced by the interference effects arising from their relative arrival times. This is borne out by Figure 3.28B, showing the total pulse as a function of acquisition depth from 2 m to 10 m.

The traces in Figure 3.28 all assume vertical propagation, which would be approximately the case for near offset receivers. However, the ghost delay time depends on the takeoff angle of the primary pulse. From the geometry of Figure 3.29 this directional ghost delay [99] is

$$t(\theta) = \frac{2 z \cos\theta}{v} \quad (3.50)$$

where  $\theta$  is the takeoff angle and  $v$  is water velocity. This variable delay complicates ghost removal and causes a point source to exhibit a directional radiation pattern. Both of these effects can influence prestack interpretation methods such as AVO.

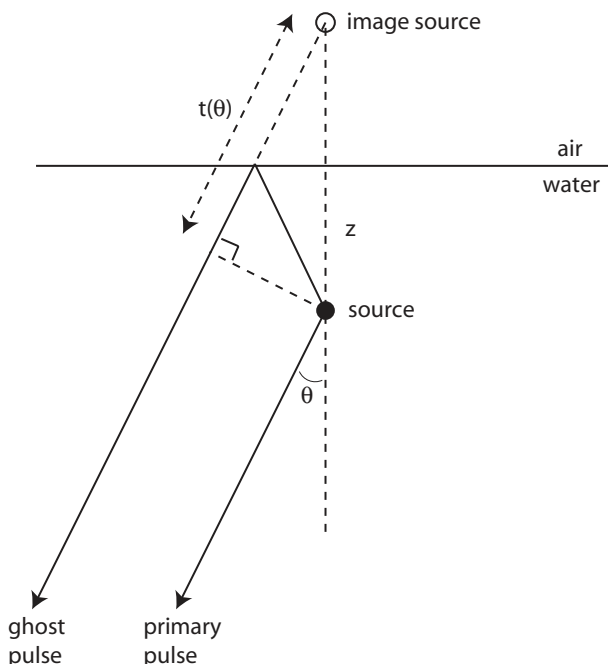


Fig. 3.29 Detailed geometry of the ghost illustrating that its time delay relative to the primary is a function of takeoff angle  $\theta$  (redrawn from [99]).

## 3.7 Velocity layering

**3.7.1 More events.** When the earth model consists of many layers, the most obvious effect is introduction of more events: a reflection is associated with each interface and more than one headwave arrival is possible. There is nothing fundamentally new here except the number of events.

Traveltime and amplitude calculations in general layered media are done numerically, since these quantities cannot be expressed by simple equations, and there is little practical benefit in listing equations for the many known special cases. One exception, however, is travelttime as a function of offset for a stack of parallel layers. Recall that reflection time,  $t(x)$ , for a single layer is

$$t^2(x) = \frac{(2z)^2}{v^2} + \frac{x^2}{v^2} = t_0^2 + \frac{x^2}{v^2} \quad (3.51)$$

where  $z$  is the reflector depth,  $x$  is the offset,  $v$  is the (constant) velocity, and  $t_0$  is zero offset reflection time. We consider a stack of  $j$  horizontal layers where layer  $i < j$  has thickness  $z_i$  and velocity  $v_i$ . For reflection from the base of the  $j^{th}$  layer, the squared reflection time [174] at offset  $x$  is given by

$$t^2(x) = c_1 + c_2 x^2 + c_3 x^4 + \dots \quad (3.52)$$

where the coefficients are given by

$$\begin{aligned} c_1 &= a_1^2 = t_0^2(x) \\ c_2 &= \frac{a_1}{a_2} = \frac{1}{v_{rms}^2} \\ c_3 &= \frac{a_2^2 - a_1 a_3}{4 a_2^4} \end{aligned} \quad (3.53)$$

which in turn depend on the function

$$a_m = 2 \sum_{i=1}^j v_i^{(2m-3)} z_i \quad (3.54)$$

As stressed by Yilmaz [212], when the offset is small compared to depth of the reflector the travelttime can be adequately approximated by the first two terms

$$t^2(x) = t_0^2(x) + \frac{x^2}{v_{rms}^2} + \dots \quad (3.55)$$

This tells us the reflection event for a horizontally layered earth will be approximately hyperbolic, and its departure from an exact hyperbola increases with offset.

What is the magnitude of the fourth-order term ignored in this equation? Figure 3.30 shows two examples. In Figure 3.30A, we see a 10-layer test case of random velocities in the range  $v_i=(2500,4500)$  km/s with layer thicknesses also random in the range  $z_i=(10,20)$  m. Reflection time from the deepest interface is shown in Figure 3.30B. The dot values are calculated using the second-order travelttime equation which, for this particular velocity model, is given by

$$t_2(x) = \sqrt{0.778925 + 0.0831447 x^2} \quad (3.56)$$

where the offset is in km. The solid curve in (B) is the fourth-order travelttime

$$t_4(x) = \sqrt{0.778925 + 0.0831447 x^2 - 0.000281673 x^4} \quad (3.57)$$

In a typical seismic survey, far offset will be about equal to target reflector depth. In this example, however, the offsets range up to three times reflector depth, a situation that might be encountered in the shallow section of a survey designed for deeper targets. But even at these large offsets, the maximum travelttime difference is only 38 ms, a time interval comparable to the period of a typical wavelet. Figure 3.30C and D show a 100-layer example over a comparable depth interval. The travelttime results show a similar divergence between the second- and fourth-order calculations with a difference of 35 ms at the far offset.

We conclude that significant non-hyperbolic moveout cannot easily be attributed to horizontal layering. But it is important to realize that some non-hyperbolic moveout occurs due to layering even in the absence of structure, lateral velocity variation, statics, or anisotropy. These other factors, however, are more likely causes of significant non-hyperbolic moveout.

**3.7.2 Multiples.** A *multiple* is any event which has experienced more than one reflection in the subsurface. We have already studied the ghost, which is a multiple event, and Figure 3.31 illustrates some other kinds. For this example, we have a single source firing into four closely spaced receivers over a 5-layer model.

## Elements of 3D Seismology

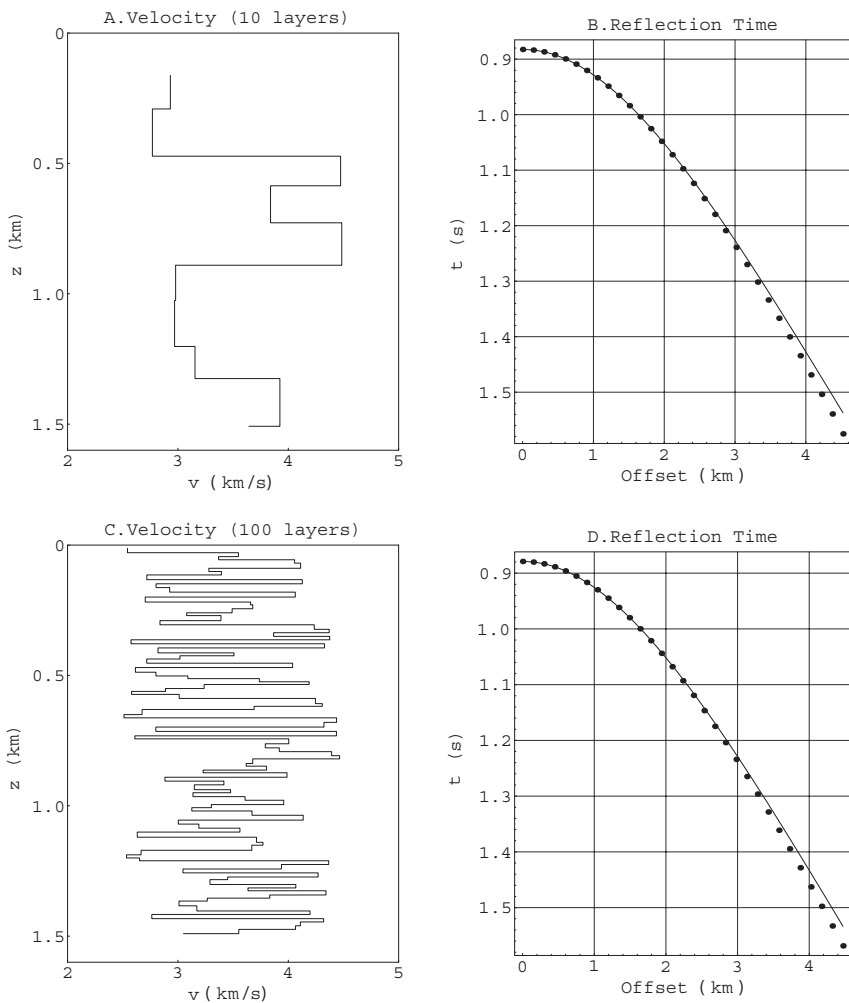


Fig. 3.30 Hyperbolic and non-hyperbolic moveout for a stack of horizontal layers. (A) Velocity model consisting of 10 thick layers with random velocities and thicknesses. (B) Traveltime curves for a reflector at the base of the 10-layer velocity model. Offsets range out to three times the reflector depth which is much greater than would be seen in field data. Dots are hyperbolic traveltimes calculated using a second-order equation. The solid line uses a more accurate fourth-order equation. Maximum difference at the far offset is 38 ms or 2.5%. (C) 100-layer random velocity model. (D) Traveltime curves for the 100-layer case show a maximum time difference of 35 ms.

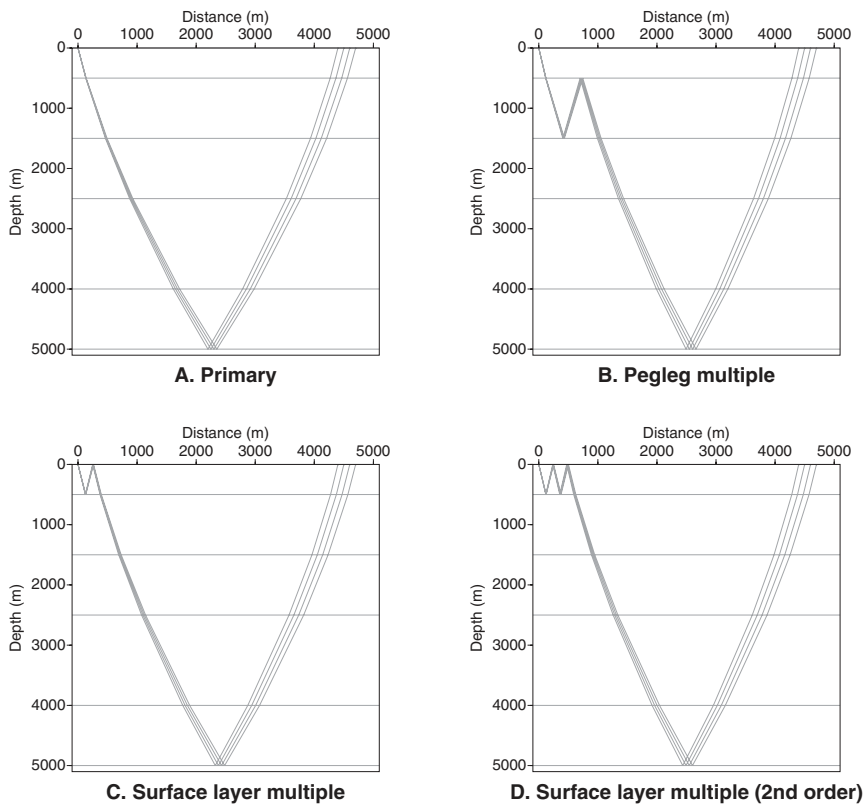


Fig. 3.31 A small sampling of multiples.

A primary event (A) is emitted from the source, bounces from a reflection point, and travels to the receiver. A pegleg multiple (B) bounces one or more times in a layer somewhere along the travel path. This is an example of an internal multiple.

When the multiple bounces from the free surface at the top of the earth model, it is called a surface layer multiple (C) and can be categorized by the number of times it has undergone multiple reflection (D). Any of the events in (B)–(D) will necessarily have longer traveltimes than the primary reflection and thus exhibit greater moveout. Equivalently, they will appear to be associated with lower average velocity than the primary.

## **Elements of 3D Seismology**

Clearly there are an infinite number of multiples even in a model with just a few layers. Any attempt to name and catalog the individual types would be fruitless. However, some general classifications are of interest.

One is the distinction between long-period and short-period multiples. A long-period multiple has additional delay time relative to the primary which is large compared to the period of the wavelet. For a typical 10–100 Hz wavelet, a long-period multiple would be one whose delay is greater than 20 ms. Long-period multiples have the potential to overlap with deeper primary reflection events, (Fig. 3.32), and thus interfere with processing and interpretation. Short-period multiples, (such as the ghost), follow so closely behind the primary that they have the effect of complicating the wavelet, a different kind of bother for processing and interpretation.

Another distinction is between free surface and internal multiples. Since the reflection coefficient from a free surface is  $-1$ , free surface multiples tend to be very strong. Internal multiples are individually weaker, but due to fine layering their net effect can be significant.

### **3.8 Classification**

We conclude this chapter by considering the general seismic event classification tree of Figure 3.33. We have discussed in some detail the various events itemized in this diagram. The fundamental goal of reflection seismology is to create an image of the subsurface for interpretation. The events that contribute to this image are shown in bold—diffractions and primary reflections. All other events are considered noise and either processed away or discounted during the interpretation process.

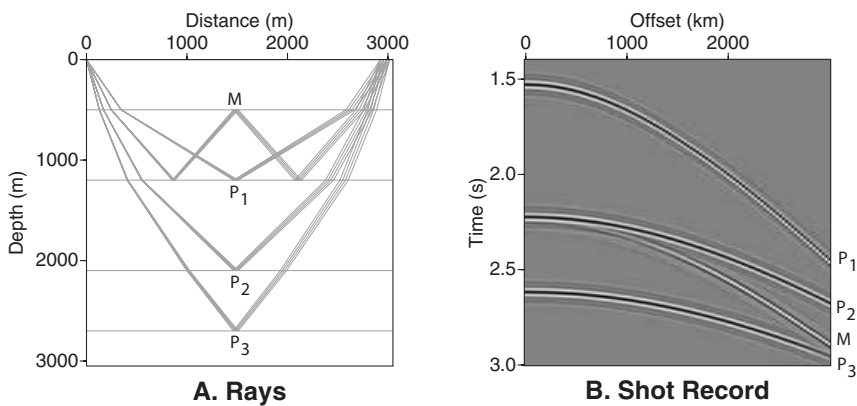


Fig. 3.32 (A) selected raypaths for a 4-layer model showing three primary reflections and one multiple. (B) A shot record over this model using offsets 0–3000 m. Note greater delay and curvature on traveltime event for the multiple (M), and that it coincides with reflection P<sub>2</sub> at near offsets.

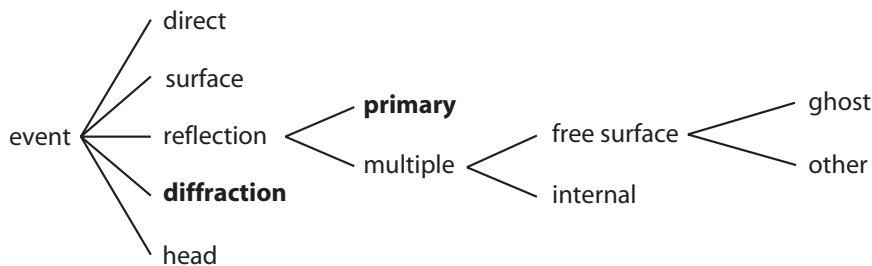


Fig. 3.33 A classification tree for events likely to be seen on seismic shot records. Diffractions and primary reflections are the raw material that seismic migration will use to create seismic images. All other events are typically considered noise.

# 4

## Reservoir Fluid Properties

The previous chapter developed an understanding of seismic events in an acoustic earth model. This is a convenient way of dealing with seismic P-wave data without addressing complicated elastic phenomena. So, in effect, the fluid medium of the last chapter was a generic proxy used to host P-waves traveling in the earth.

However, there are three actual fluids whose detailed properties are of interest to us: natural gas, petroleum, and water. The goal is to have a predictive model to calculate the density, bulk modulus, and sound wavespeed for these fluids individually or as a fluid mixture. This is important for AVO, time-lapse seismic, and fluid substitution work. This chapter follows closely the pioneering work of Batzle and Wang [13].

### 4.1 Pressure and temperature range

Our method here will be to give the relevant equations without much explanation and no derivation. Each important result will also be presented graphically. The fluid properties in this section are functions of pressure and temperature, so it is important to know the range of conditions likely to be encountered in petroleum reservoirs.

In the earth, the geothermal gradient is in general about  $25^{\circ}\text{C}/\text{km}$ . All results will be plotted on the range  $0\text{--}350^{\circ}\text{C}$  ( $32\text{--}662^{\circ}\text{F}$ ). With the standard temperature gradient, the maximum temperature corresponds to a depth of roughly 14 km (more than 40,000 ft). But these temperatures can be encountered closer to the surface, depending on local conditions or human activity such as steam or fire flood.

There are two pressure gradients in the earth. Lithostatic pressure due to overlying rock mass increases at the rate of about  $22.77 \text{ kPa/m}$  ( $1.0 \text{ psi/ft}$ ) and is called the confining pressure. The pore fluids, however, are assumed to be in pressure communication at all depth levels and therefore subject to the hydrostatic

## Elements of 3D Seismology

pressure gradient of 10.7 kPa/m (0.47 psi/ft). Pore pressure is of interest here and will be plotted 0.1–100 mPa (14.7–14,700 psi). This covers reservoirs down to depths of 9470 m (31,280 ft) depth. However, high pressures can be encountered at shallower depths if overpressure conditions exist in the reservoir.

## 4.2 Gas

Natural gas is classified by its specific gravity,  $G$ . This is defined as the ratio of the gas density to air density at standard temperature and pressure (15.6°C; 0.1 mPa),

$$G = \frac{\rho_{gas}}{\rho_{air}} \quad (4.1)$$

Gas specific gravity is a dimensionless quantity that ranges in value from about 0.56 (pure methane) to 1.8 (heavier components).

For the gas calculations in this section, we have the following quantities given and to be calculated

Given:	$P$	pressure	mPa
	$T$	temperature	°C
	$G$	gas specific gravity	
Calculate:	$\rho_{gas}$	gas density	g/cc
	$v_{gas}$	gas velocity	m/s
	$k_{gas}$	gas bulk modulus	mPa

There are several intermediate quantities but these are the final ones we really want.

**4.2.1 Gas density.** The equations are

$$\rho_{gas} = \frac{28.8G P}{Z R T_a} \quad (4.2)$$

$$T_a = T + 273.15 \quad (4.3)$$

$$Z = [0.03 + 0.00527(3.5 - T_{pr})^3] P_{pr} + (0.642T_{pr} - 0.007T_{pr}^4 - 0.52) + E \quad (4.4)$$

$$E = 0.109(3.85 - T_{pr})^2 \exp \left[ - \left( 0.45 + 8(0.56 - 1/T_{pr})^2 \right) P_{pr}^{1.2} / T_{pr} \right] \quad (4.5)$$

$$T_{pr} = \frac{T_a}{94.72 + 170.75G} \quad (4.6)$$

$$P_{pr} = \frac{P}{4.892 + 0.4048G} \quad (4.7)$$

where  $T_a$  is the absolute temperature,  $(T_{pr}P_{pr})$  are the “pseudoreduced” temperature and pressure, and  $R$  is the molar gas constant whose value is 8.3144 Joule(Kelvin\*Mole).

The behavior of gas density as a function of temperature, pressure, and  $G$  is shown in Figure 4.1. Actually plots are only shown for the two extreme cases  $G=(0.56,1.2)$ , but intermediate values can be visualized and estimated from the two graphs shown. We see that gas density is far from constant, varying from near zero to 0.5 g/cc (half the standard density of water). The high density case occurs at high pressure and low temperature, an unlikely scenario to naturally occur in the earth.

**4.2.2 Gas modulus and velocity.** The equations are

$$v_{gas} = \sqrt{1000 k_{gas}/\rho_{gas}} \quad (4.8)$$

$$k_{gas} = \frac{P \gamma_0}{1 - P_{pr} q/Z} \quad (4.9)$$

$$\gamma_0 = 0.85 + \frac{5.6}{P_{pr} + 2} + \frac{27.1}{(P_{pr} + 3.5)^2} - 8.7 \text{ Exp}[-0.65(P_{pr} + 1)] \quad (4.10)$$

$$q = [0.03 + 0.00527(3.5 - T_{pr})^3] + \frac{\partial E}{\partial P_{pr}} \quad (4.11)$$

The factor of 1000 in the velocity calculation occurs because density is expressed in units of g/cc, while all other quantities are MKS. The last term in  $q$  is messy but can be computed from the definition of  $E$  given in the gas density calculation. The variation of sound speed is shown in Figure 4.1C and D and bulk modulus variation in Figure 4.2. For  $G=1$ , the sound speed in gas at surface temperature and pressure would equal the sound speed in air (335 m/s). We see this approximately confirmed by the low pressure, low temperature region of Figure 4.1D.

## Elements of 3D Seismology

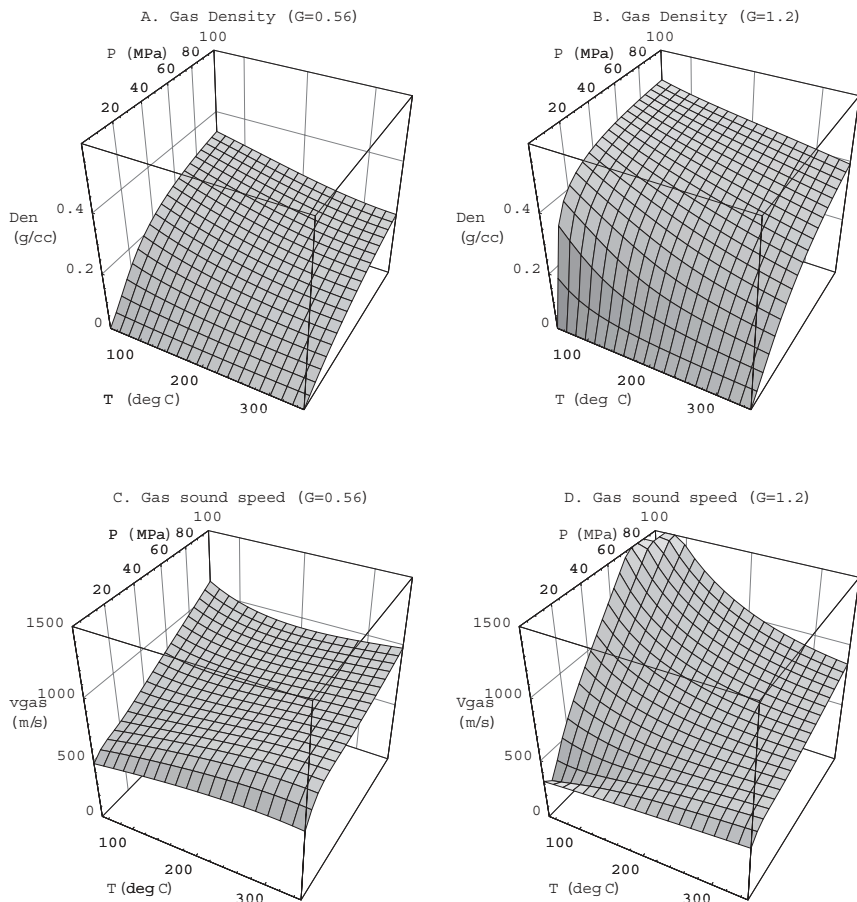


Fig. 4.1 Gas density and sound speed as a function of temperature (T), pressure (P), and gas specific gravity (G).

## 4.3 Oil

Oils are classified by American Petroleum Institute gravity ( ${}^{\circ}\text{API}$ ), which is in turn inversely related to the oil density at standard temperature and pressure.  ${}^{\circ}\text{API}$  gravity for oil ranges about 5–100. An oil with  ${}^{\circ}\text{API}$  gravity of 5 is basically tar, while  ${}^{\circ}\text{API}$  100 would be indistinguishable from a very heavy gas (say  $G=1.8$ ). Typical crude oils range from 30–45  ${}^{\circ}\text{API}$ . While crude oils with the same  ${}^{\circ}\text{API}$

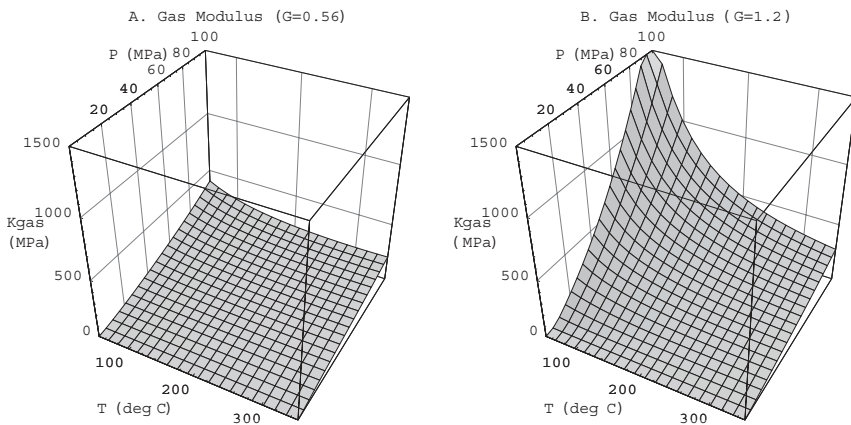


Fig. 4.2 Gas modulus as a function of temperature, pressure, and gas specific gravity (G).

gravity can have significant variability in composition and ability to absorb gasses, the API number is often the only description available [13]. It should also be noted that the results here are only valid for oils that stay constant in composition with changes in temperature and pressure.

The expressions given here are for live oil that contains saturation levels of dissolved gas. The equations include corrections for the dissolved gas, which can go in or out of solution as conditions vary. For oil calculations, the given and calculated quantities are

Given:	$P$	pressure	mPa
	$T$	temperature	°C
	°API	oil gravity	cc/g
	$G$	gas specific gravity	
Calculate:	$r_{oil}$	oil density	g/cc
	$v_{oil}$	oil velocity	m/s
	$k_{oil}$	oil modulus	mPa

## Elements of 3D Seismology

**4.3.1 Oil density.** The equations are

$$\rho_{oil} = \rho_G + (0.00277 P - 1.71 \times 10^{-7} P^3)(\rho_G - 1.115)^2 + 3.49 \times 10^{-4} P \quad (4.12)$$

$$\rho_G = (\rho_0 + 0.0012G R_G)/B_0 \quad (4.13)$$

$$\rho_0 = \frac{141.5}{API + 131.5} \quad (4.14)$$

$$R_G = 3.03 G (P \text{ Exp}[0.02878 API - 0.00377 T])^{1.205} \quad (4.15)$$

$$B_0 = 0.972 + 0.00038 \left[ 2.4R_G \sqrt{G/\rho_0} + T + 17.8 \right]^{1.175} \quad (4.16)$$

where the gas-oil ratio  $R_G$  is the volume ratio of liberated gas to remaining oil at atmospheric pressure and  $15.6^\circ\text{C}$  and  $B_0$  is Standing's volume factor. Figure 4.3 shows oil density variations with  $T$ ,  $P$ ,  $^\circ\text{API}$  and  $G$ . These demonstrate a curious behavior, density decreases with increasing pressure. This is due to an increased ability to support gas in solution as pressure increases.

**4.3.2 Oil modulus and velocity.** The equations are

$$k_{oil} = \rho_{oil} v_{oil}^2 / 1000 \quad (4.17)$$

$$v_{oil} = 2096 \left( \frac{\rho'}{2.6 - \rho'} \right)^{0.5} - 3.7T + 4.64P + 0.0115 \left[ 4.12 \sqrt{1.08/\rho' - 1} \right] T P \quad (4.18)$$

$$\rho' = \frac{\rho_0}{B_0 (1 + 0.001R_G)} \quad (4.19)$$

where  $\rho'$  is a pseudodensity based on expansion caused by gas intake. Oil modulus and velocity are shown in Figures 4.4 and 4.5 as functions of  $T$ ,  $P$ ,  $^\circ\text{API}$  and  $G$ .

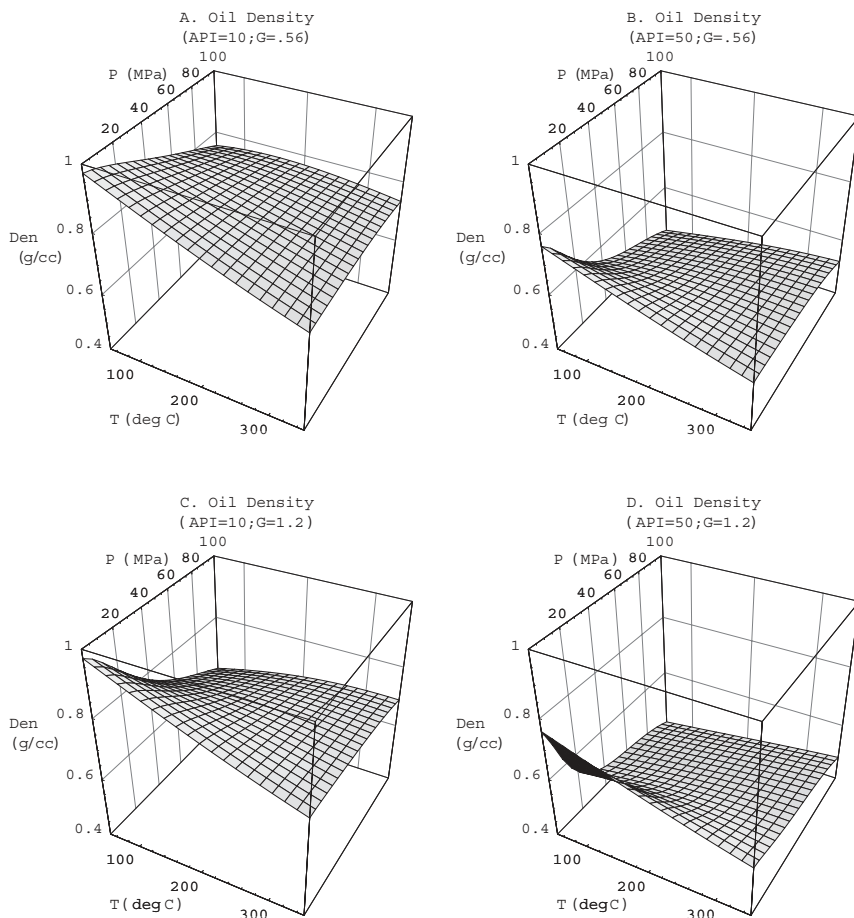


Fig. 4.3 Oil density as a function of temperature, pressure, oil gravity ( $^{\circ}$ API), and gas specific gravity (G).

All of these expressions could alternatively use the gas-oil ratio,  $R_G$ , as the independent variable rather than the gas specific gravity,  $G$ .

The plots given here differ significantly from the first edition, due to an earlier coding error. The present results have been verified by comparison with figures in the original article.

## Elements of 3D Seismology

### 4.4 Brine

Brine properties are a function of the salinity ( $S$ ), which is defined as the weight fraction of sodium chloride (ppm/1,000,000). This can range from  $S=0$  (pure water) to about  $S=0.35$  (350,000 ppm). For brine, the given and calculated quantities are

Given:	$P$	pressure	mPa
	$T$	temperature	°C
	$S$	salinity	ppm/1,000,000
Calculate:	$\rho_{br}$	brine density	g/cc
	$v_{br}$	brine velocity	m/s
	$k_{br}$	brine modulus	mPa

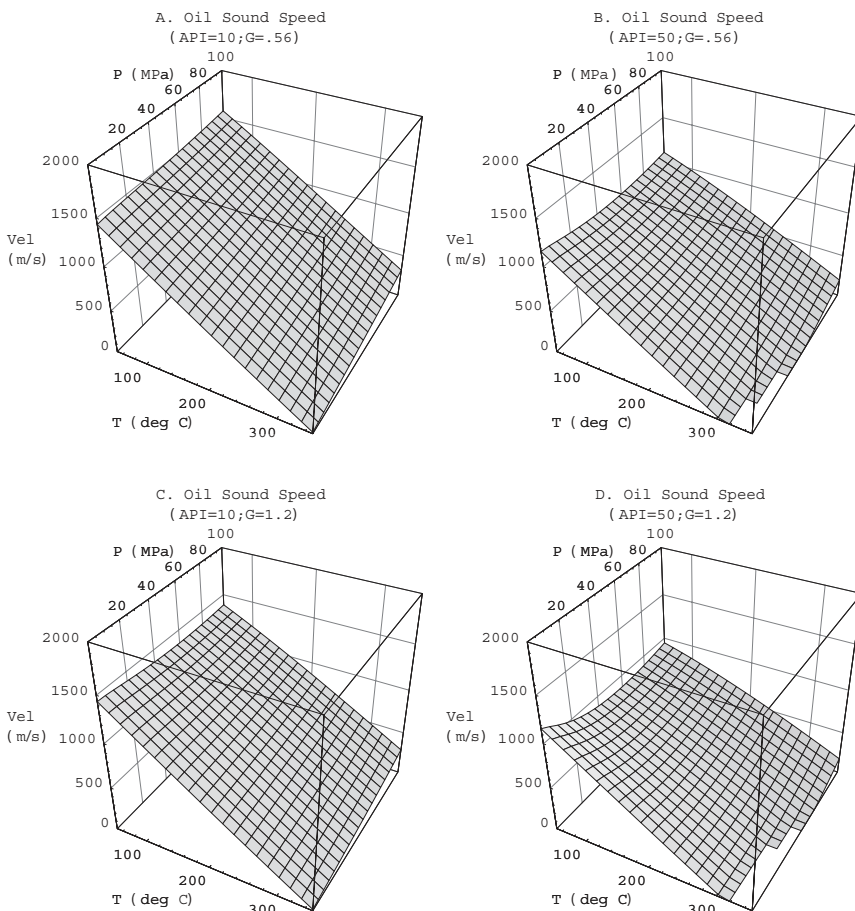


Fig. 4.4 Oil sound speed as a function of temperature, pressure, oil gravity (°API), and gas specific gravity (G).

**4.4.1 Brine density.** The equations are

$$\rho_{br} = \rho_w + S(0.668 + 0.44S + 10^{-6}(300P - 2400PS + T(80 + 3T - 3300S - 13P + 47PS))) \quad (4.20)$$

$$\rho_w = 1 + 10^{-6}(-80T - 3.3T^2 + 0.00175T^3 + 489P - 2TP + 0.016T^2P - 1.3 \times 10^{-5}T^3P - 0.333P^2 - 0.002TP^2) \quad (4.21)$$

where  $\rho_w$  is the density of pure water. Figure 4.6 shows brine density as a function of  $T$ ,  $P$  and  $S$ .

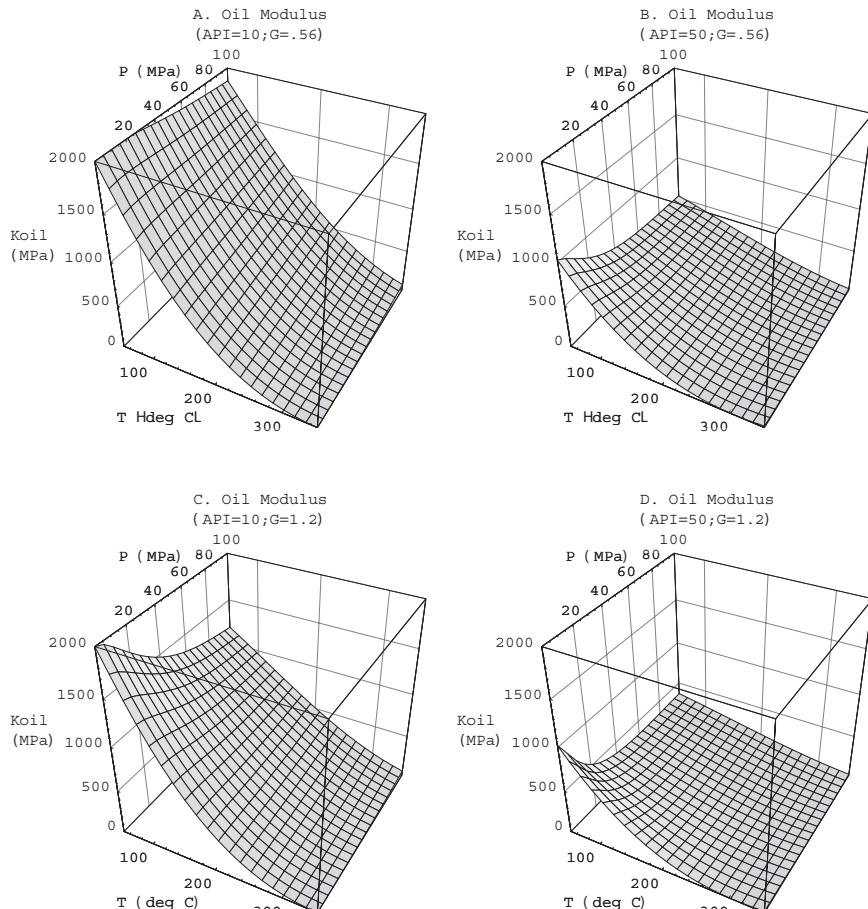


Fig. 4.5 Oil modulus as a function of temperature, pressure, oil gravity (°API), and gas specific gravity (G).

**4.4.2 Brine modulus and velocity.** The following equations apply:

$$k_{br} = k_{gf}/(1 + 0.0494R_g) \quad (4.22)$$

$$\begin{aligned} v_{br} = & v_w + S(1170 - 9.6T + 0.055T^2 - 8.5 \times 10^{-5}T^3 + 2.6P \\ & - 0.0029TP - 0.0476P^2) + S^{1.5}(780 - 10P + 0.16P^2) - 1820S^2 \end{aligned} \quad (4.23)$$

$$k_{gf} = \rho_{br} v_{br}^2 / 1000 \quad (4.24)$$

$$R_g = (0.712 \text{ Abs}[T - 76.71]^{1.5} + 3676 P^{0.64}) (10^{-4-7.786 S (T+17.78)^{-0.306}}) \quad (4.25)$$

$$v_w = \sum c_{ij} T^i P^j \quad (i = 0, 4; j = 0, 3) \quad (4.26)$$

where  $k_{gf}$  is the bulk modulus of gas-free brine. The last term in  $v_b$  is correct and supersedes a typographical error of  $820S^2$  in equation (29) of Batzle and Wang [13].

It is somewhat surprising that the most complicated expression in all this fluid work is the sound speed in pure water as a function of temperature and pressure. The 20(!) coefficients,  $c_{ij}$ , needed to calculate  $v_w$  are not given here but can be found in [13].

These expressions automatically account for modulus and velocity effects due to dissolved methane gas. Dissolved gas has a weaker effect on brine properties than oil properties and is usually insignificant. Thus  $G$  does not explicitly occur in the equations.

For brine velocity and modulus behavior, see Figures 4.6 and 4.7.

## 4.5 Fluid mixture

Gathering all this together, we want to calculate the net properties of a mix containing gas, oil, and brine. Two additional parameters are needed to describe the quantity of each component present. One way to describe the situation is using oil saturation,  $S_o$ , which is the volume fraction of oil, and gas saturation,  $S_g$ , which is the volume fraction of gas. The water saturation is then the remaining volume calculated from  $(1-S_o-S_g)$ . Of course the gas, oil, and water saturation will change as a function of temperature and pressure as gas goes in and out of solution. But at any given  $T$  and  $P$ , we are able to compute the desired quantities.

**4.5.1 Fluid density.** The density of a fluid mixture,  $\rho_f$ , obeys a simple mixing law that expresses the volume of each component and associates it with the appropriate density

$$\rho_f = (1 - S_g - S_o) \rho_{br} + S_o \rho_{oil} + S_g \rho_{gas} \quad (4.27)$$

subject to the constraint that  $S_o + S_g \leq 1$ .

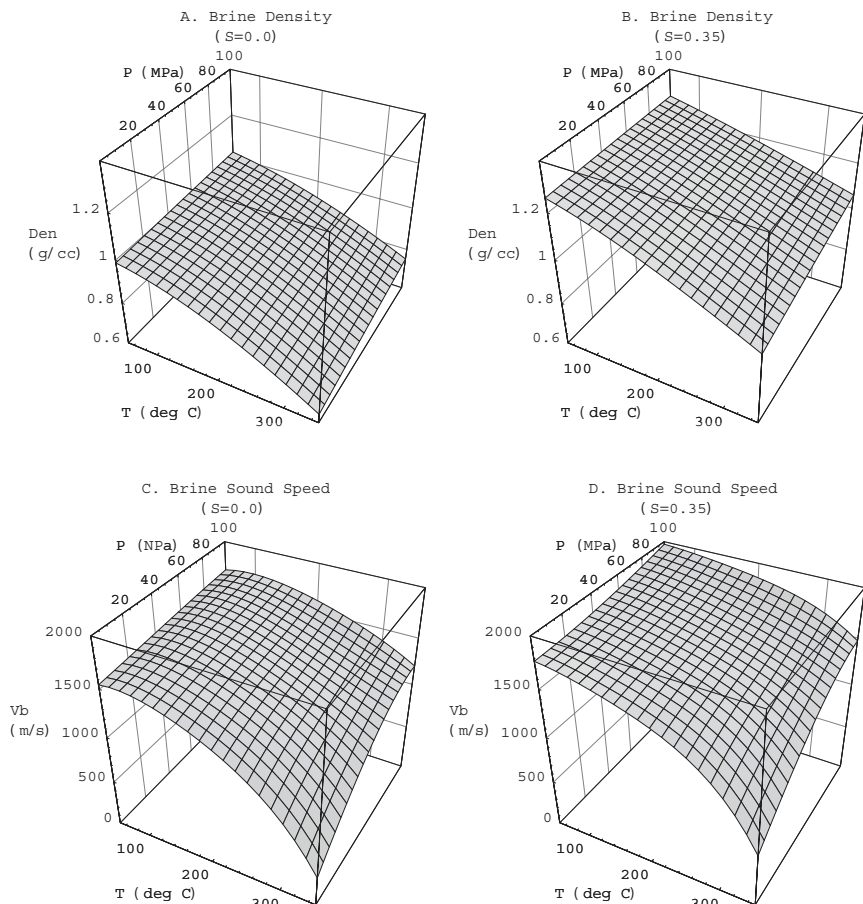


Fig. 4.6 Brine density and velocity as a function of temperature, pressure, and salinity (S).

## Elements of 3D Seismology

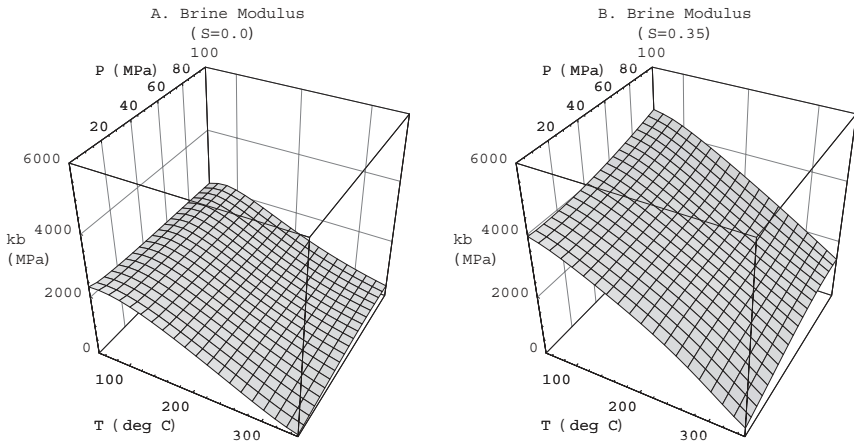


Fig. 4.7 Brine modulus as a function of temperature, pressure, and salinity ( $S$ ).

**4.5.2 Fluid modulus and velocity.** Fluid mixture modulus,  $k_f$ , involves saturations and bulk moduli averaged in a particular way

$$k_f = \left( \frac{1 - S_g - S_o}{k_{br}} + \frac{S_o}{k_{oil}} + \frac{S_g}{k_{gas}} \right)^{-1} \quad (4.28)$$

again subject to  $S_o + S_g \leq 1$ . Once the modulus and density are known the velocity is given by

$$v_f = \sqrt{1000 k_f / \rho_f} \quad (4.29)$$

Table 4.1 itemizes parameter ranges and dependencies. With the fluid mix properties depending on seven variables, it is not possible to capture all scenarios with a 3D plot or even a series of 3D plots. However, specific problems can be done, which isolate certain properties of interest. Consider for example a pore fluid mixture at 1 km depth and the same mixture at 6 km. The temperature and pressure (in centigrade and mPa) for each case can be estimated from the standard gradients

$$T = 25 z \quad (4.30)$$

$$P = 0.0107 z \quad (4.31)$$

where  $z$  is the depth in meters and we have used the hydrostatic gradient for pressure.

Quantity	Range	Units	Depends on
T	50–350	°C	
P	0.1–100	mPa	
G	.56–1.2		
°API	5–100	cc/g	
S	0–0.35	ppm/1 000 000	
$S_o$	0–1		
$S_g$	0–1		
$\rho_{gas}$	0.0015–0.5	g/cc	G, T, P
$v_{gas}$	200–1500+	m/s	G, T, P
$k_{gas}$	0.2–1500+	mPa	G, T, P
$\rho_{oil}$	0.38–0.95	g/cc	API, G, T, P
$v_{oil}$	200–2100	m/s	API, G, T, P
$k_{oil}$	200–2400	mPa	API, G, T, P
$\rho_{br}$	0.6–1.25	g/cc	S, T, P
$v_{br}$	200–1980	m/s	S, T, P
$k_{br}$	580–4700	mPa	S, T, P
$\rho_f$	0.0015–1.25	g/cc	API, G, S, $S_o$ , $S_g$ , T, P
$v_f$	200–2100	m/s	API, G, S, $S_o$ , $S_g$ , T, P
$k_f$	200–4700	mPa	API, G, S, $S_o$ , $S_g$ , T, P

Table 4.1 Reservoir fluid parameters, ranges, and dependencies. The net fluid property ranges ( $\rho_f$ ,  $v_f$ ,  $k_f$ ) are the extreme values of the individual component fluids.

At 1 km depth these expressions give  $(T,P)=(25,10.7)$  and the 6 km case is  $(T,P)=(150,64.2)$ . Fixed fluid properties for this example are salinity of 0.22, gas specific gravity of 0.56, and API gravity of 40. At each depth, we consider two scenarios: a brine-gas mixture and a brine-oil mixture.

Figure 4.8 shows sound speed in the fluid mixtures as a function of saturation. Clearly the effect of gas saturation is more dramatic than changes in oil saturation. For the 1 km depth case, introducing 10% gas lowers the velocity from 1700 m/s to about 400 m/s, a drop of 76.5%. This is the origin of the gas “bright spot” effect. The same volume fraction of oil only reduces velocity to 1600 m/s, a 5.9% drop, so people do not spend time discussing oil bright spots.

## Elements of 3D Seismology

Furthermore, the gas case is relatively flat between 20% and 80% gas saturation. This means that we have little ability to distinguish gas saturation from seismic data, but the presence of gas versus no gas has a strong effect on pore fluid velocity. The 1 km and 6 km brine-gas results indicate that the range of the gas effect is diminished with increasing depth. However, the oil saturation influence on velocity becomes greater with depth. This paradoxical result comes about from the increase in oil's ability to hold gas in solution with increasing pressure.

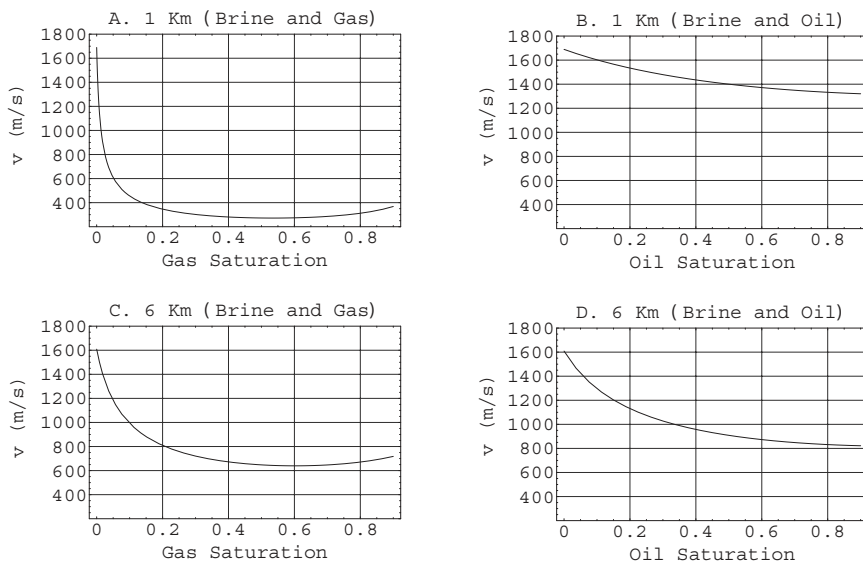


Fig. 4.8 Example fluid mixture velocity calculation. (A) and (C) Brine-gas mixture at 1 km and 6 km depths. (B) and (D) Brine-oil mixture at the same depths.

# 5

## Waves in Solids

An acoustic model of the earth is a useful first-order approximation. However, acoustic seismic simulation will not predict elastic effects (mode-converted waves, non-acoustic reflection amplitudes, etc.), and acoustic processing will deal with them improperly. Despite these limitations, industry practice at the current time is almost entirely acoustic seismic imaging, although there are circumstances where elastic effects cannot be ignored or yield fundamentally new information. In any case, it is important to understand the basic physics of elastic wave propagation.

An elastic material is a solid such as steel or glass. It is oversimplification to say that rock is an elastic material, since any rock we are likely to encounter has porosity and therefore falls under the category of poroelastic. But as we shall see, the behavior and characteristics of elastic media are the framework within which we understand porous solids.

The well of elastic wave theory is deep. A substantial library could be filled with the books published in this area from the early 1800s to the present. We will outline those features that serve our purpose of understanding current practice in petroleum seismology and point the interested reader toward two books as gateways to deeper aspects of the subject. First, chapter 13 of *Seismic Prospecting for Oil* [60] by Dix (sadly, a book now long out of print) is a wonderful introduction for the general reader. Second, volume one of *Quantitative Seismology* [3] by Aki and Richards is a comprehensive and readable survey of the mathematics and physics of elastic wave propagation.

### 5.1 Strain

Unlike fluids, a solid material can undergo deformation in response to applied forces. Inside the solid, it is useful to imagine a volume that has a cubic shape. When something happens to initiate forces in the solid, the cube can deform and

## Elements of 3D Seismology

move in various ways. If the cube changes shape in any way, it is said to be strained. For example, it can undergo contraction, shortening, lengthening, or shearing—these are all forms of strain. The cube can also move by rotation and translation in such a way that its shape does not change. These rigid displacements are not considered strains because the cubic volume does not change.

The mathematical description of strain necessarily involves the index notation that was introduced for fluid displacements. We consider a point in the solid material that has a certain rest position. The three space coordinates are taken to be

$$\underline{x} = (x, y, z) = (x_1, x_2, x_3) \quad (5.1)$$

and displacements from the rest position are

$$\underline{u}(u_x, u_y, u_z) = (u_1, u_2, u_3) \quad (5.2)$$

Each displacement is a function of time and all three space coordinates,  $\underline{u}(t, \underline{x})$ .

As an analogy, consider two people standing some distance apart and each holding an end of a rope. If they pull very hard, the rope will make a straight line between them, and for simplicity, we take this to be the rest position of the rope. We define the two people to be standing along the  $x_1$  coordinate and further define the  $x_3$  coordinate to be positive downward. With the rope pulled tight, the  $u_3$  displacement is zero, and the other two components of displacement will always be zero, unless the rope is somehow shifted toward one holder or flipped sideways.

Now imagine that the holders relax a bit, and the rope sags in the vertical direction. From experience, we know the rope will sag most in the middle and none at the end points. This sag is the vertical displacement as a function of the  $x_1$  coordinate,  $u_3(x_1)$ . If the holders change tension on the rope, then this displacement is also a function of time.

Strain is a measure of how displacements in a solid material change in space. Since there are three possible displacements, depending on three possible space coordinates, strain has nine components. Writing  $e_{ij}$  for the strain, it is defined by the dimensionless tensor quantity

$$e_{ij} = \frac{1}{2} \left( \frac{\partial u_i}{\partial x_j} + \frac{\partial u_j}{\partial x_i} \right) \quad ; \quad i, j = 1, 2, 3 \quad (5.3)$$

Returning to our rope analogy, we find the only nonzero displacement is in the 3-direction and it changes in the 1-direction, so the only nonzero strains would be

$$\begin{aligned} e_{31} &= \frac{1}{2} \left( \frac{\partial u_3}{\partial x_1} + \frac{\partial u_1}{\partial x_3} \right) = \frac{1}{2} \frac{\partial u_3}{\partial x_1} \\ e_{13} &= \frac{1}{2} \left( \frac{\partial u_1}{\partial x_3} + \frac{\partial u_3}{\partial x_1} \right) = \frac{1}{2} \frac{\partial u_3}{\partial x_1} \end{aligned} \quad (5.4)$$

While just an analogy, this result correctly points to the fact that strain is symmetric  $e_{ij}=e_{ji}$ .

The definition of strain is sufficient to describe all possible kinds of deformation. For example, pure compression of the cubic volume to make a smaller cube is a kind of strain called dilatation,  $\Delta$ ,

$$\Delta = \frac{\partial u_1}{\partial x_1} + \frac{\partial u_2}{\partial x_2} + \frac{\partial u_3}{\partial x_3} \quad (5.5)$$

which represents volumetric strain, or change in volume per unit volume. Other important quantities include three shear strains

$$\begin{aligned} e_{13} &= \frac{1}{2} \left( \frac{\partial u_1}{\partial x_3} + \frac{\partial u_3}{\partial x_1} \right) \\ e_{23} &= \frac{1}{2} \left( \frac{\partial u_2}{\partial x_3} + \frac{\partial u_3}{\partial x_2} \right) \\ e_{12} &= \frac{1}{2} \left( \frac{\partial u_1}{\partial x_2} + \frac{\partial u_2}{\partial x_1} \right) \end{aligned} \quad (5.6)$$

While it is far from obvious from these definitions, shear strain on a cube would have the effect of changing its shape while not changing its volume. In other words, whereas the opposite edges of a cube are all parallel, the new shape would have one or more edges not parallel while preserving the volume of the original cube.

## 5.2 Stress

Stress is the force per unit area that exists at interior points of a solid material. Pressure is a familiar form of stress, and units of pressure (Pascals, bars, psi, atmospheres, etc.) are also units of stress.

Since stress is force per unit area, we need to be specific as to which area we mean. Figure 5.1 illustrates that any point in the solid is the intersection of three perpendicular planes. Each dashed planar area is classified by its perpendicular axis. For example, in Figure 5.1A we see an area with orientation two, while the area in Figure 5.1B has orientation one.

A force acting at any point in the solid has three possible components, one along each coordinate axis as shown by the three lines at the center of each area. Stress,  $\tau_{ij}$ , is defined as the force in direction  $j$  acting on an area with orientation  $i$  where both indices can take on values from one to three. There are three possible area orientations and three possible force components, so stress has nine components. Like the strain, stress is a symmetric tensor  $\tau_{ij} = \tau_{ji}$ .

### 5.3 Hooke's law and elastic parameters

Strain is deformation in response to stress. Some solids are significantly deformed by small stresses, while other materials barely change even under high stress. This behavior is determined by elastic parameters of the material  $C_{ijkl}$  which relate the nine strains and nine stresses,

$$\tau_{ij} = C_{ijkl} e_{kl} \quad ; \quad i, j, k, l = 1, 2, 3 \quad (5.7)$$

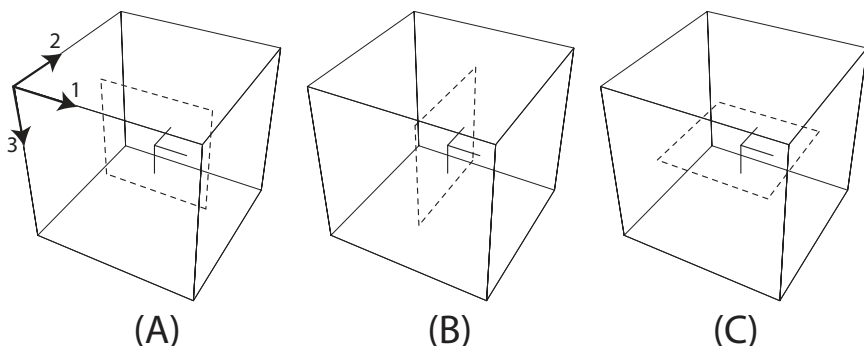


Fig. 5.1 Force and area orientations in a 3D solid. The coordinate directions are labeled 1, 2, and 3. In each volume, the dashed box represents a surface area whose orientation is determined by its perpendicular coordinate. The three lines in the center of each cube are the three possible force orientations associated with the dashed area.

In this kind of notation, a repeated index implies summation over that index. For example,  $w_i q_i$  would be shorthand for  $w_1 q_1 + w_2 q_2 + w_3 q_3$ .

The relationship between stress and strain is called Hooke's law, although the generalized form came much later than Robert Hooke (1653–1703). The object  $C_{ijkl}$  is a tensor of a higher order than stress or strain. It contains  $3 \times 3 \times 3 \times 3 = 81$  elastic parameters, also called stiffness coefficients. However, symmetry dictates there can be no more than 21 independent parameters. All other entries are linear combinations of these.

From a physical point of view, this equation might seem backward. After all, stresses cause strains not the other way round. The inverse form of Hooke's law is

$$e_{kl} = S_{klji} \tau_{ij} \quad (5.8)$$

where  $S_{klji}$  is the compliance tensor whose elements are combinations of the  $C_{ijkl}$ .

Tensor notation is an extreme example of compact notation. It is rather a nasty business to manually calculate something like a stress. Imagine that you are given functions describing the displacement field and the elastic constants. To calculate the first stress component we have

$$\tau_{11} = C_{11kl} e_{kl} \quad (5.9)$$

but the repeated  $kl$  in this equation is an implied summation over  $k=1,2,3$  and  $l=1,2,3$ . So the stress is given by

$$\tau_{11} = C_{1111} e_{11} + C_{1112} e_{12} + \dots [7 \text{ more terms}] \quad (5.10)$$

and every  $e_{kl}$  involves taking one or two derivatives. Now repeat this for the other eight components of  $\tau_{ij}$ , and you are up to around 135 derivatives. Although many of these are duplicates, these calculations are not something you would want to do every day.

Elastic materials can be simple (few parameters) or very complicated (many parameters). Like fluid bulk modulus, elastic constants have units of pressure. This comes from the general relationship

$$\text{stress} = (\text{elastic constants}) * (\text{strain}) \quad (5.11)$$

where stress is force per unit area and strain is dimensionless. As in the fluid case, density is an inertial parameter rather than an elastic constant.

We have seen that acoustic media supports one wave type and is characterized by density plus one elastic parameter (bulk modulus). The simplest elastic case, termed *isotropic elastic*, is described by density and two elastic parameters. Traditionally the two parameters are taken to be the Lamé parameter,  $\lambda$ , and the shear modulus,  $\mu$  (also called rigidity). Rigidity is related to the ability of the material to resist shear deformation. Even though there are only two independent elastic parameters, this important case has a long history, and there are several derived parameters commonly used in petroleum seismology. These include

$$\begin{aligned} k &= \lambda + \frac{2}{3}\mu \\ m &= k + \frac{4}{3}\mu \\ \sigma &= \frac{\lambda}{2(\lambda + \mu)} \end{aligned} \tag{5.12}$$

where  $k$  is the bulk modulus,  $m$  is the P-wave modulus, and  $\sigma$  is Poisson ratio. It is important to understand that there really are only two elastic parameters, but they can be combined in an infinite variety of ways to make secondary parameters.

These parameters relate back in a complicated way to the  $C_{ijkl}$ 's, for example

$$\begin{aligned} C_{1111} &= \lambda + 2\mu \\ C_{1122} &= \lambda \\ C_{1212} &= \mu \quad \dots \quad etc \end{aligned} \tag{5.13}$$

## 5.4 Equations of motion

Finding the equation of motion for a solid begins with kinetic and potential energy functions.

Kinetic energy in a solid is precisely analogous to the fluid case. A point of mass in the medium is displaced from its rest position by passage of a mechanical wave. The displacement is a function of time and the three space coordinates and the kinetic energy is

$$KE = \frac{\rho}{2} \left( \frac{\partial u_1}{\partial t}^2 + \frac{\partial u_2}{\partial t}^2 + \frac{\partial u_3}{\partial t}^2 \right) \quad (5.14)$$

where the mass density,  $\rho(\underline{x})$ , is in general a function of all three space coordinates,  $\underline{x}$ .

Part of our reason for developing the expressions for stress, strain, and stiffness coefficients was to set up the expression for elastic potential energy needed in this section. This is commonly called the strain energy function and is simply stress times strain,

$$\tau_{ij} e_{ij} = C_{ijkl} e_{kl} e_{ij} \quad (5.15)$$

where the last form follows from Hooke's law. Remember that all indices take on values from one to three, and a repeat index implies summation.

Since every index on the right side of this equation is repeated, the summation will run to completion leaving no indices at all. That is another way of saying the energy is a scalar quantity (not a vector or a tensor). At a particular point in space and time, the energy will be a number, like 7, but this number will change from point to point in the solid material and change with time.

With the elastic potential energy,  $PE$ , given by

$$PE = C_{ijkl} e_{kl} e_{ij} \quad (5.16)$$

we can form the Lagrangian as before,

$$L = KE - PE \quad (5.17)$$

and note that  $L$  still is a function of four coordinates

$$coordinates : \quad t, \underline{x} \quad (5.18)$$

and three field variables

$$field \ variables : \quad u_1(t, \underline{x}), u_2(t, \underline{x}), u_3(t, \underline{x}) \quad (5.19)$$

## Elements of 3D Seismology

but now there are up to 21 elastic parameters which can vary from point to point in the medium

$$\text{parameters : } C_{ijkl}(\underline{x}), \rho(\underline{x}) \quad (5.20)$$

forming an earth model through which the waves propagate.

From the Lagrangian, the action integral can be formed and the Euler-Lagrange equations invoked to give the equation of motion for 3D elastic waves in a general anisotropic solid,

$$\frac{\partial}{\partial x_j} \left[ c_{ijkl} \frac{\partial u_k}{\partial x_l} \right] - \rho \frac{\partial^2 u_i}{\partial t^2} = S_i \quad (5.21)$$

where  $S_i$  is the  $i$ th component of a force distribution representing the seismic source [3].

Simulation with this equation means we are given  $C_{ijkl}(x,y,z)$  and  $\rho(x,y,z)$ , and must calculate the displacements  $(u_1, u_2, u_3)$  as functions of  $(t, x, y, z)$ , thus simulating the evolving wave field. This is the direction that physics works (as in an earthquake), and the result is unique. Given the same elastic constants and density function, anyone would calculate the same wavefield.

On the other hand, inversion with this equation means we are given the wavefield displacements for all space and time and asked to find the medium parameters  $C_{ijkl}(x,y,z)$  and  $\rho(x,y,z)$ —a much harder problem. We are trying to run the physics backward, and the answer is inherently non-unique, meaning that an observed wavefield is consistent with any number of different parameter sets. The seismic inverse problem is made even more difficult because we only have the wavefield values as measured on the earth surface.

In practice, the goal of seismic data processing is not to do inversion in the sense used here, but to create an image of the subsurface. This image shows the location of boundaries or changes in  $C_{ijkl}(x,y,z)$  or  $\rho(x,y,z)$ . The difficulty of finding exactly which parameters are changing at each boundary and by how much is complicated by parameter coupling.

## 5.5 Wave types and speeds

In the isotropic elastic case, the medium parameters are  $(\lambda, \mu, \rho)$ , which we take for the moment to be constant. The equation of motion in this situation decouples into two wave equations corresponding to a longitudinal P-wave and a

transverse S-wave. The S-wave is called SV or SH as the particle motion is vertically or horizontally polarized. The P- and S-waves travel with speeds given by

$$\begin{aligned} v_p &= \sqrt{\frac{\lambda + 2\mu}{\rho}} \\ v_s &= \sqrt{\frac{\mu}{\rho}} \end{aligned} \quad (5.22)$$

and since  $\lambda$ ,  $\mu$  and  $\rho$  are all positive (by definition) it follows that  $v_p > v_s$ . It is common to characterize the elastic material by either  $(v_p, v_s, \rho)$  or  $(\lambda, \mu, \rho)$  as convenient. The wavespeed ratios are given by

$$\begin{aligned} \gamma &= \sqrt{\frac{\mu}{\lambda + 2\mu}} = \frac{v_s}{v_p} \\ \Gamma &= \sqrt{\frac{\lambda + 2\mu}{\mu}} = \frac{v_p}{v_s} \end{aligned} \quad (5.23)$$

For most rocks of interest to petroleum seismology  $v_s/v_p \approx 0.5$ .

In the vicinity of a free surface, another elastic wave can exist, which is a combination of P and S particle motion. This is the Rayleigh wave. While the air-earth interface is not exactly a free-surface, it is sufficiently close to allow the existence of Rayleigh waves. The exact Rayleigh-wavespeed,  $v_R$ , does not have a simple formula like the P- or S-wave. A common approximation (based on  $v_s/v_p = 0.577$ ) is  $v_R \approx 0.92 v_s$ . A much better approximation [111] for the Rayleigh wavespeed is given by

$$v_R \approx v_s \left[ \frac{20 - \sqrt{256\gamma^4 - 336\gamma^2 + 130}}{16\gamma^2 + 9} \right] ; \quad \gamma = v_s/v_p \quad (5.24)$$

Particle motion for the Rayleigh wave is counter clockwise (retrograde elliptical), near the free surface, and clockwise (prograde elliptical) below about one-fifth of a wavelength. All Rayleigh wave motion ceases below a depth of about one wavelength. Since the Rayleigh wave is essentially a 2D wave, it shows amplitude decay of  $1/\sqrt{R}$  and becomes increasingly predominant over 3D body waves (decay of  $1/R$ ) as we move away from the source.

The amount of energy that goes into each wave type depends on near surface elastic properties and the source geometry (point source, line source, etc.). The theory of source radiation patterns in elastic media can be found in White [200]. If measurements are made within about five wavelengths of the source location,

## Elements of 3D Seismology

there is incomplete separation of wave types. A good discussion of the character of elastic wave motion in this nearfield region can also be found in White [200] as well as Aki and Richards [3].

Figure 5.2 is a cartoon showing the four direct waves expected in land seismic data—air wave, P-wave, S-wave, and Rayleigh wave (labeled R). Each would appear as a linear event, whose speed could be estimated as described in Figure 3.3. For most earth models, the wavespeeds will relate to each other in this way

$$v_a < v_R < v_s < v_p \quad (5.25)$$

where  $v_a$  is the speed of sound waves in air.

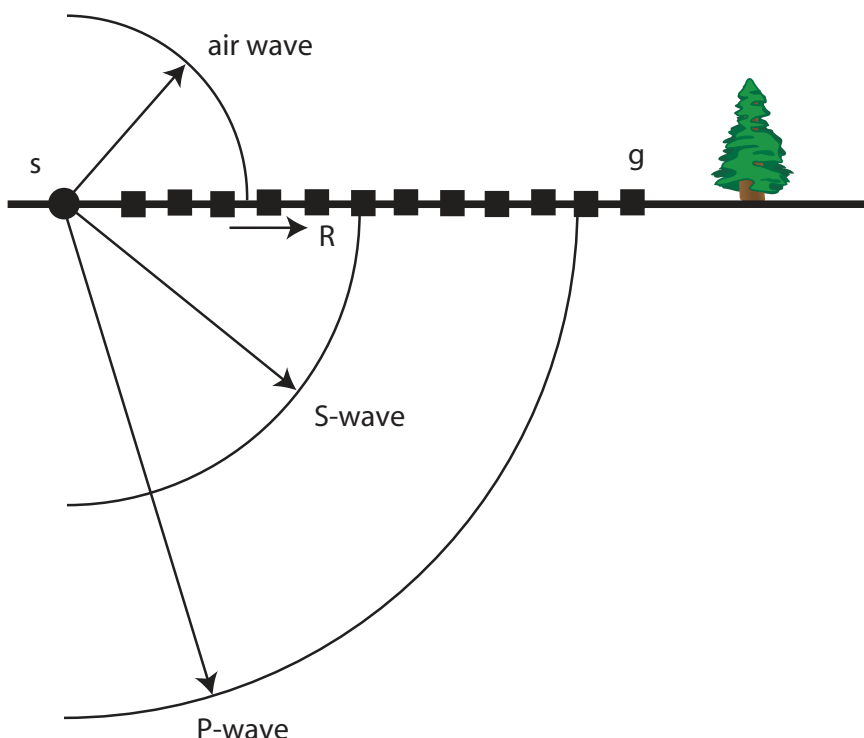


Figure 5.2 Rays and wavefronts for a source at the surface of an elastic half-space. The source is at  $s$ , each box is a receiver group location, and  $R$  is the Rayleigh wave traveling close behind the S-wave.

Figure 5.3 [131] shows an elastic wave simulation for a half-space with the following model parameters: P-wavespeed, 2 km/s; S-wavespeed, 1.2 Km/s; density, 2 g/cc. Plotted here are two amplitude components of the wavefield,  $A_x$  and  $A_z$ . The source is 10 m deep;  $(R_1, R_2)$  are two receiver positions. RW is the Rayleigh wave, S is the S-wave reflected from the free surface,  $S^*$  is a connecting wave between the Rayleigh wave and the reflected S-wave, and P is the direct P-wave with ghost.

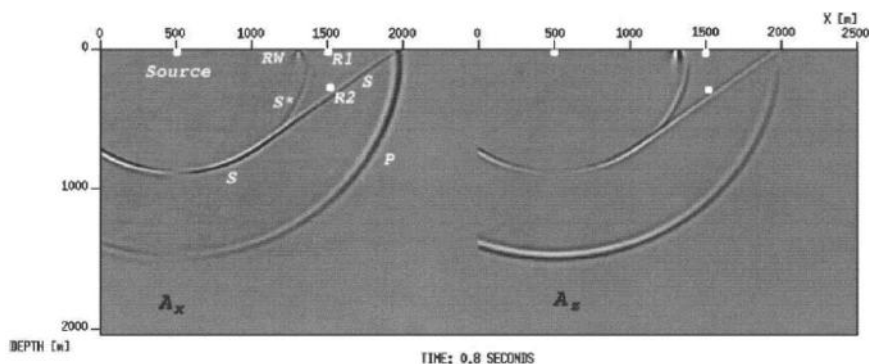


Fig. 5.3 Elastic wave simulation for a shallow buried source in a half space. The horizontal amplitude component is  $A_x$  and vertical component is  $A_z$ . Labeled waves include the Rayleigh wave (RW), reflected S-wave (S), direct P-wave with ghost (P), and the  $S^*$  wave connecting RW and S. (From [131]).

The same events are present on the  $z$ -component with different amplitudes due to the source radiation pattern and receiver directional sensitivity. The Rayleigh, shear, and  $S^*$  waves are elastic phenomena not present in acoustic modeling. Vector seismology is a term sometimes used to describe acquisition of multicomponent data and processing for elastic effects.

As with acoustic wavespeeds, we can have  $v_p(z)$ , etc. The worst case isotropic elastic scenario is  $v_p(x,y,z)$ ,  $v_s(x,y,z)$  and  $\rho(x,y,z)$ . The Earth is actually something like this, but it is difficult and expensive to treat it this way.

## 5.6 Mode conversion

Unlike acoustic waves, elastic waves can experience mode conversion at the point of reflection. Figure 5.4 shows all mode conversion possibilities for solid (elastic) and liquid (acoustic) media in contact. The rows show three possible

## Elements of 3D Seismology

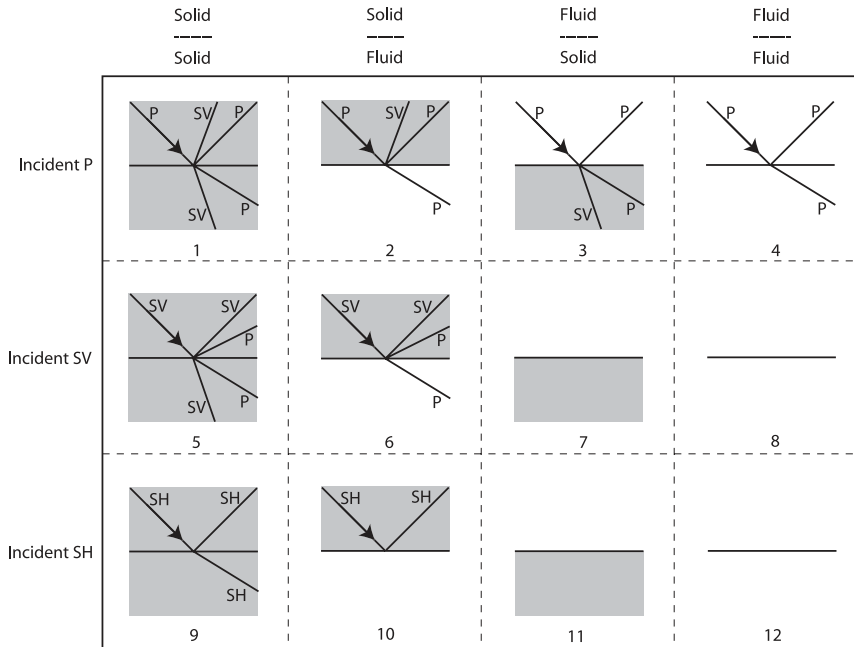


Fig. 5.4 Mode conversion cases for elastic waves. The wave types are compressional (P), shear-vertical (SV), and shear-horizontal (SH). The incident wave for each case has an arrowhead. Fluid media is shown white and solid media is gray.

incident wave types, P, SV, and SH, where the incident wave is always assumed to travel through the upper medium. The columns are associated with the four possibilities of fluid and solid contact.

A few of these cases are worthy of comment. Case 1 is the typical situation in the earth. An incident P-wave strikes an interface and is partitioned into four scattered waves: reflected P and SV and transmitted P and SV. This situation opens the possibility of mode-converted (PS) imaging where the event is a P-wave until reflection and an SV-wave from reflection point to receiver. Case 3 is typical of marine seismology, where the source is an air gun array in the water. This generates a P-wave that strikes the seafloor and partially mode converts to SV.

Case 2 shows a P-wave impinging on a solid-fluid boundary. This seems an unlikely scenario, but is very common if we just flip it upside down. Now it represents a P-wave exiting the solid earth and striking the seafloor from below

to a transmitted P-wave in the water column and reflected P and SV-waves in the solid. Case 9 shows that SH-waves do not mode convert at all, but remain a pure mode. Cases 7, 8, 11, 12 are blank because the incident wave is assumed to travel through the upper medium, and shear waves cannot travel through a fluid. Finally, we note that these results hold for oblique incidence. At normal incidence, no mode conversion occurs for any wave type.

## 5.7 Snell's law and critical angles

For an incident P-wave, all four scattering angles are determined by Snell's law. The general scattering angle relationship is

$$\frac{\sin(\text{incident wave angle})}{\text{incident wave speed}} = \frac{\sin(\text{scattered wave angle})}{\text{scattered wave speed}} \quad (5.26)$$

Applying this to the reflection geometry shown in Figure 5.5 we find

$$\frac{\sin \theta_{inc}}{v_{p1}} = \frac{\sin \theta_{rpp}}{v_{p1}} = \frac{\sin \theta_{rps}}{v_{s1}} = \frac{\sin \theta_{tpp}}{v_{p2}} = \frac{\sin \theta_{tps}}{v_{s2}} \quad (5.27)$$

where the known quantities are  $(\theta_{inc}, v_{p1}, v_{s1}, v_{p2}, v_{s2})$  and the unknowns are the four scattering angles  $(\theta_{rpp}, \theta_{rps}, \theta_{tpp}, \theta_{tps})$ .

Recall that in the fluid case, the critical angle was defined as that incidence angle which caused the transmitted wave angle to be 90 degrees. In elastic reflection, two critical angles are possible

$$\begin{aligned} \theta_{c1} &= \sin^{-1} \left( \frac{v_{p1}}{v_{p2}} \right) & ; & & v_{p2} > v_{p1} \\ \theta_{c2} &= \sin^{-1} \left( \frac{v_{p1}}{v_{s2}} \right) & ; & & v_{s2} > v_{p1} \end{aligned} \quad (5.28)$$

At the first critical angle, the transmitted P-wave bends parallel to the interface, and the SV-wave does so at the second critical angle.

## Elements of 3D Seismology

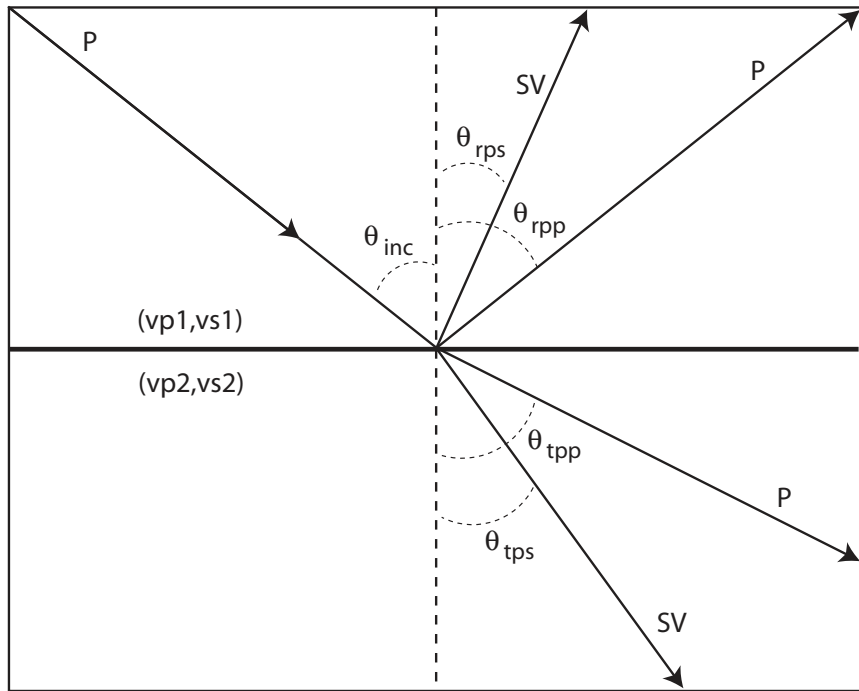


Fig. 5.5 Elastic reflection angles for an incident p-wave.

Consider, for example, a P-wave incident at  $20^\circ$  on an elastic interface separating media with these properties

$$(v_{p1}, v_{s1}, v_{p2}, v_{s2}) = (2600, 1500, 3000, 1800) \quad (5.29)$$

where all velocities are in m/s. The scattering angles are

$$(\theta_{rpp}, \theta_{rps}, \theta_{tpp}, \theta_{tps}) = (20^\circ, 11.4^\circ, 23.2^\circ, 13.7^\circ) \quad (5.30)$$

and the first critical angle is  $60.1^\circ$ . There is no second critical angle in this case because the P-wavespeed in medium 1 is greater than S-wavespeed in medium 2.

## 5.8 Velocity layering

All of the events and effects discussed in relation to layered fluids still apply in the layered solid case with the added complication of S-waves and mode-converted waves. For a single layer over a half space, we would have direct P, SV, SH, Rayleigh, and air wave direct arrivals, reflection events for P-P, P-SV, SV-P, SV-SV, SH-SH, headwaves for all these modes, and any combination of multiples.

Just considering the primary reflections for a stack of layers becomes very complicated. Imagine a P-wave hitting the first interface and generating four reflected and transmitted waves. Next, each of the downgoing rays strike another interface generating four events. The total number of downgoing events grows as  $2^N$  where  $N$  is the number of interfaces, but then each reflects and generates more rays on the way up.

The total count of primary reflections,  $C_{NM}$ , returned by an N-interface medium supporting M wave types that can mutually mode convert is

$$C_{NM} = \begin{cases} N, & M = 1 \\ \frac{M^2(M^{2N}-1)}{M^2-1}, & M = 2, 3, \dots \end{cases} \quad (5.31)$$

No mode conversion occurs in an acoustic medium because only one wave type is possible ( $M=1$ ). This means that only one primary reflection is generated at each interface and the total number of returned primaries is equal to the number of interfaces.

The isotropic elastic case of P-SV waves ( $M=2$ ) in a 10-layer earth model would return 1,398,100 reflections. If the layers are anisotropic, there are three possible wave types ( $M=3$ ) and the 10-layer case has about 3.9 billion primaries. Real data does not show this level of complexity, because most of these reflections are low energy events, but brute force ray tracing would require computing the amplitudes to figure out which events are important.

For a 10-layer acoustic case, there are 10 primaries. It is easy to see why people like to assume the earth is acoustic.

## 5.9 Elastic reflection coefficient

For a wave incident on a solid-solid interface, the amplitude associated with each of the reflected and transmitted waves is determined by the incident wave mode, the velocities and density in each medium, the scattered wave type, and the incidence angle. By far the most important case in petroleum seismology is an incident P-wave and reflected P-wave whose reflection coefficient we will call  $R_{pp}(\theta)$ .

## Elements of 3D Seismology

The boundary conditions which apply to elastic reflection are continuity across the interface of two displacements and two stresses. The conditions lead to a set of four coupled equations involving the scattering coefficients, the incidence angle, and the medium parameters. These are very complicated algebraic equations called the Zoeppritz equations.

The equations are well-represented in the literature [3]. We will examine elastic reflection behavior using three examples. Table 5.1 lists the parameters and critical angles for three different cases which correspond to Figures 5.6–5.8.

	Model Parameters						Critical angles	
	$v_{p1}$	$v_{s1}$	$\rho_1$	$v_{p2}$	$v_{s2}$	$\rho_2$	$\theta_{c1}$	$\theta_{c2}$
Figure 5.6	2.5	1.2	2.5	1.8	0.9	1.8	none	none
Figure 5.7	1.8	0.9	1.8	2.5	1.2	2.5	46°	none
Figure 5.8	1.8	0.9	1.8	3.5	1.9	2.5	31°	71°

Table 5.1 Model parameters for  $R_{pp}(\theta)$  plots in the figures indicated. Velocities are in km/s and densities are in g/cc.

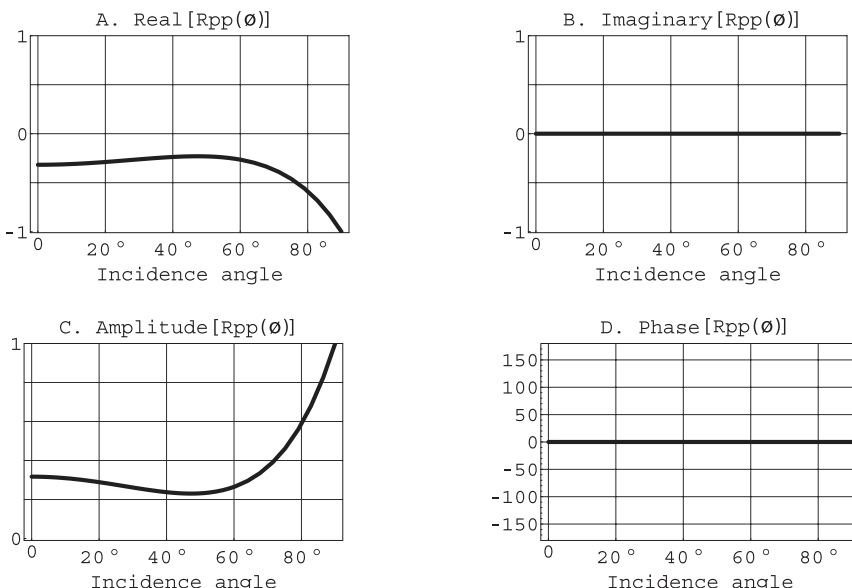


Fig. 5.6 Elastic  $R_{pp}$  reflection coefficient for a case with  $v_{p1} > v_{p2}$ . For model parameters see Table 5.1.

Figure 5.6 is a case where the upper P-wavespeed is greater than both the lower P-wave and S-wavespeeds. In this case,  $R_{pp}$  is negative for all angles of incidence. The imaginary part is always zero because there are no critical angles. Thus  $R_{pp}$  is purely real for all incidence angles. Its amplitude is (by definition) positive and approaches 1.0 at 90 degrees or grazing incidence. The phase is zero which follows from the imaginary part being zero.

In Figure 5.7, we have  $v_{p1} < v_{p2}$  but  $v_{p1} > v_{s2}$  meaning that the first critical angle  $\theta_{c1}$  exists but not the second. This critical angle of 46 degrees is evident in all of the plots as a point of discontinuity. One way to think of the critical angle is that for incidence angles less than  $\theta_{c1}$  both P and SV waves are transmitted into the lower medium. Beyond the critical angle only SV waves are transmitted. There is phase change beyond the critical angle as noted earlier for the acoustic reflection coefficient.

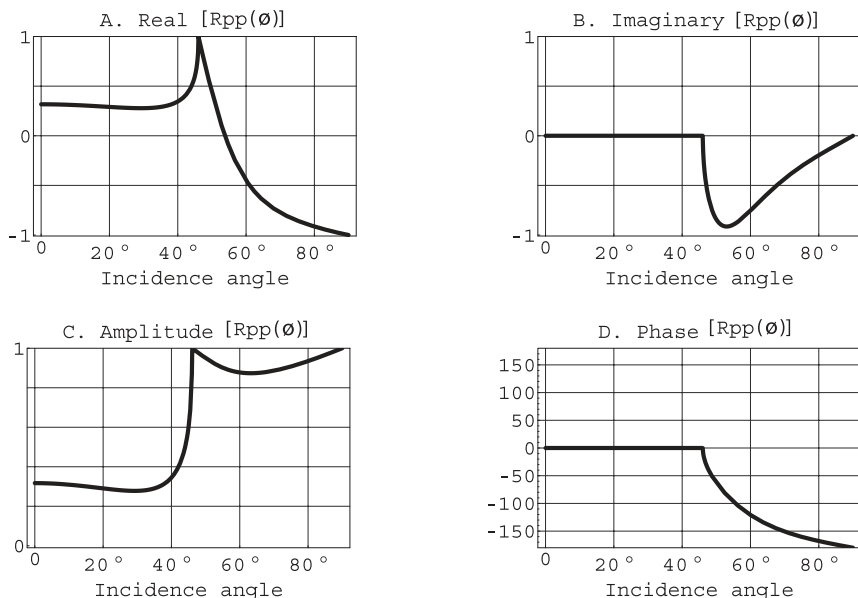


Fig. 5.7 Elastic  $R_{pp}$  reflection coefficient for a case where  $v_{p1} < v_{p2}$ , but  $v_{p1} > v_{s2}$ . The first critical angle is 46 degrees and there is no second critical angle. For model parameters see Table 5.1.

## Elements of 3D Seismology

The last case, Figure 5.8, is a very hard interface in which the lower  $P$  and  $SV$  wavespeeds are both greater than the incident  $P$ -wavespeed. Both first and second critical angles exist in this case, occurring at 31 and 71 degrees. This further complicates amplitude and phase behavior of the reflection coefficient.

It should be kept in mind that petroleum seismic data is acquired and processed in such a way that postcritical reservoir reflections are rarely encountered. The amplitude behavior utilized in AVO is variation in  $R_{pp}(\theta)$  at incidence angles less than critical.

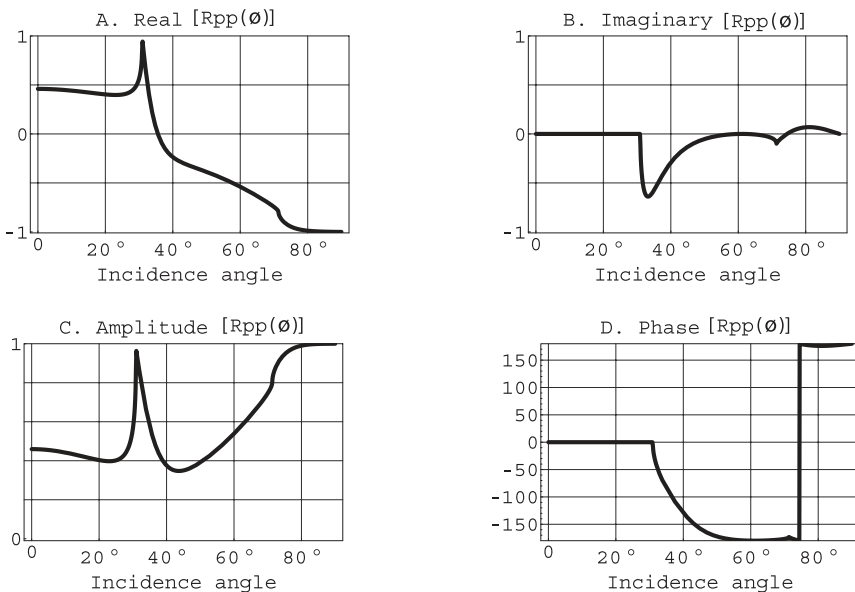


Fig. 5.8 Elastic  $R_{pp}$  reflection coefficient for a hard interface where  $v_{p1} < v_{p2}$  and  $v_{p1} < v_{s2}$ . The first critical angle is 31 degrees, and the second critical angle is 71 degrees. For model parameters see Table 5.1.

## 5.10 Reflection coefficient approximations

The exact Zoeppritz equations are very complicated, but it is often useful to work with approximate forms of  $R_{pp}$ . Many authors have published such approximations, including Bortfeld (1961), Aki and Richards (1980), Shuey (1985), Hilterman (1989), and Swan (1993) [22, 3, 166, 85, 172]. These approximations

vary in the assumptions made, including small parameter contrast across the boundary, small incidence angle, and small difference between incidence and transmission angle. Also, for a given set of assumptions, it is possible to write the resulting approximation in many ways.

Consider a P-wave incident on an interface with properties  $(v_{p1}, v_{p2}, \rho_1, v_{p2}, v_{s2}, \rho_2)$ . A widely used  $R_{pp}$  approximation due to Shuey [150] is

$$R_{pp}(\theta_{inc}) \approx A + B \sin^2 \bar{\theta} \quad (5.32)$$

where

$$\bar{\theta} = (\theta_{inc} + \theta_{tpp})/2 \quad (5.33)$$

is the average of the incident angle and the P-wave transmission angle, and where

$$A = \frac{1}{2} \left( \frac{\tilde{v}_p}{\bar{v}_p} + \frac{\tilde{\rho}}{\bar{\rho}} \right) \quad (5.34)$$

and

$$B = \frac{1}{2} \frac{\tilde{v}_p}{\bar{v}_p} - 2 \frac{\bar{v}_s}{\bar{v}_p} \left( 2 \frac{\tilde{v}_s}{\bar{v}_s} + \frac{\tilde{\rho}}{\bar{\rho}} \right) \quad (5.35)$$

In these equations an over-tilde implies parameter difference, as in  $\tilde{v}_p = v_{p2} - v_{p1}$ , and an over-bar means the parameters are to be averaged, as in  $\bar{v}_p = (v_{p2} + v_{p1})/2$ . This may not seem like a simple formula, but the exact equation would stretch out to several typeset pages.

This approximation, or one similar, is the physical basis for amplitude versus offset (AVO) analysis of prestack seismic data. The quantity  $A$  is the AVO intercept, and  $B$  is the AVO gradient.

Approximations such as this one are designed to work in the range of incidence angles and parameter contrasts likely to be encountered in petroleum seismology.

## 5.11 Anisotropy

Anisotropy is a general property of waves in which the wavespeed depends on the direction of travel (or particle motion). At any given point in the medium velocity,  $v(\theta)$ , depends on propagation direction where  $\theta$  is the propagation angle. Both P-waves and S-waves can exhibit anisotropy [179].

## Elements of 3D Seismology

Many pure solids, like quartz or calcite, have crystal symmetry that causes them to be anisotropic with respect to light or mechanical waves. This is the origin of double refraction in calcite, which is the strange effect of seeing two images when a calcite crystal is placed over text on a printed page. This is caused by light traveling at one of two speeds in the calcite, depending on its polarization direction. The same phenomena occur in seismic shear waves, where it is called shear wave splitting [52] or birefringence. It is hard evidence of anisotropy, as opposed to other factors that can mimic some anisotropic effects [204].

A classification scheme has developed in relation to anisotropy, the key terms being

- **VTI anisotropy.** This is the expected kind of anisotropy associated with a stack of thin isotropic layers [7]. It is thought to be common in shale sections throughout the world.
- **HTI anisotropy.** This is associated with vertical fractures and shear wave splitting.
- **Azimuthal anisotropy.** Associated with regional stress orientation. For example, waves traveling E–W might go faster than those traveling N–S.

In terms of elastic parameters, the simplest useful description of anisotropy involves two additional constants. The full parameter set for VTI or HTI media can be written as  $(v_{p0}, v_{s0}, \delta, \epsilon)$  and  $\rho$  where  $(v_{p0}, v_{s0})$  are vertical P- and S-wave velocities and  $(\delta, \epsilon)$  are dimensionless Thomsen anisotropy parameters [179]. The isotropic case corresponds to  $\delta = \epsilon = 0$ . Typical values of these parameters range from  $(-0.2, +0.2)$  but larger values in either direction are possible.

Both Thomsen parameters have physical interpretations. The speed of a horizontally traveling P-wave is associated with  $\epsilon$  through

$$v_{p90} = v_{p0}(1 + \epsilon) \quad (5.36)$$

The parameter  $\delta$  is related to the second-order moveout velocity for reflection from a horizontal interface,

$$t^2(x) = t_0^2 + \frac{x^2}{v_{p0}^2(1 + 2\delta)} + \frac{A_1 x^4}{1 + A_2 x^2} \quad (5.37)$$

where  $A_1$  and  $A_2$  are complicated functions of the four elastic parameters [178].

The consequences of anisotropy are many and varied:

- particle motion is not perpendicular to wavefronts,
- three wave types exist ( $qP$ ,  $qS1$ ,  $qS2$ ),
- phase and group velocity are not the same,
- moveout curves are non-hyperbolic, and
- the elastic reflection coefficient becomes a function of the Thomsen parameters.

Here is one way to think of anisotropy. In an isotropic homogeneous medium, a point source will emit waves which spread out in the form of an expanding sphere. This is a spherical wavefront. In an anisotropic homogeneous medium, the wavefront is not spherical, even though the velocity is constant from point-to-point. The wavefront will stretch, or run ahead, in the fast directions, and be delayed in the slow directions. Figure 5.9 shows two wavefronts using anisotropic parameters outside the normal bounds to make the wavefront deformation apparent. Earth parameters used to simulate these wavefronts are

$$\begin{aligned} \text{chalk} &: (v_{p0}, v_{s0}, \epsilon, \delta, \rho) = (5030, 2620, 0, 0.81, 2.7) \\ \text{shale} &: (v_{p0}, v_{s0}, \epsilon, \delta, \rho) = (3050, 1220, 0.28, 1.48, 2.3) \end{aligned} \quad (5.38)$$

where all velocities are in m/s and densities in g/cc.

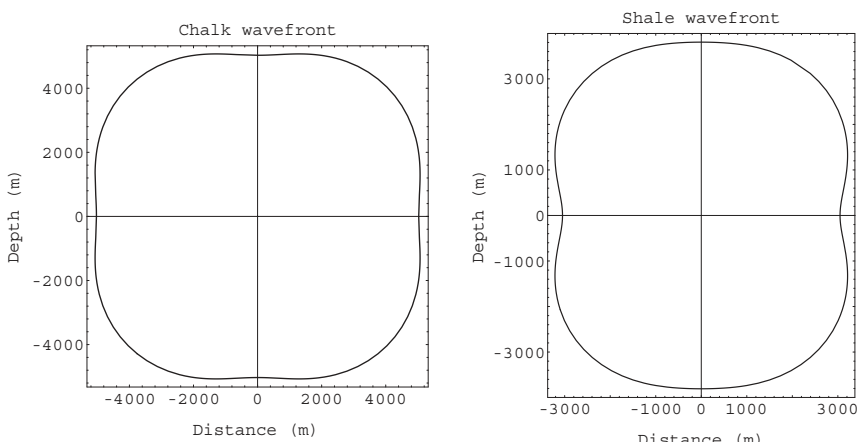


*Fig. 5.9 Wavefronts in anisotropic media are not circular even if the velocity is constant from point to point.*

## **Elements of 3D Seismology**

Intrinsic anisotropy, such as exhibited by mineral crystals, is unlikely to be encountered in petroleum seismic data because this would require an internal regularity of rock fabric that persists on a length scale of 100 meters or more. As for anisotropy induced by thin layering or fractures, it is sacred ground for some and ignored by others. There is probably a general consensus today that anisotropy of this kind is present in most real rocks but the P-wave effects are likely to be overpowered by lateral velocity variations.

The ability to account for P-wave anisotropy in seismic processing is now widespread. Where anisotropy can be demonstrated, it requires correction to avoid distortions that influence interpretation. Occasionally anisotropic effects can yield new and important information not available from an isotropic view of the subsurface. A prime example is fracture mapping from 3D P-wave seismic data [164].

# 6

## Waves in Porous Solids

### 6.1 Rock as a porous solid

In a broad sense, sedimentary rocks can be subdivided into siliciclastic (conglomerate, sandstone, shale, silt, mudstone) and carbonates (limestone and dolomite). Each group has detailed classification schemes that depend on mineralogy, rock fabric, grain size distribution, and other small scale properties. In petroleum seismology, we probe such rocks with 50–200 m wavelengths, and our waves are influenced only by the average properties over this kind of distance.

From a seismic point of view, a rock is a porous solid as shown in Figure 6.1. The solid frame of the rock is composed of one or more minerals forming grains and one or more cement-forming minerals that tie the grains together. We make the distinction because the cement minerals have a first-order effect on the overall stiffness and seismic velocity of the rock. For example, a quartz-cemented sandstone is likely to be a much stiffer rock than a sandstone with calcite cement.

But even among quartz cemented sandstones, there is a broad spectrum of stiffness from young, shallow, barely consolidated sandstone—so soft it can be crumbled by hand—to hard sandstone that a sledge hammer can barely break. That part of the rock, which is not solid, is the pore space, or porosity, expressed as a fraction (usually in the range 0.05–0.3). The pores are filled with a fluid mixture of gas, oil, and brine.

This broad-brush description may horrify a petrologist who studies the microscopic complexity of rocks or be deeply dissatisfying to a sedimentologist who classifies sandstones into categories like quartz arenite, subarkose, litharenite, etc. But these scientists have access to levels of detail in the rock unavailable from seismic measurements. As geophysicists, we tend to discuss rock types only in terms of their gross lithology, such as sandstone, shale, and limestone. From seismic measurements alone—without well log data or core measurements—we are fortunate to determine the nature of a rock formation to even this level of classification.

There is a long history of work relating seismic P-wave velocity to important rock parameters. We can segregate theories of this kind into two groups, empirical and physical (or physics-based).

### 6.2 Empirical relationships

Empirical wavespeed relationships are usually area-specific and serve as guidelines for calibration work. For example, one formula proposed in the 1950s for P-wavespeed [66] is

$$v_p = k(z T)^{1/6} \quad (6.1)$$

where  $k$  is a calibration constant,  $z$  is depth, and  $T$  is geologic age. Another form of this equation [67] is

$$v_p = k(z T L)^{1/6} \quad (6.2)$$

where  $L$  is a lithologic parameter, which serves in effect as a second calibration constant.

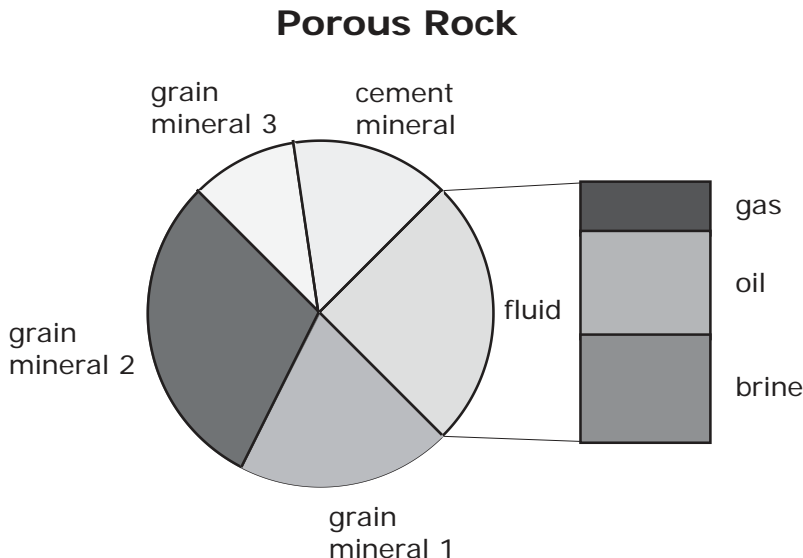


Fig. 6.1 From a seismic point of view, a rock is composed of grains, cement, and pore fluids.

There are also numerous equations relating velocity to electrical resistivity or other measurements available from well logging tools. Relationships such as these have generally fallen out of favor with geophysicists because a parameter such as depth is a composite of more fundamental parameters, including pressure, temperature, and mineralogy (through diagenesis and cementation). Similarly, geologic age is a proxy for many rock properties that deserve independent treatment.

Perhaps the most famous of the empirical velocity functions is the Wyllie [210] time average equation for P-wavespeed

$$v_p(\phi) = \left( \frac{\phi}{v_f} + \frac{1 - \phi}{v_m} \right)^{-1} \quad (6.3)$$

where  $\phi$  is porosity. The parameters ( $v_f$   $v_m$ ) are sound speeds associated with the pore fluid and pure mineral respectively. However, these values are not measured but thus serve as calibration constants.

To illustrate such a calibration process, consider the data points shown in Figure 6.2. These data are from the Glenpool field [97] of Oklahoma, specifically a well called the Self-82. The main producing formation in this area is the Pennsylvanian age Glenn sandstone and the digital log suite includes sonic and neutron porosity. There are 225 (velocity, porosity) pairs in the Glenn interval of 450–480 m depth. We see a trend of decreasing wavespeed with increasing porosity, which is typical behavior in sandstone. The data has significant scatter.

The Wyllie time average equation says this data trend has a certain mathematical form we can use in nonlinear regression. For calibration purposes, the Wyllie equation has one independent variable,  $\phi$ , one dependent variable,  $v(\phi)$ , and two parameters, ( $v_f$   $v_m$ ). If we choose initial values for ( $v_f$   $v_m$ ) and go to the first data point,  $v_1(\phi_1)$ , the equation will predict a velocity that is not equal to the observed value. This difference is calculated and accumulated for all points to form a number, which represents the misfit between this parameter set and the observed data. The next step is to update the parameters, and do it all again to get an improved misfit. The process is repeated until the misfit is minimized, meaning we have achieved the best possible fit of the data using the Wyllie equation.

This is an optimization problem and there are many ways to solve it, each with its own strengths and weaknesses. Key distinctions are selection of starting point, parameter update procedure, and definitions of the misfit function. For example, we could define the misfit as the squared difference of modeled and observed values, or the fourth power difference, or their absolute values, etc. Optimization theory is an enormous and rapidly evolving field, and the interested reader is referred to *Numerical Recipes* [149] as a starting point.

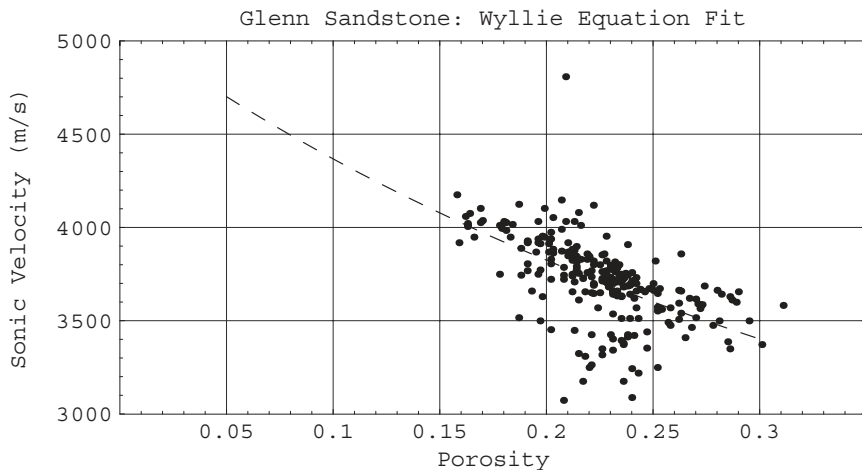


Fig. 6.2 Well log velocity-porosity points from the Glenpool Field of Oklahoma. The curve is the best fit solution using the Wyllie time average equation.

The result of calibrating the Wyllie equation against the Self-82 log data is shown as a dashed line in Figure 6.2, and the estimated parameters are  $(v_f v_m) = (1920, 5090)$  m/s. The fluid velocity seems consistent with brine and oil, while the matrix velocity is fairly close to the pure quartz P-wavespeed of 6050 m/s.

There are two kinds of uncertainty in this conclusion. First, we noted significant scatter of the input data. This strongly suggests that factors other than porosity are influencing the velocity. This uncertainty is not unique to the Wyllie equation and would be present for any equation we calibrated on this data. Second, we have uncertainty about the theoretical framework of the Wyllie equation. Smoothness of the calibration curve suggests it could just as easily have been made assuming a relationship like  $v_p(\phi) = a + b \phi + c \phi^2$ , or any number of others. In particular, our interpretation of pore fluid and matrix mineral is only as valid as the Wyllie equation itself.

We do not seek out more complicated equations for their own sake. It is attractive to use a simple equation. The danger is that results may not be meaningful. Next, we present the outline of a physics-based theory that is routinely and robustly used in seismic applications throughout the world.

### 6.3 Parameters

From earlier chapters, we already have an inventory of most parameters needed for mechanical wave propagation in a porous solid. The pore fluid is characterized by gas, oil, and brine parameters discussed in chapter 4. These

equations allow us to calculate density and bulk modulus for any mixture under reservoir pressure and temperature conditions. Since the solid part of the rock is an elastic material, it is characterized by two or more stiffness coefficients as described in the previous chapter. The porous rock case involves a few new parameters, including frame porosity, permeability, and fluid viscosity.

## 6.4 Equation of motion

Drawing on earlier results, we understand that expressions for the kinetic and potential energy will lead to the Lagrangian function, and then through the Euler-Lagrange equations to the equation of motion. Here we can describe the components of the energy functions without straying into the formidable mathematical notation and theoretical framework. The pioneering work in this field is due to Biot [19, 20], which is the headwater of a vast literature on the physics of porous solids including nonlinear theories [16].

Like any theory, Biot's work is based on certain assumptions [55]:

1. the fluid phase is connected, and disconnected pores are treated as a part of the solid matrix
2. the porous medium is statistically isotropic so that a 2D slice of any orientation would show a constant ratio of pore space to solid frame
3. the pore size is much smaller than the seismic wavelength
4. wave motion induces only small deformation
5. the solid matrix is elastic
6. no gravity is acting on density fluctuations induced by wave motion
7. no temperature changes are caused by dissipation of wave energy

Notice that assumption 2 is violated by fracture porosity, but this situation can be approximately dealt with by assuming porosity is uniformly distributed and the frame is anisotropic.

The kinetic energy for a fluid-filled porous solid is composed of several factors. These include contributions from the solid component and of the fluid mixture as seen in previous chapters. A third term is associated with local expansion and contraction of the constituents and a fourth is related to wave-induced flow of pore fluids relative to the solid frame. The relative flow will necessarily depend on permeability of the solid and pore fluid viscosity.

The potential energy (PE) for a porous solid involves individual contributions from the elastic frame and pore fluid as well as coupling terms linking the two together through porosity, permeability, and fluid viscosity. Inertial effects of relative motion between the fluid and solid frame are also included.

## 6.5 Wave types

When all of this is combined to generate the Biot theory equation of motion, it takes the form of coupled differential equations [25]. Solutions include P- and S-waves as well as a new kind of compressional wave called a Type II or Slow P-wave. Where the regular P-wave propagates primarily in the rock frame somewhat influenced by the pore fluids, the Type II wave is a sound wave in the pore fluid influenced by the rock frame [200]. It is as much diffusion phenomena as a propagating wave.

This wave exists only above a critical frequency, which is near 100 kHz [203] for rock materials, and thus it has no influence on conventional seismic data. However, it has been observed in ultrasonic core studies. In an air-filled sandpack, the Type II wave can occur at frequencies as low as a few hundred Hz [83].

Aside from the Type II wave, the primary contribution of the Biot theory is a recipe for computing composite P- and S-wavespeeds from knowledge of the elastic frame parameters, pore fluid properties, and environment parameters. This is a very important contribution since it relates seismically observable quantities back to reservoir properties.

## 6.6 Rock density

Density of the porous fluid-saturated rock obeys the mixing law

$$\rho_{sat} = \rho_m(1 - \phi) + \phi \rho_f \quad (6.4)$$

where the quantities are

$\phi$	fractional porosity	
$\rho_m$	mineral density	g/cc
$\rho_f$	pore fluid mixture density	g/cc
$\rho_{sat}$	saturated rock density	g/cc

The fluid density calls on all of the density calculations for gas, oil, brine, and the fluid mixture density equation. Mineral densities we are likely to encounter for petroleum reservoir rocks include quartz (2.65 g/cc) for sandstone and related rocks, calcite (2.71 g/cc) for limestone, dolomite (2.84 g/cc), and clay minerals (2–3 g/cc) for shale and clay-bearing sandstones. Clay mineral densities depend on precise mineralogy [195]. If more than one mineral is present in the rock matrix, a simple volume-weighted average can be used for  $\rho_{min}$ .

## 6.7 Gassmann theory and wavespeeds

While the Biot theory is powerful and elegant, it is overly complicated for simply estimating wavespeeds for use in elastic or acoustic calculations. Gassmann [75] has investigated the low-frequency limit of the Biot theory, and his results form the basis of common practice in reflection seismology. In the low-frequency limit, permeability and pore fluid viscosity have negligible influence and drop out of the theory.

The Gassmann theory allows us to calculate P and S velocities using

$$v_p = \sqrt{\frac{1000 (k_{sat} + 4 \mu_{sat}/3)}{\rho_{sat}}} \quad (6.5)$$

$$v_s = \sqrt{\frac{1000 \mu_{sat}}{\rho_{sat}}} \quad (6.6)$$

in terms of saturated rock moduli that can be written in the form [37]

$$k_{sat} = k_m \frac{k_d + Q}{k_m + Q} \quad (6.7)$$

$$\mu_{sat} = \mu_d \quad (6.8)$$

$$Q = \frac{k_f(k_m - k_d)}{\phi(k_m - k_f)} \quad (6.9)$$

where

$\phi$	fractional porosity	
$k_m$	frame mineral bulk modulus	mPa
$k_d$	dry porous frame bulk modulus	mPa
$k_f$	pore fluid mixture bulk modulus	mPa
$k_{sat}$	porous saturated rock bulk modulus	mPa
$\mu_m$	frame mineral bulk modulus	mPa
$\mu_d$	dry porous frame shear modulus	mPa
$\mu_{sat}$	porous saturated rock shear modulus	mPa

## Elements of 3D Seismology

One immediate consequence of the Gassmann theory is that shear modulus is independent of pore fluid ( $\mu_{sat}=\mu_d$ ), which means that S-wavespeed is only influenced by the effect pore fluid has on the saturated rock density. When we refer to parameters of the “dry” porous frame, this is understood to mean some level of irreducible fluid saturation because as the frame is literally dried out to zero fluid content, the properties of the frame change dramatically [203].

A key issue is the relationship between dry frame modulus and modulus of the mineral composing it. Imagine a block of pure mineral, such as quartz, which has bulk and shear moduli of ( $k_m, \mu_m$ ). As porosity is gradually introduced to make a porous frame, the moduli will necessarily change. We denote these porous frame moduli ( $k_d, \mu_d$ ). Both are functions of porosity and the pure mineral moduli

$$k_d = g(k_m, \phi) \quad (6.10)$$

$$\mu_d = g(\mu_m, \phi) \quad (6.11)$$

where  $g( )$  denotes a general function.

Aside from the fact that in the zero-porosity limit, the frame moduli and mineral moduli should be equal, there is no widespread agreement as to the nature of this function. In practice, a test function can be postulated [141], which includes one or more free parameters whose values are to be determined by a calibration procedure.

One such function is the three-parameter form

$$k_d \approx k_m (a_p + b_p \phi^{c_p}) \quad (6.12)$$

$$\mu_d \approx \mu_m (a_s + b_s \phi^{c_s}) \quad (6.13)$$

where  $(a, b, c)$  are free parameters of the theory and the subscripts correspond to P-wave or S-wave calibration constants. Special cases of this particular mathematical form include constant, linear and quadratic variation. Clearly, requiring  $a_p=a_s=1$  would assure correct behavior in the zero porosity limit, but we leave them as free parameters. This allows additional flexibility for regression in the presence of noise and uncertainty in real data.

In the usual Gassmann formulation, we need to know the shear modulus as a function of porosity. This is required even in the standard case where we only want to calculate the P-wavespeed. But finding the S-wavespeed of in-situ rock requires a full-waveform sonic log or laboratory measurement on cores. Often, neither is available. As an alternative, we use a formulation of the Gassmann theory that does not require knowledge of the shear wavespeed [128].

For this problem, the quantities given and to be found are

Given:	$k_m$	mineral bulk modulus	mPa
	$\mu_m$	mineral shear modulus	mPa
	$\rho_m$	mineral density	g/cc
	$k_f$	pore fluid mixture bulk modulus	mPa
	$\rho_f$	pore fluid mixture density	mPa
	$\phi$	fractional porosity	
	$a, b, c$	calibration parameters	

Calculate:	$m_{sat}$	saturated rock P-wave modulus	mPa
	$v_p$	rock P-wavespeed	m/s

The pure mineral properties used in sandstone and carbonate calculations are

$$\begin{array}{llll} \text{Quartz} & k_m = 37\,900 \text{ mPa} & \mu_m = 44\,300 \text{ mPa} & \rho_m = 2.65 \text{ g/cc} \\ \text{Calcite} & k_m = 76\,800 \text{ mPa} & \mu_m = 32\,000 \text{ mPa} & \rho_m = 2.71 \text{ g/cc.} \end{array} \quad v_p = 6050 \text{ m/s} \quad v_p = 6640 \text{ m/s}$$

The mineral P-wave modulus is given by

$$m_m = k_m + \frac{4}{3} \mu_m \quad (6.14)$$

which for quartz and calcite, respectively, work out to be 96,965 mPa and 119,465 mPa.

The heart of the P-wave only Gassmann theory is to substitute an equivalent P-wave modulus for each solid bulk modulus entry in Equations 188 and 190:

$$m_{sat} = m_m \frac{m_d + Q}{m_m + Q} \quad (6.15)$$

$$Q = \frac{k_f (m_m - m_d)}{\phi (m_m - k_f)} \quad (6.16)$$

As in standard Gassmann theory, it is necessary to know the modulus of the dry porous rock frame in terms of the mineral modulus and porosity. We use the form

$$m_d \approx m_m (a + b \phi^c) \quad (6.17)$$

where subscripts on the calibration constants have been dropped. Once  $m_{sat}$  has been calculated, P-wavespeed in the porous fluid-saturated rock is found using

$$v_p = \sqrt{1000 m_{sat} / \rho_{sat}} \quad (6.18)$$

You might wonder if something like the Wyllie equation can be coaxed out of the Gassmann theory. If all terms related to the dry frame are neglected, and all densities (fluid, mineral, and saturated rock) are assumed equal the Gassmann relationship becomes

$$v_p(\phi) = \left( \frac{\phi}{v_f^2} + \frac{1-\phi}{v_m^2} \right)^{-1/2} \quad (6.19)$$

an approximation involving the same parameters as Wyllie's relationship in equation 183. This can be fit to the Glenn sandstone data with  $(v_f v_m)$  being calibration constants as before (Figure 6.3).

In the porosity interval where we have data points, the fit lines are virtually identical. Numerical results of the Gassmann fit are  $(v_f v_m) = (2185, 5495)$  m/s compared to the Wyllie equation result  $(v_f v_m) = (1920, 5090)$  m/s. Our confidence in the fluid and mineral velocities found using the Gassmann approximation depend on reliability of the data points and validity of the assumptions leading to this equation. But, unlike the Wyllie equation, we know precisely what these assumptions are.

## 6.8 Attenuation and dispersion

Under the heading of attenuation, lie all those processes which conspire to weaken seismic wave amplitude with distance or time traveled. Some of these effects are present when waves propagate in fluids (geometric spreading, short period multiples, transmission losses), and others only occur when the medium is elastic (mode conversion). But when solids are porous, a different effect can come strongly into play and that is intrinsic absorption, the conversion of wave energy into heat. The terms attenuation and absorption are used interchangeably, while understanding the technical distinction. Figure 6.4 classifies various attenuation processes acting on seismic waves. In-depth discussion of attenuation and absorption is available in Aki and Richards [3].

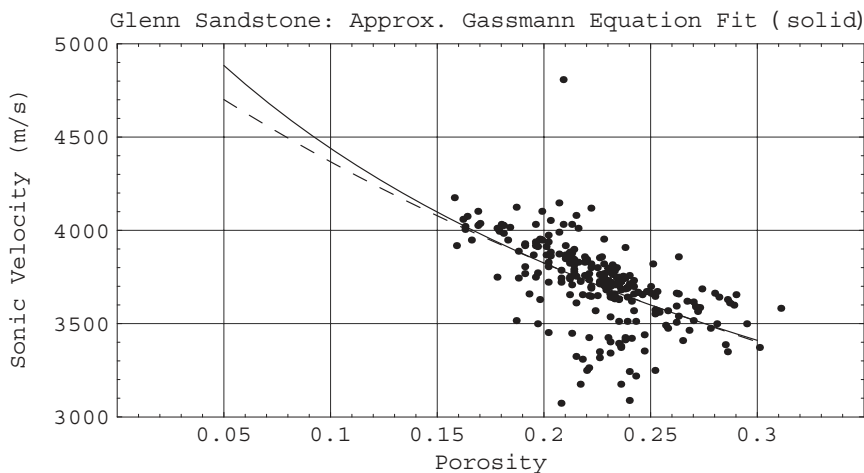


Fig. 6.3 Best fit solution to the Glenpool Field data using an approximation to the Gassmann Equation (solid line) and the Wyllie Equation (Dashed).

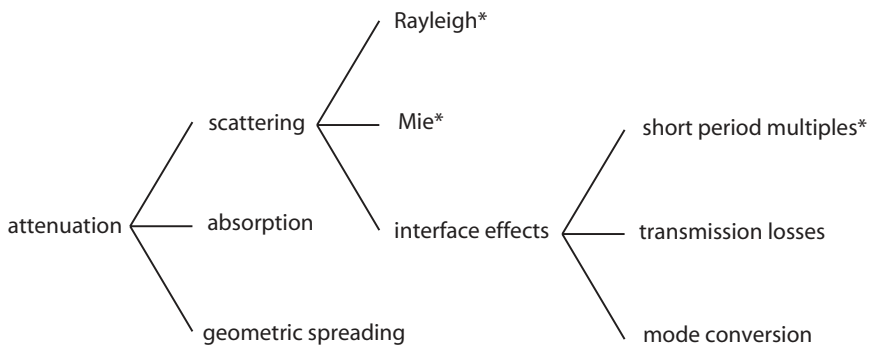


Fig. 6.4 Attenuation includes all processes which operate to cause amplitude decay in observed seismic data. Intrinsic absorption (conversion of wave energy to heat) is primarily associated with porous solids. Those attenuation processes marked with an asterisk can give rise to apparent absorption.

## Elements of 3D Seismology

Figure 6.4 also shows Rayleigh and Mie scattering [21] as attenuation effects. These relate to heterogeneities in the subsurface, which can include vugular porosity, rock fragment inclusions such as boulders in glacial terrain, karst features arising from large-scale dissolution of carbonate rocks, and irregularities associated with unconformity surfaces. From microscopic porosity to very large features, each kind of heterogeneity has a characteristic length scale,  $L$ . Scattering is controlled by a certain dimensionless ratio,  $R_s$  of this length scale to the seismic wavelength,  $\lambda$ ,

$$R_s = \frac{2\pi L}{\lambda} \quad (6.20)$$

There are three regimes to distinguish

$R_s < < 0.01$	no significant scattering
$0.01 < R_s < 0.1$	Rayleigh scattering (apparent absorption and anisotropy)
$0.1 < R_s < 10$	Mie scattering (strong app. absorption and possible diffractions)

Rayleigh scattering is familiar to most people, although they may not know it. White light from the sun scatters from molecules in the atmosphere, a process that is more effective at short wavelengths, while long wavelength (blue) light passes through relatively unaffected. This gives the sky its blue color. In the seismic case, this means Rayleigh scattering causes high frequency loss.

To put a scale on these scattering regimes, consider a seismic wave with  $\lambda=100$  m. No significant scattering will occur for objects much less than 0.15 m in size. Rayleigh scattering will occur for objects between  $L=0.15\text{--}1.5$  m and Mie scattering is operative for objects between  $L=1.5\text{--}15$  m. Typical pores in rock ( $L \approx 10^{-5}$  m) are so small they have no scattering effect at seismic wavelengths.

In seismic experiments, the source emits a pulse which can be decomposed by Fourier analysis into sine and cosine waves of fixed frequency, so there is no loss of generality in considering fixed-frequency waves. For a wave of frequency  $f$  that has been propagating  $t$  seconds in an absorbing medium, the amplitude  $A(t)$  is described by

$$A(t) = A_0 e^{-\pi f t / Q} = A_0 e^{-at} \quad (6.21)$$

where  $A_0$  is the amplitude measured at some reference position defining zero time,  $Q$  is the seismic quality factor, and  $a$  is the damping factor in units of dB/s. The dimensionless quantity  $Q$  is useful for describing the magnitude of absorption at length scales associated with surface seismic data to the shorter

wavelengths of sonic logging and ultrasonic measurements. The relationships between  $Q$  and the damping factor are

$$a = \frac{\pi f}{Q} \quad ; \quad Q = \frac{\pi f}{a} \quad (6.22)$$

showing the inverse relationship of these two parameters. Small  $Q$  corresponds to strong damping and large  $Q$  means little damping. Infinite  $Q$  implies no damping at all (a lossless medium).

Since time is distance divided by velocity, this can also be written as spatial absorption

$$A(x) = A_0 e^{-\pi f x / (vQ)} = A_0 e^{-\alpha x} \quad (6.23)$$

where  $\alpha$  is called the absorption coefficient and its relation to  $Q$  is

$$\alpha = \frac{\pi f}{v Q} \quad ; \quad Q = \frac{\pi f}{v \alpha} \quad (6.24)$$

where  $v$  is the wavespeed. Note that  $\alpha$  (like  $a$ ) is a parameter of the medium and not frequency dependent. Units for  $\alpha$  are often stated as decibels per wavelength,  $dB/\lambda$ . For most rocks this lies in the range of 0.2–0.5  $dB/\lambda$ . In these units, the absorption coefficient is approximately [51] related to  $Q$  by

$$\alpha \sim 27/Q \quad ; \quad \text{units : } dB/\lambda \quad (6.25)$$

where  $Q$ , as always, is dimensionless.

To give an example, consider 30 Hz seismic data in an area with velocity of 3000 m/s and  $\alpha=0.25$   $dB/\lambda$ . The wavelength is 100 m. For a reflector 1 km deep, the reflected wave will travel 20 wavelengths and absorption will diminish the wave amplitude by

$$A(x) = A_0 e^{(-0.25 dB/\lambda)(20 \lambda)} = A_0 e^{-5} = 0.0067 A_0 \quad (6.26)$$

## Elements of 3D Seismology

Converting the multiplying factor in the last step to decibels, we find the 30 Hz wavefield is 22 dB down just due to absorption. The 3D geometric spreading loss for this example is also 22 dB.

But absorption does more than just diminish the wave amplitude, it also has the effect of carving away high frequencies relative to low frequencies. To see this, take the previous example but change the wave frequency to 90 Hz. The wavelength is now 33 m, so there are about 60 wavelengths down and back to a 1 km target. The absorption loss for 90 Hz is

$$A(x) = A_0 e^{(-0.25 \text{ dB}/\lambda)(60 \lambda)} = A_0 e^{-15} = (3.1 \times 10^{-7}) A_0 \quad (6.27)$$

or 65 dB down, while geometric spreading is still 22 dB because it is not frequency dependent.

This calculation highlights the fact that absorption acts more aggressively on high frequencies. Absorption in the earth is such that even if we drive very high into the ground, only something like 10–100 Hz comes back. The frequencies above 100 Hz are lost to attenuation. This is evident in Figure 6.5, which shows Fourier amplitude spectra for a shallow portion and deep portion of one marine seismic trace. The loss of high frequency deep in the data is due to absorption and other factors that preferentially erode high frequencies.

Different kinds of waves (P, S, Rayleigh) can have different quality factors ( $Q_p, Q_s, Q_R$ ) and associated attenuation constants ( $\alpha_p, \alpha_s, \alpha_R$ ). When  $Q$  is discussed without reference to wave type, it is safe to assume  $Q_p$  is intended. Seismic  $Q_p$  of consolidated sedimentary rocks is in the range 50–300.

A necessary consequence of absorption is that wavespeed becomes a function of frequency, a phenomena called velocity dispersion [3]. For a given  $Q$  value the P-wavespeed at a particular frequency is given by

$$v(f) = v(f_r) \left[ 1 + \frac{\ln(f/f_r)}{\pi Q} \right] \quad (6.28)$$

where  $f_r$  is a reference frequency and  $v(f_r)$  is the velocity at the reference frequency. As an example, consider a wave measured at 20 Hz to have a wavespeed of 2000 m/s. For a sonic log operating at 15 kHz, the observed velocity will depend on the value of  $Q$ .

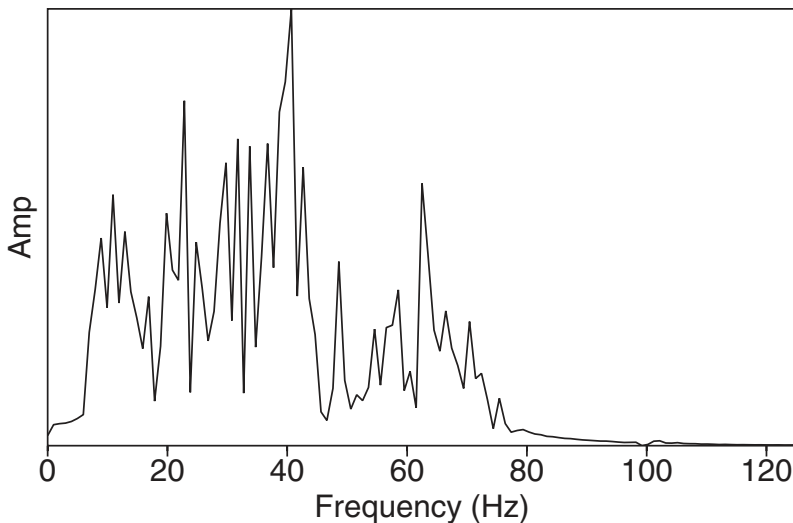
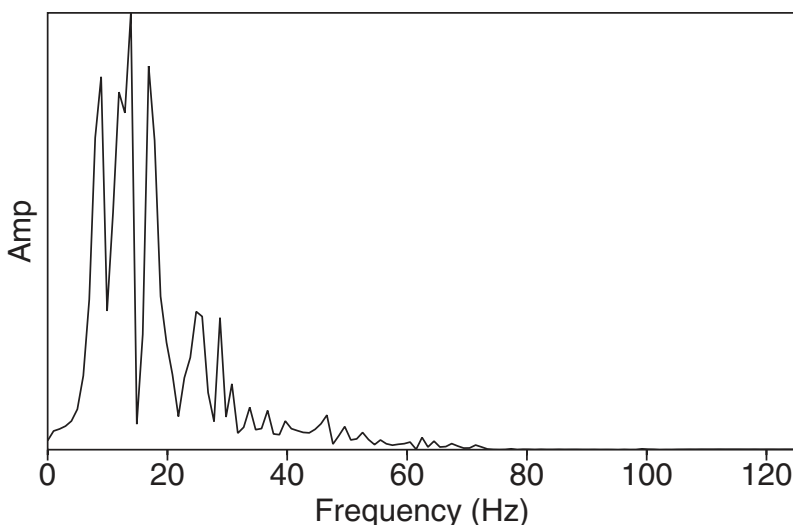
**A. Amplitude Spectrum (1.5-2.5 s)****B. Amplitude Spectrum (4.5-5.5 s)**

Fig. 6.5 Absorption and related processes cause loss of high frequency energy in seismic reflection data. (A) Fourier amplitude spectrum for a single marine seismic trace in the window 1.5–2.5 s. Bandwidth is 5–80 Hz. (B) Amplitude spectrum from the same trace in the window 4.5–5.5 s. Due to loss of high frequencies, bandwidth is now 5–30 Hz.

Figure 6.6A shows that for  $Q=50$ , the sonic velocity will be 2085 m/s, for  $Q=100$  it will be 2045 m/s, and for  $Q=300$  the velocity is 2015 m/s. Which velocity is correct? They all are. Dispersion makes for a strange world. Plotting the same results on a log-linear plot, Figure 6.6B, shows the linear relationship between wavespeed and log-frequency for any  $Q$ .

### 6.9 Rock velocity ranges

From our understanding of the factors affecting porous rock velocity, it is not surprising that wavespeed in real rocks is highly variable. Table 6.1 gives a list of velocity and density ranges derived from various published sources. The sound speed in air as listed in the table is only an average value. A good approximation at standard pressure can be obtained using

$$v_{air} = 331.4 + 0.6 T_c \quad (6.29)$$

where  $T_c$  is the temperature in centigrade, and the velocity is in m/s.

The high velocity and density cases for rock types in Table 6.1 correspond to very low porosity and strong cementation. The extreme opposite case occurs near the surface of the earth, where chemical and mechanical processes act to break down competent rock. This is termed the weathering layer or low-velocity layer (LVL). Cox [51] gives an extensive list of near-surface materials and their properties, a few of which are listed in Table 6.2. Values of  $Q$  in the weathered layer can range 2–10, which has the effect of strongly filtering high frequencies out of the seismic wavefield. Variations in weathering layer thickness and velocity cause traveltime delays (called static shifts) in reflected arrivals.

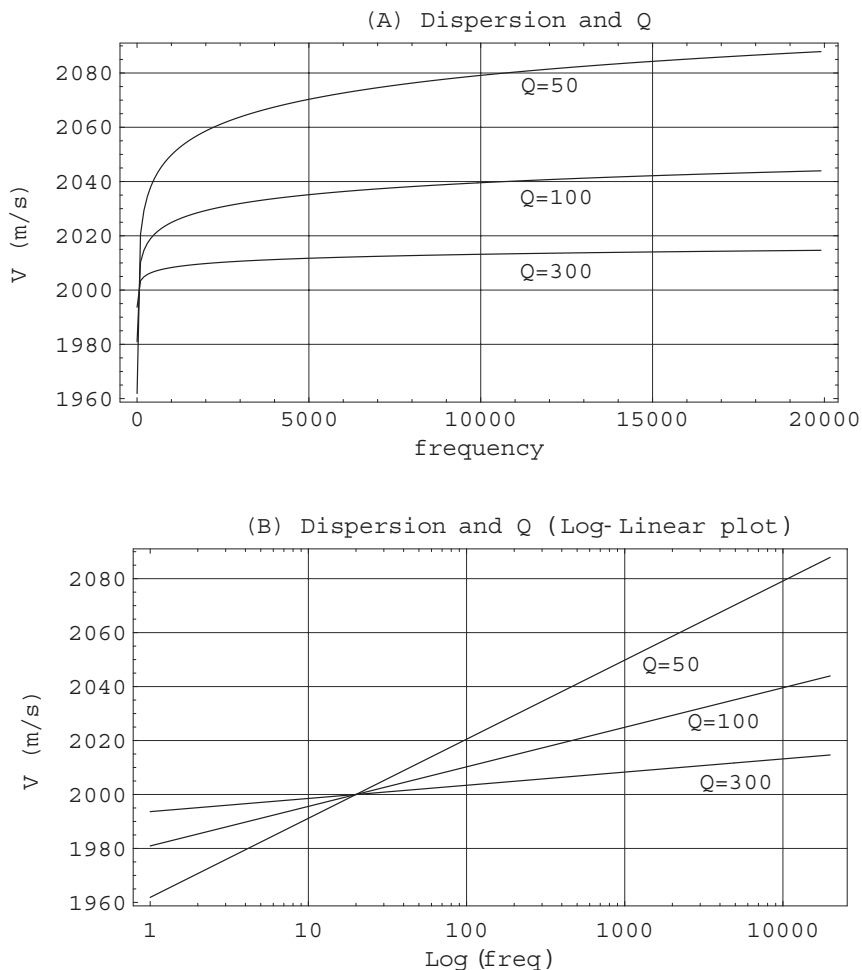


Fig. 6.6 In attenuating media velocity becomes a function of frequency, a phenomena called dispersion. (A) In this example a wave is measured at 20 Hz to have a wavespeed of 2000 m/s. The velocity that would be measured on a 15 kHz sonic log depends on the  $Q$  value. (B) The same results on a log-linear plot demonstrate that velocity varies linearly with  $\log$  (frequency).

## Elements of 3D Seismology

Material	Vp (m/s)	Vs (m/s)	$\rho$ (g/cc)
Air	332		0.0013
Water	1400–1600		1
Sandstone	2000–4300	700–2800	2.1–2.4
Chalk	2200–2600	1100–1300	1.8–3.1
Limestone	3500–6100	2000–3300	2.4–2.7
Dolomite	3500–6500	1900–3600	2.5–2.9
Salt	4450–5500	2500–3100	2.1–2.3
Granite	4500–6000	2500–3300	2.5–2.7
Basalt	5000–6400	2800–3400	2.7–3.1
Quartz	6049	4089	2.65
Calcite	6640	3436	2.71

Table 6.1 Approximate range of P-wave velocity, S-wave velocity, and density in rocks and other materials (from various sources, including [141] and [128]). Actual values for a specific rock and depth cannot be generally predicted but must be measured.

Material	Vp (m/s)	Vs (m/s)
Aerated soil	170	
Loam	800–1800	
Clay	300–2500	100–600
Glacial till (dry)	430–1040	
Glacial till (saturated)	1730	
Sub waterbottom mud	45–1500	

Table 6.2 Properties of some unconsolidated near-surface materials (selected from [51]).

## Part II

*Acquisition:  
Gathering Seismic Data*

# 7

## 2D Land Acquisition

Acquisition geometry for 2D seismic data contains many elements common to 3D acquisition. We will review 2D acquisition by going, in detail, through items in the geometry section of the line header for a specific West Texas seismic line (Fig. 7.1) shot for Unocal in 1990. Where it will clarify matters, throughout the description the original item name will be placed in capitals and parentheses (e.g., *traces/record*) for reference. In this chapter, we deviate from the preferred metric system because the line header lengths are in English units. However, the concepts given here are equally valid for a 2D seismic line shot with metric intervals. Rather than go pedantically through the items from first to last, we subdivide them into topics.

With respect to the general topic of seismic data acquisition, there are a number of ways to subdivide the subject [100]. A natural one is land, marine, and transition zone. A second is to consider subsystems—source, receiver, recording, positioning—but this classification depends heavily on the application. A third approach is to distinguish hardware from field procedures. In general, we follow the third approach here.

### 7.1 Historical summary

The history of reflection seismology using artificial sources stretches back on theoretical grounds into the late 1800s [196], but the application to petroleum exploration can be associated with the year 1917. At that time, Fessenden was granted a U.S. patent for the use of reflected and refracted sound waves to locate mineral bodies. From that time forward, there is a long, storied history associated with development and commercialization of reflection seismology, including the first seismic oil discovery in 1924 (Orchard field, Fort Bend County Texas), formation of Geophysical Research Corporation in 1925, and widespread use by the 1930s.

## Elements of 3D Seismology

From the earliest days, land seismic data was shot in a non-overlapping fashion termed *100% coverage*. By this we mean the first shot had a spread of receivers, and the second shot was placed (usually) half way into that spread so reflection points (for a horizontal layer) were continuous. Things changed in 1956, when Harry Mayne was granted a patent for common reflection point seismic profiling. This shooting technique generates a multiplicity of data associated with each reflection point in the earth that can be exploited to vastly improve the quality of subsurface information. Under the name common midpoint (CMP) shooting, this technique is at the heart of all modern 2D and 3D seismic acquisition techniques.

## 7.2 Hardware

**7.2.1 Source.** This line was shot using vibroseis, a controlled source patented in 1954 by Crawford and Doty of Conoco [53]. Previous to this time, explosives were the exclusive land seismic source. The advantages offered by a controlled land source are compelling, including safety, reduced environmental damage, efficiency, and ability to tailor the source spectral content and power.

Think of reflection seismology as an echo location technique (which it is), and imagine you are standing on a scenic overlook trying to induce an echo from a distant canyon wall. If you shout “I” you will shortly hear the sound “I” come back. It will be weaker due to geometric spreading and scaling by a reflection

RECORDING PARAMETERS AND GEOMETRY			
LINE PROGRESSING	NW - SE	INSTRUMENT	M/S DFS V
SOURCE	VIBROSEIS	GROUND SYSTEM	DFS VII
TRACES/RECORD	240	FIELD FILTER	
GEO DIMENSIONS	20 X 110 FT	B/1B DB-128/72 DB HZ	
GEOPHONE MODEL	GSC 200 10HZ	NOTCH	OUT
GEOPHONES/GROUP	24	SAMPLE INTERVAL	2 MS
PHONES/STRING	12	SWEEP LENGTH	12 SEC
PHONE SPACING	10 FT INLINE	RECORD LENGTH	15 SEC
GROUP INTERVAL	80 FT	SWEEP FREQUENCY	VARI-SWEEP
SOURCE INTERVAL	160 FT	8-60	12-72
SOURCE/ARRAY	INLINE-107 FT	20-96	24-108
UNIT MOVEUP	0 FT	32-132	36-144
UNIT SPACING	53 FT	VARIABLE TAPER SEE OBS	
SWEEPS PER UNIT	8	SPREAD:	
NUMBER OF UNITS	3	TR1	TR120
		TR121	TR240
		9720 - 200--X--200 -	9720

Fig. 7.1 Part of line header from a Unocal land 2D seismic line. The processing part of the line header is not shown.

coefficient, and it will arrive at a time we could calculate from sound speed in air and distance to the canyon wall. Conversely, from knowledge of the sound speed and traveltime, we could calculate distance to the wall. If there were two canyon walls, the echo would be “I...I” where the dots denote some time delay. The situation so far described is akin to shooting seismic with an explosive source that acts for a few milliseconds to generate a short-duration chirp like the word, “I.”

Now consider the same situation except you shout, “I say I say back.” If there is just one canyon wall, the echo will be the same phrase delayed and weaker. The time of flight for this complex signal can be determined by listening for the first “I,” and we can find the distance traveled as before. But what if there are two canyon walls? The echo will sound something like “I say I I say say I back say back.” This is an interleaved version of what we shouted coming back at us twice. Knowing the exact emitted phrase, we can determine that two (and only two) reflections took place and the traveltime for each.

This situation is like the vibroseis case. A long, complex signal (called a *sweep*) is emitted, undergoes several reflections in the earth, and the receiver observes a mix of many time-delayed copies of the sweep. Vibroseis correlation is the process, which uses the original sweep and observed data to unravel all of this. It is a kind of pattern recognition technique; the correlation process slides the sweep across the recorded trace, and where it finds a copy of the sweep, it kicks out a spike or a wavelet that is as close to a spike as possible. The correlated trace is saved for further processing and interpretation. Vibroseis correlation is typically done in the field.

In Figure 7.2, four example sweeps are shown as amplitude spectra in time-frequency ( $t,f$ ) plots. Each sweep is 10 seconds long and has a time sample rate of 4 ms for a Nyquist frequency of 125 Hz. The ( $t,f$ ) representation clearly shows how frequency content of the sweep evolves with time. Vibroseis correlation can distinguish a 10–80 Hz upsweep from an 80–10 Hz downsweep, a fact, which can be exploited to increase vibroseis shooting efficiency by using two simultaneous sources [151]. Even though all of these sweeps put 10–80 Hz energy into the earth, a Fourier amplitude spectrum of the entire sweep shows that different frequency bands are enhanced or diminished depending on the details of the sweep. This is illustrated in Figure 7.3. The nonlinear sweeps (C) and (D) contain more high frequency energy to partially compensate for the loss of high frequencies as seismic waves pass through the earth.

Sweep technology is a whole field of study, and the interested reader is referred for details to Laster [100] and Yilmaz [212].

Back on our seismic line, we find a source array consisting of three vibroseis trucks (*number of units*) spaced 53 ft apart (*unit spacing*) for a total length of 107 ft (*source/array*). This is basically bumper to bumper. Figure 7.4 gives a scaled drawing of the shooting geometry including source array. The source array plays

## Elements of 3D Seismology

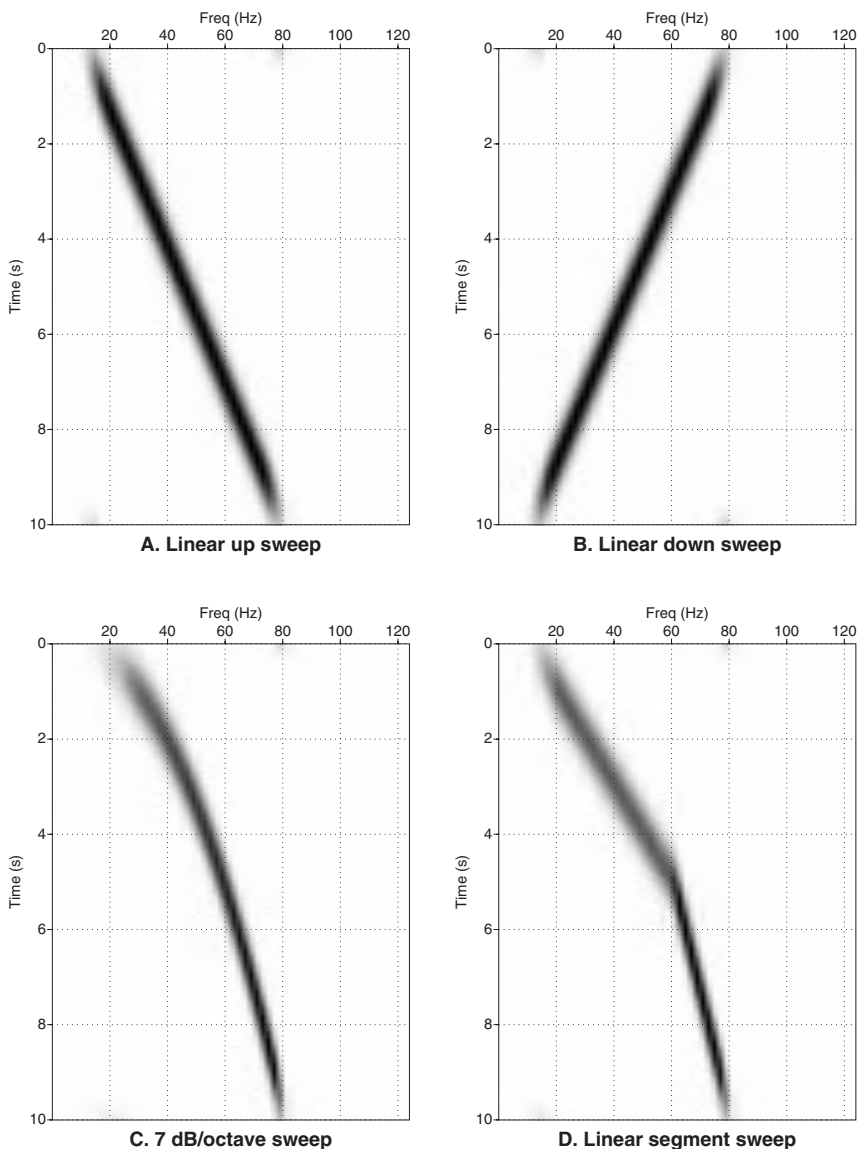


Fig. 7.2 Four vibroseis sweeps shown as time-frequency amplitude spectra. All four sweeps put 10–80 Hz energy into the subsurface, but the amount of energy associated with any given frequency can be different depending on the sweep details. (A) and (B) are linear sweeps, while (C) and (D) are nonlinear.

a role in attenuating surface wave energy, but the primary use of multiple sources is to increase the amount of power put into the earth, thus generating a stronger signal. One attraction of vibroseis is the ability to precisely tailor the source signal and have multiple twenty-ton trucks pounding energy into the ground over a period of several seconds. To generate the equivalent energy with explosives would generate quite a crater [193].

The sweep details are also given in the header. The sources vibrate for 12 s (*sweep length*). Due to vertical stacking (discussed later), there are eight individual sweeps ranging from 8–60 Hz to 36–144 Hz for a total frequency input of 8–144 Hz. Without further information, we would assume each individual sweep is a linear up sweep. The phrase *variable taper see obs* is telling us that each sweep ramps up to full power in a different way, and we should have a look at the observer sheets for details. The observer is the field person in charge of the data recording, and observer notes are the final word on what actually happened in the field.

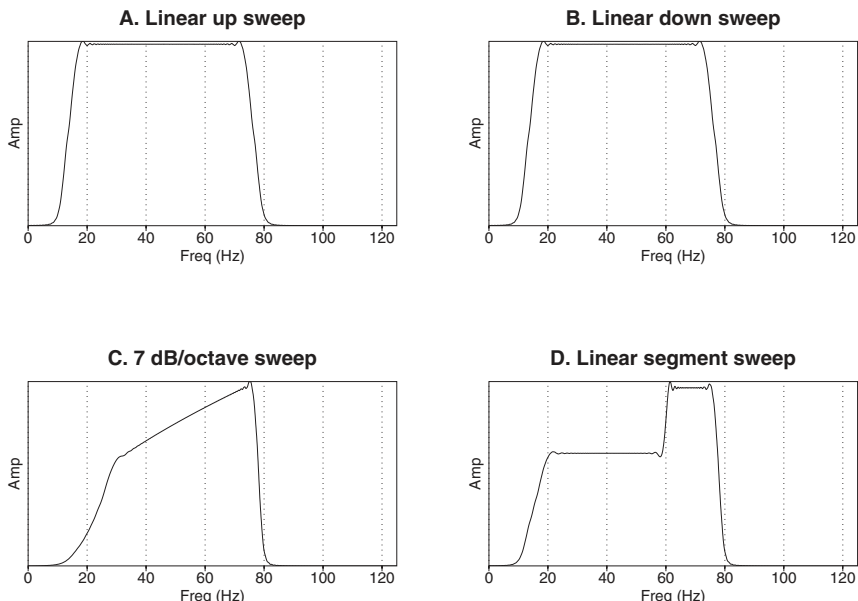


Fig. 7.3 Fourier amplitude spectra of the sweeps in Figure 7.2. These show which frequencies reside in the sweep and in what proportion. The nonlinear sweeps (C, D) are much richer in high frequency energy than the linear sweeps (A, B).

**7.2.2 Receiver.** For land data, the fundamental receiver unit is a geophone sensitive to vertical ground motion (see Fig. 7.5). As the geophone moves with the ground (it has to since the spike is stuck in the ground), we have a conductor (wire coil) moving in a magnetic field (from the permanent magnetic core). This device is thus generating current proportional to particle velocity (time derivative of particle displacement) of the earth surface. The result is electrical current flowing out the wires, and going (ultimately) to an analog-to-digital converter.

This is a single-component receiver that is sensitive only to vibration. Multi-component (MC) geophones are used to observe shear waves or other elastic phenomena. The MC phones can be three-component (3C) or 2C, where the 2C measured directions are usually vertical and radial from the source. The 2C receiver is designed to measure P-P, P-SV, and SV-SV data, which from a vertical vibrator source will ideally be confined to the vertical and radial components of motion.

A geophone is a very sensitive device for detecting motion of any kind. As an example, one American art museum near an active fault zone has hundreds of geophone-like motion detectors built into the floor of a main exhibit hall housing

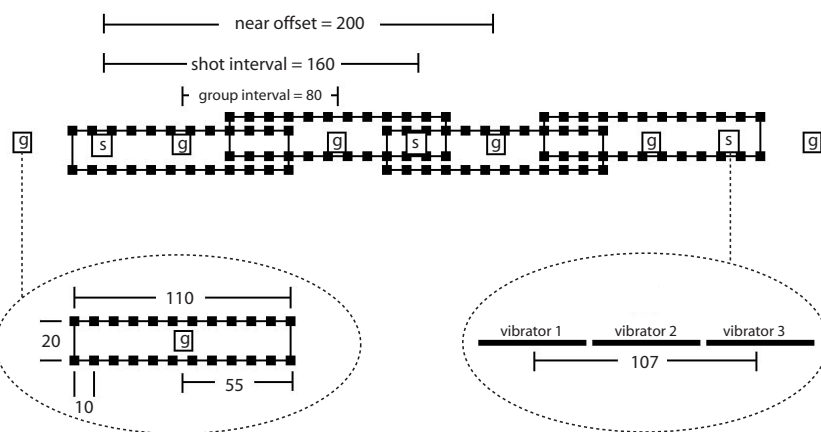
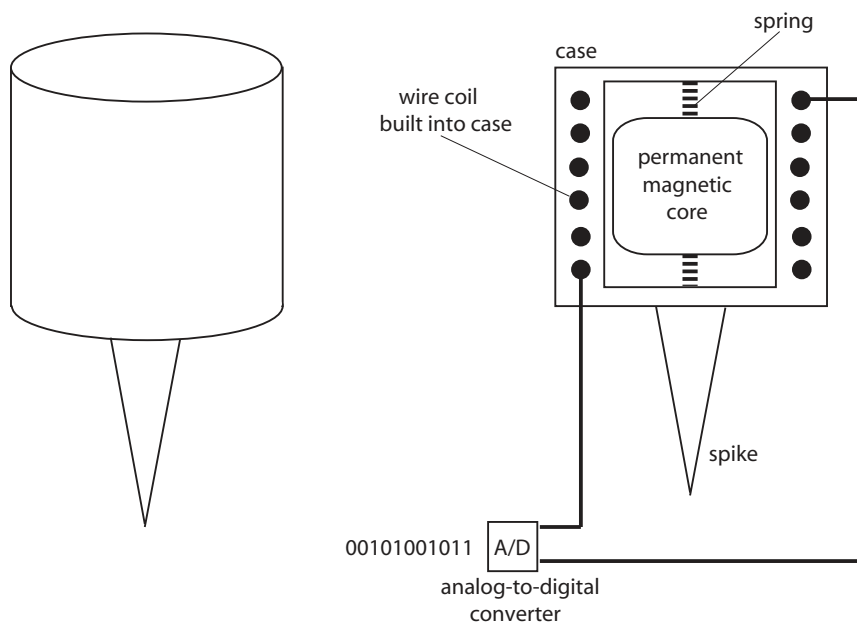


Fig. 7.4 Map view scaled drawing of 2D land shooting geometry described in the Unocal line header of Figure 7.1. Boxes marked g are receiver group flag locations, and s boxes are shot locations. All dimensions are in feet, and details are given for the source and receiver arrays in the dotted ellipses. Receiver arrays partially overlap and are shown staggered for clarity.

some of the best preserved Greek and Roman statues in the world. Should an earthquake be detected, the statues are on active pedestals that take signals from floor sensors as ground motion input and hydraulically adjust so that the statues remain unperturbed, at least until ground motion is strong enough to collapse the entire building.

A side benefit of this system is a grid of motion sensors that can serve as one component of a security system. Were an unwelcome intruder to drop in, each footstep could be mapped from floor sensor data, and should the culprit pause, his pulse could easily be detected. A heartbeat is a very strong signal compared to ground motion from a seismic source many kilometers away.

Our 2D seismic line used a geophone array consisting of 24 individual geophones (*geophones/group*) on the perimeter of a rectangle 110 ft long and 20 ft wide (*geo dimensions*). The long dimension is parallel to the direction the line is



*Fig. 7.5 Outside and inside view of a geophone. When the case and embedded wire coil move in response to ground motion, the spring-held magnet lags behind. Since a conductor is moving in a magnetic field, current is generated. This is fed along wires to a converter where it becomes a digital signal.*

## Elements of 3D Seismology

being shot. The geophone has a 10 Hz (*geophone model*) resonant frequency, which means it is reliable for frequencies above about 10 Hz.

The geophone array, or group, consists of two strings of 12 geophones (*phones/string*) hardwired together. All 24 elements of the geophone array are analog summed to form the output signal. This represents one channel going into the recording system.

The role of the geophone array is to pass reflections, which come from below and thus strike all geophones at the same time. But source-generated ground roll

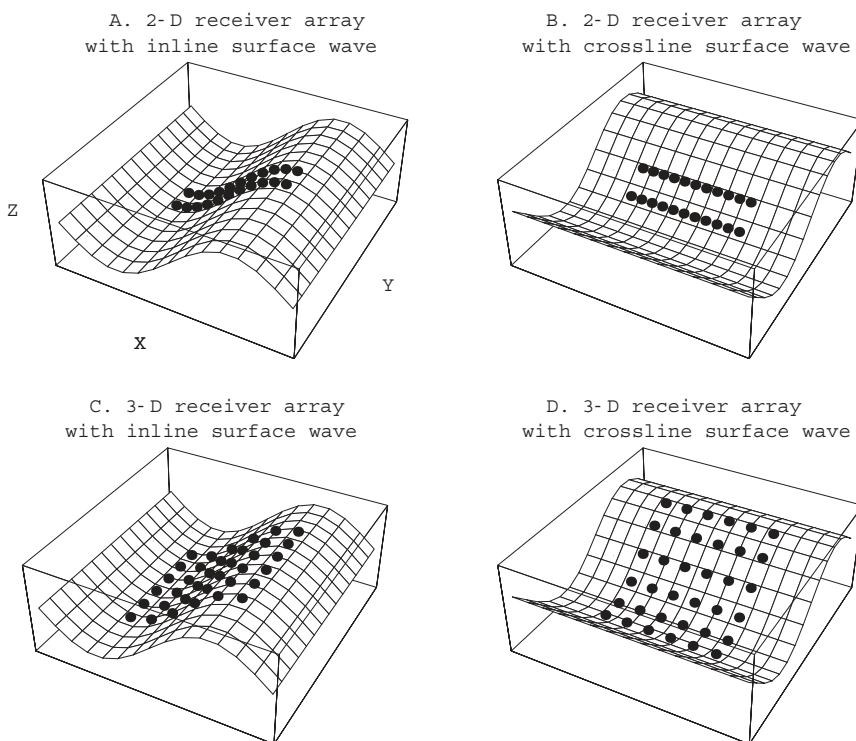


Figure 7.6 Concept of 2D and 3D receiver arrays where *x* is the inline direction and *y* is the cross line direction. (A) A 2D array cancels an inline surface wave because half of the geophones are going up, while the other half are going down. (B) The same array cannot cancel a surface wave going in the crossline direction. (C) and (D) A 3D array has equal power to reject inline and crossline surface waves.

moves along the array past different geophones at different times; some geophones are moving up, while others are moving down. If the array is properly designed, these surface waves will pass the array without generating a net signal. The center-to-center distance between geophone arrays (*group interval*) is 80 ft.

Since this is a 2D line, the receiver array is a long rectangle designed to deal with surface waves traveling along the line. For 3D shooting, we want to reject surface waves going in any direction. Figure 7.6 shows how a square array might better accomplish this goal. But remember, the receiver array is only part of the story. It is the combined response of both source and receiver arrays, which determines actual surface wave suppression.

**7.2.3 Recording system.** When a shot fires, each group (*geophone array*) that is live will begin sending analog data, which is digitized (*analog-to-digital conversion*), to form digital data. Where the A/D conversion takes place depends on the equipment in use. The data could travel analog along a wire cable to the recording unit and be digitized there, or it could come out of the group as analog data and be digitized at that point to be sent via wire or wireless connection to the recording unit. A third possibility is that each geophone could directly output a digital signal. This is not current practice except for some multicomponent geophones.

When data streams in from the geophone groups, it enters the recording system, which has a finite number of recording channels. The recording system used in our line has 240 data input channels (*traces/record*). In early 2003, one major seismic contractor reported that during the prior two years their 2D land crews averaged about 500 active channels. One 2D survey, however, used more than 2500 channels.

### 7.3 Field procedure

Ahead of any actual seismic acquisition, a survey party lays out the shooting plan using flags for source points (usually red) and receiver groups (usually blue). The group flags are taken to be the geometric center of the array.

The  $(x,y,z)$  coordinates of each shot and receiver are required for processing. This is generally obtained using differential global positioning system (GPS). GPS is operated by the U.S. Department of Defense and consists of 24 satellites in 12-hour orbits. At any given time, every point on earth is within view of six or seven satellites. Phase-encoded signals from the satellites in view are compared to a signal from the hand-held GPS unit to determine coordinates of the observer. In differential mode, one GPS unit is stationary at a known coordinate, and a rover GPS unit is used to find relative position that can be converted into absolute coordinates. Differential GPS positioning accuracy (about 1 m) is more than adequate for seismic surveying requirements.

## Elements of 3D Seismology

Our seismic line header includes a small sketch:

TR1	TR120	TR121	TR240
9720	— 200 —	X	— 200 — 9720

The X here is the shot location, the TR labels indicate how traces from each receiver group are organized in the recorded data, and the lower numbers are offsets. The far offset is 9720 ft, the near offset is 200 ft, and the data is shot symmetric-split-spread (the source is in the middle). In 2D data with offsets on either side of the shot, the offsets are signed—negative offset on one side of the shot and positive offsets on the other.

Notice that the near offset (200 ft) is not an integer number of group intervals (80 ft). This tells us the shot points lie between the receiver points, a fact incorporated into Figure 7.4.

**7.3.1 Vertical stack.** At each source point, the three vibroseis units sweep in unison for 12 s (*sweep time*) while the recording system listens for 15 s (*listen time*). The three second difference between sweep time and listen time is the final trace length after vibroseis correlation. After each sweep, listen time, and a short delay, the shot is repeated and the result added to the first sweep. This continues a total of eight times (*sweeps per unit*) for each source point. This is called vertical stacking and helps attenuate random noise. The vertical stack of this line is eight, so it would be said to have an eight-fold vertical stack.

Vertical stack has the effect of increasing acquisition time and thus driving up acquisition cost. An eight-fold vertical stack is fairly high for a 2D seismic line. Field tests and economic estimates are required to determine what level of vertical stack is justified for a particular project. Vertical stacking is rarely used in land 3D data because the number of shots involved is so large that it is economically difficult to justify.

**7.3.2 Roll and cabling.** In our 2D line, there are 240 live receiver groups for each shot. Once the shot was finished, the shot point rolled ahead 160 ft (*source interval*). The vibroseis trucks physically move ahead this distance to the next shot point, but no receivers move. In fact, the 240 live groups for any given shot are just a few of the groups actually laid out on the ground. What happens when a source moves is that certain receiver groups are taken offline, and others are taken online, meaning they are connected to the recording system. Which receivers are live for which shots is called cabling information.

Figure 7.7 is a simple diagram illustrating some important points about the way our data was shot. In each drawing, *s* and *g* mean source and group location respectively; a circle on the subsurface reflector is a reflection point; and a circle on the acquisition surface is a midpoint. The midpoint for a source-receiver pair is the surface location halfway between them. For a horizontal reflector, the

midpoints are directly above the reflection points. Only three groups are shown in the drawing for clarity. In (B) the second shot is shown along with first shot elements as dashed lines. Notice the shot moveup is such that two of the reflection points are visited twice. Although more difficult to see, two midpoints are also common to both shots.

This is termed common midpoint (CMP) shooting. From a processing point of view, a seismic trace does not live at the shot or the receiver location, but at the midpoint. The number of traces that are associated with any given midpoint location is termed the CMP fold, or simply fold, of the data. The fold for a 2D line,  $F_{2d}$ , can be calculated from

$$F_{2d} = \frac{N_c}{2} \frac{dx_g}{dx_s} \quad (7.1)$$

where  $N_c$  is the number of recording channels and  $(dx_g, dx_s)$  are the group and shot interval, respectively. The midpoint interval,  $dx_m$ , for a 2D seismic line is

$$dx_m = \frac{1}{2} \text{Min}(dx_s, dx_g) \quad (7.2)$$

where  $\text{Min}(a,b)$  means we take the smaller of the two values in parentheses.

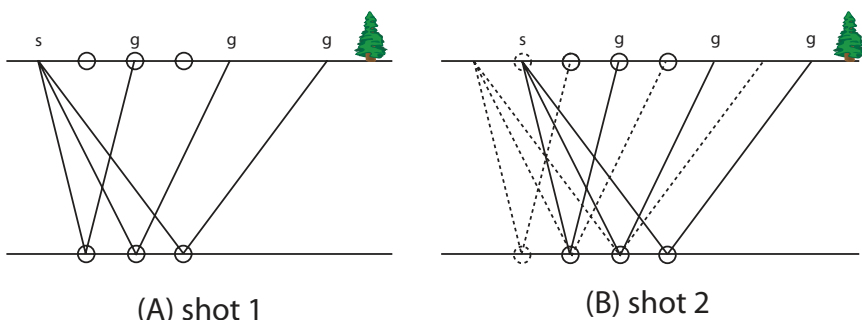
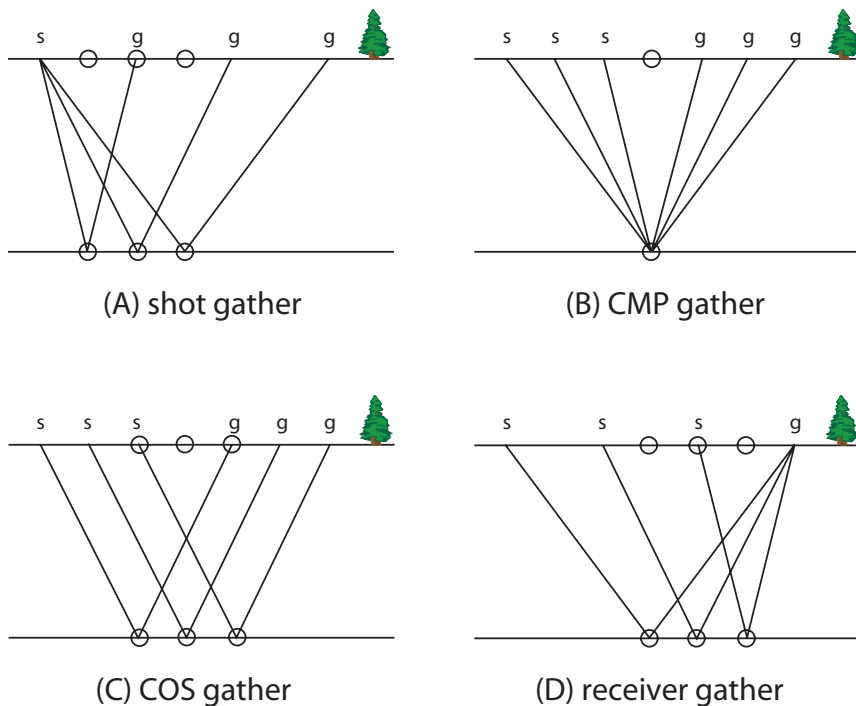


Fig. 7.7 Seismic data is acquired in shot profiles. (A) Rays from a shot ( $s$ ) into three receiver groups ( $g$ ). The circles on the reflecting horizon are reflection points and those on the acquisition surface are midpoints. (B) When the shot moves forward, two midpoints and two reflection points are visited again. Elements of the first shot are shown as dashed lines.

## Elements of 3D Seismology

Bringing these two concepts together, a 2D seismic line can be thought of as a collection of many midpoint gathers, spaced  $dx_m$  apart, each consisting of  $F_{2d}$  traces. Another view (equally valid) is to consider the line as composed of a collection of many shot gathers spaced  $dx_s$  apart, each consisting of  $N_c$  traces.

When all of the traces associated with one shot are gathered together, it is called a shot record, shot profile, or common shot gather. While the shot record is the fundamental unit making up a seismic line, the data in the entire line can be sorted in various ways as shown in Figure 7.8. In the CMP gather (B), we see a single midpoint. There are many seismic processes which operate in the CMP domain. A common offset gather (C) pulls together all those with equal distance from the source.



*Fig. 7.8 When several shot profiles have been acquired it is possible to sort, or gather, a subset of traces from the entire data set in various ways. (A) Rays, midpoints, and reflection points for a single shot gather. (B) A common midpoint gather (CMP) is the collection of all traces having the same midpoint. (C) A common offset section (COS) or gather is the collection of all traces whose source-receiver distance is the same. (D) A common receiver gather pulls together all traces which came from the same receiver group.*

A near offset section is very useful for understanding data quality and general structural style of the subsurface. The common receiver gather (D) is used to isolate problems associated with individual receivers. For example, a bad receiver will generate one noisy trace per shot, and its location with the shot record will move as the shot moves. Associating the bad traces with a particular receiver may be difficult until common receiver gathers are viewed.

Notice that in all the data sorts of Figure 7.8, the midpoints are directly above the reflection points. Figure 7.9 shows this concept breaks down in the presence of subsurface dip. In particular, the CMP gather no longer relates to a single reflection point, a phenomenon called reflection point dispersal. Since midpoints are surface coordinates in our control, they are independent of subsurface

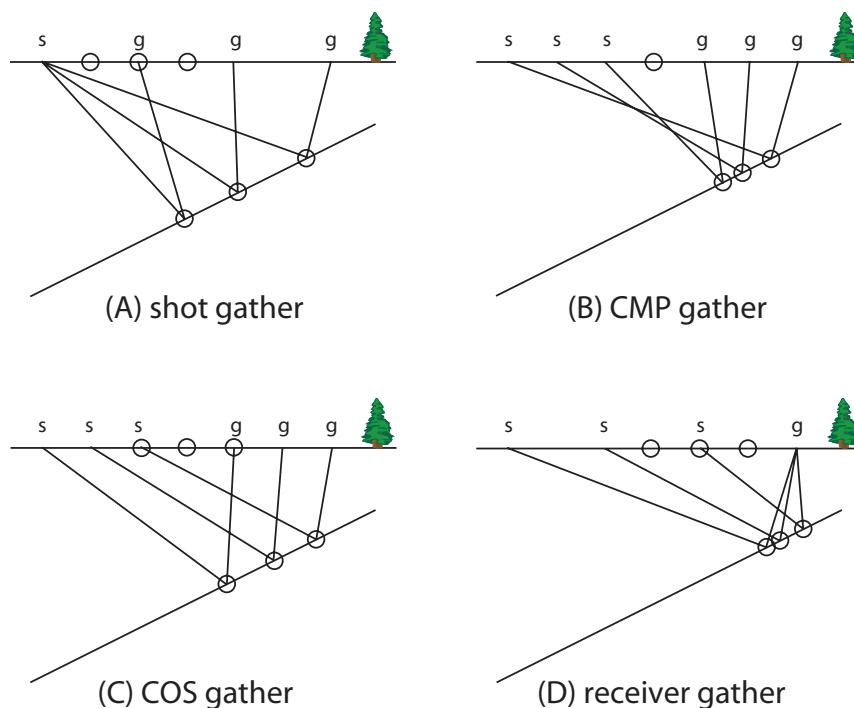


*Fig. 7.9 In the presence of dip reflection points are no longer directly beneath midpoints. Note that midpoint locations, being surface coordinates, have not moved relative to Figure 7.8. Thus the preferred term for modern seismic acquisition is CMP shooting .*

## **Elements of 3D Seismology**

conditions, but not so reflection points (lateral) and depth points (vertical). It is for this reason that the preferred term is common midpoint (CMP) shooting rather than common depth point (CDP) or common reflection point (CRP).

An essential feature of seismic imaging is associated with Figure 7.9B. In a modern survey, there will be dozens of traces associated with each midpoint location. Since the earth consists of many reflecting interfaces, the reflection points will be distributed in 3D space depending on the details of subsurface velocity and structure.

However, after processing the data in various ways, all prestack traces having the same midpoint will be stacked (summed) together to give a single trace that lives at that midpoint. This stack trace is an approximation to the zero offset seismic trace that would have been recorded at this location. The stack traces are displayed together to form a 2D stack section or 3D stack volume. Anticipating later discussions, the final seismic image is created by the process of migration applied to either the stack or prestack traces.

## **7.4 SEGY headers and sorting**

To understand how data sorts can be made, it is necessary to think about how seismic data is stored on a computer. The exact format for seismic data is a matter of mutual consent. The ubiquitous format described here is named Society of Exploration Geophysicists format Y (SEGY).

As shown in Figure 7.10, a SEGY data file is like a snowman full of tadpoles. The top ball is the binary line header, and the middle ball is the extended binary-coded decimal interchange code (EBCDIC) line header. These contain information common to all traces in the file (e.g., samples per trace). EBCDIC is an IBM mainframe format for text files that is virtually extinct. When the EBCDIC header is retrieved from tape, it is converted to industry standard ASCII format so we can read it.

An individual seismic trace is represented as a structure with a trace header and a data tail. The trace header is defined to have exactly 240 bytes. It contains all the identifying information which makes this trace unique in the seismic survey, including source/receiver ( $x, y$ ) locations and elevations, offset, time, date, trace number within line, shot number, CMP number or coordinate, and so on.

Here is the dump of nonzero header words and value ranges for a small 2D seismic line (not the one in Fig. 7.1).

```
trac1=(1,55320) tracr=(2,55321) fldr=(309,770) tracf=(1,120)
ep=(1313,1776) cdp=(1842,2887) cdpt=(1,120) trid=1 nvs=1
offset=(149,3125) gwdep=(1313,1776) scalel=1 scalco=1
sx=(8390,18053) sy=(-11904,-5532)
gx=(5781,17928) gy=(-11821,-3812)
cunit=1 swevel=(131,1176) ns=1500 dt=4000 igc=16448 igi=16448
corr=16448 sfs=16448 hcs=(7093,17986) year=-1 day=(-11876,-4667)
timbas=(1,461) grnors=(303,304) otrav=(123,124)
```

Don't be surprised if you have no idea what this means. Even experts must regularly look up header word definitions, but these numbers tell us a lot about the data set. It has 55,320 traces (*trac1*) consisting of shot records numbered 309–770 (*fldr*). Each shot record has 120 traces (*tracf*) and common midpoints range 1842–2887 (*cdp*). The maximum CMP fold is 120 (*cdpt*), a fact that tells us the group interval must be twice the shot interval. Offsets range from 149 to 3125 m (*offset*); the time sample rate is 4 ms (*dt*); and the number of samples per trace is 1500 (*ns*).

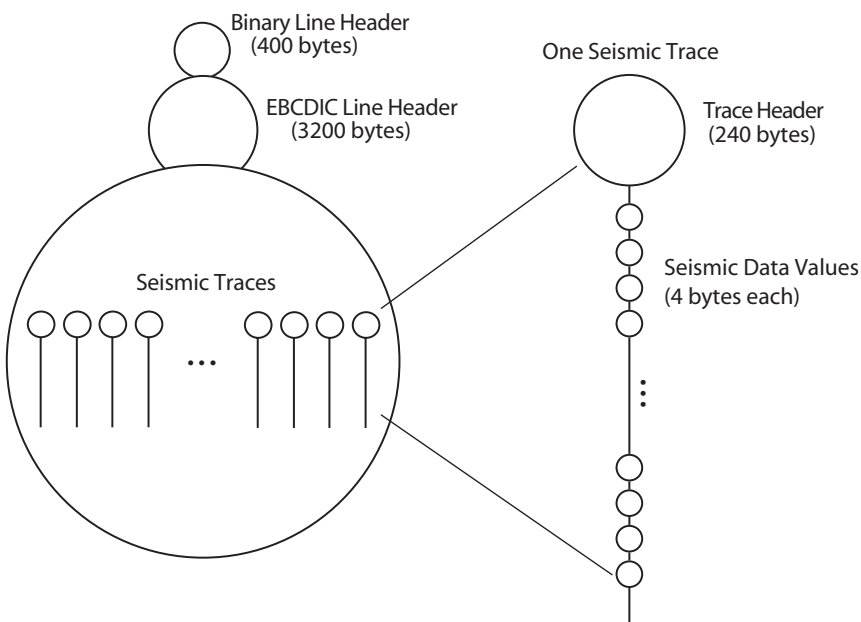


Fig. 7.10 How seismic data are stored in a SEGY format file: a snowman full of tadpoles.

## Elements of 3D Seismology

Since all the offsets are positive, we know the shot was off the end of the live receiver spread. The fact that the shot and group  $(x,y)$  coordinates are all changing, tells us the line was not shot along either the  $x$  or  $y$  coordinate axis. It is possible to use these coordinates to make diagnostic plots as in Figure 7.11.

It is interesting that despite the prevalence of 3D seismic data, the SEGY trace header is inherently 2D. There is no standard header field for azimuth, bin  $x$  and  $y$  coordinates, etc. There is some movement toward a new SEG standard for 3D data including a revised standard issued in May 2002. However, this is an incremental fix. Many would prefer a fundamental change to the SEGY structure so it is inherently 3D. The many varieties of 2D would then be special cases.

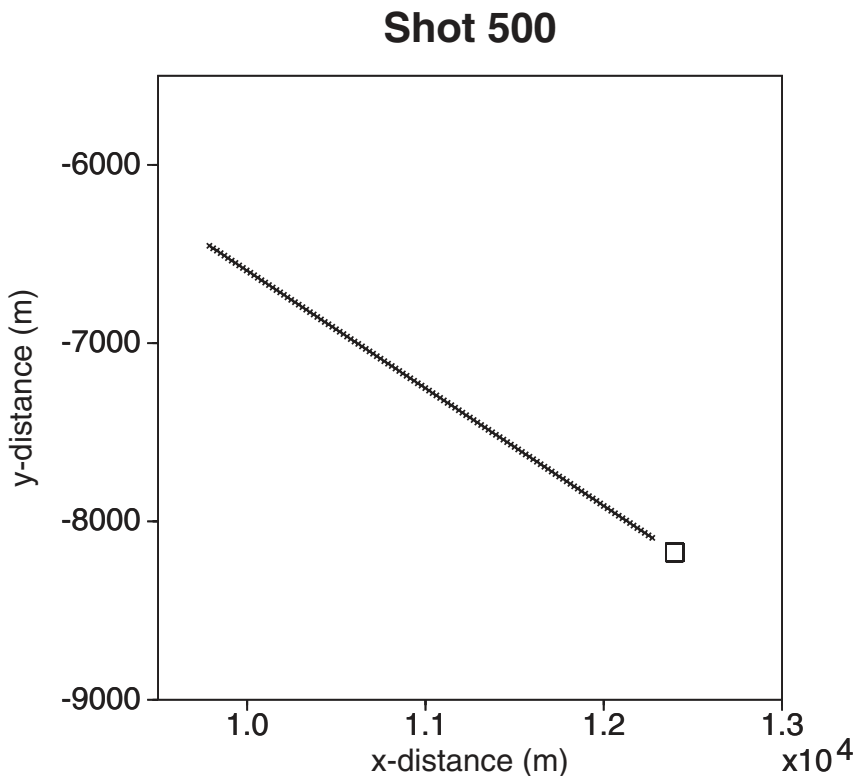


Fig. 7.11 Seismic trace headers contain all necessary information for understanding how the data was acquired. Here shot and group coordinates have been used to plot the location of the source (box) and receivers (crosses) for a single shot record.

# 8

## Financial Aspects of 3D Seismic

Here we consider the economics of 3D surveys. Economics are affected by some geophysical decisions, such as sampling density and survey area, as well as numerous non-geophysical factors. These include market prices for petroleum and natural gas, leasing situations, drilling costs, etc.

The detailed engineering of the survey (source and receiver locations, fold map, etc.) is only done after economic feasibility has been determined.

### 8.1 The big picture: stock price

Petroleum exploration and production (E&P) companies are the consumers of seismic data. For a publicly traded E&P company, long-term success is judged on stock performance. Stock price is a trailing indicator of company management, but there are also market-wide factors [163] beyond company control. Positive factors include growing money supply, tax cuts, low interest rates, political stability (or expectations of it), and high employment.

Negative factors include tight money, increased taxes, high interest rates, political unrest, international conflicts, and recession. For an E&P company in particular, time variability of the oil price, Figure 8.1, is a first-order control on business operations including economic decisions concerning seismic data acquisition. Gas producers face similar price fluctuations. However, due to long-range transportation issues for natural gas, historical price variations are regional rather than global.

Of those things in company control, stock price is based largely on assets, earnings, and dividends. Therefore, 3D seismic data can impact these factors.

- **Assets** include booked reserves and carry over cash from the previous financial year. The company assets are a floor on stock price called the

## Elements of 3D Seismology

*book value.* When a stock drops to book value or below, investors are indicating they see no near-term growth potential in the company. Since 3D seismic can narrow uncertainty in reserve estimates, it may increase reserves (assets) in various ways. It can also help limit downside reserve surprises.

- **Earnings** are generated by revenue from hydrocarbon production and other sales, minus production and sales expenses. Earnings and earnings growth are prime stock price factors over long periods of time. The price-earnings ratio, or PE, is a closely watched quantity. A PE above the market average for similar companies indicates that investors see growth potential in company stock, and they are willing to pay extra for it. 3D seismic can help maximize earnings by lowering expenses related to the number and placement of development wells.
- **Dividends** are paid from current year cash. As dividends go up, earnings go down. So long as dividends are stable or show some steady growth, they affect stock price very little. However, cutting dividends or dividend growth can be seen as a sign of financial trouble and thus lowers the stock price. Dividends are a stock valuation factor largely unrelated to 3D seismic.

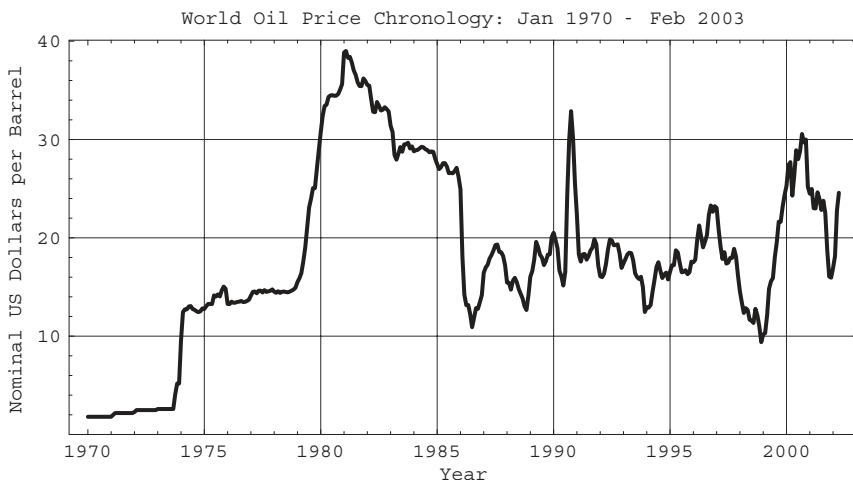


Fig. 8.1 History of world oil prices in U.S. dollars. Prices are not adjusted for inflation (Data: U.S. Department of Energy [187])

In summary, 3D seismic is only one part of the financial picture for an E&P company, but it can be an important part if used properly.

## 8.2 Economics

Any 3D survey is an economic undertaking [98]. For an exploration or production project, there is always a fixed budget. The question is how to allocate funds between seismic and drilling activities so as to maximize return on invested capital. The connection is that seismic data reduce drilling risk, and 3D seismic reduces risk more than an equivalent coverage of 2D seismic. There is ample scientific evidence [28] that 3D seismic is superior to even a dense grid of 2D lines for structural, stratigraphic, and reservoir interpretation.

One comparison that arises concerns shooting a 3D survey or a grid of 2D lines. For land data in the United States, there is a choice between shooting the 3D survey or a 400-800 m grid of 2D seismic. While these are cost equivalent, they are not equivalent in reducing drilling risk. Seismic data is only 3D if it is shot 3D, meaning most bins have full azimuth coverage. Interpolating 2D lines on a dense grid into a 3D volume is not the same as a true 3D data set. At best, it provides a smoothed estimate of the 3D data volume one would have recorded [94].

Another common comparison is made between the 3D survey cost and dry hole cost. One could argue in this case that the choice is to drill two wells with a certain dry hole risk (unknown) or shoot 3D and drill one well with a different dry hole risk (unknown, but lower).

In general, these economic models are too simple to really describe even the basic economics of a 3D seismic survey.

## 8.3 The exploration process

The petroleum exploration business can be considered from a financial point of view to be a value-added exercise. An exploration project is an expensive long-term undertaking. The life cycle from concept to initial production can be 10 years or more. An international project life cycle contains these phases and associated seismic activities:

<b>Strategic planning</b>	Inventory spec and trade data available in the area
<b>Play generation</b>	Acquire, process, and interpret 2D seismic, predesign 3D
<b>Acreage acquisition</b>	Full 3D design
<b>Prospect definition</b>	Acquire, process, and interpret 3D
<b>Initial discovery</b>	Calibrate 3D with well control and VSP
<b>Appraisal</b>	Extend 3D and possible next generation 3D.

## **Elements of 3D Seismology**

The current trend is to apply full cycle economics to an exploration project whenever possible. This is common among major oil companies working international projects, but U.S. land operators tend to do component economics.

- **Full cycle economics.** Rate of return targets are calculated by bundling all parts of the exploration project life cycle from prerelease feasibility studies to selling costs of final refined product. Only integrated E&P companies own all components in this chain and are in a position to practice full cycle economics.
- **Component economics.** Each major step (3D seismic, drilling, etc.) in the exploration project must meet rate of return targets individually.

### **8.4 A savings/gain model**

Here we will look at a component economic analysis for proprietary 3D seismic data. The economic model is divided into savings and gains from which net value, profit, and rate of return can be developed [98].

This discussion is approximate, but gives a good indication of the economic profile of a proposed 3D survey. However, the reader should be aware that it ignores cash flow issues such as timing of costs and expenses. We are not attempting a full accounting of the survey and its effects, just a first-order estimate.

A land or marine 3D survey will only be done if it makes economic sense. We must save or gain money for the survey to be viable. The survey must generate a profit or avoid a loss.

The total cost of a 3D seismic survey,  $C_{3d}$  is given by

$$C_{3d} = C_a + C_p + C_i \quad (8.1)$$

where  $C_a$  is acquisition cost,  $C_p$  is processing cost, and  $C_i$  is interpretation cost. Costs can be external or internal. External costs are dollar amounts paid to other organizations, while internal costs are transactions that occur within or between parts of the E&P company itself. These can be actual dollar amounts paid to other business units or allocated resources such as time, equipment, and computing.

Few petroleum companies own and operate their own production seismic crew, so we can consider all acquisition costs to be external. Included in acquisition cost is permitting, which can represent a substantial portion of the total acquisition cost in some situations (up to 30% for U.S. onshore or transition zone). Processing costs are a mix of internal and external. Big companies will have a specialty processing group but still let seismic contractors do routine processing jobs. In smaller oil companies processing is completely outsourced.

Interpretation costs are almost entirely internal since prospects and reservoir recommendations come from interpreting the seismic data. There is a trend (small but growing) to outsource routine 3D interpretation work (fault picking, tying synthetics, horizon picking), making it an external cost. In general, we can say that external costs are easy to quantify (you have invoices), and internal costs are not. In any case, accurate cost estimates and monitoring are a vital factor for any successful 3D project.

Consider an oil field on which we propose to shoot a 3D seismic survey. We must imagine two future scenarios for the field—one with the 3D data and one without it. To calculate the value of the 3D survey, we must estimate, by whatever means, several key field parameters in each future scenario.

**8.4.1 Savings.** Two kinds of savings are associated with 3D seismic data. These are savings from reduced risk of drilling dry holes or marginal producers and reducing the number of wells required to produce the total reserve.

It is necessary in this analysis to try and quantify the avoided risks. How many dry holes and marginal producers are likely to be avoided by using the 3D data and what are the net costs of such wells? Money not spent on these unsuccessful wells is money saved, but some income would have been generated by production from marginal wells.

Savings,  $S$ , are calculated as

$$S = C_{dha} + C_{mpa} - V_{lmp} - C_{3d} \quad (8.2)$$

where  $C_{dha}$  is the cost of dry holes avoided,  $C_{mpa}$  is the cost of marginal producing wells avoided, and  $V_{lmp}$  is the dollar value of lost marginal production from marginal wells not drilled.

The cost of dry holes avoided depends on the number of dry holes avoided,  $N_{dha}$ , and the dry hole cost,  $C_{dh}$ ,

$$C_{dha} = N_{dha} C_{dh} \quad (8.3)$$

Similarly, the cost of marginal producers avoided is

$$C_{mpa} = N_{mpa} C_{pw} \quad (8.4)$$

where  $N_{mpa}$  is the number of marginal producers avoided and the production well cost is  $C_{pw}$ .

## Elements of 3D Seismology

We use the production well cost, since this is the cost incurred to complete a well whether it is marginal or not. A rule of thumb is that production well costs are about 1.5–2.0 times dry hole cost, but this varies greatly with well depth and operating conditions. To calculate value of the production lost from marginal producing wells not drilled, we use

$$V_{lmp} = N_{mpa} V_{mp} \quad (8.5)$$

where  $V_{mp}$  is the dollar value of hydrocarbons produced by an average marginal well.

**8.4.2 Gains.** Savings are only part of the picture; gains are the rest. Gains are achieved by increasing the total volume of recoverable reserves less any extra production well costs to extract this new reserve. Gains can be defined as dollar value of additional recoverable reserve directly attributed to the survey.

Gains,  $G$ , are calculated as

$$G = V_{nr} - C_{apw} \quad (8.6)$$

where  $V_{nr}$  is the dollar value of new reserves attributable to the 3D seismic survey, and  $C_{apw}$  is the cost of any additional production wells drilled to extract the new reserves. The additional production well cost is given by

$$C_{apw} = N_{apw} C_{pw} \quad (8.7)$$

where  $N_{apw}$  is the number of additional production wells.

**8.4.3 Net value, profit, and rate of return.** With these definitions in place, the 3D seismic survey net value,  $V_{net}$  is savings plus gains

$$V_{net} = S + G \quad (8.8)$$

The net value must be adjusted for various expenses on the additional reserves that are produced. However, it is also possible that no additional reserves can be attributed to the 3D seismic survey, or even negative reserves. An example of negative reserves would be a 3D survey, which demonstrates a suspected untapped fault block is actually in communication with the main field. Typical expense ratios are .2–.4 (20–40%) depending on country, partnership arrangements, etc.

We capture all expense items (tax, royalties, etc.) on produced hydrocarbon in a fractional expense factor,  $E$ , and apply it only to the value (if any) of additional reserves. This allows us to calculate the profit,  $P$ , as

$$P = \begin{cases} V_{net} - V_{nr} E & V_{nr} > 0 \\ V_{net} & V_{nr} \leq 0 \end{cases} \quad (8.9)$$

This agrees with our expectation that a profit of zero means we recover the invested capital and nothing more.

As with any investment, we want to calculate the rate of return on the capital we invest in the 3D seismic survey. Taking the long-term view from initiation of the survey to complete production and sale of additional reserves attributable to it, we find the lifetime rate of return,  $R_l$  is

$$R_l = \frac{C_{3d} + P}{C_{3d}} - 1 = \frac{P}{C_{3d}} \quad (8.10)$$

Rates of return are usually quoted in percentage terms which would be our definition times 100. A lifetime rate of return of 0% means that we have recovered the money invested in the survey; 100% means you recovered this amount twice, and so on.

While lifetime rate of return may seem like a natural measure, it is better to express financial performance of an investment in terms of annualized rate of return. For one thing, the annualized rate of return allows comparison with U.S. Treasury bond yields, which are taken to be the risk-free rate of return available to investors at any given time. Investments with greater risk, such as seismic surveys or drilling, must offer a correspondingly higher rate of return to attract investors.

Annualized rate of return is based on the finance equation for time-value of money.

$$FV = PV(1 + i)^n \quad (8.11)$$

where  $PV$  is present value,  $FV$  is future value,  $i$  is rate of return per period, and  $n$  is the number of periods. Solving this for the rate of return per period gives

$$i = \left[ \frac{FV}{PV} \right]^{1/n} - 1 \quad (8.12)$$

## Elements of 3D Seismology

Furthermore, if the number of periods represents years, this gives the annualized rate of return of the investment.

As an example, imagine you buy \$20,000 worth of stock in a growth company, hold the shares six years, then sell it all for \$28,500. What is the annualized rate of return on your investment?

$$\begin{aligned} i &= \left( \frac{28\ 500}{20\ 000} \right)^{1/6} - 1 \\ &= (1.425)^{.16667} - 1 \\ &= .0608 \\ &= 6.08\% \end{aligned} \tag{8.13}$$

Or you buy \$28,500 worth of stock in a growth company hold the shares six years and sell for \$20,000. What is the annualized performance of this investment?

$$\begin{aligned} i &= \left( \frac{20\ 000}{28\ 500} \right)^{1/6} - 1 \\ &= (.701754)^{.16667} - 1 \\ &= -0.05732 \\ &= -5.73\% \end{aligned} \tag{8.14}$$

This is a company growing in the wrong direction.

For a 3D seismic investment, the annualized rate of return,  $R_a$ , is given by

$$R_a = \left( \frac{C_{3d} + P}{C_{3d}} \right)^{1/n} - 1 \tag{8.15}$$

where  $n$  is the life of the project in years.

As an example, parameters for a 3D seismic survey project are shown in Table 8.1, and the calculated economic quantities in Table 8.2.

Once annualized rate of return is estimated, the decision whether or not to make the 3D seismic investment is one of relative value. For the example here, few would invest money in a 3D seismic survey when very nearly the same rate of return can be had risk-free in government securities. Also, the seismic dollars are

in competition with drilling, refining, and other capital investments an integrated E&P company must make. The seismic rate of return needs to be in line with internal company targets, which in turn are driven by external factors.

Added reserves typically drive 3D seismic economics. Gains can be very big, and savings are usually smaller. But there are situations where high well costs can mean big savings, even if the survey is expensive, and little or no additional reserves are discovered.

In summary, to determine economic feasibility we must estimate the future parameters listed in Table 8.3.

Some of these items can be robustly estimated while others are much less certain.

Symbol	Value	Description
$C_{dh}$	\$ 22/bbl	Hydrocarbon price
$C_{pw}$	\$ 650,000	Dry hole cost
$N_{dh}$	\$ 1,400,000	Production well cost
$N_{mpa}$	2	Number of dry holes avoided due to 3D survey
$N_{apw}$	3	Number of marginal producers avoided
$C_{3d}$	90,000 bbl	Avg marginal prod from each marg well avoided
	\$ 6,000,000	Cost of 3D survey
	1,200,000 bbl	Add reserves attributable to 3D survey
$E$	3	Add prod wells required to extract new reserves
$n$	35 %	Expense factor
	14 years	Life of project (time to extract reserves).

Table 8.1 Parameters for a 3D seismic survey project.

Symbol	Value	Description
$S$	\$ -6,440,000	Savings generated by 3D seismic
$G$	\$ 22,200,000	Gains generated by 3D seismic
$V_n$	\$ 15,760,000	Net value of 3D seismic
$P$	\$ 6,520,000	After tax profit from 3D seismic investment
$R_l$	108.67 %	Lifetime rate of return
$R_a$	5.39 %	Annualized rate of return

Table 8.2 Economic quantities for this parameter set.

## Elements of 3D Seismology

Parameter	Unit (assuming oil)
Dry hole cost	\$/ well
Producer cost	\$/ well
Reserves without 3D	bbl
Reserves with 3D	bbl
Oil price	\$/bbl
Dry holes avoided	number
Marginal producers avoided	number
Marginal well production	bbl/well
Additional producers required	number
Fractional expense ratio	number

Table 8.3 Estimate of future parameters.

## 8.5 Some industry trends

One important factor concerning economic justification of a 3D seismic project is where in the life cycle of a field the survey is done. If shot in the early life of a field, the 3D costs are weighed against all future benefit provided by the survey. However, if the 3D is acquired in the late stages, it is more difficult to make rate of return targets because the field has less potential. These facts have resulted in a steady move toward shooting 3D seismic earlier in the field development cycle [87] as evidenced by Figure 8.2.

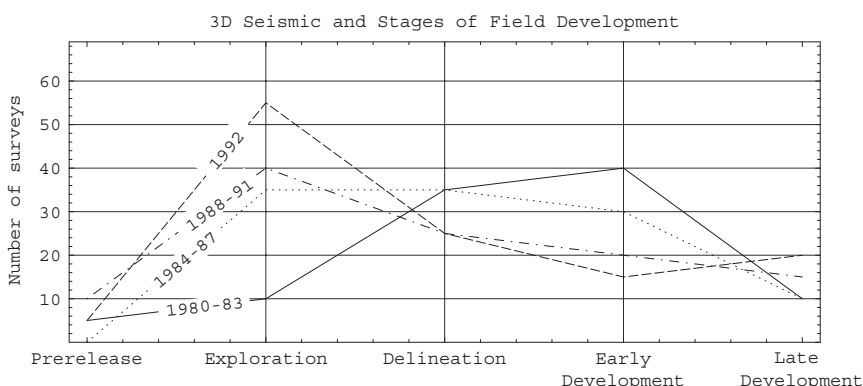


Fig. 8.2 3D Seismic surveys acquired by Exxon 1980–92 showing the trend toward shooting 3D data earlier in the field development Cycle (modified from [87]).

Costs for land 3D acquisition vary widely from area to area, depending on terrain, permitting, and other factors. However, the general trend is toward more efficient field procedures and falling costs on a dollar per prestack trace basis. Figure 8.3 shows some historical acquisition and pricing trends from a jungle environment [15].

The large scale industry trends [64] are associated with 2D versus 3D and land versus marine. Figure 8.4 shows that cumulative investment in 3D seismic data is growing at the expense of investment in 2D data. Several trends are evident from Figure 8.5, including

- rapid decay of land 2D seismic investment
- a 1996/7 peak in land 3D work
- slow decay of marine 2D
- the emergence and financial dominance of 3D marine data

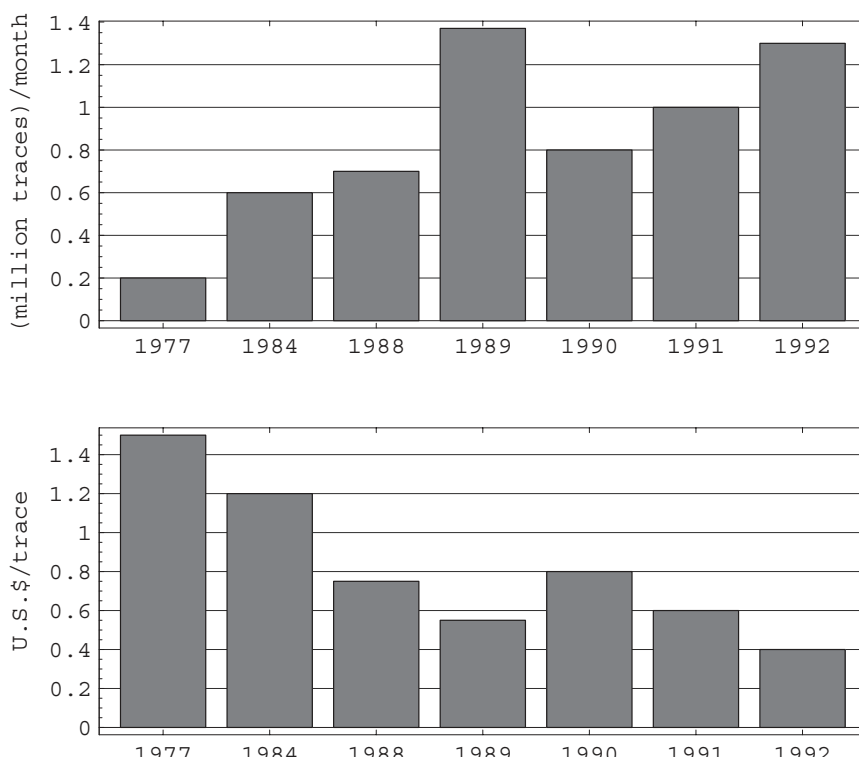


Fig. 8.3 Historical trends for land 3D seismic in a jungle environment. Improved efficiency leads to falling prices on a prestack trace basis (modified from [15]).

## Elements of 3D Seismology

Finally, we get some idea of the sheer magnitude of just the U.S. seismic industry by noting that a recent (year 2000) private survey estimated that more than 4.1 million km of non-exclusive 2D seismic data reside in data libraries [64]. As for non-exclusive 3D, something like 900,000 square km have been acquired. This is more than three times the surface area of onshore Texas.

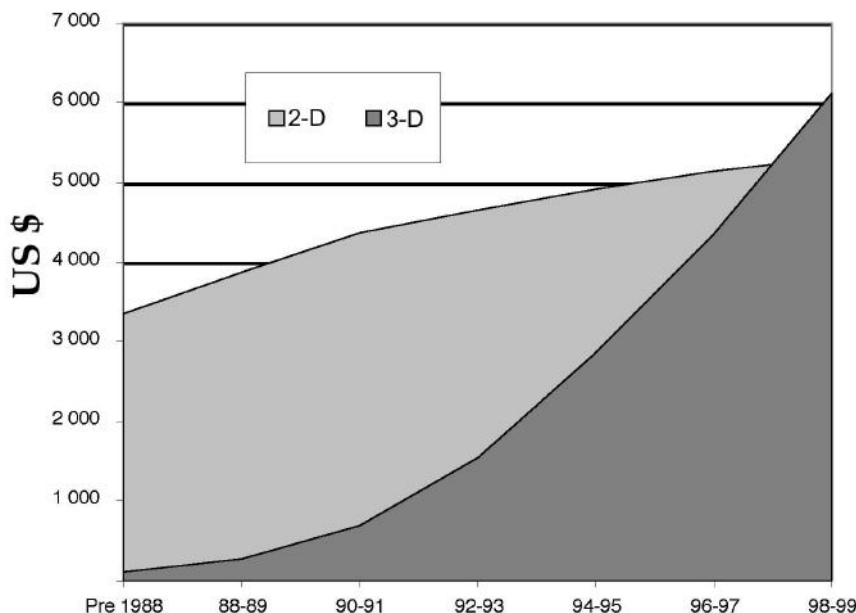


Fig. 8.4 Cumulative investment in 3D and 2D Seismic data in billions of U.S. dollars (from [64]).

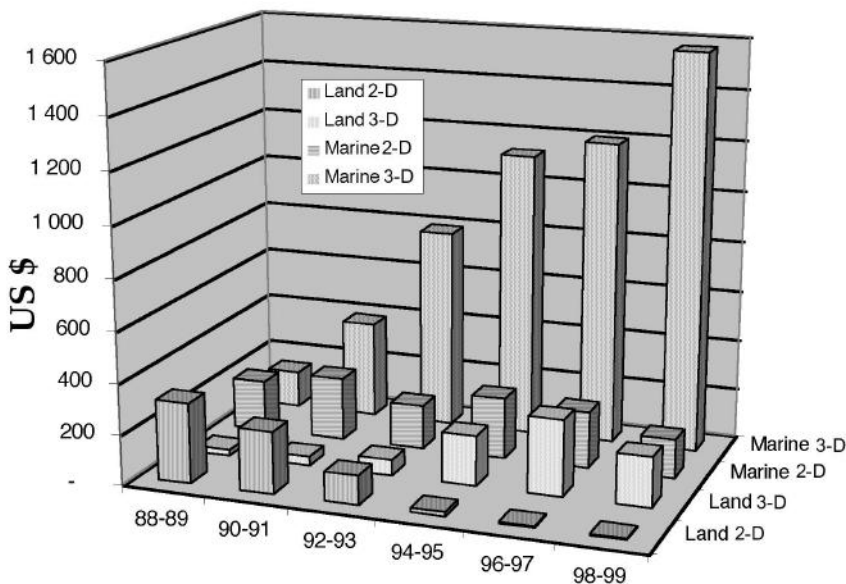


Fig. 8.5 Investment trends in seismic data in billions of U.S. dollars. Note the decline of land 2D and emerging dominance of Marine 3D (From [64]).

# 9

## Survey Predesign

Major items that drive survey design can be divided into three categories. Operational issues include physical access to the acquisition area, supply logistics, cultural interference and noise, and interference from other surveys [27]. Economic issues involve the survey budget, field and prospect economics, and seismic crew costs and availability. Important geophysical issues, Table 9.1, concern us in this chapter. The parameter choices discussed here are common to 2D and 3D data and have strong influence on data quality.

Acquisition parameter	Geophysical concern	Determining factor(s)
Sweep band	Vertical resolution	velocity ( $v$ )
Sweep length	Signal-to-noise (S/N)	Ambient noise
Source effort	Signal-to-noise (S/N)	Ambient noise
Listen time	Target depth and diffractions	Depth, $v$
Shot and group interval	Spatial aliasing	$v_{min}, f, \theta_{max}$
Receiver array	Ground roll	( $v, f$ ) of ground roll
Recording spread layout	Aperture, fold, azimuth	
Recording spread size	Image area	Target size, depth

Table 9.1 General acquisition parameters can be related to geophysical concerns and factors that influence the values we might choose.

### 9.1 Acquisition parameters

Example 3D onshore U.S. acquisition parameters [54] are shown in Table 9.2. For a marine 3D survey, the summary of acquisition parameters will look something like Table 9.3, which is for Mississippi Canyon data in the Gulf of Mexico [176].

## Elements of 3D Seismology

Parameter	Example
Sweep band	12-96 Hz
Sweep length	10 s
Source effort	6 vibrators, 6 sweeps
Listen time	4 s beyond sweep
Source/receiver interval	660/110 ft
Receiver array	12 phones in 25-ft circle
Recording spread layout	768 channels
Recording spread size	1.5 × 1.0 miles

Table 9.2 Acquisition parameters for a land 3D seismic survey [54]. The recording spread size represents the area of live receiver groups for each shot, not the total area of the survey.

Parameter	Example
Acquisition date	1999
Data acquired by	CGG
Shoot orientation	North-South
Recording instrument	Syntron 480
Streamer type	Syntron
Receiver array	12 phones in 25-ft circle
Positioning	GPS/DGPS
Airgun source	4180 cubic inches
Gun depth	7.5 m ± 1 m
Shotpoint interval	62.5 m per CMP line
CMP crossline separation	45 m
Group interval	25 m
Recording channels	288 and 240 per streamer
Streamer depth	9 m ± 1.5 m
Streamer Length	4 x 7200 m and 4 x 6000 m
Record length	12.288 s
Sample interval	4 ms
Nominal fold	57.6

Table 9.3 Acquisition parameters for a Gulf of Mexico marine 3D marine survey [54].

## 9.2 Time sample rate

When a shot initiates a seismic wavefield, it propagates until measured by the receivers. In order to create the best possible image, it is necessary to sample the wavefield properly in time and space. Figure 9.1 shows the idea of adequate time sampling. Imagine the high frequency curve is sampled at the dot locations, and we try to reconstruct this original curve. Clearly, the dots are too widely spaced in time to do this. We would reconstruct instead the lower frequency curve shown. This effect is called temporal aliasing or simply aliasing. Any frequency in our data above a magic value will be aliased. This important frequency is called the Nyquist frequency (see appendix A).

For a given time sample rate,  $dt$ , the highest frequency that can be reliably measured is the Nyquist frequency,  $f_{nyq}$  given by

$$f_{nyq} = \frac{1}{2 dt} \quad (9.1)$$

For consistent amplitude control, the highest actual frequency in the data,  $f_{max}$  should not exceed one-half of the Nyquist frequency. Using this rule, the design condition for  $dt$  is

$$dt \leq \frac{1}{2} \left[ \frac{1}{2 f_{max}} \right] = \frac{1}{4 f_{max}} \quad (9.2)$$

a situation described as running at half-Nyquist. The farther the survey is run under Nyquist, the less worry there is of distorting amplitudes important to AVO and reservoir property prediction.

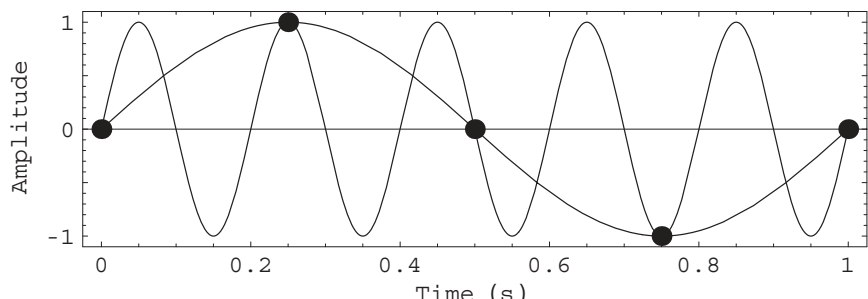


*Fig. 9.1 The concept of aliasing in one dimension (time). The high frequency curve is sampled at the dot locations. An attempt to reconstruct it from the sampled points fails because the time sample rate is too large.*

## Elements of 3D Seismology

Nyquist frequency is the primary reason for choosing a time sample rate, but there is another issue to consider in areas of subtle structure. Imagine a prospect that hinges on 10 m of closure at 600 m depth in rocks with interval velocities of 4600 m/s. If the maximum signal frequency in the data is 70 Hz, then a time-sample rate of 4 ms is adequate from our Nyquist calculation. However, the traveltime difference for a location on and off structure is just one time sample:

$$dt = \frac{2 dz}{v} = \frac{20}{4600} = .004 \text{ s.} \quad (9.3)$$

In order to get a few additional points for confidence, the time sample rate could be lowered to 1 ms. This would incur little or no extra acquisition cost. But processing at 1 ms, rather than 4 ms will be more expensive.

It is common practice to acquire, process, and interpret at different time sample rates. Each time the sample rate is doubled, the data size is cut in half. (This is the size of the data file on a computer, not size of the survey area.) A typical modern marine survey might acquire at 1 ms, process at 2 ms, and interpret at 4 ms.

We can make some general comments about time sample rate.

1. When the recommendation is between two standard values, the safe choice is to use a smaller dt
2. When careful amplitude control is important, use a time sample rate that runs between 1/2 and 1/3 of Nyquist
3. Using a smaller dt costs almost nothing at acquisition time (storage media only)
4. Processing cost and data size in bytes are inversely proportional to dt (smaller dt means more expensive processing)
5. Structural resolution may also be a consideration in areas of subtle structure

### 9.3 Offset range

Few seismic surveys are shot with a single target horizon in mind, rather an interval of interest extends from the shallowest to the deepest target. Ideally the maximum offset in the data will be at least equal to the deepest target

$$x_{max} \geq z_{max} \quad (9.4)$$

From typical velocity increase with depth this condition will result in incidence angles at the deep target of something like 20–25 degrees.

The far offsets are important in showing significant moveout that can be exploited in processing to estimate NMO and migration velocities.

Offset much beyond the maximum target depth will likely introduce head waves and phase changes associated with post critical reflection. In all probability, these will be muted and thus not be available to contribute to the seismic image.

## 9.4 Listen time

It would do little good if a seismic survey were shot and processed with 3 s of data and it turned out that the target horizon was at 4 s.

A rule for maximum recording time,  $t_{max}$  is

$$t_{max} \geq \frac{1.4}{v_{avg}} \sqrt{x_{max}^2 + 4z_{max}^2} \quad (9.5)$$

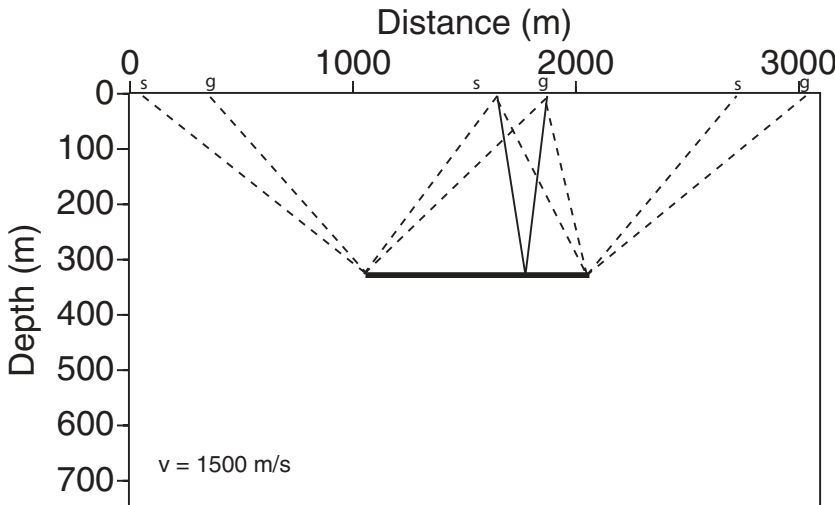
where  $v_{avg}$  is the average velocity from the acquisition surface to the reflector,  $x_{max}$  is the maximum offset, and  $z_{max}$  is the target depth. Applying the rule for maximum offset gives a simplified form

$$t_{max} \geq \frac{3.13 z_{max}}{v_{avg}} \quad (9.6)$$

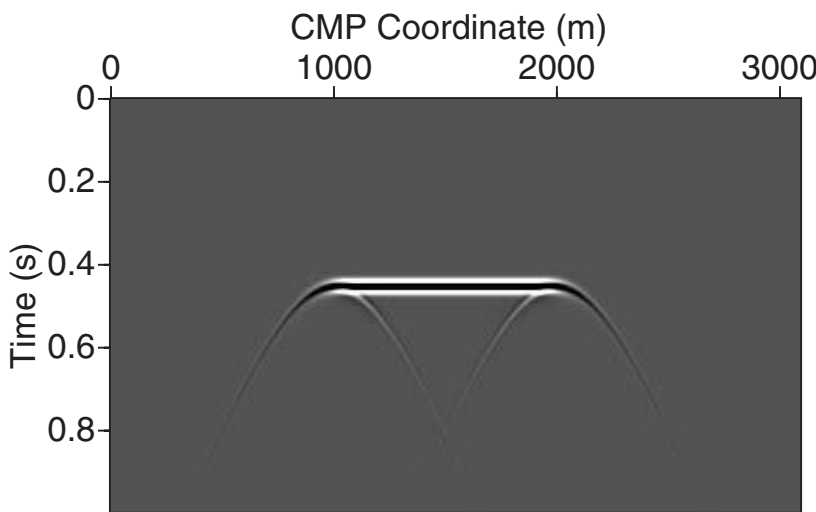
This formula represents 140% of the reflection time to a horizontal reflector at target depth. The 40% pad allows enough time for diffractions and moderately dipping reflections. Figure 9.2A illustrates this point with an earth model consisting of a single reflector floating in a constant velocity (1500 m/s) background. We imagine a common offset experiment progressing from left to right. A shot-receiver pair near zero distance shows a dashed raypath representing diffraction from the near end of the reflector.

For a shot-receiver near 3000 m, the same argument applies to diffraction from the right-hand end of the reflector. At an intermediate point near 2000 m, we have dashed diffraction rays from each end of the reflector and a solid reflection path. The seismic data in Figure 9.2B shows the horizontal reflection event and two endpoint diffractions. The maximum recording time for a seismic survey must capture both the reflection and the diffractions.

The equation given above for  $t_{max}$  should be used as a conservative estimate since deeper events may be of interest, and because curved ray effects are not taken into account. A longer  $t_{max}$  is needed if very steep dips or turning waves are



**A. Earth Model**



**B. Common Offset Section (200 m)**

Fig. 9.2 (A) Common offset experiment over an earth model consisting of a reflector segment floating in a constant velocity medium. Two kinds of events are returned, reflections (solid) and diffractions (dashed). (B) Seismic data from the experiment showing reflections and diffractions. We need to record enough time for both. Migration will use the diffraction energy to rebuild the reflector terminations.

expected. By turning waves, we mean a seismic wave with a travel path such as shown in Figure 9.3. These are only likely to be present in soft, clastic basins. The Gulf of Mexico (above salt) is a prime example, but turning waves have been reported worldwide from similar basins.

We can make the following general comments about listen time.

1. The recording time will usually be an integer number of seconds
2. The safe choice for recording time is to use a larger value rather than a smaller one
3. Extra time should be allowed for steep dips and turning waves

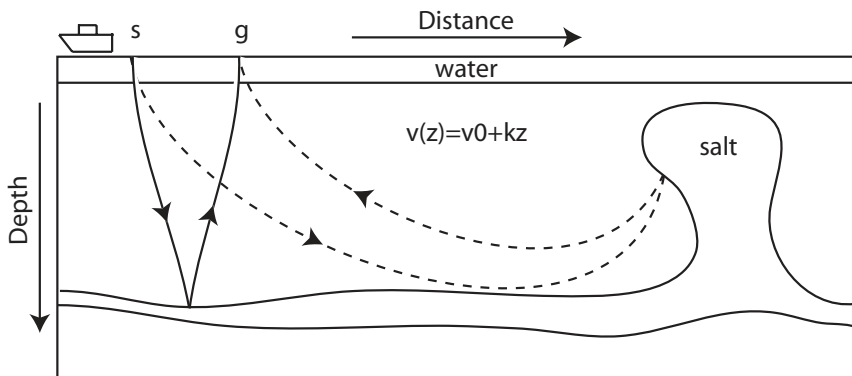


Fig. 9.3 Turning waves (dashed raypath) can occur in basins with gradual increase of velocity with depth such as the linear velocity profile shown here. The downrange travel distance and reflection time for turning waves is much greater than ordinary reflection events (solid raypath).

## 9.5 Spatial sampling and aliasing

Spatial aliasing is a consequence of trace spacing relative to frequency, velocity, and slope of a seismic event. With adequate trace spacing, points along a seismic event are seen and processed as a continuous event. When trace spacing is too coarse, individual points do not seem to coalesce to a continuous event, confusing not only the eye but processing programs as well. This can seriously degrade data quality of the final seismic image.

Figure 9.4 shows one way to describe spatial aliasing. In this view, spatial aliasing is based on trace-to-trace time delay. Since the delay is related to trace spacing, the issue is really one of midpoint interval which, in turn, is determined by shot and receiver intervals.

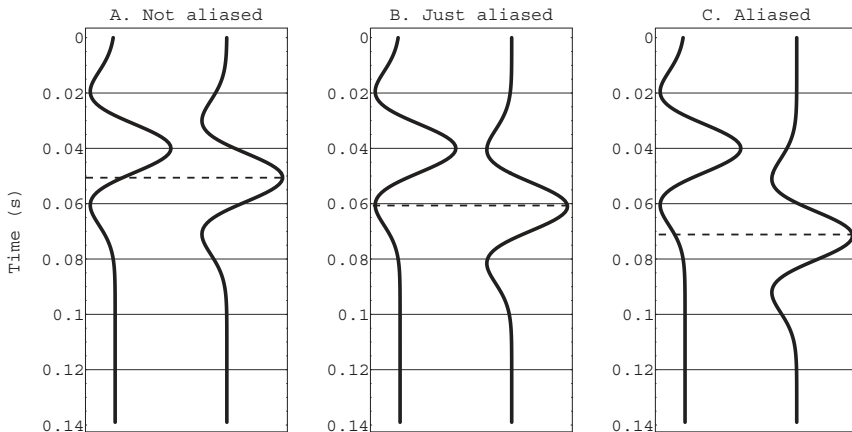


Fig. 9.4 Spatial aliasing occurs when moveout between adjacent traces is greater than half the dominant period of the wavelet. The dominant period of the wavelet used here is 20 ms. (A) Since the delay is less than the half-period these traces are not spatially aliased. (B) The delay is now exactly equal to the half-period. (C) Strong aliasing is present here since the delay is much greater than the half-period.

As discussed earlier, the midpoint interval,  $dx_m$ , for a 2D line with shot interval  $dx_s$  and receiver group interval  $dx_g$  is

$$dx_m = \frac{1}{2} \operatorname{Min}(dx_s, dx_g) \quad (9.7)$$

The spatial aliasing condition on midpoint is

$$dx_m \leq \frac{v_{int}}{4 f_{max} \sin \theta} \quad (9.8)$$

where  $v_{int}$  is the interval velocity near (or immediately above) the target,  $f_{max}$  is maximum signal frequency and  $\theta$  is the physical dip angle of the reflecting bed. We could also write this inequality as a condition on either shot or group interval, if the other is held constant. The unaliased midpoint interval grows with target depth due to increasing  $v_{int}$  and decreasing  $f_{max}$ . We note for design purposes that diffraction limbs (Figure 9.2) appear as  $\theta=90^\circ$  events.

Midpoint interval is a first order economic factor. For 2D data, as the midpoint interval decreases, acquisition cost increases more or less linearly. Although the formula as given is correct, it is often applied in such a way as to

achieve a larger (less expensive) midpoint interval. Any such trade-off introduces the risk of spatial aliasing and the question reduces to whether that risk is acceptable. We can quantify this with an example.

Consider a 10–80 Hz survey shot for a 45-degree dipping target with interval velocity 4000 m/s. The safe midpoint interval for this situation is

$$dx_m \leq \frac{4000}{4 * 80 \sin 90^\circ} = 12.5m \quad (9.9)$$

where we have used  $\theta=90^\circ$  to account for the possibility of diffractions associated with faulting. It is common to design based on dominant, rather than maximum, frequency. This choice gives a recommended midpoint interval of 20 m. What are the consequences of this choice?

This question has several answers, one of which is a condition on frequency as it relates to dip

$$f \leq \frac{v_{int}}{4 dx_m \sin \theta} = \frac{50}{\sin \theta} \quad (9.10)$$

where  $f$  is now the maximum unaliased frequency. For the  $45^\circ$  target we find frequencies above 70 Hz are aliased. Not a great loss, perhaps, since our bandwidth only extends to 80 Hz. However, the effect on diffraction energy digs deeper into the bandwidth. For that part of the diffraction curve with an apparent 70-degree dip, frequencies above 53 Hz are aliased. To be sure, most of the diffraction energy is loaded toward smaller dips, but preservation of the entire bandwidth will allow migration to do a better job. Going in the other direction, using average velocity in place of interval velocity will recommend a midpoint interval smaller (more expensive) than actually needed.

The spatial aliasing condition is a physical limit. Given enough money, we can shoot data with a midpoint interval of 1 m, but there is no additional information or imaging value to be had. On the other hand, violating the spatial aliasing condition without a compelling reason can quickly degrade image quality of the data.

Spatial aliasing is not difficult to recognize in real data, (see Fig. 9.5). The main problem with spatial aliasing is the detrimental effect it has on two expensive processes: dip moveout and migration.

Figure 9.6 gives a synthetic migration example. The spatial aliasing we have described is a consequence of wavefield sampling. This is often termed data aliasing to distinguish it from operator aliasing that can occur during dip moveout or migration [17].

## Elements of 3D Seismology

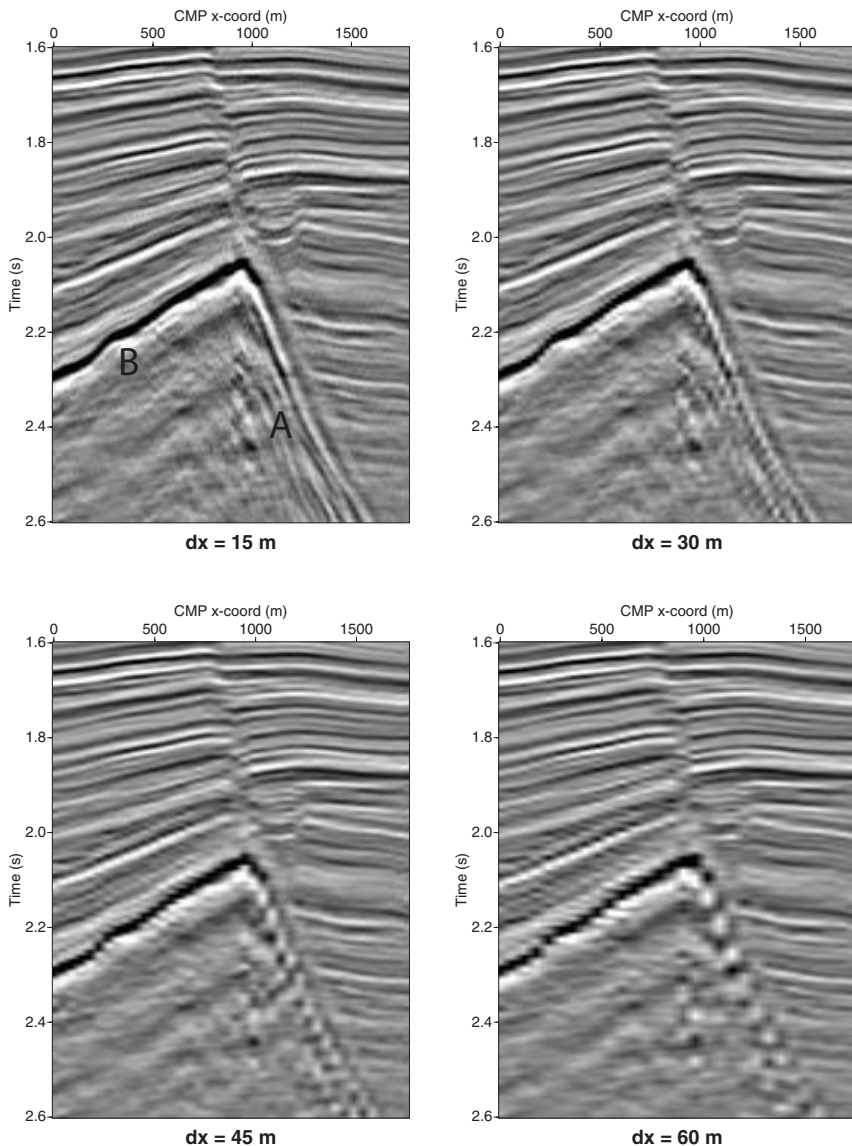


Fig. 9.5 Spatial aliasing is controlled by CMP interval as shown in this migrated 2D section. As originally shot ( $dx=15$ ), even the steepest events A and B are unaliased. At  $dx=30$ , event A shows aliasing as evidenced by the false dip alignments sloping up and to the right. The situation worsens at  $dx=45\text{ m}$  till A has the “string of pearls” appearance typical of strong spatial aliasing. At  $dx=60\text{ m}$ , B and those events parallel to it, are clearly aliased.

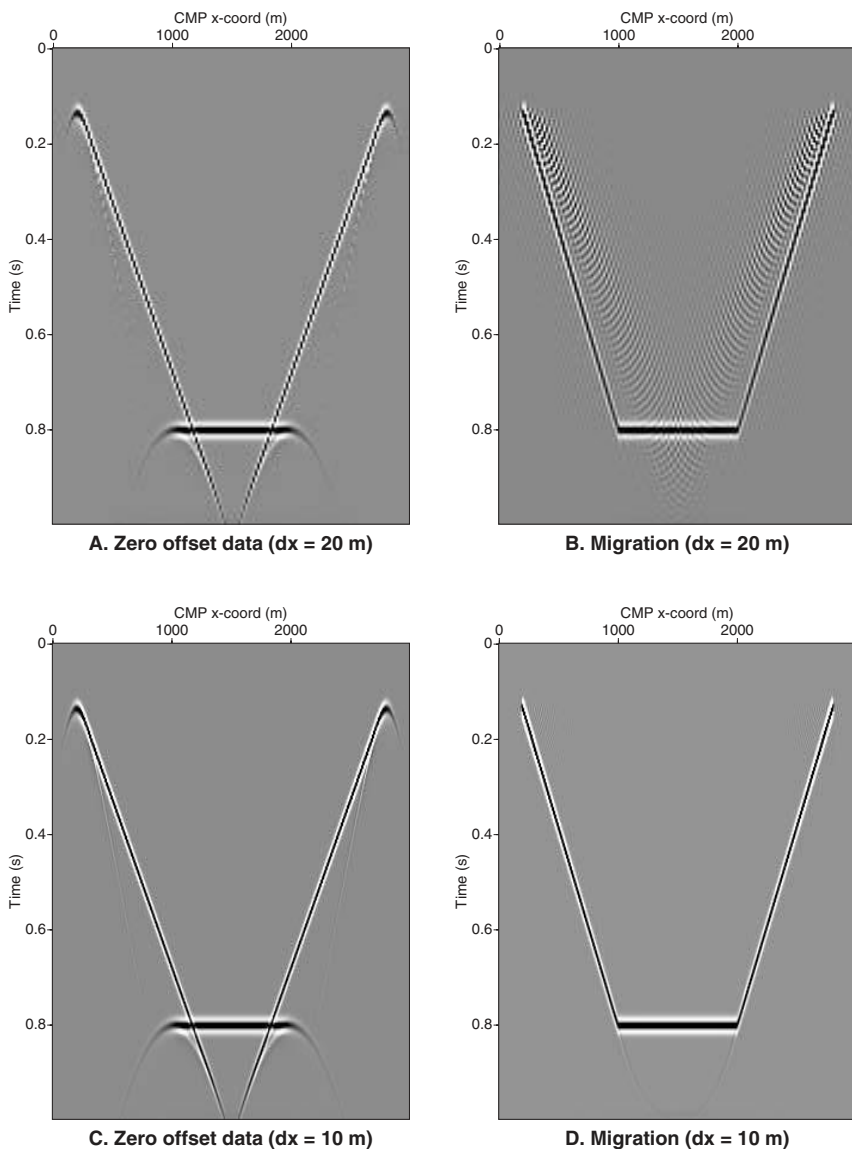


Fig. 9.6 Spatial aliasing degrades migration results. (A) Zero offset section with two steep aliased events and an unaliased horizontal one. The trace spacing of 20 m is too big for the steep events. Horizontal events are never aliased. (B) Migration of the data shows properly located reflections along with strong migration artifacts caused by data aliasing. (C) Zero offset section with 10 m trace spacing is not spatially aliased. (D) Unaliased data are properly handled by migration to yield correctly positioned reflections and virtually no artifacts.

## Elements of 3D Seismology

We can make some general statements about spatial aliasing.

1. The safe choice is to use a smaller CMP interval
2. The required CMP interval will be small for shallow and big for deep targets
3. Use maximum signal frequency and 90-degree dip for safest CMP interval
4. A smaller midpoint interval costs more at acquisition time
5. The aliasing condition is the same in 2D (CMP interval) or 3D (bin size)

## 9.6 Total signal-to-noise improvement

Seismic data always contains noise as well as signal. The signals are primary reflections and diffractions. Any other kind of event or random jitter is considered noise. Figure 9.7 classifies some common kinds of noise.

The signal-to-noise ratio,  $R_{sn}$ , describes signal strength relative to noise strength. It is the ratio of peak signal amplitude to average maximum noise amplitude in a time window that may include some or all of the trace. While “average maximum” may sound like an oxymoron, we mean exactly that because the actual average of wave-like noise will tend to zero. In practice the signal-to-noise ratio is not easy to quantify because of difficulty in separating signal and noise.

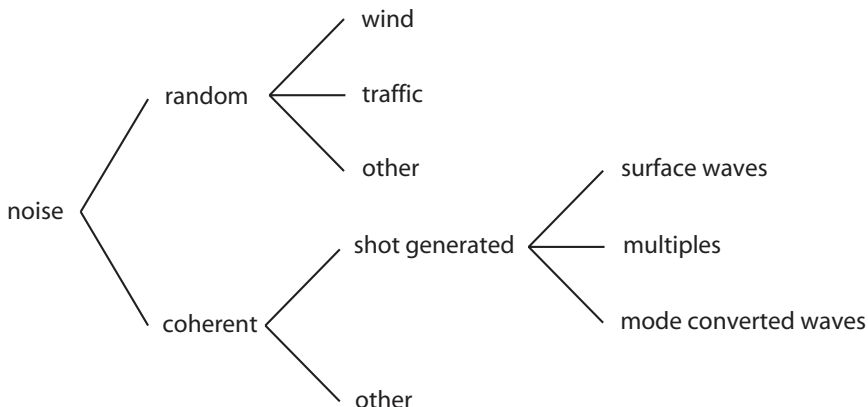


Fig. 9.7 Classification of noise types likely to be encountered in land or marine seismic data. Some items here may be considered signal if the survey is designed to measure them (e.g., mode converted waves). Although the term “random” is common in connection to noise, it does not necessarily imply true random behavior in a statistical sense.

Modern recording with 24- or 32-bit analog-to-digital conversion allows very small signals to be faithfully recorded. But these small signals are only useful if the signal-to-noise ratio is high. The process of vibroseis correlation, in particular, can significantly improve  $R_{sn}$  and raw  $S_N$  is usually taken to be that observed on correlated field traces.

The primary method of  $R_{sn}$  enhancement is stacking. As discussed earlier, there are two kinds of stacking. Vertical stacking is the repetition of a shot profile in the field with the result from each shot being added to the previous shots. The typical fold of vertical stack,  $F_v$ , is between one and eight. Common midpoint stacking is a data processing step, where all traces associated with a certain position on the earth surface are added to give a single trace at that position. The number of traces added in CMP stacking is the CMP fold,  $F_{cmp}$ , and typical numbers are 20 (low-fold land 3D) to 200 (2D marine).

In either stacking process,  $R_{sn}$  is improved against incoherent noise by the square root of the number of traces summed in the stack  $\sqrt{N}$ . Figure 9.8 illustrates this concept.

The net effect of both vertical and CMP stacking is to produce a signal-to-noise improvement factor  $I_{sn}$  of

$$I_{sn} = \sqrt{F_v F_{cmp}} \quad (9.11)$$

The final signal-to-noise ratio,  $R_{snf}$  will then be given by

$$R_{snf} = R_{snr} I_{sn} \quad (9.12)$$

where  $R_{snr}$  is the raw signal-to-noise ratio associated with the output of a geophone group. If we knew  $R_{sn}$  for the output of a single geophone the improvement factor would include the number of geophones per group,  $N_g$

$$I_{sn} = \sqrt{F_v F_{cmp} N_g} \quad (9.13)$$

This factor can represent a first-order improvement in data quality.

## Elements of 3D Seismology

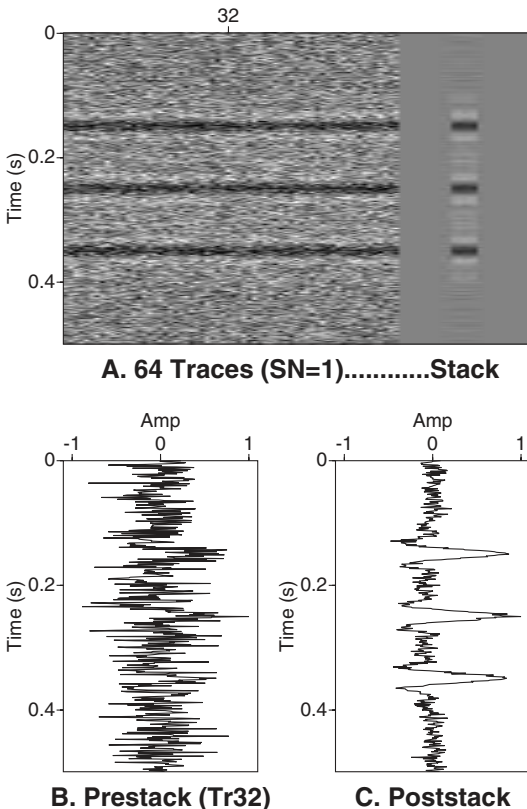


Fig. 9.8 Stacking tends to cancel random noise. (A) Three identical signals are embedded in random noise on 64 traces with  $R_{sn}=1.0$ . These traces are summed sideways (stacked) to make the stacked trace shown on the right, which is repeated several times for visibility and offset from the prestack data by blank traces. (B) A graph of prestack trace 32 confirms that with a signal-to-noise ratio of one, the noise is, on average, just as strong as the signal. (C) The stack trace shows clear stand-out of the three signals. Theoretically, the peak signal amplitude in this case should be  $\sqrt{64}=8$  times the average peak noise amplitude.

Here are some comments on signal-to-noise ( $R_{sn}$ ) ratio and improvement.

1.  $R_{sn}$  is ambiguous to quantify and not used as a hard design criteria
2.  $R_{sn}$  is the main thing that makes data look “good” versus “bad”
3. Vertical stack improves  $R_{sn}$  but is an expensive field procedure because it increases acquisition time
4. The geophone array is an important factor in  $R_{sn}$  improvement as well as attenuation of surface waves
5. Stacking of any kind reduces incoherent noise but not shot-generated noise

# 10

## Land Shooting Geometry

The development of 3D seismic on an industrial scale required the parallel development of recording systems, computers, and processing technology. The first large scale 3D seismic survey was undertaken in 1971 by Geophysical Service Incorporated on behalf of an industry consortium [100, 162]. By the mid-1980s, 3D seismic was in wide use, and today it is the standard form of petroleum seismic data throughout the world. Now 2D seismic data continues to be acquired but represents an ever smaller segment of the seismic industry.

Rather than track the history of 3D seismic acquisition, we will concentrate on a few fundamental geometries that lead naturally to template shooting, which is the most common method in use today.

### 10.1 Coordinates and related quantities

Whether we are considering land or marine 3D shooting, Figure 10.1, a seismic trace is created when the wavefield from a shot is recorded by one receiver group. Thus a trace is associated with a shot coordinate  $x_s$  and a group coordinate  $x_g$  both in 3D space

$$\begin{aligned}\underline{x}_s &= (x_s, y_s, z_s) \\ \underline{x}_g &= (x_g, y_g, z_g)\end{aligned}\tag{10.1}$$

From these position vectors, we can calculate the midpoint coordinate

$$\underline{x}_m = \frac{1}{2} (\underline{x}_s + \underline{x}_g) = \frac{1}{2} (x_s + x_g, y_s + y_g, z_s + z_g)\tag{10.2}$$

and the offset vector

$$\underline{x}_o = \underline{x}_s - \underline{x}_g = (x_s - x_g, y_s - y_g, z_s - z_g)\tag{10.3}$$

## Elements of 3D Seismology

Notice the midpoint and offset definitions include  $z$ -coordinates corresponding to elevation. However, in practice the  $z$ -values are moved whenever possible to a common datum plane (constant  $z$ -coordinate) through the process of static corrections. In cases of extreme topography, this process fails and the full 3D shot and receiver coordinates are used by prestack migration or wave equation datuming algorithms.

Assuming that topography is such that shot and group can be moved to a datum plane, both midpoint and offset become functions of  $(x,y)$  only. Specifically, the offset vector is

$$\underline{x}_o = \underline{x}_s - \underline{x}_g = (x_s - x_g, y_s - y_g) \quad (10.4)$$

For a 2D line, we can define any axis to be the inline direction. Using the  $x$ -coordinate in this way, the 2D offset becomes  $x_o = x_s - x_g$ , which can be positive or negative depending on the relative position of shot and receiver. Thus in 2D shooting, we have the concept of signed and unsigned offset.

In 3D, the offset is defined as the absolute distance between shot and receiver

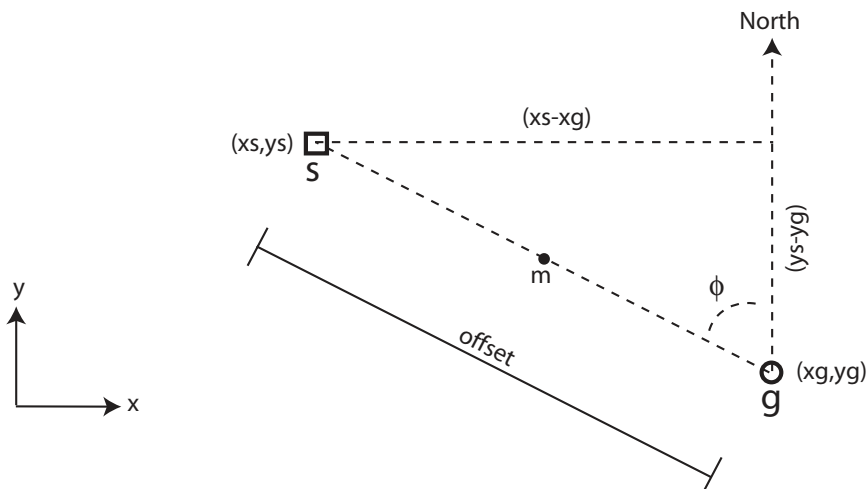


*Fig. 10.1 Map view geometry and definitions for a single seismic trace, including location of shot (s), receiver group (g), and midpoint (m). The offset and azimuth angle ( $\phi$ ) are also shown.*

$$x_o = |\underline{x}_o| = \sqrt{(x_s - x_g)^2 + (y_s - y_g)^2} \quad (10.5)$$

and the role of offset sign is superseded by the azimuth,  $\phi$ . Azimuth is an angle measured counterclockwise relative to north from the viewpoint of the receiver looking at the shot, (see Fig. 10.1). The azimuth is calculated from shot and receiver coordinates as

$$\phi = \tan^{-1} \left( \frac{x_s - x_g}{y_s - y_g} \right) \quad (10.6)$$

which can be implemented to give azimuth values from either 0–180 or 0–360 degrees.

Reciprocity assures us that interchange of shot and receiver leaves the measured data unchanged, and this is usually invoked to use the 0–180 degree azimuth definition. However, for detailed analysis of data acquired with shot and receiver arrays, as well as multicomponent receivers, reciprocity may become suspect and the 0–360 degree definition can be used.

An example calculation may help to bring these definitions into focus. Figure 10.2 shows a shot and receiver with coordinates of

$$\begin{aligned} \underline{x}_s &= (x_s, y_s) = (100, 230) \\ \underline{x}_g &= (x_g, y_g) = (150, 200) \end{aligned} \quad (10.7)$$

where the units are meters and any elevation differences have been adjusted to the datum  $z_s=z_g=0$ . This trace has a midpoint coordinate of

$$\underline{x}_m = \frac{1}{2} (100 + 150, 230 + 200) = (125, 215) \quad (10.8)$$

the offset is

$$x_o = \sqrt{(100 - 150)^2 + (230 - 200)^2} = 58.3 \text{ m} \quad (10.9)$$

and the azimuth is

$$\phi = \tan^{-1} \left( \frac{100 - 150}{230 - 200} \right) = 59^\circ \quad (10.10)$$

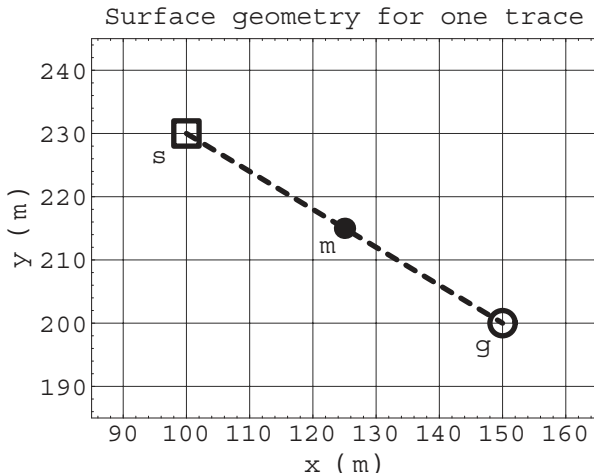


Fig. 10.2 An example of shot (s), group (g), and midpoint (m) for a single trace.

## 10.2 Cross spread method

The cross spread, or crossed array, is a fundamental acquisition geometry described in detail as early as 1972 [194]. It involves one source line and one perpendicular receiver line as illustrated by Figure 10.3. As an evolution of 2D shooting, the cross spread is formed by rotating the receiver line 90 degrees to the shot line. This causes the midpoints to move offline, forming an image area.

Figure 10.4A illustrates a cross spread consisting of  $n_s=11$  shots and  $n_g=11$  receiver groups. The shots are shown as squares running parallel to the  $x$ -axis and receivers are circles aligned parallel to the  $y$ -axis, but this choice is arbitrary. The shot and receiver intervals for this example are

$$\begin{aligned}(dx_s, dy_s) &= (20, 0) \\ (dx_g, dy_g) &= (0, 20)\end{aligned}\tag{10.11}$$

where all distances are in meters. The image area consists of  $n_s n_g=121$  midpoints with intervals of

$$\begin{aligned}dx_m &= \frac{1}{2} \text{Min}(dx_s, dx_g) = 10 \\ dy_m &= \frac{1}{2} \text{Min}(dy_s, dy_g) = 10\end{aligned}\tag{10.12}$$

where  $\text{Min}(a,b)$  means the smaller of (a,b) should be used. This 3D midpoint interval calculation is clearly an extension of the 2D midpoint spacing rule.

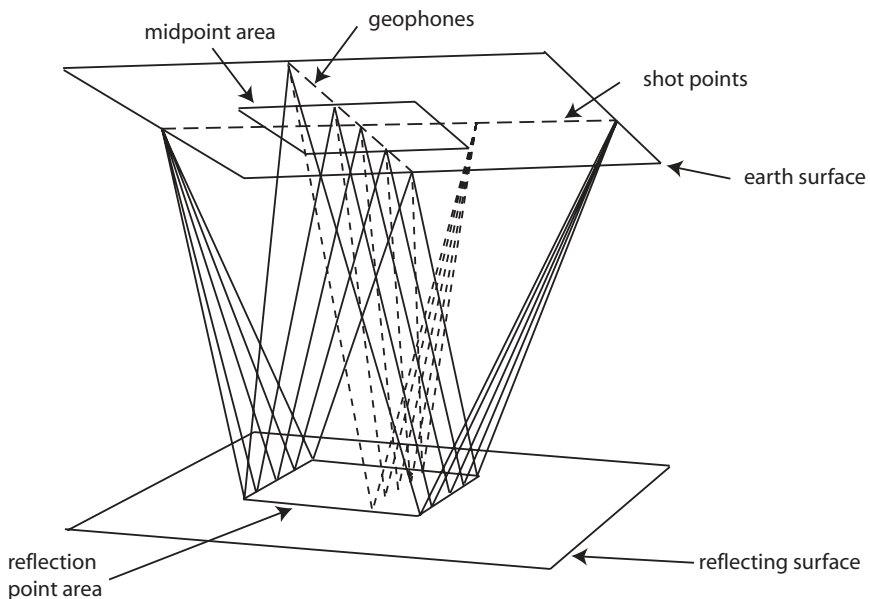


Fig. 10.3 Raypath sketch of cross spread shooting (modified from [194]).

Figure 10.4B shows a line connecting each shot-receiver pair. The orientation of this line represents the azimuth, and its length is the offset. The distribution of azimuths and offsets are shown as histograms in Figure 10.4C and D. From these we see that offsets around 85 m and 105 m dominate the data, an effect called offset clustering.

For various processing reasons, a more uniform distribution of offsets is preferred. One way to achieve this is to skid the shots or receivers half a station, as shown in Figure 10.5. This has the effect of smoothing out the offset distribution while leaving midpoint intervals unchanged (but shifted) and azimuth distribution only slightly modified. In 2D acquisition, this technique is termed shooting between the flags.

The azimuth distribution is very important since data is truly 3D only if it has a full azimuth distribution. To take an extreme example, consider a series of closely spaced 2D lines shot in such a way that a large area of midpoint coverage is acquired. One could say it is a 3D survey. However, since the azimuth distribution is limited to the 2D shooting direction, it is simply a collection of 2D lines and not a 3D survey. This is more than quibbling over words. The seismic image volumes generated in these two cases would be significantly different, with the 3D result a more reliable indicator of the subsurface.

## Elements of 3D Seismology

For 2D acquisition, all shots and receivers lie in a line, which is termed the inline direction. For 3D we distinguish inline and crossline directions. However, this can lead to confusion since several definitions are possible. For example, we could define inline as the direction the line was shot, or parallel to shots or receivers, or some arbitrary direction [165]. We will sidestep this issue by distinguishing the directions as  $x$  and  $y$ , rather than inline and crossline.

In addition to the actual shot, group, and midpoint coordinates associated with a cross spread (or any 3D shooting), a grid is superimposed on the survey area. Each cell in this grid is called a bin, and the natural bin size is determined

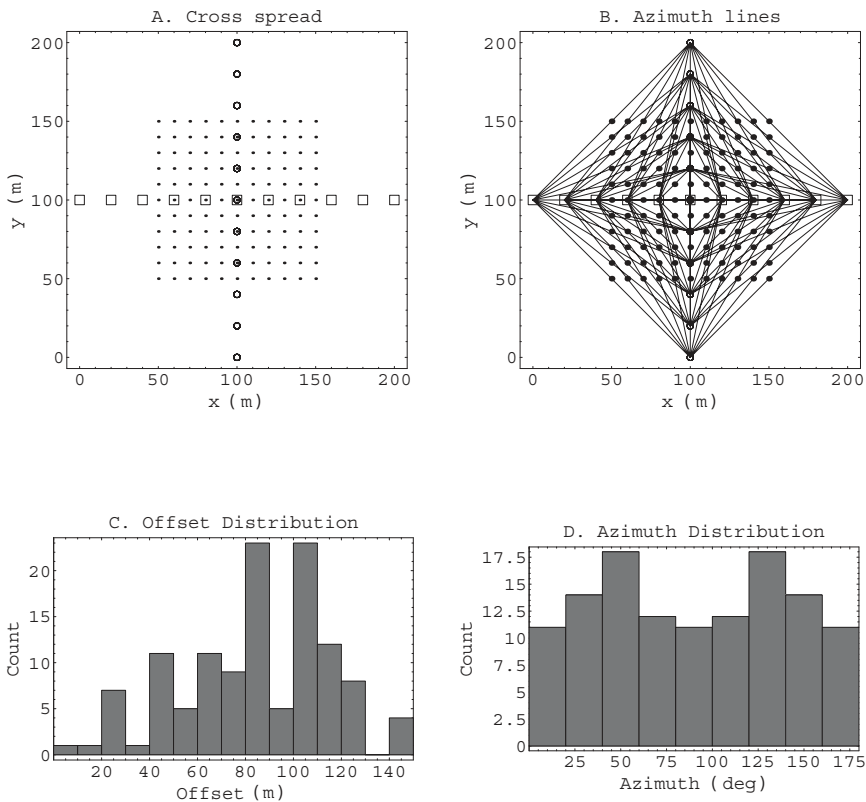


Fig. 10.4 Cross spread shooting. (A) shot points (squares), receiver groups (circles) and midpoint locations (dots). (B) Collection of azimuth lines connecting each shot and receiver with the midpoint at the line center. (C) and (D) Histograms of all offsets and azimuth angles. Two dominant offsets occur because of orthogonal shot and receiver lines.

by the midpoint intervals. For the example shown in Figure 10.4, the bin dimensions are

$$\begin{aligned} dx_b &= dx_m = 10 \\ dy_b &= dy_m = 10 \end{aligned} \quad (10.13)$$

We note this is the bin size determined by acquisition parameters. While prestack interpolation is an important part of modern seismic data processing [156], the natural bin size determines physical resolution and

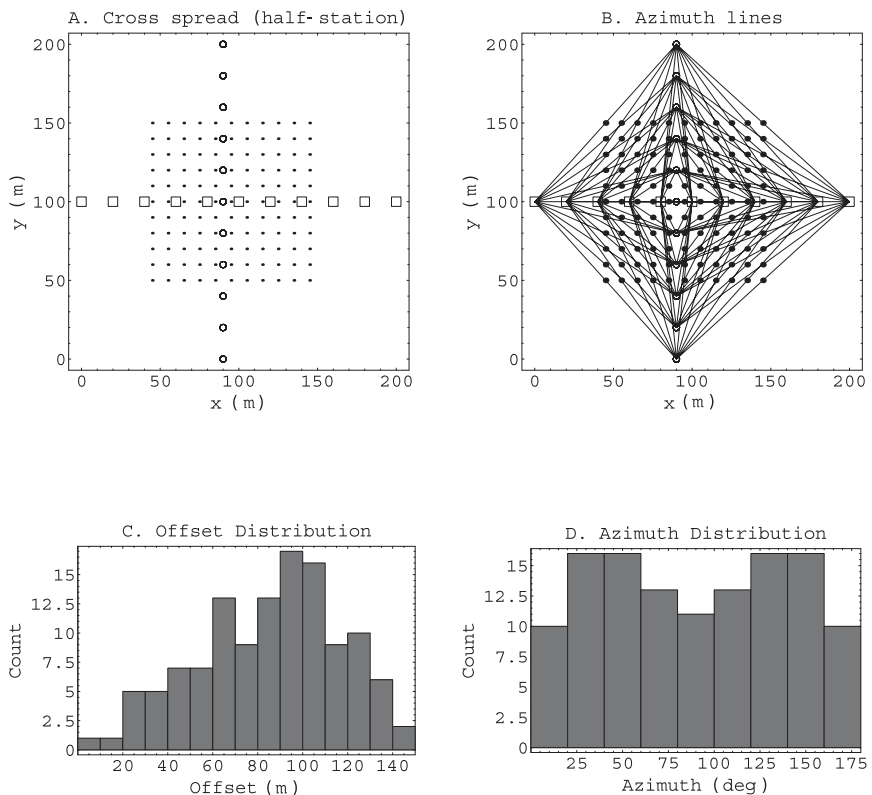
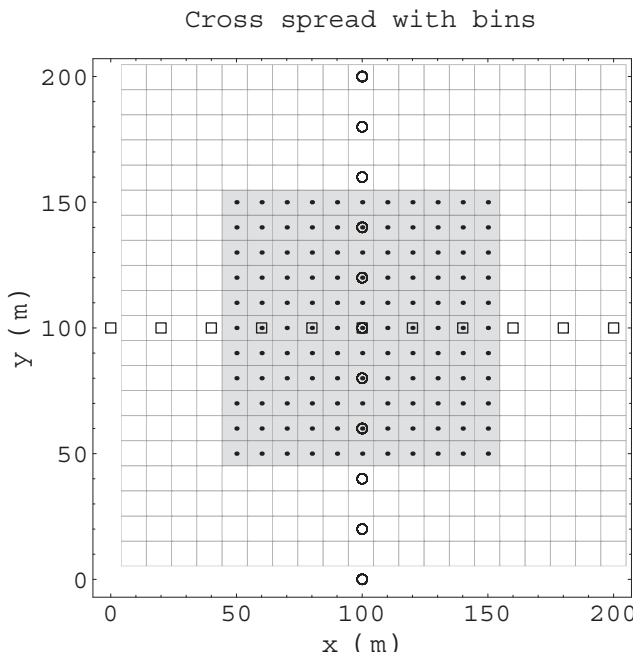


Fig. 10.5 Cross spread shooting with non-coincident shot and receiver stations. This breaks the symmetry enough to give a better distribution of offsets.

information content of the data [191]. Each bin is a capture area that contains all traces (midpoints) falling inside it. The number of traces in each bin is the CMP fold, also called the fold of stack. As seen in Figure 10.6, the cross spread geometry is single fold, meaning there is one trace per bin.



*Fig. 10.6 Cross spread showing bins and fold. Maximum CMP fold is one (gray), so non-overlapping cross spread shooting is a single fold technique.*

### 10.3 Swath method

By the mid-1970s, swath or wide line shooting was in commercial use [162]. The swath method is a continuous extension of cross spread shooting, where the source line is extended through many short perpendicular receiver lines.

Figure 10.7 shows an example of swath shooting geometry. The parameters describing this technique include shot interval ( $dx_s=20$  m), number of shots ( $n_s=11$ ), group interval ( $dy_g=20$  m), receiver line interval ( $dx_g=40$  m) and the number of receiver lines ( $n_{gl}=4$ ). As usual, we interchangeably use the terms receiver and group. The midpoint intervals are calculated as before,

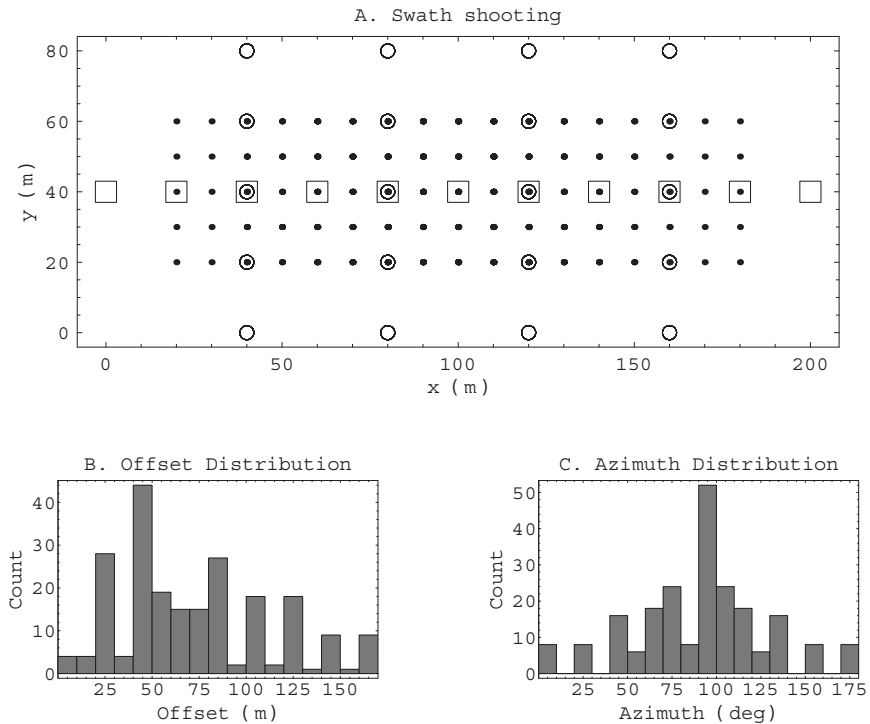


Fig. 10.7 Swath shooting technique.

$$\begin{aligned}
 dx_m &= \frac{1}{2} \text{Min}(dx_s, dx_g) = 10 \\
 dy_m &= \frac{1}{2} \text{Min}(dy_s, dy_g) = 10
 \end{aligned} \tag{10.14}$$

which are also the natural bin dimensions. As the source walks through the receiver lines, we can think of the process as generating midpoint lines parallel to the shot direction, the number of midpoint lines being equal to the number of groups per receiver line.

Since this swath is elongated in the E-W direction, we expect a dominance of 90-degree azimuths as clearly seen in Figure 10.7. In the limit of one receiver channel per line, all receivers and shots would be in the same line, and the situation shown would reduce to 2D shooting with only one azimuth.

## Elements of 3D Seismology

The CMP fold for this swath is variable as seen in Figure 10.8 with the maximum fold being four.

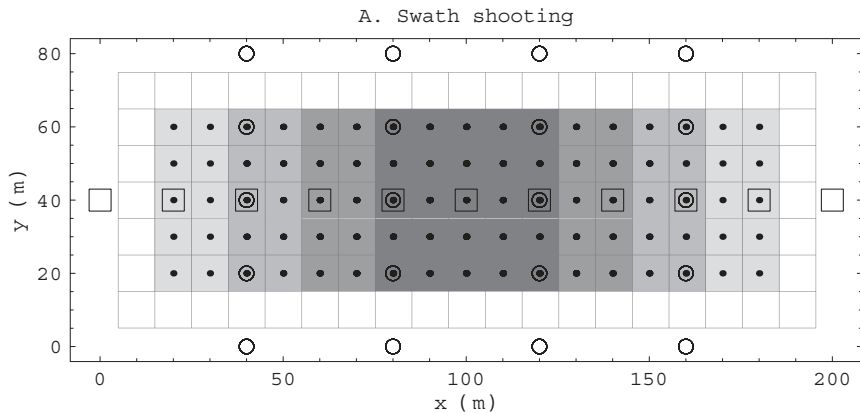


Fig. 10.8 Swath shooting with bins and CMP fold. This particular example has a maximum fold of four.

## 10.4 Fringe

A 3D survey should give reliable information across the target. However, we must accept and plan for edge effects in the data. Figure 10.9 shows a schematic drawing of the various areas associated with a survey. Remember, the final image will only extend as far as the midpoint coverage.

The area containing source and receiver locations is the acquisition area, while the image area contains all midpoint locations. The area between the two is called the acquisition fringe, in which we need permits and access, but get no midpoint coverage and therefore no image. Part of the image area is unreliable due to various edge effects (build-up of CMP fold, reflections lost to migration distance, etc.). This is called the fold/migration fringe. Finally, inside all the fringes lies the sweet spot, where data is most reliable. Ideally the target should lie completely in the sweet spot. Figure 10.10 shows the image area for a land 3D seismic survey, and the shades of gray represent CMP fold. Edge effects associated with fold build-up are evident.

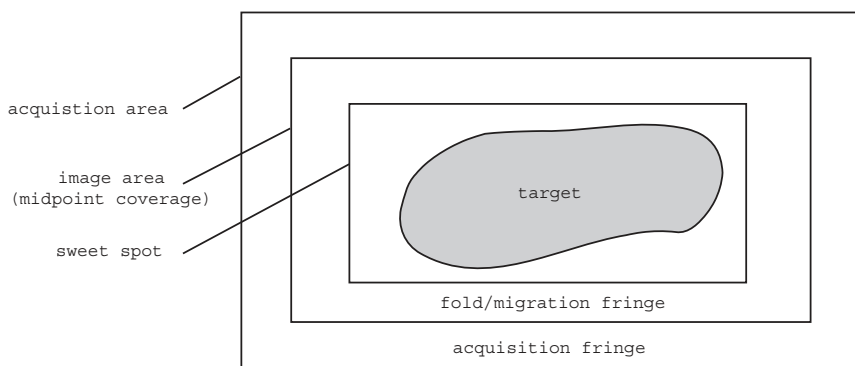


Fig. 10.9 Map view of areas and fringes in a 3D seismic survey.

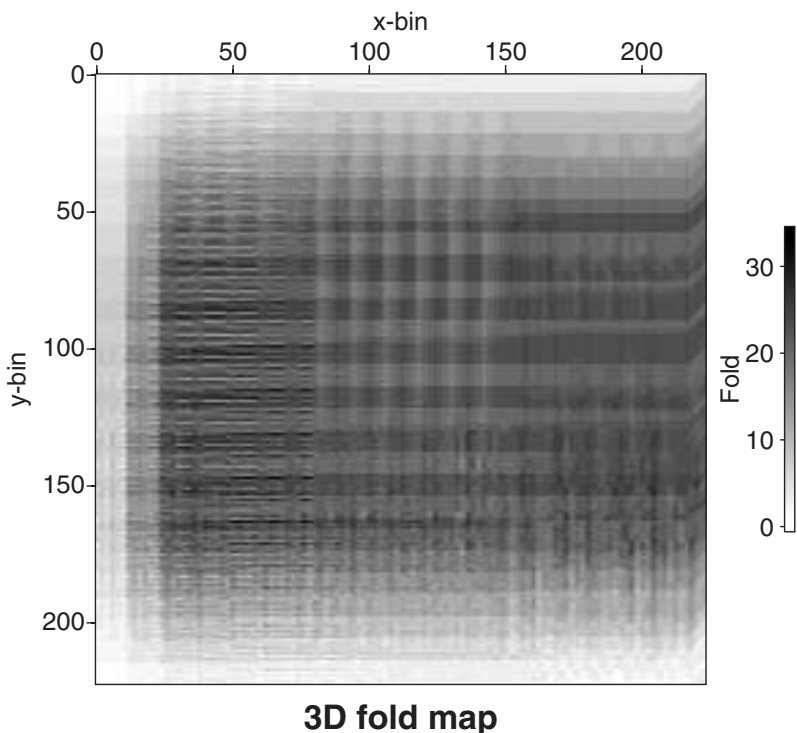


Fig. 10.10 Fold map for an onshore U.S. 3D seismic survey. Note edge effects associated with fold build-up.

### 10.5 Perimeter or loop method

Perimeter shooting involves sources and receivers placed on the perimeter of a regular or irregular area. Typically the source and receiver lines are coincident, and all the receivers on the perimeter are recorded for all the shots.

In Figure 10.11, there are two horizontal source lines and two vertical receiver lines. The result is a maximum fold of two, Figure 10.12. If the area were completely surrounded by sources and receivers, the maximum fold would be higher, and the fold can be further increased by including interior source or receiver lines.

One way to understand how midpoint coverage works is to consider a patch of receivers and a source point well away from it, as in Figure 10.13. The midpoint coverage generated from this one shot into the receiver grid is a midpoint grid,

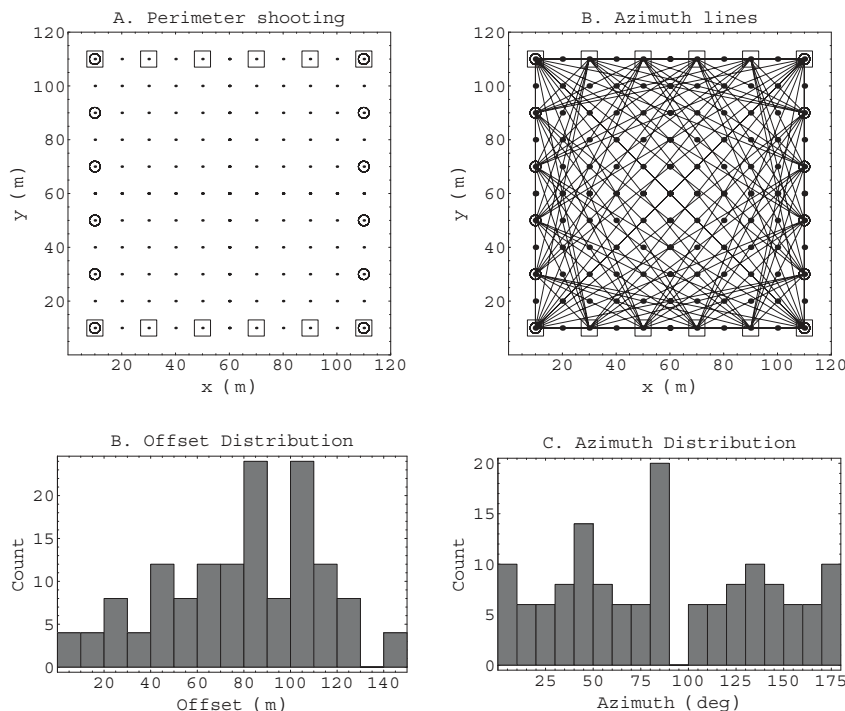


Fig. 10.11 (A) Perimeter shooting method showing sources (square), receivers (circle), and midpoints (dot). (B) Azimuth lines connecting each shot and receiver. (C) and (D) Histograms showing offset and azimuth distribution.

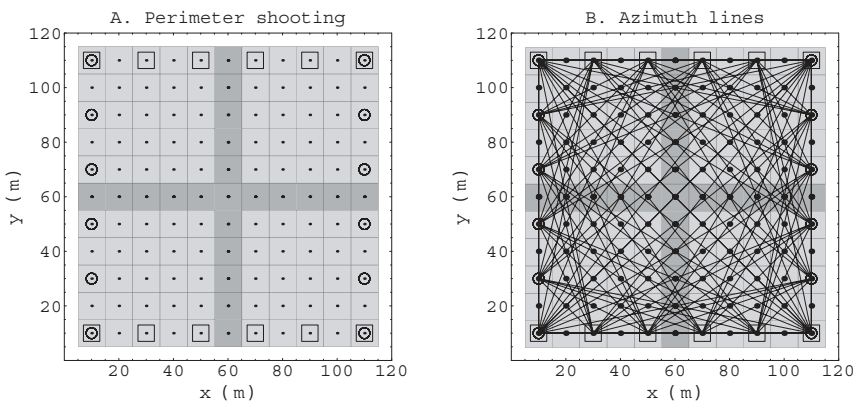


Fig. 10.12 (A) Bins and CMP fold for a perimeter shooting example. Maximum fold is two. (B) Same with azimuth lines as overlay.

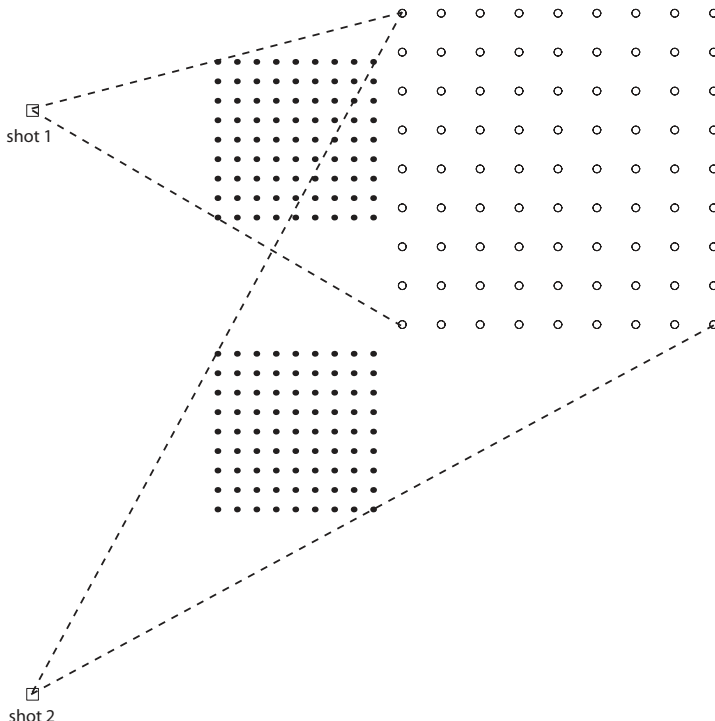


Fig. 10.13 Shooting into a patch of receivers gives a collection of midpoints that is a half-scale version of the receiver geometry. Here two shots generate two non-overlapping midpoint patches from the same receiver patch.

## Elements of 3D Seismology

which is a half-scale version of the receiver geometry. This makes 3D very flexible at undershooting obstacles—that is, we can image under a part of the earth where no sources or receivers can be placed. Figure 10.14 shows this idea works even for irregular receiver areas and geometries.

Perimeter shooting gives the most CMP image coverage for the least surface and source effort. Figure 10.15 illustrates a simple geometry with one interior line. There is no acquisition fringe.

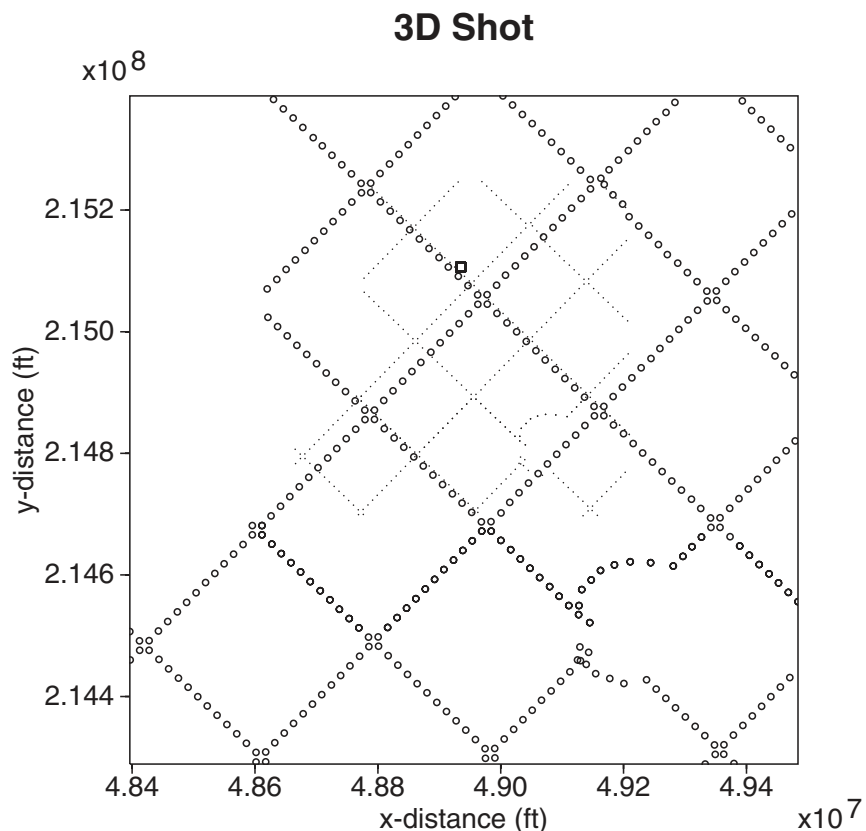


Fig. 10.14 This 3D shot record has one source (square), 416 receivers (circles), and the same number of midpoints (dots). Note the midpoints are a half-scale version of the receiver positions as seen from the source. A receiver grid irregularity in the lower right corner represents a surface obstruction. Receiver groups have been offset to avoid it.

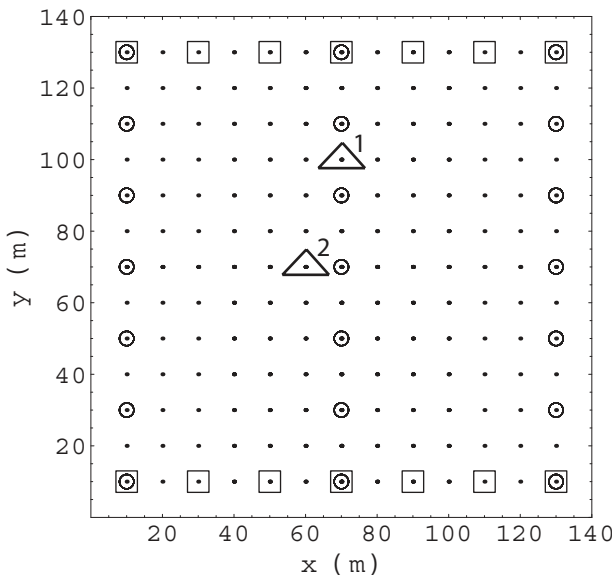


Fig. 10.15 Midpoint plot of a perimeter survey with one interior receiver line. The fold is 3 at location 1, and 4 at location 2.

## 10.6 Cabling, template shooting, and fold

To this point we have assumed that all receivers are live for all shots. This is seldom the case in real data except for very small surveys. For larger survey areas, only part of the receivers laid out on the ground are live for any given shot. The details of which receivers are live for which shots is termed cabling. If all receivers are live for all shots, the survey is said to be shot static.

Cabling is an issue for two reasons. First, the recording system has only a finite number of data channels (one channel per receiver group). Second, by controlled cabling we can tailor the survey to meet fold, offset, azimuth and other design criteria.

Template shooting involves simple cabling. The area to be shot is laid out with as many receivers as are available. The source is located in one corner of the receiver spread. Centered on the source is an imaginary template or box. The template is usually square, but may be a rectangle, circle, or something more complicated. All receiver groups on the interior of the template are live and all others are dead. The source position moves in a regular fashion along parallel lines

## Elements of 3D Seismology

to roll through the survey area. As the source position moves, the template may or may not move with it, depending on the precise roll-along procedure utilized.

For large surveys, this roll-along is very efficient. Receivers behind the template can be picked up and laid out ahead for continuous shooting. The size of the template is one of many design parameters, which can be tested in computer simulation to find a suitable parameter set.

Table 10.1 lists the parameters, design equations, and example values for template shooting. This subject has been studied in depth by Vermeer [191], and we follow his parameterization of the problem while casting it in our notation.

Figure 10.16 is a map-view sketch of the example given in Table 10.1. Note that receiver lines are considered to run parallel to the  $x$ -axis and shot lines parallel to the  $y$ -axis. However, this simply defines the line direction for each as the direction of fine sampling. In a symmetric arrangement where all intervals are equal, this distinction would be meaningless. Some authors strongly advocate symmetric sampling, but we will retain the more general case here.

Some quantities in Table 10.1 require comment. The acquisition footprint is the total area of live receivers for each shot, and the midpoint footprint is the single fold image area generated by each shot. As these quantities increase, the survey acquisition becomes more efficient, assuming that acquisition time per shot does not increase accordingly.

As the shot location moves relative to the receiver lines, the receiver template may or may not move, but the farthest a source will ever be from a live group is called the maximum near offset. This is an important parameter since static correction estimates require near offset data.

The example survey has a shot density of  $66.7/\text{km}^2$  and receiver group density of  $80/\text{km}^2$ . This implies shots are relatively more expensive than receivers for this particular survey. There are circumstances where the opposite is true. For example, transition zone (coastal marine) shooting involves difficult deployment of expensive receiver systems, while the source is a standard air gun array. In this case, we would want to a design that minimizes receiver density rather than shot density.

The template aspect ratio tells us how closely the template of live receiver groups approximates a square (aspect ratio = 1). As square template implies full azimuth coverage, while a very large or very small aspect ratio indicates the template is significantly elongated, and azimuth coverage will be correspondingly narrower. From an aspect ratio point of view, the example in Table 10.1 is far from optimum. A 2D line is the extreme case with aspect ratio equal to zero or infinity.

When 3D fold is not an integer, we can expect that the survey will not attain a constant fold value in the sweet spot. In addition to integer 3D fold, integer 2D

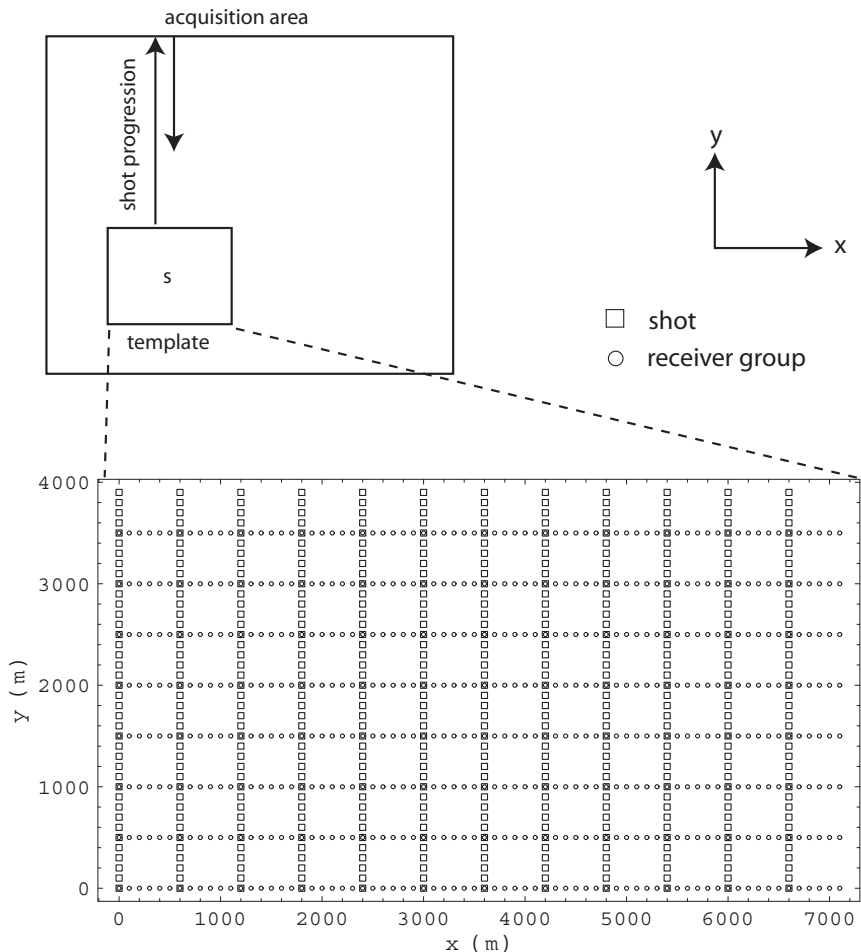
Independent Parameters	Symbol	Example
station intervals	$(dys, dx_g)$	(25,25) m
line intervals	$(dx_s, dy_g)$	(600,500) m
maximum offsets	$(x_{mo}, y_{mo})$	(3600,2000) m
Dependent Parameters	Symbol and Formula	Example
bin size in x-direction	$dx_b = \frac{1}{2} \text{Min}(dx_s, dx_g)$	12.5 m
bin size in y-direction	$dy_b = \frac{1}{2} \text{Min}(dys, dy_g)$	12.5 m
receiver spread length	$x_{sl} = 2 x_{mo}$	7200 m
shot spread length	$y_{sl} = 2 y_{mo}$	4000 m
acquisition footprint area	$a_{af} = x_{sl} y_{sl} / 10^6$	2.88 km <sup>2</sup>
midpoint footprint area	$a_{mf} = a_{af}/2$	1.44 km <sup>2</sup>
template aspect ratio	$r_a = x_{mo} / y_{mo}$	1.8
maximum near offset	$x_{no} = \frac{1}{2} (dx_g^2 + dy_g^2)^{1/2}$	250 m
far offset	$x_{fo} = (x_{mo}^2 + y_{mo}^2)^{1/2}$	4118 m
2D x-fold	$f_{2dx} = x_{mo} / dx_s$	6
2D y-fold	$f_{2dy} = y_{mo} / dy_g$	4
3D fold	$f_{3d} = f_{2dx} f_{2dy}$	24
number of receiver lines	$n_{gl} = 2 y_{mo} / dy_g$	8
number of channels per line	$n_{cl} = 2 x_{mo} / dx_s$	288
number of active channels	$n_c = n_{gl} n_{cl}$	2304
number of shots per km <sup>2</sup>	$n_{skm} = 10^6 / (dx_s dys)$	66.7 km <sup>-2</sup>
number of groups per km <sup>2</sup>	$n_{gkm} = 10^6 / (dx_g dy_g)$	80 km <sup>-2</sup>
x-distance to full fold	$x_{ff} = \frac{1}{2} (x_{mo} - dx_s)$	1500 m
y-distance to full fold	$y_{ff} = \frac{1}{2} (y_{mo} - dy_g)$	750 m

Table 10.1 Design parameters and equations for orthogonal, shot-centered template shooting (modified from [191]). These equations assume receiver lines run parallel to the x-axis, shot lines are parallel to the y-axis, the number of receiver lines is even, and the number of channels per receiver line is even.

fold in each direction is also required to avoid fold striping. Fold striping is undesirable because it gives rise to signal-to-noise and data quality variations unrelated to geologic changes. This is particularly disruptive to amplitude and phase information. Any map-view variations in the data, which shadow the acquisition geometry, are considered acquisition footprint artifacts [84].

For a real survey, there are many reasons that a nice regular grid of sources and receivers may not be possible, a good example being Figure 10.14. But there are many locations where such a survey can be shot, and the design equations

## Elements of 3D Seismology



*Fig. 10.16 Template shooting geometry for land 3D seismic data corresponding to the example in Table 10.1. For clarity, every fourth shot and receiver group are shown along the fine sampling directions. The acquisition area is swept by a template of live receivers moving with the shotpoint.*

given here would then be valid. Another issue with the real world is that shot and receiver intervals are constrained to take on only certain values. For U.S. work, these are values that divide evenly into a mile (5280 ft). For metric work, the intervals must usually divide into a kilometer.

## 10.7 Crooked line 2D

In our discussion of 2D seismic data acquisition, it was assumed that the line was straight. Access problems in mountainous terrain or other settings can lead to crooked seismic lines. As a line becomes more and more crooked, the midpoints disperse away from a straight line to cover an area enclosing the shot and receiver locations, (see Fig. 10.17). If the midpoint crossline smear is less than the midpoint interval, the line can be processed as a standard 2D line. If the spread is greater than this, but not too much greater, the data can be projected onto a processing line called the slalom line.

For severely crooked 2D lines, the situation evolves into a 3D imaging problem [135,136]. The actual midpoint coverage in Figure 10.17 can be considered an irregular swath of 3D data and imposed onto a larger regular 3D grid, as shown in Figure 10.18.

## Elements of 3D Seismology

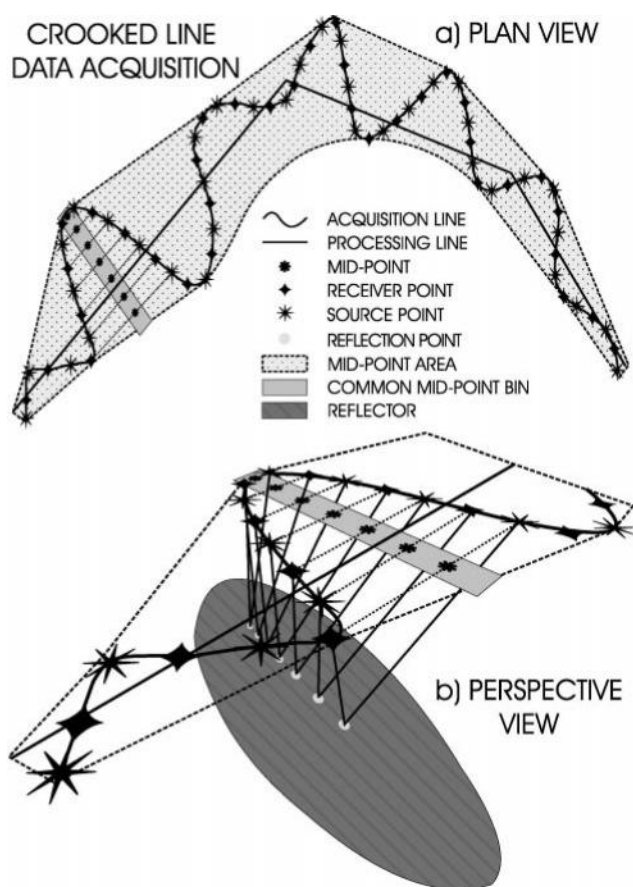
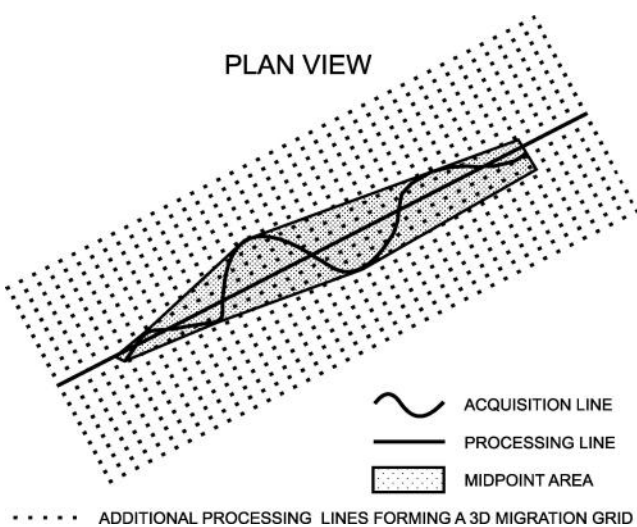


Fig. 10.17 Schematic 2D crooked line geometry. (A) Plan view showing midpoint coverage area and other features. (B) Schematic perspective view of a section of crooked line and reflection from a dipping reflector (from [135]).



*Fig. 10.18 Schematic midpoint geometry of a 2D crooked line in a 3D midpoint grid (from [136]).*

# 11

## Land 3D Design Optimization

There are many trade-offs in the design of any seismic survey. For 2D seismic, there are so few parameters that experience can effectively be used to achieve an optimum design. In 3D, the situation is different. Marine 3D is strongly constrained by hardware arrangements, including number and length of streamers, and the fact that the source is in a fixed position relative to the live receiver spread. But land 3D has complete flexibility with respect to design, and this means that determining an optimum shooting arrangement is more challenging.

The aim is to achieve certain target values, such as fold and bin size, while working with standard station spacings and using no more than the available number of recording channels. This can be set up as an optimization problem to find the *best* set of acquisition parameters to meet these goals [117]. By providing an objective measure for the quality of a survey design, both experts and non-experts can contribute to the design process. Here we will treat the problem from a physical standpoint, but it can be carried through to financial optimization as well [133].

We take the point of view that a seismic survey adequately sampled on the acquisition surface is sufficient to image any subsurface configuration. Calculation of subsurface sampling, illumination, and resolution, however, require detailed knowledge of the subsurface [78].

### 11.1 Optimization and inversion

There is a vast and rapidly growing literature associated with the theory of optimization; this is partly mathematical and partly computer science. We will briefly describe optimization to put the current chapter in context, and as acknowledgment that optimization is applicable to nearly every facet of seismic work from acquisition to interpretation.

## Elements of 3D Seismology

Optimization is intimately related to inverse problems [161]. Figure 11.1 illustrates the general inversion problem. This figure is generic in the sense that it applies to survey design optimization as well as more ambitious inversion problems in seismology and other fields. Action items are shown in ovals, while results or data files are in rectangle boxes.

For the 3D design problem, we start with a set of station intervals and channels in each direction (*initial parameters*), and then calculate (*simulation*) all the survey design quantities such as bin size and far offset (*simulated data*). This is compared to the target parameters, and a decision is made whether the solution is good enough (*accept*) or not (*reject*). If the solution is rejected, the parameters

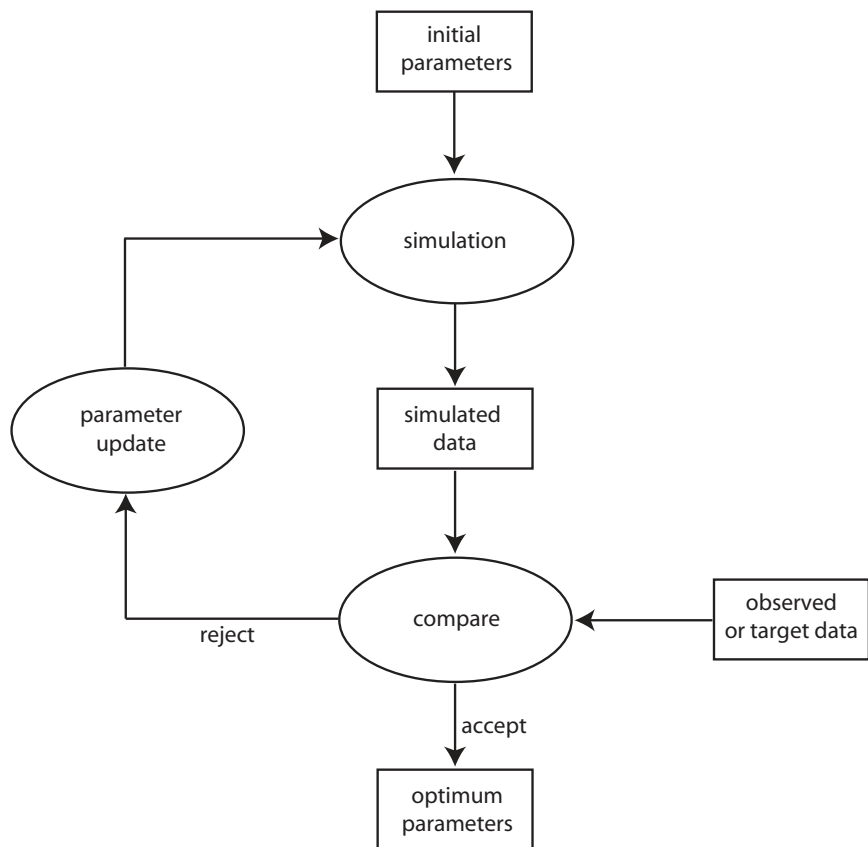


Fig. 11.1 General inverse problem.

are updated, another simulation is done, another compare, and so on. The process can stop when the match is acceptable or a maximum number of iterations is exceeded or some other stopping criteria is invoked.

To give just one example of another kind of inversion, the parameters could be gridded velocities in a 2D earth model, and the observed data could be field seismic shot records. The result of such an inversion would be an earth velocity model that is most consistent, in some sense, with the observed shot records. This is a difficult problem because the parameter space is large (earth velocities and densities), the simulation step is expensive (lengthy wave equation modeling), and convergence is slow requiring many iterations. It is the subject of much recent research [61].

The key elements of the inversion process are the simulation, compare, and parameter update steps. The physics or mathematical understanding of the problem is contained in the simulation. In the case of 3D survey design, the simulation step uses the template shooting equations of Table 10.1. It is possible to classify optimization methods in many ways, one of which is the nature of the comparison and parameter update actions. In manual inversion, these steps are done by human input. Someone views the simulated data and visually compares with the target data, and based on the intuitive mismatch, the parameters are updated by hand. This is rarely done in seismic work but occasionally used in 1D problems, such as gravity profile inversion.

In catalog inversion, the parameters are updated by selection from a catalog of allowed values. An inversion process that cycles through all possible parameter values is called an exhaustive search. This is only possible when the number of parameters (i.e., the dimension of the parameter space) is small. For large parameter spaces, such as the seismic inversion example, an exhaustive search is extremely inefficient. In automatic inversion, both compare and parameter update steps are accomplished by computer optimization methods.

In the compare step of an inversion process, it is necessary to define a function, which quantifies the mismatch between simulated and observed data. This can be as simple as the squared difference or something more complex. The misfit function is also called the cost or objective function. All these names suggest its key role in the optimization problem.

If there are  $N$  parameters to be estimated, the cost function can be thought of as an  $N$ -dimensional surface, and the goal is to find the deepest valley in the surface. This minimum represents the very best set of parameters in the sense that they minimize the cost function. But there are likely other valleys not quite so deep that can easily trap inversion procedures. The distinction between global and local minimization methods is another way to classify optimization techniques. No one wants to settle for a local minimum, but some problems are so difficult that we have little choice.

Luckily the inversion problem for 3D survey design can be solved for the globally optimum solution. We discuss it because it is important in its own right but also as a compact pointer to the use of optimization in other areas of petroleum seismology.

### 11.2 Assumptions, target variables, and constraints

We assume the data will be acquired using the shot-centered template method and that the equations in Table 10.1 apply. This acquisition method is common and very flexible with swath shooting as a special case. There are six independent parameters for this acquisition technique, the four station intervals ( $dx_s, dx_g, dy_s, dy_g$ ) and two maximum offsets ( $x_{mo}, y_{mo}$ ). Alternatively, we could use the number of receiver lines  $n_{gl}$  and the number of channels per line  $n_{cl}$  in place of the maximum offsets.

Effectively, the collection of equations in Table 10.1 says that given ( $dx_s, dx_g, dy_s, dy_g, x_{mo}, y_{mo}$ ), we can simulate a unique set of dependent parameters as listed in the same table. However, there are many valid acquisition parameter sets ( $dx_s, dx_g, dy_s, dy_g, x_{mo}, y_{mo}$ ) that give very nearly the same set of dependent parameters. For a typical case, there are millions of total possibilities with hundreds of designs that deliver the correct fold, bin size, channel usage, etc.

We acknowledge that for many logistical and financial reasons, perfect template shooting may not be possible. But such cases would still benefit from using an optimum design as a starting point.

We are interested in finding an optimum design, which best matches certain target quantities. Specifically, these target variables are

Target values:

```
tf3d      = 3D fold
ttol      = tolerance on 3D fold
tdxb      = bin size in x direction
tdyb      = bin size in y direction
txnr      = maximum near offset
txmax     = far offset
tnc       = number of recording channels available
```

In addition to these target variables, we can further refine the search by introducing preference weights and a shot-receiver density flag,

```
w1 = relative importance of matching near offset [0.0-1.0]
w2 = relative importance of matching far offset [0.0-1.0]
w3 = relative importance of getting a square template [0.0-1.0]
flag = minimize shots (3), receivers (2) or neither (1)
```

There are several constraints involved in getting a valid design; these include

- **3D fold.** The 3D fold must be an integer (hard constraint); otherwise the fold will vary from bin to bin and generate fold striping. This can introduce amplitude errors and other non-geologic variations into the data (i.e., acquisition footprint).
- **3D fold tolerance.** While 3D fold must be flat, we might be satisfied if it is just close to the target fold. For example, we might allow any flat fold between 20 and 25. The fold tolerance is an integer (hard constraint) between 0 and the allowed value (soft constraint).
- **2D fold.** Each 2D fold needs to be an integer (hard constraint).
- **Bin size.** The target bin size in each direction must be honored precisely (hard constraint).
- **Maximum near offset.** This should be honored approximately (soft constraint). The maximum near offset is the farthest that a shot will ever be from a live receiver group. Near offsets are important for statics processing.
- **Far offset.** We are satisfied with a far offset that is simply close to the desired value (soft constraint). Far offsets are important for velocity analysis.
- **Channels.** The total channels used cannot exceed the available number of channels (hard constraint).
- **Square template.** Template aspect ratio is a proxy for azimuth distribution. A square template assures full azimuth, while a thin template compromises azimuth coverage. A perfectly square template is not generally possible or necessary (soft constraint).
- **Shot and group density.** This describes the number of shots and receivers per square kilometer (hard constraint when activated). The relative cost of deploying and maintaining sources and receivers can be an important factor in optimum survey design. If shots are more expensive, then shot density should be minimized and vice versa when receivers are expensive. If the costs are similar, then the best design can be found while ignoring shot and receiver density.
- **Intervals.** The shot and receiver intervals can only take on certain allowed values (hard constraint). We will assume metric units and allowed station intervals are 10, 20, 25, 30, 40, 50, 60, 80, 100, 200, 300, 400, 500, 600, 800, 1000, 1200, 1600, 2000, 4000 meters.

### 11.3 A direct method

Before discussing a method that works, it is instructive to consider a direct approach that does not. It is tempting to define the following cost function

$$\begin{aligned} \text{cost} = & w_1 \left( \frac{f_{3d} - \tilde{f}_{3d}}{f_{3d}} \right)^2 + w_2 \left( \frac{dx_b - \tilde{d}x_b}{dx_b} \right)^2 + w_3 \left( \frac{dy_b - \tilde{d}y_b}{dy_b} \right)^2 + \\ & w_4 \left( \frac{x_{no} - \tilde{x}_{no}}{x_{no}} \right)^2 + w_5 \left( \frac{x_{fo} - \tilde{x}_{fo}}{x_{xfo}} \right)^2 + w_6 \left( \frac{n_c - \tilde{n}_c}{n_c} \right)^2 + w_7 (r_a - 1)^2 \end{aligned} \quad (11.1)$$

The first six terms on the right-side of this equation are aimed at achieving the target 3D fold,  $x$ -bin size,  $y$ -bin size, maximum near offset, far offset, and number of channels. Each penalty term is normalized to guard against the cost function being dominated by larger parameters. For example, typical bin sizes are 10–20 m, while far offsets might be 4000 m. Without normalization, any solution would quickly lock onto the correct far offset, while bin sizes would not converge to the target values. The last term in the cost function promotes a square template.

Minimizing this cost function by calculus-based methods, such as conjugate gradient or steepest descent, will fail because the system of equations is ill-posed. This means the inversion process does not converge to a solution. To assure convergence would require additional conditions that are not natural to the problem.

From such an approach, all target parameters could be matched exactly. But the acquisition parameter set would be unusable due to nonstandard shot and receiver intervals, as well as a noninteger number of channels. It may be possible to use such output as a starting point for manually adjusting intervals and channels to get a valid result, but there is no guarantee the result will be an optimum design.

There are three issues here:

1. There are far too many permutations to manually tweak this kind of result on a regular basis.
2. The method can only guarantee a local minimum, and we want the global minimum.
3. Since many acquisition parameters should be integers, this is really a problem in combinatorial analysis not minimization of a continuous function.

## 11.4 Method 2

To overcome all three of these issues, a hybrid method can be developed based on semi-exhaustive search and optimization [118]. The algorithm is outlined in the following pseudocode:

```

for all allowed intervals{
    select (dxs,dxg,dys,dyg)
    calculate binsize
    if (binsize=ok) {
        for (ncl=20 to tnc/2) {
            for (ngl=2 to tnc/ncl) {
                calculate nchannels
                if (nchannels=ok) {
                    compute other dependent parameters
                    if (3dfold=ok & 2dfolds=ok & s_g_density=ok) {
                        calculate cost function
                        if (cost=smallest) {
                            keep parameters (dxs,dxg,dys,dyg,ncl,ngl)
                        } // end cost if
                    } // end fold+density if
                } // end channel if
            } // end ngl loop
        } // end ncl loop
    } // end binsize if
} // end interval loop
}

```

In this way we progress through all 20 intervals for the shot and receiver spacing in each direction, passing solutions with the correct bin size. Next, we loop over the number of receiver lines and groups per line, and pass solutions that use no more than the available number of channels. Now all other parameters are calculated, and we pass solutions that have acceptable 3D fold, integer 2D fold in each direction, and honor our shot-receiver density preference. For solutions that make it this far, we calculate a cost function based on matching offsets and template aspect ratio

$$cost = w_1 \left( \frac{x_{no} - \tilde{x}_{no}}{x_{no}} \right)^2 + w_2 \left( \frac{x_{fo} - \tilde{x}_{fo}}{x_{fo}} \right)^2 + w_3 (r_a - 1)^2 \quad (11.2)$$

where these terms have the meaning described earlier.

## Elements of 3D Seismology

### 11.5 Examples

We can apply this method to reproduce the example in Table 10.1, and find it is not optimum with respect to template squareness. The target variables are taken from the table except that far offset and number of channels have been rounded up.

```
Design 3D v3.0
Aug. 8, 2003
Target variables:
tf3d      = 3D fold
ttol      = tolerance on 3D fold
tdxb      = bin size in x direction
tdyb      = bin size in y direction
txno      = maximum near offset
txfo      = far offset
tnc       = number of recording channels available
Enter Values For: tf3d ttol tdxb tdyb txno txfo tnc ...
24 0 12.5 12.5 250 4120 2500
```

For this example to be an optimum design, it is necessary to ignore the template aspect ratio and request minimum shot density. These choices are captured in the optimization weights and flag parameter.

```
w1 = relative importance of matching near offset [0.0-1.0]
w2 = relative importance of matching far offset [0.0-1.0]
w3 = relative importance of getting a square template [0.0-1.0]
flag = minimize shots (3), receivers (2) or neither (1)
verb = verbose output flag (0 = final solutions only)
Enter Values For: w1 w2 w3 flag verb ... 1 1 0 3 0
```

The output of the program is a list of result values defined here:

```
Result values:
f3d      = 3D fold
tol      = absolute diff of target and result 3D fold
dxb      = bin size in x direction
dyb      = bin size in y direction
xno      = maximum near offset
xfo      = far offset
nc       = total recording channels used
dxs,dys = shot interval in x and y
dxg,dyg = receiver interval in x and y
ncl      = channels per rec line (x-dir)
ngl      = number of rec lines (y-dir)
f2dx,f2dy = 2D fold in x and y
```

```
xmo,ymo = max offset in x and y
ra       = template aspect ratio
nskm,ngkm = number of shots and receivers per unit area
working ...
```

Now the program does the work and returns the top three designs, which are those having the smallest cost function values.

-Top 3 Candidate Solutions-

```
options: w1=1  w2=1  w3=0  flag=3
```

-One-

```
cost = 1.7367944e-06
```

```
Given:    tf3d,ttol,tdxb,tdyb,txno,txfo,tnc =
          24,0,12.5,12.5,250,4120,2500
```

```
Result:   f3d,tol,dxb,dyb,xno,xfo,nc =
          24,0,12.5,12.5,250.312 4118.25,2304
```

```
Pars:     dxs,dys,dxg,dyg,ncl,ngl = 600,25,25,500,288,8
```

```
Misc:    f2dx,f2dy,xmo,ymo,ra,nskm,ngkm =
          6,4,3600,2000,1.8,66.6667,80
```

-Two-

```
cost = 0.0036885741
```

```
Given:    tf3d,ttol,tdxb,tdyb,txno,txfo,tnc =
          24,0,12.5,12.5,250,4120,2500
```

```
Result:   f3d,tol,dxb,dyb,xno,xfo,nc =
          24,0,12.5,12.5,250.312 4386.34,2304
```

```
Pars:     dxs,dys,dxg,dyg,ncl,ngl = 600,25,25,500,144,16
```

```
Misc:    f2dx,f2dy,xmo,ymo,ra,nskm,ngkm =
          3,8,1800,4000,0.45,66.6667,80
```

-Three-

```
cost = 0.0052423277
```

```
Given:    tf3d,ttol,tdxb,tdyb,txno,txfo,tnc =
          24,0,12.5,12.5,250,4120,2500
```

```
Result:   f3d,tol,dxb,dyb,xno,xfo,nc =
          24,0,12.5,12.5,250.312 3841.87,2304
```

```
Pars:     dxs,dys,dxg,dyg,ncl,ngl = 600,25,25,500,192,12
```

```
Misc:    f2dx,f2dy,xmo,ymo,ra,nskm,ngkm =
          4,6,2400,3000,0.8,66.6667,80
```

The top design reproduces the Table 10.1 example. The fold is 24, bin size is correct, maximum near offset is 250, far offset is 4118, 2304 out of 2500 channels are used, and the 2D fold in each direction is an integer. The template aspect ratio is far from the ideal value of one consistent with our choice to ignore this parameter, (w3=0). All shot and receiver intervals are standard values.

## **Elements of 3D Seismology**

Note that solution two is nearly as good as solution one, in fact better, if we care about the aspect ratio. A template aspect ratio of 0.45 is 55% deviation from a square, while a value of 1.8 is 80% from that goal.

Here is some indication of how hard it was to solve the problem.

1,042,536 = Cases with correct bin size and acceptable channel count.

80 = Cases with acceptable fold and shot/rec density.

1.45 secs = Compute time.

More than 1 million parameter sets were determined to have correct bin size in both directions and acceptable channel count. Of these, 80 were found with 3D fold within the prescribed limits (exactly 24 in this case), integer 2D fold in both directions, and acceptable shot-receiver density. The cost function was evaluated for these 80 designs, and the lowest value identified the top solution. This took under 2 seconds on a typical desktop computer.

This design example is summarized as Example 1 in Table 11.1. Example 2 is the same problem, except that we additionally request a square template. Several optimization results change, including far offset, 2D folds, number of receiver lines, and channels per line. But the target goals are met, while achieving a better template aspect ratio (0.8 versus 1.8). On the downside, the far offset is now 6.7% short of the target value. To match both near and far offset targets, all other things being equal, would require more than 2500 channels. The effort to simultaneously match a small near offset target and large far offset typically drives up the number of channels.

Example 3 in Table 11.2 differs from Example 2 only in requesting a design with minimum receiver density. This gives a design with 66.7 shots per square kilometer, down from 80 in example 2. But the strict 24-fold requirement is a severe constraint, and both near and far offset targets are poorly met. In Example 3, the algorithm is given more latitude by requesting a  $36 \pm 10$  fold and 5000 channels to work with. As a result, the near and far offsets are now closely matched, the fold has gone up to 42 and channel usage to 2688, which was just outside the scope of channels available for example 3. The receiver density in example 4 has gone up to 80, a necessary consolation to match the near and far offset simultaneously.

Although this optimization scheme is developed for orthogonal template shooting, any 3D acquisition method for which design equations are known could be implemented the same way. These few examples demonstrate the infinite variety of cases that could, and do, arise.

Target Parameters		Example 1	Example 2
3D fold		24	24
3D fold tolerance		0	0
bin size in x direction		12.5 m	12.5
bin size in y direction		12.5 m	12.5
near offset		250 m	250
far offset		4120 m	4120
number of channels available		2500	2500
near offset weight		1	1
far offset weight		1	1
square template weight		0	1
min shots(3), recs(2), neither(1)		3	3
Optimization Results			
station intervals	$(dy_s, dx_g)$	(25,25) m	(25,25)
line intervals	$(dx_s, dy_g)$	(600,500) m	(600,500)
maximum offsets	$(x_{mo}, y_{mo})$	(3600,2000) m	(2400,3000)
bin size in x direction	$dx_b$	12.5 m	12.5
bin size in y direction	$dy_b$	12.5 m	12.5
template aspect ratio	$r_a$	1.8	0.8
maximum near offset	$x_{no}$	250 m	250
far offset	$x_{fo}$	4118 m	3842
2D x-fold	$f_{2dx}$	6	4
2D y-fold	$f_{2dy}$	4	6
3D fold	$f_{3d}$	24	24
number of receiver lines	$n_{gl}$	8	12
number of channels per line	$n_{cl}$	288	192
number of active channels	$n_c$	2304	2304
number of shots per km <sup>2</sup>	$n_{skm}$	$66.7 \text{ km}^{-2}$	66.7
number of groups per km <sup>2</sup>	$n_{gkm}$	$80 \text{ km}^{-2}$	80

Table 11.1 Optimum design examples. Example 1 gives the same design seen in Table 10.1, but it is the best design only if template aspect ratio is completely ignored. Giving equal weight to matching far offset and achieving a square template results in Example 2. The key distinctions in this solution are a better aspect ratio (i.e., 0.8 is nearer to 1.0) at the expense of missing the far offset target by 280 m (6.7%).

## Elements of 3D Seismology

Target Parameters		Example 3	Example 4
3D fold		24	36
3D fold tolerance		0	10
bin size in x direction		12.5 m	12.5
bin size in y direction		12.5 m	12.5
near offset		250 m	250
far offset		4120 m	4120
number of channels available		2500	5000
near offset weight		1	1
far offset weight		1	1
square template weight		1	1
min shots(3), recs(2), neither(1)		2	2
Optimization Results			
station intervals	$(dy_s, dx_g)$	(25,25) m	(25,25)
line intervals	$(dx_s, dy_g)$	(400,600) m	(400,500)
maximum offsets	$(x_{mo}, y_{mo})$	(2400,2400) m	(2800,3000)
bin size in x direction	$dx_b$	12.5 m	12.5
bin size in y direction	$dy_b$	12.5 m	12.5
template aspect ratio	$r_a$	1	0.93
maximum near offset	$x_{no}$	300 m	250
far offset	$x_{fo}$	3394 m	4104
2D x-fold	$f_{2dx}$	6	7
2D y-fold	$f_{2dy}$	4	6
3D fold	$f_{3d}$	24	42
number of receiver lines	$n_{gl}$	8	12
number of channels per line	$n_{cl}$	1920	224
number of active channels	$n_c$	1536	2688
number of shots per km <sup>2</sup>	$n_{skm}$	100 km <sup>-2</sup>	100
number of groups per km <sup>2</sup>	$n_{gkm}$	66.7 km <sup>-2</sup>	80

Table 11.2 Optimum design examples. Example 3 changes the previous examples only in demanding a solution that minimizes the number of receivers per square kilometer. Such a design would be suited to an area where receiver deployment is expensive, such as transition zone acquisition. Example 4 is a related case using up to 5000 channels to achieve 3D fold of  $36 \pm 10$ , while still minimizing receiver density. The added flexibility allows a solution to be found which better matches near and far offset targets, but to do so requires a receiver density of 80 groups per square kilometer.

# 12

## Marine Acquisition Methods

Marine seismic surveys are of generally higher quality and have better subsurface accuracy than land data. The reasons include a lack of a weathering layer, no coupling problem between the medium (water) and the receiver, and pressure measurements are less ambiguous than ground motion measurements. Marine data also have problems not found in land data, including water bottom multiples, source-receiver ghosts, and much more complicated positioning issues.

### 12.1 Towed receiver systems

In towed seismic acquisition, the receivers are embedded in long streamers, or cables, that are towed at shallow depth behind a ship. This represents the vast majority of worldwide marine 3D data shot today. A specific example of recent 3D seismic shooting parameters [143] in the Gulf of Mexico includes

Receiver group interval	25 m	Channels per streamer	240
Number of streamers	6	Streamer separation	100 m
Streamer length	6000 m	Streamer depth	8 m
Source volume	3750 ci	Source interval	25 m
Source type	sleeve air gun	Shooting type	flip-flop
Source depth	7 m	Source line interval	50 m

resulting in a bin size of 12.5 by 25 m. The shot spacing depends, in turn, on ship speed and time delay between shots. For example, the 25 m shot spacing seen here could be achieved by a ship speed of 2.5 m/s and 10 s shot interval.

**12.1.1 Receiver cable.** The streamer cable was developed for antisubmarine warfare during World War II. Modern cables are 2.5–3 inches in diameter, plastic cased, neutrally buoyant, and filled with oil. Designed to have about 1% positive buoyancy relative to sea water, they will float for easy recovery.

## **Elements of 3D Seismology**

The basic receiving element is a pressure sensitive hydrophone composed of a small solid-state device called a piezoelectric ceramic crystal. This has the property that, when it is subjected to stress during the passage of a sound wave, emits a weak electrical signal. A hydrophone is small and very robust, having no moving parts. Cables are built with a receiver hardwired every meter or so. The desired receiver interval can be obtained by software linking of several individual receivers.

Note that hydrophones and geophones measure different quantities to record seismic wave arrivals. The particle motion seen by a geophone is a vector quantity, even if we only measure the vertical component as is typical in land surveys. The pressure measured by a hydrophone is a scalar quantity, so there is no such thing as a three-component hydrophone.

However, hydrophones are able to distinguish pressure waves from directional acceleration such as ship lurch, wave activity, etc. This is accomplished by using two polarized elements, which reinforce the pressure wave and cancel unwanted accelerations. From the output of a single hydrophone, it is not possible to determine the propagation direction of pressure waves, but since the sound speed in water is known, direction can be determined from relative time delays between receivers.

Modern streamers are up to 12 km long, contain over 10,000 individual elements, and are composed of up to 100 interchangeable sections. Before 1979, all marine cables were analog. Each receiver fed a wire pair that passed to the ship for recording, and analog to digital (A/D) conversion occurred on the ship. Space available in the cable set a limit of about 96 channels per streamer. By 1985, digital cables were in use with up to 240 channels. Hydrophone signals were carried along analog wire pairs to A/D converters built into the cable or connections between cable sections. Also by 1985, individual hydrophone digitizers were available, allowing a higher number of channels per cable.

Figure 12.1 is a sketch of the hardware configuration for a standard marine cable. The lead-in cable is a heavy, armored section that depresses the cable to approximate operating depth and isolates it somewhat from vibration and pitching of the ship. Farings are rubber strips that minimize water turbulence due to transverse dragging of the lead-in cable. Without farings, strum and flutter noise would be transmitted to the streamer. The stretch section is usually made of nylon rope or similar resilient material with loosely coiled electric wires from the streamer. This section can stretch up to one-third of its length to further attenuate vibration and lurching of the lead-in cable and ship.

Depth controllers (birds) keep the cable at the design operating depth with an accuracy of about 1 m. They are pressure sensitive and have wings that lift or lower the cable in response to depth changes. The birds can be preset or electronically controlled during the survey. Finally, the tail buoy is attached to the end of the cable by about 200 m of line and is essential for recovery if the cable is severed. The buoy contains a light beacon, positioning equipment, and other electronics.

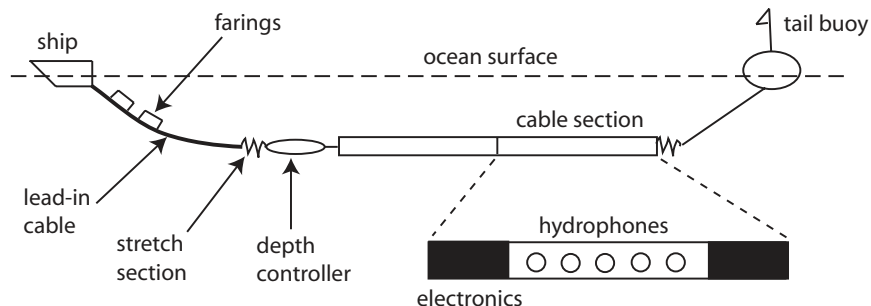


*Fig. 12.1 Schematic of marine cable hardware configuration.*

Figure 12.2 illustrates the concept of multiple steamer acquisition. The progress of ship and streamer technology can be judged from industry facts [147]. The year 1993 saw the first surveys to use five cables towed by a single ship, and by 1994 some 10-cable work was being done with two ships towing five cables each. Also by 1994, a six-cable single ship system was in use, and the first full onboard seismic processing system came online. A six-cable operation could acquire up to  $1000 \text{ km}^2$  of data per month.

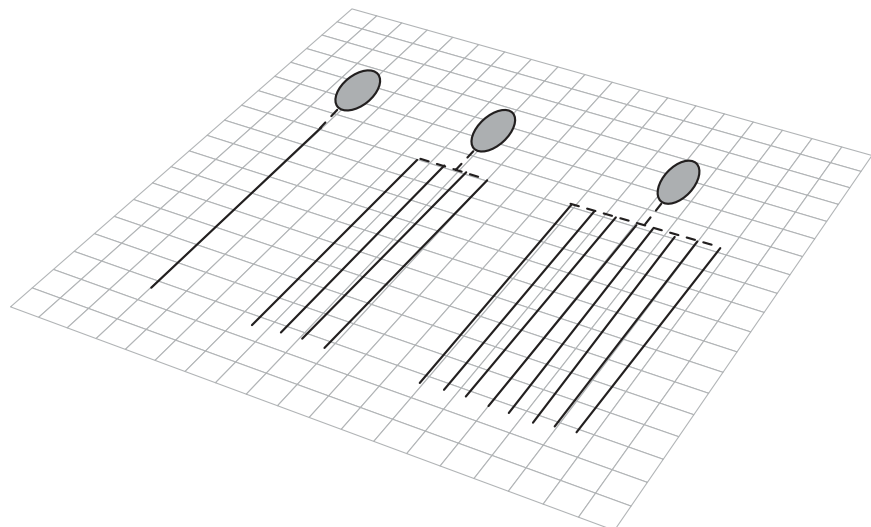


*Fig. 12.2 Schematic of selected multiple cable marine acquisition configurations. The gray oval represents the towing ship, which is also the source ship.*

## Elements of 3D Seismology

A jump in acquisition capability occurred in 1995 with the introduction of Ramform ships. Where classic vessels were limited to towing about six streamers, Ramform ships could, in principle, tow many more. Single ship eight-streamer acquisition began in 1995. As early as 1996, it became possible to shoot 2000 km<sup>2</sup> per month with sustained rates of 1500. The current industry record (North Sea 2001) for a single ship is 72 km of active cable in the water, consisting of 16 streamers each 4.5 km long. It is a record likely to fall before you read this.

With each improvement, the total cost goes up, but cost per square kilometer goes down. This is another way of saying that 3D surveys are getting bigger and more efficient with each improvement in the acquisition system.

Upgoing pressure waves reflect from the ocean surface to generate receiver ghost events. Since the streamer is shallow (less than 20 m), the ghost has a very small time delay relative to the primary arrival. Rather than a separate event, the ghost appears as an unwanted complication of the wavelet, including ghost notches. These are undesirable zeros in the wavelet amplitude spectrum. The frequency,  $f_g$ , of the ghost notch depends on cable depth,  $z_c$ , as

$$f_g = \frac{n v}{2 z_c \sin \theta} \quad (12.1)$$

where  $n$  is an integer,  $v$  is sound speed in water, and  $\theta$  is the direction of wave propagation (relative to vertical).

Figure 12.3 illustrates the dependence of ghost notch frequency on cable depth for  $n=(1,2,3)$ , these being the first, second, and third ghost notches. Results are plotted up to 500 Hz, which is the Nyquist frequency for 1 ms time sampling common in marine seismic acquisition. Figure 12.3 (A) assumes the propagation angle is zero (vertical travel), and in (B) the angle is 70 degrees. The typical angle range encountered in marine surveying is 0–30 degrees. Notice that for cable depths greater than 10 m, the first ghost notch is encroaching on the seismic band of 10–100 Hz (shaded). Consistent cable depth control is important to ensure the ghost notch is stationary throughout the data. Optimum cable depth is a trade-off between moving the ghost notch out of the seismic band and avoiding near surface wave action.

When conditions allow it, ghosting of vertical waves can be minimized by making the ghost delay equal to one-half of the wavelet dominant period. This corresponds to the cable being one-quarter wavelength deep,

$$z_c = \frac{\lambda_{dom}}{4} = \frac{v}{4f_{dom}} \quad (12.2)$$

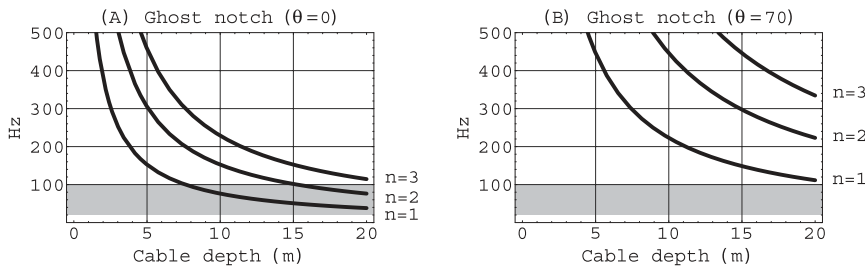


*Fig. 12.3* Ghost notch frequency versus cable depth. It is preferable to have the ghost notch outside the seismic band of 10–100 Hz (shaded). The angle  $\theta$  refers to travel direction of the wave being recorded (vertical is  $\theta=0$ ).

**12.1.2 Source array.** Many seismic sources have been developed over the half-century since offshore seismic acquisition began. Most of these have fallen to only historical status, including explosives, which served as the first marine seismic source. Currently available sources [207] include a spring-loaded plate device called a Boomer, 300–3000 Hz; up to 50 m depth of penetration (DOP), sparkers, which generate an air bubble using an electric arc (50–4000 Hz; 100s of meters DOP), and water guns that operate with compressed air to expel high pressure water (20–1500 Hz; variable DOP).

These sources, and others unlisted, are rarely used in commercial petroleum seismology. Although water guns were of great interest at one time, they suffered from unwanted precursor noise, which added complexity to the source wavelet. The marine source universally used today is the air gun. This generates sound waves in response to an electrical trigger by quickly releasing high pressure air. Many air gun types are available, with sleeve guns being among the most popular. A sleeve gun exhausts compressed air through 360-degree ports near the center of the cylindrical gun. This generates a more spherical air bubble than other designs and minimizes the amount of unbalanced force acting on the gun during each shot.

The gas bubble generated by an air gun grows until inward forces from the water overcome expansion forces. It then collapses, recompressing the air, which leads to another expansion phase and another outgoing sound wave in the water. Clearly, it is desirable to minimize the bubble pulse and one measure of air gun efficiency is the primary-to-bubble amplitude ratio.

## Elements of 3D Seismology

Figure 12.4 is a synthetic air gun wavelet with two bubble pulses visible. For this example, the primary-to-bubble ratio is about 4, similar to wavelets measured in the field. The bubble pulse typically has lower dominant frequency than the primary. Between the ghost and bubble pulse, the net effect of an air gun and water surface is to generate a much more complicated source wavelet than we find on land data.

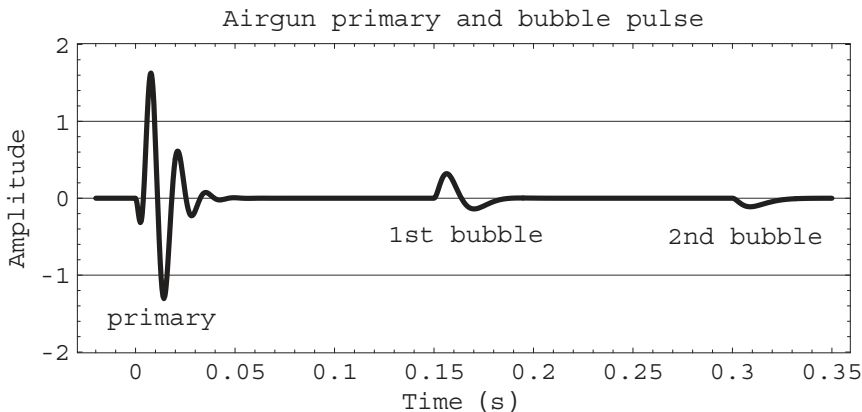


Fig. 12.4 Model wavelet for a single air gun showing primary pulse and two bubble pulses.

Industrial grade seismic sources consist of many air guns combined to form an array. An example of source array geometry and scale is shown in Figure 12.5. In this case, there are three subarrays of six air guns each. Individual air guns generate characteristic frequencies. Big air gun signals are rich in low frequencies and high frequencies dominate for small ones. A standard source array will have individual air guns with volumes of 30–300 cubic inches and a total volume of 3000–7000 cubic inches. Comments made earlier concerning the receiver ghost also apply to the source ghost.

The air gun array is designed with several goals in mind [89]:

- **Give more power.** Using more guns puts more power into the system, which in turn should give more returned signal power.
- **Assist in bubble cancellation.** By using several guns at slightly different depths, and perhaps firing at slightly different times, the net bubble oscillation can be minimized though not eliminated.

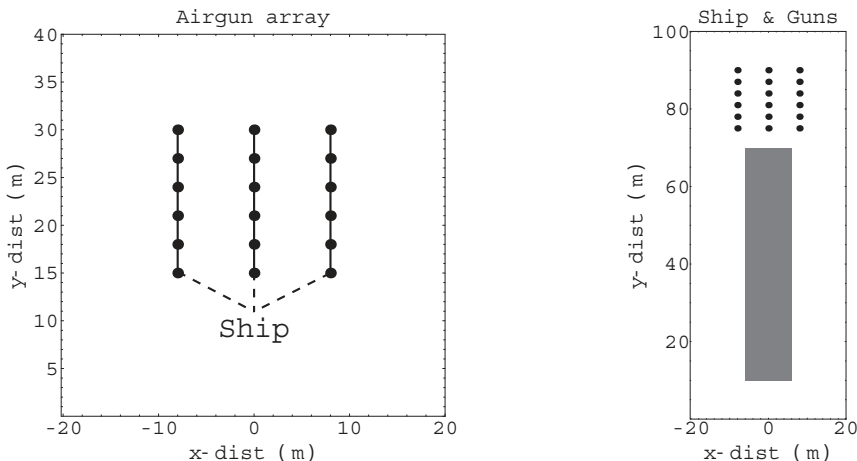


Fig. 12.5 Map view of a standard air gun array consisting of 3 sub arrays and 18 individual air guns. On the right, the air gun array is shown to scale against the footprint of a 60 m vessel (shaded).

- **Give desired frequency content.** Like individual bells in a bell choir, big guns emit low frequencies and the small ones emit high frequencies. By combining the highs and lows, any desired frequency range can be generated in the net pulse.
- **Control directivity.** An individual air gun emits power almost evenly in all directions, but one effect of the ghost is to make the radiated power angle dependent. Each individual gun shows this directivity, and there is a net directivity for the entire array. It is desirable that the net power from the entire array be focused between about zero and 40° (measured from vertical). This will put most of the power into reflection events rather than direct arrivals and refractions.

An air gun array develops strong directivity for sound waves with short wavelengths. As always, “short” is a relative term. In the source array problem, we define short relative to a typical linear dimension,  $L$ , of the source array. This can be recast as a condition on frequency given by

$$f \geq \frac{v}{L} \quad (12.3)$$

where  $v$  is sound speed in water. For the example in Figure 12.5, we have  $L=20$  m and the condition is  $f \geq 75$  Hz. For frequencies much below 75 Hz, the array will

## Elements of 3D Seismology

radiate sound like a point source, uniform in all directions. For frequencies well above 75 Hz, the power emitted in various directions will be substantially different.

Marine source arrays should be as small as possible. An air gun array with cross line dimension as small as 50 m can degrade 3D migration results [89].

**12.1.3 Acquisition geometry.** Methods like cross spread, perimeter, and template shooting are only feasible for land data, where source and receiver positions are easily controlled and receiver spread roll along is possible. Although fixed receiver systems are becoming more popular, the vast majority of marine seismic surveys are acquired using towed cables. These acquisition geometries are all extensions of the single source and single cable configuration. For 2D shooting, the source lies in the line of the cable, while for 3D work, the cable (or source, or both) are offset from the ship track.

Most marine surveys are acquired with the parallel line method. The simplest parallel line 3D coverage is obtained using a single source line (the source boat track) and two receiver lines (cables).

Figure 12.6 illustrates dual cable shooting. In (A) the shot (square), receivers (circles), and azimuth lines are shown. The 500 m cable is unrealistically short to allow clear illustration. In (B) the midpoints are shown forming two CMP tracks behind the ship parallel to the receiver cables. The midpoint intervals are clearly related to group and cable intervals. This is the geometry of a single shot record. Not shown is the source spacing in  $x$  or  $y$ . This information would be required to find the final  $x$  and  $y$  CMP spacing and to calculate CMP fold; 3D coverage is built up by cruising the ship back and forth in parallel lines.

The offsets and azimuths present in this shot record are shown as histograms in (C) and (D). The offsets are very uniformly distributed, which is a consequence of the precisely spaced group centers along the cables. The real difficulty in towed marine seismic acquisition is evident in the azimuth histogram. By its nature, a towed system has limited aperture, meaning that azimuth values are constrained to a narrow corridor along the shooting direction. Compared to a land survey this azimuth distribution is very poor.

Improvement in azimuth distribution is possible through the use of more cables, such as the six-streamer example of Figure 12.7. The azimuth distribution is much better, but this is not an improvement we would see in real data because the cable in this example is only 500 m long. For a more realistic 5 km cable, Figure 12.8 indicates that even a six-streamer configuration has poor azimuth distribution.

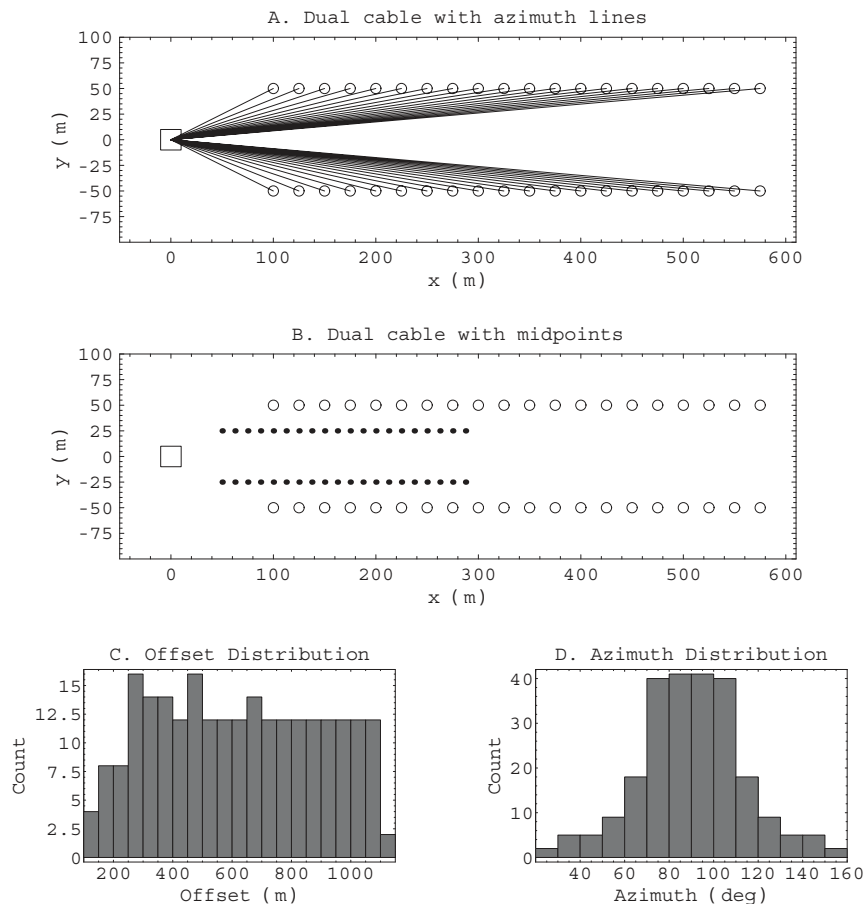


Fig. 12.6 Geometry of a single source, dual receiver, parallel line marine survey. The midpoints are for one shot record. Shot interval and shot-line interval are not shown.

## Elements of 3D Seismology

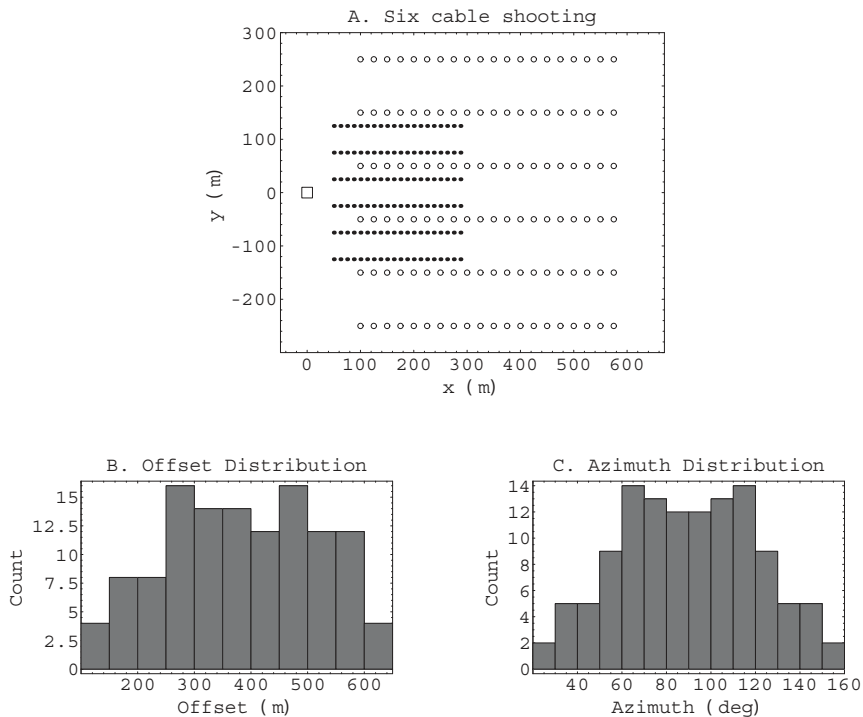


Fig. 12.7 Shooting with six cables generates six midpoint tracks and improved azimuth distribution.

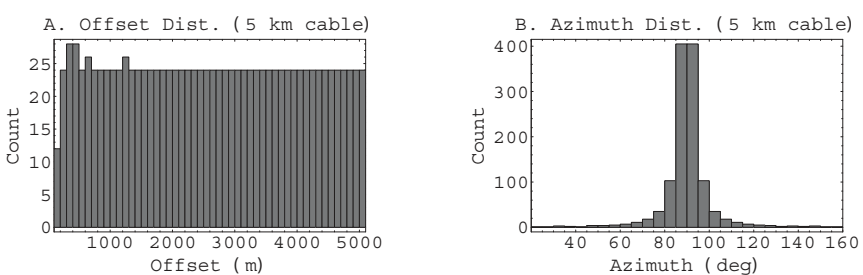


Fig. 12.8 Six-cable acquisition results a narrow azimuth distribution when the cables are long, 5 km in this example. The cross line dimension of the receiver footprint (600 m) is about half of the current industry record.

**12.1.4 Flip-Flop shooting.** One way to improve efficiency without increasing the number of cables is to have more than one source towed behind the ship [56]. If these sources are fired simultaneously, they will simply have the appearance of an extended source array, which smears the data away from discrete midpoints. However, if the sources are fired alternately, then the smearing effect is avoided, and new midpoint tracks are generated. This is termed flip-flop shooting and is illustrated in Figure 12.9.

**12.1.5 Positioning.** For accurate processing of 3D seismic data, it is necessary to know the (x,y,z) coordinates of the source and each receiver for every shot. Navigational sensors are deployed on the ship, cables, and tail buoys to provide positioning data.

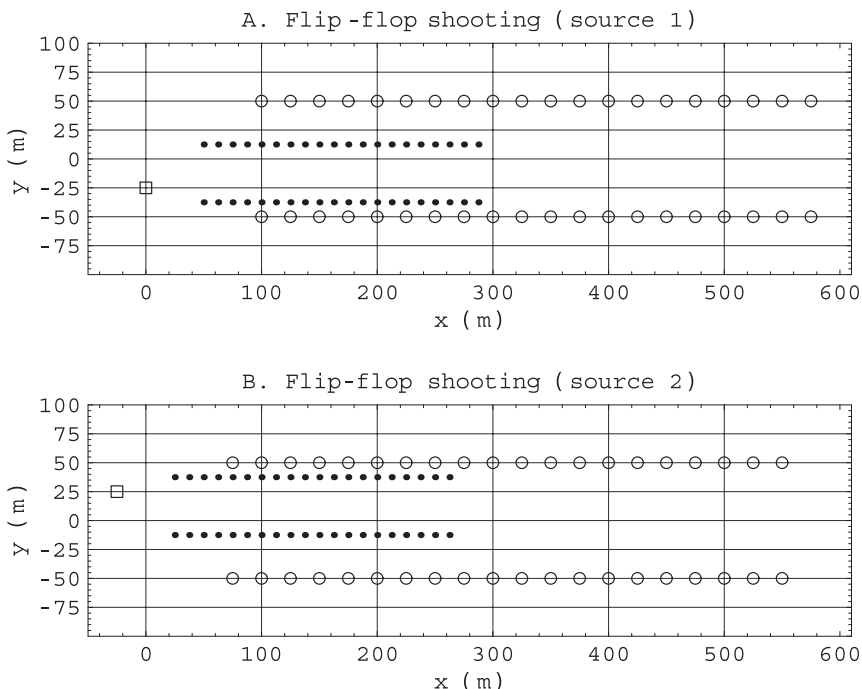


Fig. 12.9 Flip-flop shooting involves two sources towed behind a single ship. (A) When the first source fires, two CMP tracks are generated. (B) After a preset delay, the second source fires creating two additional CMP tracks. Meanwhile source array 1 is recharging, the ship and cables are moving forward, and flip-flop shooting continues.

## Elements of 3D Seismology

Figure 12.10 shows the configuration of positioning elements for a seismic ship towing three cables. Differential Global Positioning System (DGPS) provides primary navigation along with radio-positioning equipment. Active components include high-frequency acoustic and laser ranging. Laser-ranging systems are much more accurate than acoustic ones. These give precise traveltime measurements but need a clear line of sight. Tail buoys are equipped with radio positioning and acoustic receivers.

Along each cable are a series of acoustic ranging receivers and depth controllers called birds. The individual elements have observational standard deviations on the order of 2–3 m and 0.5 degree azimuth. However, the probable positioning error in a field setting is a complex interplay of all elements [79]. These results suggest an overall relative accuracy of about 5 m in positioning and 3 degrees in azimuth. Absolute positioning from GPS and radio navigation is about 10 m.

Acoustic ranging systems use signal generators on the ship's hull and tail buoy pinging into receivers along the cable. Typical distance between acoustic receivers is 75 m [206]. Acoustic ranging accuracy depends on accurate estimates of the local sound speed in water and precise traveltime measurement from generator to receiver. Sound speed in near-surface water is a function of temperature and salinity

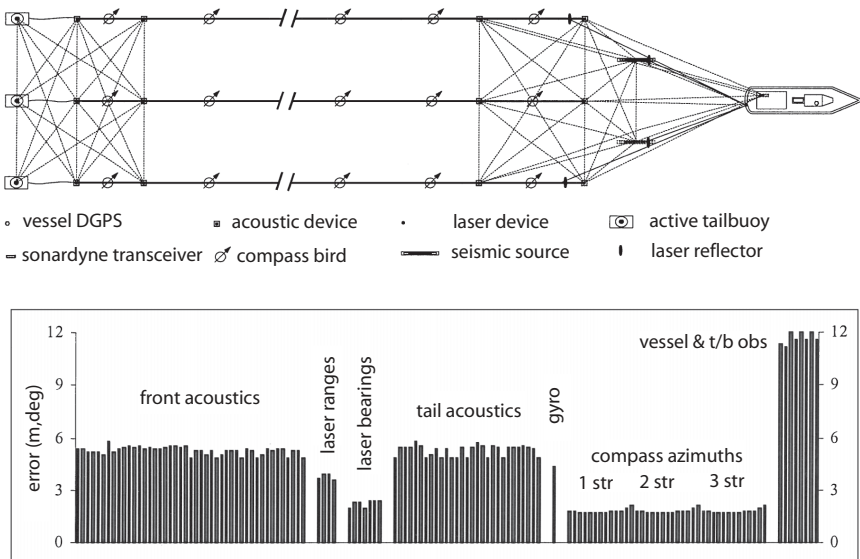


Fig. 12.10 Positioning systems on a typical marine seismic ship and internal reliability estimates for a single shotpoint (from [79]).

$$v_w = 1449.14 + 4.57 T + 1.40 (S - 35) \quad (12.4)$$

where  $v_w$  is in m/s,  $T$  is temperature in  $^{\circ}\text{C}$  ( $-4^{\circ}\text{C} < T < 30^{\circ}\text{C}$ ), and  $S$  is salinity in parts/1000 ( $0 \leq S \leq 37$ ).

**12.1.6 Cable feathering.** When a ship tows one or more long streamers, these are subject to lateral forces due to currents and tides. These forces can push the cable away from the ship track and result in significant cable curvature. This effect is called cable feathering and is illustrated in Figure 12.11. One effect of cable feathering is to broaden the data azimuth distribution, but it also degrades survey repeatability important in time-lapse seismic work.

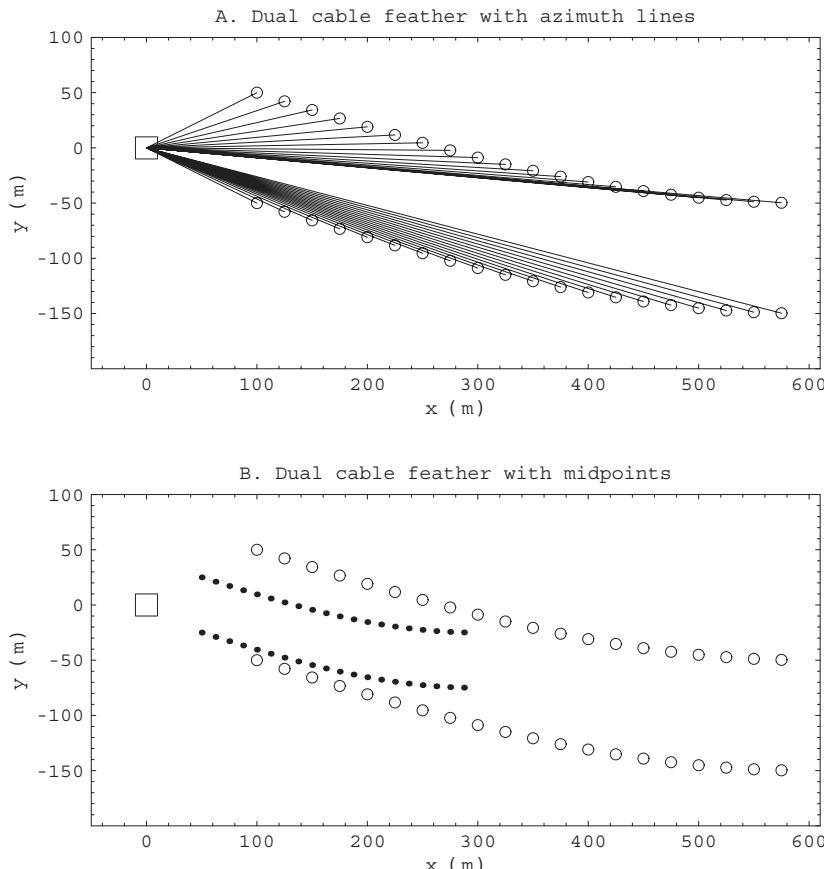


Fig. 12.11 Cable feathering is the deformation of towed streamers due to cross currents or tides.

## 12.2 Fixed receiver systems

In certain circumstances a fixed receiver system, rather than towed cables, are the preferred form of marine seismic acquisition. This can be due to strong currents, heavy ship traffic, or dense surface obstructions (e.g., drilling platforms). Fixed receiver methods allow much better control on azimuth distribution in the data, close to what can be achieved on land. Using fixed receivers leads to improved survey repeatability that is vital in time-lapse seismic.

In areas with drilling platform clusters, active shipping channels, or other cultural obstacles, acquisition with towed streamers is not feasible. In these situations, 3D data can be gathered using a small number of receivers in fixed position on the water bottom and a standard air gun array towed in a regular shooting pattern. The cost per trace is significantly higher than shooting with towed cables. In current practice, fixed receiver systems are deployed if operating conditions require it, if time lapse seismic is planned, or if mode converted imaging is of prime importance. An example of the last case is the use of multicomponent bottom cable for PS imaging through gas clouds [105].

For transition zone areas, buoy and telemetry systems use individual receivers or small groups of receivers deployed on the seafloor in very shallow water. Figure 12.12A is a schematic diagram of a telemetry system. Surface buoys transmit data to the recording unit. There are various strategies for accomplishing this from real-time transmission to onboard storage of data generated by many shots. The data can be downloaded to an electronic dock when the receiver buoys are recovered at the end of each shooting day. The source is typically a barge-mounted air gun array.

Ocean bottom cable (OBC) is a shallow water system in which receiver cables are deployed on the ocean floor, Figure 12.12B. The cable is secured to the sea floor via back-dragging to engage slanted vanes or the cable is burrowed into the bottom. Consistent long-term coupling of the cable to the sea floor is very important. Noise is low because receivers are below wave base and away from ship vibration, and midpoint coverage is achieved by cruising source ship(s) in a regular pattern. OBC is generally limited to water depths less than 150 m, but special systems can operate down to 2000 m.

Multicomponent bottom cable is becoming common, measuring three particle velocity components plus pressure [36]. This allows particle velocity measurement of shear and mode converted waves. Together with the hydrophone pressure data, the geophone data can be used for identification and suppression of seafloor multiples. However, OBC data can suffer from long period ghosting [12]. The vertical ghost delay,  $t$ , for a receiver at depth  $z_g$  is

$$t = \frac{2z_g}{v_w} \quad (12.5)$$

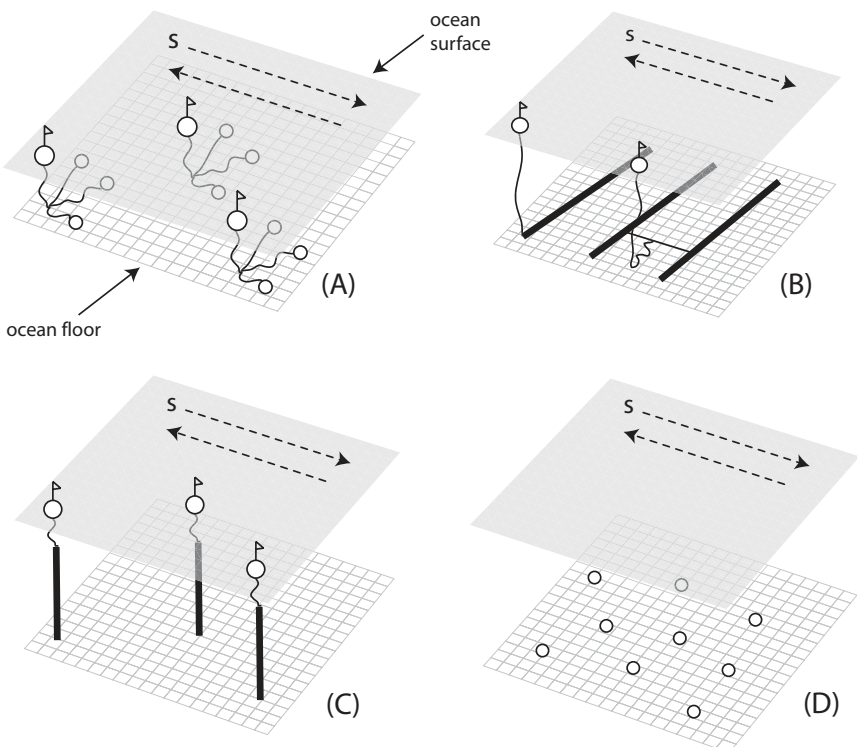


*Fig. 12.12 Schematic diagram of marine seismic acquisition using fixed receivers. (A) Telemetry systems are used in the very shallow water of land-sea transition zones. (B) Ocean bottom cable is designed for shallow open ocean settings. (C) Vertical cable is sometimes deployed in intermediate to deep water. (D) Ocean bottom seismometers are used in deep water.*

where  $v_w$  is the water velocity.

Vertical cable, Figure 12.12C, is an acquisition technique sometimes used in moderate to deep water. Developed in the early 1990s, it involves cables vertically suspended between a bottom anchor and surface buoy. This offers a low noise environment and shooting methods similar to bottom cable. The vertical arrangement of receivers allows new kinds of processing, including separation of upgoing and downgoing energy, which is useful for removal of deep water multiples.

For deep water applications, the only instrument in current use is the ocean bottom seismometer (OBS) deployed as shown in Figure 12.12D. OBS is a

## Elements of 3D Seismology

system which can operate in up to 6000 m of water and consists of a three-component receiver and hydrophone pressure sensor on the ocean floor. An OBS unit is self-contained with no umbilical link to the surface.

There are various configurations, but a typical one for petroleum seismic applications is a continuous recording capability of 30 days at 2 ms time sample rate (about 5 Gb of data). OBS units are expensive and therefore few are deployed. Data density is made up by shooting a tight source pattern with a surface ship as shown in Figure 12.13. OBS gives vector seismic response that allows processing for shear and mode-converted waves.

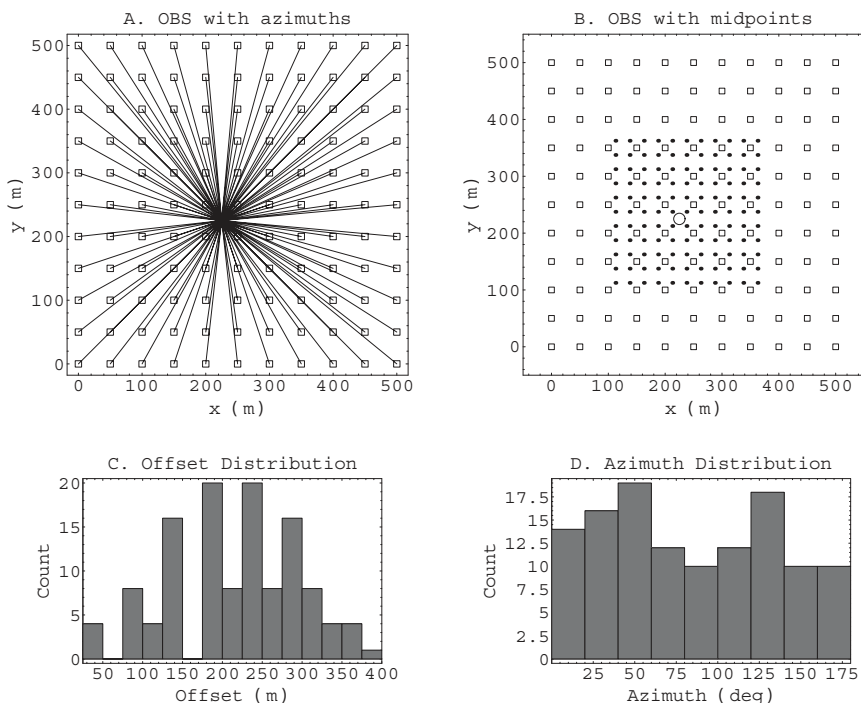


Fig. 12.13 OBS acquisition involves a dense grid of shot points firing into a sparse collection of receivers. (A) One hundred source points (boxes) shooting into a single receiver (circle) with azimuth lines shown. (B) The same configuration now showing midpoint coverage. (C) The offset distribution is broad with some clustering as expected from orthogonal shooting. (D) Azimuth coverage of OBS surveys can approach that of land data.

We make note of the fact that any of the marine seismic fixed receiver systems can be permanently installed for use in time-lapse seismic work. Integrated with downhole sensors of various kinds, permanent seismic installations can be used passively to monitor fracture mechanics of the reservoir, as well as supply periodically updated active-source seismic images. This emerging branch of production technology is sometimes called the instrumented oil field.

## 12.3 Marine acquisition and the environment

Many aspects of seismic acquisition have potential environmental impact that must be managed and minimized. This is an area of overlap between business interests and government regulations, both of which vary on local and national scales.

In the United States, there is a body of regulation associated with the Endangered Species Act (ESA), which protects habitat not only of species in danger of extinction, but also those that might become threatened in the foreseeable future. For marine seismic, this primarily relates to transition zone work on public land, which has the potential to impact marsh and swamp habitat.

The seismic contractor is required to prepare a biological assessment at the direction of the governmental agency involved. The contractor is also responsible for adhering to ESA on private land by making reasonable efforts to determine if endangered species are present and working with the governmental agency to devise a plan of action.

One example in the literature [50] involves a 3D survey covering part of the Aransas National Wildlife Refuge. Endangered species in the survey area included the whooping crane and interior least tern. To avoid interference with nesting, certain non-standard shooting logistics were required at an added cost of about \$270,000.

Another issue is the impact of marine seismic acquisition on fisheries. Receivers are passive devices, so this is primarily concerned with source characteristics. To cite one example, the Canadian Department of Fisheries and Oceans (DFO) has developed safeguards during the last 30 years for explosive and air gun sources used in lakes, rivers, and ocean settings. These guidelines take the form of overpressure or peak particle velocity as measured at the substrate-water interface or, equivalently, as proposed depth of burial or setback distance of an explosive charge from the fish habitat. Current guidelines [208] allow an overpressure of 1.00 bar (14.5 psi) or a peak particle velocity not greater than 13 mm/s.

An issue that has received increasing attention in the last decade is the impact of seismic acquisition on marine mammals. The Canadian DFO guidelines address seismic operations and the effect they can have on the distribution and

## **Elements of 3D Seismology**

behavior of whales. Specifically, "...no explosive seismic source is to be knowingly detonated within 500 m of any marine mammal, and there must be no visual contact by an observer using 7x35-power binoculars" [208].

Tagging studies have been undertaken in the Gulf of Mexico [35] on sperm whales by a U.S. research group that included the Minerals Management Service, National Marine Fisheries Service, and the Office of Naval Research. The goal was to document whale behavior before, during, and after encroachment of seismic work boats. It is now certain that seismic air gun sources influence the behavior of marine mammals, but it is not yet known if this is significant or harmful. Cooperative worldwide studies between seismic contractors, governmental agencies, and E&P companies are sure to continue.

# 13

## Data Dimensionality and Components

The term 4D is commonly used in seismic work, as well as in some medical and computational fluid dynamics applications. In the seismic case, this can be a confusing and misleading term, and our purpose here is to clarify the role of data dimensions and components and move toward a consistent and sustainable way of describing data. First, it is useful to consider 2D data as indicated in Figure 13.1(A).

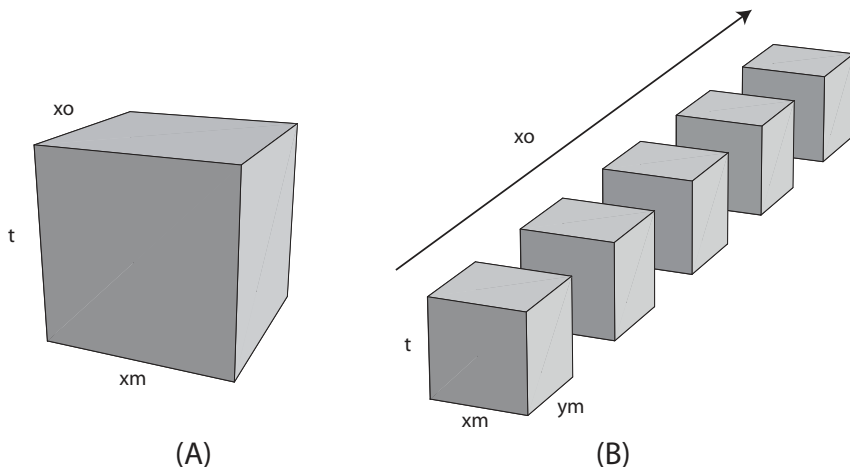


Fig. 13.1 (A) Prestack 2D data is a 3D volume. (B) Prestack 3D data is a collection of common offset cubes, a 4D object.

## Elements of 3D Seismology

The data as seen by the interpreter is indeed a 2D image with a vertical reflection time ( $t$ ) axis and horizontal axis of common midpoint ( $x_m$ ). The seismic processor, however, sees the data before stacking, when there is another dimension, offset ( $x_o$ ). There is also the implied information that typical land 2D data are the result of exciting the earth with a vertical source component ( $c_{sz}$ ), and measurements taken with a receiver sensitive only to the vertical component ( $c_{gz}$ ) of earth surface vibrations. So, we could justifiably say a 2D prestack data set is a function of five quantities

$$2D : t, x_m, x_o, c_{sz}, c_{gz} \quad (13.1)$$

In what sense is this object two dimensional? To begin with, we should distinguish  $(t, x_m, x_o)$  as data dimensions and  $(c_{sz}, c_{gz})$  as data components. Furthermore, in naming the object, the vernacular usage is to only include poststack dimensions (the offset dimension is summed by CMP stacking) and not mention components unless we have more than just vertical ones. To summarize, we can consider 2D data as 2D in this sense

$$2D : t, x_m, \{x_o, c_{sz}, c_{gz}\} \quad (13.2)$$

where the items in curly brackets are implied but not used in naming.

Going up to 3D data means we have two CMP coordinates  $(x_m, y_m)$ . Thus prestack 3D data is a 4D object with dimensions  $(t, x_m, y_m, x_o)$ . It would be nice to draw this, but how can we visualize a 4D object? A 1D line is a collection of 0D points (yes, a point is zero dimensional), a 2D plane is a collection of 1D lines, and a 3D volume is a collection of 2D planes. So, it makes sense that a 4D object can be considered as a collection of 3D volumes. Applying this to prestack seismic data, we note that all the near offset traces in a 3D survey form a volumetric data set by themselves. The next larger offsets form another cube, and so on up to the far offsets.

The 3D prestack data can thus be considered as a collection of common offset cubes as shown in Figure 13.1B. Even though only five offsets are shown, real data will contain up to 100 or more. Since we are still assuming vertical source and receiver components, the data in Figure 13.1B is a function of

$$3D : t, x_m, y_m, \{x_o, c_{sz}, c_{gz}\} \quad (13.3)$$

As with the 2D case, we call this 3D seismic because the dimensions are  $(t, x_m, y_m)$  and the bracketed items are implied.

Now imagine that this entire 3D survey is repeated every few years. This adds another time dimension we might call vintage ( $T$ ). We now need to draw a 5D object to illustrate the prestack data. Clearly, this will be a collection of 4D objects of the type in Figure 13.1B. This 5D object is shown in Figure 13.2A. Now we reach the crux of the matter. Should we call these data 4D or time-lapse 3D (TL3D)?

There is a case for both. To be consistent with the definitions above, we write the data dependencies in this case as

$$4D : t, x_m, y_m, T, \{x_o, c_{sz}, c_{gz}\} \quad (13.4)$$

The medical imaging community has clearly endorsed the term 4D for this kind of data, although they do not have the complications of offset and source/receiver components. Other scientific disciplines are split on whether to call this time-lapse 3D or 4D data.

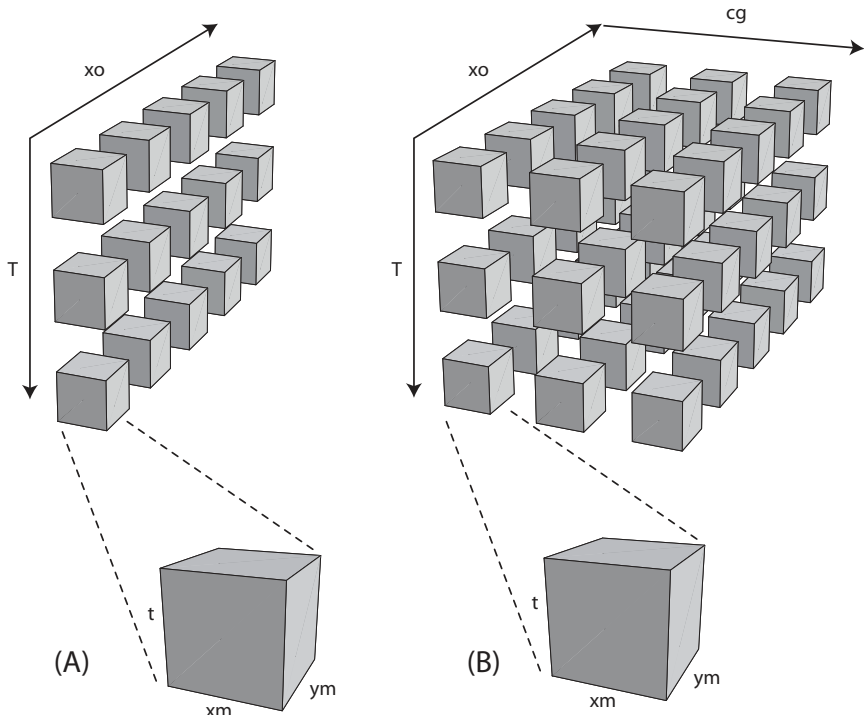


Fig. 13.2 (A) A Multiple vintage prestack 3D data set is a 5D volume that is called 4D or TL3D seismic data. (B) Recording multiple receiver components adds another dimension.

## Elements of 3D Seismology

But many geophysicists see inconsistency lurking. If 4D sounds logical, then consider this. What do we call a repeated 2D seismic survey? The vintage axis adds a new dimension and our naming convention would give

$$3D? : t, x_m, T, \{x_o, c_{sz}, c_{gz}\} \quad (13.5)$$

which is in direct conflict with the standard meaning of 3D seismic data. This problem goes away if we term these data TL2D clearly distinguishing them from single vintage 3D data. Perhaps the only way to be consistent is to use the prefix time-lapse for a multiple vintage seismic survey of any kind.

While on the subject, we may as well push it to the limit and see how this all extends to the confusing world of multicomponent seismic data. Figure 13.2 (B) shows data initiated by a vertical source but measured with three component receivers. This could arguably be termed 6D according to our recipe

$$6D? : t, x_m, T, \{x_o, c_{sz}\}, c_{gx}, c_{gy}, \{c_{gz}\} \quad (13.6)$$

that would, of course, be a confusing and ambiguous term. Would TL 5D be any better? Probably not. For the sake of consistency, the term for these data should be TL3C3D, where the 3C denotes the three-receiver components ( $r_x, r_y, r_z$ ). Our consistency is not perfect, however, since the 3C includes the vertical component which was only implied in all other names.

We are almost done. The ultimate seismic experiment is shown in Figure 13.3. Here we have multiple vintage 3D seismic generated by sources acting in each of the (x,y,z) directions and shooting into three component receivers. Each source acts along only one axis (x,y, or z) or somehow spans this 3D space. We know this is the ultimate experiment because there are only three space coordinates in our 3D world. We have excited them all with sources and measured them all with receivers. No matter how complicated the subsurface and the returning wave motions, this is enough information to completely capture it. Our naming convention for this case is

$$TL9C3D : t, x_m, y_m, T, \{x_o\}, c_{sx}, c_{sy}, c_{sz}, c_{gx}, c_{gy}, c_{gz} \quad (13.7)$$

We term it nine-component, because each of the three source components shoots into each of the three receiver components. Three times three equals nine, hence the name. It is worth noting that this kind of vector seismic data requires specialized and expensive processing (elastic migration, etc). While we know in

theory how to migrate it, computers are insufficient to do it repeatedly in a reasonable amount of time.

None of our current naming conventions may persist. Eventually someone will coin a phrase that sticks—maybe “vector 4D seismic”—and we will all have to live with it. As a final thought, the data in Figure 13.3 are multicomponent and prestack. Before interpretation this massive amount of information would be processed to a reflectivity image of some kind

$$\text{Image}(t, x_m, y_m, T) \quad (13.8)$$

which is indeed a 4D object, although we prefer to call it TL3D. So the discussion of naming conventions is likely to continue.

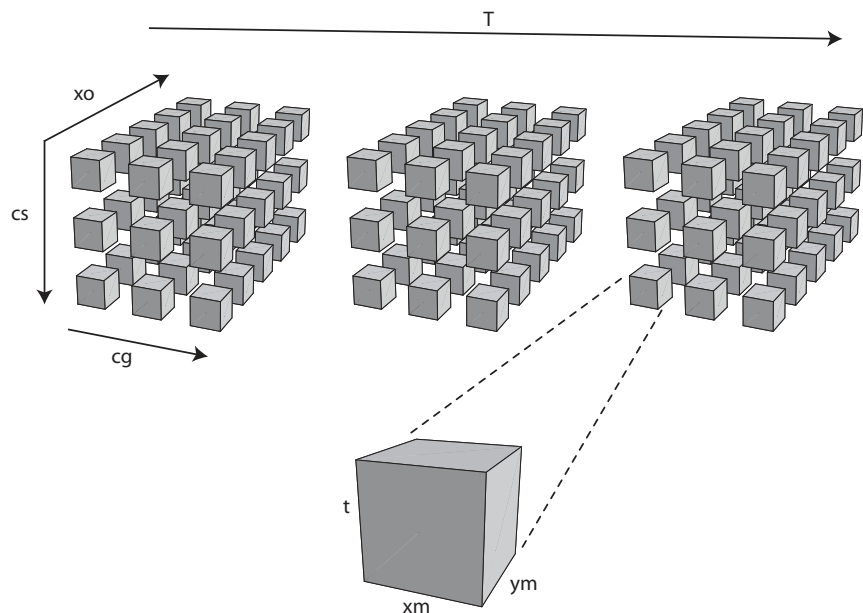


Fig. 13.3 The ultimate seismic experiment: 2 midpoint coordinates, 3 source components, 3 receiver components, offset, and multiple vintages

## Part III

*Data Processing:  
Creating the Seismic Image*

# 14

## Processing and Binning Overview

### 14.1 Why do we need to process seismic data?

Raw seismic data bears no resemblance to features inside the earth. It is primarily an expression of the experimental details of how it was acquired. Seismic data processing draws on our full knowledge of wave propagation effects and acquisition geometry to create geologically meaningful images of the subsurface.

A bewildering array of processes are applied to seismic data. Most fall into one of four categories: wavelet, travelttime, amplitude, or noise.

- **Wavelet adjustments.** Vibroseis correlation, deconvolution, filtering, phase rotation.
- **Travelttime corrections.** Statics (elevation, weathering, residual), normal moveout (and velocity analysis), dip moveout, migration (and velocity analysis).
- **Amplitude corrections.** Geometric spreading, attenuation, various forms of gain ( $t^n, e^{at}$ , normalization, automatic gain control, etc.).
- **Noise reduction.** Vibroseis correlation, vertical stack, mute, CMP stack, filtering (frequency, f-k, radon, etc.), multiple suppression.

A popular free processing system, SeismicUn\*x, contains about 250 individual programs developed from the late 1970s to the present. Allowing for many of these to be graphics and utilities, there are still more than 150 core seismic processing programs. The field of seismic data processing is enormous. Published contributions stretch back to the beginnings of reflection seismology in the 1920s and accelerate with the introduction of digital computers in the 1960s. Our treatment of the subject is, at best, a selective overview of those topics of first-order importance. The interested reader who yearns for more detail is referred to the classic data processing text by Yilmaz [211], the same author's recent 2000 page treatise [212], or individual papers cited in specific subject areas.

## Elements of 3D Seismology

The traveltime observed on field seismic data represents travel from the source to a reflection point to the receiver. After a series of traveltime corrections the final earth image involves only vertical traveltimes.

Figure 14.1A illustrates the need for static corrections, which are bulk time shifts applied to field seismic traces. The physical raypath (solid) bends sharply at the base of weathering because of very low velocity in the weathering layer relative to the subweathering layer. Thus travel through the weathering is nearly vertical. Static corrections adjust for elevation changes as well as lateral variations in weathering layer thickness and velocity. Using time shifts, the data is modified to the approximate time (dashed raypath) that would have been observed on a horizontal datum plane if the weathering layer and topography were absent.

Such corrections are useful and robust but can be expected to fail in the presence of

1. significant lateral velocity variation in the weathering or subweathering
2. extreme topography (large elevation changes over short distances)
3. extreme subweathering topography

When statics corrections are inadequate for any of these reasons, more sophisticated methods can be applied, such as wave equation redatuming or migration from topography. Since statics are relatively simple to compute and apply, they are used whenever possible.

Whether the data is acquired on a flat surface or corrected to the datum plane, the raw traveltime is along a reflection path such as the solid one shown in Figure 14.1B. There are three dynamic traveltime corrections in standard seismic processing: normal moveout (NMO), dip moveout (DMO), and migration. A dynamic time correction is one in which the time axis is stretched or compressed. Starting with the raw reflection time (path 1), NMO reduces time to what would have been seen at the midpoint (path 2). This is done by removing the traveltime effect of offset one trace at a time, but as seen in the Figure 14.1B we lose track of the reflection point in the process.

DMO moves data across midpoints and adjusts times to the normal incidence path through the original reflection point (path 3). Note that paths 2, 3, and 4 only separate due to reflector dip. Migration is a multichannel process that maps data onto a vertical travel path through the reflection point (path 4). It is only after migration that the traveltime in seismic data represents vertical reflection time which can be related to measured depth in wells.

The final product of seismic data processing is a 3D volume or 2D section. In the interpretation phase, there may be many additional processes applied to

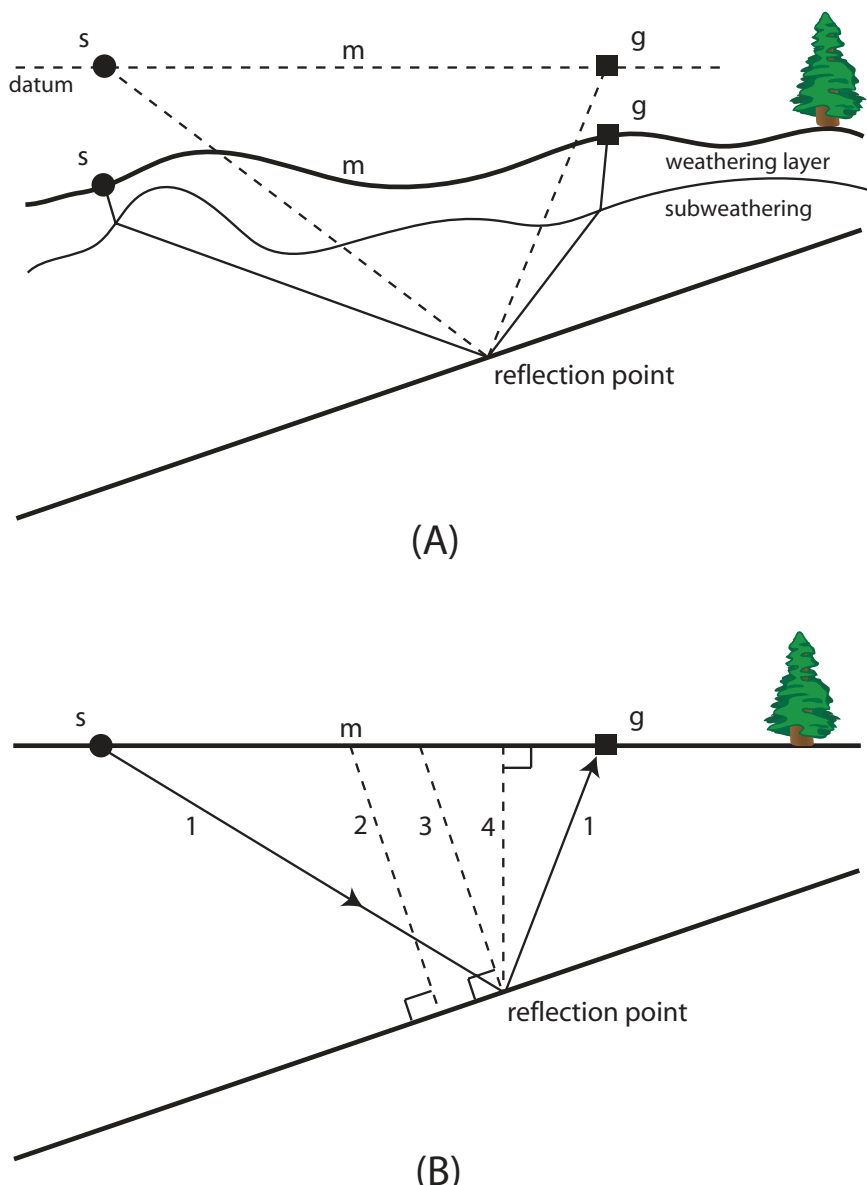


Fig. 14.1 Traveltime corrections to seismic data. (A) Static corrections modify traveltimes from the physical raypath (solid) to a hypothetical one (dashed) that would have been observed on the datum plane. (B) Raw traveltimes from the datum plane (path 1) is corrected by NMO (path 2), DMO (path 3), and migration (path 4).

## **Elements of 3D Seismology**

seismic data to generate attributes. Some of these are visual attributes designed to bring out subtle features in the data that would not otherwise be visible. Items in this category are not unique to seismic data and their generation is more properly termed image processing rather than seismic processing.

Examples include edge detection, coherency, Hilbert attributes (instantaneous amplitude and phase), shadow processing, smoothing, and lateral gradient operations. Other attributes are based on the physics of wave propagation to generate images, which are quantitative estimates of rock or fluid properties. Impedance inversion and fluid factor images are two examples.

### **14.2 Filtering and noise removal**

A central theme in processing is the removal of noise from seismic data. Noise can take many forms, from surface waves to multiples to direct arrivals and head waves. These are examples of source-generated, or coherent, noise. We can also expect ambient noise in the environment during data acquisition due to wind, various kinds of vehicle traffic, wave action, and cultural interference.

A common strategy to remove noise is shown in Figure 14.2. The original  $(t,x)$  domain data, Figure 14.2A, consists of several lines with different slopes. For whatever reason, we want to remove events with slopes going down and to the left (noise) without degrading other events (signal). Note the signal and noise overlap in the  $(t,x)$  domain. If they did not overlap, then we could directly mute (replace with zeros) the unwanted lines. In Figure 14.2B a transform has been applied to the data. In this case, it is a 2D Fourier transform (FT) which maps the data into frequency-wavenumber space.

Appendix A describes the 2D Fourier transform in some detail. While this transform is very useful in seismic applications, many other transforms exist and more are constantly being developed. The idea is to have some kind of transformation that takes data with overlapping signal and noise and have these separate in the transform space. The 2D FT is ideal for the slope filtering we need in this example.

The filtering process consists of determining which slope values to kill and then applying the filter. Figure 14.2C shows a tapered wedge of zero values in the area of transform space containing what we consider noise. After inverse transform back to the original space, Figure 14.2D, the signal events remain and the noise is removed. As is typically the case, the data is improved, but some artifacts remain indicating the filtering operation is not perfect.

The most common form of filtering used in seismic data processing is frequency filtering. The Lena image, a standard image processing subject, is useful to demonstrate the effect of seismic style frequency filtering. The human visual system is very adept at finding subtle differences in faces, as evidenced any

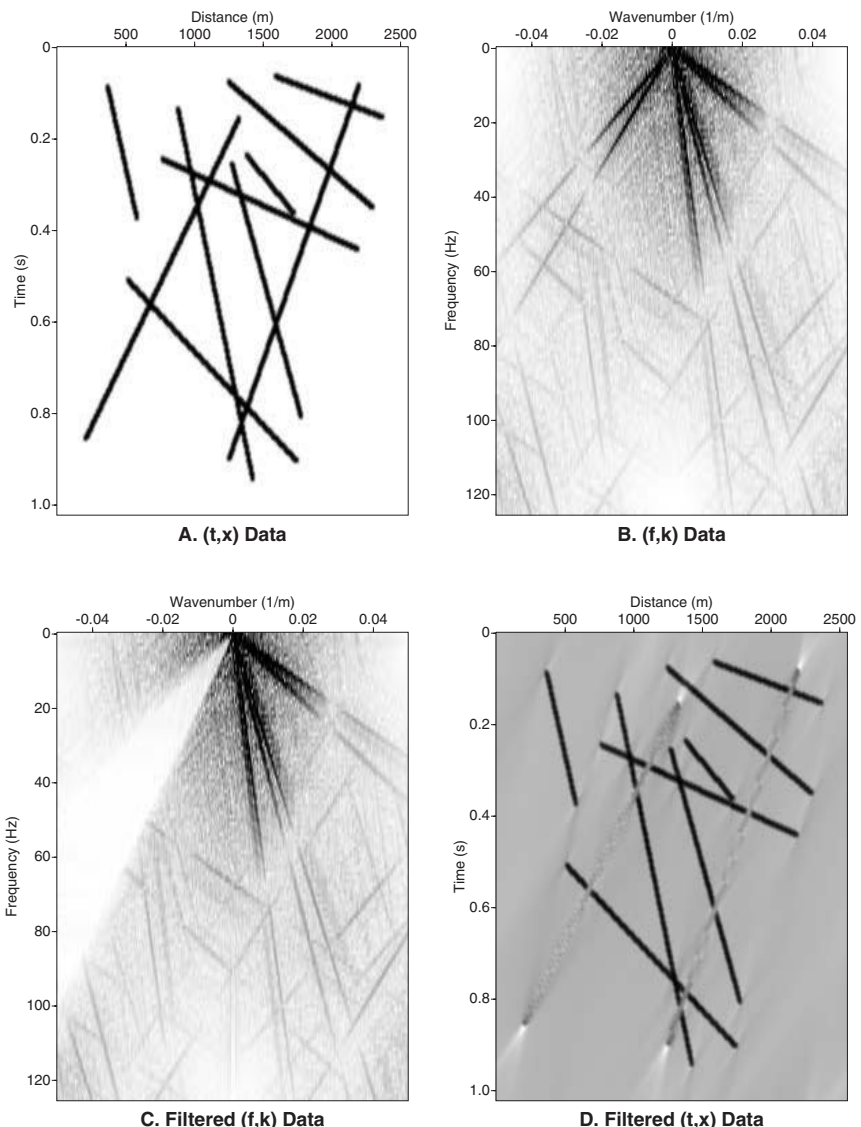


Fig. 14.2 Slope filtering is an example of a common noise removal strategy. (A) Original  $(t,x)$  data consisting of several lines. We consider lines sloping down and left to be noise. (B) Amplitude spectrum of the data after 2D Fourier transform (FT). (C) In order to remove the noise events, a filter is applied in  $(f,k)$  space by zeroing out a wedge of data containing the unwanted slopes. (D) After inverse 2D FT, the events are removed, but not perfectly.

## **Elements of 3D Seismology**

time you recognize a face in a crowded room. In Figure 14.3A the Lena image is shown unfiltered.

To simulate a seismic scale in this example, each column in the image is treated as a seismic trace with time sample rate of 4 ms. Applying a one dimensional Fourier transform to each trace in the  $(t,x)$  image creates an  $(f,x)$  domain version of Lena that is shown as amplitude spectrum traces in Figure 14.3B. A 15–60 Hz bandpass frequency filter has been applied to generate the data in Figure 14.3C, and inverse FT of this data creates the filtered  $(t,x)$  Lena image of Figure 14.3D.

The filtered Lena image shows three effects systemic to seismic data. First, missing low frequency data means that area shading is lost. Dark shadows on the hat and the white hatband are equally missing in the filtered image. This fact means that seismic images will not contain photographic-style area shading that one would see in an outcrop, where color might distinguish limestone from shale.

Second, missing low frequencies also mean loss of subvertical, or steeply dipping, information. For example, the horizontal line of the mouth is well preserved, but vertical lines of the nose are lost. This tells us that seismic data is much better at imaging low slopes than steep slopes. These two effects taken together mean that seismic is an edge detection technique, delivering images of interfaces in the earth, and it does a better job on low slope events.

Third, missing high frequencies degrade detail and resolution. An effect easily confirmed through comparison of the unfiltered and filtered versions.

### **14.3 Processing flow**

Land or marine 3D data processing is a significant undertaking. If we think of 3D CMP coverage as a collection of many 2D CMP lines, 3D processing must be dozens or hundreds of times more involved than 2D processing. A typical marine 3D survey may have a few hundred million prestack traces, while the number in a long 2D survey will rarely exceed 500,000.

Some processing steps are unique to 3D, but most are common to 2D and 3D. Figure 14.4 shows an example processing flow that could be applied to either 3D or 2D seismic data. Some processes are unique to land data, specifically those items related to vibroseis and statics.

Some seismic processes are single channel, meaning that one input trace generates one output trace. Trace processes are identical for 2D and 3D except for the vast number of traces in 3D. Single channel processes include gain, deconvolution, application of NMO, frequency filtering, and wavelet processing.

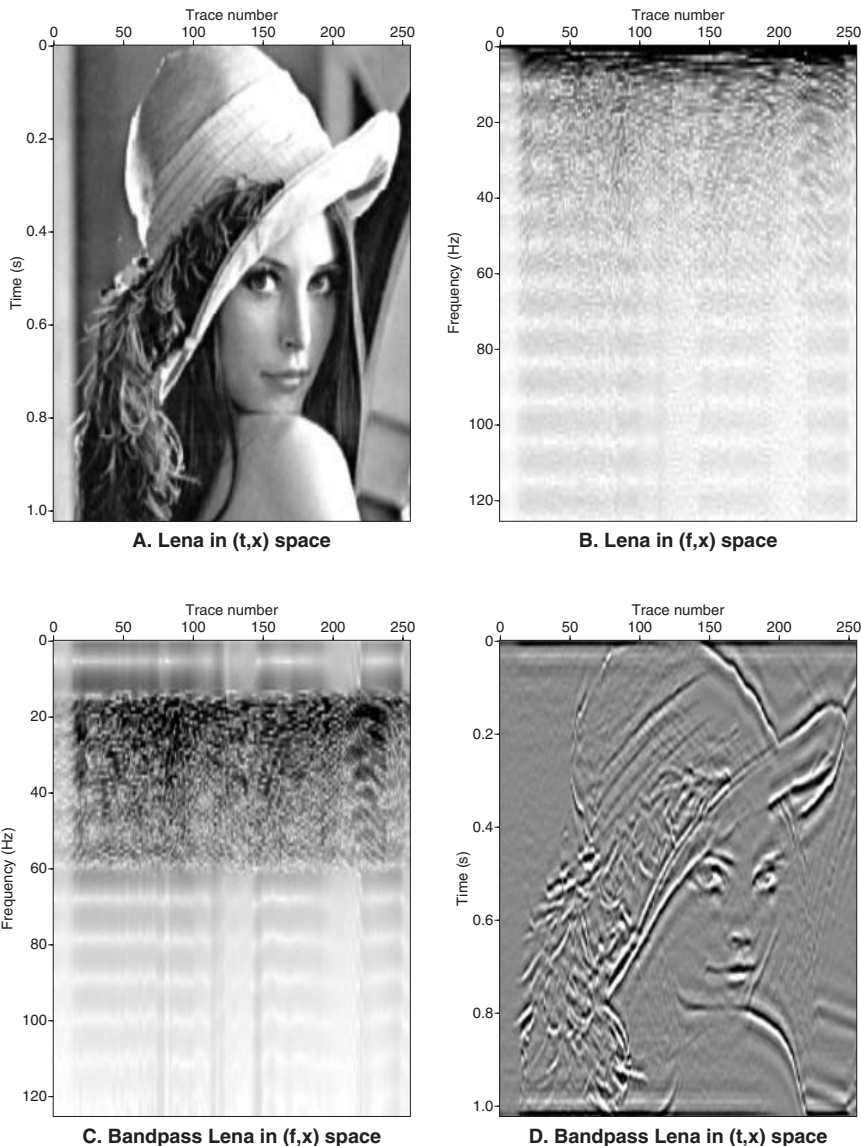


Fig. 14.3 bandpass filtering illustrated on seismic lena. (A) Lena as  $(t,x)$  data. (B) Amplitude  $(f,x)$  spectra of the data after 1D Fourier transform. (C) Filtered amplitude spectra simulating seismic bandwidth. (D) Filtered Lena in the  $(t,x)$  domain. Note that area shading is lost along with steep slopes and overall image detail.

## Elements of 3D Seismology

Multichannel processes can be one of three types: (1) One input trace influences many output traces, (2) many input traces influence one output trace, or (3) many input traces influence many output traces. In any case, multichannel processes tend to be much more involved and expensive in 3D than 2D.

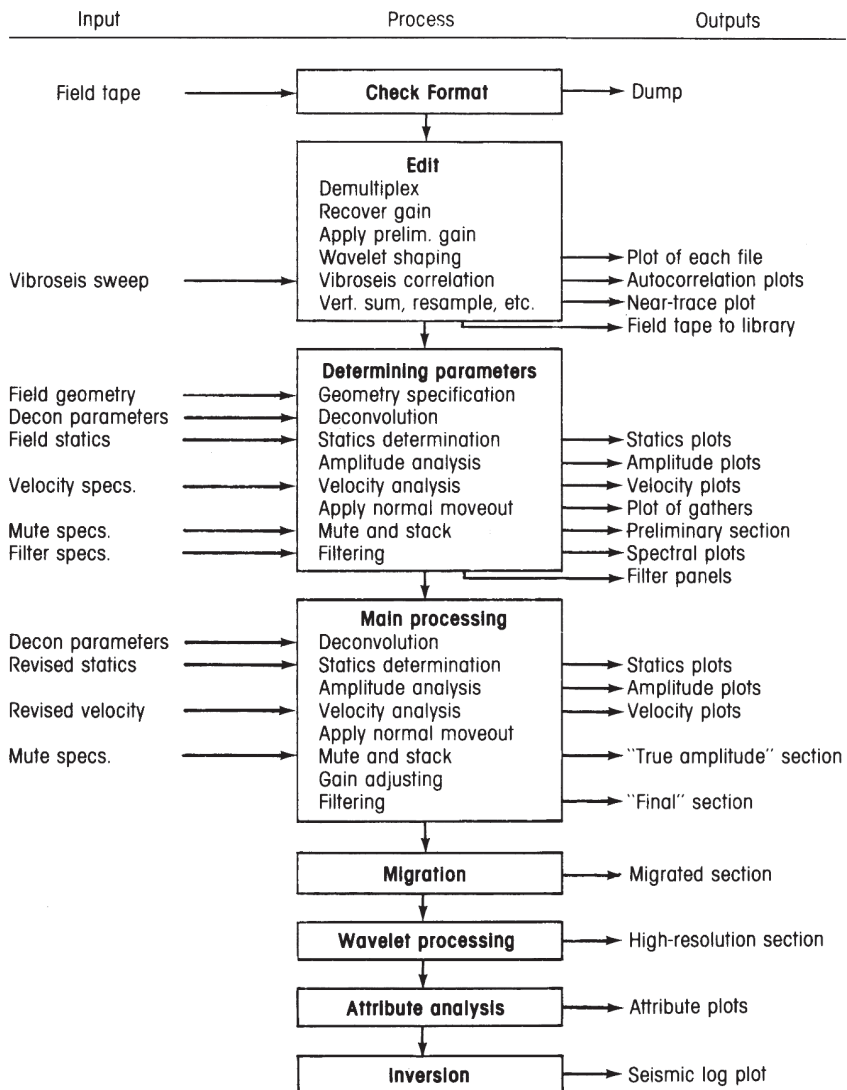


Fig. 14.4 An example processing flow (from [165])

Examples include NMO velocity analysis, multiple suppression, CMP stack, DMO, and migration.

Figure 14.5 shows the relative compute time of different seismic processes. The processing times in this graph all relate to a marine data set consisting of 100 2D shot records, each containing 120 traces for a total of 12,000 prestack traces and 320 poststack traces. Trace length is 1500 samples per trace.

Figure 14.5A includes standard prestack processes, common midpoint stack, and poststack time migration. Starting from the bottom item, these are in the order they would be applied and represent components of a typical 2D or 3D processing job. All of the processing times have been normalized to poststack time migration to facilitate comparison. Clearly DMO is the most expensive prestack process.

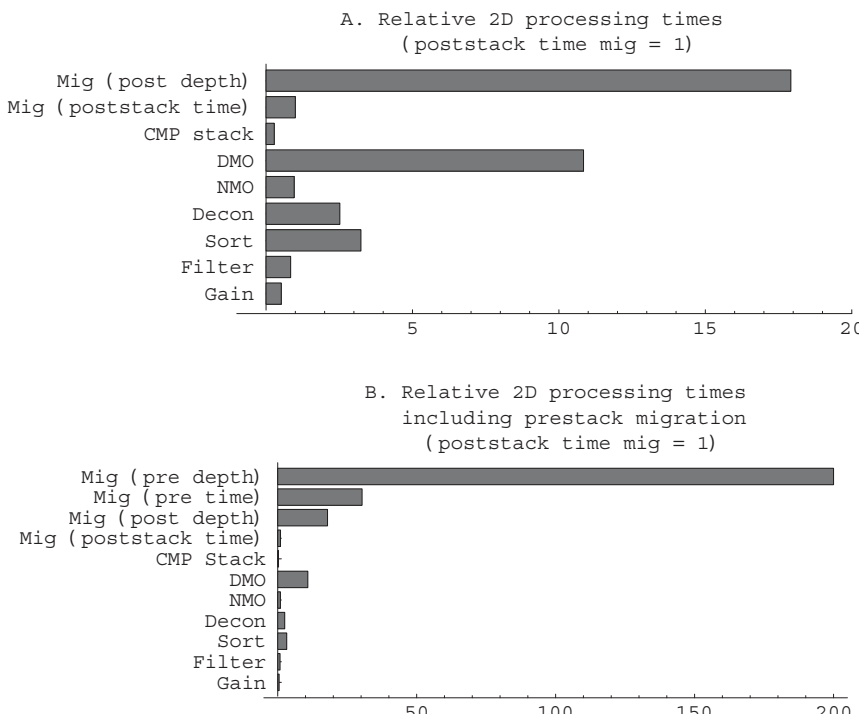


Fig. 14.5 Processes and computing effort for a 12,000 trace data set consisting of 100 2D shot records. If prestack migration is used then all processes beyond filter are eliminated.

## Elements of 3D Seismology

In Figure 14.5B, the same processing times are shown along with prestack time and depth migration. Note that DMO combined with poststack time migration is considerably less expensive than prestack time migration. When subsurface conditions are not too extreme, these two processing paths yield similar results. Prestack depth migration is the ultimate imaging algorithm and by far the most expensive. A large scale 3D survey might contain billions of traces, and the compute time to process it will increase accordingly, but not necessarily in a linear fashion. For really large data sets, something as simple as sorting can be substantial computing task.

In modern petroleum seismology, we process seismic data to create image sections or volumes, which are then interpreted. But raw data in the form of shot records was directly interpreted for many decades. To give one example, for the simple case of zero dip and constant (or layered) velocity, both average velocity and depth can be calculated from two points along a reflection hyperbola in a CMP gather. If the (time,offset) coordinates of two widely separated points along the reflection hyperbola are  $(t_1, x_1)$  and  $(t_2, x_2)$ , then

$$\begin{aligned} v_{avg} &= \left[ \frac{x_2^2 - x_1^2}{t_2^2 - t_1^2} \right]^{1/2} \\ z &= \frac{1}{2} \left[ \frac{x_2^2 t_1^2 - x_1^2 t_2^2}{t_2^2 - t_1^2} \right]^{1/2} \end{aligned} \quad (14.1)$$

where  $x_2 > x_1$  and  $t_2 > t_1$ . Knowledge of direct arrival and headwave traveltimes further allows near surface velocities to be estimated. On an elaborate scale, this is the basis of computing refraction statics to correct for weathering layer variations.

You can apply these equations to the land shot record [211] in Figure 14.6. This shows many features common on seismic field data including direct arrivals, head waves, reflections, and statics.

## 14.4 Bins

The 2D seismic data are sorted into CMP gathers, each of which is theoretically associated with one point on the earth's surface. The 3D data are more irregular and require the concept of a midpoint bin as introduced earlier, Figure 14.7. This irregularity comes from cable feathering in marine data or access, topography, or design problems in land data.

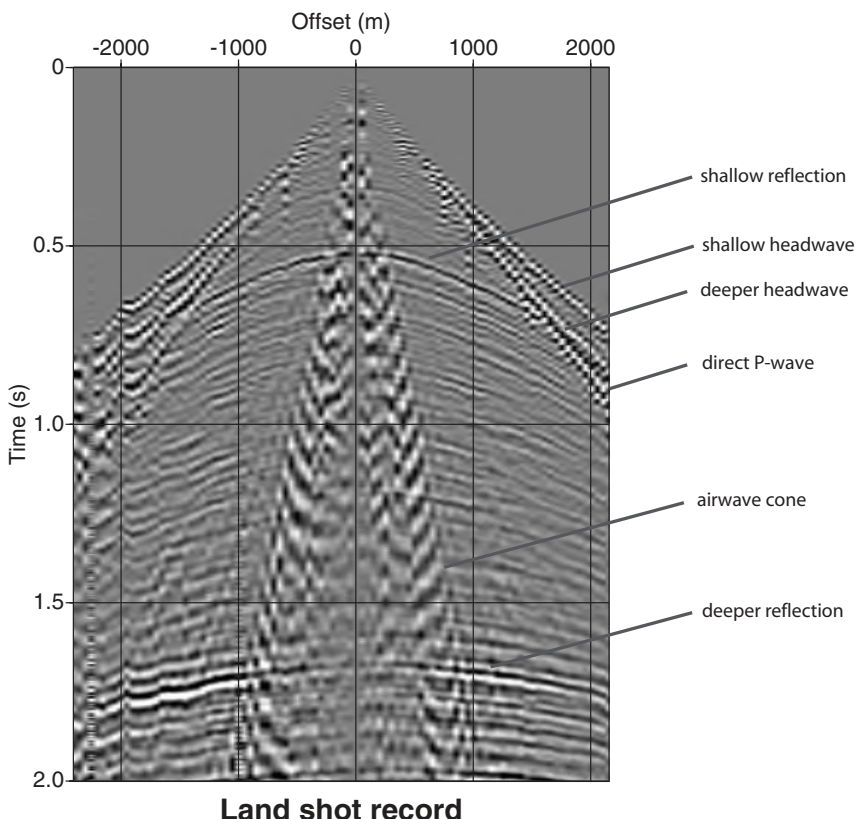


Fig. 14.6 A land shot record from Alaska. Several kinds of events are indicated on the right side of the record. The first arrival energy may be a direct wave or headwave depending on the offset and details of the subsurface. Static problems are seen as sharp lateral changes in first arrival times (e.g., near  $-2000\text{ m}$  offset) which persist for all times. Reflection events show hyperbolic traveltimes with increasing offset—the normal moveout effect. This figure can be used to estimate average velocity and depth of reflection events as well as direct arrival and refraction velocities. (Data from [211]).

The bins are of fixed size and all midpoints falling into the bin area are captured to form a 3D CMP gather. The fold of each bin is the number of captured traces. Ideally the actual midpoints will cluster near the bin center. Through the CMP stacking process, all traces within a bin are summed to create a single stack trace, as shown in Figure 14.8. This trace is associated with the geometric center of the bin for subsequent processing.

## Elements of 3D Seismology

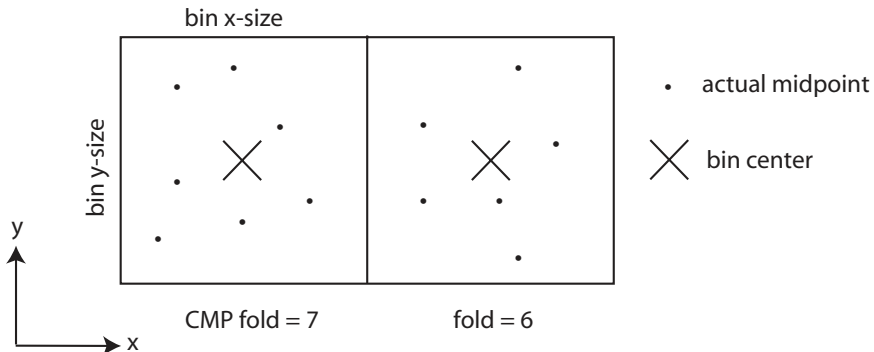


Fig. 14.7 Capturing traces (midpoints) into a 3D bin.

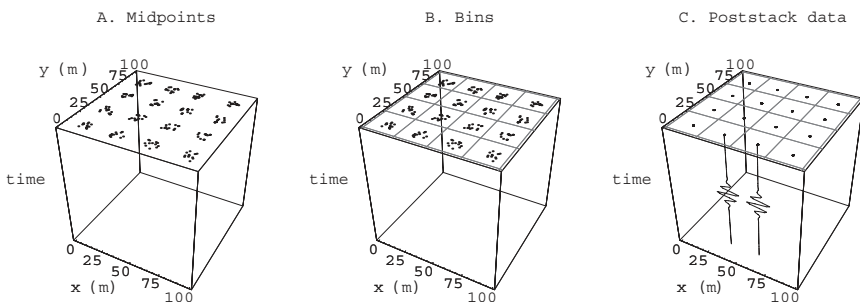


Fig. 14.8 Schematic diagram of binning and CMP stacking. (A) Each prestack trace has a midpoint. (B) The bin grid is superimposed on the midpoints and all prestack traces in a bin are captured into it. (C) After 3D common midpoint stacking, each bin contains one poststack trace.

**14.4.1 Bin size calculation.** For prestack processing, the traces in a bin are associated with the geometric center of the bin. This introduces errors since the traces do not have the same actual midpoint, but these amplitude and traveltime differences are small if the bin is properly sized. The general condition for bin size dimension is the same as the antialiasing condition on 2D midpoint spacing

$$(dx_b, dy_b) \leq \frac{\lambda}{4 \sin \theta} = \frac{v_{int}}{4 f_{max} \sin \theta} \quad (14.2)$$

where  $v_{int}$  is the interval velocity in the vicinity of the target, and  $\theta$  is the maximum anticipated physical dip.

To be technically correct, the velocity used should be that immediately above the reflecting interface. Considering the seismic wavelength is 60 m or more, it makes more sense to use an averaged interval velocity near the target. The variable  $\theta$  is often used to justify a non-square bin where steep dips are expected in one direction but not the other. However, this is a serious trade-off that risks spatial aliasing and, as always, fault diffraction limbs appear as 90° events.

The alert reader may wonder about the plausible situation of zero dip. In this case,  $\sin \theta=0$ , and the equation says the bin size is infinite. While not very useful, this result is correct. From a spatial aliasing point of view, if there is no dip, then the distance between adjacent traces can be as large as you like—10 kilometers is fine. But in practice, even for very low dips, we want traces close enough together to image fine-scale features of exploration interest like channels and reefs.

The safest rule for bin size is to ignore the dip altogether and design for ninety-degree dip

$$(dx_b, dy_b) = v_{int}/(4 f_{max}) \quad (14.3)$$

This will ensure that the data is not spatially aliased in the binning process, and that traces gathered within a bin are similar enough not to destructively interfere. If the bins are taken too large, processing is affected, and the final migrated data cube will be a degraded image. This can strongly influence subtle interpretations involving amplitude and stratigraphy.

Both interval velocity and maximum data frequency are functions of depth, as shown schematically in Figure 14.9. In soft clastic basins like the Gulf of Mexico, a good first order trend of interval velocity increase with depth is

$$v(z) = v_0 + k z \quad (14.4)$$

where the gradient is about  $k=0.4$ . This velocity function is shown in Figure 14.9A. Dominant frequency, on the other hand, diminishes with reflector depth due to attenuation, something like the function shown in Figure 14.9B. The velocity and frequency determine the wavelength as a function of depth, Figure 14.9C, and the bin size, Figure 14.9C. The heavy line is the bin size that would be valid for all dips up to 90 degrees and the light line corresponds to bin size valid up to 45 degrees.

In this example, to get an unaliased image of the sea floor would require a bin size of about 5 m x 5 m (up to 90 degree dips) or 7.5 m x 7.5 m (up to 45 degree dips). A deeper target at about 4000 m would require a bin of 25 m x 25 m (90 degrees) or 37.5 m x 37.5 m (45 degrees).

## Elements of 3D Seismology

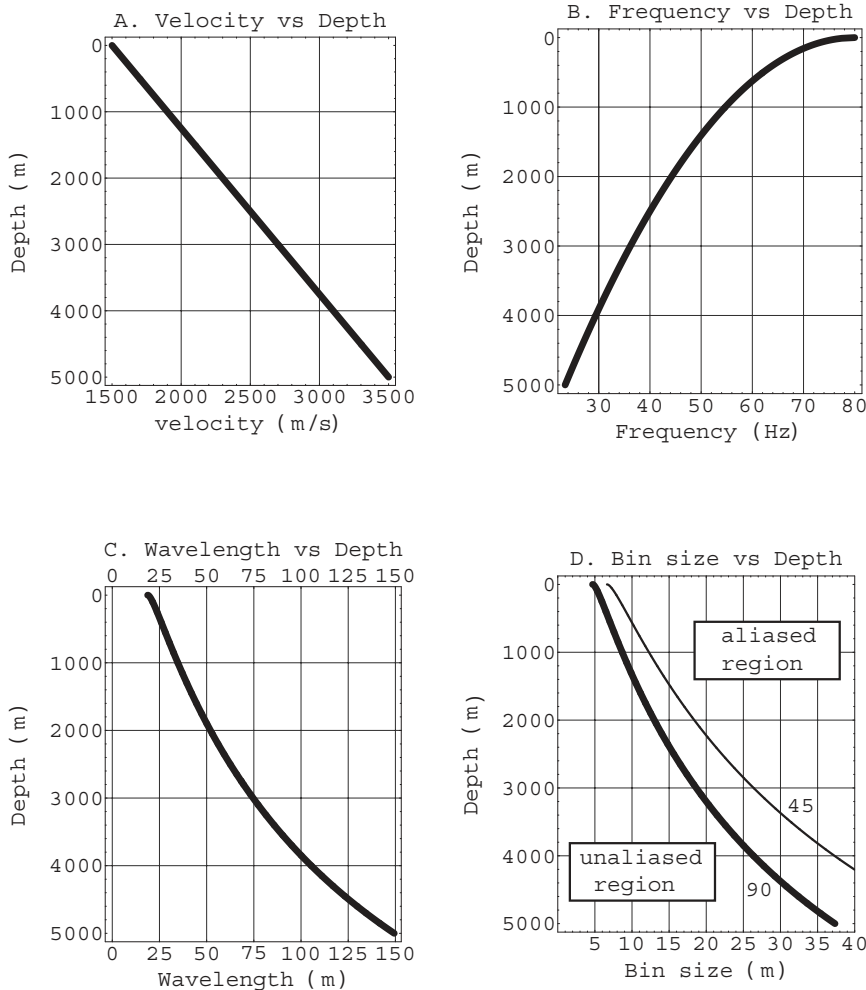


Fig. 14.9 Bin size recommendations for shallow and deep targets can be quite different. (A) Interval velocity tends to increase with depth in the earth due to compaction, lithification, and increasing temperature and pressure. (B) Dominant frequency in reflection seismic data decreases with reflector depth due to various forms of attenuation. (C) Both effects cause wavelength to increase with target depth. (D) Recommended bin size increases with target depth, but also depends on the maximum dip. A bin valid for all dips up to 90 degrees (heavy line) is smaller than a bin valid only up to 45 degrees.

From a purely scientific point of view, marine data should always be acquired with a 5 m bin which will give unaliased imaging of everything from the sea floor down. However, if CMP fold, image area, and other design goals are held constant, the number of prestack traces,  $n_{pre}$ , will increase as

$$n_{pre} \propto \frac{1}{(dx_b dy_b)^2} \quad (14.5)$$

where  $(dx_b, dy_b)$  are the bin dimensions.

For example, if the fold and survey area are held constant, cutting the bin size in half generates four times as many prestack traces. Furthermore, most would agree that acquisition cost is proportional to the number of prestack traces while processing has an even more rapid nonlinear dependence. The conclusion is that acquisition plus processing cost,  $C_{ap}$ , is at least proportional the number of prestack traces,

$$C_{ap} \propto \frac{1}{(dx_b dy_b)^2} \quad (14.6)$$

and this may well be an underestimate. Bin size is a first order economic parameter and a first order geophysical imaging parameter. Physics argues for a small bin, finance argues for a big one. Guess who usually wins.

Typical bin sizes in the Gulf of Mexico and similar basins worldwide range between 12.5 m x 12.5 m up to 20 m x 40 m with an accelerating trend toward uniform application of the smaller bin size. Figure 14.9D tells us that in such a basin a 12.5 m x 12.5 m bin should give unaliased data up to 90 degrees for any target below 2000 m depth.

The bin size calculations here are based on constant velocity and therefore straight rays. A more realistic approach [15, 116] is to assume a linear  $v(z)$  function. Bin calculations based on constant velocity can always be used, but tend to be overly conservative (bin size too small) and thus waste money.

**14.4.2 Effects of fold and offset variation.** Seismic data is acquired in shot profiles, but primarily processed in the CMP bin domain. Thus 3D shooting necessarily introduces fold and offset variations from bin to bin. This can cause shadow images of the acquisition geometry to leak into the data. This is undesirable because it can interfere with geologic features in the data that are important interpretation targets. If any pattern associated with acquisition geometry leaks into the data, we say the acquisition footprint is visible, an effect best seen in time slices and horizon amplitude maps.

## Elements of 3D Seismology

Bin-to-bin variation in offset, azimuth, and fold are of concern for several reasons [154]. Clustering of offsets within CMP's limits sensitivity to velocity analysis essential for stack response, dip moveout, and migration. Near offsets are required to achieve good static corrections, and long offsets are essential to high-resolution NMO velocity analysis because the moveout is greatest at the far offset.

If CMP fold changes from bin-to-bin, this introduces signal-to-noise variations called *fold striping*. This occurs because as fold changes, so does the ability of CMP stacking to attenuate random noise and multiples. If both offset and fold variations are present, it creates waveform inconsistencies that influence interpretation, particularly amplitude work. The main concern with azimuth is not consistency from one bin to the next, but that a full range of azimuths are consistently present.

It is really quite simple. Inside the sweet spot of 3D seismic survey, we want every bin to have (1) all offsets, (2) all azimuths, (3) constant fold from bin to bin, and (4) a tight cluster of midpoints at the bin center. The last item is important because any spatial aliasing calculation to determine bin size assumes that the actual midpoints are near the bin center. If two traces are in opposite corners of a bin, the distance between them is greater than the design limit represented by the bin size.

As developed here, the bin size arises from a natural clustering of midpoints due to shot and receiver intervals. The data can be rebinned to a larger or smaller bin, but the natural bin size is set at acquisition time. In practice, the midpoints may not be clustered at all because of logistics, access, or any number of other shooting problems. For towed streamer marine data, tides and currents guarantee midpoints will be widely scattered. There are several strategies for dealing with this situation [33, 156].

**14.4.3 Anatomy of a bin.** At one level of understanding, a bin is a very simple object, really nothing more than an imaginary cell drawn on the earth surface with an  $x$  and  $y$  dimension. But the internal detail of a particular bin is difficult to predict for a large 3D survey. Here we describe the internal structure of a single 3D bin and identify those features that are important for quality control and influence later processing and interpretation. Figure 14.10 shows a synthetic 3D bin.

Figure 14.10A shows azimuth lines connecting all sources and receivers that contribute to this bin. The actual bin is a 25 m  $\times$  25 m square area centered at (0,0). To contribute to this bin, a trace must have its true midpoint within the boundaries of the bin. From the plot we see a wide distribution of azimuth. That is, the sources and receivers surround the midpoint without large gaps in angular coverage. A close up of the bin and actual midpoint locations is shown in Figure 14.10B. As desired, this bin has a tight spread of midpoints clustered on the bin center.

The offset distribution within the bin is shown in Figure 14.10C. These range from the near offset of 250 m to far offset of 3500 m. The offsets have been sorted in ascending order to show uniformity of coverage. This bin has good offset distribution in the sense that nearly all offsets between the designed near (250 m) and far offset (3500 m) are represented. Figure 14.10D shows the azimuth distribution within the bin. As with the offsets, the azimuths are sorted

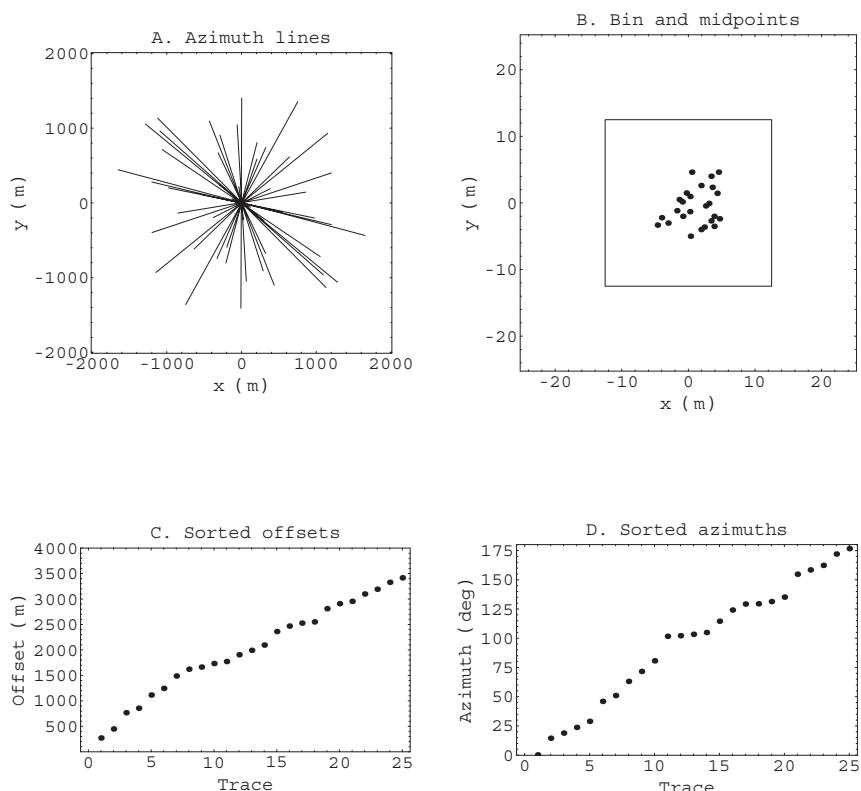


*Fig. 14.10* Detailed view of one synthetic 3D bin. This bin has good distribution of all important properties. (A) A  $16 \text{ km}^2$  area showing azimuth lines connecting sources and receivers whose midpoints fall in a  $25 \text{ m} \times 25 \text{ m}$  bin. Invoking reciprocity, we do not distinguish which end of each line represents the source or receiver. (B) Detail view of the bin area and midpoint scatter. The CMP fold is 25. (C) Each trace has an unsigned offset. By plotting the sorted offsets we see an even distribution of all values between the designed near offset of 250 m and far offset of 3500 m. (D) The sorted azimuths confirm that this is a full azimuth bin with values 0–180 degrees.

## **Elements of 3D Seismology**

in ascending order. No bin is perfect in showing all azimuths, but this bin has a good distribution covering most directions.

It is important to understand the detailed internal structure of 3D bins and their important properties. As an example consider the 3D bins shown in Figures 14.11–14.13.

The bin in Figure 14.11 shows excessive midpoint scatter but good distribution of offsets and azimuth. The risk here is spatial aliasing from diagonal midpoints being too widely separated. The Figure 14.12 bin is healthy except for the offset distribution, which shows that only middle offsets are present. The risk here is poor velocity analysis (missing far offsets) and poor static corrections (missing near offsets). The bin in Figure 14.13 has an azimuth problem. The azimuth range of 75–125 degrees makes this 3D data little better than a grid of east-west trending 2D lines, and the image volume will suffer because migration requires full azimuth data to do its job correctly.

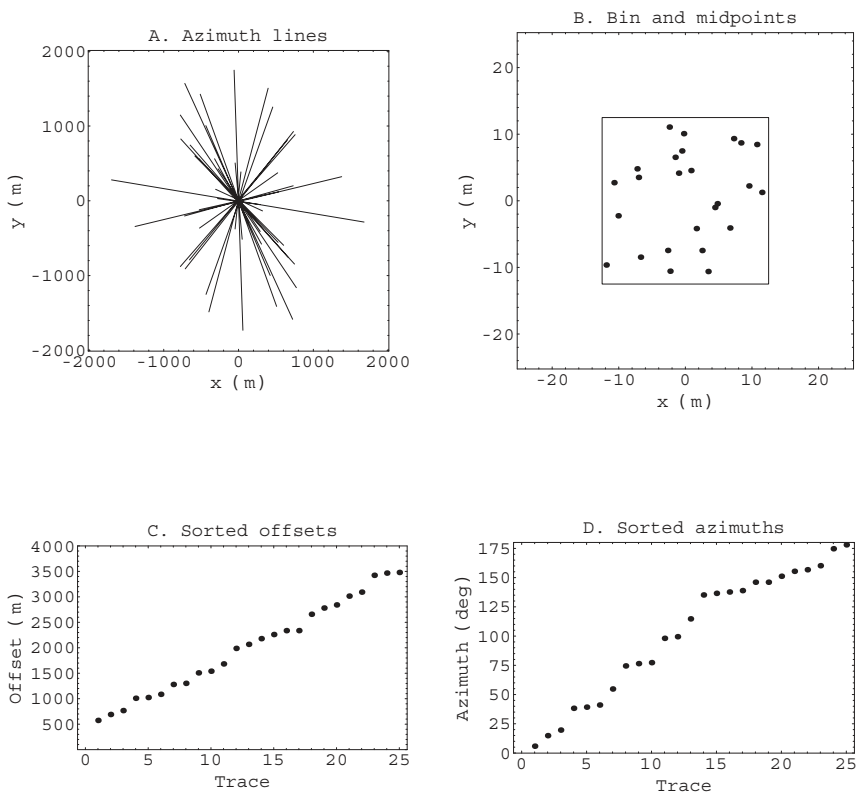


Fig. 14.11 Synthetic 3D bin with excessive midpoint scatter.

## Elements of 3D Seismology

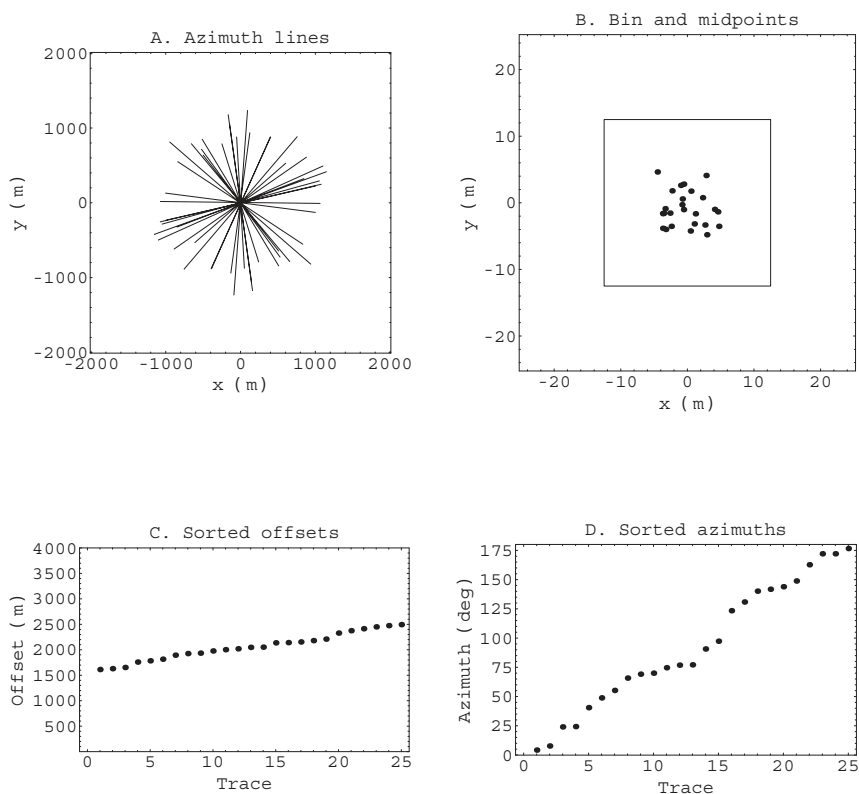


Fig. 14.12 Synthetic 3D bin with poor offset distribution.

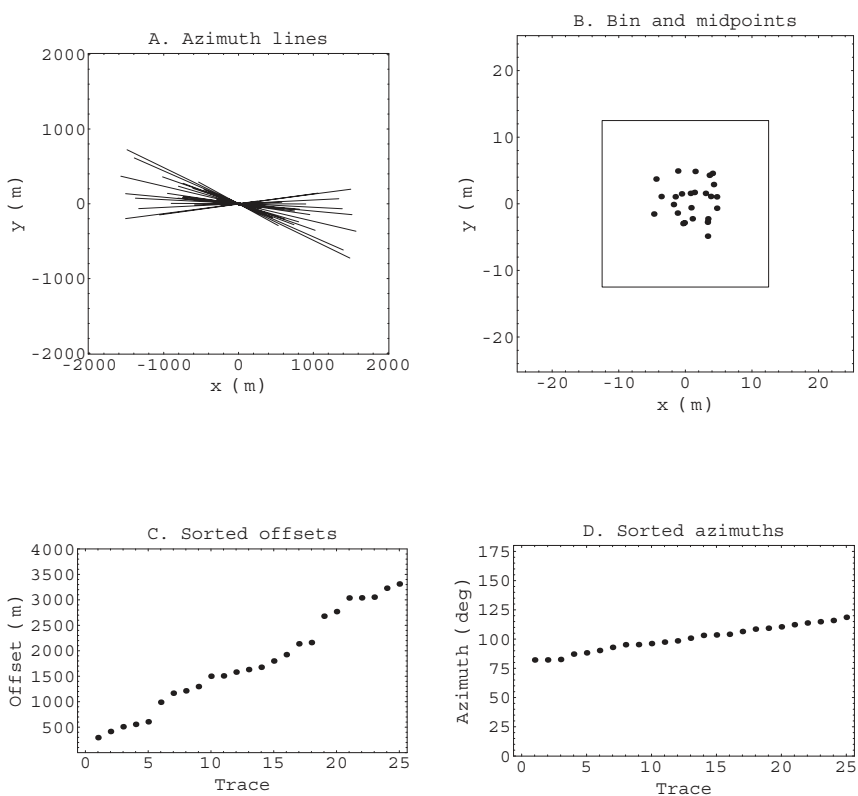


Fig. 14.13 Synthetic 3D bin with narrow azimuth coverage.

# 15

## Computing

Geophysics is tightly linked to computing power, yet many geophysicists will never log on to a supercomputer. They live in a world populated by workstations and desktop computers. The work is interpretation, log analysis, synthetic seismograms, and report preparation. They get along just fine without supercomputers. But the geophysicist who does not understand computers is at the mercy of those who do.

Progress in modern processing and interpretation runs parallel to advances in computer hardware, numerical algorithm developments, and multidimensional visualization techniques. Here we consider computer hardware issues of data storage and processing speed in the context of large seismic data sets.

### 15.1 RAM and disk storage.

Figure 15.1 is a schematic diagram of the components making up a generic computer system.

We start at the beginning with the lowly bit, the fundamental binary unit of information and data storage. From bits we define larger information units:

1 bit	=	8 bits		
1 byte	=	32 bits (PC,WK)	=	4 bytes
1 word	=	64 bits (SC)	=	8 bytes
1 kilobyte	=	1024 bytes		
1 megabyte	=	(1024) <sup>2</sup> bytes	=	1 Mb [~ 10 <sup>6</sup> bytes]
1 megaword	=	(1024) <sup>2</sup> words	=	8 Mb (SC)
1 gigabyte	=	(1024) <sup>3</sup> bytes	=	1 Gb [~ 10 <sup>9</sup> bytes]
1 terabyte	=	(1024) <sup>4</sup> bytes	=	1 Tb [~ 10 <sup>12</sup> bytes]
1 petabyte	=	(1024) <sup>5</sup> bytes	=	1 Pb [~ 10 <sup>15</sup> bytes]
1 exabyte	=	(1024) <sup>6</sup> bytes	=	1 Eb [~ 10 <sup>18</sup> bytes].

## Elements of 3D Seismology

The terms *petabyte* and *exabyte* are not in common use because individual disks that large are not yet available. With developments in nanoscale technology, petabyte disks are projected to be available around the year 2010. To put the petabyte into perspective, such a disk would hold nearly 60 years of continuous DVD quality video. Even petabyte disk farms are very rare today. For example, NCAR (U.S. National Center for Atmospheric Research) only passed the petabyte mark in January 2003. Exabyte disks (not to be confused with a tape manufacturer of the same name) are probably several decades away.

A disk farm is a multidisk data storage facility attached to a supercomputer or computer network. A disk farm is sometimes called a disk vault or disk array.

We distinguish among three computer classes: the personal computer (PC), work station (WK), and supercomputer (SC). This classification is fuzzy but based primarily on processing speed as well as RAM and disk storage. The computer operating system (OS) is loosely correlated with the classes as well. The dominant OS for PC class machines is some form of Windows™, while UNIX is most common on work stations, and ubiquitous on supercomputers.

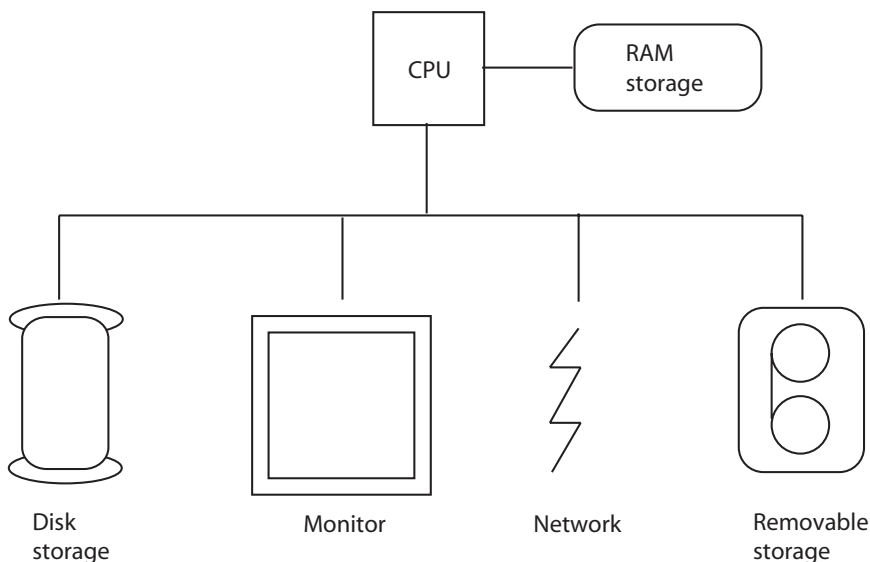


Fig. 15.1 Elements of a single processor computer system. (CPU = central processing unit; RAM = random access memory).

To bring the machine classes into perspective, we can list upper limit of RAM and disk storage to be found in computers today.

RAM			Disk		
PC	=	512 Mb	PC	=	80 Gb
WK	=	4 Gb	WK	=	600 Gb
SC	=	10 Tb	SC	=	2 Pb

Supercomputers only exist to solve large computationally challenging problems, which means they are loaded with RAM and disk. The supercomputer numbers given here are for Japan's Earth Simulator, which became operational in March 2002 and is used to model atmospheric, ocean, and solid earth physics.

We have seen in chapter 7.4 that petroleum seismic data is composed of many individual traces in SEGY file format. The actual seismic data are a string of floating point numbers each of which has a size of 4 bytes, or 32 bits. Oddly, these 32-bit floating point numbers are in an archaic format called IBM float, which is about as useful as cuneiform. In processing centers around the world, it must be translated to the modern IEEE 32-bit form billions of times each day.

The number of bytes,  $N_b$ , in a SEGY seismic data set depends on the number of traces,  $N_{tr}$ , and the number of time samples per trace,  $N_t$ ,

$$N_b = (4 N_t + 240) N_{tr} + 3600 \quad (15.1)$$

where the 4 in this equation arises because each sample is a 4-byte floating point number; the 240 is the number of bytes in each trace header; and 3600 is the number of bytes in the two line headers (see Fig. 7.10). It is often useful to calculate  $N_t$  or  $N_{tr}$  from the byte count

$$N_t = \frac{1}{4} \left[ \frac{N_b - 3600}{N_{tr}} - 240 \right] \quad (15.2)$$

These equations assume line headers are included. If they have been removed (common in data processing), the equations are

$$N_{tr} = \frac{N_b - 3600}{4 N_t + 240} \quad (15.3)$$

### 15.2 The 2D survey size.

We can calculate how much disk space is needed to store a 2D seismic line in SEGY format. Here is an example.

1 sample value	=	4 bytes
6 secs data @ .002 sec sample rate	=	3000 samples/trace
3000 * 4 + 240 (header)	=	12,240 bytes/trace
192 channel * 1000 shots	=	192,000 traces
192 000 traces * 12 240 bytes/trace	=	2,350,080 000 bytes
add line headers 3600 bytes	=	2,350,083,600 bytes
2,350,083,600 / (1024) <sup>3</sup>	~	2.19 Gb

If the shot interval is 25 m, this represents a 25 km line.

From the previous RAM and disk storage numbers, we conclude that the 2D seismic line can fit in RAM of a large workstation, and fit on the disk but not in RAM of a high-end desktop computer. The RAM issue is important because processes like prestack migration prefer to hold the entire data set plus work space in RAM. If it can't all be stuffed into RAM, we are left with a significant data management problem.

### 15.3 The 3D survey size.

Do things get better for 3D seismic data? Hardly. Large 3D surveys today can contain billions of prestack traces. This calculation shows the data storage requirements for a medium-sized 3D data set composed of 500 2D lines like the previous one.

500 2D lines	=	500 lines * 2.16 Gb/line	[96,400,000 traces]
	~	1094 Gb	
	~	1.07 Tb	

This amount of data would overwhelm any PC or work station. It will fit in RAM of maybe ten supercomputers in the world, but everyone else will have to be satisfied with finding enough pasture for it on the disk farm. Remember this is a 96-million trace example. You can imagine the issues associate with a billion trace survey.

### 15.4 Processing speed

RAM and disk storage are two parts of a seismic computing bottleneck. Another is processing speed. It is of little use to squeeze seismic data into computer RAM if, once there, it takes forever to process it.

The fundamental unit of processing is the floating point operation (flop), and the basic unit of processing speed is the number of floating point operations that can be achieved in one second (flops). A floating point operation is a basic arithmetic procedure (add, subtract, multiply, divide) as implemented in computer code. More advanced operations, such as a square root or trigonometric function, take several flops to complete. For this reason, computationally intensive programs are carefully analyzed to minimize such function calls on inner loops.

Processing speed is defined here in terms of floating point operations because seismic applications are floating point processes, but many other metrics of performance are used in non-scientific computing. Two examples are million instructions per second (MIPS) and a combination of floating point and integer arithmetic speed (SPEC marks). Floating point processing speed units are

flop	=	floating point operation + - * /
flops	=	floating point operations per second
1 megaflop	=	$10^6$ flops = 1 Mf
1 gigaflop	=	$10^9$ flops = 1 Gf
1 teraflop	=	$10^{12}$ flops = 1 Tf
1 petaflop	=	$10^{15}$ flops = 1 Pf
1 exaflop	=	$10^{18}$ flops = 1 Ef

Petaflop and exaflop are not yet in common use. We don't have machines that fast. The current world speed record for computer processing is around 36 Tf in performance.

The alert reader will see inconsistent use of prefixes between megabyte and megaflop. A megabyte is  $1024^2$  bytes, but a megaflop is  $1000^2$  flops. This convention is ingrained and not likely to change.

There are many different ways to achieve high flop rates. None of them are cheap. First, a single CPU can be constructed to achieve multi-gigaflop performance, but it tends to be made of exotic materials and generate so much heat that special cooling equipment is needed. Second, a single machine can have many standard or specialized CPUs with hardware connections, a configuration termed massively parallel.

A third approach is to build a cluster of networked machines (nodes), each of which has several CPUs. The dominant form of cluster in technical computing today is the Beowulf cluster, which uses the free Linux operating system to run applications and manage network traffic between nodes. A fourth type of supercomputer is a cluster of clusters, with the individual clusters communicating across high speed Internet. This is called grid computing, and it has not yet found wide application in petroleum seismology but clearly represents the future of massively parallel computing.

## Elements of 3D Seismology

Scientific programming becomes a more complex undertaking with each move to a new level of parallel computing architecture. The days of processing data with a few simple loops are going fast. Now the programmer must decompose the problem into parts that can be passed to nodes or clusters and then reassembled into a final product, all the while enforcing crash-resistance and midjob restart capability.

Upper limits on floating point performance in the various computer classes are

PC:

Intel P4 3.06 GHz = 1 Gf (1 cpu)

WK:

Intel P4 3.06 GHz = 16 Gf (16 cpu)

SC:

Earth simulator = 35.9 Tf (5120 cpu)

HP ASCII-Q = 7.7 Tf (4096 cpu)

IBM ASCII White = 7.2 Tf (8192 cpu)

MCR Linux Cluster = 5.7 Tf (2304 cpu)

HP Alpha Server = 4.4 Tf (3016 cpu)

Intel ASCII red = 2.4 Tf (9632 cpu)

The PC and WK numbers are as of June 2003 and the SC values are accurate through November 2002.

We should all realize that any list of supercomputer speed is extremely volatile. It certainly needs to be updated every six months or so. The fastest machine listed (Earth Simulator at the Yokohama Institute for Earth Sciences) has only been online since March 2002. The *Top500* Internet site [182] maintains current and historical lists of the 500 fastest computers in the world, as measured by the Linpack [119] floating point benchmark.

There are some clear trends in the *Top500* list which has been maintained since 1993. The teraflop barrier was broken by the top machine in 1998, and it is expected the number 500 machine will have Tf performance by 2005 (the current number 500 machine is rated at 245 Gf). Performance of the top machine has a clear logarithmic trend that allows us to say, with some certainty, that the first petaflop computer will come online about the year 2009, at which time the number 500 machine will have 10 Tf performance. If the trend continues to hold, the first exaflop machine will be operational around the year 2020.

By way of comparison, the human brain contains about  $10^{11}$  neurons, each of which has 10,000 or so synapses, and all these switch 1000 times per second. If we take synapse operations as equivalent to floating point operations, the brain executes  $10^{18}$  operations per second or is roughly equivalent in processing power to an exaflop computer.

## 15.5 Speed and 3D migration

The 3D prestack depth migration is the classic example of our extreme need for computing speed. Assume migration involves one million floating point operations per data sample. This is the effort it takes to broadcast each input amplitude along a unique image surface that resembles a lumpy bowl. A major part of the work is tied up in calculating the exact geometry of this surface.

We can estimate how much time is required for 3D prestack depth migration of the data set specified earlier. First, we need the total number of floating point operations.

Data size:	3000 samp/trace * 96,000,000 traces	
		= $2.88 \times 10^{11}$ data samples
Assume prestack depth mig		= 1,000,000 operations/sample
total floating point operations		= $2.88 \times 10^{17}$

The time required for this number of operations on the fastest PC currently available is

$$\text{PC time} = (2.88 \times 10^{17}) / (10^9) = 2.88 \times 10^8 \text{ seconds},$$

which sounds like a long time, because it is. This theoretical processing time works out to 80,000 hours or just more than nine years.

A top workstation could do it in seven months. But both of these estimates are wildly optimistic. In reality, on either a PC or workstation, this job would go on forever due to disk thrashing since the data will not fit in RAM memory. A good rule of thumb in the computer world is that nothing works at theoretical speed.

To run the 3D prestack depth migration on the world's fastest computer should take a little over two hours, but again this is a theoretical number based on a dedicated machine. The qualifier, "dedicated," is added to highlight the fact that it is unusual to have a supercomputer working on only one problem at a time. More likely jobs are queued up like traffic on a Los Angeles freeway, thus slowing work on any given job. On the second fastest computer in the world today, the job time calculates out to about ten hours but all of our cautionary comments still apply.

The conclusion is not that 3D prestack depth migration is an impossible computer task. Rather, we are only trying to appreciate the scale of the problem in the context of current and future computing capabilities. Seismic processing is world-class in terms of data size and algorithm complexity, and the trend is toward much larger surveys and multiple components. Shortcuts that will generate final results faster are continuously being developed and the need for this work will accelerate in the future.

# 16

## Creating the CMP Stack

Long before the advent of prestack migration, a processing flow developed to sequentially remove residual wave propagation and acquisition geometry effects in seismic data. Where prestack migration bundles all this functionality in one grand program, the traditional approach isolates each effect for analysis and optimum removal. The CMP stack approach is still the industry standard unless subsurface conditions dictate the use of prestack migration.

Here we briefly describe the individual steps that lead to the CMP stack, approximately following the order in which they are applied.

### 16.1 Gain

Seismic waves emitted by a source array travel to a subsurface reflection point, then back to the receiver array. Several phenomena influence the wave amplitude including source directivity, geometric spreading, various forms of attenuation, and receiver directivity. The observed amplitudes are a composite of these unwanted effects and the reflection coefficient. We want to preserve reflection coefficients because they contain information about impedance contrasts in the subsurface.

It is not feasible to remove each of these amplitude effects individually since they are coupled in various ways. Rather, a general amplitude modification process, called *gain*, is applied with certain parameters chosen by the user.

Various kinds of amplitude balancing are often applied. For example, shot balancing will remove shot-to-shot variability in source strength, and receiver balancing can be used to compensate for variations in receiver sensitivity.

## Elements of 3D Seismology

The physical processes of geometric spreading and attenuation are addressed through application of a gain function of the form

$$p_1(t) = t^a e^{bt} p_0(t) \quad (16.1)$$

where  $p_0(t)$  is the ungained prestack data,  $p_1(t)$  is the gained data, and  $(a,b)$  are parameters determined by the processor. Figure 16.1A shows a 2D shot record from a marine survey. Without gain, the only visible energy is at shallow times and near offsets. Geometric spreading represents  $1/r$  amplitude decay. For constant velocity, this is equivalent to a time decay of  $1/t$ .

Allowing for another power of time to account for various attenuation processes [48], the time decay goes approximately like  $1/t^2$ . Removal of this amplitude behavior is accomplished by our general gain function with  $(a=2, b=0)$  shown in Figure 16.1B. By comparison, the parameter set  $(a=0, b=2)$  gives the result in Figure 16.1C. It should be evident that gain decisions made in processing can preserve or destroy geologically meaningful amplitude variations in the data. Robust effects like bright spots will generally survive any reasonable gain function, but subtle features such as AVO must be carefully preserved.

When structural imaging is the only goal, automatic gain control (AGC) is often applied. This preserves the root-mean-square amplitude in a user-defined window. The example in Figure 16.1D uses a 500 ms window. AGC makes all events visible and appear balanced, but relative amplitude information is lost. Reflections of equal strength on an AGC section may represent vastly different reflection coefficients. When the AGC window contains only noise, even very weak noise, this is scaled up to give the impression of strong noise, particularly at early times before the first break. This precursor noise is a universal characteristic of prestack data with AGC, unless it has been muted out after AGC.

## 16.2 Deconvolution

Deconvolution is the general inverse process to convolution. Since convolution of two time functions ( $g_1(t), g_2(t)$ ) is simply multiplication in the frequency domain

$$g_3(f) = g_1(f)g_2(f) \quad (16.2)$$

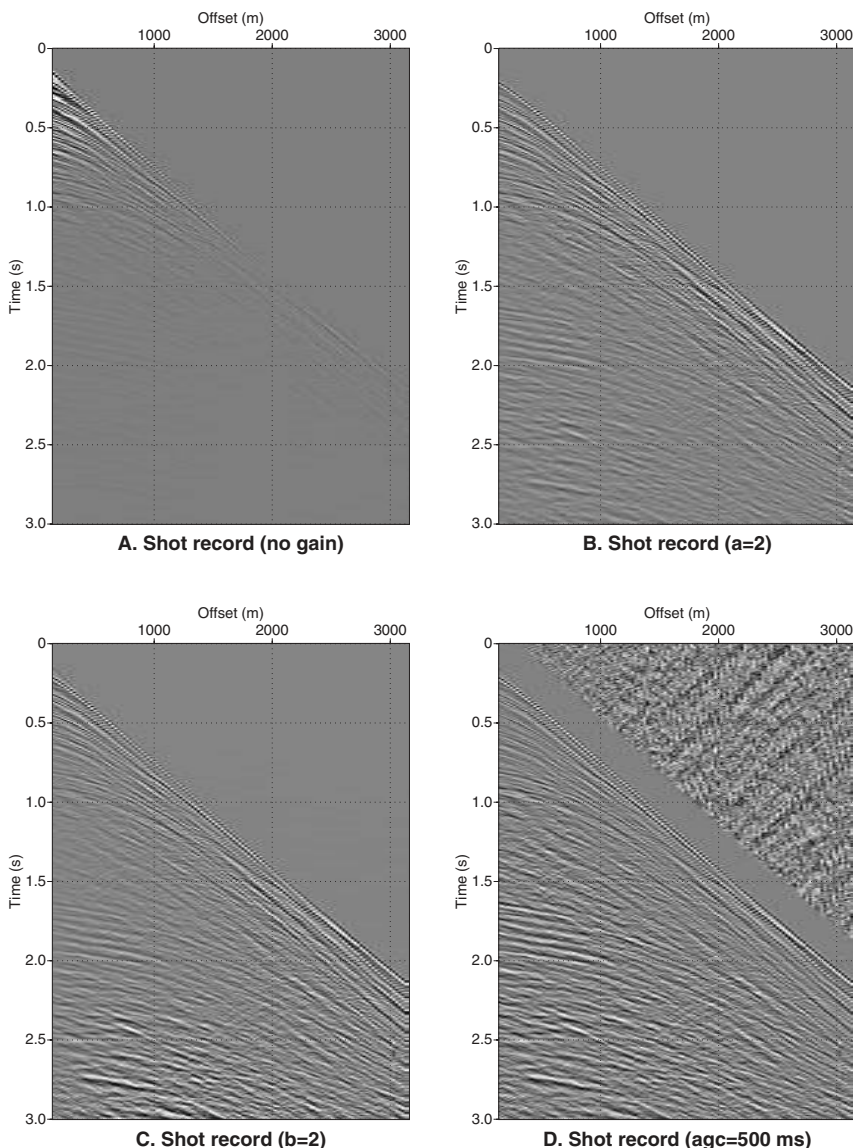


Fig. 16.1 Gain is applied to prestack data to remove unwanted amplitude decay effects associated with wave propagation and acquisition geometry. (A) A 2D marine shot record without gain. (B) Data after  $t^2$  gain which approximately removes geometric spreading and attenuation. (C) Data after  $e^{2t}$  gain. (D) Data after automatic gain control using a 500 ms window. All events are visible, but relative amplitude information is lost.

## Elements of 3D Seismology

then deconvolution is division

$$g_1(f) = \frac{g_3(f)}{g_2(f)} \quad (16.3)$$

For example, if  $g_1(t)$  is a reflection coefficient (RC) series, and  $g_2(t)$  is a wavelet, then  $g_3(t)$  is a seismic trace created by convolution. In theory, deconvolving the trace with respect to the wavelet returns the RC series. Although we write these expressions in the frequency domain, they are usually computed in the time domain.

Figure 16.2A is synthetic zero offset data consisting of a horizontal seafloor reflection at about 70 ms and a deeper dipping reflection. Water bottom reverberations set up a chain of multiples that complicate the image and would interfere with interpretation. Functionally we can describe this data as a double convolution

$$g_4(f) = g_1(f) \ g_2(f) \ g_3(f) \quad (16.4)$$

where  $g_4(t)$  is the data in Figure 16.2A,  $g_1(t)$  is the desired primary RC series,  $g_2(f)$  is the wavelet, and  $g_3(f)$  is the multiple RC series.

Autocorrelation is a way of scanning a trace against itself [165] and Figure 16.2B shows the autocorrelation of the first ten data traces. This contains two important pieces of information: (1) the wavelet at zero lag indicates a period of about 20 ms, and (2) multiples are present with a period of about 65 ms.

Deconvolution with respect to the wavelet is done by running a deconvolution program and telling it to design an optimum inverse filter up 40 ms long and apply it to the data. This is spiking deconvolution. Since the wavelet period falls in this range and the multiple period does not, the program sniffs out the wavelet, inverts it, and applies this inverse to make the first deconvolution result

$$g_{d1} = \frac{g_4(f)}{g_2(f)} = g_1(f) \ g_3(f) \quad (16.5)$$

as shown in Figure 16.2C. Each event in the data now has a compact appearance because an oscillating wavelet has been replaced by an approximate spike. The autocorrelation of this result, Figure 16.2D, clearly shows a more compact wavelet and the multiples which are still present.

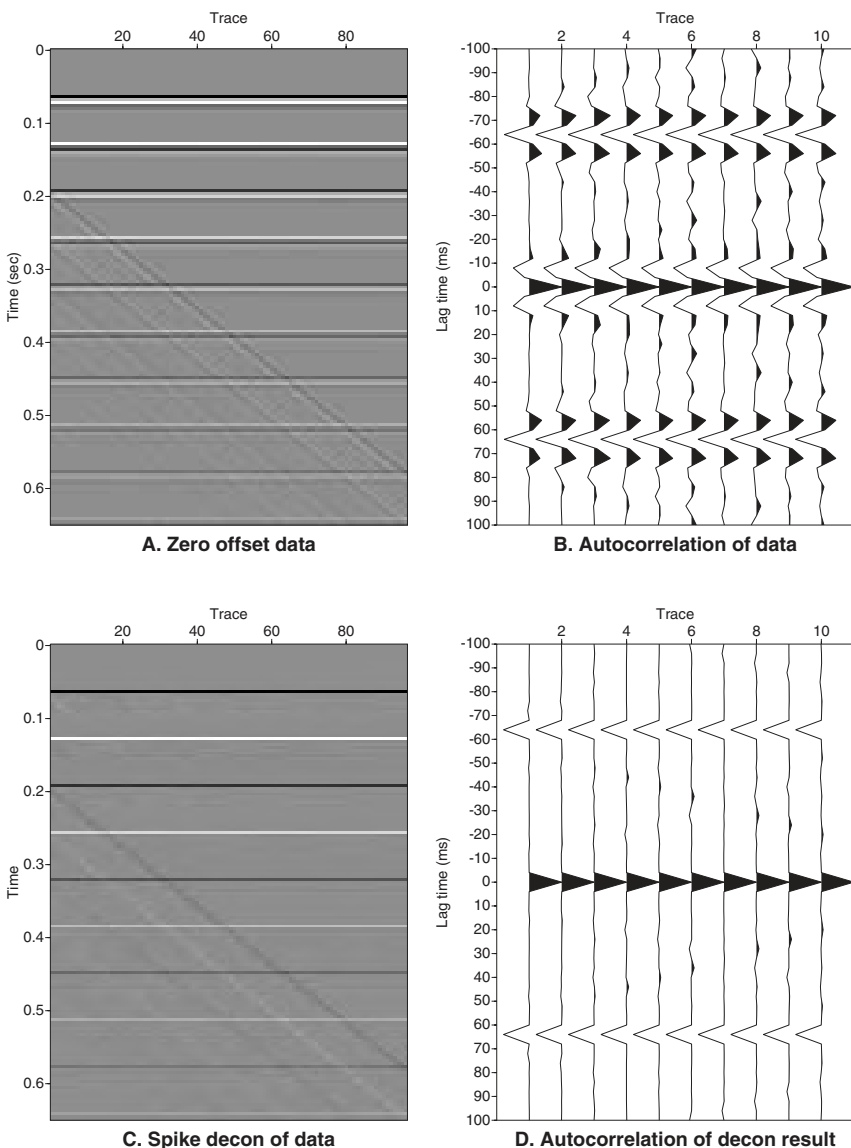


Fig. 16.2 Spiking deconvolution. (A) Synthetic zero offset marine data with seafloor multiples and a dipping event. (B) Autocorrelation of the data indicates a wavelet period of 20 ms (around zero lag) and multiple period of 65 ms. (C) After spiking deconvolution, each event is much more compact in time. (D) Autocorrelation of the spiked data confirms the tighter wavelet and continued presence of multiples.

## Elements of 3D Seismology

To attenuate the multiples, we run deconvolution again, this time telling it to seek and destroy any recurring features in the data with 50–160 ms periods. The multiple period lies in this range, but the wavelet period does not. This is gap or predictive deconvolution and when applied to the data in Figure 16.2C, it gives the result in Figure 16.3A. The autocorrelation in Figure 16.3B now shows a compact wavelet and little evidence of multiples. In symbols, this second pass of deconvolution is

$$g_{d2} = \frac{g_{d1}(f)}{g_3(f)} = g_1(f) \quad (16.6)$$

which is an approximation of the primaries-only reflection coefficient series. The complete synthetic example of spiking plus predictive deconvolution is shown in Figure 16.4.

While deconvolution is a powerful process, there are limitations. It requires multiples to be perfectly periodic, which is true only for zero offset data. For prestack data multiples are not periodic in shot records and only approximately so in common offset sections. There are more advanced tools than deconvolution for removing prestack multiples.

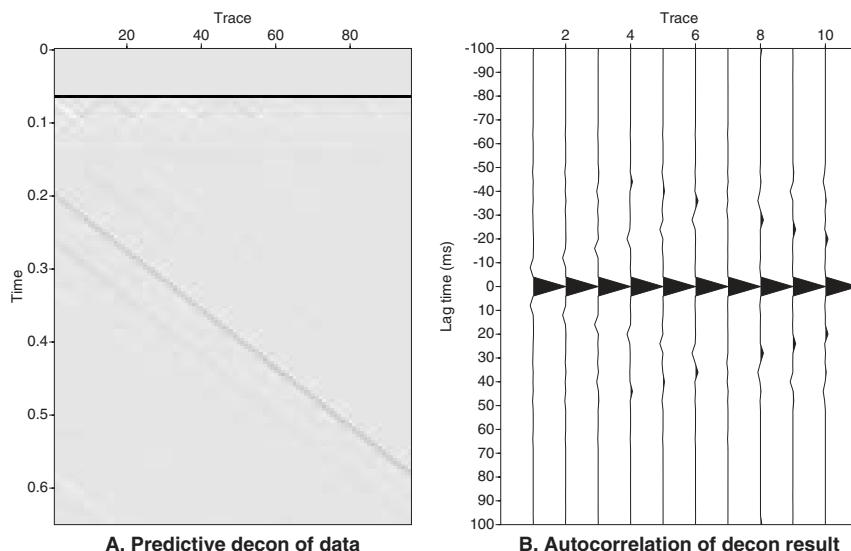


Fig. 16.3 Gap deconvolution removes periodic multiples. (A) The result of applying predictive deconvolution to the data in Figure 16.2C. Aside from minor artifacts, we now have data with a compact wavelet and the remaining multiples are very weak.

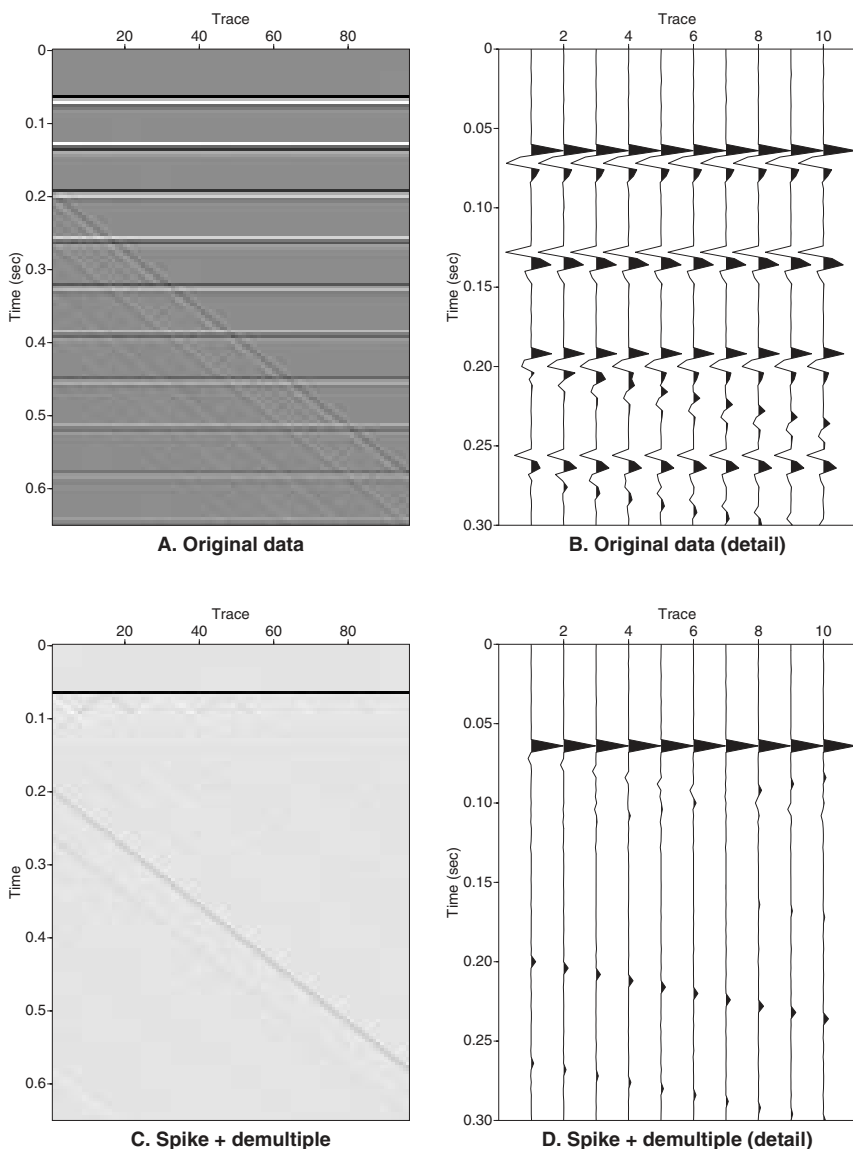


Fig. 16.4 Summary of synthetic deconvolution example. (A) Synthetic zero offset marine data with seafloor multiples and a dipping event. (B) Detail of data showing complicated wavelet and strong multiples. (C) Data after spiking and gap deconvolution. (D) Detail of deconvolution result.

## **Elements of 3D Seismology**

Another requirement of spiking deconvolution is that the wavelet be minimum phase because only such a wavelet has a sable finite inverse [211]. Lucky for us, real sources usually generate minimum phase data.

Figure 16.5 illustrates the action of deconvolution on common offset marine data. Autocorrelation of the data shows a 25 ms wavelet and evidence of internal multiples with a period of about 60 ms. Furthermore, we suspect seafloor multiples are present although the displayed autocorrelation window is not long enough to show the 200 ms period they should have.

The first pass of deconvolution performs spiking deconvolution with a minimum gap of 1 and maximum of 25 ms. To suppress multiples, we run predictive deconvolution with a minimum gap of 40 ms (to hit the interbed multiples) and a maximum gap of 200 ms (for seafloor multiples). This result is shown in Figure 16.5C. In this data, the multiples were weak and the wavelet was well-behaved, so deconvolution results are not very dramatic. But resolution and reliability of the data for interpretation is much improved.

### **16.3 Sorting**

At various stages of processing, it is necessary to sort the data. Since trace headers contain prestack geometry information, the sorting is done on header fields. For large 3D data sets, sorting can be a big computational issue. Sorting a billion objects is not trivial.

Figure 16.6 illustrates some typical data sorts form a 2D marine survey. Seismic acquisition always delivers shot record data, Figure 16.6A. Prestack depth migration is often done on shot records to save sorting time. In a conventional processing flow gain, spiking deconvolution, and filtering can be done in shot records. Common offset data, Figure 16.6B, is useful to preview subsurface structural complexity and is the domain in which DMO is usually applied.

Common receiver gathers, Figure 16.6C, are not commonly used in processing but can be useful to identify bad traces. Common midpoint gathers, Figure 16.6D, play a key role in conventional processing. NMO velocity analysis is only applied in CMP gathers, and many NMO programs assume the input data is CMP sorted. For 3D data, an additional sort is possible, that of common azimuth.

Each of the sorts shown here have an associated spatial sampling interval. Thanks to the work of Vermeer [191] it is now understood that spatial sampling should be adequate to avoid spatial aliasing and be equal in all domains. This is termed symmetric sampling, and it should be implemented as far as financial considerations allow.

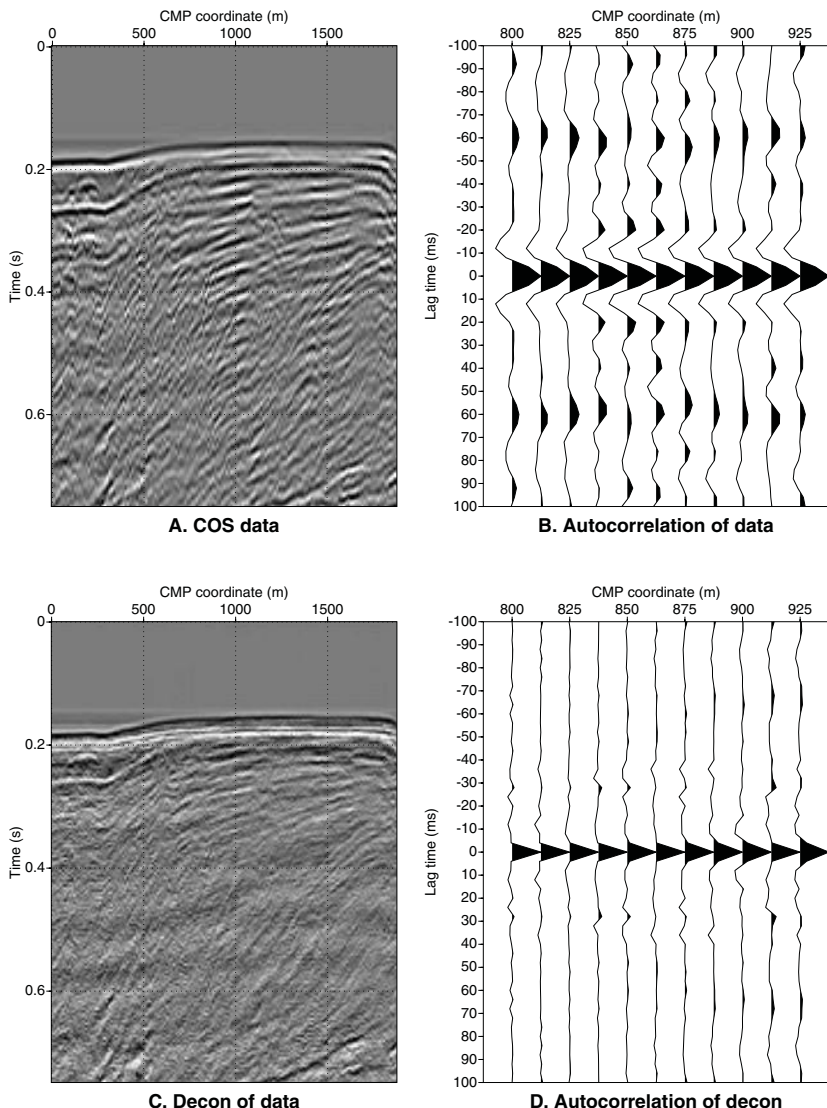


Fig. 16.5 Deconvolution of 2D marine common offset data. (A) The common offset data. (B) Autocorrelation of the data showing a 25 ms wavelet and 60 ms internal multiples. (C) Result of applying gap deconvolution after spiking deconvolution. (D) Autocorrelation of deconvolution result showing tighter wavelet and diminished multiples.

## Elements of 3D Seismology

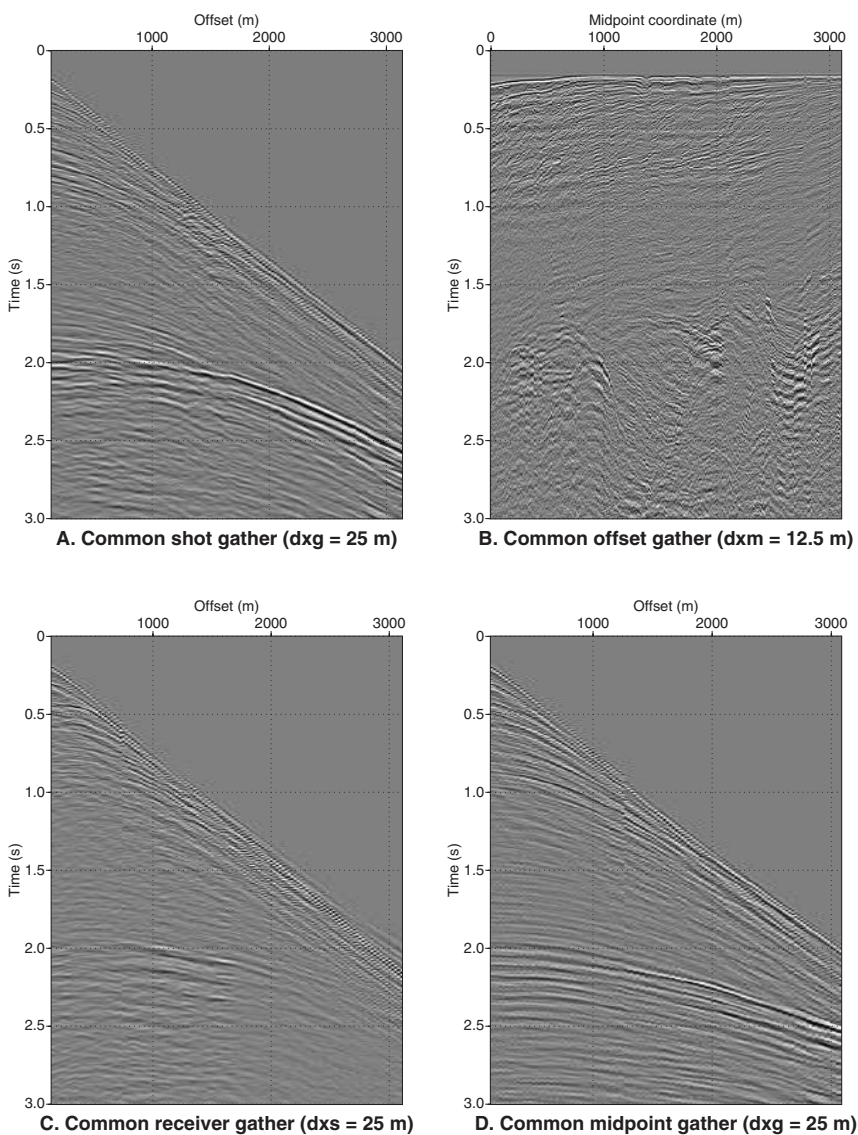


Fig. 16.6 Common data sorts illustrated on a 2D marine seismic line.

## 16.4 Normal moveout

From knowledge of wave propagation, we know that reflection times will increase with increasing offset. This is the NMO effect, and its removal is the normal moveout process. For a horizontal reflector the constant velocity reflection time varies according to

$$t^2(x) = t_0^2 + \frac{x^2}{v^2} \quad (16.7)$$

where  $t_0$  is the zero offset time,  $x$  is the offset, and  $v$  is the velocity. The NMO correction,  $\Delta t_n(x)$ , is the time shift necessary to convert the observed time at any offset to the zero offset time

$$\Delta t_n(x) = t(x) - t_0 = \sqrt{t_0^2 + \frac{x^2}{v^2}} - t_0 \quad (16.8)$$

This is not a simple bulk shift but a time-variant stretch of the trace with more stretch occurring at far offsets and small times.

Figure 16.7A shows a synthetic CMP gather. The reflection from a single horizontal interface and the expected hyperbolic moveout is easily seen. We can take the Fourier transform (FFT) of this data, one trace at a time, and plot the amplitude spectra as shown in Figure 16.7B.

In this example, the data bandwidth is a uniform 10–80 Hz at all offsets. When NMO is applied to the data, Figure 16.7C, the event is flat in the CMP gather, meaning that the traveltime is now  $t_0$  at all offsets. Note the NMO process has introduced wavelet changes, particularly at far offsets. These changes are best understood in the Fourier domain.

The amplitude spectra after NMO in Figure 16.7D show reduction in bandwidth with offset. As the wavelet is stretched in the time domain by NMO, its frequency content is compressed until at the far offset it is down to 5–30 Hz. This is an undesirable effect because it reduces seismic resolution and strategies are currently being developed to overcome it.

In practice the severely stretched portions will be muted through a technique called stretch mute illustrated in Figure 16.8. This operates on the concept of percentage stretching. For example a 10–80 Hz wavelet will have a dominant period of 14 ms. If NMO stretches this wavelet to have a period of 28 ms, it is a 100% stretch. Figures 16.8B–D illustrate the effect of various stretch mute thresholds. Random noise has been added to the input data to clearly display the mute area after NMO. It is undesirable to leave severely stretched events in the CMP data because this lowers the stack bandwidth and thus degrades resolution. A 50% stretch is close to standard practice.

## Elements of 3D Seismology

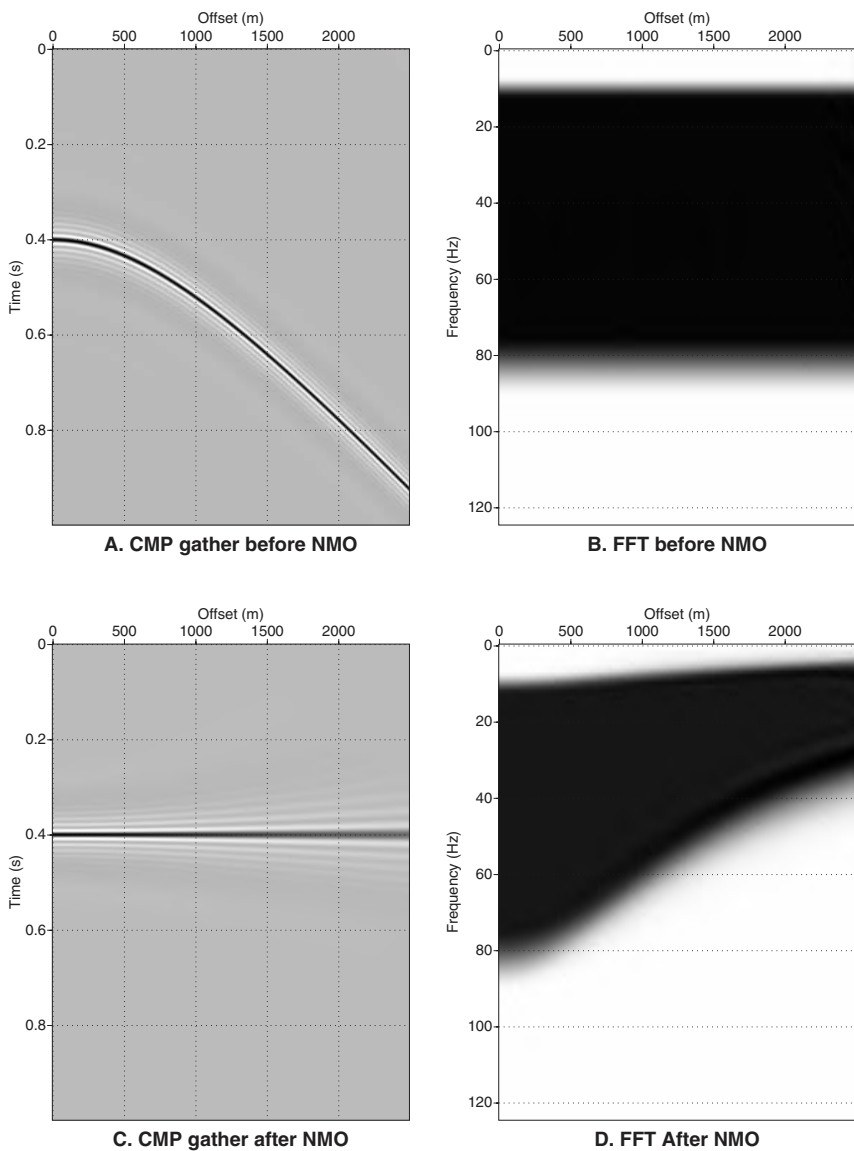


Fig. 16.7 NMO stretch illustrated on a synthetic CMP gather. (A)–(B) Before NMO the data has uniform 10–80 Hz bandwidth at all offsets. (C)–(D) NMO has the effect of stretching the wavelet, which compresses the bandwidth.

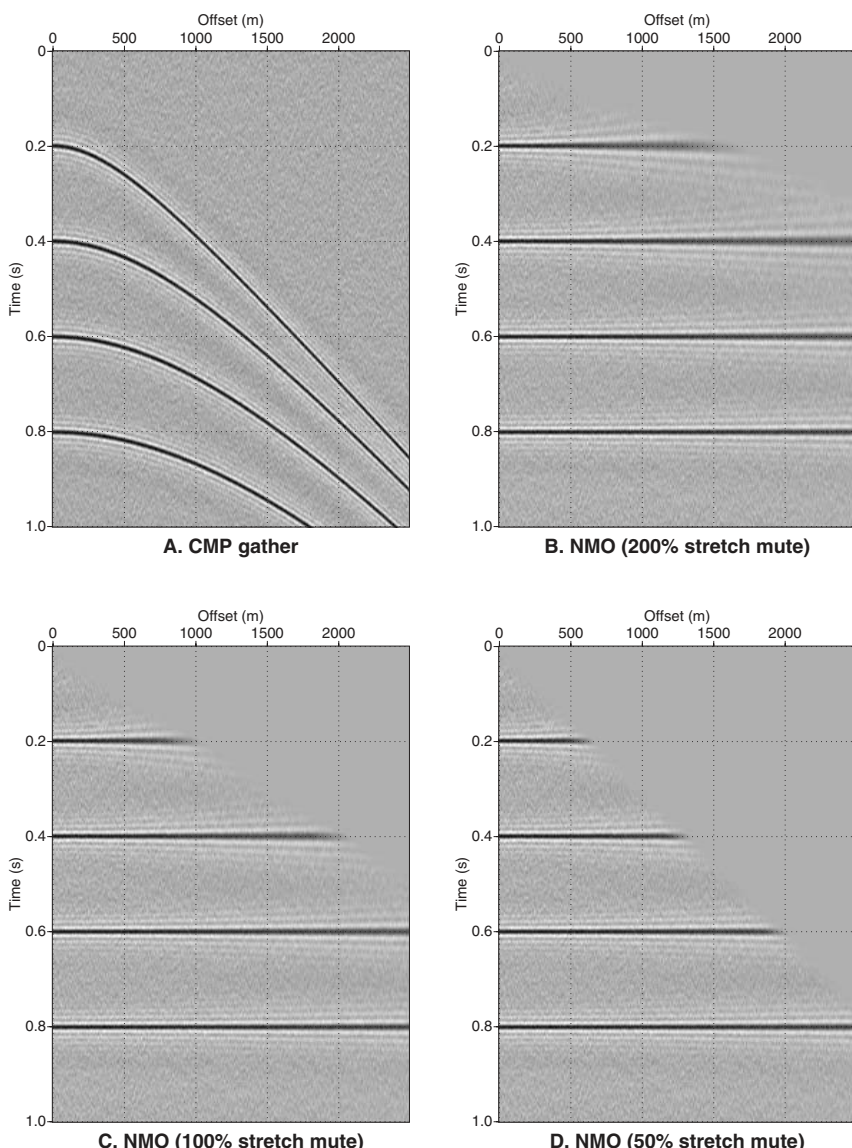


Fig. 16.8 NMO stretch mute illustrated on a synthetic CMP gather. (A)–(D) NMO with various stretch mute thresholds.

Since the NMO equation involves velocity, it is necessary to get the velocity right if events are to be flat after NMO. Figure 16.9 demonstrates the effect NMO velocity errors have on event flattening. NMO works hardest at small times and far offsets, therefore shallow events are more sensitive to velocity errors.

Sensitivity of event flattening to NMO velocity can be exploited as a velocity analysis tool. Consider the CMP data shown in Figure 16.10A. We could apply NMO to this data with a velocity of say 1500 m/s, then stack the data, meaning that we add all the traces together to create one stack trace. If 1500 m/s is the correct velocity for any event, then NMO will flatten it, and the stack will have a strong spike at this time.

If however the velocity is wrong, the event will not be flat and will be weak on the stack trace. Now we repeat this process for 1550 m/s, 1600 m/s, and so on. The result is a velocity analysis panel as shown in Figure 16.10B. Note the velocity indicator is smeared out for the deepest reflector because our leverage for determining the velocity is reflector curvature, and there is less curvature on deep reflectors. In other words, velocity resolution decreases with depth.

A processor will interpret (yes that is the correct word) a velocity panel such as this to pick time-velocity pairs that are joined to form an interpolated NMO velocity function for this CMP gather, Figure 16.10C. Applying this velocity function to the CMP data does indeed flatten all events at all times. This is a very commonly used velocity analysis technique, but many others are available [211].

From our knowledge of wave propagation in thinly layered media, we know that NMO velocities approximately represent root-mean-square (RMS) average velocities from which interval velocities can be estimated. In practice the interval velocities derived in such a fashion are not of sufficient accuracy for use in depth conversion or depth migration. These velocities must be determined independently. Time migration, on the other hand, uses an RMS velocity model and NMO velocities are sometimes taken as a first order model, which is then refined by migration velocity analysis.

These concepts are applied to a 2D marine CMP gather in Figure 16.11. The velocity analysis panel for this data shows two clear trends near 0.5 s, one fast, one slow. This indicates a sequence of shallow multiples (slow) and associated primary reflections (fast). By picking the fast trend, the processor knows CMP stacking will tend to reinforce the flattened primary events and attenuate the multiples.

The effect of anisotropy on NMO velocity analysis is illustrated in Figure 16.12. In Figure 16.12A, we see a synthetic CMP gather generated using isotropic velocities and Figure 16.12B is an isotropic velocity scan, which correctly identifies the isotropic velocities. The CMP data in Figure 16.12C was generated using the same velocities as Figure 16.12A (now used as vertical velocities) and with 10% anisotropy ( $\delta=-0.1$ ,  $\epsilon=0.1$ ).

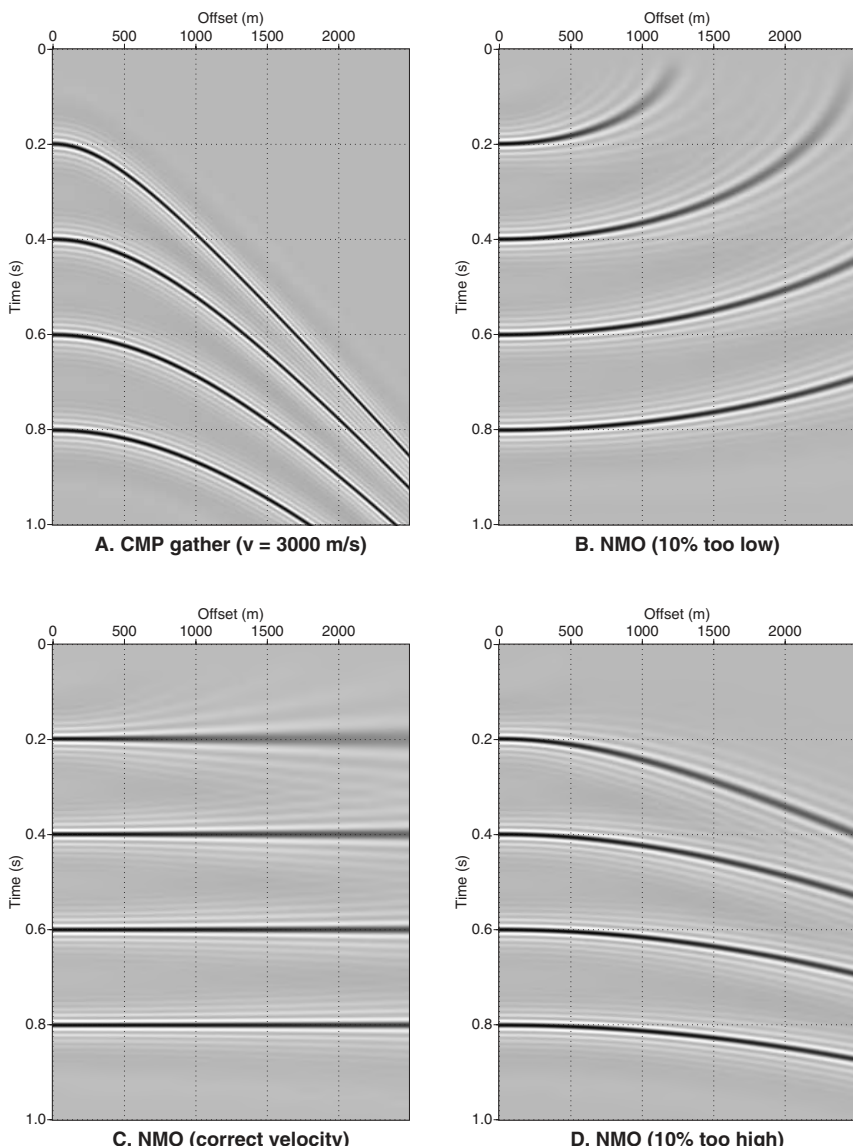


Fig. 16.9 NMO velocity errors cause events to have residual curvature after NMO. (A) Synthetic CMP gather modeled using a constant velocity of 3000 m/s. (B) Too low a velocity causes NMO to over correct and results in concave upward residual curvature. Since shallow events have more curvature, they are more sensitive to velocity errors. (C) Correct velocity flattens all events at all times. (D) Too high a velocity causes NMO to undercorrect and results in concave downward residual curvature.

## Elements of 3D Seismology

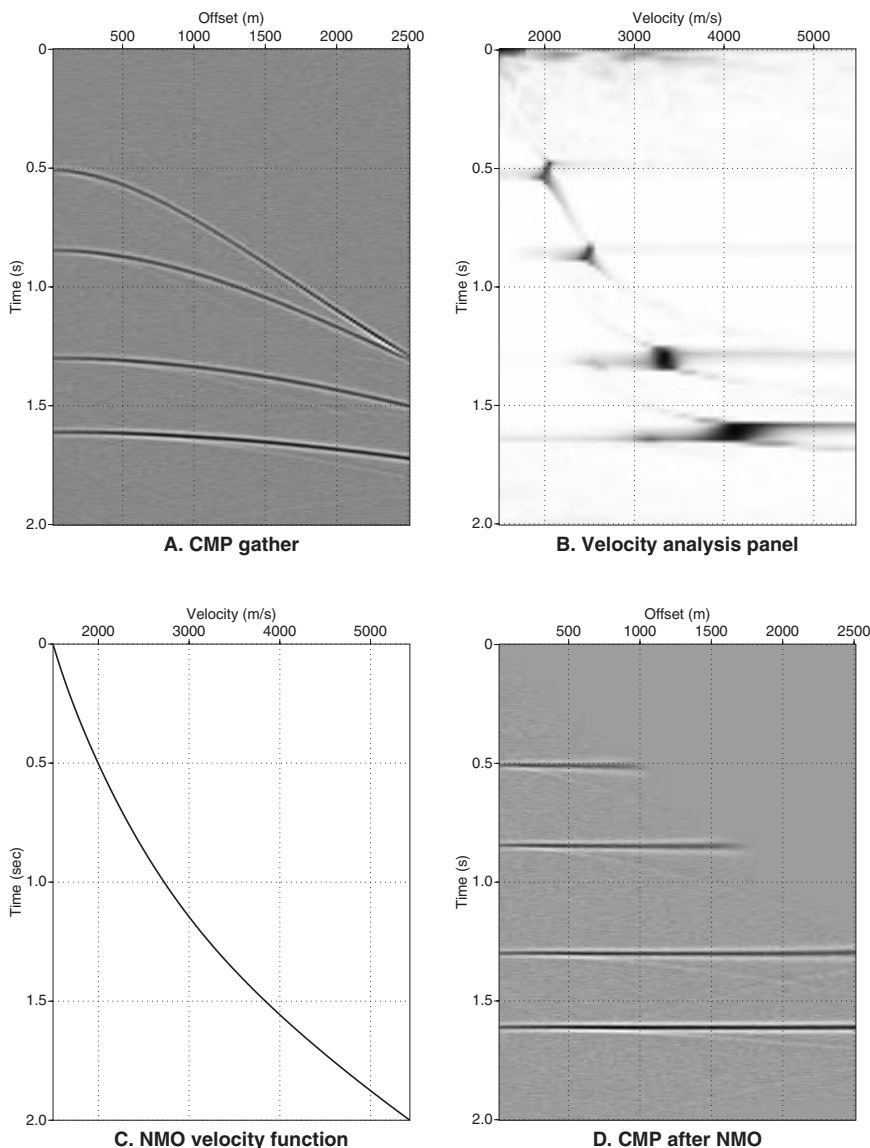


Fig. 16.10 NMO velocity analysis. (A) Synthetic CMP gather with four events. (B) The velocity analysis panel is constructed by applying NMO and stack for a range of velocities. When the velocity is correct for an event, it will be flat in the CMP domain and contribute strongly to the stack. (C) The processor interprets the velocity panel for this CMP to determine an NMO velocity function. (D) Applying the NMO velocity function to the CMP data flattens all events at all times.

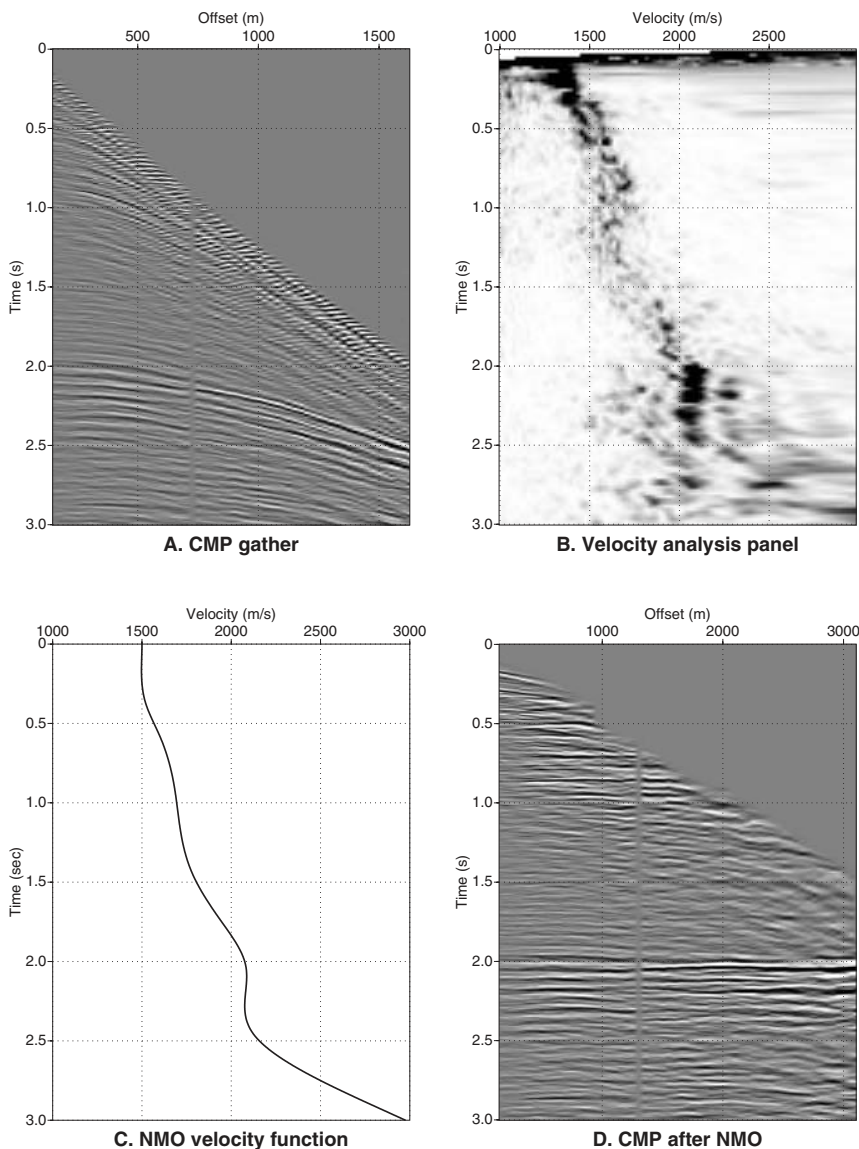


Fig. 16.11 NMO velocity analysis of a 2D marine CMP gather. (A) The CMP data consists of 60 traces with near offset of 150 m and group interval of 25 m. (B) The velocity analysis panel shows a well defined trend of increasing velocity with depth. It also distinguishes primary events (fast) from multiples (slow), which exist at the same time. The fast trend is picked to stack in primary reflections. (C) Interpreted NMO velocity function for this CMP. (D) CMP gather after NMO using the interpreted velocity function.

## Elements of 3D Seismology

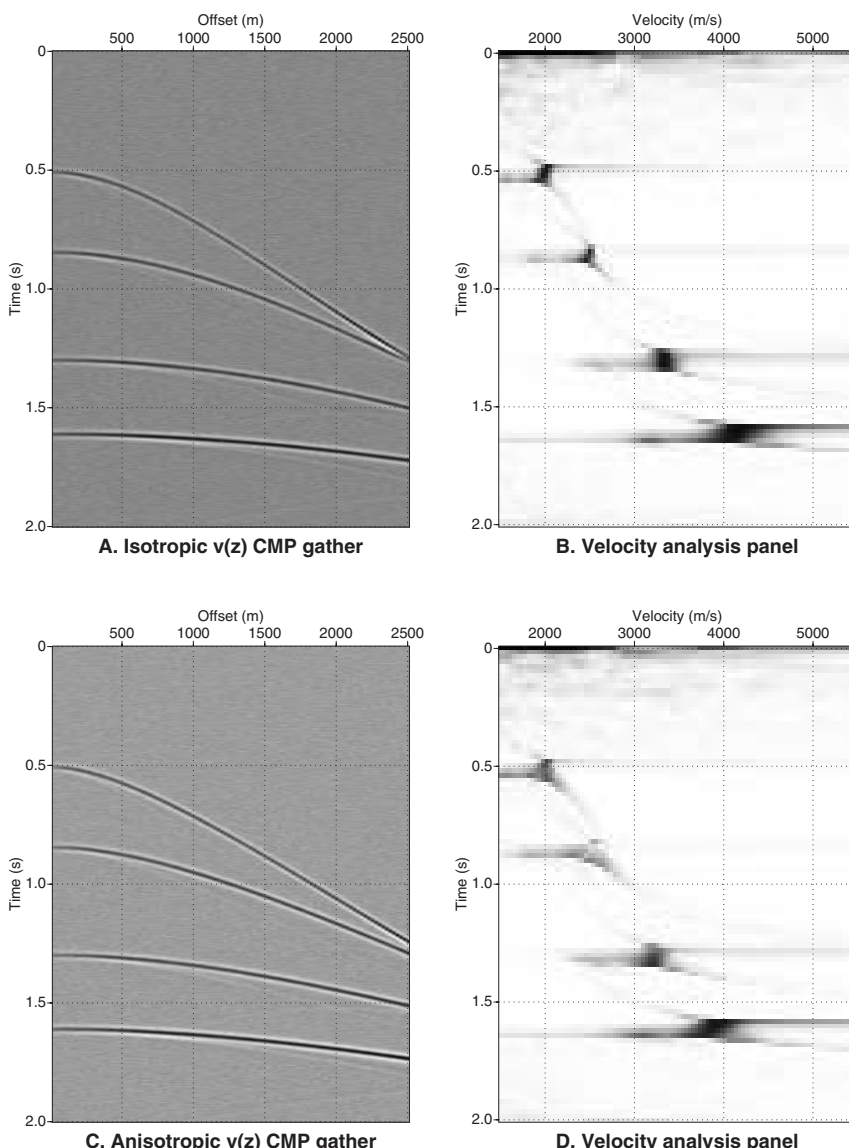


Fig. 16.12 Effect of anisotropy on NMO velocity analysis. (A) CMP gather generated using isotropic velocities. (B) Isotropic velocity analysis gives correct results. (C) CMP gather generated using velocities which are 10% anisotropic. (D) Isotropic velocity analysis is weakly effected by the presence of anisotropy.

An isotropic velocity scan, Figure 16.12D, is fooled into thinking the deep velocity is 3900 m/s rather than the correct value of 4100 m/s. Notice also that the velocity indicators are smeared and weak. These are both clues that the moveout curves in Figure 16.12C are not hyperbolic. Velocity analysis that includes anisotropy parameters could be applied in this case to precisely flatten the events and simultaneously give subsurface anisotropy estimates for later use in migration.

But in real data, how certain are we that anisotropy is present and causing the non-hyperbolic moveout behavior? A more likely candidate is lateral velocity variation. Figure 16.13A shows a CMP gather generated from a  $v(z)$  velocity model. As in earlier examples, the velocity analysis, Figure 16.13B, correctly identifies the velocities.

Figure 16.13C shows a CMP gather over the same earth model, except velocity varies laterally by 10% across the spread. This results in non-hyperbolic moveout that the velocity scan interprets according to the velocity of the best fit hyperbola. The deep reflector whose average lateral velocity is 4100 m/s is incorrectly seen as a 3100 m/s event. This is a much stronger effect than an equivalent level of anisotropy.

When moveout is non-hyperbolic, the most likely causes (in descending order) are

1. statics due to variations in the weathering layer
2. lateral velocity variation below the weathering layer
3. anisotropy
4. fourth order moveout due to fine horizontal layering

## 16.5 Dip moveout

Dip moveout (DMO) is a process that is almost universally applied to seismic data before CMP stacking. DMO has an intimate relationship to prestack migration. We defer the detailed description of DMO to a later chapter and here only describe its role in conventional seismic processing.

Consider the synthetic CMP gather shown in Figure 16.14A. The earth model for this data consists of four horizontal reflectors, which are the first, second, fourth, and fifth events on the CMP gather. The third event at  $t_0=0.8$  s has a 45-degree dip. This could be a physical dip associated with some geological feature, a diffraction curve, or a fault plane reflection. In any case, the fact that it has 45-degree dip gives the appearance of higher velocity,

$$v_a = \frac{v}{\cos \theta} = \frac{2600 \text{ m/s}}{\cos 45^\circ} = 3675 \text{ m/s} \quad (16.9)$$

where  $v_a$  is the apparent velocity,  $v$  is the NMO velocity for a horizontal reflector, and  $\theta$  is the dip.

## Elements of 3D Seismology

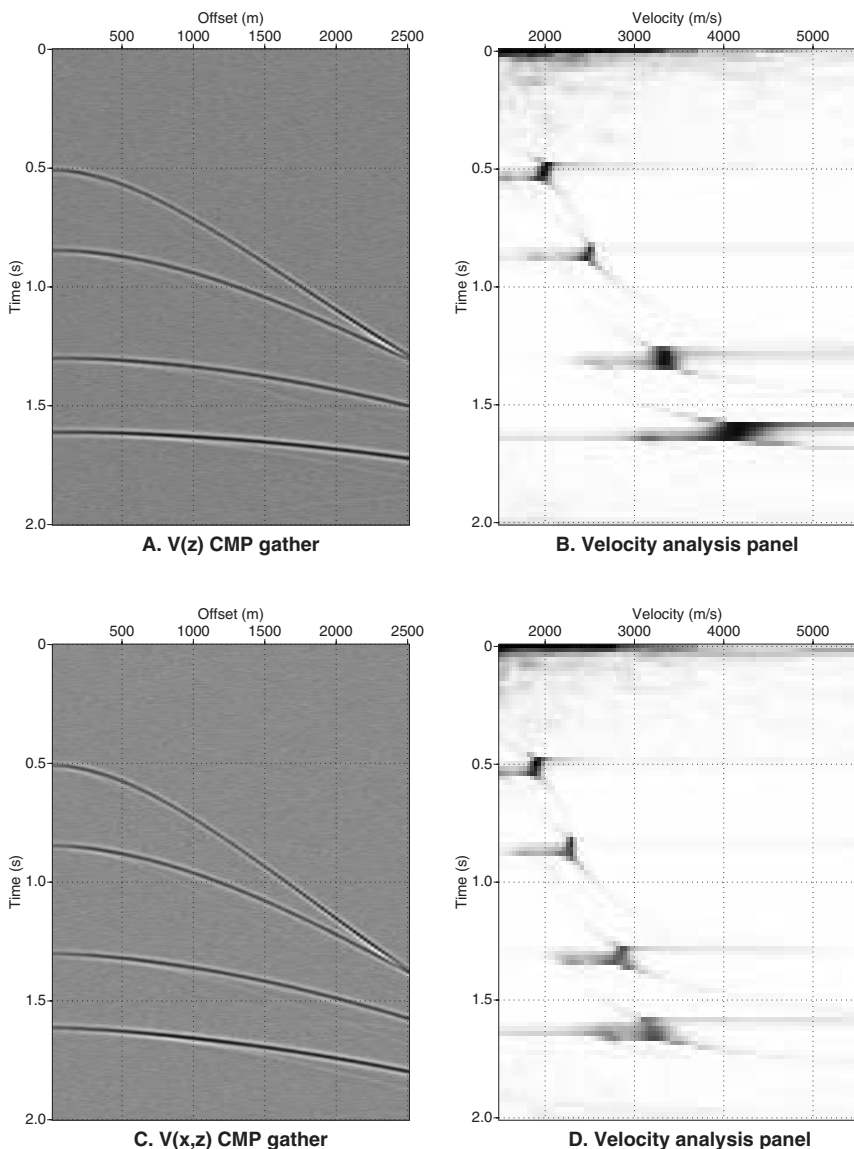


Fig. 16.13 Effect of lateral velocity variation on NMO velocity analysis. (A) CMP gather generated using  $v(z)$  velocities. (B) Velocity analysis gives the correct results. (C) CMP gather generated using a lateral velocity gradient of 10% velocity change across the shot spread. (D) The velocity analysis is strongly effected by the lateral velocity variation, even though the actual velocities at this midpoint location are the same as those in (B).

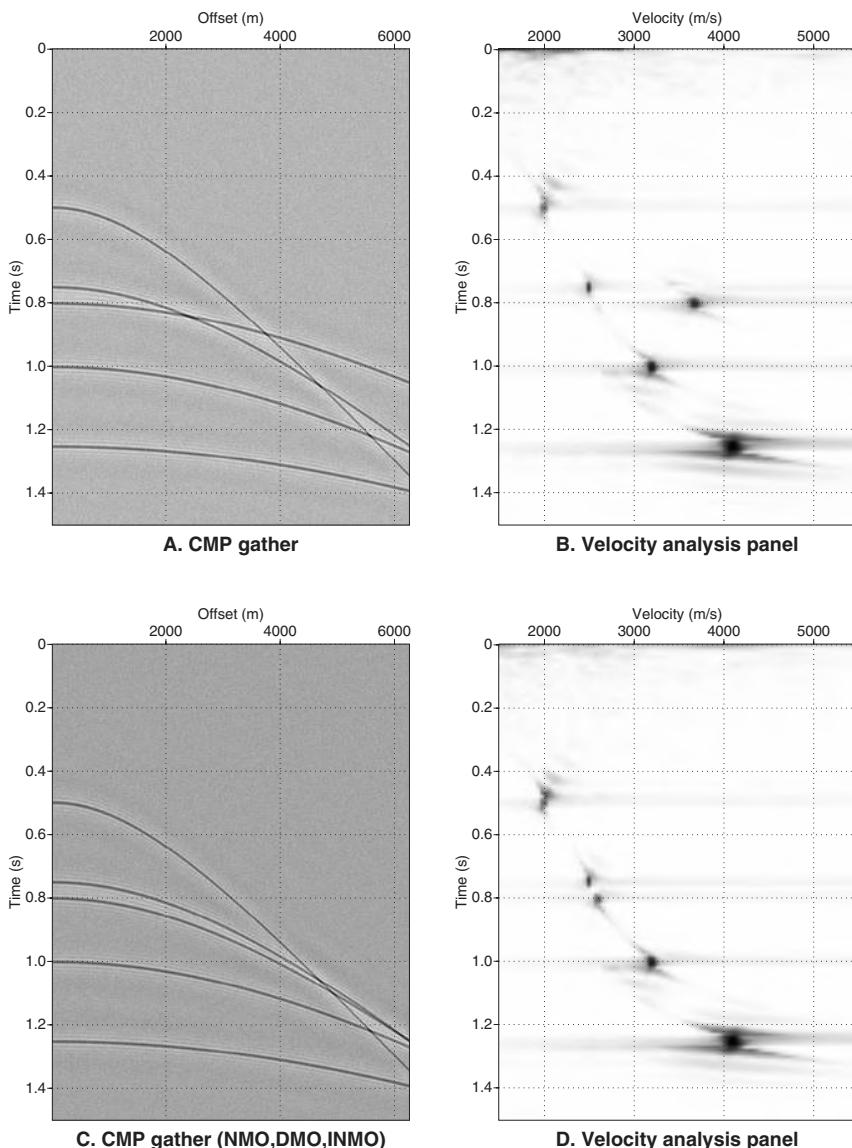


Fig. 16.14 The role of dip moveout in NMO velocity analysis. (A) CMP gather with five reflection events. The reflection at 0.8 s has a 45-degree dip and all others have zero dip. (B) Velocity analysis sees the dipping event with a much higher velocity than horizontal events at the same time. (C) CMP gather after the processing sequence of NMO, DMO, and inverse NMO has been applied. (D) Velocity analysis shows the dipping event now appears along the velocity trend of the horizontal events.

This calculation is verified by the velocity analysis panel in Figure 16.14B that shows a trend associated with the horizontal reflectors and the dipping event well away from this trend at the apparent velocity of 3675 m/s. Before about 1980 (when DMO was introduced) the processor working with this data at 0.8 s had to make a choice. By choosing a velocity near 2500, the horizontal event will be flattened, but the dipping event will be severely under corrected. This means the horizontal event will stack in correctly while the stacking process would largely cancel the dipping event. On the other hand, choosing a velocity near 3600 m/s would stack in the dipping event and attenuate the horizontal one. Picking a velocity half way between is the worst choice since neither event would stack in.

DMO comes to the rescue in this case. The procedure for using DMO has five steps:

1. apply NMO using a regional velocity function
2. apply DMO
3. apply inverse NMO using the regional velocity function
4. do detailed NMO velocity analysis
5. apply NMO using the detailed velocities

In Figure 16.14C, the same CMP gather is shown after application of NMO, DMO, and inverse NMO. Note the dramatic change in the traveltimes for the dipping reflector. Velocity analysis of this CMP gather confirms that this event can now be flattened by picking a velocity along the trend of the other events. The beauty of DMO is it will do this for all dips in one pass. Even though we have seen the action of DMO in the CMP domain, it operates by moving data across midpoints in the common offset or common shot domain.

One way to describe the action of DMO is that it allows all dips to pass equally into the stack section for use as raw material in migration. The classic example is horizontal sediments in contact with a near vertical salt face, a situation common in the Gulf of Mexico and elsewhere. With NMO, we could either create a good image of the sediments or the salt face. With DMO, we can do both.

## 16.6 Common midpoint stacking

The final step in creating the stack section is common midpoint stacking. Figure 16.15 shows a synthetic example. The data consists of 30 CMP gathers containing 60 traces each. The midpoint and group intervals are both 25 m. The near offset is zero and the far offset is 1500 m. In Figure 16.15A, we see three of the CMP gathers. The earth reflectivity model consists of three horizontal reflectors and one dipping reflector. On the CMP gathers, the dipping event is seen as a hyperbolic curve that moves deeper as we move to larger CMP numbers.

The velocity analysis for CMP 21 in Figure 16.15B shows the dipping event scans in a very high velocity compared to the other events. Applying NMO based on velocity picks from the horizontal events gives the NMO corrected gathers in Figure 16.15C. Note the dipping event is under corrected as we could have predicted.

The actual CMP stacking operation is a horizontal summation of all the traces in each CMP gather. The number of traces in each CMP gather is called the fold of stack, but is actually the maximum fold. For example, the data in Figure 16.15C has a maximum fold of 60 because we have 60 traces per CMP, but the fold at 0.4 s is about 20 due to the mute cut. When someone says something like, “the data is 36 fold,” this is the maximum fold, and we should understand that the actual fold is a function of time.

Figure 16.15D shows the stack section, which consists of 30 traces because we had 30 CMP gathers. The horizontal events are strong and consistent because we stacked with the best velocities for them. The dipping event, however, is weak and inconsistent. From the previous discussion, we know the solution to this problem is to use dip moveout, but this example clearly shows that CMP stacking without DMO acts like a dip filter driven by the processor’s velocity picks.

The event above 0.4 s in Figure 16.15D is much weaker than the other horizontal events, even though they are of similar amplitude on the prestack gathers. This occurs because the number of live traces being summed at the shallow event is less than half of the full fold. The effect was kept in this example for illustration. But in practice, we keep stack amplitudes balanced by dividing the output amplitude at each time sample by the number live traces that contributed to it.

The stacking process tends to cancel random noise in the data. This results in a signal-to-noise ratio improvement of  $\sqrt{N_f}$  where  $N_f$  is the fold. The prestack data in Figure 16.15 has a signal-to-noise ratio of 20 and the stacking process improves this to about  $20\sqrt{60} = 150$ .

The same sequence of displays is shown for a 2D marine seismic line in Figure 16.16. The data consists of 300 60-fold CMP gathers. Only the velocity analysis for CMP 1 is shown, but velocities were picked on CMPs 1 and 300, and these are interpolated to all intermediate CMPs. The NMO-corrected gathers are shown in Figure 16.16C and the stack section in Figure 16.16D. Note full fold of 60 is not achieved until about 2 seconds.

For quality control, it is useful to view CMP gathers just before CMP stacking. At this point of processing, they contain a wealth of information. They can be reviewed for fold versus depth, muting, event flattening, noise levels, uncorrected statics, and multiples. In 2D, it is sufficient to perform this kind of QC every half kilometer or so and, in 3D, perhaps on a one kilometer grid.

## Elements of 3D Seismology

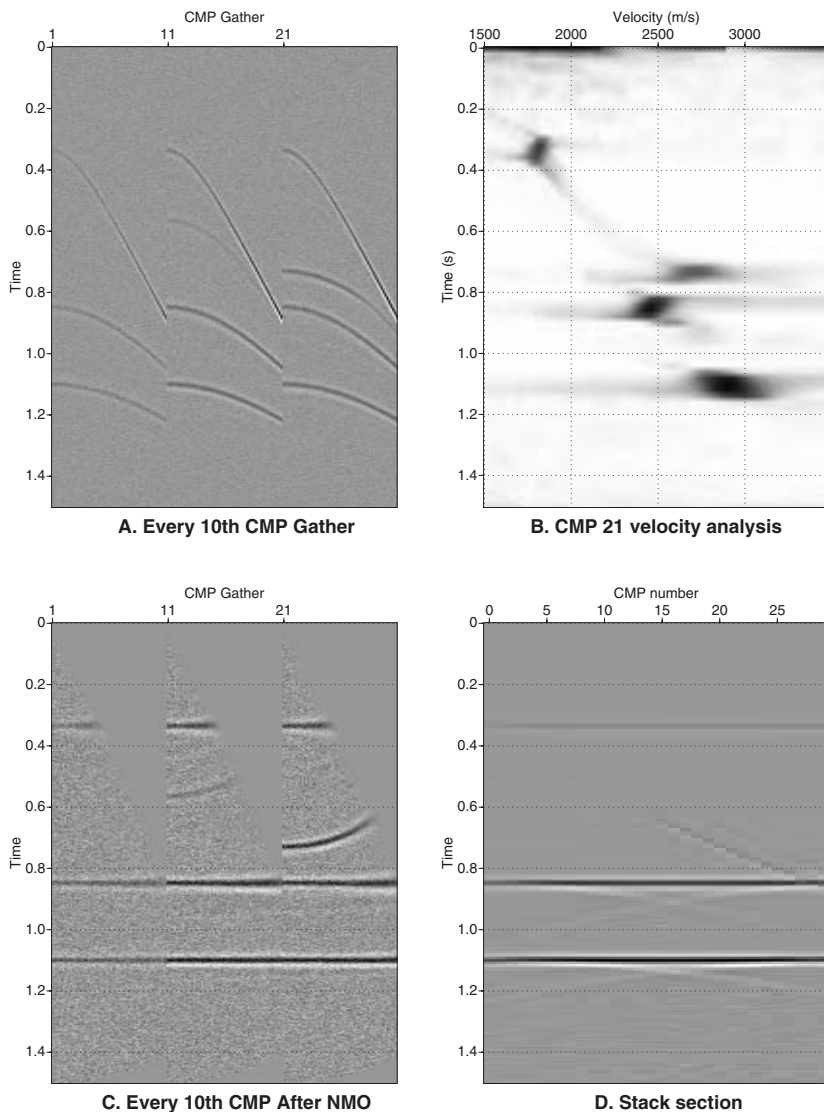


Fig. 16.15 Common midpoint stacking illustrated on synthetic data consisting of 30 CMP gathers of 60 traces each. (A) Display of every 10th gather shows four events. (B) Velocity analysis of CMP 21 shows event 2 has a anomalously high velocity indicating the reflector is dipping. (C) NMO-corrected CMP gathers created using NMO velocities appropriate for horizontal reflectors. The dipping event is over-corrected. (D) CMP stack created by summing all traces in each CMP gather. The shallow event is very weak because fewer nonzero traces contributed to its sum. The dipping event is weak because NMO without dip moveout acts as a dip filter.

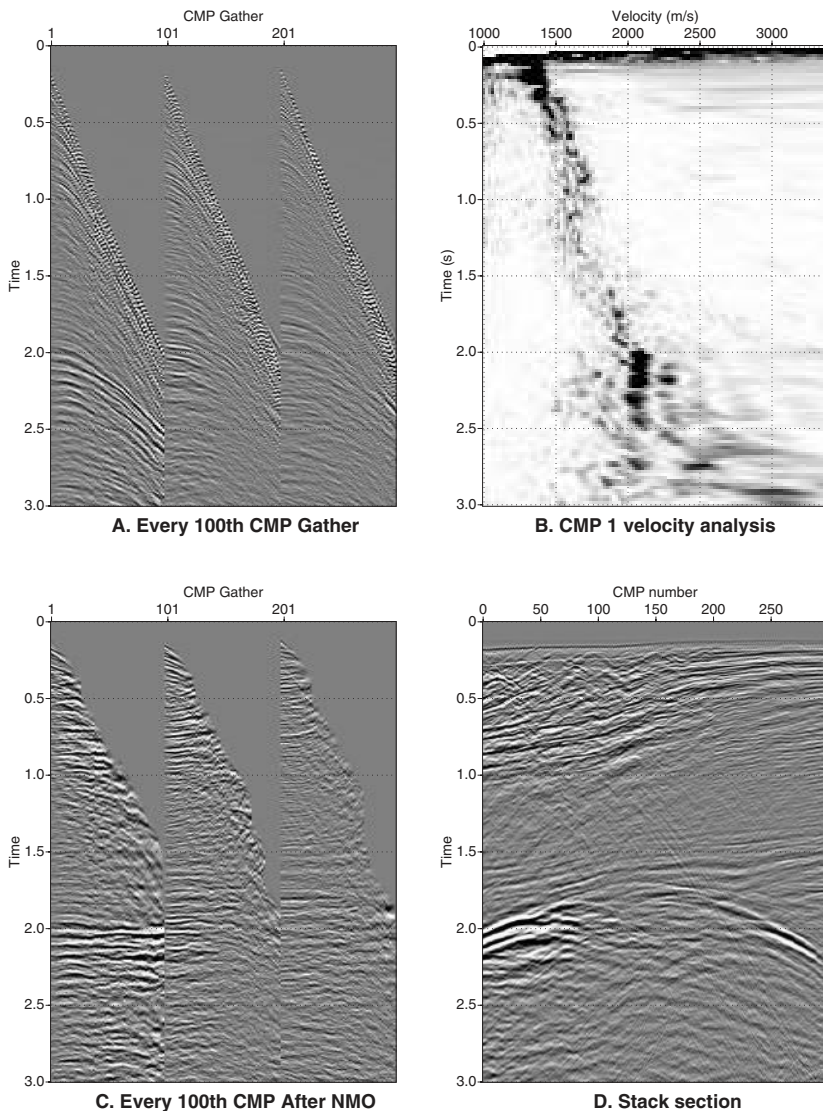


Fig. 16.16 CMP stacking of 2D marine seismic data. (A) Display of every 100th CMP gather. Gain is the only process that has been applied. (B) Velocity analysis of CMP 1. (C) Display of every 100th CMP gather after NMO. Velocities vary with time and CMP based on velocity analyses at CMPs 1 and 300. (D) CMP stack of the NMO corrected gathers. Maximum fold of stack is 60.

## 16.7 Statics

Static corrections are performed very early in the processing flow, but we have delayed discussing them because they are intimately related to stack response. This is an extensive and involved subject that can only be addressed here in terms of the basic phenomena and processing approaches. For a detailed treatment, the interested reader is referred to the comprehensive work by Cox [51].

One way to think about static problems is to use an analogy from optics. Imagine that you are looking through an old window in which the glass has variable thickness. The appearance of objects beyond the glass will be distorted and will change as you look through different parts of the window. The weathering layer plays this same role in seismic data introducing distortion in seismic images that must be removed before they can be considered reliable.

We introduce the nature of statics through the example in Figure 16.17. The earth model in Figure 16.17A consists of an acquisition surface with a simple step in topography and a deep horizontal target interface. Between these, exists a near surface weathering layer also called the low velocity layer (LVL). The LVL has smooth variation in thickness of 100–400 m and a 100 m step thickness increase. Velocity in the LVL varies laterally across the line, but subweathering velocity is constant.

If a zero offset seismic experiment is run across this model and displayed as a time section, it would look like Figure 16.17B. Even though the acquisition surface is not flat, it looks flat on a time section because all traces are plotted from time zero. Interpretation of this raw data would lead to the conclusion that a 40 ms structural high exists between 2 and 3 km distance. In fact, this structure is entirely false, created by topography and variations in weathering thickness. Countless dry holes have been drilled throughout the world on false structures associated with near surface problems.

To remove the effect of topography we define a datum plane and adjust traveltimes to those that would have been observed from the datum. There are two steps to this: (1) subtract the reflection time from acquisition surface to base of weathering, and (2) add the reflection time from base of weathering to datum. The procedure requires detailed knowledge of the weathering velocity and thickness, knowledge that cannot generally be derived from production seismic data but requires a separate refraction survey. The term refraction statics denotes that this kind of work has been done.

After correction of topographic statics, the data has the appearance shown in Figure 16.17C. The base of weathering and target reflector discontinuities at 2 km distance are now gone because these were only associated with surface topography. But effects still remain due to lateral velocity and thickness changes in the weathering layer. From a refraction survey, a set of travelttime corrections could be derived to remove the effect of the LVL. In effect this means taking the

data down to the base of the weathering layer then moving it back up to the datum using the subweathering velocity. The result of applying these refraction statics is the data in Figure 16.17D. At this point the target reflection is correctly imaged as horizontal and if the data were to be depth converted using the subweathering velocity, this target would be correct in depth.

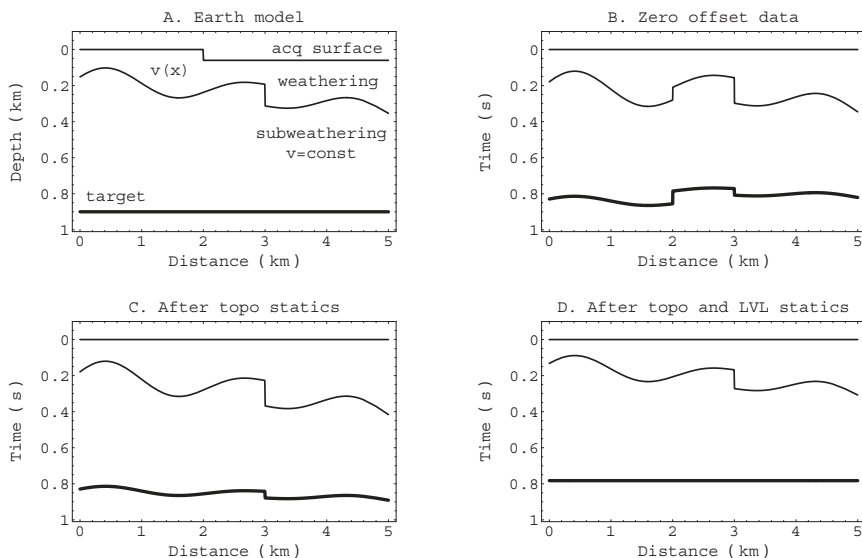


*Fig. 16.17 Effect of statics on zero offset data. (A) Earth model with topography and weathering layer. (B) Zero offset section shows a false structure at the target level. (C) After removal of topography statics, the target is improved, but still has distortion due to lateral changes in weathering layer thickness and velocity. (D) Refraction statics remove the effect of weathering layer variations and restore the correct target geometry.*

Figure 16.18A shows a CMP gather with strong statics. The earth model includes a complicated near surface over three horizontal reflectors. Statics have the effect of bending the reflection curves until they are nonhyperbolic. Velocity analysis will clearly suffer because it is nothing more than a hyperbolic scan. Applying NMO and stack, we form the brute stack shown in Figure 16.18B. The reflections are wavy and blurred because of uncorrected statics.

## **Elements of 3D Seismology**

A process called residual statics can be applied to determine short wavelength static corrections. By short wavelength, we mean topography or weathering layer effects that change significantly over the length of the spread, in this case 3000 m. Figure 16.18C shows the stack that results if residual statics are applied. The rapid lateral variations have been removed, but long wavelength problems are still in the data. Both residual and refraction statics were applied to create the stack in Figure 16.18D.

We have only touched on the topic of static corrections, but it should be clear that they are a very important data processing step. Uncorrected statics are one of the few problems that can introduce false structure.

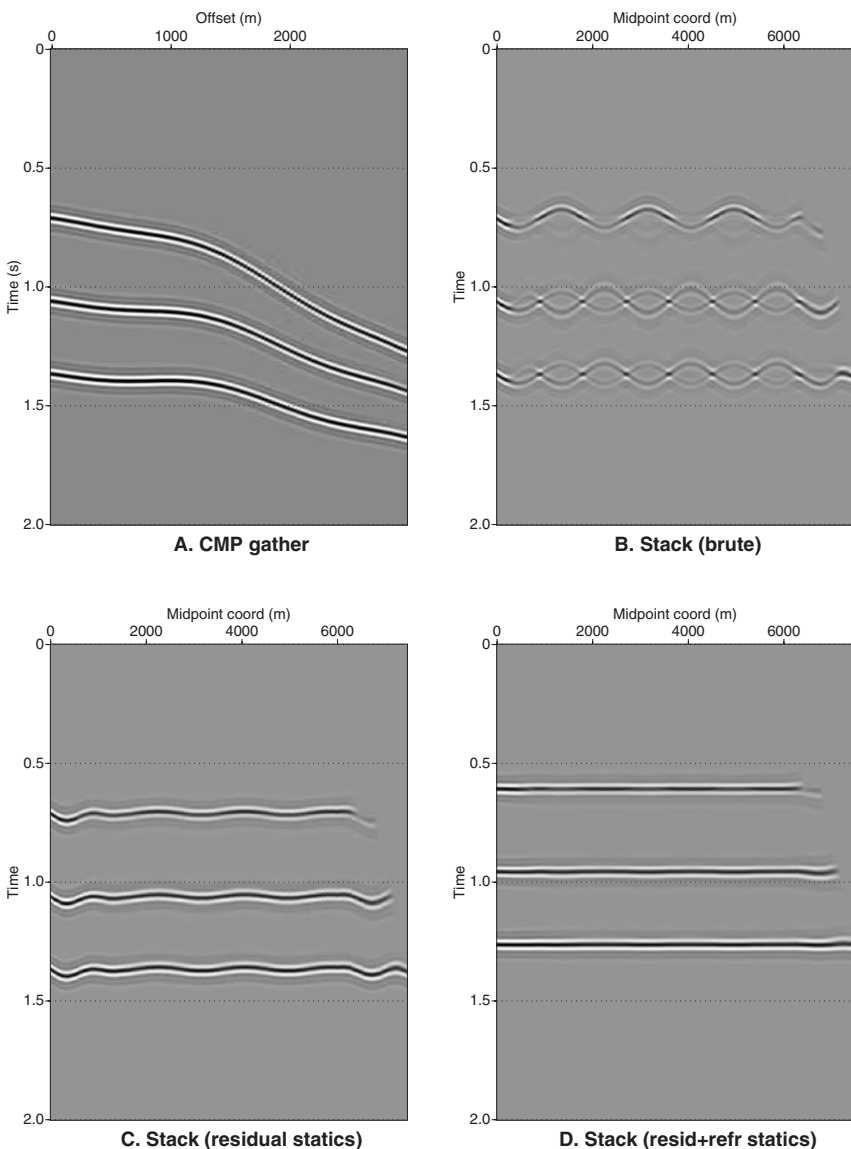


Fig. 16.18 CMP stacking and statics corrections. The earth model consists of a complicated near surface and three horizontal reflectors. (A) CMP gather with significant statics. (B) The brute stack is created by summing after NMO, but static corrections have not been applied. Statics cause misalignments that blur and degrade the stack. (C) Residual statics remove most effects that are caused by rapid lateral changes in the near surface. (D) Refraction statics remove long wavelength near surface effects to create the final stack.

# 17

## Migration I: Concepts

Migration is a process that compensates for effects introduced by wave propagation and acquisition geometry. It is a subject of great breadth and challenging mathematical complexity. For an advanced, yet very readable, account of migration, the reader is referred to Claerbout [48] and a comprehensive treatment is available in Yilmaz [211]. Here we develop the conceptual framework of migration and present theoretical results only when it serves to reinforce the discussion.

Until migration is applied to seismic data, it can be very misleading to think of the image as a cross section of the earth. Dipping events are misplaced, lateral resolution is low, and a wide array of effects influence the data to confuse interpretation. Before the advent of digital migration in the late 1960s, there were any number of books and manuals on pitfalls of seismic interpretation. These pitfalls were largely concerned with event characteristics—buried foci, triplication, fault diffraction, etc.—that are fixed by migration.

Migration can be viewed in many ways. Here we consider the basic operation in terms of impulse and line responses.

A 2D stacked section is a collection of traces, and each trace is a collection of data values. Each individual data value forms an impulse or spike as input to the migration process. Every spike will be processed to create an output space, which we call the migrated section. If the data consists of only a single impulse in a field of zero values, the migration output will be a migration impulse response. This is the microscopic behavior of migration, and it varies as the migration is prestack or poststack, 2D or 3D, and constant velocity or variable velocity.

The large-scale result of migrating any number of traces with nonzero data is simply the superposition, or constructive interference, of many such impulses. Although the total response is a superposition of point responses, it is difficult to anticipate what the migrated result will be for complicated input data.

## Elements of 3D Seismology

Stated differently, if we know how to migrate one sample on one trace, then we know how to migrate every sample on every trace. We do this and add up the results to get the migrated image. This is really pretty amazing when you think about it.

From an operational point of view, any kind of migration can be considered as a process where the input is unmigrated data and the output is the migrated image: `mig[data]=image`. Depending on the input data type and kind of migration, the image can be 2D, 3D, or time lapse. Other names for the migrated image are reflectivity image, reflectivity map, migrated data, and earth image.

The inverse of migration is the process of simulation or modeling, which creates seismic data from an assumed earth model: `mod[earth]=data`. However, migration and modeling are not an invertible transform pair. That is to say, cascading migration and modeling (`mig[mod[earth]]`) does not return the earth model as it would in an exact transform pair. Rather this cascaded process returns a reflectivity image identifying places in the subsurface where impedance changes. This is due to the fact that seismic data is band limited in frequency and has a finite wavenumber aperture.

The first is due to attenuation of seismic energy by earth materials, and the second is a consequence of data acquisition being limited to the earth's surface. Unlike medical imaging where the patient can be surrounded with sources and receivers, seismic imaging is fundamentally aperture-limited.

### 17.1 Constant velocity migration and modeling pairs

Consider the point diffractor shown in Figure 17.1. The earth model consists of a constant velocity half-space and an embedded object or feature that is small compared to the seismic wavelength. For convenience of notation, we define the origin to be at the point on the acquisition surface directly above the diffractor. Figure 17.1A describes the geometry of prestack data where source and receiver are separated by some offset. The total traveltimes is the sum of the time from source to scatterer and from the scatterer to receiver

$$t = t_s + t_g = \frac{1}{v} \left( \sqrt{x_s^2 + z^2} + \sqrt{x_g^2 + z^2} \right) \quad (17.1)$$

where the symbols are defined in Figure 17.1A. This is known as the double-square-root equation [48]. The special case of zero offset is shown in Figure 17.1B, where the source and receiver are coincident at the point  $x$ . The travel time in this case is given by

$$t(x) = \frac{2}{v} \sqrt{x^2 + z^2} \quad (17.2)$$

which follows from the previous equation with  $x_s=x_g$ .

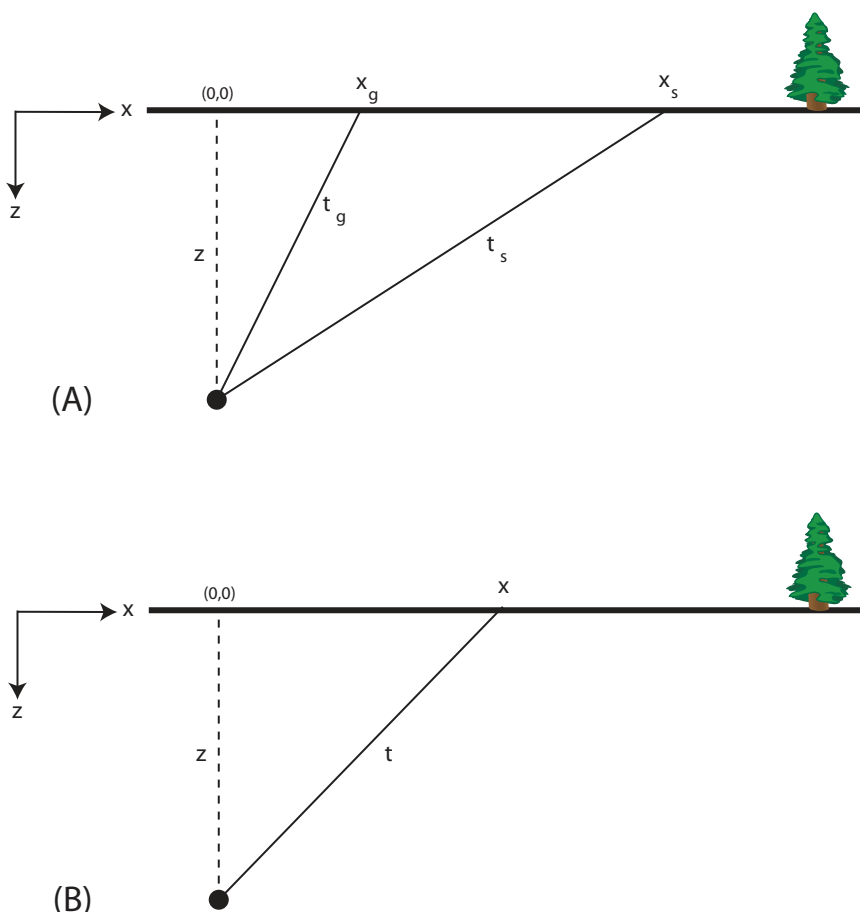


Fig. 17.1 Point diffractor geometry. The origin is taken to be on the acquisition surface directly above the diffractor. (A) In prestack data the source and receiver are separated, giving a one-way time,  $t_s$ , from source to the point diffractor and a one way time back to the receiver,  $t_g$ . Total traveltimes is the sum of these two times. (B) For zero offset data, the source and receiver are at the same location denoted by  $x$ . The traveltimes is the two-way time from this point to the diffractor. A CMP stack section is approximately zero offset data.

## Elements of 3D Seismology

This equation has two distinct meanings. If we take diffractor depth and velocity as known parameters, then the equation is

$$t^2 - \left(\frac{2x}{v}\right)^2 = \left(\frac{2z}{v}\right)^2 \quad (17.3)$$

which is the standard form of a hyperbolic curve in  $(t,x)$  space. Thus the zero offset traveltime curve for a point diffractor is hyperbolic.

If, on the other hand, we have data consisting of a single trace with an amplitude spike at a known time, this equation is

$$x^2 + z^2 = \left(\frac{vt}{2}\right)^2 \quad (17.4)$$

which is a circle in  $(z,x)$  space with radius of  $vt/2$ . Thus an amplitude spike on the data corresponds to a circular reflector in the output data. Figure 17.2 illustrates these twin meanings of the traveltime equation.

It is important to clearly understand this duality. As an analogy, consider that you are standing in a field over a small cavern. You stand with both feet together (this makes it a zero offset thought experiment), one foot representing the source and the other the receiver. Somewhere away from the cavern, you imagine sound waves emitting from your right foot, hitting the cavern, and returning to be measured by your left foot. You make a note of the reflection time.

Now you step toward the cavern and repeat the experiment. Since you are closer to the scattering object, the time of flight is a bit smaller. You step again toward the cavern and the reflection time again gets smaller. As you progress along the line (making this a 2D experiment), you ultimately find a minimum traveltime directly over the cavern. Progressing farther, the times begin to increase again. This is precisely the situation shown in Figure 17.2A and B.

Now consider a related experiment. This time you repeat the measurements exactly as before, but to your surprise, your left foot senses no scattered energy. As you move along the line, you always get the same null result until you stand at one particular surface location. Here you get a return and note the traveltime. You complete the experiment by moving farther along the line always with a null result.

How are we to interpret these observations? What could be in the subsurface that is consistent with the measured data? To figure it out, you go back to the magic point where you got a response and think about it. Let's say the subsurface velocity is 1500 m/s and the time you measured was one second. Since that is a

two-way time out and back, it means that whatever the seismic waves bounced from is 750 m away from where you are now. It could be a horizontal interface directly beneath you, but that would have given a response at all surface locations and so must be rejected as a possibility.

Similarly any dipping plane reflector is inconsistent with the data. Since you do not know what direction the reflection came from, you have to assume it could come from any direction. What is the shape of a reflector that in any downward direction is 750 m away from one point on the acquisition surface? It must be a circle in the vertical plane of your imaginary seismic line.<sup>1</sup> This is the 2D constant velocity poststack migration impulse response as illustrated in Figures 17.2C and D.

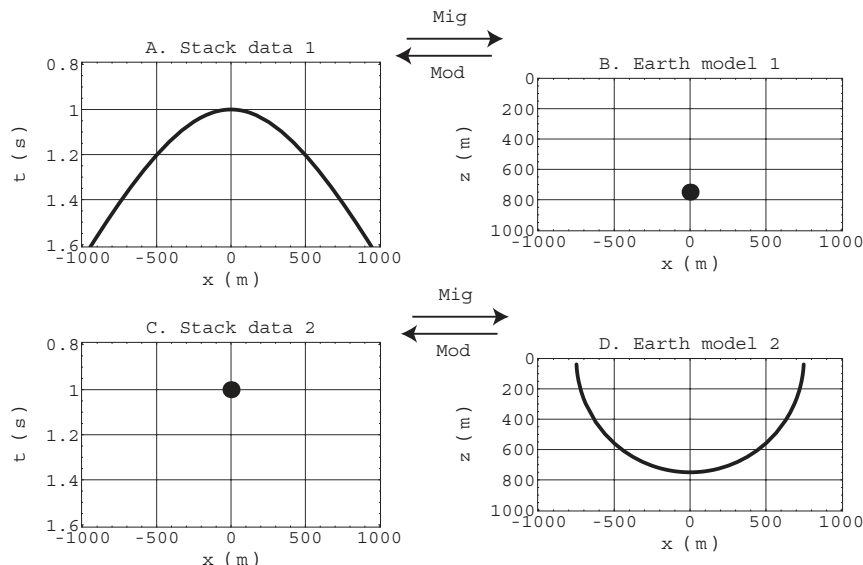


*Fig. 17.2 The 2D impulse responses for zero offset migration and modeling. Velocity is 1500 m/s. (A) Stack data over a point diffractor in the earth is a hyperbolic curve. Migrating this data gives the earth model in B. (B) Point diffractor earth model. Simulation of zero offset seismic data over this model will generate the data in A. (C) Stack data consisting of a single nonzero amplitude spike. Migration of this data will generate the earth model in D. (D) Earth model consisting of a circular reflector. Zero offset data generated across this model will be the data in C.*

---

<sup>1</sup>It may also be a 3D bowl, but you cannot conclude this from a 2D experiment.

When a migration program does this for every blip of amplitude on every trace and adds it all together, we get an image of the subsurface. Where real reflectors live, the individual circles add up to show them. Where there are no reflectors, the circles are random in amplitude and sign and tend to cancel. Thus the image is formed by superposition. Figure 17.3 shows this process in action.

The input stack data in Figure 17.3A shows several features which occur in unmigrated data to confuse interpretation, including edge diffractions, a buried focus with triplication at  $(t, \text{cmp}) = (0.55, 2400)$ , and misplaced dipping events. Migration has rebuilt reflector terminations from endpoint diffractions, anticlines have become narrower, synclines broader, and dipping reflection segments have moved updip and steeper.

## 17.2 Dip from seismic slope

The effect of migration on a sloping line segment in the data is to make it steeper, shorter, and move it updip. This is seen in Figure 17.4 along with the fact that a horizontal line is unchanged by migration (although endpoint diffractions are collapsed).

Analysis of the line response relates dip and migration distance [47]. On unmigrated stack data the relationship is

$$\sin \theta = \frac{v}{2} \frac{dt_s}{dx_s} \quad (17.5)$$

where  $dt_s/dx_s$  is the time slope. The slope can be measured on the stack section by selecting an interval along the reflection event and laying this off as the hypotenuse of a triangle. If the data being analyzed is migrated data with a time axis, the dip can be estimated from

$$\tan \theta = \frac{v}{2} \frac{dt_{mt}}{dx_{mt}} \quad (17.6)$$

where again the quantities  $(dt_{mt}, dx_{mt})$  are the legs of right triangle laid off on the reflection of interest. This is illustrated in Figure 17.5. Finally for migrated data in the depth domain, the dip is the usual geologic definition that would be used with outcrop measurements

$$\tan \theta = \frac{dz}{dx} \quad (17.7)$$

## 17.3 Migration distance

It is clear from Figure 17.4 that dipping reflection segments in stack data move laterally under the action of migration. This is termed migration distance or sometimes migration aperture. The migration distance  $x_{mig}$  for a constant velocity earth is given by

$$x_{mig} = z \tan \theta \quad (17.8)$$

where  $z$  is the depth of a point on the reflection segment and  $\theta$  is the geological dip.

The exploding reflector model [48] is a powerful concept in reflection seismology that helps understand the importance of migration distance. Figure 17.6A shows an earth model that includes a steep reflector segment. The exploding reflector concept says that we can think of this segment as exploding and radiating energy to the surface as indicated by the parallel wavefront segments. In order to capture the returned energy, we need to have midpoint coverage where the exploding reflector wavefronts emerge. If the survey does not include midpoints in this area, then the energy from the reflector will not be received, and the reflector will not be imaged.

In Figure 17.6A we do not have the necessary midpoint coverage. Even if we have receivers in the emergence area, Snell's law tells us that raypaths, such as the dashed one shown, will contain no energy. Midpoint coverage is the key concept not receiver coverage. Migration distance must be considered in seismic survey design to avoid disappointment associated with this problem. Due to ray bending, migration distance for variable velocity is generally much less than the constant estimate.

## 17.4 Variable velocity migration and modeling pairs

The effect of strong velocity variation on migration is to complicate the point and line responses shown above. Instead of being perfect geometric curves, they are distorted circles, hyperbolas, and lines. The point responses are shown schematically in Figure 17.7. A reflection segment, which is straight on the stack section, will not be straight on the migrated output in a variable velocity earth. The detailed shape depends on the actual velocity model.

## 17.5 3D migration

The migration and modeling pairs discussed previously are 2D, in which case an input data point maps to a 2D curve. The extension to 3D for a constant velocity earth is not difficult. For a point diffractor in the earth, the traveltime is a surface as shown in Figure 17.8A.

## Elements of 3D Seismology

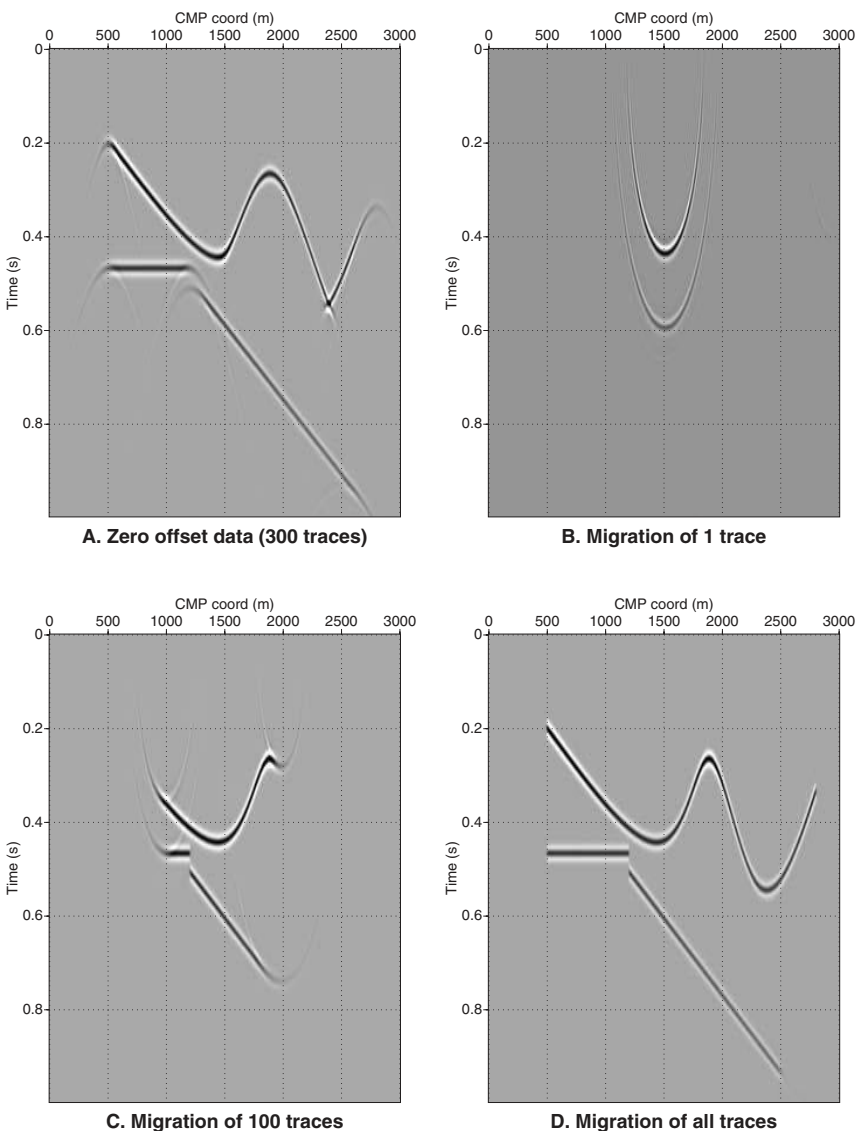


Fig. 17.3 Poststack migration spreads each input amplitude along its appropriate circular impulse response. Velocity is 1500 m/s. (A) Input stack data. (B) Migration of only the center trace yields the migration impulse response centered on the input trace location for an event just below 0.4 s and another at 0.6 s. In a 1:1 depth display, these would be circles. (C) Migrating the center 100 traces gives a partial image due to constructive interference of many impulse responses. These tend to cancel except in reflector locations. (D) The complete migration shows true structural configuration of the subsurface.

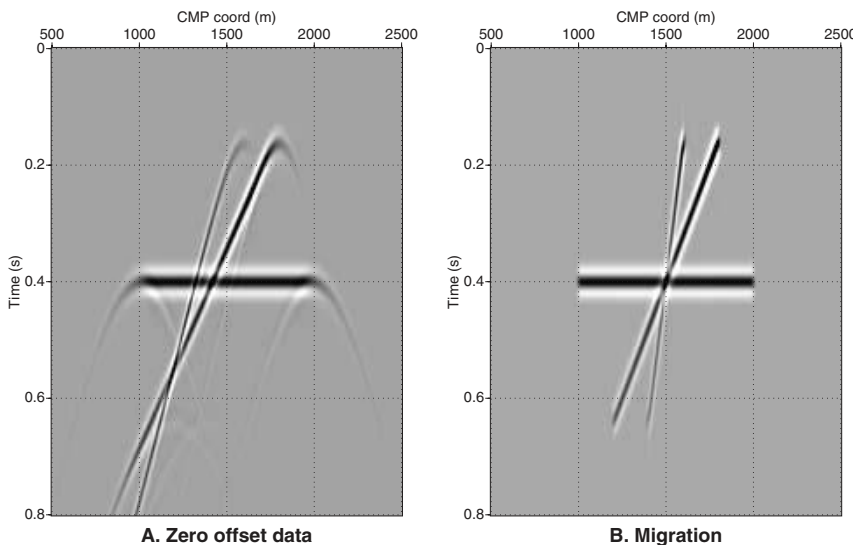


Fig. 17.4 Line response for constant velocity poststack migration. (A) Input data is zero offset data for three reflector segments with dip of 0, 30, and 60 degrees. Velocity is 1500 m/s. (B) Migration result showing the reflector segments have moved up-dip and steeper.

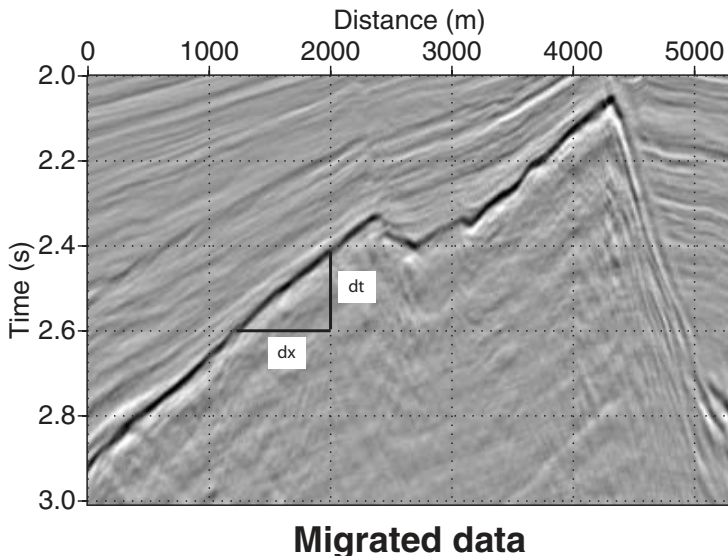
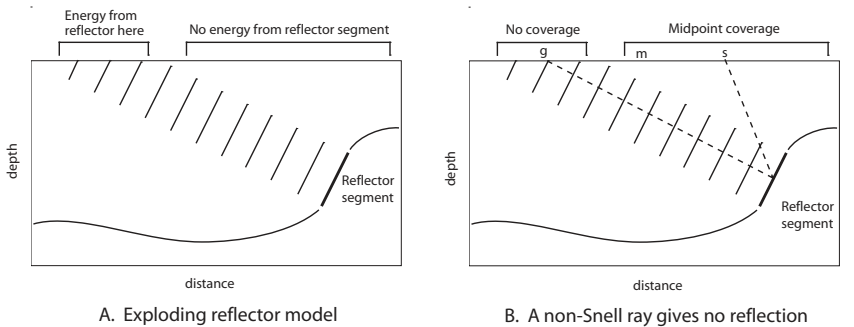
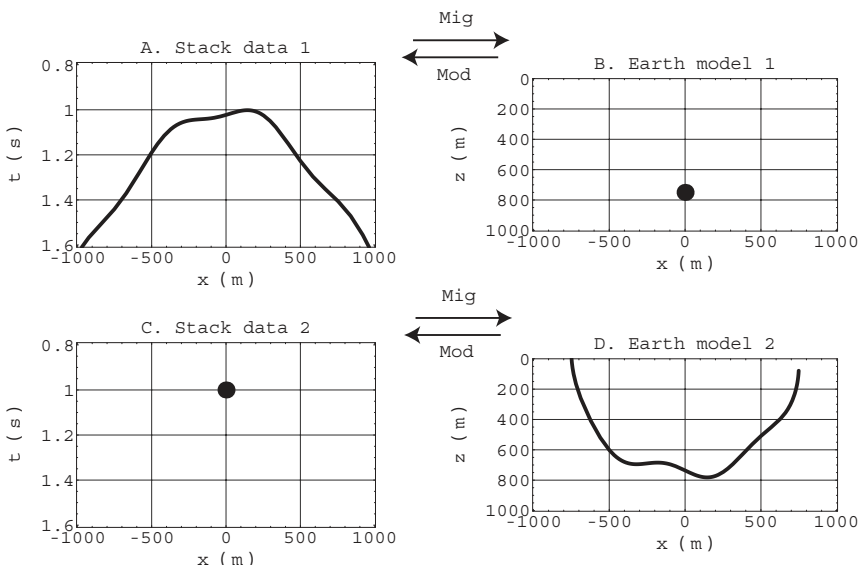


Fig. 17.5 Seismic slopes can be very misleading. This is a panel of migrated data with a prominent basement reflection. Seismic velocity above the basement reflector is about 2500 m/s. The measured quantities ( $dt, dx$ ) indicate local dip of about 11 degrees.

## Elements of 3D Seismology



*Fig. 17.6 A missed opportunity. The midpoint coverage does not extend far enough to capture energy from the reflector segment of interest. Therefore, it cannot be imaged by the acquired data.*



*Fig. 17.7 Point responses for variable velocity migration and modeling.*

The impulse response of 3D zero offset migration follows the same logic as the 2D thought experiment discussed previously, only now we move to every location on a survey grid and get the null return, except at one location. This can only be true if we are standing at the center of an upward-facing spherical shell

as shown in Figure 17.8D. One way to think of 3D migration is that each bit of input amplitude is broadcast along this, its appropriate migration surface in the output space. As all samples are processed, the migrated image in the output data volume emerges by superposition.

The prestack versions of 2D and 3D migration impulse responses are extensions of the poststack ideas outlined previously. Figures 17.9 and 17.10 illustrate the geometry of prestack migration impulse responses for constant

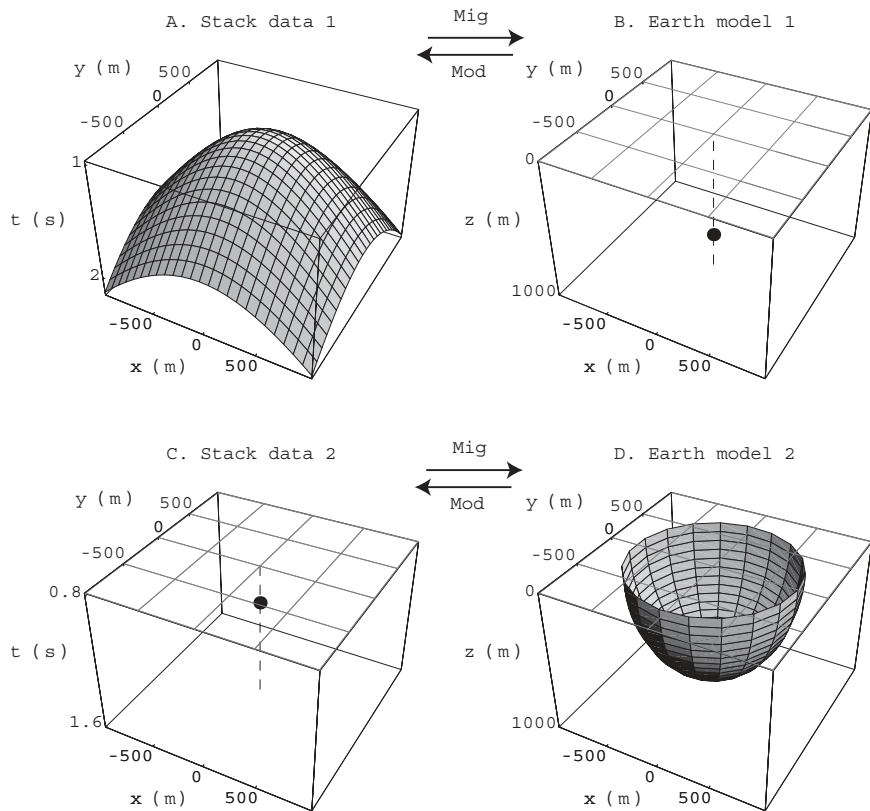


Fig. 17.8 Point response of 3D zero offset migration and modeling in a constant velocity earth ( $v = 1500 \text{ m/s}$ ).

## Elements of 3D Seismology

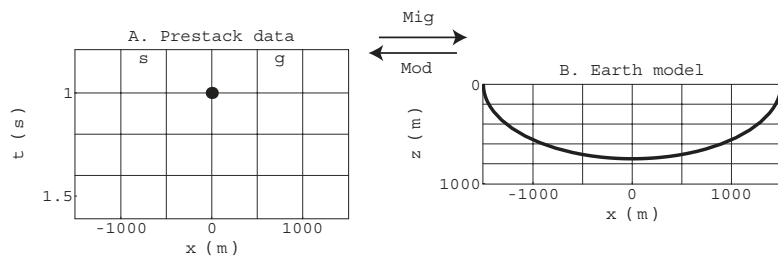


Fig. 17.9 Impulse Response for Constant Velocity 2D Prestack Migration. (A) The input data is a single trace with a single amplitude spike. This trace has a source (*s*) and receiver (*g*) location, but the trace is considered to live at the midpoint. (B) Prestack migration gives an ellipse whose foci are at the source and receiver locations. Traveltime from the source to any point on the impulse response and back to the receiver is a constant. (See also Fig. 19.2)

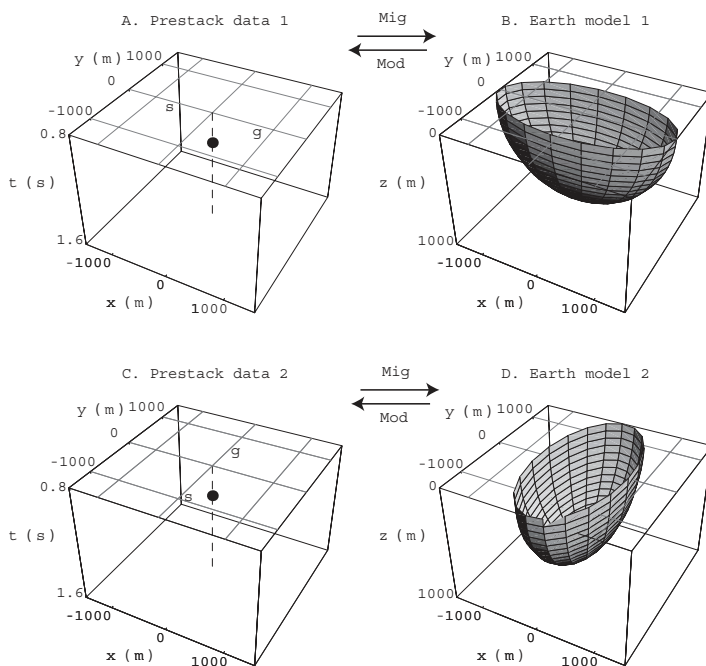


Fig. 17.10 Point response of 3D prestack migration and modeling in a constant velocity earth ( $v = 1500 \text{ m/s}$ ). (A) A 3D prestack trace with one amplitude spike. The azimuth of this trace is E-W. (B) The 3D migration result is an ellipsoid with foci at the source and receiver locations. Total traveltimes for this surface is a constant. (C) A prestack trace with N-S azimuth. (D) The prestack migration impulse response is now oriented with its long axis N-S.

velocity. For a variable velocity earth, all of the impulse responses will be lumpy versions of the curves and surfaces already shown. Table 17.1 itemizes all possible cases for migration impulse response geometry.

Input data	Dimension	Velocity	Impulse response
poststack	2D	constant	circle
poststack	2D	variable	lumpy circle
poststack	3D	constant	hemisphere
poststack	3D	variable	lumpy hemisphere
prestack	2D	constant	ellipse
prestack	2D	variable	lumpy ellipse
prestack	3D	constant	ellipsoid
prestack	3D	variable	lumpy ellipsoid

Table 17.1 Summary of migration impulse response geometry.

## 17.6 Lateral resolution in 2D and 3D data

Lateral resolution of seismic data is the ability to see small scale features in map view. Examples are channels, small reefs, and amplitude patches associated with anomalous reservoir properties. Before migration, lateral resolution is limited by the area of the Fresnel zone. Sharp lateral variations in reflectivity or structure are smeared across this area. Migration improves lateral resolution from the Fresnel zone radius to a theoretical limit of one-half wavelength.

A 2D migration can only collapse the Fresnel zone in the migration direction, whereas 3D migration collapses the Fresnel zone completely to the theoretical limit in both directions as illustrated in Figure 17.11.

Figure 17.12 further illustrates this important concept by considering a hypothetical grid of 2D lines. The amplitude feature as seen in an unmigrated time slice (B) has a different appearance after 2D x-migration (D) and 2D y-migration (F). This is due to lateral resolution being improved only along the migration direction. As seen in Figure 17.13D, 3D migration improves resolution in all directions to reveal the true amplitude feature.

We can use two measures to quantify the importance of migration in any particular case. The first measure,  $\alpha$ , is the ratio of migration distance to optimum CMP interval. Large  $\alpha$  means migration will move events sideways a significant number of traces. The second measure,  $\beta$ , is the ratio of pre- and post-

## Elements of 3D Seismology

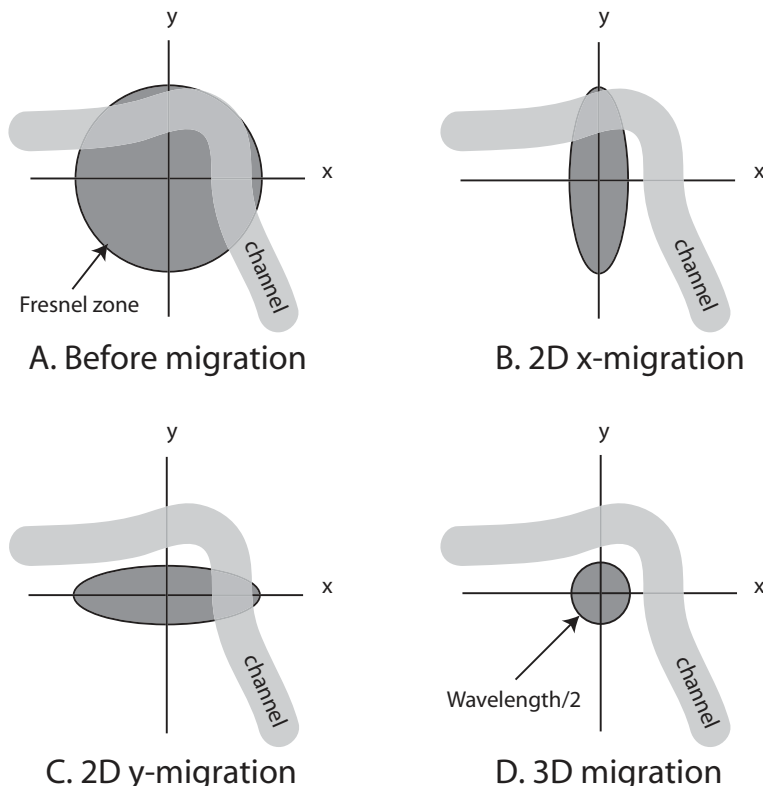


Fig. 17.11 Lateral resolution in unmigrated seismic data is controlled by the Fresnel zone. A geologic feature, such as a channel, will influence the trace if it passes through the lateral resolution zone. Migration improves resolution by collapsing the Fresnel zone to about one-half wavelength. A 2D migration can accomplish this only in the direction the line was shot, leaving cross line resolution unchanged. A 3D migration achieves optimal lateral resolution.

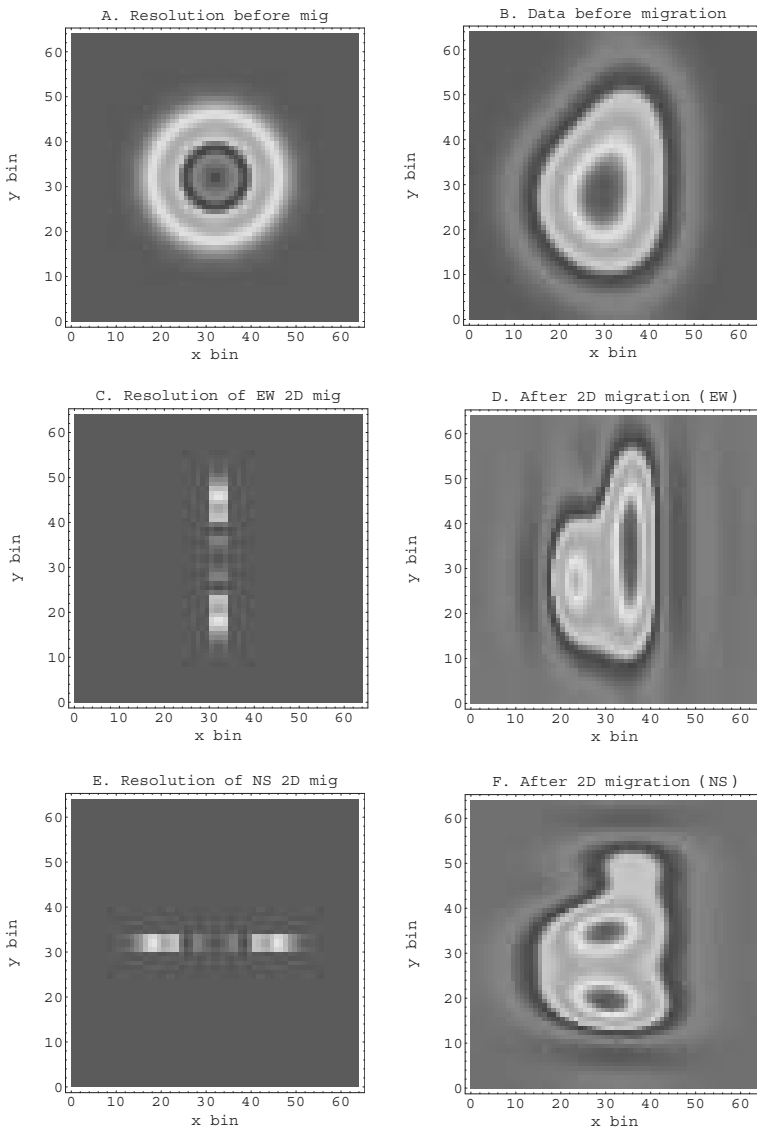


Fig. 17.12 Effect of 2D migration on lateral resolution (LR) in a time slice. In each row, the approximate LR is shown on the left and the data time slice on the right. Even a dense grid of 2D lines can indicate a confusing amplitude distribution within a time or horizon slice. (A) LR of unmigrated seismic data is the Fresnel zone. (B) The unmigrated amplitude anomaly appears to be a broad featureless object. (C) LR for 2D x-migration. (D) 2D x-migration result showing improved LR in the x-direction but no improvement in the y-direction. (E) LR for 2D y-migration. (F) After 2D y-migration the feature is well-resolved in y but not x.

## Elements of 3D Seismology

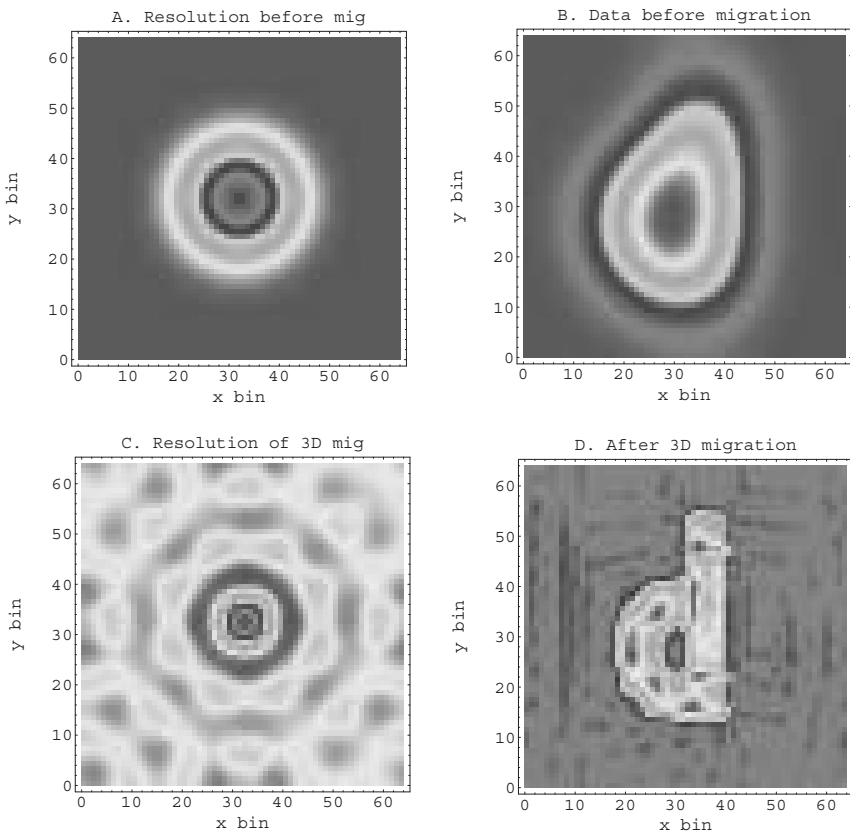


Fig. 17.13 A 3D migration gives optimum lateral resolution. (A) Unmigrated resolution. (B) Timeslice of unmigrated data with amplitude anomaly. (C) Resolution after 3D migration is about one-half of the seismic wavelength. The figure is a bit deceptive due to display clipping; it is actually a much smaller feature than the Fresnel zone in (A). (D) After 3D migration, the anomaly is clearly defined and significantly different than either 2D result in the previous figure.

migration lateral resolution. Large  $\beta$  means lateral resolution is improving significantly. The equations can be written in terms of either reflector depth or zero offset reflection time,

$$\alpha = \frac{4fz}{v} \sin \theta \tan \theta = 2 t_0 f \sin \theta \tan \theta \quad (17.9)$$

$$\beta = \sqrt{1 + 8 f z/v} = \sqrt{1 + 4 f t_0} \quad (17.10)$$

where  $\theta$  is the dip and  $f$  can be either dominant or maximum frequency. Dominant frequency is probably a good thing to use, but actually each frequency has its own  $(\alpha, \beta)$ . Note that  $\alpha$  and  $\beta$  are dimensionless quantities.

Migration will have significant effects if  $\alpha \gg 1$  or  $\beta \gg 1$ . A key idea is that migration is necessary even for data shot in an area with little or no dip. For zero dip, the  $\alpha$  measure will always be zero because migration does not move horizontal reflection events. But if we are mapping amplitude effects for a 50 Hz target reflection at 2 s, we find  $\beta=20$  which is a vast improvement in lateral resolution. The amplitude anomalies of interest will be much better resolved on migrated data than stack data.

There are several reasons why migration may not achieve the theoretical resolution of one-half wavelength, including inappropriate migration algorithm, operator aliasing, aperture problems, migration velocity errors, excessive noise, or spatially aliased input data.

## 17.7 Survey design for linear $v(z)$

Now that we understand migration distance and the key role it can play in survey design, we can quickly outline the theory of seismic survey design in linear  $v(z)$  media. Many design parameters implicitly assume velocity is constant. In a basin like the Gulf of Mexico (GOM), velocities have a smooth increase with depth plus occasional velocity jumps associated with salt, gas, or overpressure. A good first approximation to the background velocity model is to assume velocity increases linearly with depth [115, 116].

Consider a dipping target (i.e., reflector segment) embedded in a continuous linear  $v(z)$  media. We assume the surface velocity, velocity gradient, depth of target, dip of target, and highest desired unaliased frequency are all known quantities. The problem is to calculate appropriate bin size, zero offset reflection time, migration distance, and maximum depth achieved by the seismic ray. The definition of variables used here are itemized in Table 17.2.

For constant velocity, these quantities are simple and well known

$$dx_c \leq \frac{v}{4 f \sin \theta} \quad (17.11)$$

$$t_0 = \frac{2 z}{v \cos \theta} \quad (17.12)$$

Variable	Description
$dx_c$	Bin size for constant velocity
$dx_v$	Bin size for linear velocity
$\Delta t$	Time delay between adjacent traces
$f$	Highest unaliased frequency
$k$	Velocity gradient
$x_m$	Midpoint
$p$	Ray parameter
$v$	Constant velocity
$v_0$	Surface velocity
$v(z)$	Linear velocity function
$t_0$	Normal incidence reflection time
$\theta$	Dip of target (horizontal = 0)
$\theta_0$	Ray take-off angle (vertical = 0)
$x$	Horizontal coordinate
$x_c$	Migration distance for constant velocity
$x_v$	Migration distance for linear velocity
$y$	Midpoint coordinate
$z$	Depth coord; depth of reflection point
$z_{max}$	Maximum ray depth

Table 17.2 Definition of variables for linear  $v(z)$  survey design.

$$x_c = z \tan \theta \quad (17.13)$$

$$z_{max} = z \quad (17.14)$$

When calculating the constant velocity bin size,  $dx_c$ , it is typical to use dominant frequency, although higher signal frequencies are at risk of spatial aliasing. For variable velocity media, it is also typical to use average velocity to the target. Figure 17.14 shows the similarity between the constant velocity and  $v(z)$  geometry. The standard constant velocity spatial aliasing diagram [212] is shown in Figure 17.14A. The traveltime for midpoint  $x_{m2}$  is smaller than the time observed at  $x_{m1}$ .

Spatial aliasing is avoided if this delay is less than one-half the dominant period of the wavelet. Note that all of the delay,  $v dt/2$ , appears to occur near the acquisition surface. In Figure 17.14B, the  $v(z)$  geometry is given. Time delay in this case is clearly associated with the region near the reflector not the acquisition surface. The rays stay parallel passing through a stack of constant velocity layers because the ray parameter is constant for rays in general  $v(z)$  media [177].

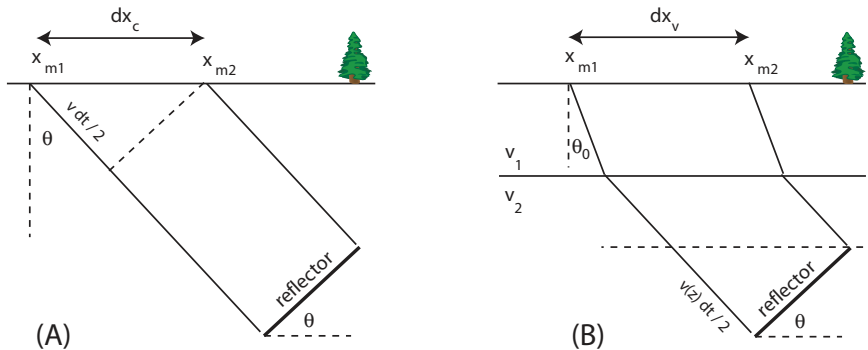


Fig. 17.14 Spatial aliasing geometry. (A) Constant velocity case. (B) Geometry for  $v(z)$ .

The linear velocity equations [115] for 3D design are

$$v(z) = v_0 + k z \quad (17.15)$$

$$p = \frac{\sin \theta}{v(z)} = \frac{\sin \theta_0}{v_0} \quad (17.16)$$

$$\theta_0 = \sin^{-1} \left[ \frac{v_0}{v(z)} \sin \theta \right] \quad (17.17)$$

$$dx_v \leq \frac{v(z)}{4 f \sin \theta} \quad (17.18)$$

$$t_0 = \frac{2}{k} \operatorname{Log}_e \left[ \frac{\tan(\theta/2)}{\tan(\theta_0/2)} \right] \quad (17.19)$$

$$x_v = \frac{\cos \theta_0 - \cos \theta}{p k} \quad (17.20)$$

$$z_{max} = \begin{cases} \frac{1}{k} \left( \frac{1}{p} - v_0 \right) & \text{if } \\ z & \text{if } \end{cases} \quad (17.21)$$

Figure 17.15A compares recommended bin size based on constant velocity and linear  $v(z)$  using parameters typical of the GOM. The constant velocity bin is calculated using average velocity to the target. We see the constant velocity bin

## Elements of 3D Seismology

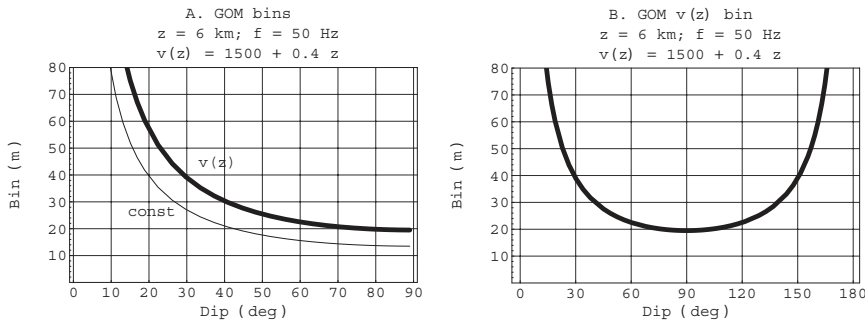


Fig. 17.15 Recommended Bin Size as a Function of Dip. (A) The  $v(z)$  bin is always larger than the constant velocity one. (B) The smallest  $v(z)$  bin size occurs at 90° dip.

is always smaller than the  $v(z)$  bin. This means that honoring linear  $v(z)$  allows the use of a larger bin and thus saves acquisition cost. Figure 17.15B shows the linear  $v(z)$  bin is valid for 0–180 degree dips. This example also shows the smallest bin requirement occurs at 90° dip. Therefore a bin properly designed for 90° dip is adequate for all dips beyond 90°.

There can be a great difference between constant velocity and linear  $v(z)$  migration distance, and this is second only to bin size in design importance. In the example of Figure 17.16A, ignoring curved rays would indicate a need to shoot data 8.5 km down dip of the target, but honoring ray bending due to linear  $v(z)$  argues for a much smaller down dip survey extension of 3.5 km.

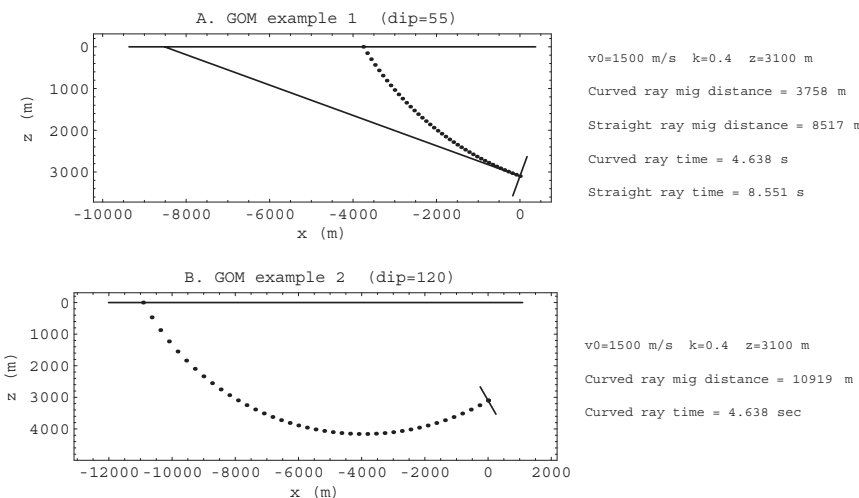


Fig. 17.16 (A) Plot and calculated values for an example in the Gulf of Mexico. Constant velocity assumptions overestimate traveltimes and migration distance. (B) Gulf of Mexico turning wave example for 120-degree dip.

# 18

## Migration II: Classification and Velocity Analysis

Migration is an important and expensive process that is applied to reflection seismic data before it is interpreted. Because it is the last major process to hit the data, it is likely to be blamed for things like inconsistent amplitudes and lack of structural detail, even though these problems may arise from acquisition problems or other processing issues. Petroleum E&P companies are the end users of seismic data, but they process little of the data they interpret.

The migration process may be performed by a contractor, another E&P company (perhaps a lease or project partner), or the company itself. The work may be done by a processing division (typical for a contractor or major E&P company) or an internal specialty processing group. The latter is likely in a secondary E&P company or on a high profile project in a major E&P company.

Dealing effectively with the migrator(s) saves time, confusion, and money. To do this, you need to know about the different kinds of migration and the issues of suitability and sensitivity associated with each. It is a waste of time and money to remigrate data because an inappropriate migration technique was recommended or requested.

### 18.1 Kinds of migration

Here we develop a classification scheme for migration [113]. We classify migration for the same reason that people classify anything—it brings order out of apparent chaos and gets everyone talking the same language.

Dimensionality is the first consideration. Migration is either 2D or 3D.

- **2D.** This is appropriate only for a pure dip line. Even so, there remains a large crossline Fresnel zone that can blur stratigraphic targets.

- **3D.** The correct thing to do but it requires 3D data. A close grid of 2D lines can be merged into a 3D data volume and migrated, but this is unsatisfactory. The 3D migration of 3D data can be one-pass or two-pass. One-pass migration does not decompose the survey arbitrarily but treats it as true 3D data. Two-pass migration involves 2D migration along the inline direction then a second pass along the crossline direction. This is a patch for using 2D migration programs on 3D data. Two-pass migration is only valid for mild lateral velocity variations. It is still of some theoretical interest but is no longer in wide commercial use.

The next issue concerns the type of data input to migration. This can be either poststack or prestack seismic traces, and the migration that is performed is thus termed poststack or prestack.

- **Poststack.** Migration of the CMP stack data volume, which is considered to be zero offset data. The standard decoupled processing flow is applied, and DMO is almost always applied before CMP stacking so that all dipping events are preserved in the stack data. This is much less expensive than prestack migration but also less accurate in complicated areas. Poststack migration can often be accomplished on workstation class machines.
- **Prestack.** Migration of the entire prestack data volume. Every blip of amplitude on every prestack trace is broadcast over a unique 2D or 3D migration impulse response. This is a coupled process that combines the functions of NMO, DMO, and poststack migration. This means that two velocity analysis steps (NMO, poststack migration) have been combined into one. Typically the only processing applied before prestack migration is deconvolution, some gain corrections that are not incorporated in the migration, and static corrections if they are not severe. For a large survey, prestack migration requires supercomputer class machines and still takes a very long time. For migration velocity analysis, the data, or significant subsets of it, must be migrated repeatedly. Prestack migration is much more expensive than poststack migration (see Fig. 14.5).

The last classifying term involves the level of physics put into the algorithm, primarily the handling of velocity variation. From Snell's law, we know that as velocities change, seismic rays should bend, but not all migrations honor this fact. It is much less expensive to only approximately honor ray bending, if doing so will still generate a geologically accurate image. But in many cases, the more closely we honor the physics the better the image will be and the higher the cost. To describe this situation, we use the terms *time migration* and *depth migration*.

- **Time.** Any migration that is accurate only for constant velocity or  $v(z)$  is termed time migration. Within the time migration family are methods that

are exact for arbitrary  $v(z)$  and those that are really constant velocity algorithms that can approximately incorporate vertical velocity variations.

Time migration is fast enough to be done repeatedly for easy velocity analysis, and it is relatively robust with respect to velocity errors. Time migration can be patched for  $v(x,y,z)$ , but is inferior to depth migration for strong lateral velocity variations.

- **Depth.** Any migration technique that is accurate in the presence of strong lateral and vertical velocity variations is termed depth migration. Geologic examples of strong lateral velocity variation would include salt overhangs, subthrust or subsalt areas, extreme topography, or a combination of such features. As far as possible, depth migration bends rays accurately through the velocity field and accounts for wave theory amplitudes. All of this costs computer time and thus money.

Depth migration is generally too expensive to be run repeatedly for migration velocity analysis, so specialized methods are developed that allow the absolute minimum number of migration runs to get the velocity right. As nature would have it, depth migration is very sensitive to velocity errors. Clearly depth migration is much more expensive than time migration.

In summary, the terms depth and time are used to distinguish those algorithms that handle lateral velocity variations and properly bend rays (depth migration) from those that do not (time migration).

An additional classification into scalar migration and vector migration is not yet common. The difference is one of input data type, earth model parameters, and physics. For vector migration, we require multicomponent data. The migration velocity model will consist of both P-wave and S-wave velocities and the migration algorithm will need to incorporate elastic processes such as mode conversion. On a world-wide volume basis, the vast majority of data currently acquired and processed is single component (scalar) and the distinction of scalar versus vector migration remains largely a research topic. However in some marine basins there is an accelerating trend toward vector migration of 4C OBC data. The successes are sometimes aggressively promoted giving a skewed perception that the practice is ubiquitous.

We note that time versus depth migration is not related to whether the migrated data are output with a time or depth axis. Any migration can be output in terms of vertical reflection time or vertical depth. In current practice, it is common to output the migrated data in time and then depth convert particular horizons using all available velocity and depth information. But in areas of strong lateral velocity variation, depth migration is often output directly in depth.

## Elements of 3D Seismology

Since migration depth accuracy is limited to about one-half wavelength, this means that the migrated depth section often needs final adjustment based on well data.

Bringing all this together, we can identify those items which are less accurate and less expensive—2D, poststack, time- from those that are more accurate and more expensive—3D, prestack, depth. We live in a world of jargon and migration is no exception. A given migration method can be identified by concatenating these terms in a certain order. For example we can say 2D poststack time migration or 3D prestack depth migration.

As mentioned earlier, it is important to realize that we never migrate data just once. To determine migration velocities, we must iterate the migration. There are clever ways of avoiding repeated migration of the entire data volume, but iterating even partial migrations can add up. The major cost factor is the number of input traces. Adding more input traces means more cost.

For a given number of input traces, depth migration will be more expensive and hopefully more accurate than time migration. But when should we request depth migration and when will time migration suffice? What about poststack and prestack? The controlling factors are structural complexity and lateral velocity variation. A qualitative decision graph is shown in Figure 18.1. You could get a good argument going about exactly where the bounding lines should be drawn and how to quantify the coordinate axes. Lateral velocity change greater than about 40–50% over something like 10 wavelengths is definitely strong, although much greater velocity gradients are possible. A steeply dipping sediment-salt interface in the Gulf of Mexico can exhibit a 100% change in the space of a few dozen meters. As for quantifying structural complexity, we leave that to the geologists.

Migration should be 2D or 3D, depending on whether the data is 2D or 3D. However to hold down costs, selected 2D lines are often extracted from the 3D data for detailed prestack depth migration. These 2D lines should be extracted in the dip direction, if one exists, to minimize out-of-plane effects.

Note the occurrence of prestack time migration in Figure 18.1. At first sight this kind of migration seems curiously unwise. Much extra expense is incurred by working with prestack data, but no improved image can be expected because only time migration physics is going into the algorithm. Not long ago it seemed that the main role of prestack time migration was to prepare data for AVO analysis. We want to migrate before AVO for lateral resolution improvement but not spend big money on depth migration and related velocity analysis. Furthermore, we have more faith in time migration amplitude behavior.

But there is growing evidence [81] that for structurally complex areas, the standard processing flow of NMO, DMO, CMP stack, poststack depth migration is just not appropriate. The reasons are still being debated, but it is clear that better images come from prestack time migration than the standard processing

flow. Plus, as you load more velocity variation into DMO, it approaches the cost of prestack depth migration. This is not to say that DMO and the standard flow should never be done; it is just worthwhile to consider what is appropriate for a particular area.

Figure 18.1 shows the minimum requirement for kind of migration. You can always over-kill a problem by using a kind of migration more general (read expensive) than required. For example, you could request prestack depth migration in an area of subtle structure and gentle velocity variation. However, the improvement over poststack time migration in this case is minimal and the added cost would be significant.

In summary, there are two things that make a migration more expensive: either you put more data into it, or you put more physics into it. More data comes from 3D versus 2D and prestack versus poststack. How much physics we put in is implied by the terms time migration (less physics) and depth migration (more physics).

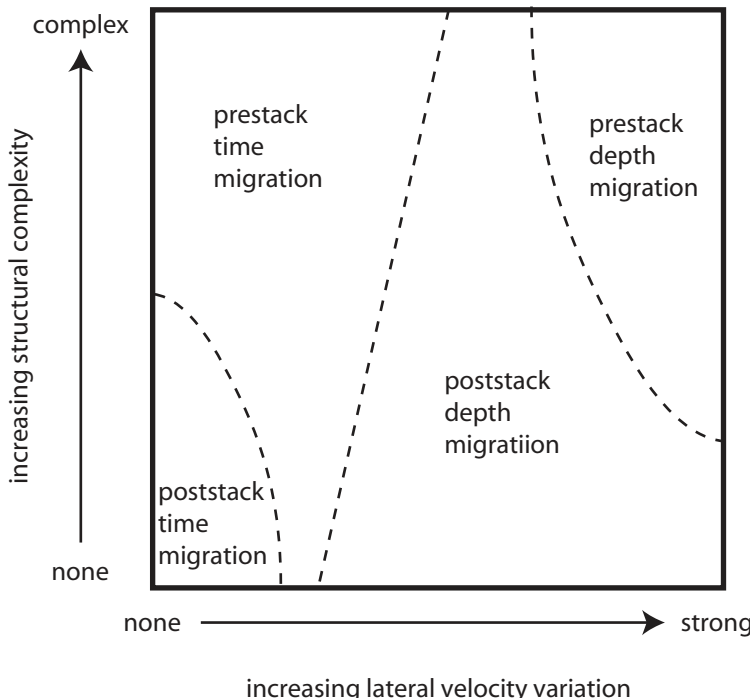


Fig. 18.1 Qualitative decision diagram for migration.

## 18.2 Stolt migration theory

The general mathematical framework of migration is much too broad to be developed here in any detail. But it is instructive to give one example.

Migration by Fourier transform [171] is a 2D or 3D method applicable to poststack or prestack data. It is a widely used time migration algorithm that in its simplest form assumes constant velocity although it can be extended to  $v(z)$  media. It is also known as Stolt migration, phase shift migration, and F-K migration. It is the fastest of all migration techniques. We will consider the 2D constant velocity poststack case. This discussion draws heavily on Fourier theory as presented in appendix A.

The starting point is the 2D constant velocity wave equation

$$\frac{\partial^2 p}{\partial x^2} + \frac{\partial^2 p}{\partial z^2} - \frac{1}{v^2} \frac{\partial^2 p}{\partial t^2} = 0 \quad (18.1)$$

where  $p(t,z,x)$  is a time-dependent wavefield in a two-dimensional  $(z,x)$  earth. We can take the Fourier transform of this equation with respect to all three coordinates. This is a mapping from physical space  $(t,z,x) \rightarrow (\omega, k_z, k_x)$  where  $(k_z, k_x)$  are vertical and horizontal wavenumbers and the result is

$$\left( -k_x^2 - k_z^2 + \frac{\omega^2}{v^2} \right) p(\omega, k_z, k_x) = 0 \quad (18.2)$$

For this equation to be true, the quantity on the left side must be zero at every point in  $(\omega, k_z, k_x)$  space. There are two possibilities. One possibility is that  $p(\omega, k_z, k_x)$  is zero, but this is a trivial case because it implies the original wavefield is zero for all space and time. The other possibility is that

$$\left( -k_x^2 - k_z^2 + \frac{\omega^2}{v^2} \right) = 0 \quad (18.3)$$

This is what we are after because it gives a relationship between the transform variables of  $(t,z,x)$ . It says that if we are dealing with data that obeys the wave equation, then  $(\omega, k_z, k_x)$  are not independent variables. Anticipating later developments, we solve this for the vertical wavenumber

$$k_z = \frac{\omega}{v} \sqrt{1 - \left( \frac{vk_x}{\omega} \right)^2} \quad (18.4)$$

A zero offset section or CMP stack is wavefield data as a function of time and CMP coordinate,  $p(t,x)$ . We can take the Fourier transform of this data, with respect to both coordinates, to form  $p(\omega,k_x)$ . No magic yet, just our data in frequency-wavenumber space. But if we assume a velocity, the  $k_z$  equation allows us to calculate a  $k_z$  value at every point in  $(\omega,k_x)$  space and thus create  $p(k_z,k_x)$ , which can be inverse Fourier transformed to give  $p(z,x)$  – migrated data.

If that went by a little too fast, here is the algorithm as a program sketch.

```

p(w,kx) = FFT[p(t,x)]
choose v
for all w {
    for all kx {
        kz = (w/v) sqrt(1 - (v kx/w)^2)
        p(kz,kx) = p(w,kx)
    }
}
p(z,x) = IFFT[p(kz,kx)]

```

Naturally there are implementation details not shown here, such as interpolation of complex numbers, but basically that's it. The first and last steps run at FFT speed and the inner loop is not very complicated; so the whole thing is very fast.

We can see the action of Stolt migration by looking at data before and after migration in the Fourier domain. Figure 18.2 illustrates migration on three dipping reflector segments. Note the expected inverse relationship of dips in the physical and Fourier domains– a horizontal  $(t,x)$  event is vertical in  $(\omega,k)$  space. The slope of each dipping event in the Fourier domain is changed by migration in accordance with the  $k_z$  formula shown previously.

In our example, the output vertical axis is migrated time (vertical two-way traveltime) rather than depth. Since the velocity is known, we can choose to have it either way, but using the time axis is better for illustrating the Fourier domain behavior of migration. Because it involves a square root mapping, Stolt migration has been described as NMO in the frequency domain. The appearance of this example would be the same if any migration technique were applied. Stolt migration is one of many ways to accomplish it.

## 18.3 Overview of algorithms

Any given kind of migration can be accomplished in many ways. The detail of how migration is done is referred to as the algorithm.

Two popular Fourier transform methods are Stolt and Gazdag migration (also known as *phase shift migration*). These are time migration methods valid for  $v(z)$  and naturally incorporate turning waves. For mild  $v(x,y,z)$ , there is an

## Elements of 3D Seismology

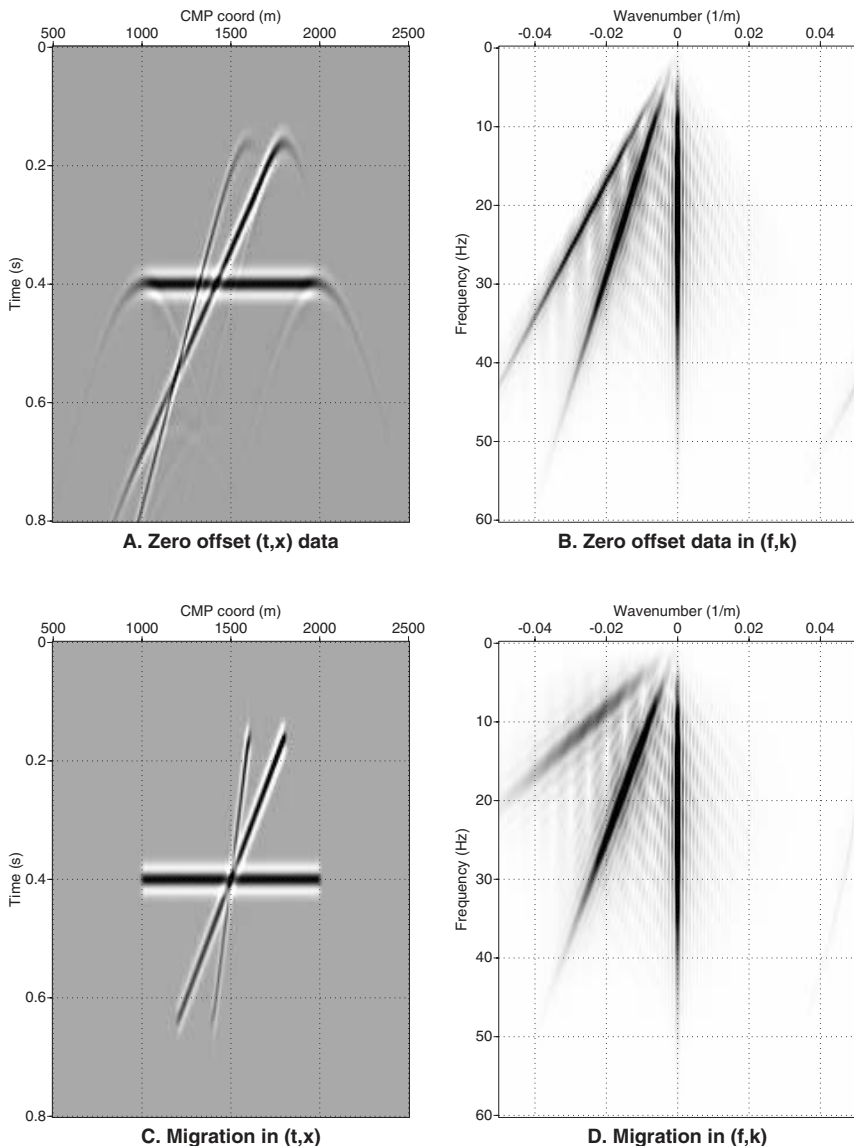


Fig. 18.2 Migration action in the Fourier domain. (A) Stack data before migration. (B) Frequency-wavenumber plot of the stack data. (C) Migration result. (D) Migration result in Fourier domain.

extended form of Gazdag migration called *phase shift plus interpolation* (PSPI), which can be applied to prestack or poststack data. Spatial Fourier transforms in Stolt migration require uniform trace spacing, which often must be accomplished by data interpolation. Gazdag migration does not have this complication because only the time axis is transformed and time sampling is always regular.

Wave equation methods use some form of direct or indirect finite difference application of the wave equation. These methods include reverse time migration and various forms of dip-limited FD algorithms. These are generally depth migration techniques, which use the wave equation directly and tend to have good amplitude control and naturally generate very smooth images without compromising resolution. Finite difference techniques tend to be relatively expensive and require the data to be interpolated onto a regular grid before migration. Forms that incorporate anisotropy and turning waves are known.

Kirchhoff migration operates in the physical time-space domain and therefore naturally handles irregular data. This is the most commonly used depth migration technique especially for 3D. It operates one trace at a time and can be applied to data sorted in any way. If coded properly, good amplitude control is possible, but in complex areas the output image may contain sharp discontinuities and other artifacts. These arise because Kirchhoff migration is based on high frequency approximations and geometrical optics. Extreme ray bending may leave holes in the image that wave equation methods would smooth over.

Kirchhoff allows migration of a subset of the survey area, a technique called *targeted prestack depth migration*. Operator aliasing can be a problem. This is a kind of spatial aliasing that occurs in the steepest parts of the migration impulse response, that is say it is introduced by the migration itself (as opposed to data aliasing). Kirchhoff migration can be programmed to allow turning waves and good velocity analysis tools exist. The dominant method is velocity field updating based on event curvature in common image gathers.

Many other migration techniques have been developed, but Kirchhoff, Fourier, and wave equation finite difference are the workhorses of the industry. For prestack time migration, Fourier methods are probably the most commonly applied since they allow robust and quick velocity analysis. Kirchhoff migration dominates the prestack depth migration market, but prestack wave equation migration is an area of active research that promises improved amplitude control in difficult situations, such as subsalt AVO analysis.

## 18.4 Kirchhoff depth migration methodology

One should understand that prestack depth migration is a complicated undertaking and involves many choices on the part of the processor. Even if the physics and programming are perfect in the migration program, the output

## Elements of 3D Seismology

quality is strongly dependent on the expertise of the user. Parameter choices made for migration will largely determine the data quality as seen by the interpreter. Of course acquisition problems like spatial aliasing may be present before processing, and this will further influence data quality.

We focus here on Kirchhoff 2D prestack depth migration. As an example of such a depth migration program, consider the following self-documentation for sumigtopo2d. This program is part of the SeismicUn\*x processing package freely available from the Center for Wave Phenomena at The Colorado School of Mines.

```
SUMIGTOPO2D - Kirchhoff Depth Migration of 2D poststack/prestack  
data from the (variable topography) recording  
surface
```

```
sumigtopo2d  infile=  outfile=  [parameters]
```

Required parameters:

```
infile=stdin      file for input seismic traces  
outfile=stdout    file for common offset migration output  
ttfile          file for input traveltimes tables
```

The following 9 parameters describe traveltime tables:

```
fzt      first depth sample in traveltime table  
nzt      number of depth samples in traveltime table  
dzt      depth interval in traveltime table  
fxt      first lateral sample in traveltime table  
nxt      number of lateral samples in traveltime table  
dxt      lateral interval in traveltime table  
fs       x-coordinate of first source  
ns       number of sources  
ds       x-coordinate increment of sources  
fxi     x-coordinate of the first input trace  
dxi     horizontal spacing of input data  
nxi     number of input trace locations in surface
```

Optional Parameters:

dt= or from header (dt)	time sampling interval of input data
ft= or from header (ft)	first time sample of input data
dxm= or from header (d2)	sampling interval of midpoints
surf="0,0;99999,0"	Recording surface
"x1,z1;x2,z2;x3,z3;..."	
fzo=fzt	z-coord of first point in output trace
dzo=0.2*dzt	vertical spacing of output trace
nzo=5*(nzt-1)+1	number of points in output trace
fxo=fxt	x-coordinate of first output trace

<code>dxo=0.5*dxt</code>	horizontal spacing of output trace
<code>nxo=2*(nxt-1)+1</code>	number of output traces
<code>off0=0</code>	first offset in output
<code>doff=99999</code>	offset increment in output
<code>noff=1</code>	number of offsets in output
<code>fmax=0.25/dt</code>	frequency-highcut for input traces
<code>offmax=99999</code>	max abs offset allowed in migration
<code>aperx=nxt*dxt/2</code>	migration lateral aperture
<code>angmax=60</code>	mig angle aperture from vertical
<code>v0=1500 (m/s)</code>	reference velocity value at surface
<code>dvz=0.0</code>	reference velocity vertical gradient
<code>ls=1</code>	flag for line source
<code>jpfile=stderr</code>	job print file name
<code>mtr=100</code>	print information every mtr traces
<code>ntr=100000</code>	max input traces to be migrated

**Notes:**

1. Traveltime tables were generated by program rayt2dtopo (or any other one that considers topography) on relatively coarse grids with dimension ns\*nxt\*nzt. In the migration process, traveltimes are interpolated into shot/geophone positions and output grids.
2. Input seismic traces must be SU format and can be any type of gathers (common shot, common offset, common midpoint, and so on).
3. If velocity analysis is desired, migrated traces are output in CMP gathers with dimension nxo\*noff\*nzo.
4. If the offset value of an input trace is not in the output offset array, the nearest one in the array is chosen.
5. Amplitudes are computed using the reference v(z) velocity profile specified by the parameters v0= and dvz=.
6. Input traces must specify source and receiver positions via the header fields tr.sx and tr.gx. Offset is computed automatically.

Author: Zhenyue Liu 03/01/95 CSM  
 Trino Salinas 07/01/96 CSM Added topo

We are interested in the conceptual use of such a program rather than detailed application to a particular data set. Like any Kirchhoff migration, this one can directly operate on shot records. Figure 18.3 illustrates how a 2D seismic line is composed of overlapping shot records, which involves the shot interval, group interval, and span of midpoint coverage.

## Elements of 3D Seismology

The first step for prestack migration is construction of an interval velocity model  $v(x,z)$  that spans the same range as the data midpoint coverage. The first pass at such a model might come from a linear velocity gradient or perhaps interpolation of upscaled sonic logs or vertical seismic profile velocity information. The simple velocity model shown in Figure 18.4A has both vertical and lateral linear velocity gradients. Dark shades are high velocity.

With this velocity model in mind, consider a prestack seismic trace with a source at 1000 m and a receiver at 2000 m. Further consider only the amplitude value on this trace at 1 s. What Kirchhoff migration wants to do is broadcast this amplitude along a curve representing every point in the subsurface which has the following property. Traveltime from the source to the subsurface point and then to the receiver is exactly 1 s. It would be possible to embed traveltimes in the migration code, but that would be extremely inefficient. For example, the location at 1000 m might be home to many receivers as the acquisition process rolls over it. But the traveltimes to all points in the subsurface is the same for any receiver that occupied this location.

This leads to the idea of traveltimes and ray fans, which are a prominent item in the *sumigtopo2d selfdoc*. Figure 18.4B shows one way traveltimes from the 1000 m location to all points in the subsurface for take off angles up to 60 degrees. This is the traveltime table that will be invoked for our trace's source location.

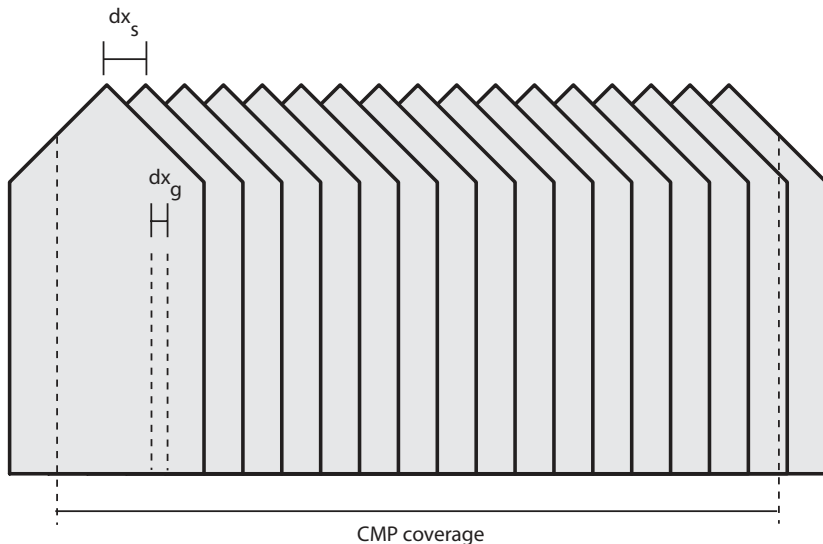


Figure 18.3 A 2D prestack seismic line is a collection of overlapping shot records. The shot interval, receiver interval, and span of CMP coverage are indicated.

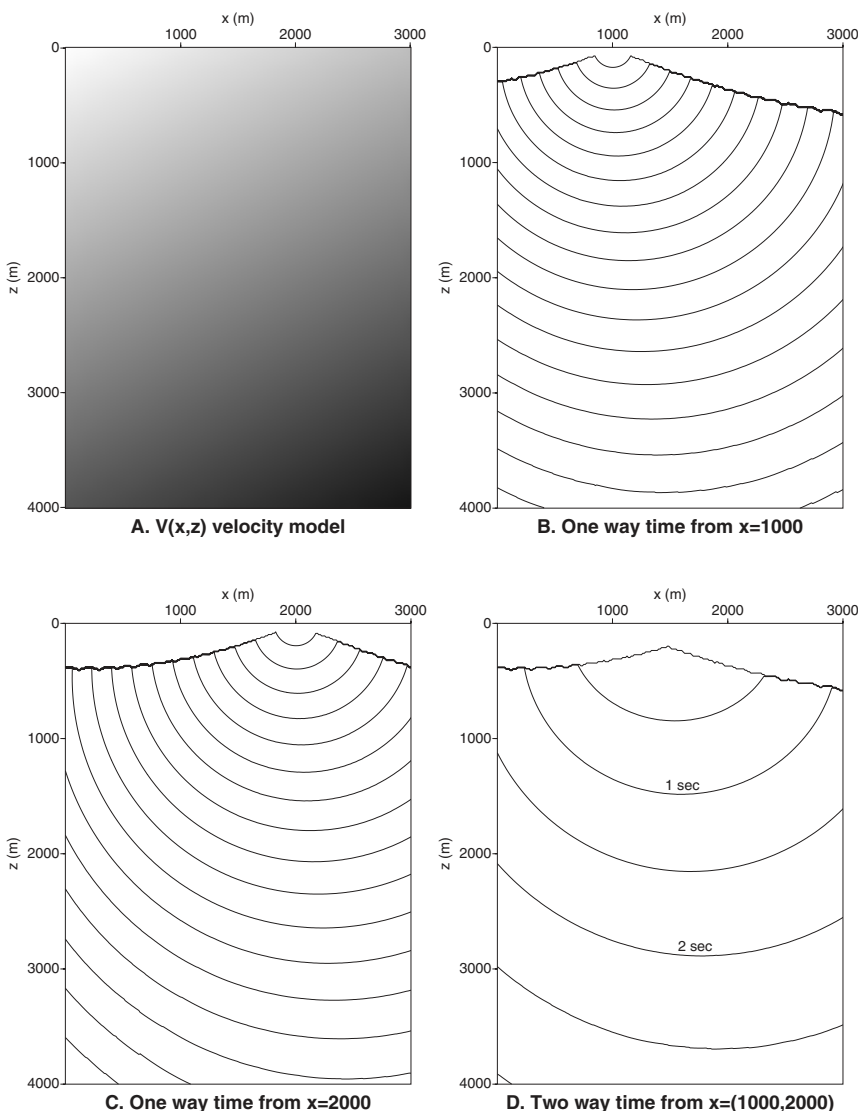


Fig. 18.4 Traveltimes for prestack depth migration. (A) A 2D velocity model with vertical and lateral velocity gradients. Higher velocities are indicated by darker shades. (B) One way traveltimes computed from location at 1000 m by combined ray tracing and eikonal solver. This is the source traveltime table. Contour interval 100 ms. (C) Traveltimes from a receiver location at 2000 m. Contour interval 100 ms. (D) By summing the source and receiver one-way times, we get the reflection time curves. Contour interval is 500 ms. Each contour is an impulse response for prestack depth migration.

## Elements of 3D Seismology

Each contour is 100 ms and this traveltimes map has been computed by a combination of ray tracing and solution of the eikonal equation

$$\left(\frac{\partial \tau}{\partial x}\right)^2 + \left(\frac{\partial \tau}{\partial z}\right)^2 = \frac{1}{v^2(x, z)} \quad (18.5)$$

where  $\tau(x, z)$  is the traveltimes at each point in the depth model. This equation can be derived directly from the wave equation, if it is assumed that seismic wave amplitude and traveltimes are separable functions. This is a good assumption at the frequencies encountered in petroleum seismology.

In addition to a source traveltimes table, we need one for the receiver location at 2000 m. This is shown in Figure 18.4C again with a contour interval of 100 ms.

We find the reflection time from any subsurface point into these source and receiver locations by summing the individual source and receiver one way times. The result of this summation is Figure 18.4D shown with a contour interval of 500 ms. Once the traveltimes curve is known, then migration reduces to spreading the input amplitude along this curve with some amplitude adjustments for various wave propagation effects. Each contour in Figure 18.4D is a 2D prestack depth migration impulse response. Each is an ellipse with the property that the source and receiver locations (1000, 2000) are the foci.

With the full form of this two way traveltimes map, we are ready to migrate all samples on the trace. To migrate an entire line, we need a collection of travel tables that span the CMP coverage area. Ray fan spacing depends on lateral velocity variation in the subsurface. More ray fans mean more computer time. For a  $v(z)$  medium, only one ray fan is needed because traveltimes would be the same for a fan anywhere along the line.

To summarize, Kirchhoff prestack depth migration has the following major steps: (1) build initial velocity model, (2) compute traveltimes tables, (3) do the migration.

## 18.5 Migration velocity analysis

When there is significant velocity variation in the subsurface, migration cannot be performed just once to produce a final product. The reason is because the migration velocities are unknown and must be determined by the migration itself. Migration velocity analysis is the repeated migration of a data set or part of it to find the best migration velocity model. For prestack depth migration, this can be a very lengthy and expensive procedure, especially in 3D. How well the velocities are determined will affect the final migrated result.

Migration velocities are important because migration is one of the few seismic processes which can create or remove structural features in the data

(uncorrected statics are another). Furthermore, migration is fairly sensitive to velocity errors with depth migration being much more sensitive than time migration.

Figure 18.5 gives an idea of how sensitive poststack time migration is to velocity errors and how this can be used to estimate velocities. Figure 18.5A is zero offset for a constant velocity earth composed of a folded reflector, a fault, and a point diffractor. This data was simulated using a velocity of 1500 m/s. If we migrate it using a velocity that is 10% too low, the result is Figure 18.5B. The only strong clue there is a problem is the point diffraction hyperbola which has not completely collapsed. Close examination shows residual diffractions on the reflector endpoints as well. This is an under-migrated result.

Figure 18.5C is the image created by migration with the correct velocity. All features are focused. Figure 18.5D results if the migration is done with a velocity 10% too high and again unfocused energy is seen. This is an over-migrated result with characteristic migration smiles. This is the basis of focusing analysis as a tool for prestack depth migration. Clearly without point diffractors to key from, it would not be a very sensitive tool.

If migration velocities are incorrect, the first thing to go is image detail, then the possibility of false structure arises. Even though the features in this data appear at the same times for all these migration velocities, they represent different depths. The horizontal reflection segment in Figure 18.5 C occurs at 0.466 s, which corresponds to a depth of 350 m at the correct migration velocity of 1500 m/s. In the over-migrated example Figure 18.5 D, this event occurs at the same time, but represents a depth of 385 m because the migration velocity is 1650 m/s. The migrated depth,  $z_m$ , is related to the true depth,  $z$ , by

$$z_m = \frac{v_m}{v} z \quad (18.6)$$

where  $v_m$  is the migration velocity and  $v$  is the correct velocity.

Prestack depth migration is even more sensitive to velocity errors. A common procedure in Kirchhoff depth migration is to migrate the prestack data, then output the migrated multioffset data as common image gathers (CIGs). These are like CMP gathers in that they are associated with one surface position. But a CMP gather represents zero offset traveltime while a CIG represents vertical depth beneath the surface location as seen by each migrated offset trace.

Just as events in CMP gathers should be flat after NMO when velocities are correct, events in CIG gathers should be flat after prestack depth migration. Figure 18.6 shows the idea. A synthetic prestack data set was created over two point

## Elements of 3D Seismology

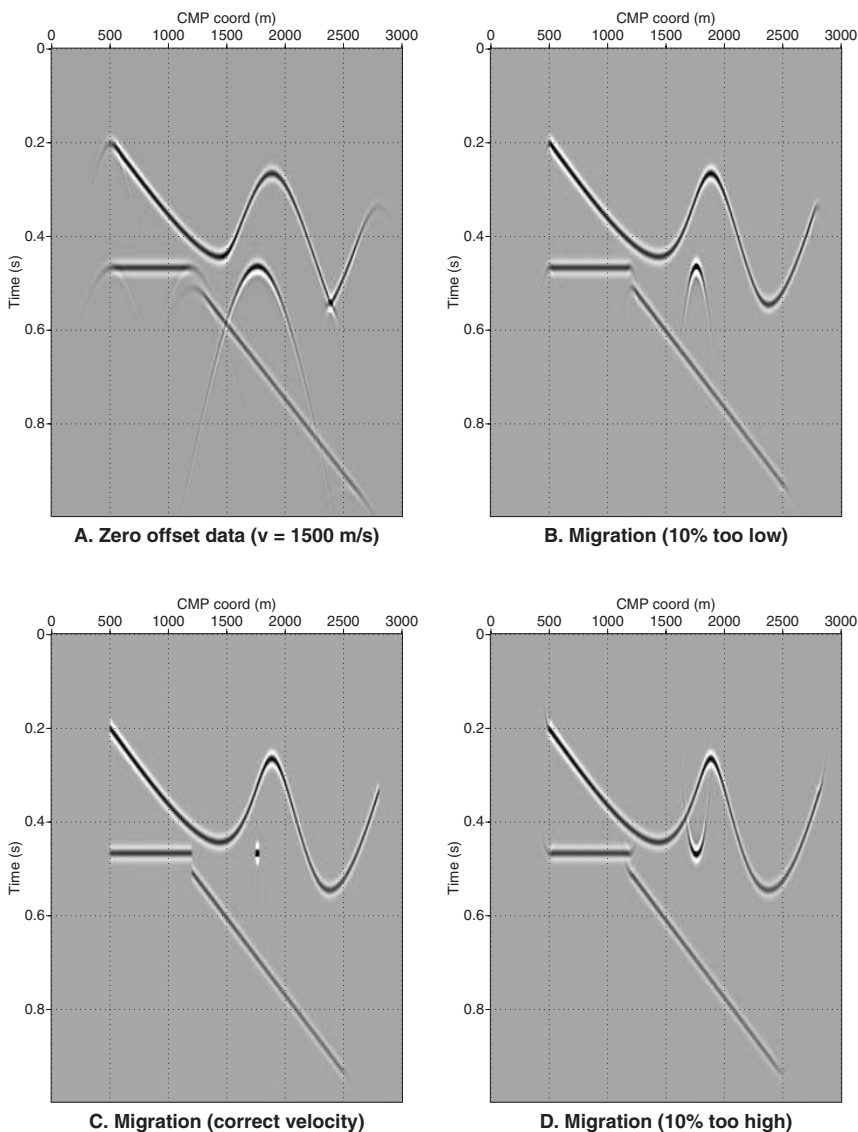


Fig. 18.5 Sensitivity of poststack migration to velocity error. (A) Constant velocity zero offset data (1500 m/s). (B) Poststack migration with too low a velocity leaves residual diffractions indicative of under-migration. (C) All features are in focus after migration using the correct velocity. (D) If the velocity is too high, the data is over-migrated resulting in characteristic migration smiles.

diffractors (650 m and 800 m) using a velocity of 4000 m/s. When this data is pre-stack migrated at 3000 m/s an output CIG, Figure 18.6A, shows residual curvature and depth error. In the CIG domain the migrated depth [213] is given by

$$z_m = \sqrt{\beta^2 z^2 + (\beta^2 - 1)x^2} \quad (18.6)$$

where  $x$  is the offset,  $\beta=v_m/v$ , and  $z$  is the true depth. Note that for zero offset this reduces to the equation given above.

Migration with the correct velocity gives a CIG, Figure 18.6B, in which the events are flat and correctly positioned in depth. If the migration velocity is 5000 m/s the CIG, Figure 18.6C, shows downward residual curvature and depth error. To summarize, in the CIG world too low a migration velocity causes a shallow smile, and too high a velocity gives a deep frown. CIG flattening is probably the most common form of prestack depth migration velocity analysis in use today.

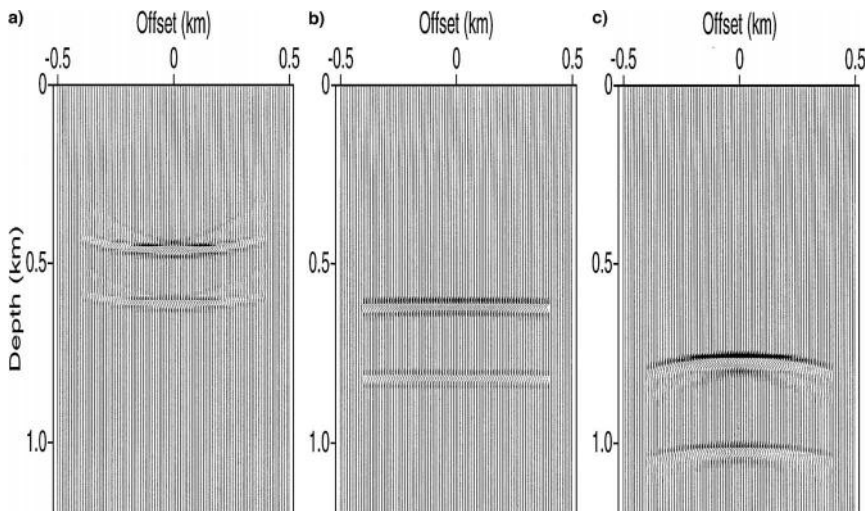


*Fig. 18.6 Sensitivity of prestack depth migration common image gathers (CIGs) to velocity error (from [213]). The data (not shown) was created using a velocity of 4000 m/s over an earth model consisting of two point diffractors 650 m and 800 m deep. (A) CIG after migration using 3000 m/s. Note residual curvature (smile) and depth error. (B) Migration at correct velocity results in CIG events that are flat and correct in depth. (C) Using 5000 m/s to migrate the data gives CIG events that are too deep and show residual downward curvature (frown).*

# 19

## Historical Perspective

### 19.1 Progress in seismic processing

It seems appropriate to pause and consider progress in seismic data processing during the last couple of decades. The first thing to consider is the scope of the assignment. In the last 20 years there have been 267 monthly or bimonthly issues of the journal *Geophysics*, which can be used as a gauge of progress. Conservatively estimating 10 papers per issue related to seismic topics, it follows that something like 2700 individual papers span the period. Any thought of a detailed account must be abandoned. We will touch here on the first order advances in seismic data processing, those things that have changed the way work is done around the world every day.

First a distinction. By seismic data processing, we mean any computational technique that attempts to remove noise or wave propagation effects in order to create an image of the subsurface. Once this image is created, there is another universe of methods to mine the data for further information. Examples include attribute analysis, coherency, AVO analysis, etc. While these image processing and extraction methods are very important, they are not properly in the scope of this chapter. Similarly the entire field of seismic inversion is a topic important but separate.

**19.1.1 Dip moveout.** By 1982 the broad outlines of prestack migration were taking firm shape. But even for 2D, the problem was beyond existing computer power. Furthermore, prestack migration was already known to be very sensitive to velocity errors, meaning that more than one pass of prestack migration was needed.

One approach to deal with this difficulty was to decouple the prestack migration process into separate steps. In this view, prestack migration was normal moveout, followed by a mystery process, followed by common midpoint stacking, followed by poststack migration. The mystery process had the obligation to do whatever was necessary in order for this decoupled processing flow to give precisely the same results as prestack migration. It was unreasonable to expect the results to match in complex terrain or situations with strong lateral velocity variations, but under mild conditions the goal seemed achievable.

## Elements of 3D Seismology

Since the detailed history of DMO is discussed later, we only note here that a working commercial implementation was available by 1978, and DMO was in general use by 1984. During the next two decades, DMO progressed to include velocity variation (vertical and lateral), mode conversion, anisotropy, and 3D implementation.

Some migration purists see DMO as a trick—an annoying distraction of resources and effort that should have gone into the real problem of prestack migration. Perhaps. But DMO served a definite purpose in bridging the gap between 1980-era computer power and the computational needs of prestack migration. If the subsurface is well-behaved, DMO is a perfectly valid process. It was a major data processing milestone and is still in routine use today.

**19.1.2 Anisotropy.** The tendency of seismic waves to have directional velocity was well known 50 years ago, and the theory was worked out in detail 50 years before that. But the fact is that anisotropy was profoundly ignored in seismic data processing until the late 1980s.

Why? Anisotropy is an elastic effect. It seemed unlikely you could do anything to estimate it or remove its effects without measuring three component data to observe the full elastic wavefield. The effects of anisotropy were generally considered in terms of shear waves—shear wave splitting, polarization, etc. But there was very little shear wave work ever done, at least relative to the amount of standard P-wave work.

There was a flurry of S-wave enthusiasm in the 1970s when it seemed that shear wave data held a promise of higher resolution, something potentially worth the cost of shooting multicomponent data. This was based on the fact that S-wave velocities are about one-half those of P-waves, so at similar frequencies the shear wavelength should be about half of the P wavelength. Sadly, nature did not cooperate. Higher shear wave attenuation caused S-waves to come in with about half the expected frequency for no net improvement in resolution. So life went on as before.

This changed in 1986 when Thomsen demonstrated that anisotropy influences P-wave data that we had been processing for 60 years. Furthermore, a clean, well-defined set of anisotropy parameters were proposed, which made immediate sense to everyone. This is one of those happy points in time where someone deeply understood a problem, wrote clearly about it, and gave the world something we could actually use. Once you look for it, anisotropy is everywhere. The important thing is this—if the subsurface is significantly anisotropic and you process your data assuming it is not, then the image you get is degraded. Then amplitudes are wrong, reflector segments are not at the right depth or the right lateral location, fault terminations get smeared, and so on. The interpreter can be compromised by the processor's isotropic worldview.

Since 1986 there has been an enormous amount of work describing

- the types of anisotropy we are likely to encounter
- how to exploit anisotropic effects in P-wave data
- how to estimate anisotropy parameters from surface seismic data

We now have anisotropic NMO, DMO, and migration with more algorithms coming out monthly. But caution is in order, because as we have seen in the case of NMO velocity analysis, it is difficult to distinguish P-wave anisotropy effects from the generally stronger effects due to lateral velocity variation.

**19.1.3 The 3D processes.** While this discussion is about processing, we understand that advances in acquisition drive data processing changes. The last two decades have seen the development of many important acquisition techniques—crosswell, bottom cable, telemetry, ocean bottom seismometer, vertical cable, etc. But no acquisition change was bigger than 3D. The roots of 3D shooting stretch all the way back to the 1930s but there was only so much that could be done before computers. The situation changed in the mid-1980s when 3D became the industry standard.

Many processes developed for 2D data were applied straight away to 3D. These were mainly single-channel processes (one trace in, one trace out), which required no substantial modification for 3D work. But the multichannel processes were a different story. Normal moveout, for example, might seem to be the same in 2D and 3D. After all, it just applies a transformation to the time axis based on source-receiver separation. But what if NMO is applied to a trace with 2000 m of offset in the E–W direction, then to another with 2000 m offset in the N–S direction? Although 2D NMO does not distinguish these cases, 3D NMO allows for the possibility that velocity is a function of azimuth.

NMO is just one example. We could also mention DMO, migration, surface consistent processes (statics, deconvolution), multiple suppression (a huge problem), and velocity analysis of various kinds. In addition to the thorny issues of understanding how such processes should work in 3D, there is the sheer trace count. A big 3D seismic survey in 1984 would have something less than 2 million traces; a large one today has something more than 2 billion. A thousand-fold increase in 20 years.

By way of comparison, Moore's Law states that the number of transistors on a printed circuit will double every 18 months, and as the transistors go, so goes the speed. Curiously this 1964 law gives a good fit to computing changes right through today. The last 20 years have seen 13 intervals of 18 months, so whatever the computer speed was in 1984 it is now  $2^{13}$ , or about 8000, times faster. Sounds great. We have 1000 times more data and are processing it with computers 8000 times faster so everything should be done in one-eighth of the time it took in 1984.

## Elements of 3D Seismology

But speed is only part of the computer situation. There is also memory, disk space, networking, and dealing with massively parallel architectures. In fact, our data processing needs far outdistance available computer power and they always have. What we would like to do in a minute can take hours or days. This situation is unlikely to change. As compute power increases, we will be applying ever more sophisticated seismic processes to ever larger data sets.

**19.1.4 Depth migration.** If we are to limit discussion to the last 20 years, then we must consider that migration was a mature seismic process in 1984. Seismologists knew about lateral positioning errors almost as soon as people started shooting data. There was important work in the 1950s by Hagadorn and others. In the early 1970s Claerbout worked toward a comprehensive view of what migration was and how to do it. Then the great foundation papers came in 1978—Kirchhoff migration by Schneider, phase shift migration by Gazdag, and F-K migration by Stolt. The first and third were 3D, while the third also developed prestack migration.

The big advances of the 1980s were in the field of depth migration, particularly prestack depth migration. The need for this technology arose from the failure of traditional techniques. A processing flow of NMO, DMO (after 1984), common midpoint stack, and poststack migration, gives a satisfactory image for much of the world.

But exploration was pressing into deeper water, snooping around salt overhangs, testing subsalt rock formations, dealing with extreme topography, and trying to image overthrust areas. All these cases involve significant 3D lateral velocity variation. When things get tough enough, everything is a migration problem. Under these extreme conditions, the decoupled processing flow simply fails to provide a geologically meaningful image, and prestack depth migration is needed.

Standard processes are ultimately based on constant velocity physics or perhaps  $v(z)$ . In a continuum of progress, the migrators have incorporated more and more physics into the migration process—anisotropy, 3D shooting geometry, and strong variations in  $v(x,y,z)$ . There has been remarkable theoretical progress in finding new ways to implement migration—various Fourier domains, finite difference (including reverse time), Gaussian beams, screen propagators, and the venerable time-space domain Kirchhoff migration.

As mentioned earlier, Kirchhoff depth migration is the dominant technique in use today, perhaps because of its superior ability to accommodate arbitrary  $(x,y,z)$  coordinates for each source and receiver. Increasingly during the late 1980s and early 1990s, the burden of traveltime computation was spun off from Kirchhoff migration and sequestered in ray tracers of every increasing complexity. Radiation patterns, attenuation, various elastic wave phenomena, anisotropy, multipathing, and whatever else we think is important can ultimately

be worked into the ray tracer. The migration program itself begins to look more and more like a database to match up traveltime tables and amplitudes.

The last two decades deserve to be remembered as the foundation age of seismic depth migration. Progress will continue, but the foundation is only built once.

## 19.2 A brief account of dip moveout

In addition to general comments about progress in seismic processing, it is useful to give one detailed account. We take dip moveout as the subject.

You can talk about NMO all day long without mentioning migration. DMO is another matter. In fact, an early version (1979) of DMO had the cumbersome, but descriptive, title of prestack partial migration. But at least a year earlier, there was a DMO processing product on the market. It was named DEVILISH an acronym for Dipping Event Velocity Inequality Licked.

DMO is a good example of how progress is made in seismic processing. The development is very recent and to put things in perspective, Table 19.1 gives a rather detailed chronology of major advances in DMO. We could make a similar table for migration or any number of other processes.

The first column in Table 19.1 is a shorthand notation for the achievement followed by the authors and publication dates. Since DMO progressed so quickly, most advances were first given as abstracts at national geophysical meetings. But these abstracts did not all show up later as peer reviewed publications. In such a case, we also list the first published author on the subject. For a detailed account of the early history of DMO, the interested reader is referred to the excellent summary in Hale [88].

At certain times, there were several authors who simultaneously presented key advances. This happened in 1984 with respect to 3D, in 1988 for amplitude preservation, and in 1990–91 for vertical velocity variation. These cases are denoted in the table by the entry “several.”

This table is not comprehensive. The geophysical literature contains more than 200 references to DMO in some form or another. Every effort has been made to confirm the claimed priority for each advance and any remaining errors reside with the author.

**19.2.1 Dip moveout just isn’t normal.** During acquisition, a source and receiver are some distance apart (the offset), and a prestack trace is recorded. From earlier discussions, we know that NMO removes offset from prestack data. In the computer, we adjust the trace to simulate one that would have been recorded at

## Elements of 3D Seismology

the midpoint half-way between the source and receiver. This new trace is a zero-offset trace, and stacking all such traces that live at this midpoint yields a stack trace. All the stack traces plotted side by side form the stack section, which is raw material for poststack migration processing.

<i>Advance</i>	<i>Authors</i>	<i>Meeting Abstr.</i>	<i>Publication</i>
DMO	Judson et al.	1978	
DMO ellipse geometry	Deregowski and Rocca		1981
Widespread use	Hale	1983	1984
Shot record	Biondi and Ronen	1986	1987
Inverse DMO (amplitude preserving)	Ronen Liner and Cohen	1988	1987
Amplitude preserving	several Sorin and Ronen	1988	1989
Anisotropy	Uren and Gardner		1990
3D	several	1984	1991
Wave equation amplitude	Jorden Liner	1987	1991
Mode converted	Harrison Alfaraj and Larner	1990 1991	1992
Linear $v(z)$	several Dietrich and Cohen	1990 1992	1993
General $v(z)$	several Hale and Artley	1991	1993
Anisotropy + $v(z)$	Larner and Hale Larner	1992	1993
<i>Algorithms</i>	<i>Authors</i>	<i>Meeting Abstr.</i>	<i>Publication</i>
Finite difference	Yilmaz and Claerbout		1980
Offset continuation	Bolondi et al.		1982
Log stretch	Bolondi et al.		1982
$f-k$ domain	Hale	1983	1984
$t-x$ domain	Berg	1984	
	Hale		1991
Dip decomposition	Jakubowicz	1984	1990
Before NMO	Forel and Gardner		1988
$t-x$ shot record	Hearn	1989	
General coordinates	Liner		1990
Finite difference shot record	Pleshkevitch	1994	
Radon domain	Wang	1995	1999

Table 19.1 Summary of progress in dip moveout. Unless otherwise stated, the advances are related to the common offset implementation of DMO.

Figure 19.1 is another view of the NMO idea. On the left is a field trace with one reflection event. NMO assumes the reflection comes from a horizontal interface as shown in the middle figure. This is an important and restrictive assumption. The NMO correction adjusts observed traveltimes (dashed path) to zero-offset traveltimes as seen from the midpoint (solid path). During NMO, the event is moved up in time, but is not moved across traces. Technically, we are changing time coordinates from raw time,  $t$ , to NMO time,  $t_{nmo}$ .

But what if the interface is not horizontal? All we know is the reflection time, and it is tempting to think that the reflecting point could be anywhere. But this is not the case. Suppose the original traveltimes is 1 s, and we know the velocity is 3000 m/s. The total distance traveled has got to be 3000 m. So all valid reflector positions have one thing in common. The total distance from source to reflection point to receiver is constant, namely 3000 m. As we have mentioned in an earlier discussion of prestack migration, this is just the definition of an ellipse with the source and receiver at each focus. Figure 19.2 shows such an ellipse.

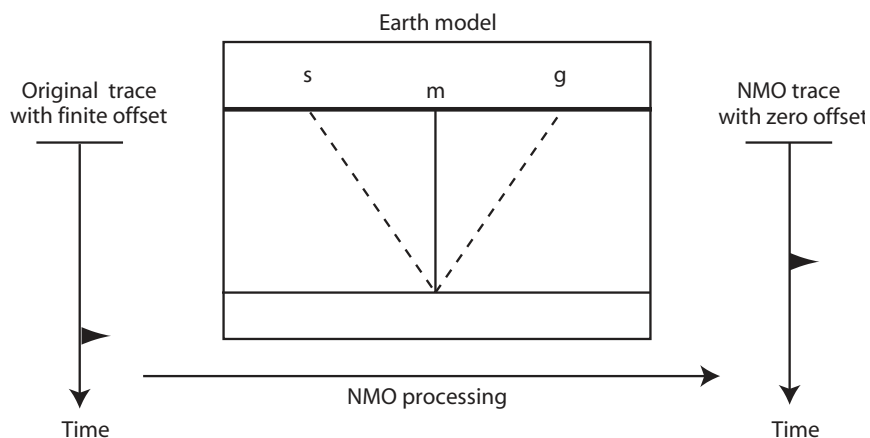


*Fig. 19.1 NMO is a process applied to prestack data. Here the effect is shown on a single trace with one reflection event (left). NMO assumes that the reflection comes from a horizontal interface in the earth (center). Using a velocity function supplied by the processor, NMO adjusts the original time (dashed) to that which would have been observed at the midpoint. The solid path is two-way time down and back, which must be less than traveltimes along the dashed path. So the job of NMO is to move the reflection event up the trace (right). Note NMO operates on one trace at a time, which makes it inexpensive.*

## Elements of 3D Seismology

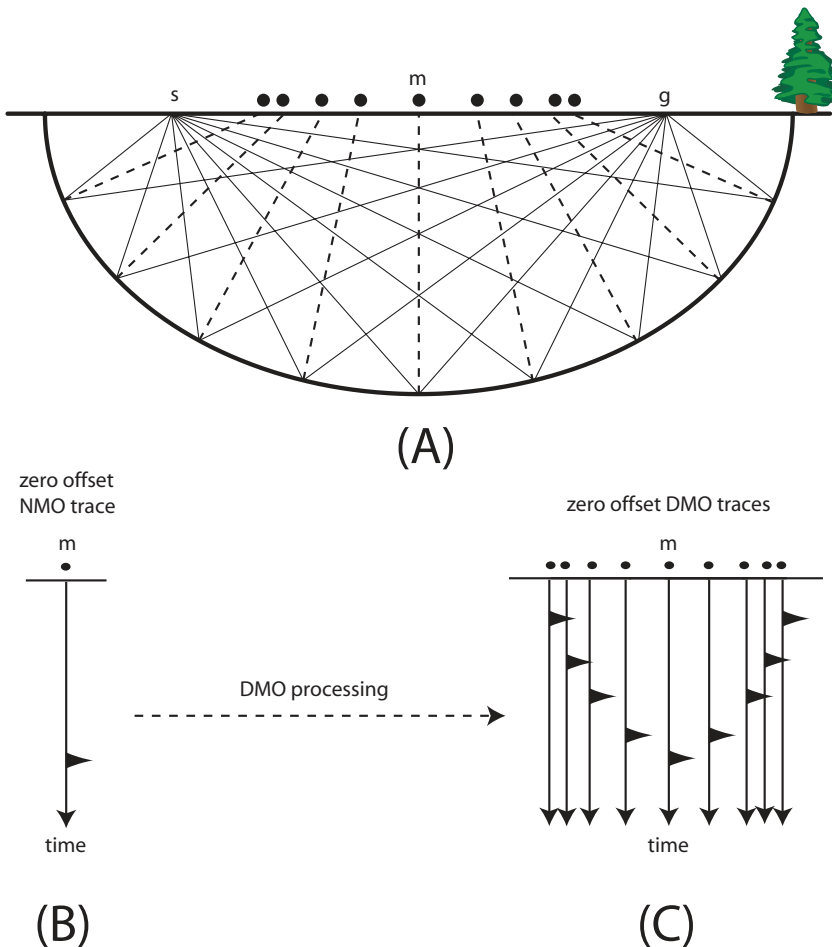


*Fig. 19.2 DMO is a process which is applied after NMO. (A) Prestack geometry showing the original shot location (*s*) and receiver location (*g*). For one trace with one reflection event, all possible travel paths (solid rays) have the same length from source to reflection point to receiver. The geometrical shape with this property is an ellipse with source and receiver at the foci, the prestack migration ellipse. Each dot is a possible zero offset trace location associated with a zero offset ray (dashed). NMO assumes the reflector is horizontal (vertical dashed path), while DMO does all the other cases (nonvertical dashed paths). (B)–(C). The action of DMO is to take the NMO corrected event and broadcast it across several nearby traces along a time curve, which is the DMO impulse response. This means DMO is a multichannel process and therefore expensive.*

Remember the goal is to remove offset and thus create a zero offset section. NMO gives one of many possibilities and DMO gives all the rest. In Figure 19.2A, some of the possible original travel paths are shown as solid lines along with the single travel path after NMO (dashed vertical), and the many travel paths after DMO (dashed nonvertical). The source ( $s$ ) and receiver ( $g$ ) locations are shown, as well as the midpoint ( $m$ ). Each dot is a zero offset location (there are many more of these than shown). Only beneath the midpoint location does the ellipse have zero dip. NMO calculates the zero offset time at this location. The traveltime curve in Figure 19.2C is determined from the dashed zero offset raypaths in Figure 2A. Note that at the midpoint DMO does not change the NMO time but away from the midpoint it does.

From Figure 19.1 we saw that NMO is a process that takes one trace in and gives one trace out. DMO is different. One trace into DMO generates many traces out—all of which live between the original source and receiver locations.

Consider Figure 19.3A showing a common offset section containing two filtered amplitude spikes on one trace. The other traces are there but have no amplitude values on them. Every trace in this section has an offset of 800 m, so we can consider the live trace to have its source at the tickmark labeled 0 and the receiver at 800. The effect of NMO is to move the spikes shallower on the same trace but not to move energy between traces. Note the time axis now represents NMO time, meaning that NMO is really a coordinate transformation of the time axis from raw time to NMO time.

DMO of the data in Figure 19.3B throws each spike out along an ellipse with surface intercepts at the source and receiver positions, thus the DMO impulse response only lives between the source and receiver. This is sometimes called the DMO smile. An important feature of constant velocity DMO is that the DMO smile is still a 2D object, even when DMO is applied to 3D data. In other words, the DMO operator in 3D is like a sagging wire that hangs between the source and receiver surface locations.

There is a lot of important action in the second row of Figure 19.3. If the raw spikes in Figure 19.3A are prestack migrated, then we generate the prestack migration impulse responses in Figure 19.3D. In 3D these curves would become ellipsoidal bowls as discussed earlier. If the NMO data Figure 19.3B is thrown directly into poststack migration, we get the result Figure 19.3E.

Poststack (zero offset) migration is supposedly appropriate because NMO has removed the effect of offset. But actually, NMO has done the right thing only for zero dip beds. Therefore, the migrated result, (Fig. 19.3E), only agrees with the correct result, (Fig. 19.3D), at the bottom of each ellipse where the dip is zero. The combination of NMO+DMO removes offset in a way that is correct for all dips.

## Elements of 3D Seismology

So poststack migration of the NMO+DMO data is the same as prestack migration of the raw data. Note the times at which the spikes occur in Figure 19.3B coincide with the bottom of all the ellipses in Figure 19.3C–E. This is another way of saying that DMO and migration do not adjust traveltimes in the case of zero dip.

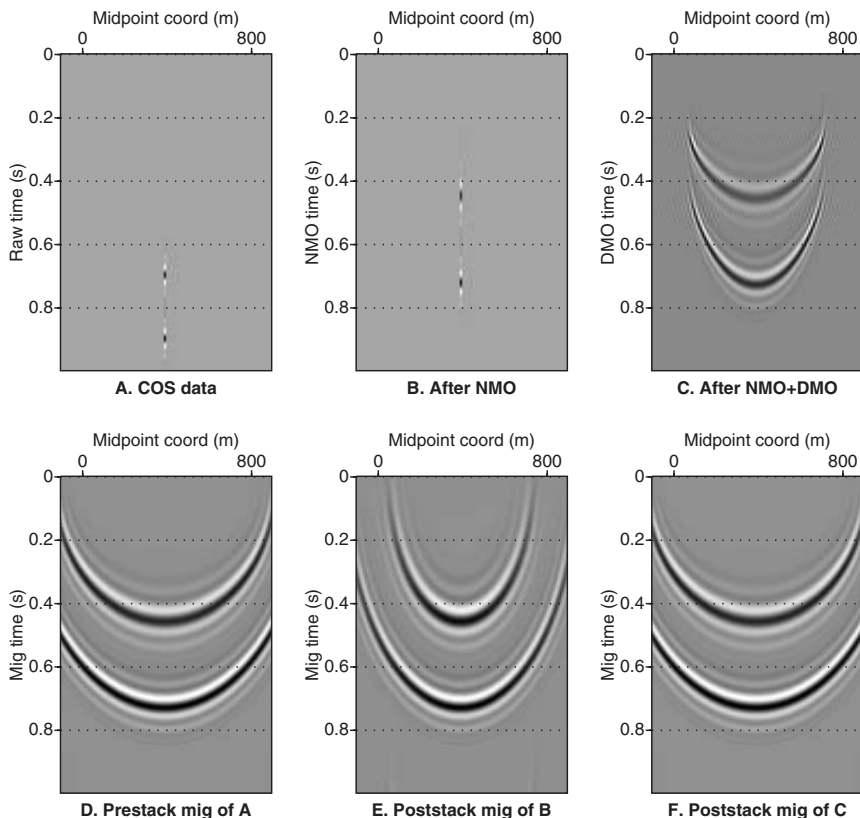


*Fig. 19.3 Numerical example illustrating the effects of NMO, DMO, and migration. (A) Common offset data with two spikes on the center trace. The source and receiver locations for the live trace are at (0,800). (B) NMO shifts the spikes up in time on the same trace. (C) DMO throws the NMOd spike amplitude out along a curve to handle all possible dips. This curve is called the DMO smile (or ellipse, or impulse response). Notice the DMO smile only lives between the original source and receiver positions. (D) Prestack migration of the raw data gives the correct prestack migration impulse response. This is an ellipse with source and receiver at the foci. (E) Poststack migration of the data after NMO is not correct except for zero dip. (F) Poststack migration of the data after NMO+DMO gives the same correct result as D.*

In summary, panels D and F in Figure 19.3A are identical because in the constant velocity case prestack migration is equivalent to NMO followed by DMO followed by poststack migration. More on that later.

Now here is some magic. By creating the DMO smile, all possible dips are handled simultaneously. We do not need to know what the dip is in the earth. By processing all traces with DMO, the actual reflections will emerge in their correct zero offset locations because they are tangent, at some point, to DMO smiles.

DMO is nearly independent of the velocity so long as the velocity is constant. Specifically, velocity only determines the shallowest time along the DMO ellipse. This is one of the things that initially excited everyone about DMO. Its weak dependence on velocity is one reason it is still so widely used. This is unlike NMO and migration, which need detailed velocity information and are quite sensitive to it.

Figure 19.4 is another way of showing how DMO works. Imagine a single spike of amplitude on a 2D common offset section. The effect of DMO is to

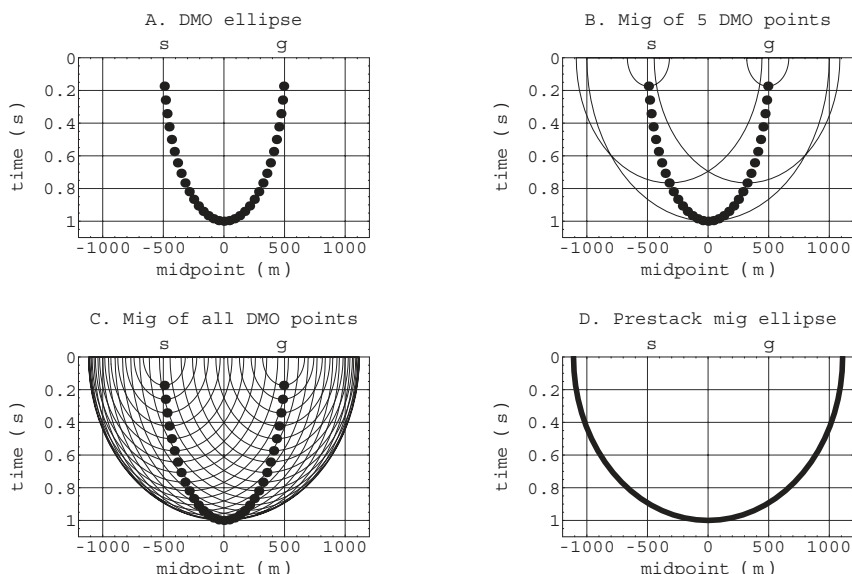


Fig. 19.4 How DMO and poststack migration work together in a constant velocity situation. (A) The dots represent the DMO ellipse for a trace whose source (s) and receiver (g) are shown. (B) Poststack migration has been applied to five of the dots. Each migrated dot spawns a semi-circle. (C) All DMO dots have been poststack migrated. The resulting migration curves are tangent to the prestack migration ellipse. In real data, wavelets (instead of lines) cause interference that tends to reinforce along the outer curve and cancel at interior points. In effect, we will only see the outer curve. (D) The prestack migration impulse response.

broadcast this spike along the DMO smile shown with dots. In Figure 19.4 B, we poststack migrate only five of the DMO dots to see what happens. Each of the five dots spawns a semi-circle and, in Figure 19.4 C, all the DMO dots are migrated. The poststack migration curves are tangent to yet another curve—the prestack migration ellipse. In real data, the interior points would tend to cancel, leaving only the perimeter curve. The migration curves are said to osculate and form the outer curve.

**19.2.2 Velocity variation.** Early researchers understood that DMO is not quite independent of velocity. But the constant velocity formulation improved data so much compared to just using NMO that processors did not worry much about velocity variation.

The effect of vertical velocity variation depends on the strength of the velocity gradient. When the velocity is a weak function of depth, the DMO impulse response is squeezed narrower than the constant velocity version. This small gradient effect is illustrated in Figure 19.5.

The squeezed DMO ellipse is still a 2D object stretching like an elliptical wire between the source and receiver. But as the velocity becomes a significant

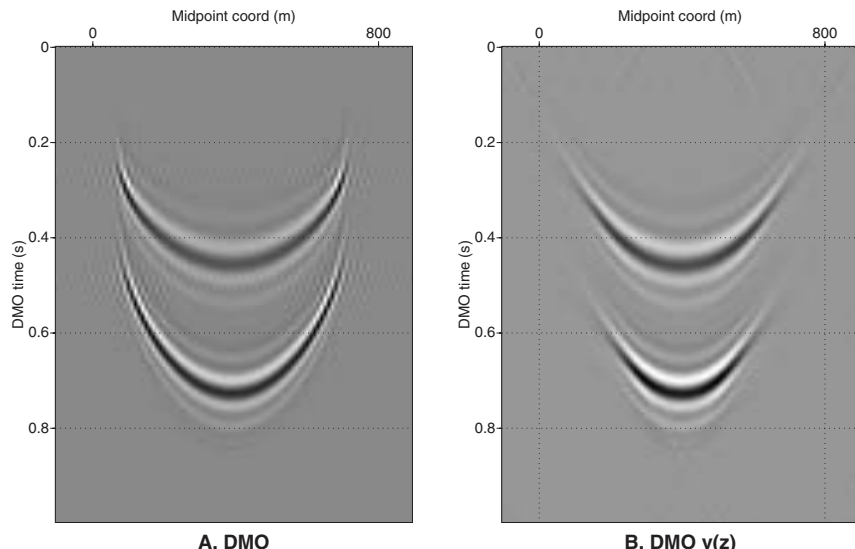
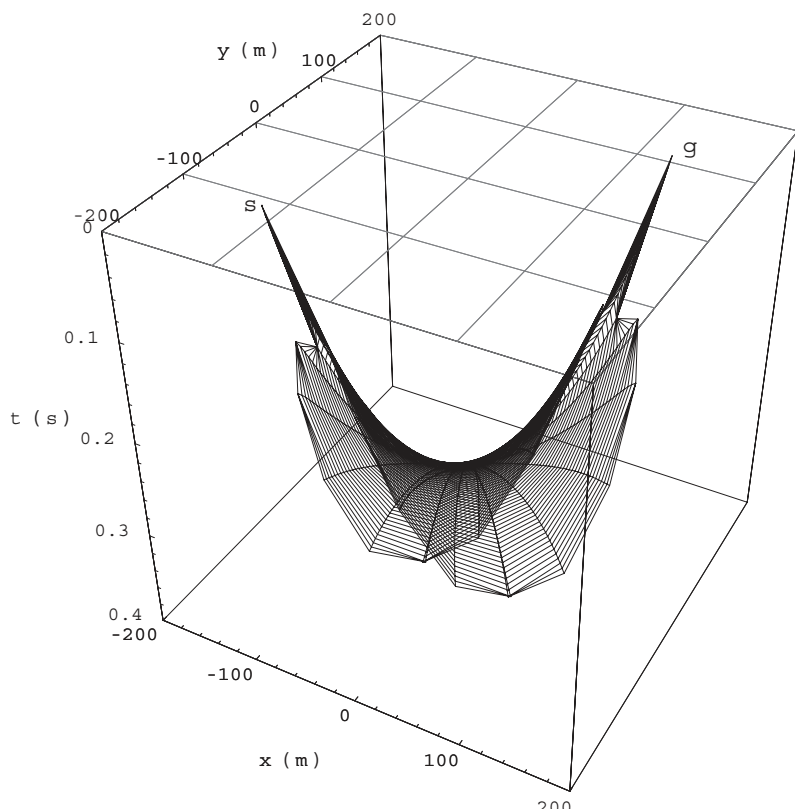


Fig. 19.5 The effect of weak vertical velocity variation on the DMO impulse response. (A) Constant velocity DMO ellipse. (B) For small vertical velocity variation the effect on DMO is to squeeze the ellipse a bit narrower.

function of depth, the DMO ellipse begins to spread in the direction perpendicular to the source-receiver azimuth, becoming a saddle-shaped 3D operator [129]. Figure 19.6 is an attempt to show this 3D DMO saddle. It is not hard to imagine that spreading data over a 3D saddle is much more expensive than spreading along to a 2D wire.

Most people who talk about velocity variation and DMO are referring to vertical velocity changes. If there are strong lateral changes, then DMO becomes about as expensive as prestack depth migration. So most people do not bother with DMO in that situation.



*Fig. 19.6 When strong vertical velocity variation is present, the DMO operator is no longer a 2D wire stretching from the source to receiver. Rather it spreads out to become a saddle-shaped 3D operator. This causes DMO to become more expensive. (Redrawn from graphic data provided by Craig Artley)*

**19.2.3 Anisotropy.** As we have seen, anisotropy is a general effect that causes seismic waves to propagate at different speeds depending on the direction of travel. From Figures 19.1 and 19.2, it is clear that NMO and DMO involve rays traveling at various angles. If anisotropy is present, then both processes need to account for it.

Recall that NMO moves events up on the same trace. The anisotropy effect on NMO is to move these events up a different amount, but they are still confined to the same trace. NMO is affected by anisotropy but not drastically.

DMO is a different story. It has a much more intimate relationship to dip and steep ray angles than does NMO. Anisotropic DMO is controlled by a parameter called eta,  $\eta$ , which can range from about (-0.2,+0.2) with  $\eta=0$  being the isotropic case. Figure 19.7 gives a fair idea of the situation. Figure 19.7A illustrates common offset spikes. Applying isotropic DMO gives the usual DMO impulse response.

Negative  $\eta$  generates the data in Figure 19.7C, which shows the DMO smile is broader than the isotropic impulse response. For positive  $\eta$ , Figure 19.7D, the result is a drastic departure from the isotropic case. The operator is narrower, more angular, and shifted up in time.

It seems fair to say that anisotropy has a stronger influence on DMO than mild vertical velocity variation. But this can reverse if the  $v(z)$  is drastic enough to warp the DMO operator into a 3D saddle. In the real world, velocity variation is always present and cannot be ignored. If anisotropy can be demonstrated to exist, then it too must be dealt with to generate the best possible image.

As a final comment on DMO, we note that when subsurface conditions become too extreme, decoupled processing fails to give a reliable migrated image. The good news is that we have a single grand process called prestack depth migration to use in this situation. The bad news is that it costs more than all the decoupled processes combined, including DMO (See Fig. 14.5).

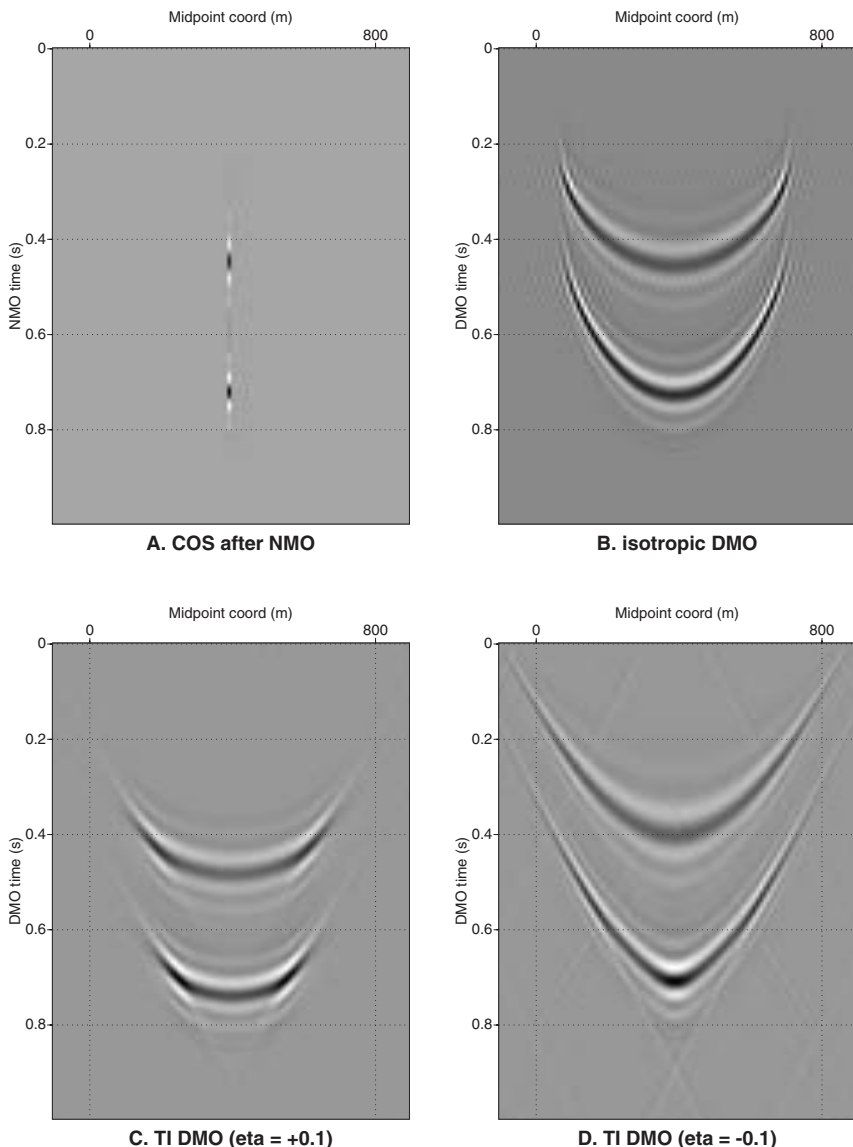


Fig. 19.7 DMO and anisotropy. (A) Common offset section with one live trace containing two filtered spikes. (B) Isotropic DMO impulse responses. (C) Anisotropic DMO with positive  $\eta$  gives a broader impulse response that is not shifted very much in time. (D) Negative  $\eta$  causes DMO impulse response to shift dramatically in time and become narrower.

## Part V

*Interpretation:  
Extracting Geologic Information  
From Seismic Data*

# 20

## Synthetic Seismogram, Tuning, and Resolution

### 20.1 Creating the synthetic seismogram

A seismic source initiates a wavefield that interacts with the earth. The waves are partially transmitted and will never return to be measured by receivers at the earth's surface. But part of the wavefield is reflected and returns to the surface. The measured field at the surface is the seismic response of the earth at that location. The fundamental problem addressed in seismic modeling, or simulation, is calculation of the seismic traveltimes and amplitude response for a given earth model and recording geometry.

We know from earlier chapters that the earth model consists of those physical properties that influence seismic wave propagation. For an elastic earth, these include compressional wavespeed, shear wavespeed, and mass density. For an acoustic earth model, we only need a sound speed and mass density.

All 1D seismic concepts are still present and important in 2D seismic work, which in turn underlay 3D seismic. At the heart of 1D seismic are well logs and the creation of a synthetic seismogram (or simply synthetic) for seismic event identification and depth conversion [146]. If a vertical seismic profile is available for a particular well, then a synthetic seismogram is not needed. The VSP gives direct measurement time, depth, and waveform. An alternative to a full synthetic is to convert a sonic log to time and velocity then directly overlay this on the seismic data. A third possibility is to overlay impedance in this way.

The purpose of 1D simulation is to create the zero offset seismic trace that theoretically would have been recorded at a well location based on logs recorded

## Elements of 3D Seismology

in the well. This trace is the synthetic seismogram. The assumptions that underlie a standard synthetic seismogram are

1. the source and receiver are coincident at the well location
2. the geological dip is zero
3. the well bore is vertical
4. velocity, density, and depth log readings are accurate
5. the velocity field varies only with depth

Of these assumptions, the most difficult to justify in many situations is number two because the subsurface has significant structure. In such a case, we compute the synthetic as outlined below, even though Snell's law says that downgoing rays would bend away from the vertical well bore. This means the synthetic vertical traveltimes are not physical traveltimes. But if the field data at the well location has been properly migrated, it will also represent vertical traveltime which can be tied to the synthetic.

**20.1.1 Earth model.** A  $v(z)$  velocity model is needed to create a synthetic or convert other well information from depth to time. This velocity information can come from a variety of sources. These can be listed in order of preference.

1. **VSP.** A vertical seismic profile (VSP) is recorded by using a source at the surface and many receiver locations down the well. The receivers record full traces for interpretation and receiver spacing is determined by spatial aliasing considerations, usually something like 3 m. This gives actual traveltimes from the surface to points in the earth. It is the best and most direct method of associating seismic events with geologic horizons. The VSP considered here is relatively inexpensive, and often called a zero offset VSP, meaning that only a single source position is used and that it is as close to the wellhead as possible. There are also multioffset and multiazimuth VSPs which use many source locations. These are much more expensive and sometimes useful for local, high resolution imaging. However, a zero offset VSP is sufficient for event identification and other standard uses.
2. **Sonic log with checkshots.** A checkshot survey is sort of like a baby VSP. The receivers are sparsely placed down the well, usually on key geologic boundaries. The measured quantity is just the first arrival time, unlike the full trace recorded in a VSP. The checkshots are used to correct for any drift due to missing log intervals or hole problems. This makes the calculated traveltimes more reliable.
3. **Sonic without checkshots.** Sonic logs provide good local velocity information but are prone to drift when converted to traveltime due to hole problems during sonic log acquisition.

4. **Checkshots without sonic.** Checkshots provide very coarse velocity information, perhaps five or six traveltimes for the entire well. This is generally useful only to identify a few key reflectors, certainly not suitable to build a detailed subsurface model for use in a synthetic seismogram.
5. **Processing velocities.** This kind of velocity information tends to have a large margin of error and be sampled too coarsely in depth for use in making a synthetic seismogram.

In summary, a zero offset VSP is the best way to directly relate seismic events to geologic horizons. If one is not available, then a sonic with checkshots can be used to create a synthetic.

Density information also contributes to the production of a synthetic. Although density can be estimated from sonic if the local lithology is known, independent density information is preferable (e.g., from a neutron density log).

The earth is assumed to consist of a stack of horizontal layers. Figure 20.1 shows the numbering scheme for layers and interfaces.

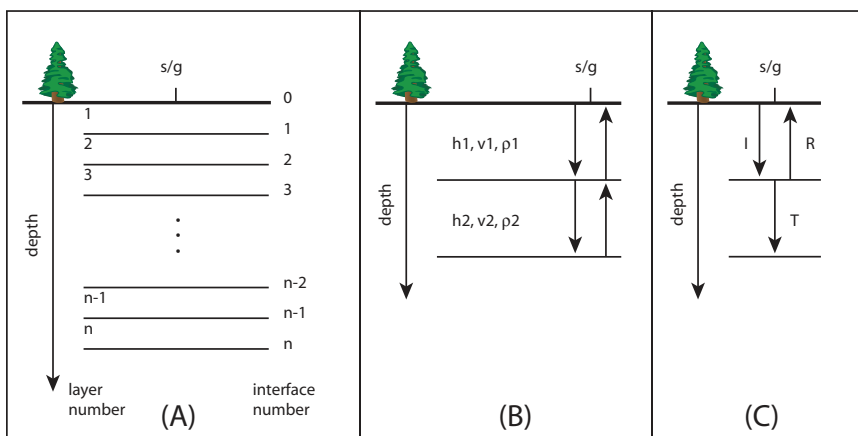


*Fig. 20.1 (A) Earth model for 1D seismic simulation. (B) Detail of top two layers showing that each has three parameters: thickness ( $h$ ), velocity ( $v$ ), and density ( $\rho$ ). From this we can calculate reflection times and reflection coefficients. (C) Detail showing the concept of incident ( $I$ ), reflected ( $R$ ), and transmitted ( $T$ ) waves.*

## Elements of 3D Seismology

A sonic log typically operates with a depth sampling rate of five samples per meter, so there can be many thousands of layers in a sonic-derived layered velocity model. The measured quantity in a sonic log is reciprocal velocity (or slowness) in units of microseconds per foot ( $\mu\text{s}/\text{ft}$ ), which can be converted to m/s using

$$v \text{ (m/s)} = \frac{304 \text{ } 800}{sonic \text{ } (\mu\text{s}/\text{ft})} \quad (20.1)$$

**20.1.2 traveltimes.** The source sends energy out in all directions, but we are only interested in the part that returns to the receiver. Since offset is assumed to be zero, the source and receiver are at the same point on the earth surface. We begin by calculating reflection time to the first interface. The general relationship for traveltime is

$$time = \frac{distance}{velocity} = \frac{d_1}{v_1} + \frac{d_2}{v_2} + \frac{d_3}{v_3} + \dots \quad (20.2)$$

where the second form allows for breaking up the distance into constant velocity segments. This is like estimating driving time—you go 30 km at 60 kph, then 60 km at 80 kph, etc. Total driving time is just the sum of the segment times. Applying the general formula to reflection from interface 1 gives

$$t_1 = 2h_1/v_1 \quad (20.3)$$

where the thickness of layer 1 is  $h_1$  and its velocity is  $v_1$ . To calculate reflection time from interface 2, we segment the distance into two parts and find

$$t_2 = 2h_1/v_1 + 2h_2/v_2 = t_1 + 2h_2/v_2 \quad (20.4)$$

Note that the last form shows we need find  $t_1$  only once and can reuse it for calculating  $t_2$ . Mathematically this is called a recursion and is computationally very efficient. From here we extend easily to reflection from the next interface and the general case for the  $n$ th interface

$$t_3 = t_2 + 2h_3/v_3 \quad (20.5)$$

$$t_n = t_{n-1} + 2h_n/v_n \quad (20.6)$$

In this way, we find a reflection time associated with each interface. Figure 20.2B shows that these are markers down the seismic trace we are constructing, but what do we put at each time?

**20.1.3 Reflection coefficients.** Notice that the previous traveltime calculation does not involve the density. We are effectively making a sound with the source and waiting for the echo to come back to the receiver. The time delay depends only on thicknesses and velocities. But density does play a role in determining the strength of the echo. As discussed in chapter 3.2.2, normal incidence reflection is associated with a reflection coefficient given by

$$R_0 = \frac{\rho_2 v_2 - \rho_1 v_1}{\rho_2 v_2 + \rho_1 v_1} \quad (20.7)$$

$$= \frac{I_2 - I_1}{I_2 + I_1} \quad (20.8)$$

where  $I=\rho v$  is the acoustic impedance. By computing all  $R_0$  values for the layered velocity model and placing each at its appropriate time, we create the reflection coefficient series. It is a time series of reflection coefficients as shown in Figure 20.2C.

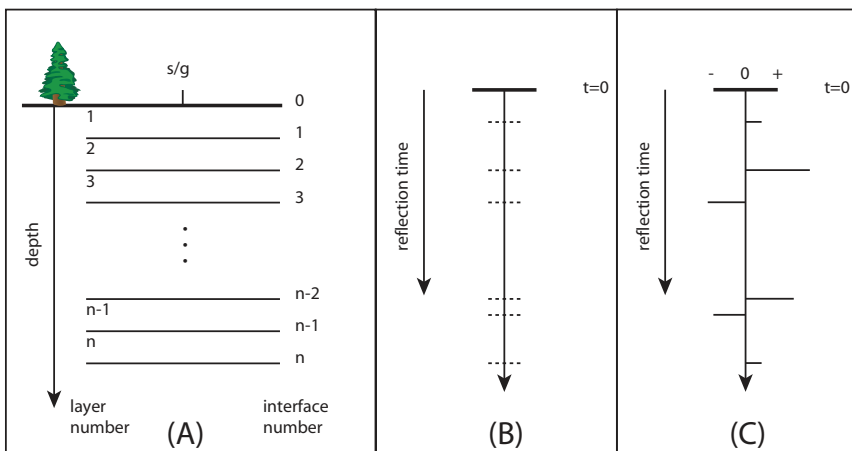


Fig. 20.2 (A) Earth model for 1D seismic simulation. (B) Traveltimes give time locations on the trace, which are the interface echo times. (C) Reflection coefficients are placed at the time locations to form a reflection coefficient series. This is a seismic trace without the wavelet or noise. Note that in A the vertical axis is depth, while in B and C it is reflection time. Well data live in the depth domain and seismic data live in the time domain.

## Elements of 3D Seismology

**20.1.4 Wavelet.** If it were possible, we would gladly acquire and process seismic data to give the reflection coefficient series. Unfortunately echoes from inside the earth are not spikes. Instead, we get a wavelet with finite duration in time. Even if a pure spike is put in the ground, the earth modifies it and returns a wavelet.

Mathematically we can think of a wavelet as built by the summation of many cosine curves. The equation for one cosine curve (one component of the wavelet) is

$$\cos(2\pi ft) \quad (20.9)$$

where  $f$  is the frequency in Hz and  $t$  is time in seconds. Figure 20.3A shows a plot of four such cosines with frequencies of 1, 2, 3 and 4 Hz. The 1 Hz curve is the widest one, and so on. The wavelet is formed by summing these four curves to get the pulse shown in Figure 20.3C. The dominant frequency of this wavelet is

$$f_{dom} = (f_1 + f_2)/2 = (1 + 4)/2 = 2.5 \text{ Hz} \quad (20.10)$$

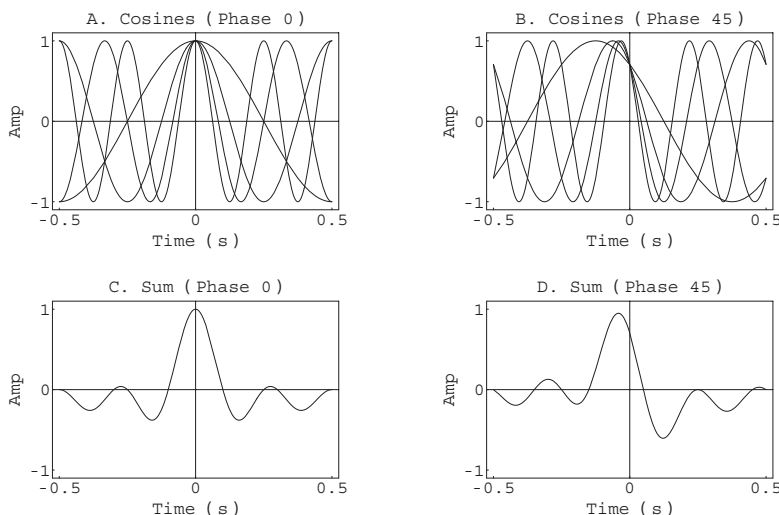


Fig. 20.3 Building a wavelet from cosine curves. (A) Four zero-phase cosines with frequencies of 1, 2, 3, and 4 Hz. (B) The same cosines, except the phase is now 45 degrees. (C) Summation of the zero phase cosines gives a zero-phase wavelet with dominant frequency of 2.5 Hz. (D) Wavelet with 45-degree phase shift and 2.5 Hz dominant frequency.

Clearly this example is not a real seismic wavelet which would have an  $f_{dom}$  of something like 40 Hz.

Each component can also have a phase factor,  $\phi(f)$ ,

$$\cos(2\pi ft + \phi(f)) \quad (20.11)$$

The effect of a constant phase ( $45^\circ$ ) is shown in Figure 20.3B and D. The frequency content is still 1–4 Hz, but the 45-degree wavelet is quite different than zero phase. Figure 20.4 illustrates wavelets with various phases.

The last extension to the cosine formula is

$$A(f) \cos(2\pi ft + \phi(f)) \quad (20.12)$$

where  $A(f)$  is a frequency-dependent amplitude factor. The way it is written, the height can be different for each frequency component, so we can make a plot of amplitude against frequency to form the amplitude spectrum of the wavelet, a

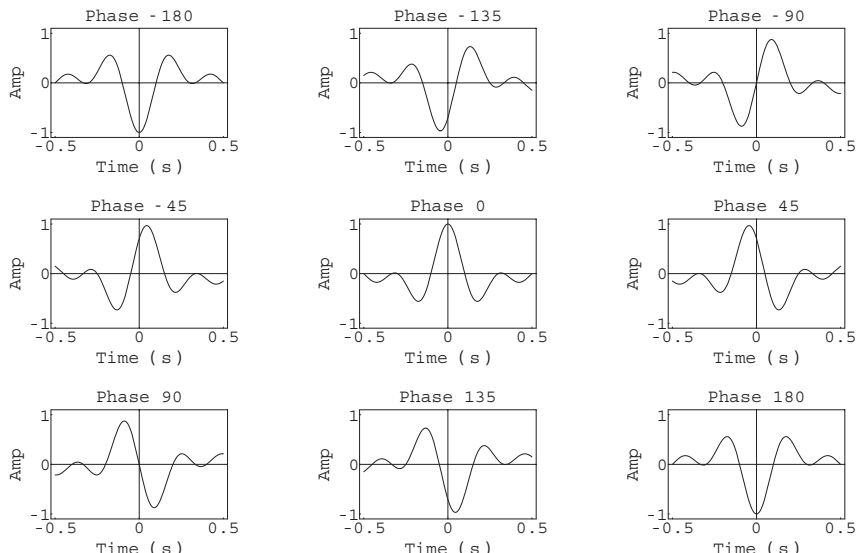
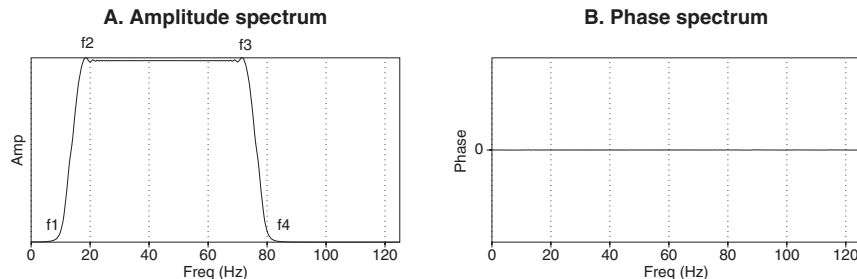


Fig. 20.4 Constant phase wavelets ranging from  $-180$  to  $+180$  degrees. The center of each wavelet is at time zero.

## Elements of 3D Seismology

topic that is discussed in more detail in appendix A. Figure 20.5 shows an idealized case defined by four frequencies ( $f_1, f_2, f_3, f_4$ ). It is common to call  $(f_2, f_3)$  cut-off frequencies and  $(f_1, f_4)$  truncation frequencies. These define the frequency content of the wavelet. The phase spectrum in this example is zero, meaning all frequency components have zero phase.



*Fig. 20.5 Frequency and phase characteristics of an idealized wavelet. On the left is an amplitude spectrum showing which frequencies live in the wavelet (here  $f_1 \rightarrow f_4$ ). The right plot shows the wavelet phase, in this case zero for all frequencies.*

The sinc function can be used to represent a zero phase wavelet

$$w(t) = \frac{\sin(2\pi f(t - t_0))}{2\pi f(t - t_0)} \quad (20.13)$$

where  $f$  is the dominant frequency, and  $t_0$  is the center time.

There are some important things to note about phase. A phase shift of 180 or -180 degrees is called a polarity reversal relative to zero phase. It is equivalent to multiplying every amplitude in the entire wavelet by -1. A wavelet phase of 90 or -90 degrees is very dangerous, if it is undetected and the wavelet phase is assumed to be zero. This is because the response of a thin bed as seen by a zero phase wavelet is indistinguishable from a single interface as seen by a 90-degree wavelet.

For interpretation, a zero phase wavelet is good for three reasons:

1. it is strongly peaked in the sense that sidelobes are minimized
2. it is symmetric giving optimum vertical resolution
3. its peak amplitude is located at the center of the wavelet

If the phase is nonzero, but known, there is no problem. The phase can be easily rotated to zero so that wavelet phase is not an issue at interpretation time. If phase is unknown, estimates can be made from a VSP, a synthetic, or statistical analysis of the data itself.

**20.1.5 Convolutional model.** We want to combine the wavelet and the reflection coefficient series in a way that is consistent with observed properties of real seismic data. From the viewpoint of classical physics, this problem was solved by 1940 [152]. It drew on 19th century ideas about partial differential equations in which a Green's function impulse response is convolved with a source function. The seismic case was digitally implemented during the 1950s [155, 184].

The fundamental connection between a seismic trace and its constituent wavelet and RC series is the convolutional model

$$p(t) = \mathcal{W}(t) * r(t) + n(t) \quad (20.14)$$

where  $p(t)$  is the seismic trace,  $\mathcal{W}(t)$  is the wavelet, the asterisk denotes convolution,  $r(t)$  is the reflection coefficient series, and  $n(t)$  is noise.

This equation is the anatomy of a seismic trace and is the fundamental basis of all seismic interpretation. When we extract amplitude information from seismic data, there is a tacit assumption that the amplitude is proportional to the reflection coefficient, which is a residue of the convolutional model. Similar statements could be made about extracting traveltime or wavelet phase information.

One might argue that prestack analysis, such as AVO, is not based on the convolutional model because all of our 1D seismic assumptions are violated. But the convolutional model is much more general than the way we use it here to create a zero offset synthetic. In prestack data, the traveltimes are computed by Snell's law through a detailed earth model, and angular elastic reflection coefficients are associated with these times to form the reflection coefficient series. This is then convolved with the prestack wavelet to form a convolutional model of the prestack trace.

The importance of this connection cannot be overstated and for physical meaning of interpretation products such as amplitude, time structure, and attributes, we must look to the convolutional model.

How does convolution actually work? Briefly described, the job is to hang the wavelet on every spike of the reflection coefficient series. It is a simple concept. Think of the wavelet as a sideways hat and the reflection coefficient series as a tall pole, where every reflection coefficient is a nail. In convolution, we hang the hat on each nail. If it is a long nail, then we hang a tall hat and a short nail, a short hat.

## Elements of 3D Seismology

A negative reflection coefficient is a nail sticking out the other side of the pole. In addition, there may be some nails in the pole that we did not put there, but we hang hats on them anyway, and they represent noise. We finally add up all the hats to make the synthetic seismic trace.

In the frequency domain (appendix A) the convolutional model can be written as

$$p(f) = w(f) r(f) + n(f) \quad (20.15)$$

Considering the noise-free case, this can be written in polar form as

$$\begin{aligned} p &= A_p e^{i\theta_p} \\ &= A_w e^{i\theta_w} A_r e^{i\theta_r} \\ &= A_w A_r e^{i(\theta_w + \theta_r)} \end{aligned} \quad (20.16)$$

where  $A_p$  is the amplitude spectrum associated with function  $p$  and  $\theta_p$  is the phase spectrum. The last form of this expression tells us the amplitude spectrum of the trace is controlled by the wavelet amplitude spectrum.

Even though the reflection coefficient spikes contain all frequencies, convolution with the wavelet truncates any frequencies outside the wavelet bandwidth. Furthermore, the phase of the trace is the sum of the wavelet phase and that of the reflection coefficient series. This is examined in some detail in appendix A. Amplitude and phase spectrum plots for real seismic data are shown in Figure 20.6.

The seismic trace generated using well logs and the convolutional model is called a synthetic seismogram, although this term is also applied to simulated data from other numerical modeling methods (synthetic CMP gathers, numerical shot records, etc.). When a VSP is unavailable, the synthetic seismogram is the link between wellbore information and seismic data. It is the primary tool that allows geologic horizons to be associated with reflections in the seismic data.

**20.1.6 Examples.** The simplest synthetic seismogram is a two-layer case as shown in Figure 20.7 Not very exciting, but it does show all the elements—velocity model, density model, computed impedance, reflection coefficient series, and the synthetic trace based on two different wavelets. From the equations given previously, we can confirm the traveltime and reflection coefficient amplitude are correct.

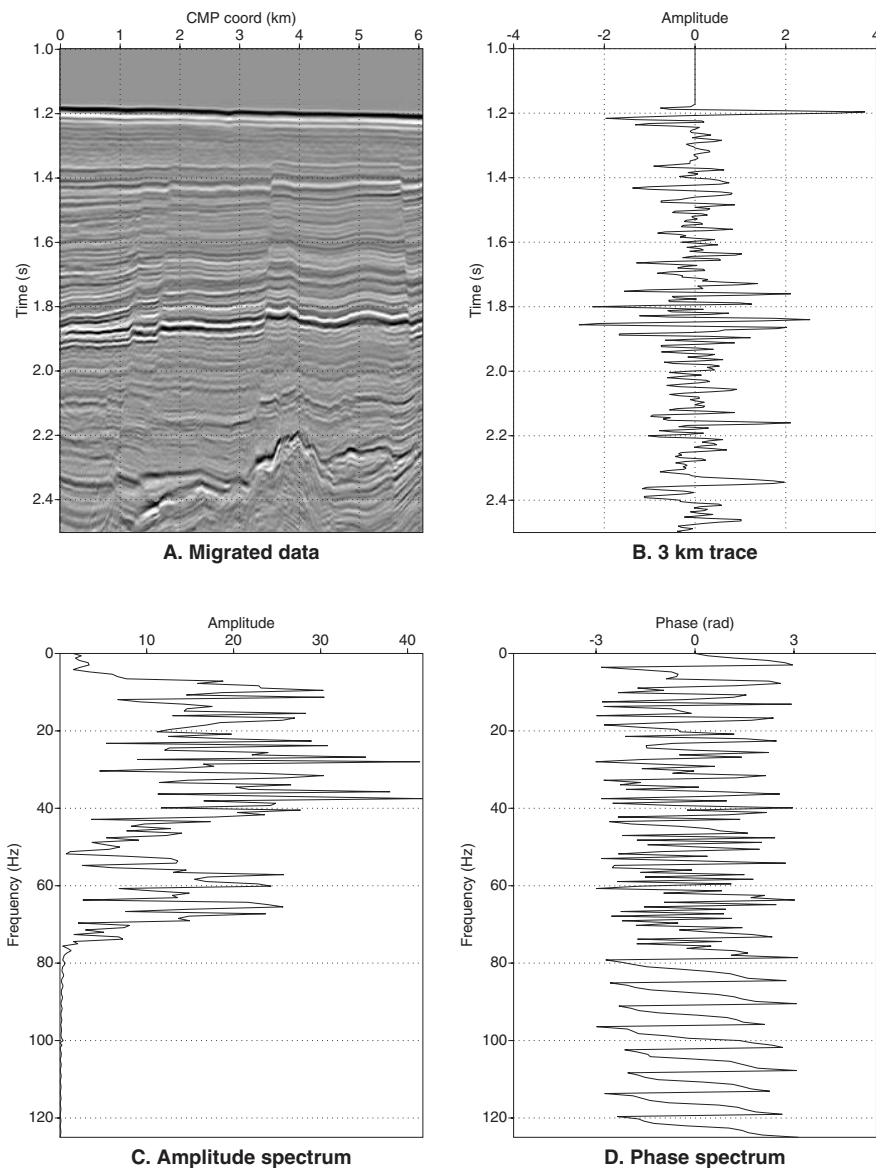


Fig. 20.6 Frequency and phase characteristics of seismic data. (A) A section of migrated 2D data. (B) Display of one trace from the center of the section. (C) Amplitude display for the trace showing a bandwidth of about 5–75 Hz. (D) The phase spectrum is a complicated combination of reflection coefficient phase and wavelet phase.

## Elements of 3D Seismology

In terms of physics, the reflection coefficient is positive for this model, but for seismic exploration purposes we want to highlight cases where impedance decreases across an interface as these are often associated with interesting rock property or pore fluid situations. Thus the SEG polarity convention would consider the reflection event in Figure 20.7 to have negative polarity.

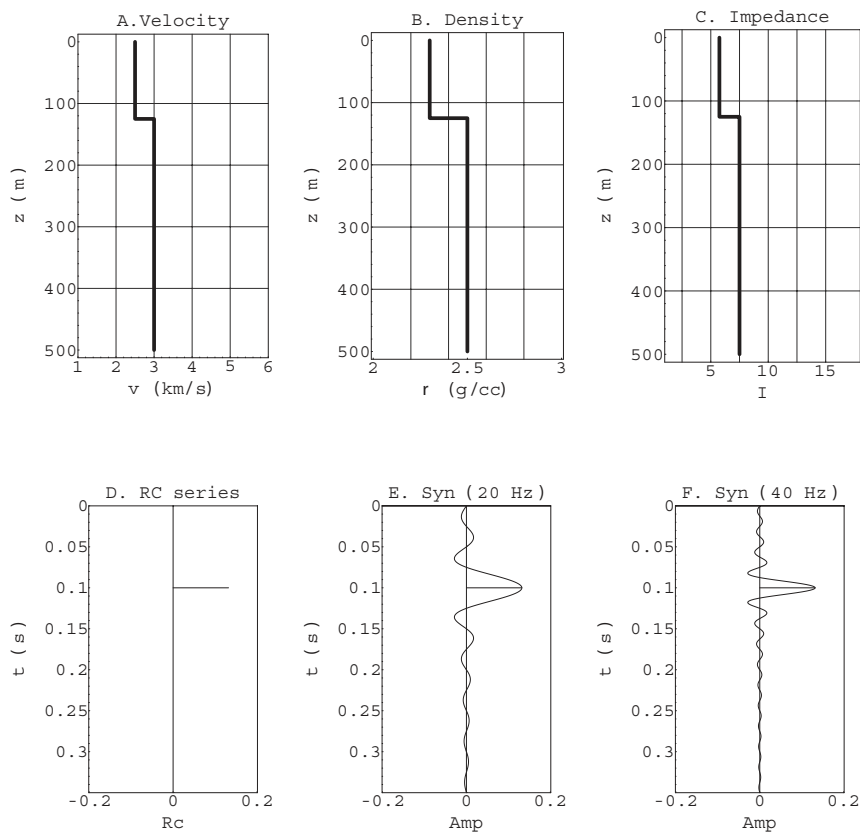


Fig. 20.7 Synthetic seismogram for a two-layer model. (A) Compressional wave velocity model. (B) Mass density model. (C) Acoustic impedance model formed through multiplication of velocity and density. (D) Reflection coefficient series consisting of a single spike. (E) Synthetic seismogram computed using a sinc wavelet with dominant frequency of 20 Hz. (F) Synthetic with a 40 Hz sinc wavelet.

A model with three layers (two interfaces) is a bit more interesting. In Figure 20.8, we see a middle layer 55 m thick with interval velocity of 3000 m/s. Whether this is a thick or a thin bed in a seismic sense depends on the wavelet that is probing it. The reflection time through the layer is 36 ms

$$t = \frac{2z}{v} = 0.036 \text{ s} \quad (20.17)$$

where  $z$  is the layer thickness. By comparison a 20 Hz wavelet has a dominant period of 50 ms.

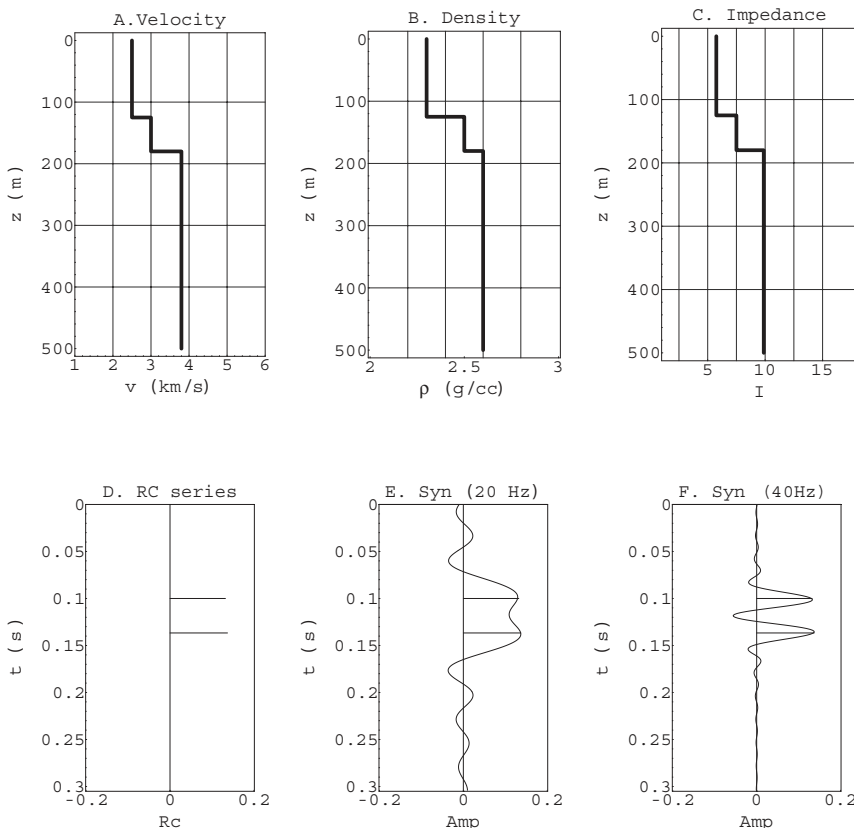


Fig. 20.8 Synthetic seismogram for a three-layer model. With a 20 Hz wavelet the spikes are poorly resolved, but they are clearly separated at 40 Hz.

## Elements of 3D Seismology

This means the wavelets associated with the two reflection coefficients in this synthetic have a significant amount of overlap. This is clearly the 20 Hz synthetic trace. With a 40 Hz wavelet (period of 25 ms), the reflection coefficients are separated enough to be easily distinguished. This leads to the idea of a seismic vertical resolution limit discussed below.

A seven-layer model is shown in Figure 20.9. Peaks and troughs in the 20 Hz result have only a loose affiliation with the reflection coefficient traveltimes or amplitudes. In the 40 Hz synthetic, each reflection coefficient is associated with a distinct maxima (peak or trough), but there are also maxima that arise from

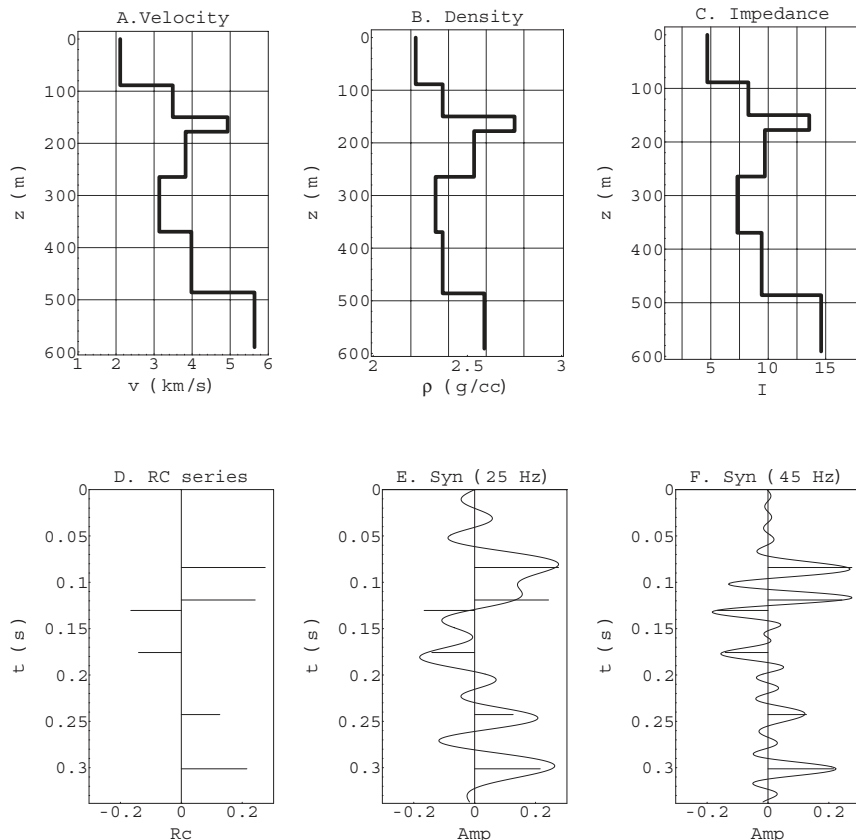


Fig. 20.9 Synthetic seismogram for a model with 7 layers. Peaks and troughs are only loosely affiliated with reflection coefficients in the 20 Hz case. Even at 40 Hz the association is not perfect.

wavelet interference effects. An example is the twin peaks at about 0.2 seconds. These events are quite strong, yet neither is associated with a reflection coefficient.

In real data and real velocity models from well control, the level of complexity is much greater than we see in this simple synthetic. The lesson here is that one must cautiously postulate a connection between any feature on a seismic trace and underlying reflection coefficients. The burden of proof is on the interpreter that such a relationship exists and is robust across the survey area. Synthetic seismograms play a key role in establishing such relationships and understanding their variability across a mapped area.

Remember, the goal is to match a synthetic seismogram to migrated field data. Migration is needed since only then does the time axis represent vertical traveltime, which can be compared with well log measurements.

The matching process involves simulating a seismic trace from well logs and user parameters (wavelet frequency and phase), then manually, or statistically, aligning the simulated trace with the field trace(s) in the vicinity of the well. This is normally done over some limited interval in the well, probably centered on the reservoir target. If the fit is not good enough, then the parameters are changed (updated) and another comparison is made, in effect forming a manual optimization loop. This continues until a match is achieved.

In practice, synthetic seismograms are rarely a perfect match to field data [91]. There are many reasons for this, some of which are listed below.

- **Frequency.** Sonic logging operates in the kilohertz frequency range (high frequency, short wavelength), while seismic data are typically 10–90 Hz (low frequency, long wavelength). This means that the sonic log is influenced by a tiny volume of rock compared to a seismic wave passing the borehole. Furthermore, attenuation ( $Q$ ) and thin layering effects (Backus averaging) make the measured sonic velocities different from velocities influencing surface seismic data. An uncorrected error of a few percent can lead to erroneous correlation between seismic events and geologic horizons.
- **Anisotropy.** Sonic logging measures velocity in the vertical direction, while seismic waves travel at significant angles away from the vertical. If anisotropy is present, then velocity depends on the direction the wave is traveling. It is not uncommon to see a 10–15 percent difference between horizontal and vertical velocities, but without downhole measurements this is difficult to distinguish from  $v(x,z)$  effects.
- **Borehole problems.** Sonic log data may be contaminated by washouts and other borehole problems, while long-wavelength seismic waves are not. Checkshots may be contaminated as well. Reconciling the two

## Elements of 3D Seismology

involves purifying the logs, rejecting unusable checkshots, and applying sonic log environmental and dispersion corrections [26].

- **Wavelet.** The user is required to specify the wavelet, and it is easy to get it wrong. Some advanced software products scan the data and attempt to extract the wavelet. Wavelet estimation in real seismic data is complicated by vertical and lateral variability in the wavelet [73]. These problems ideally should be addressed in coordination with the creation of synthetic seismograms.

A small commercial synthetic seismogram is shown in Figure 20.10. A more elaborate example is given in Figure 20.11. This involves several tracks of information and the correlation between stacked field data and the synthetic.

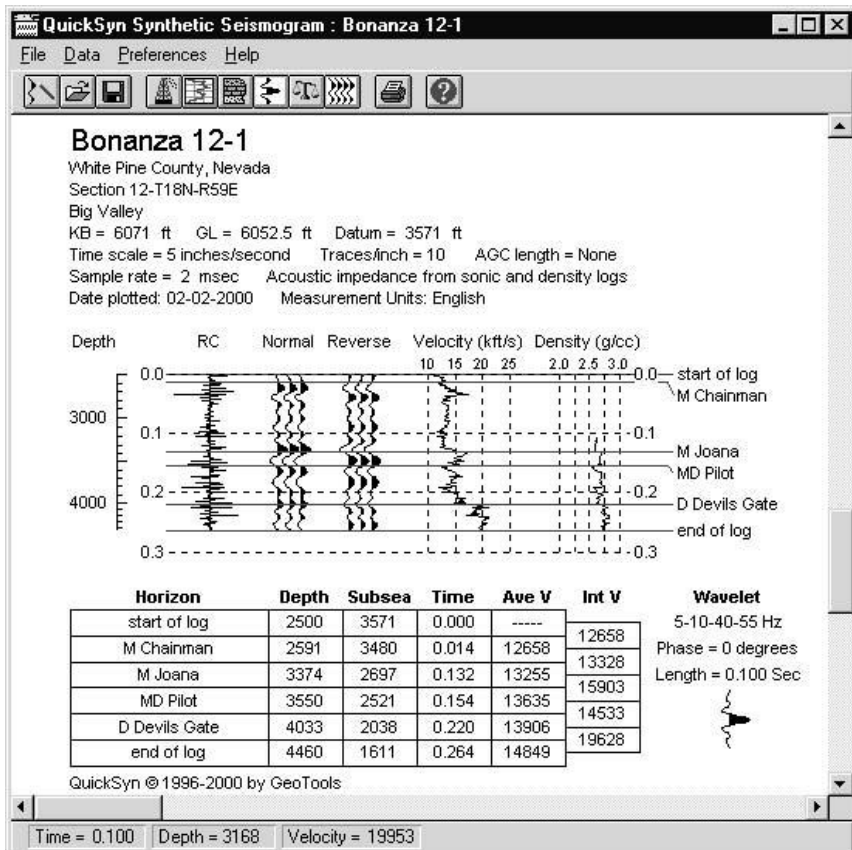
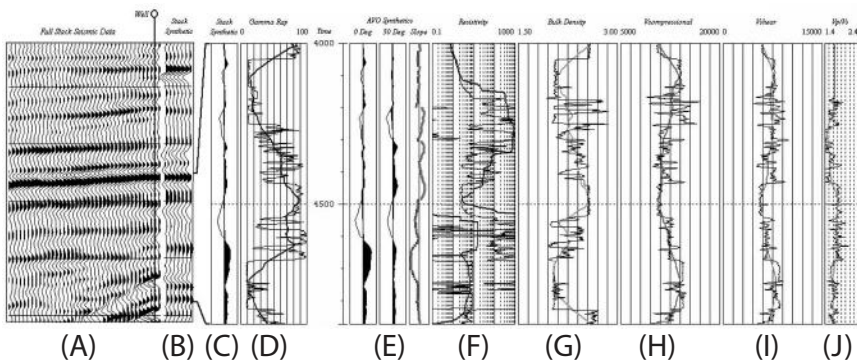


Fig. 20.10 A commercial synthetic seismogram (courtesy Geotools)



*Fig. 20.11 An elaborate commercial synthetic seismogram and several tracks of additional information. (Modified from [108])* (A) Stack of field seismic data showing well location. (B) Stack zero offset synthetic seismogram. (C) Detail of stack synthetic over 850 ms window. (D) Gamma ray log with seismic-scale running average (SSRA) curve. (E) Zero and thirty degree synthetic AVO intercept traces together with the AVO slope synthetic. (F) Resistivity log with SSRA curve. (G) Bulk density log with SSRA curve. (H) Sonic P-wave velocity with SSRA curve. (I) Sonic S-wave velocity with SSRA curve. (J) VP/VS ratio with SSRA curve.

This case is interesting as one of the few published examples of applying Backus averaging to upscale well log measurements to match surface seismic data. Apart from any measurement errors in sonic log and density data, we know of two physical corrections required for upscaling to seismic wavelengths.

First, Backus averaging should be applied in a moving window of length comparable to the surface seismic wavelength. Although the top-down Backus averaging in Figures 2.5 and 2.6 is independent of frequency,  $\lambda$ -windowed Backus averaging is a frequency dependent operation, since the local wavelength depends on frequency. The other upscaling operation is also frequency dependent, and that is sonic velocity correction for dispersion due to attenuation ( $Q$ ). Both  $\lambda$ -windowed Backus averaging and  $Q$  compensation act to reduce observed sonic velocities. The modified velocities are more nearly representative of those influencing long wavelength surface seismic data.

**20.1.7 Transmission loss.** Our synthetic seismogram calculation involved only reflection coefficients. This is the standard practice, but there are published accounts of the important role of internal multiples and transmission effects. It was known by 1960 that internal multiples can set up interference patterns that complicate any effort to associate geologic horizons with specific seismic events

## Elements of 3D Seismology

[209]. In such cases, the best solution is VSP analysis, which allows the direct identification of primary reflections versus multiples.

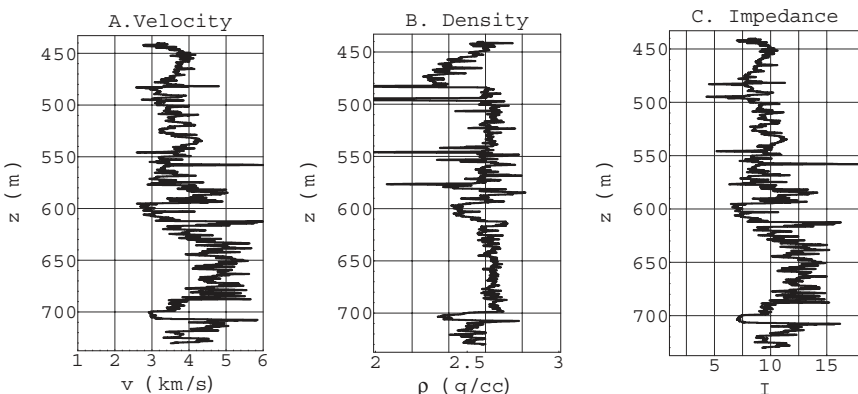
The role of transmission coefficients is less well studied, but we can form some broad conclusions by considering a test case. Figure 20.12 shows log data from a well (Self-82) in the Glenpool field [96] of northeastern Oklahoma (USA). In a general sense, the geological setting is one of little structural relief in mixed clastic and carbonate rocks of Permian to Cambrian age. The total stratigraphic section is about 750 m thick underlain by granitic basement rocks.

Figure 20.12A is a plot of sonic velocity from 440 m below surface to total depth. The depth sample interval is 0.15 m. A density log over the same interval provided the density values in Figure 20.12B. The product of these two curves gives the acoustic impedance shown in Figure 20.12C. The impedance units are strange,  $\text{km g}/(\text{cm}^2 \text{ s})$ , but not important since we are only interested in using this curve to calculate reflection and transmission coefficients which are dimensionless.

Recall from chapter 3.2.2 that the normal incidence transmission coefficient is given by

$$T_0 = \frac{2 I_1}{I_2 + I_1} \quad (20.18)$$

where the subscripted 1 refers to the incident wave layer and, as usual, the impedance is  $I=\rho v$ . As the seismic energy goes down, reflects, and returns to the



*Fig. 20.12 Well log curves for the self-82 well in the Glenpool field of northeastern Oklahoma. (A) Sonic velocities from about 440 m to total depth. (B) Bulk density for the same interval from a density log. (C) Acoustic impedance log generated by multiplying the velocity and density at each depth level.*

surface any given interface above, the reflector is passed twice, once on the way down and again on the way up. Using the subscripts now in an absolute sense (1 being shallower), the downgoing transmission coefficient is

$$T_d = \frac{2 I_1}{I_2 + I_1} \quad (20.19)$$

the upgoing is

$$T_u = \frac{2 I_2}{I_2 + I_1} \quad (20.20)$$

and the two-way transmission coefficient is given by

$$T_2 = \frac{4 I_1 I_2}{(I_2 + I_1)^2} = \frac{4 R_I}{(1 + R_I)^2} \quad ; \quad R_I = I_1/I_2 \quad (20.21)$$

where  $R_I$  is the top-down impedance ratio. A plot of this expression is shown in Figure 20.13. Note that when there is no impedance contrast ( $R_I=1$ ) there is perfect transmission ( $T_2=1$ ).

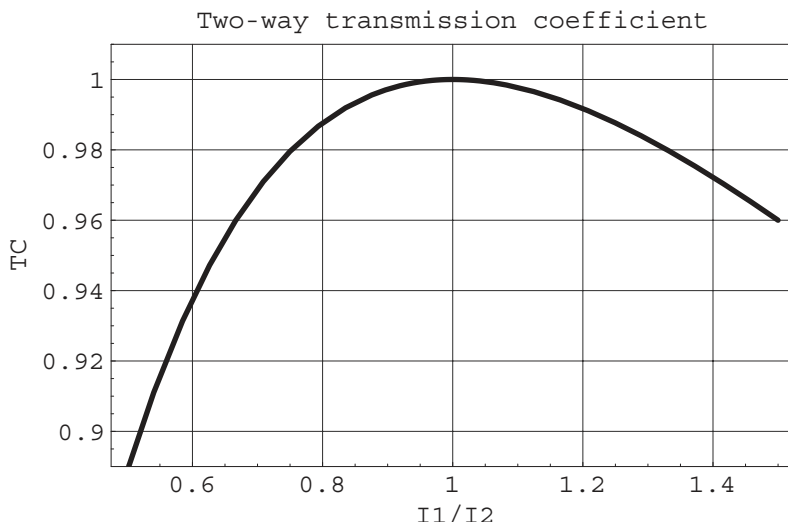


Fig. 20.13 Two-Way transmission coefficient as a function of impedance contrast. This coefficient is near 1 for any but the largest impedance jumps.

## Elements of 3D Seismology

In forming a synthetic seismogram, the transmission loss to depth level  $z$  is the product of all overlying two-way transmission coefficients. This is illustrated using the Self-82 well in Figure 20.14. The reflection coefficients and one-way transmission coefficients are shown in Figure 20.14A–C. This section of rock contains some strong impedance contrasts giving some large reflection coefficients. An area of soft sediments, such as the Gulf of Mexico, would generally have smaller reflection and transmission coefficients, so the results given here require calibration to local conditions.

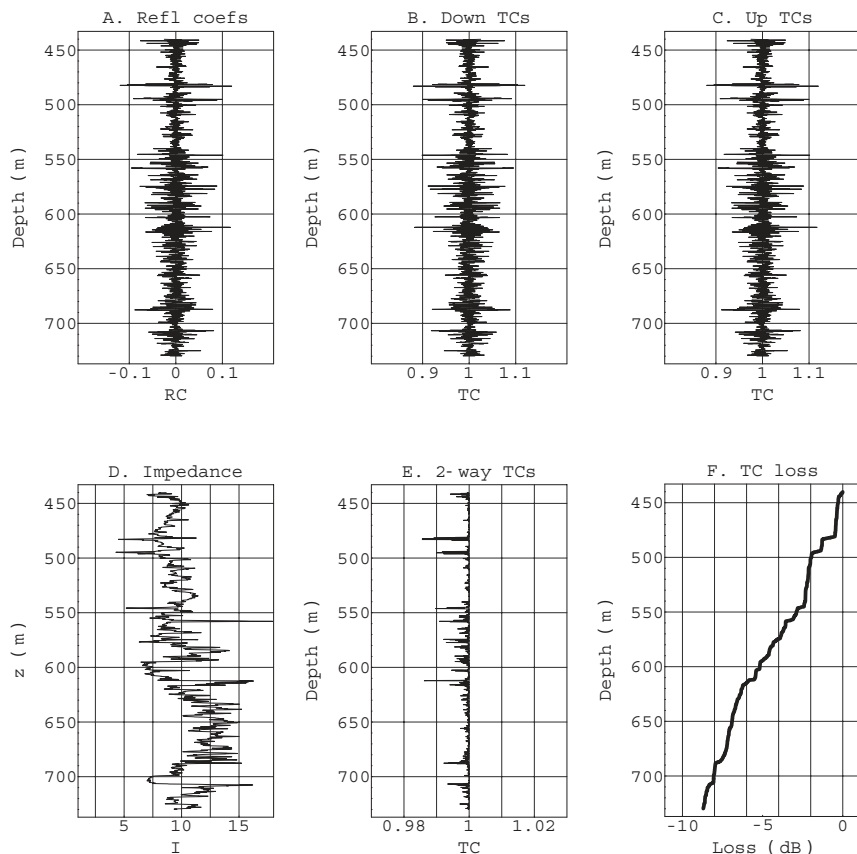


Fig. 20.14 Seismic zero offset transmission loss in the Self-82 well. (A) Zero offset reflection coefficients. (B) Downgoing transmission coefficients. (C) Upgoing transmission coefficients. (D) Acoustic impedance log. (E) Two-way transmission coefficients. (F) Two-way transmission loss (dB) versus depth. Incident wave amplitude is taken to be 1.0 at the top of the log interval.

In Figure 20.14D and E the impedance log and two-way transmission coefficients are shown. As expected, the two-way TCs deviate from 1.0 only when large impedance contrasts are encountered. Finally, Figure 20.14F is the cumulative transmission loss in dB. To form this curve, the seismic amplitude is assumed to be 1.0 at the top of the log interval, and we are plotting the amplitude loss incurred by deeper and deeper reflections.

It is interesting that a few strong contrasts in the subsurface play such an important role in overall transmission loss. A loss curve, such as Figure 20.14F, is one way of naturally segmenting the subsurface into meaningful units. To a fair approximation, the loss curve is linear with depth. Allowing for two-way travel, this gives a reflected wave transmission loss, in this particular case, of 0.014 dB/m. Since the horizontal scale is in dB, this means the transmission loss has the mathematical form

$$A(x) = A_0 e^{-\alpha x} \quad (20.22)$$

where  $x$  is the distance traveled,  $A_0$  is the reference amplitude, and  $\alpha$  is an absorption coefficient. It follows that transmission effects mimic intrinsic absorption phenomena, which are of the same mathematical form. When a processor applies an  $e^{bt}$  gain it is effectively an attempt to undo the action of both absorption and transmission loss.

## 20.2 Tuning

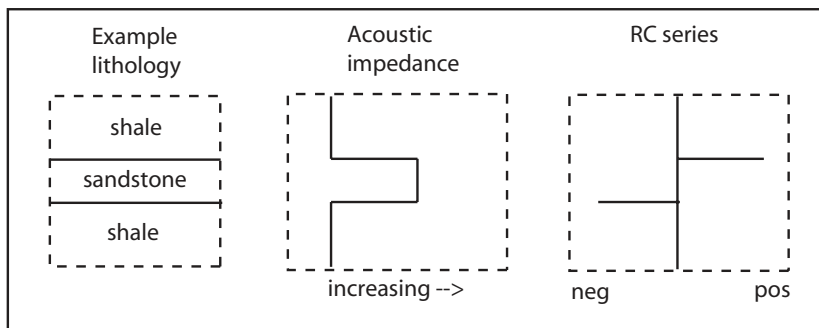
Key concerns in any seismic project are tuning and resolution. Vertical resolution is the ability to identify individual peaks on a seismic trace with the top and base of a geologic unit. Lateral resolution is the ability to see fine-scale features in map or cross sectional view, such as pinnacle reefs or channel features. Both tuning and resolution are based on local velocity near the feature of interest and frequency content of the wavelet.

We have seen that a synthetic seismogram is the sum of many overlapping wavelets and thus has a fundamental connection to interference phenomena. Interference is also involved in determination of optimum marine source depth, source and array directivity functions, vertical and common midpoint stacking, and image construction by dip moveout and migration.

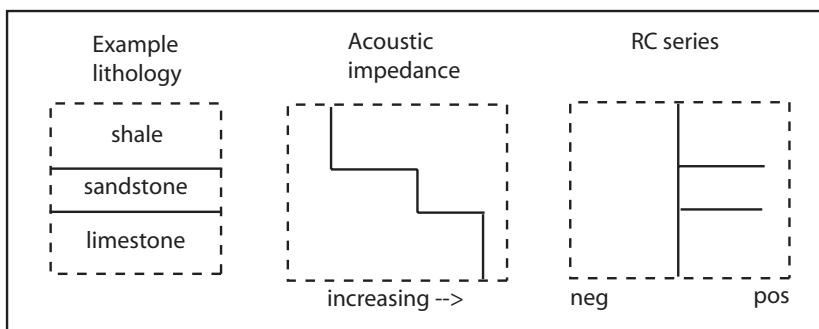
Interpretation must deal with interference phenomena arising from thin beds [201, 202] in the form of vertical resolution limits and tuning. Thin bed analysis considers the interference of reflections from the top and base of the bed. There are two fundamentally different cases, Figure 20.15.

## Elements of 3D Seismology

In Figure 20.15A, we consider a hypothetical sandstone with positive reflection coefficient at the top and a negative coefficient at the base. We assume each reflection coefficient has equal amplitude and opposite polarity, and that the wavelet is zero phase. If the bed is sufficiently thick, distinct positive and negative reflections proportional to the reflection coefficients are visible. As the sandstone approaches zero thickness, the reflection coefficients cancel and the net amplitude goes to zero.



(A)



(B)

*Fig. 20.15 Thin bed cases. (A) An embedded high or low impedance layer forms the opposite polarity case which gives rise to tuning phenomena. (B) A double step increase or decrease of impedance has equal polarity reflections from top and base of the thin layer. This is the vertical resolution case.*

For intermediate cases, the two reflections interfere in a complicated way. Figure 20.16 shows how wavelets align to develop tuning. The tuning effect is an anomalously high amplitude related to a magic thickness rather than any interesting rock or fluid property changes. This occurs when the bed has a thickness of one-quarter wavelength. In the case shown, the tuning amplitude boost is about 22%. We can expect to see this effect in real data, but the details will strongly depend on the actual wavelet in the data. This is illustrated in Figure 20.17, which is a classic tuning curve display for a sinc wavelet and a Ricker wavelet. In each plot, the maximum amplitude of the summed top+base trace is shown as a function of bed thickness. The clear peak in each case at  $\lambda/4$  is the tuning thickness,

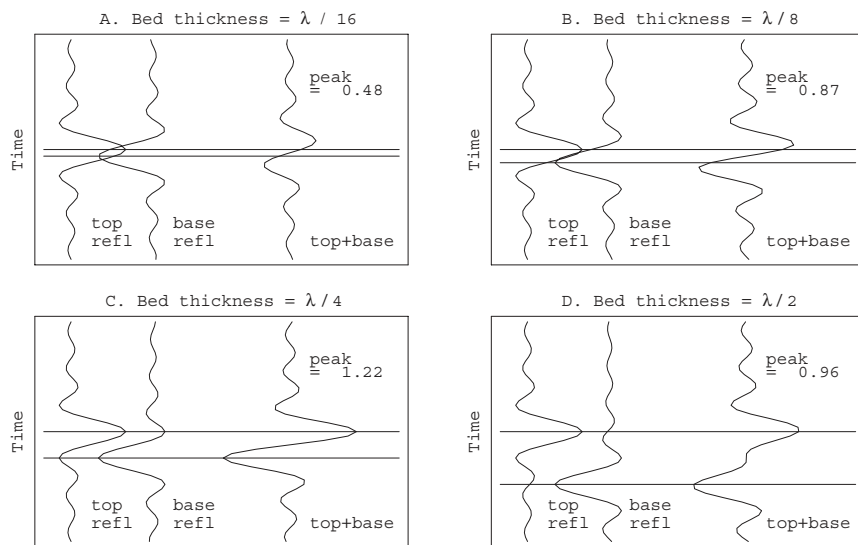


*Fig. 20.16 Alignment of wavelets to develop tuning. In each panel the two traces on the left are the top and base reflections. The reflection coefficients underlying these are unit amplitude but opposite polarity. The trace on the right in each panel is the summed trace that would be observed on migrated seismic data. When the bed thickness is one-quarter of the wavelength, the summed amplitude is a maximum. This is the tuning effect.*

## Elements of 3D Seismology

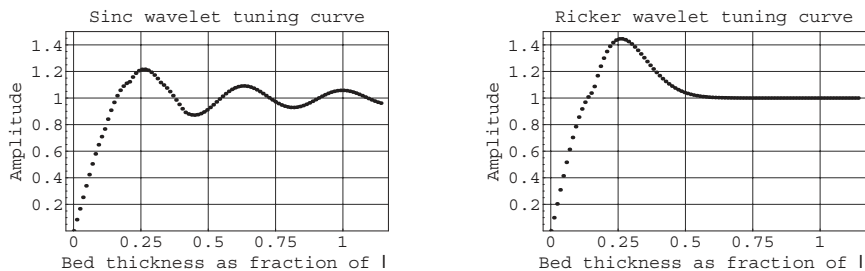


Fig. 20.17 Another view of tuning. Each plot is the maximum amplitude of the summed top+base wavelet as a function of bed thickness. Tuning curves such as this are sensitive to the wavelet, which is evident in comparing the results using a sinc wavelet and a ricker wavelet. High-amplitude tuning occurs in both cases when the bed is one-quarter of a wavelength thick. Other alignments called second and third tuning are seen in the sinc wavelet plot because it is an oscillatory function. These peaks give an amplitude boost much smaller than first tuning and thus are seldom seen on real data.

$$z_{tun} = \lambda/4 = v/(4f) \quad (20.23)$$

For example, a 2000 m/s thin bed will show tuning in a 40 Hz survey when the bed is 12.5 m thick. The frequency in this equation is usually taken to be the dominant frequency, but actually every frequency has its own tuning thickness. This is the physical basis of spectral decomposition tuning analysis [126].

With sufficient well density, tuning effects can be removed from horizon amplitude maps in a process called detuning. If well control is sparse, statistical methods are available for approximately detuning the data [28].

The results shown in this section assume we really have a zero phase wavelet. However, as mentioned earlier, there is a fundamental ambiguity between the tuning waveform and a 90° phase shift. The problem is seen by comparing the 90-degree wavelet in Figure 20.5 and the net tuning wavelet in Figure 20.16C. This net response arises from two closely spaced reflection coefficients convolved with a zero phase wavelet, yet it is indistinguishable from the case of a single reflection coefficient

convolved with a 90-degree wavelet. As an interpreter works to map features of beds at or below the tuning thickness, wavelet phase becomes increasingly important.

## 20.3 Resolution

Now consider the case of a thin bed where both top and base reflections are the same sign. Figure 20.18 shows individual top and base reflections as well as the net reflection response for a thin layer model where the top and base polarities are the same. The net response is a single peak for very thin beds, but

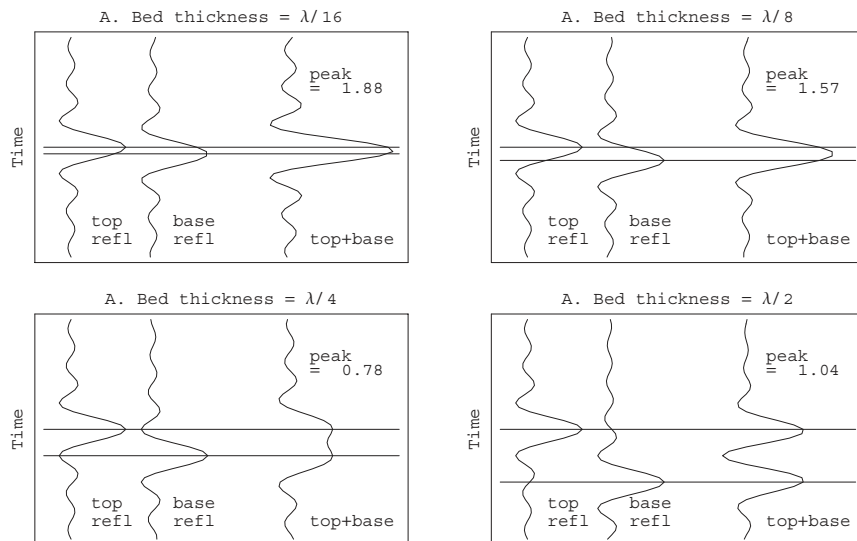


*Fig. 20.18 Alignment of wavelets to define vertical resolution. In each panel, the two traces on the left are the top and base reflections. The reflection coefficients underlying these are unit amplitude and the same polarity. The trace on the right in each panel is the summed trace that would be observed on migrated seismic data. When the bed thickness is one-quarter of the wavelength, the summed net trace begins to show two peaks rather than the single peak seen for thinner beds. Thus  $\lambda/4$  is the vertical resolution limit of reflection seismic data as well as the tuning thickness.*

## Elements of 3D Seismology

separates into two peaks when the bed thickness is  $\lambda/4$ . This is the vertical resolution limit of seismic data.

When the bed is just this thick, the top and base reflections are time-shifted by half of the dominant wavelet period. Thinner beds merge into a single event; thicker

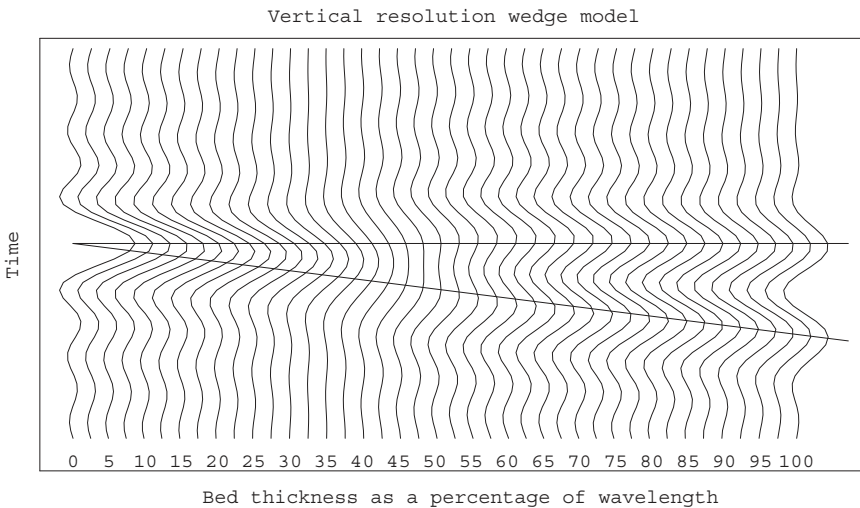


Fig. 20.19 Another view of vertical resolution. Each trace sees a different bed thickness as the wedge (thin bed) pinches out to the left. The bed thickness at each trace location is annotated as a percentage of wavelength. The vertical resolution limit occurs when the reflection trace shows two peaks corresponding to the bed being one-quarter wavelength thick.

beds are seen as distinct top and base peaks. Figure 20.19 shows a wedge model useful for visualizing gradual changes that occur near resolution thickness [202].

Figure 20.20A illustrates changes in vertical and lateral resolution with depth. This graph assumes a linear velocity model suitable for the Gulf of Mexico and nonlinear dominant frequency trend that is close to that seen in real data. The solid curve is the vertical resolution limit and lateral resolution is shown dashed. In panels (B)–(D), we see various depth intervals on 150 migrated traces from a 3D Gulf of Mexico survey. These have been depth converted with the same linear velocity

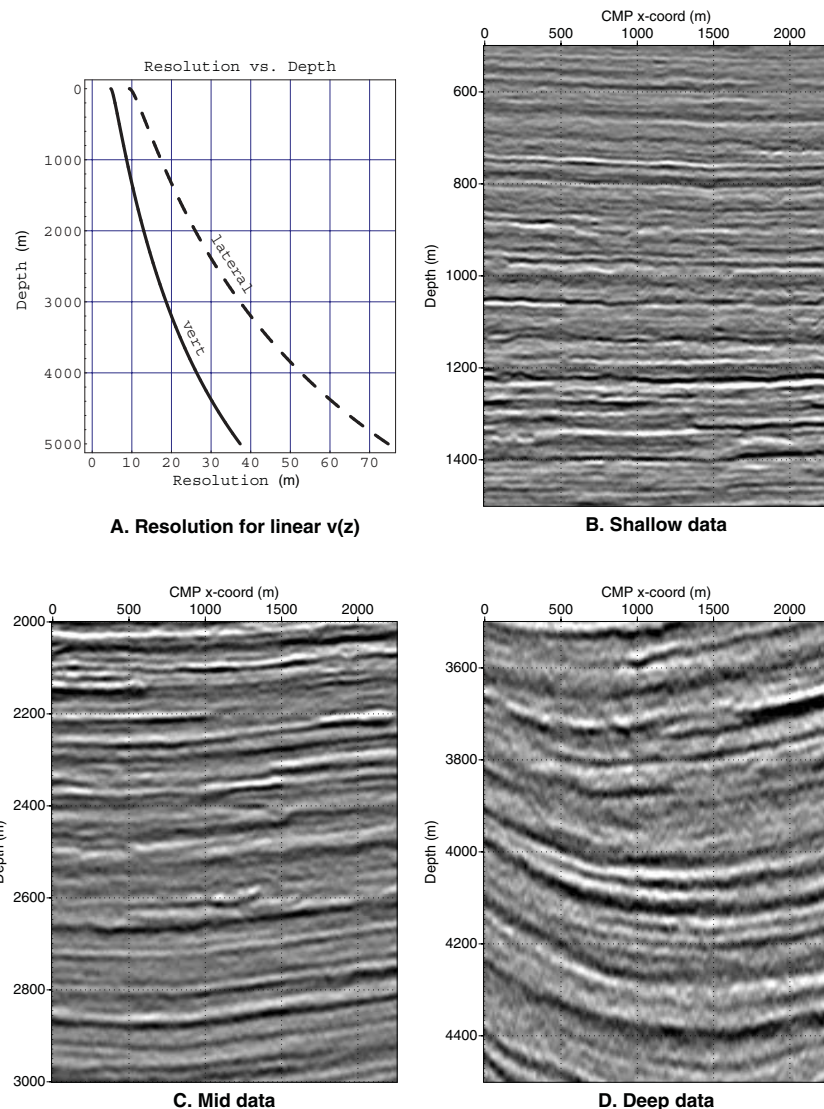


Fig. 20.20 Resolution versus depth in seismic data from the Gulf of Mexico. (A) Approximate vertical (solid) and lateral (dash) resolution as a function of depth. This curve is based on a Gulf of Mexico linear velocity model and a nonlinear model of dominant frequency versus depth. (B) Shallow section from a 3D Gulf of Mexico survey. Depth conversion was done with the same linear velocity model. (C) Medium depth data on the same traces. (D) Deep data on the same traces. The loss of detail with depth is visual confirmation of reduced resolving power.

## Elements of 3D Seismology

function used to create Figure 20.20A. Notice the general loss of detail with depth that is typical of seismic data, and serves as visual confirmation of resolution loss.

It is sometimes possible to estimate bed thickness below the resolution limit. This technique hinges on subtle changes in amplitude, waveform, or related physical properties. Tuning curves (Fig. 20.17) can be the physical basis of subresolution thickness mapping. Specifically, below tuning thickness there is an approximately linear relationship between amplitude and bed thickness. Another

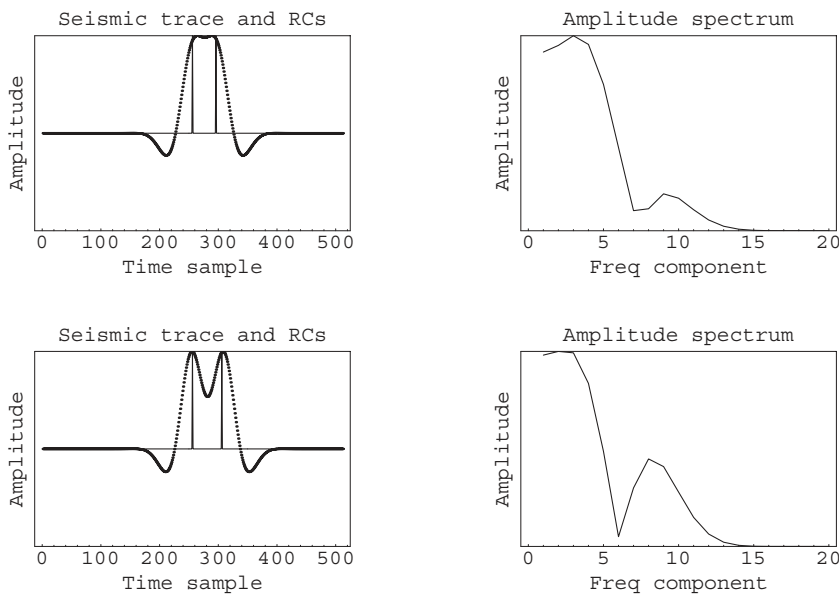


Fig. 20.21 There are clues to thickness below the resolution limit including Fourier domain phenomena. Here we see two reflection coefficient spikes near the resolution limit and an associated notch in the trace amplitude spectrum. Even below the resolution limit (upper plot), the notch can be seen and used to estimate subresolution thickness.

method exploits the fact that closely spaced spikes introduce notches in the amplitude spectrum. This effect is detailed in appendix A and shown on a synthetic case in Figure 20.21.

Subresolution mapping clues tend to be sensitive to noise and precise knowledge of the wavelet. As a result, the risk of getting it wrong grows rapidly (probably exponentially) as the bed drops below resolution thickness. A prospect which turns on subresolution thickness mapping is a higher risk project than one dealing with seismic thick beds. Well control helps because seismic is very good at interpolating information between wells, but is less successful at extrapolating away from them.

The difficulty of subresolution thickness mapping should not be confused with subresolution bed detection, which only attempts to establish whether or not a thin feature exists. With good quality 3D data, it may be possible to detect thin beds well below the resolution limit, although interference from nearby reflections and even modest noise levels can overwhelm these subtle amplitude effects. This is best done by recognizing characteristic patterns, such as channel forms, on time slice or horizon amplitude maps. Table 20.1 provides a summary of thin bed phenomena one is likely to see in seismic data.

Some general things to remember about tuning and vertical resolution are

1. they occur at the same thickness
2. detuning is possible if several wells are available
3. thickness mapping below the resolution limit is higher risk

Case	Seismic effect	Top and base $R_0$ polarities
$h \geq \lambda/4$	Top and base reflections distinct	Equal
$h = \lambda/4$	High amplitude tuning	Opposite
$h \rightarrow 0$	Amplitude increases	Equal
$h \rightarrow 0$	Amplitude decays to zero	Opposite
$h = \lambda/25$	Limit of detectability	Opposite or equal

Table 20.1 Summary of vertical resolution and tuning thin bed behavior in seismic data. The thin bed has thickness  $h$  and  $\lambda$  is the local seismic wavelength.

4. various indicators can be used to estimate subresolution thickness
5. detecting very thin beds requires unusual circumstances related to signal quality and geology

# 21

## Introduction to Interpretation

### 21.1 What does it mean to interpret seismic data?

The basic purpose of seismic interpretation is to extract all available geologic information from the data. This includes structure, stratigraphy, rock properties, and perhaps reservoir fluid changes in space and time. Our goal is to present the broad outlines of what can be inferred from petroleum seismic data and the physical basis of that interpretation. The physical basis is critical because any interpretation concept, display, or product must ultimately make sense in terms of reflection physics as well as be geologically compelling. The body of knowledge associated with seismic interpretation is enormous and growing rapidly with several hundred studies published each year. The reader interested in a comprehensive treatment of the subject is referred to the standard text by Brown [28]. It is recommended for anyone deeply involved in 3D seismic interpretation.

It used to be that geophysicists interpreted individual shot records, but as the amount of data increased, it was not feasible to work with prestack data by hand. Stack sections, migrated sections, and data cubes all changed the way we interpret. Migration, in particular, rendered obsolete a whole repertoire of tricks for dealing with the pitfalls of unmigrated data. In a similar way, 3D data make specialized knowledge of how to work with 2D strike lines a dying art.

Driven by computer and electronics technology, oil industry economics, and software life cycles, the interpretation of seismic data is growing in importance and complexity. There is no indication that this pace of change will decelerate.

### 21.2 Background information

A successful interpretation begins long before the data are loaded into a workstation. Here we list some of the information that should be gathered as necessary background knowledge for a thorough interpretation project.

## **Elements of 3D Seismology**

You will seldom have the luxury of time or access to gather all of the items listed here. Often an interpretation project is inherited, and you may be expected to “hit the ground running” with little time for background.

However, you ignore this part of the interpretation process at your own risk. It could be embarrassing, or worse, to recommend a structural prospect in an area known only for stratigraphic production. Remember, knowledge is power. The more background knowledge you have, the more power you have to make good prospects.

### **Structure**

1. Understand the regional tectonic setting. What are analogous structural settings in other parts of the world?
2. The structural style is important. Are you expecting thrust faulting or salt structures? Is the expected structure complex? If so, is the kind of migration you have chosen appropriate for such structures?
3. What are the maximum dips expected? Did the survey planning take this properly into account? Remember that fault diffractions behave like 90°dips.
4. Are the structures fully 3D? Are you expecting locally useful dip lines?
5. How complex is the faulting? Heavy faulting makes stratigraphic interpretation more difficult. In a growth fault area, start thinking about horizon slices along fault planes.
6. In a marine survey, is there any rough seafloor topography? Low velocity pockets in the shallow sediments could produce buried static problems. If seafloor topography is irregular then multiples are more likely to leak into the final migrated image.

### **Lithology**

1. Is the section generally clastic or carbonate? What lithologic interfaces are sure to show up as reflectors? Can any of these be used to confirm the wavelet is zero phase?
2. Are there any salt formations known in the area? Suspected? Salt in a young clastic basin will require prestack depth migration for imaging near or under the salt. Subsalt imaging in a carbonate or hard-rock clastic basin may not require prestack migration because of smaller sediment-salt velocity contrasts.

3. Are there strong contrasts in lithology, like thick shale over thick limestone? If severe ray bending is expected, then start planning for depth migration.
4. Is there any salt, anhydrite, limestone, or dolomite in the shallow section? These could generate strong multiples. Has this problem been addressed in processing? Have refraction statics been applied? If not, be alert for false structure due to long wavelength statics.
5. For marine data, is this an area of soft or hard seafloor? A hard seafloor is very efficient at reflecting energy back into the water column. This may be useful in confirming polarity of the data or wavelet phase (but subfloor layering will confuse phase estimates). Beware of dipping multiples from a hard seafloor. In shallow water, this sets up a waveguide that swamps reflection data. In deep water, it generates long period multiples that are very difficult to remove in processing.
6. For land data, what are the surface and weathering layer lithologies? Do these change across the survey area? Are refraction statics necessary and, if so, have they been applied?

## **Stratigraphy**

1. Understand age relationships and depositional environments of key formations. What is a modern analog of this depositional environment? If it does not exist anywhere on earth today, you may have a tough time selling the concept.
2. What are the relationships between structure, stratigraphy, and production in the area? For example, sand bodies might be known to accumulate next to up-to-the-basin faults.
3. Are there subtle stratigraphic features of interest, such as pinnacle reefs or meander channels?

## **Well control**

1. How many wells are in the area? What companies drilled them? What was (is) the exploration concept? What is the chronology of the drilling activity, and how has the exploration concept evolved?
2. Know which wells have synthetic seismograms. Synthetics can be on raw or upscaled sonic velocities, with or without multiples, and with or without transmission effects. Find out details of how the synthetics were generated so that you will be able to high-grade the information they provide. There is little probability that all synthetics will fit the field data

## Elements of 3D Seismology

equally well, and you will have to decide which ones to believe. If they all fit perfectly, be very suspicious.

3. Become familiar with petroleum shows and tests as well as drilling and production problems.

### Seismic velocity

1. What are the sources of fine-scale velocity control in the area? Vertical seismic profiles or sonic logs (with checkshots) are the best sources and are the key link between seismic events and geologic horizons, Figure 21.1. Sonic velocities benefit from upscaling, but VSP velocities generally do not (the frequency is closer to surface seismic data).
2. What are the available sources of velocity for depth conversion? VSP, well logs, or seismically derived?

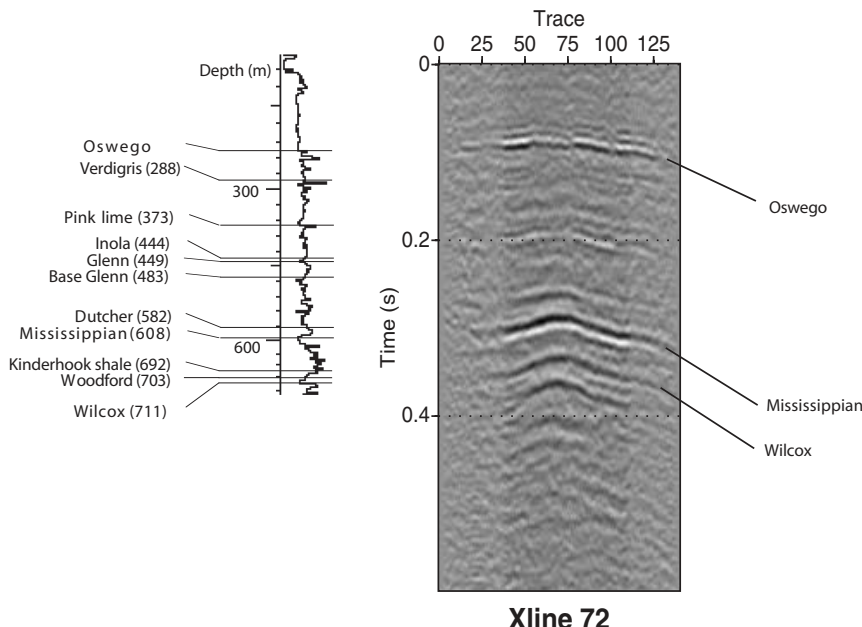


Fig. 21.1 Sonic log converted to time and annotated with geologic tops. The seismic data is from a 3D survey near the Glenpool field in Oklahoma. Production in the survey area is associated with structural closure on the Wilcox.

3. Is the kind of migration used for your data appropriate for the kind of velocity variation in the area?
4. Dipole sonic logs can give P-wave and S-wave velocity as a function of depth.
5. Cross Dipole sonic can give indications of anisotropy associated with vertical fracturing.

## **Production**

1. Learn everything you can. What are the producing formations? What are the lithology, structural setting, and stratigraphy of the reservoir(s)? Pressure data can indicate fault separation or communication across leaky faults.
2. Understand how the economic evaluation of prospects works in your company. This could save you a lot of wasted effort.

## **Literature and legends**

1. Read as many reputable articles on the area as you can. If you read and understand an article per week, in one year you will be an expert.
2. Listen for ideas that “are in the air.” You might hear that some old-time geoscientist had an idea that you are now able to follow-up with modern seismic data. Be open-minded!

## **Other data**

1. Gravity data is often useful to delineate major basement features.
2. Magnetics can play a role similar to gravity, plus has unique response to large-scale salt bodies.
3. Look carefully at all the data you can before interpreting the new 3D data. Is older 2D or 3D data available in the area? Note vintage of data. A common problem with older 2D seismic data is large trace spacing, which results in spatial aliasing and narrow bandwidth that gives the data a ringy appearance. If possible, look at the data with and without interpretation.
4. Be aware of surface geology that may be an indicator of subsurface structure and stratigraphy. It is all too easy to ignore the obvious.

### The 3D data before interpretation

1. Note any acquisition problems: skips, location errors, gun failures, etc.
2. Note any processing problems. Know the frequency content and estimated wavelet.
3. Scan selected CMP gathers generated immediately before stack. We have seen examples in Figures 16.11 and 16.16. Look for flattening of primary events, curved events that indicate residual multiples, and the mute cut that tells when full fold is achieved. Amplitude work in the mute zone can be influenced by variable CMP fold as the mute cut changes over the survey area.
4. Note migration. What kind was used? Why? What method? Why? If possible, get plots from migration velocity analysis. Work with research types until you understand these plots and can judge for yourself that the velocities were competently determined.

If all of this sounds like a laundry list, that's because it is. It is my list of important things to consider when an interpretation project starts up. Make your own list. Include what works and what does not, what is important, what surprises you, and what you do not understand. The famous physicist Richard Feynman once pointed out that there are no such things as hard problems and easy problems, only problems you understand and those that you do not understand. Don't assume you will remember it; write it down. You will be glad you did.

### 21.3 Interactive interpretation systems

Working with 3D seismic data requires the use of computer interpretation systems. There are many of these on the market and the list changes rapidly. The systems can be grouped in various ways: hardware platform, operating system, cost, or parent company. A list of some seismic interpretation systems is given in Table 21.1.

Each system is identified by product name, the company and parent company that produce it, the operating system it is designed for, and whether it is a volume- or slice-based system. In a volume interpretation system, the 3D data is presented as an interactive cube and all interpretation functions can be performed in the volume mode. A slice interpretation system presents the 3D data as a stack of slices, and interpretation proceeds from slice to slice.

This list given here is not comprehensive, but it does contain the major players in the seismic interpretation software market. Prices range from a few thousand dollars for some of the PC systems to a few hundred thousand dollars

Product	Company	Parent Company	OS	Volume or slice based
2d/3dPAK	SMT	SMT	Windows	slice
Charisma	Geoquest	Schlumberger	UNIX	slice
EarthCube	Landmark	Halliburton	UNIX	volume
Earthworks	Genetek	Genetek	UNIX	slice
Geotracker	Tigress	Tigress	UNIX,Windows	volume
GeoViz	Geoquest	Schlumberger	UNIX	volume
IESX	Geoquest	Schlumberger	UNIX	slice
Samuel 2D/3D	Mathewson	Mathewson	Linux	slice
SeisVision	Geographics	Halliburton	Windows	slice
SeisWorks 2D/3D	Landmark	Halliburton	UNIX	slice
SeisX 2D/3D	Paradigm	Paradigm	UNIX,Windows	slice
Tigress	Tigress	Tigress	UNIX	slice
VoxelGeo	Paradigm	Paradigm	UNIX,Windows	volume
VuPAK	SMT	SMT	Windows	volume

Table 21.1 Seismic interpretation software systems. Landmark and Geoquest each have over 40% of the market in dollar terms. Items are sorted alphabetically by product name.

for a UNIX-based heavy duty interpretation environment. What we consider the interpretation system often consists of many linked applications. All listed products include 2D and 3D seismic interpretation, basic geologic and log analysis, and mapping functionality. On the high end, a full Landmark install will likely include SeisWorks 2D/3D, EarthCube, Syntool, Stratworks, ZAP, TDQ, OpenWorks, and a commercial database program.

Every effort was made to generate a complete list of systems available at the time of writing. By definition, any such list is immediately out of date, but serves as a useful guide to the diversity of seismic interpretation systems. This list does not represent an endorsement of any particular system by the author, and any omissions are unintended.

In addition to software cost, you can expect to pay 8–18% of the original purchase price in annual software maintenance fees. The hardware cost ranges from about \$5000 (PC) to over \$50,000 (WK).

## 21.4 Interactive interpretation project components

The following is a description of tasks and effort for a hypothetical 150 square kilometer 2D/3D seismic interpretation project involving 200 wells [157]. Major headings and approximate work effort in man-days (MD) are shown in

## Elements of 3D Seismology

bold, followed by general task descriptions. The tasks are not necessarily chronological, and it is assumed the interpretation is entirely interactive (i.e., performed on an interpretation workstation). The effort for each major task is shown graphically in Figure 21.2A and in Figure 21.2B, where the efforts have been normalized to shortest task (3D visualization). Normalizing in this way makes it easier to upscale the results to larger or smaller projects.

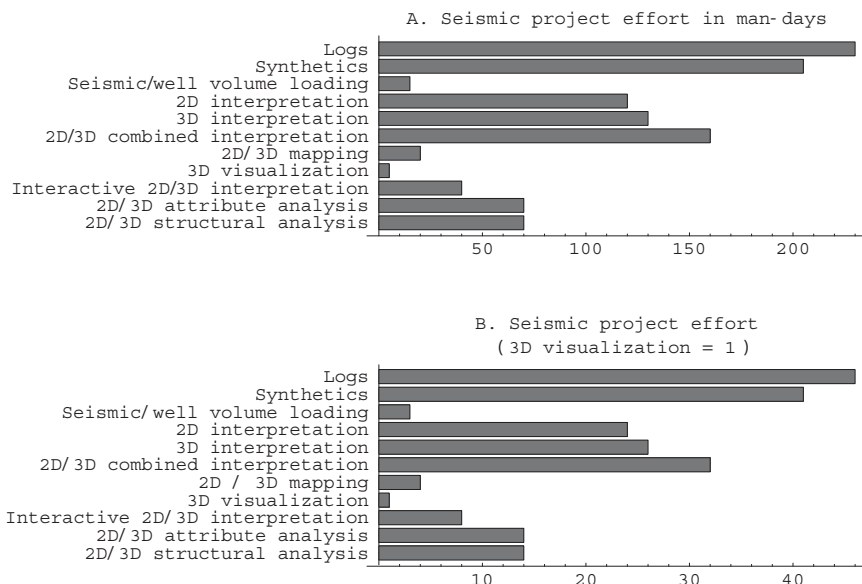


Fig. 21.2 Time and effort for major seismic interpretation tasks. (Data from [157])  
(A) Effort for each task given in man-days. (B) Effort normalized to the quickest task (3D visualization).

It is important to understand that software gives valid results only through human guidance— both software expertise and seismic interpretation expertise are needed.

1. **Logs (230 MD)** load LAS and ASCII; multiple log curve display; log editing and scaling; interpretation data (tops, fill options, etc.); log attributes and analysis; log correlation cross sections; well gridding and contouring.

2. **Synthetics (205 MD)** sonic only; density only; sonic and density; check shot; synthetic display; wavelet design; phase match synthetic to seismic.
3. **Seismic/well volume loading (15 MD)** 2D seismic data; 3D seismic data; quality control (histogram, editing, scaling); interactive line tie analysis; phase rotate and bulk shift; grid balancing (2D, 3D, wells); well data (ASCII, UKOOA, SEGY); log curves; horizons; faults; culture.
4. **2D Interpretation (120 MD)** single line; arbitrary line; autotracking; flattening; horizons, faults, flags (pick across ties).
5. **3D Interpretation (130 MD)** single line; arbitrary line; autotracking; time and horizon slice; flattening, horizons, faults, flags (pick across ties).
6. **2D/3D Combined interpretation (160 MD)** single line; arbitrary line; autotracking; time and horizon slice; flattening, horizons, faults, flags (pick across ties).
7. **2D/3D Mapping (20 MD)** gridding, contouring.
8. **3D Visualization (5 MD)** data display.
9. **Interactive 2D/3D interpretation (40 MD)** interactive 3D cube.
10. **2D/3D Attribute analysis (70 MD)** geostatistics; impedance inversion; AVO; multicomponent analysis.
11. **2D/3D Structural analysis (70 MD)** ray trace depth inversion; velocity analysis; time to depth conversion.

# 22

## Data Volume

Interpretation of 3D seismic data requires an understanding of the migrated data volume and how it can be dissected and interrogated.

The situation with conventional 2D data is a good place to start. As discussed in chapter 13, 2D prestack data is a volume of data whose dimensions are  $(N_p N_x N_o)$  where  $N_t$  is the number of time samples per trace,  $N_x$  the number of midpoints, and  $N_o$  the number of offsets. A seismic amplitude value resides at each point in this array. This 3D object is collapsed to a 2D seismic section by CMP stacking, which is simply summing over offsets after appropriate processing. After poststack migration, the 2D image is ready for interpretation. As we have seen, another path to the migrated image is direct prestack migration, in which the offset summation step is imbedded. In either case, the 2D migrated image is an array with dimensions  $(N_p N_x)$ . Figure 22.1 illustrates summation through CMP stacking or prestack migration to collapse the offset axis and to create a 2D panel of data.

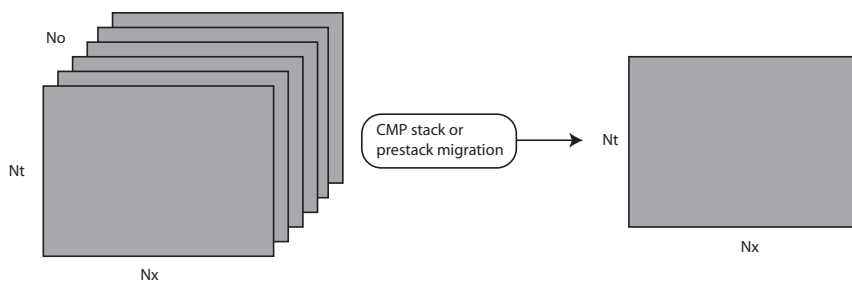


Fig. 22.1 Building a 2D image section from the 2D prestack data volume. You can think of the prestack data as composed of multiple 2D common offset sections.

## Elements of 3D Seismology

A 3D prestack data is a hypervolume with dimensions  $(N_p N_x N_y N_o)$ , where  $(N_x N_y)$  are the number of midpoints in the  $x$  and  $y$  directions. As with 2D, at each point in the prestack data, there is a value representing the seismic amplitude. CMP stacking or prestack migration again collapses the offset axis, resulting in an image volume as shown in Figure 22.2.

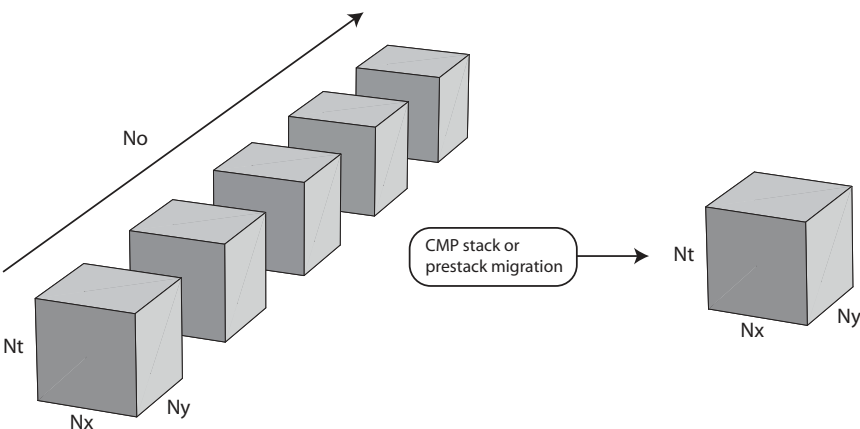
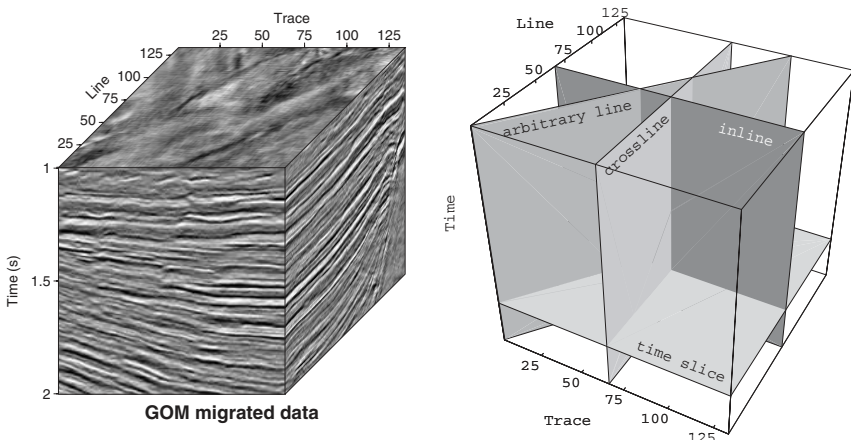


Fig. 22.2 A 3D image volume is formed by summation of prestack common offset volumes.

In all discussions that follow, we assume the seismic data volume is oriented correctly. In map view, each survey has a unique outline of live traces defining the image area. A trace is live if it contains non-zero amplitude values. In the shallowest part of any 3D survey, most of the traces appear dead (all amplitudes are zero), but this is simply due to the mute zone. Irregular surveys are usually padded out to a rectangular shape using dead traces. The live image area can be used with the processing report and well spots to confirm correct orientation of the survey. This sounds silly, but it is easy to get wrong because there are many orientation possibilities for a cube.

### 22.1 Data 2D subsets

As it arrives from the processor, a migrated 3D seismic data set is organized into lines composed of traces, just as 2D prestack data is composed of common offset lines. In the computer, these are all merged into a dense cube of data that can be sectioned, or sliced, in several ways, Figure 22.3. A consistent nomenclature is important for efficient communication between individuals and interpretation groups. The names given here are consistent with Brown [28].



*Fig. 22.3 Migrated 3D data are delivered from the processor organized into lines consisting of traces. These are merged into a dense cube of data on the interpretation system. Some standard slices of the data cube are shown on the right.*

Vertical cuts through the data cube are called lines or sections. Some common sections are inline (fixed line number) and crossline (fixed trace). The horizontal coordinates of (line, trace) can be kept or converted to (inline, crossline) or (x-bin, y-bin). A vertical section that is neither inline nor crossline is an arbitrary line and may be straight, curved, or segmented in map view as needed to intersect locations of interest. Figure 22.4 shows an example from the Gulf of Mexico.

For marine work, there is some agreement that inline is taken to be the direction of boat movement (parallel to receivers) and crossline is perpendicular to this. For land surveys, there is no uniform definition of inline and crossline.

Horizontal or subhorizontal cuts through the data cube are called slices. A time slice is a horizontal cut of a time cube, Figure 22.3, and a depth slice is a horizontal cut of a depth cube. Depth slices are only available if the data is delivered from the processor converted to depth or is converted to depth by the interpreter.

In addition to these simple plane slices, it is possible to follow a particular feature through the data and thereby generate a surface representing its structural configuration in the data volume. These tracking surfaces may be associated with reflection from a geologic horizon, fault plane, or fluid contact. Fault and fluid

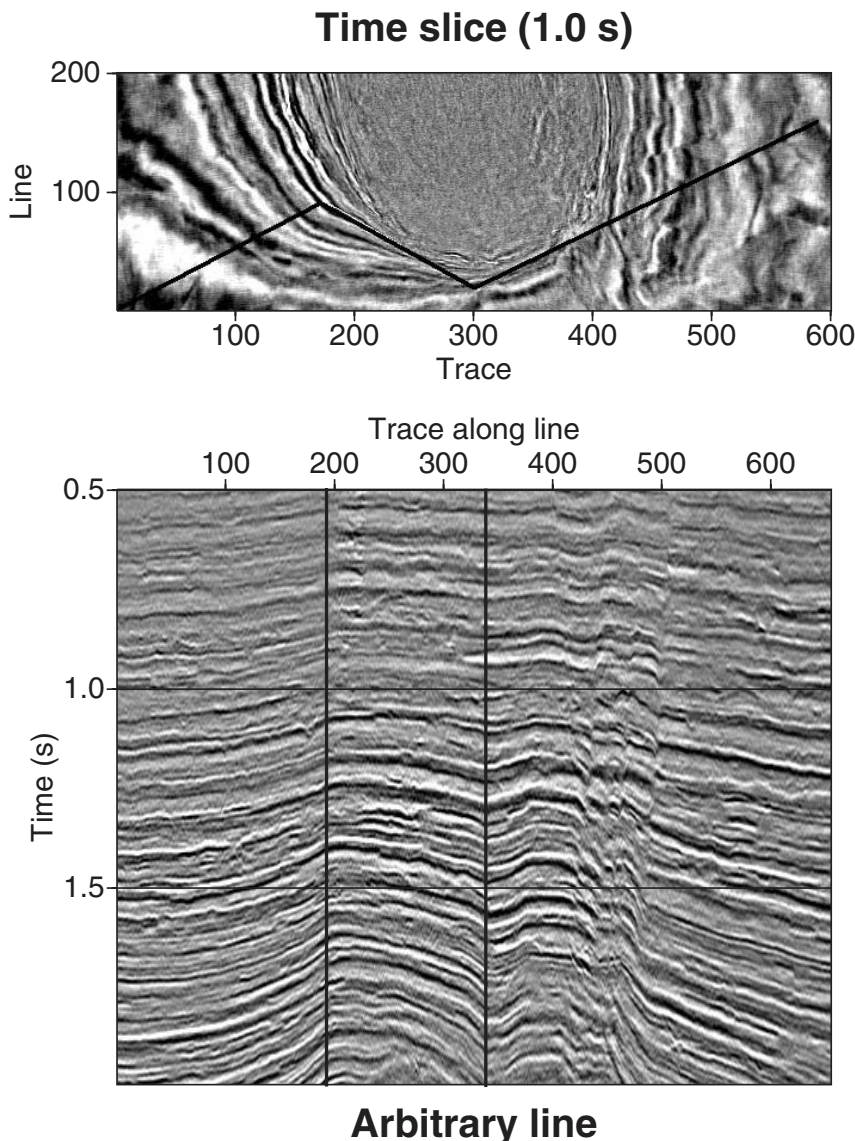


Fig. 22.4 An arbitrary line can be extracted from 3D data by defining a trajectory in map view as illustrated in this Gulf of Mexico example. The time slice shows the arbitrary line passing near a salt dome.

contact slices require very high quality data with clear mappable features. Worldwide these are rarely observed in seismic data, although in some basins, the Gulf of Mexico being one, they are not uncommon.

Plate 1 shows some 3D displays of information generated by horizon tracking. The surface represents time structure of the reflection event. From the tracking process, we also have the seismic amplitude at each point on this surface. This is often called the amplitude map of the horizon. The amplitude can be plotted alone as a 2D map or combined in a single 3D graphic with time structure. Plate 1D illustrates this concept.

## 22.2 Display of seismic data

There are four common ways of displaying seismic data as illustrated on a 2D section in Plate 2. A wiggle plot shows seismic amplitude as a horizontal deflection from baseline. This line plot can be displayed with or without area fill (variable area) on peaks or troughs. Wiggle plots are useful when it is important to see details of the waveform. In a grayscale image, seismic amplitude is assigned a gray value between black and white. If 256 shades of gray are used, then the image depth is 8 bits ( $2^8=256$ ).

Seismic interpretation systems with 16 bit and 32 bit graphics are now common. In terms of amplitude accuracy, 8 bit is adequate for most seismic applications. With 256 gray values to represent the amplitude range between the maximum negative value and maximum positive value, the amplitude resolution is 1 part in 256 or 0.4 %. Few things we do in petroleum seismology are accurate to better than one percent. However, to the human eye there is a noticeable difference between 8 bit and higher depth graphics, and there is merit to the logic that we should use the most accurate graphics systems available since subtle features might otherwise be lost.

In a color image, seismic amplitude is assigned an RGB (red-green-blue) color code or one of many other color models [28]. Be aware that many polarity and color conventions are in use. When color conventions for a project get confusing, always go back to the physical basis. An impedance increase generates a reflection coefficient. Is this considered positive or negative? What is the color associated with this situation? Keep it simple and stay close to the physics.

The fourth display method is inherently 3D. For each of the image types discussed previously, the 2D seismic data section is displayed as an array of pixels, each pixel being a basic 2D graphic element that can take on a grayscale or color value. In a volumetric display, the primitive graphic element is the voxel that is

## **Elements of 3D Seismology**

basically a small cube in 3D space. Like a pixel, it can be shaded by a gray or color value, and it has the additional property of transparency. This allows the display of 3D seismic data as a semi-transparent volume in which selected amplitude ranges are opaque and all others are transparent.

Plate 3 gives an example from the southern North Sea Basin [62]. Like all advanced visualization methods, voxel images help interpreters and decision makers to better understand spatial relationships in complex data. The real work of interpretation is often done in conventional slice mode, then imported for advanced visualization and presentation.

### **22.3 Interpretation products**

There is technology stretch in the area of seismic data interpretation. Large E&P companies routinely do volumetric interpretation involving specialized immersive environment viewing rooms [62] and software costing hundreds of thousands of dollars. Plate 4 displays two screen shots from this kind of high-end data analysis. The amount of information in a large 3D seismic volume is staggering, even before adding in leasehold information, surface equipment, and borehole data such as digital logs, VSP, pressure and production data, etc. Meanwhile for medium and small petroleum companies, the typical approach is slice-based interpretation on PC systems. Well control is worked in one horizon at a time and the projects tend to be smaller.

Volumetric data visualization is a broad and rising tide in fields as diverse as medical imaging, numerical modeling, and entertainment. We are heavy users and adapters of this technology, but even our visualization needs are dwarfed by the entertainment industry. For example, a 120-minute animated feature film consists of about 180,000 frames (24 per second) and each frame takes 6–90 hours of computer time to render.

For any seismic project, there is a bewildering array of possible plots and displays that can be used to describe interpretation results. A project review presentation will almost always be required. This is not a chore to be dreaded, but should be embraced as an opportunity for direct access to decision makers.

Remember the listener has limited time. Points must be made quickly and supported by clear unambiguous graphical displays. It is all too easy to load everything you know into a presentation and leave the audience confused. Voltaire had it right when he said, “The key to being a bore is to tell everything you know.” Be selective, concise, and brief. Seek out the advice of people who know a lot about color, articulation of form, composition, spatial relationships, and conveying complex visual information in efficient ways. They are called artists.

There are common elements that show up in many project presentations. Vertical seismic sections with and without interpretation quickly show structural setting and important amplitude features such as bright spots. A movie loop is often useful as a tool to quickly scan vast amounts of data. Time slices as shaded images reinforce the structural setting and amplitude variations. Horizon and fault slices in time or depth show lateral variation of seismic amplitude or a related quantity. These can be image, contour, or perspective plots. The prospect map can show combined structure, stratigraphy, amplitude, well control, surface equipment, lease map, and proposed locations. Additional maps can show attributes of various kinds, perhaps with multiple overlays.

Any prospect has a key feature. It may be a fault, four-way closure, AVO behavior, pinchout, or any number of other things. Make this key feature the centerpiece of your presentation and think carefully about the kind of display that will best convey the information you want to the listener. Like a good attorney, you want to make a compelling case, then stop talking.

# 23

## Structure

The field of structural geology is fully as broad and complex as petroleum seismology. It would be an endless diversion to give even an overview of structure concepts and methods. We must assume a basic understanding of deformation, static stress and strain, rock failure, fault types and occurrence, and large-scale tectonic influence on local structural elements. It is the combination of petroleum seismic data and expertise in structural geology that forms a powerful tool for structural analysis.

Mapping the structure of a 3D reflection surface involves the use of both horizontal and vertical sections in the data cube. Vertical sections afford the best view of general structural style and correlation of events across faults, but can be misleading due to apparent dip. Even in a 3D data cube, observed dips (or seismic slopes) are apparent unless the vertical section is extracted in the local dip direction. In horizontal sections, automatic time structure contours are seen by the intersection of each reflection event, analogous to a geologic subcrop map. This view also gives a direct estimate of horizontal resolution, is the primary tool for fault location and connectivity analysis, and shows true strike leading to true dip.

The 3D seismic gives a much better map of fault patterns than any grid of 2D seismic lines. It is usually the case that an area previously mapped with 2D data and remapped with 3D data will show an increase in the number and orientation of faults. This can dramatically alter reservoir engineering decisions concerning placement of wells and enhanced recovery systems [1].

Seismic interpretation has evolved significantly over the last 20 years. Some changes are related to computer technology, while others are geophysical or geologic advances. However, the basic goal of seismic interpretation remains: identify likely hydrocarbon accumulations to reduce drilling risk. This begins with structural mapping based on seismic and well control. The goal is a complete structural framework and one or more horizon depth maps throughout the image area.

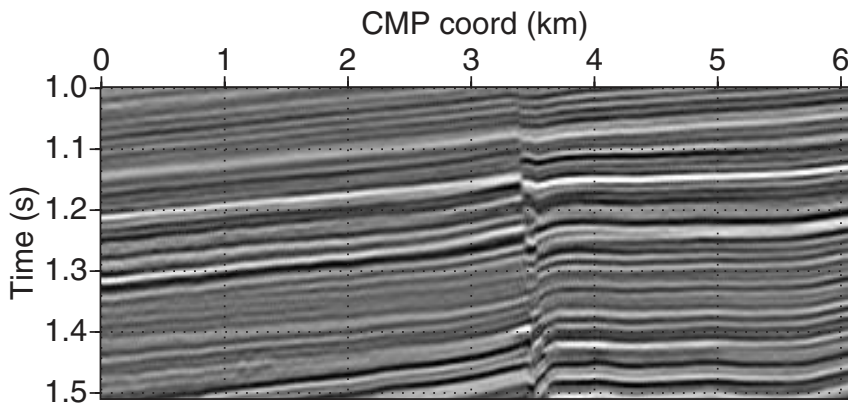
Once seismic events have been associated with geologic horizons using VSP or synthetics, structural interpretation proceeds in three basic steps: (1) fault detection and mapping, (2) horizon tracking, and (3) time-to-depth conversion.

### 23.1 Fault detection and mapping

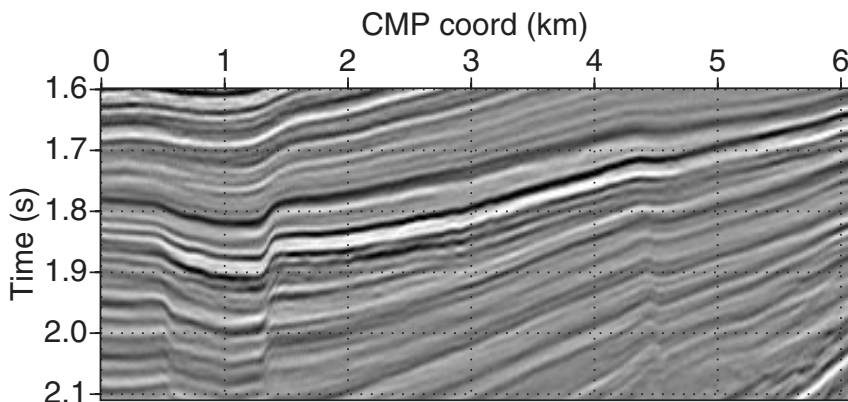
Since faults can act as petroleum traps and flow barriers, their identification and mapping is an important aspect of seismic interpretation. Fault throw (displacement) can be vertical, lateral, or some of each. Subvertical faulting is seen best on vertical seismic sections, while lateral (strike-slip) faults are better seen in horizontal sections.

Faulting often has the effect of degrading seismic image quality. This can be due to increased structural complexity, diffraction from small fault blocks, or scattering from fault zones themselves. Some faults simply may not be visible on seismic data.

1. In vertical sections faults are identified from
  - (a) Aligned bed terminations are the best evidence (Figure 23.1A)
  - (b) Aligned abrupt dip changes (Figure 23.1B)
  - (c) Aligned dim amplitude also called dim-out or fault shadow
    - i. May imply pure strike-slip fault, small offset faulting, or fracturing
    - ii. Gas migration along fault or fracture can cause shadowing
    - iii. Common in strike lines where faults are nearly parallel to line
    - iv. Better visibility on color images plotting absolute amplitude
  - (d) Fault plane reflection
    - i. Best seen on prestack data or DMO stack section [88]
    - ii. Relatively rare world-wide but not uncommon in Gulf of Mexico
    - iii. Coincident with bed terminations in final migrated section
2. In horizontal sections faults are indicated by
  - (a) Time slice—lateral displacement of amplitude bands (Figure 23.2)
  - (b) Horizon slice—linear or dendritic amplitude anomaly
    - i. Horizon needs to be trackable across the fault .
    - ii. Amplitude effects can be very subtle and image enhancement is often required. This can be artificial illumination, horizontal gradient maps, or coherency [8].
    - iii. Beware of faults that are parallel to the acquisition grid because they have a higher probability of being false indicators related to acquisition footprint.



**A. Bed terminations**



**B. Abrupt dip changes**

Fig. 23.1 Evidence of faulting in a vertical seismic section from SE Asia. (A) Aligned bed terminations form a prima facie case for faulting. In this case it appears to be a simple fault above 1.2 s grading to a compound fault zone below. (B) Abrupt dip changes form a continuum between folded and faulted rocks. The geological fault may well extend into regions that only appear folded on seismic data due to resolution limits.

## Elements of 3D Seismology

Qualitative fault interpretation only demonstrates the presence of the fault. Quantitative analysis includes fault type, orientation, azimuth, precise location at the target horizon, and throw. If a fault is viewed in a seismic section normal to strike, the vertical component of throw can be estimated from  $\Delta z = \Delta t \cdot v/2$ , where  $\Delta t$  is the time throw on the fault and  $v$  is the average interval velocity between the upthrown and downthrown block.

Calculation of fault throw on migrated seismic data requires that interval velocity at the target be known. If a sonic log is available, then sonic interval velocity can be used after appropriate upscaling. Without sonic information, useful estimates can still be made if an approximate velocity function is known. For example, if we are working with migrated data from a soft clastic basin, the average interval velocity can be well approximated by a linear velocity function [95]. The set of equations that apply in this case are well-known [177]. Velocity at depth  $z$  due to a velocity gradient  $k$  is given by

$$v(z) = v_0 + k \quad (23.1)$$

average velocity to this depth is

$$v_a(z) = v_0 + k \cdot z/2 = v(z)/2 \quad (23.2)$$

and interval velocity for a given vertical reflection time is

$$v(t) = v_0 \left[ 1 + \frac{2 k t}{4 - k t} \right] \quad (23.3)$$

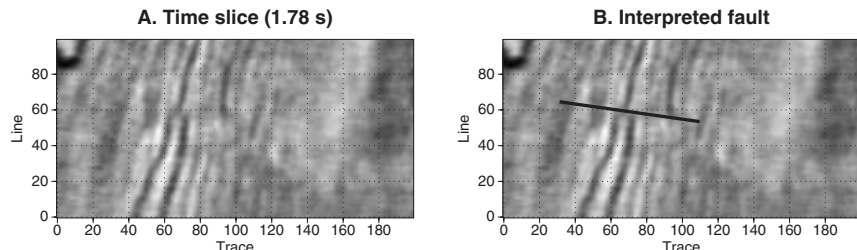


*Fig. 23.2 Faulting evidenced by lateral displacement of amplitudes in a time slice. Interpreted fault is indicated on the right image. Data is from the Stratton Field of south Texas [102].*

The depth for a given vertical reflection time is

$$z(t) = \frac{2 v_0 t}{4 - k t} = v_a(t) t/2 \quad (23.4)$$

and the vertical component of fault throw,  $\Delta z$ , for a given vertical time throw,  $\Delta t$ , is

$$\Delta z = v(t) \Delta t/2 \quad (23.5)$$

As an example, consider the migrated data section in Figure 23.3. This is marine data from a soft clastic basin in SE Asia, and we want to estimate fault through of the dotted event. To illustrate the method, we assume the velocity model

$$v(z) = 1500 + 0.4 z \quad (23.6)$$

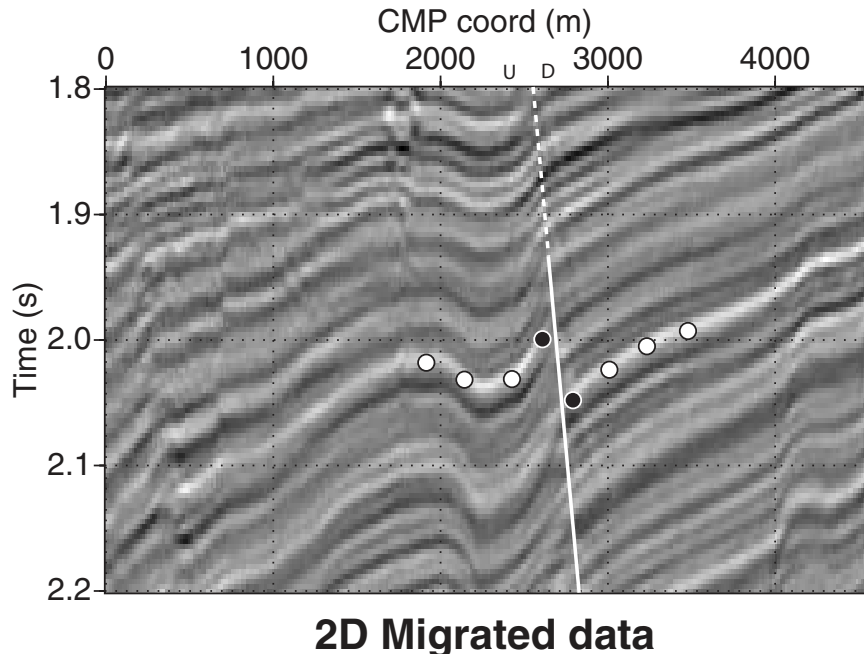


*Fig. 23.3 Estimating depth and fault throw using a linear velocity model.*

## Elements of 3D Seismology

where the interval velocity is in m/s and depth is in meters. From the figure, the average travel time of the up thrown and down thrown blocks is 2.050 s, giving a depth of

$$z(t) = \frac{2 v_0 t}{4 - k t} = \frac{2 * 1500 * 2.05}{4 - 0.4 * 2.05} = 1934 \text{ m} \quad (23.7)$$

The average interval velocity at this level is

$$v(t) = v_0 \left[ 1 + \frac{2 k t}{4 - k t} \right] = 1500 \left[ 1 + \frac{2 * 0.4 * 2.05}{4 - 0.4 * 2.05} \right] = 2274 \text{ m/s} \quad (23.8)$$

Time offset on the fault is 0.05 s which corresponds to a vertical throw of

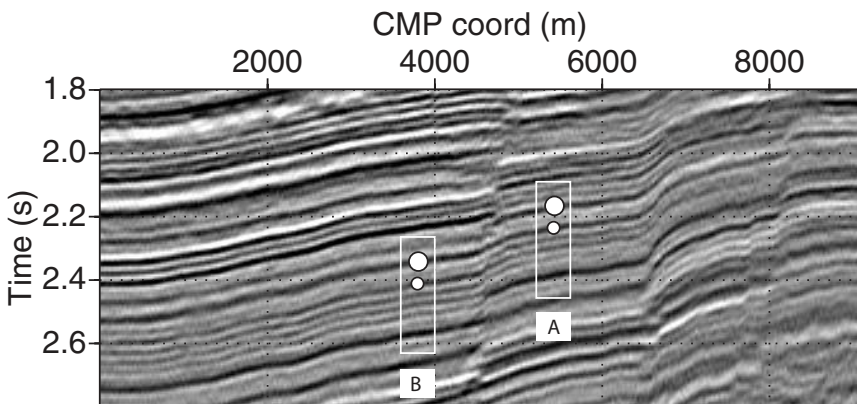
$$\Delta z = v(t) \Delta t / 2 = 2274 * 0.05 / 2 = 57 \text{ m} \quad (23.9)$$

When seismic reflections are followed away from well control, and a fault is intersected, it may be necessary to jump-correlate events of interest. This is simply the identification of a common event on each side of the fault, but the procedure may be complicated by stratigraphic thickening or thinning across the fault. A seismic jump correlation is shown in Figure 23.4. When a conflict exists between wells on either side of a fault and a seismic jump correlation, the well information takes precedence.

An important part of structural interpretation is detailed markup of the data. Plate 5 shows part of such a marked-up section. Depth, fault throw, and dip estimates use a linear velocity model. Dip calculated on a 2D or 3D seismic section can be apparent or true depending on the line orientation. Consider a dipping plane in a 3D volume, Figure 23.5. Of all possible vertical sections through the cube, only one gives the true dip, but every horizontal section gives the true strike. Since dip and strike are, by definition, perpendicular, the strike orientation can be used to infer the dip direction but not the magnitude. If the apparent dip in a given direction is known, and true dip azimuth is known, there are standard structural geology techniques to compute true dip.

## 23.2 Time structure and horizon tracking

It is necessary to map fault patterns before horizon tracking because the faults will naturally segment the survey area into blocks. Within each block, auto-picking can be used to map an event of interest, and a composite map can then



## Migrated 2D data

Fig. 23.4 Jump correlation across a fault. A small panel of data, labeled A, is outlined on the right side of the fault. Two key horizons are marked. The data panel was copied, then moved across the fault and adjusted until a satisfactory fit was made at B. Note the apparently continuous event connecting the small dot at A with the large dot at B. This is a false correlation.

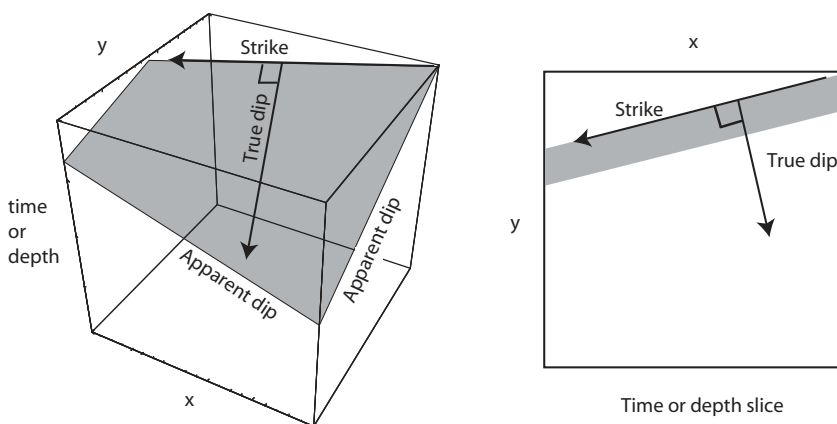


Fig. 23.5 Strike and dip relationships for a single dipping 3D plane, and the appearance of true strike in a horizontal slice.

## Elements of 3D Seismology

be constructed. The goal is to create a time structure map that represents geometry of the reflection surface in the 3D data volume.

The simplest way of finding time structure contours for a seismic event is to view time slices. By mapping the intersection of an event with a sequence of time slices, a time structure map can be manually generated. Figure 23.6 illustrates this idea using a salt dome contact in the Gulf of Mexico. Making an entire time structure map in this fashion is far too tedious.

The primary tool for generating a time structure map is automatic tracking of the horizon. However, automatic tracking can be expected to fail when significant faulting or noise is present. It is the interpreter's responsibility to

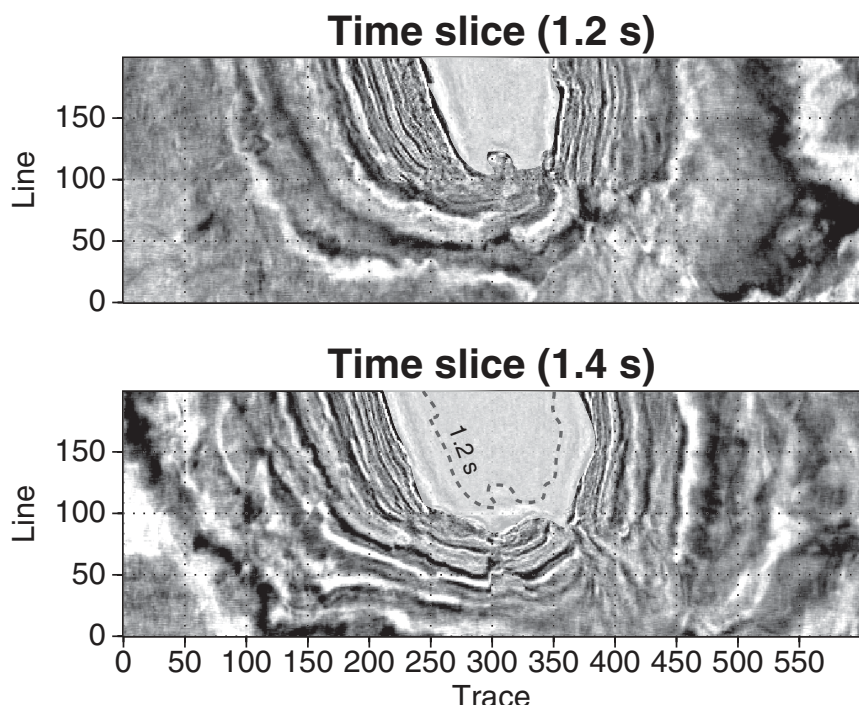


Fig. 23.6 Time slices directly show time structure contours. These Gulf of Mexico time slices cut across a salt dome (shaded white). The perimeter of the salt-sediment interface on any time slice is the time structure contour of that contact. On the 1.4 s time slice the 1.2 s time structure contour is shown for reference (dashed). Bin size is 25 x 25 meters.

correlate reflectors of interest across faults and poor data areas, then automatic tracking can extract reliable horizon results within each continuous area.

For a 3D seismic horizon, both traveltime and amplitude are available at each bin location. Extracting this information leads to a time structure map  $t(x,y)$  and a horizon amplitude map  $a(x,y)$ . In practice, there is great choice in what amplitude-related quantity to extract along the horizon.

For example, we could extract the peak amplitude, RMS amplitude over a window centered on the peak amplitude, logarithmic trace curvature at the first zero crossing, or any number of other measures. Wave physics tells us it is the peak amplitude that has some chance of being proportional to the underlying reflection coefficient, and this requires the interface to be vertically isolated. Whatever amplitude measure is extracted for mapping, its use should be justified in terms of reflection physics.

In horizon tracking, the user selects one or more seed points on an event and a criteria for following it between seed points and throughout the data volume. The search method could be as simple as scanning the next trace for the maximum amplitude within a certain dip window or as sophisticated as a cross correlation or semblance estimate in a user-defined window. The mechanics of autopicking [62] are illustrated in Plate 6 for 2D and 3D data.

Plate 7 a shows a representative line from the Glenpool survey with the Devonian Wilcox horizon highlighted. Autopicking throughout the survey area results in the time structure and horizon amplitude maps shown in Plate 7B and C. In this case, the amplitude measure is simply peak amplitude of the Wilcox in each bin.

### 23.3 Time-to-depth conversion methods

If several wells have penetrated the horizon of interest, a wells-only depth map can be constructed by some form of interpolation of the well control points. These serve as  $(x,y,z)$  data points that can be used to generate a depth structure surface by methods such as contouring, gridding, or kriging. Though we think of the well information as hard data, a map based on even dense well control points is non-unique. Essentially we are constructing a surface based on a finite, clustered set of points in 3D space, and the surface may not be continuous due to faulting or erosion. Clustering of wells introduces further complications and non-uniqueness. Of course, we must generate some kind of map from the well data, but the point is to understand it is only an approximation to the actual geological surface.

Depth conversion is the process of combining seismic time structure, well control, and velocities to create a depth structure map or volume. There are

## Elements of 3D Seismology

several depth conversion techniques [199], and each is intimately connected to migration. Which method is best in a given situation depends on the kind of migration applied before interpretation, the strength of lateral velocity variations in the subsurface, and the amount of well control.

Vertical ray depth conversion assumes the migrated traveltimes represents information from directly below each bin location. This method gives depth from the acquisition surface or datum using well control to derive average velocities. In areas of gentle structure and weak lateral velocity variation, the vertical ray method is quick and reasonably accurate for time migrated data. If the data has been depth migrated and displayed in time, the vertical ray method works even in the presence of lateral velocity variations. If a densely drilled shallow horizon is available and can be correlated into the seismic data, the vertical ray depth conversion can proceed from this horizon and thus avoid complications associated with the weathering layer at the earth surface.

Image ray depth conversion [199] accounts for the fact that time migration does not correctly bend rays. Figure 23.7 shows a simple example in which a fault is imaged through a high velocity wedge. Even if velocity in the wedge is constant, its change in thickness introduces a lateral velocity gradient. Since time migration does not strictly enforce Snell's law, the migration traveltimes are not vertical, but along image rays. Depth conversion must take this into consideration.

Ray depth migration (also called section or map migration) is the most accurate form of depth conversion for interpreted horizons. It operates on the unmigrated zero offset data and incorporates the refraction effect. Depth conversion is accomplished along rays that intercept the reflector at normal incidence.

Volumetric depth conversion stretches time migrated data to a depth cube using a  $v(x,y,z)$  velocity model. This is basically vertical ray depth conversion applied to the entire data cube, rather than individual time structure surfaces and is subject to the same comments made earlier.

Prestack depth migration operates directly on the prestack seismic data to create a depth volume. This is common in complex situations such as subsalt imaging in the Gulf of Mexico. The resulting depth image is unlikely to match well control without manual warping.

Finally, we note there is increasing awareness that important aspects of marine seismic data, particularly in deep water, are affected by variations in water velocity [124]. In the months-long time period required to shoot a large 3D survey, seasonal changes in water velocity can lead to reflection traveltimes mis-matches that require special treatment in processing.

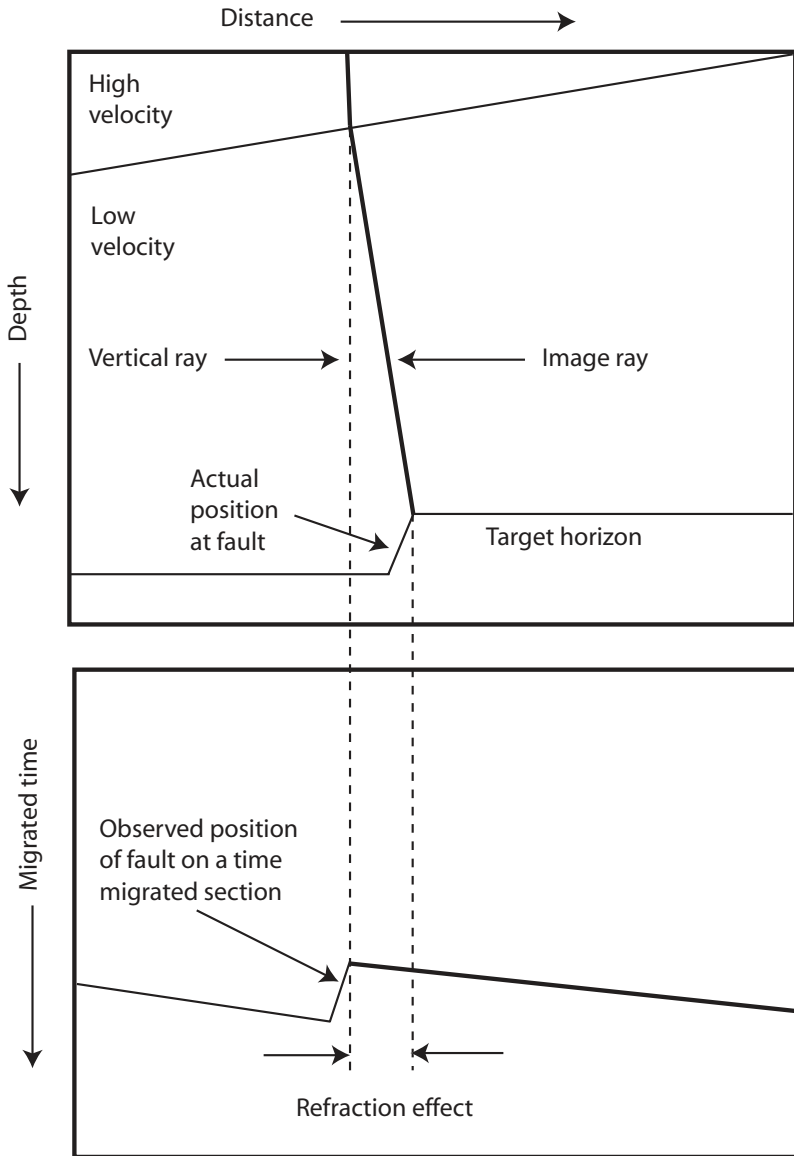


Fig. 23.7 Image rays and depth conversion. The high velocity wedge introduces a lateral velocity gradient. In such a case time migration traveltimes are not along vertical rays, but image rays that bend according to Snell's law. Vertical ray depth conversion of the time section will show the fault in the incorrect position. Image ray depth conversion will transform the time data to depth along image rays, and the fault will be correctly located. (Redrawn from [199]).

## 23.4 A vertical ray case history

To illustrate the major components of a depth conversion project, we will consider a case history from offshore Irian Jaya in eastern Indonesia described by Keho and Samsu [95]. An area map is shown in Plate 8A. The goal is to map reservoir structure in the Vorwata area. The reservoir is Jurassic Roabiba Sand, but direct mapping from seismic is not possible because the Roabiba is a weak, discontinuous reflection. Depth maps were constructed on the top Miocene Kais and interval thickness from Kais to base of Cretaceous. Adding a well-based Jurassic shale isopach to the base Cretaceous depth map delivered the final Jurassic Sand depth map. This map was generated using seismic data and wells v1–v4 on the Vorwata structure and several other wells in the area. The depth map was used to locate and make depth predictions for seven additional Vorwata wells.

We will describe the seismic depth mapping procedures used to derive the top Kais and base Cretaceous depth maps. Plate 8B shows an interpreted seismic section from the study area. Despite the appearance of this section, the Kais is actually a gently sloping feature. On this line, the Kais formation ranges 340–1980 m depth across a span of 70 km, which calculates out to an average dip of 1.3 degrees. Layers one and two for the depth conversion process are labeled on this section. Layer one extends from acquisition surface to top Kais and layer two from Kais to base of Cretaceous.

The depth conversion is accomplished using a two-stage linear velocity function. Layer one is clastic and velocity variation with depth is almost entirely due to compaction. The velocity function used to model this layer is

$$v_a(z) = v_0 + k_1 z \quad (23.10)$$

where  $v_a$  is the average velocity from surface to top Kais,  $v_0$  is the surface velocity,  $k_1$  is the layer one velocity gradient, and  $z$  is depth to the top Kais. Using a time structure map for the top Kais (not shown) and several well penetrations,  $v_a$  can be computed at each well location using the log pick and seismic time pick ( $v_a=2z/t$ ). To calibrate the layer one linear velocity model, a crossplot is made between the average velocity and Kais depth as shown in Plate 9A. The best fit line to this data ( $R^2=0.98$ ) is given by the equation

$$v_a(z) = 1662 + 0.32 z \quad (23.11)$$

where velocities are in m/s and depths in meters. The excellent linear fit of these points justifies use of the linear velocity model. Since the velocity gradient is associated with compaction and cementation trends in layer one, it is taken as a constant across the survey area.

At each well location, we now know the average velocity and depth to top Kais, and the velocity gradient. This allows the calculation of surface velocity through the relationship

$$v_0(x, y) = v_a - k_1 z \quad (23.12)$$

which is shown in Plate 9B. This map was created by contouring the  $v_0$  values at each well. If the linear velocity model were a perfect representation of subsurface velocities for layer one, then  $v_0$  would be a constant. The fact that it is a slowly varying function is a second quality indicator of the linear velocity model.

Given the  $v_0(x, y)$  map of Plate 9B, the fixed velocity gradient from Plate 9A, and the observed top Kais time picks  $t(x, y)$  (not shown), an average velocity map can be constructed at each bin location in the 3D survey using

$$v_a(x, y) = \frac{v_0(x, y)}{1 - k_1 t(x, y)/2} \quad (23.13)$$

The  $v_a(x, y)$  map in Plate 10A shows average velocity gently increasing to the east as the top Kais deepens. The top Kais depth map is then generated by grid operations using

$$z_{tk}(x, y) = v_a(x, y) t(x, y)/2 \quad (23.14)$$

Plate 10B is the top Kais depth map constructed in this way and shows gentle deepening to the east. The fact that the picked time values do not undergo any lateral displacement means this is a vertical ray depth conversion procedure, albeit a very careful one.

The next step is to generate an isopach map for layer two which goes from top Kais to base Cretaceous. A second linear velocity function is used for to model the average interval velocity of this layer

$$v_{ai} = v_0 + k_2 z_m \quad (23.15)$$

where  $v_{ai}$  is the average layer two interval velocity,  $v_0$  is the surface velocity,  $k_2$  is the layer two velocity gradient, and  $z_m$  is the depth to the midpoint of the top Kais to base Cretaceous.

## Elements of 3D Seismology

It is the average interval velocity we want, rather than the instantaneous interval velocity [127], because multiplying  $v_{ai}$  by the vertical travel time in this layer gives the layer thickness. Unlike layer one, lithology in layer two grades laterally between clastics and carbonates. Within the linear velocity framework, it is possible to accommodate this fact and construct clastic and carbonate fraction maps; details are contained in the original article [95].

The base Cretaceous time structure map, Plate 11A, is considerably more complicated than the top Kais depth map indicating structural, stratigraphic, and lithologic variability. The layer two average interval velocity can be built from the relationship

$$v_{ai}(x, y) = \frac{v_0(x, y) + k_2 z(x, y)}{1 - k_2 \Delta t(x, y)/2} \quad (23.16)$$

where  $v_0(x, y)$  and  $k_2$  are determined as described for layer one,  $z(x, y)$  is the top Kais to base Cretaceous depth grid, and  $\Delta t(x, y)$  is the top Kais to base Cretaceous isochron (time interval) grid. The base of Cretaceous integrated depth map  $z_{bc}$  is then generated by grid operations using

$$z_{bc}(x, y) = z_{tk}(x, y) + v_{ai} \Delta t(x, y)/2 \quad (23.17)$$

where  $z_{tk}(x, y)$  is the top Kais depth map. This map is shown in Plate 11B.

The accuracy of this map was tested by results from seven wells drilled after the v4 well. The mean depth error between predicted and observed base Cretaceous was  $-0.11\%$  with a maximum error of  $1.87\%$ . In absolute terms, the mean error is  $-4.3$  m and the maximum is  $72.8$  m. Depth errors over  $30$  m occur in only two wells and these are  $10$  and  $11$  km from the nearest control points.

Velocity maps in this type of depth conversion are important quality control indicators. For example, anomalies in the  $v_0$  map at well locations may indicate bad seismic time picks or well depth picks and smooth  $v_0$  variations may indicate broad areas of structural uplift or lateral lithology changes.

## 23.5 Structural uncertainty

Uncertainty and error analysis are important topics in seismic data interpretation. A depth map based on seismic data has uncertainties related to preprocessing, stacking, migration, interpretation, and the depth conversion itself.

Some of these can be quantified, for example the misplacement of a point in 3D space due to migration velocity uncertainty [180] is given by

$$\Delta x = -2z \frac{N_x}{N_z} \frac{\Delta v}{v} \quad (23.18)$$

$$\Delta y = -2z \frac{N_y}{N_z} \frac{\Delta v}{v} \quad (23.19)$$

$$\Delta z = z \left( 1 - \frac{N_x^2 + N_y^2}{N_z^2} \right) \frac{\Delta v}{v} \quad (23.20)$$

where  $(\Delta x, \Delta y, \Delta z)$  are the location uncertainties of a point actually located at  $(0, 0, z)$ ,  $(N_x, N_y, N_z)$  are the reflection surface normal vector components at the point,  $\Delta v$  is velocity uncertainty, and  $v$  is the velocity. These relationships are valid until strong lateral velocity variations are present.

To help understand the nature of these important equations, consider a reflection point 3 km deep. If the reflector has zero dip, then the normal vector components are  $(N_x, N_y, N_z) = (0, 0, 1)$  and the position uncertainty reduces to

$$\Delta z = z \frac{\Delta v}{v} \quad (23.21)$$

meaning that velocity errors only have the effect of vertical misplacement of horizontal reflectors. A 5% velocity error acts through migration to introduce a depth error of

$$\Delta z = 3000 * 0.05 = 150 \text{ m} \quad (23.22)$$

Structural uncertainty analysis is valuable in the design of optimum well trajectories as shown in Figure 23.8.

## Elements of 3D Seismology

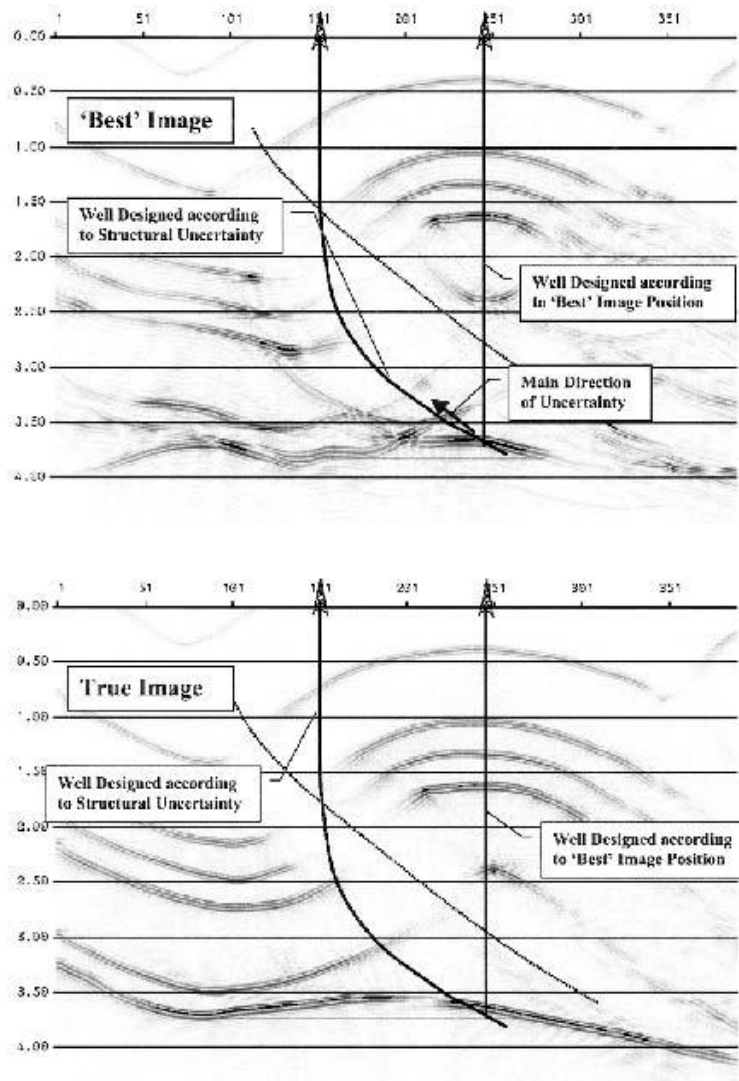
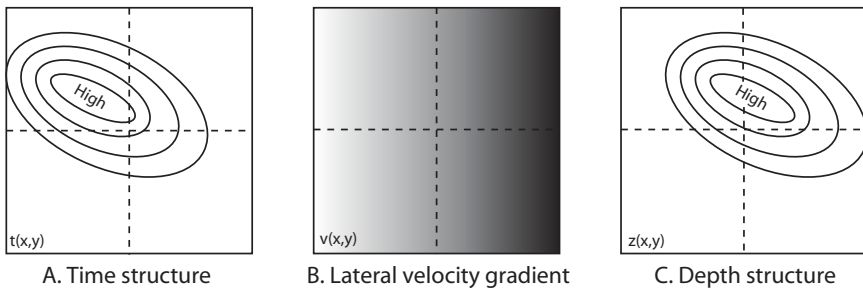


Fig. 23.8 Structural uncertainty analysis determines the direction of maximum uncertainty so that well trajectories can be designed accordingly. In this synthetic example, a vertical well based on the best available structural seismic image is significantly down dip on the actual structure. A deviated well aligned with the maximum uncertainty direction increases the probability of accurately intercepting the target (From [180]).

## 23.6 Extreme velocity variation

Time structure can be misleading. Apparent structural closures and other features can be due to lateral velocity variations above the mapped horizon as illustrated in Figure 23.9. When the gradients are weak, the effect may barely be noticeable. For strong gradients, the method of depth mapping from tracked time surfaces can fail altogether.



*Fig. 23.9 Time structure can be misleading. (A) Time map generated from a seismic cube. (B) Velocity contour map from well control or other data. Half-velocities are used because the time map represents two-way reflection time. Dark shades indicate higher velocity. (C) Vertical ray depth map created by multiplying grid A\*B. This map is a better estimate of true subsurface structure than the time structure map, because lateral velocity variations have been taken into account. But if the gradient is strong enough, the depth conversion should proceed along image rays not vertical rays.*

For subsalt, subthrust, and other difficult settings, depth migration is increasingly used to directly generate a migrated depth volume. Horizon tracking within this volume will yield a depth map, but data quality in such difficult circumstances rarely supports autotracking. In clastic-salt basins such as the Gulf of Mexico, the effect of salt is to introduce extreme distortion to any seismic image plotted with a time axis. In Figure 23.10 a Gulf of Mexico velocity model is displayed in depth and time. As the salt thickness changes laterally, it sets up strong lateral velocity gradients which bend deeper features into confusing shapes. Migration results displayed in time can be very misleading in subsalt interpretation and other situations involving extreme lateral velocity variation.

## Elements of 3D Seismology

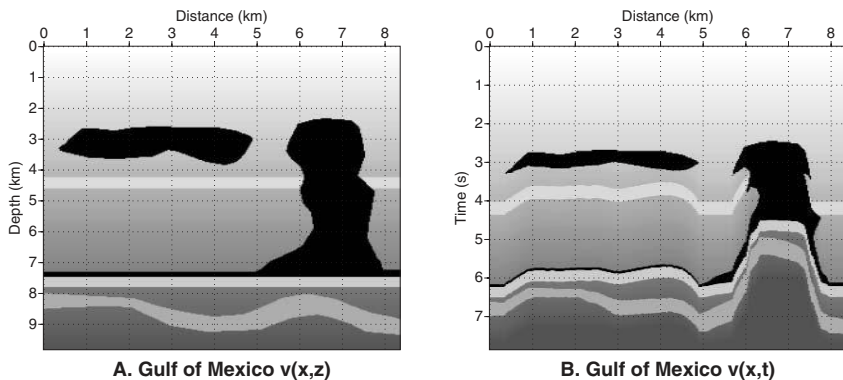


Fig. 23.10 Example of depth structure versus time structure from the Gulf of Mexico. (A) Depth image of GOM velocities. The background velocity model (in m/s) is  $v(z)=1500+.4z$ , which is typical of the region. Salt velocity is about 5000 m/s. An ideal migration displayed in depth would have this same geometry. (B) Result of vertical ray depth-to-time conversion of the GOM velocity field to simulate geometry of an ideal migration displayed in time. Note the extreme distortion of time sections in an area of strong lateral velocity variation.

# 24

## Stratigraphy

The subject of stratigraphy and sedimentation is concerned with rock features ranging in size from  $10^{-5}$  m (grain size) to  $10^5$  m (depositional systems). Our interest here is a basic understanding of those stratigraphic features likely to be visible in seismic reflection data. With the bandwidth limitation of surface seismic data, this means features thicker than a few tens of meters and lateral extent of twice that.

Large-scale stratigraphic features seen in 2D seismic data are evidenced by bed terminations. Stratigraphic bed terminations seen in seismic data occur in only a few ways as illustrated in Figure 24.1. From these basic building blocks, complex geologic relationships can be deduced through the principles of seismic stratigraphy [188] developed in the 1970s and sequence stratigraphy [189] a decade later.

From the mid-1980s on, 3D seismic data afforded a direct map view of stratigraphic features that was never available from even a grid of 2D seismic lines. This revolution is continuing with more and better ways to pull stratigraphic information from 3D seismic data.

### 24.1 Stratigraphy and 2D seismic data

Sedimentary systems can be divided into the two broad categories of clastics (sandstone, shale, etc.) and carbonates (limestone, dolomite, etc.). Clastic deposition is related to continental erosion and shoreline proximity, and carbonate sediments are largely produced *in situ* rather than transported over large distances.

A relationship that applies to either kind of sedimentation is the accommodation space equation [186]

$$\dot{T} + \dot{E} = \dot{S} + \dot{W} \quad (24.1)$$

## Elements of 3D Seismology

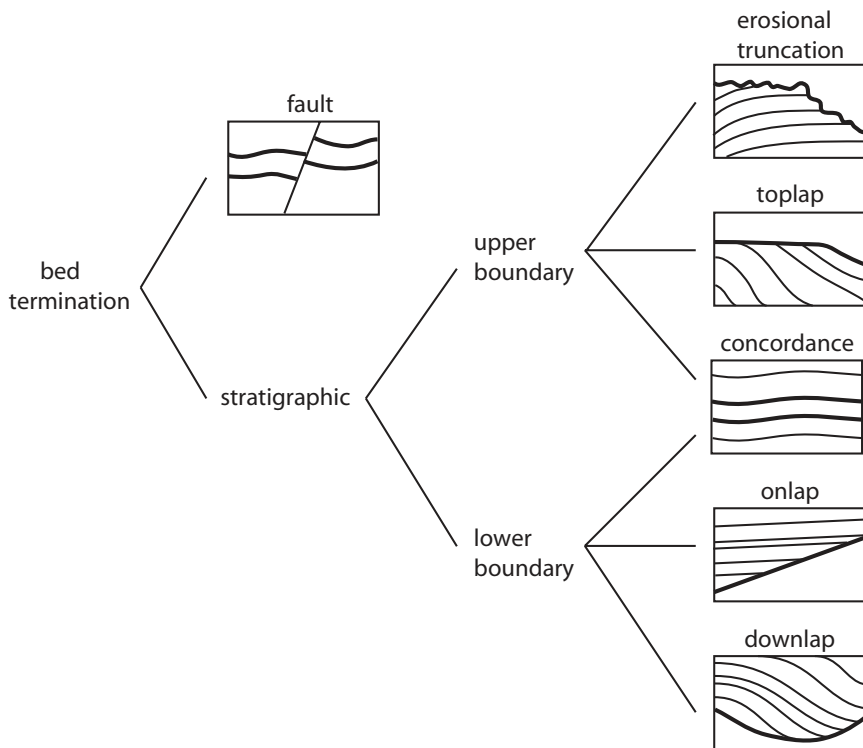


Fig. 24.1 Classification of bed terminations likely to be observed on seismic data. Stratigraphic terminations are fundamental components of seismic stratigraphy using 2D seismic data.

where a dot denotes differentiation with respect to time,  $\dot{T}$  is rate of tectonic subsidence,  $\dot{E}$  is rate of eustatic sea level rise,  $S$  is rate of sedimentation, and  $W$  is rate of water depth increase. Figure 24.2 is a sketch defining the quantities in this equation.

The idea of global sea level change is imbedded in the accommodation space equation, but it also describes local situations related to tectonic movements, glacial rebound, and other effects. The causes of eustatic sea level change can be classified into five broad categories (Figure 24.3). Over geologic time eustatic sea level fluctuates in response these drivers. This results in characteristic, large-scale sedimentation units termed depositional sequences, Figure 24.4, as sea level falls, passes through a low stand, rises, passes through a high stand, and repeats.

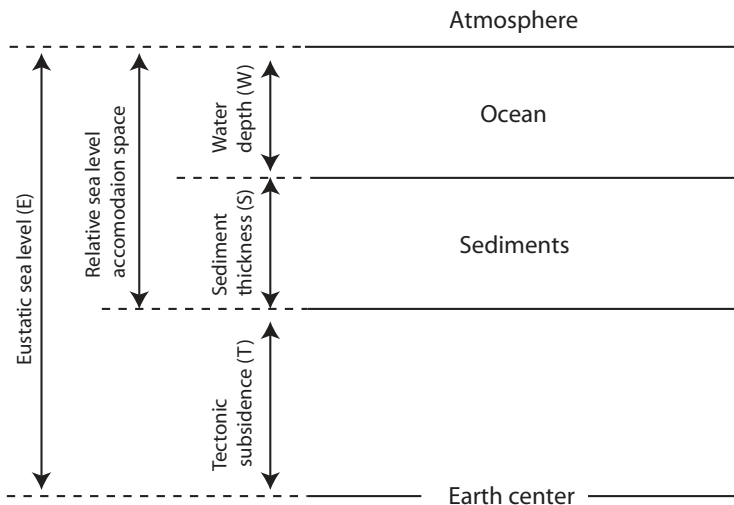


Fig. 24.2 Definition of terms related to eustatic sea level and the accommodation space equation.

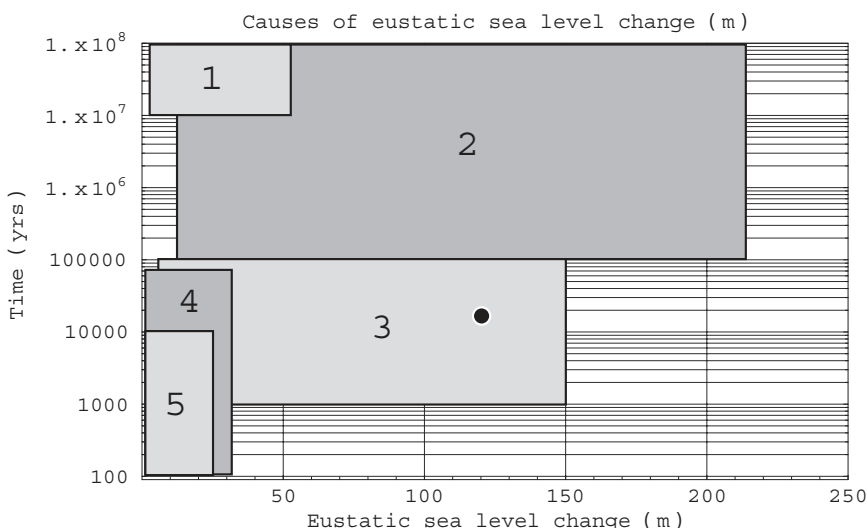


Fig. 24.3 Causes of eustatic sea level change. (Data from [186]) (1) Filling of ocean basins with sediment derived from continental weathering. (2) Changes in rate of sea floor spreading. (3) Continental and mountain glaciation. The dot represents our current situation, in which glacial melting over the last 18,000 years has resulted in sea level rise of 120 m. (4) Changes in groundwater volume. (5) Ocean temperature changes.

## Elements of 3D Seismology

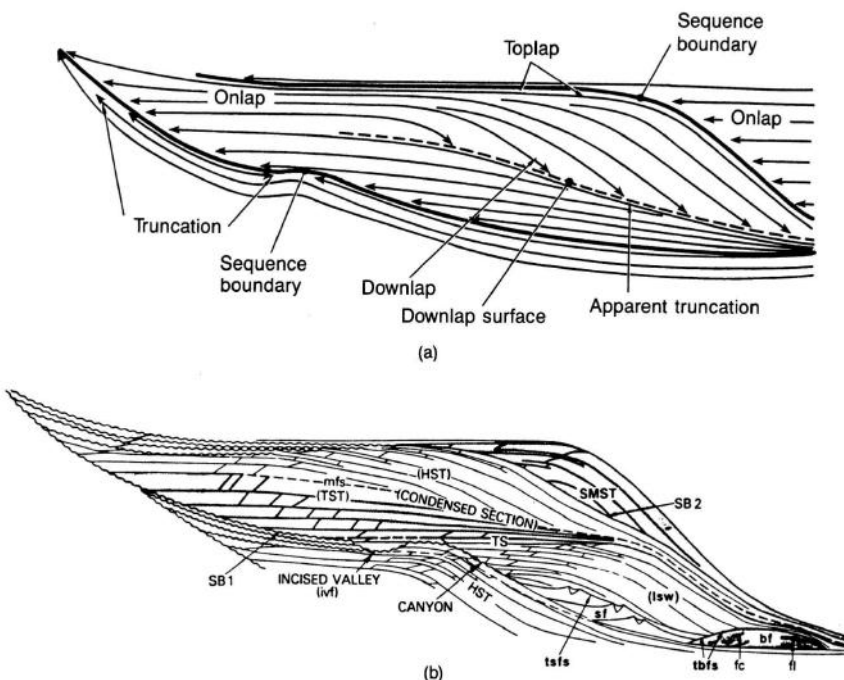


Fig. 24.4 System tracts and the seismic patterns that indicate sea-level changes. Coastal onlap is evidence of a rise of sea level, a seaward and downward shift in onlap is evidence of a fall of sea level, and a landward movement of sediment packages is evidence of transgression. (a) Types of reflection terminations. (b) System tracts; a stratigraphic sequence begins with a sea-level fall at the end of a highstand tract (HST) and ends with the next highstand tract. A lowstand tract (LST) is the first unit after a large sea-level fall, lying on top of a type 1 sequence boundary (SB1). It is subdivided into basin-floor fan (bf), slope fan (sf), and lowstand wedge (lsw). A rapid rise of sea level produces a transgressive tract (TST), at the top of which there lies the maximum flooding surface (mfs) and a thin, fossil-rich condensed section. The first unit after a sea-level fall that does not fall below the shelf edge (type-2 sequence boundary, SB2) is a shelf-margin tract (SMST). (From Vail, 1987, 2, 4.) (Figure and caption from [165])

A depositional sequence is the largest in a hierarchy of stratal units consisting of (progressing largest to smallest) sequence, systems tract, parasequence set, parasequence, bedset, bed, lamina set, and lamina. Only the first three may have length and thickness scales sufficient to be observable on surface seismic data, although thinner features may be mappable on VSP or crosswell data [96]. Standard well log analysis is useful down to the bed level, and specialized down-hole tools (e.g., formation microscanner) can see down to the lamina scale.

Stratigraphic bed truncations indicating sequence stratigraphic elements can often be mapped from long 2D seismic lines. The key features are stratigraphic terminations associated with strata boundaries, such as unconformities. Figure 24.5 gives example data sections illustrating terminations into the upper boundary. Unconformities are of particular importance. They are easily recognized and indicate a relative low stand of sea level. Lower boundary truncation examples are shown in Figure 24.6. Figure 24.7 shows part of a classic prograding delta sequence from a regional line offshore West Africa.

Seismic stratigraphy, at one time, was used to date sediments in remote areas away from well control. This was done by reference to a global sea level curve with local corrections for glacial rebound and other effects. It is now known that sea level curves alone are not sufficient to determine the age of a stratigraphic interval. The primary value of seismic stratigraphy today is the identification of likely reservoir and source rocks. These occur in predictable locations within the complex of rock units comprising a depositional system. For example, the prograding delta of Figure 24.7 is likely to have sand-rich sediments near the top of each clinoform, because this was a high energy, near shore depositional environment. Other examples of sand-rich areas include basin floor fans, turbidites, and incised valley fill.

In principle, seismic sequence stratigraphy should benefit from 3D seismic data since arbitrary vertical lines can be extracted from the data volume. This would allow truncation features to be viewed in a dip direction, which is not always the case for 2D lines. Unconformities and bed terminations occur at all scales, but most 3D seismic surveys are too small to map the regional features vital to seismic stratigraphic interpretations. As 3D surveys become larger, we can anticipate that 3D seismic sequence stratigraphy will emerge as an important interpretation technique over the next decade or so.

## 24.2 Stratigraphy and 3D seismic data

The emergence of 3D data was a great advance for stratigraphic studies of seismic data. Structural features are easily seen in vertical 2D sections. But stratigraphic features are essentially subhorizontal and very subtle, usually indicated only by variations in amplitude, phase, and termination. In going from 2D to 3D seismic data, stratigraphic analysis shifted from reflector geometry studies in vertical sections to time slice and horizon amplitude studies.

A few stratigraphic features are most evident in vertical sections (pinnacle reefs, bed terminations, etc.), but most can only be appreciated in plan view. The visibility of a subtle stratigraphic feature like a sand channel is very different in vertical and horizontal sections. A vertical seismic section will only image a subtle anomaly with small amplitude variation or character change in composite waveform. The width of the anomaly will depend on the relative orientation of channel and seismic profile as well as the size of the stratigraphic feature.

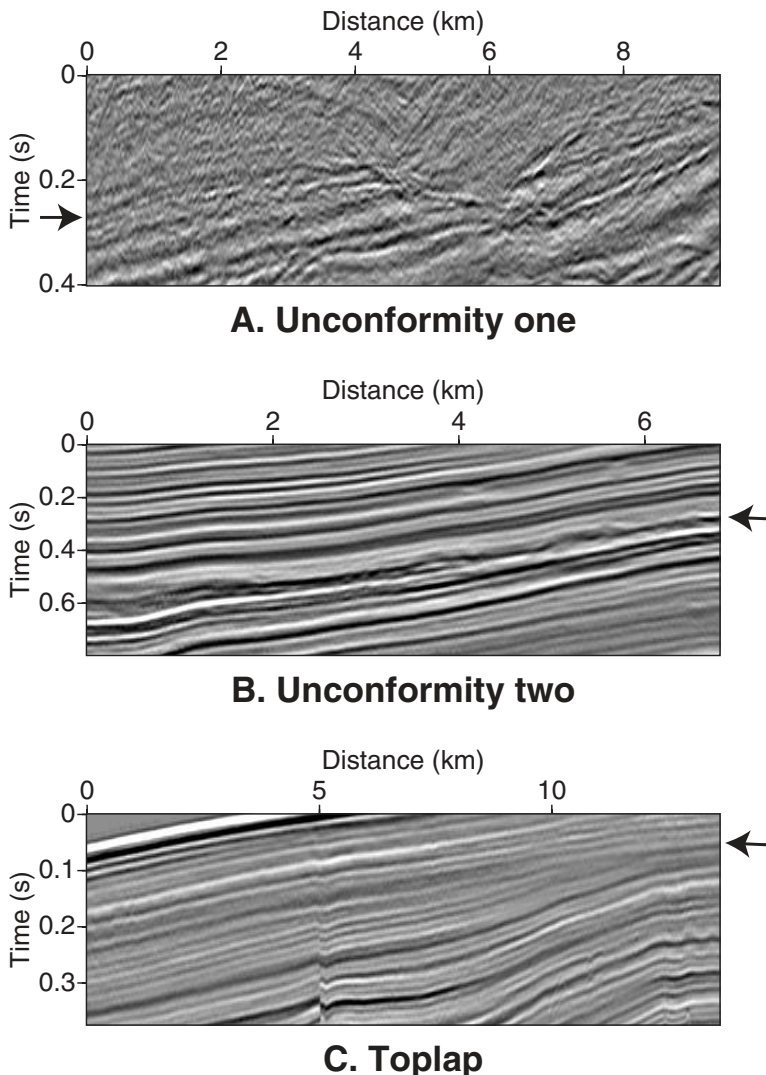


Fig. 24.5 Seismic sequence stratigraphy is an interpretation method that extracts stratigraphic information from long 2D seismic lines. These three panels illustrate the common stratigraphic truncations associated with the upper boundary (arrow) of a sediment package. Data from West Africa (A) and SE Asia (B,C). (A) An angular unconformity cutting deeply into layered sediments. The featureless zone above the unconformity is likely a section of deep water shale. (B) A more subtle unconformity is evidenced by rough surface scattering and gradual truncation of the beds below. (C) Toplap is indicated by beds truncating from below into a surface of nondeposition.

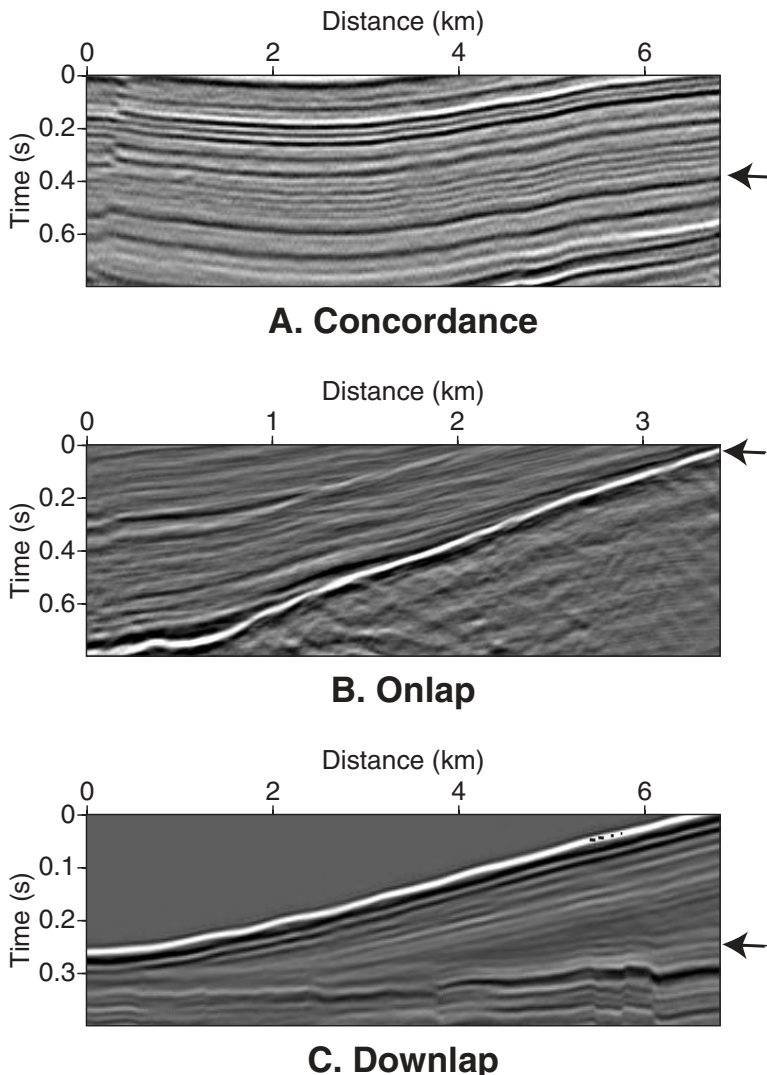
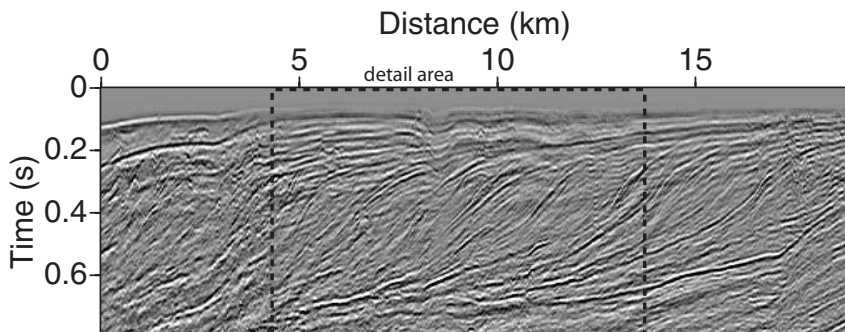
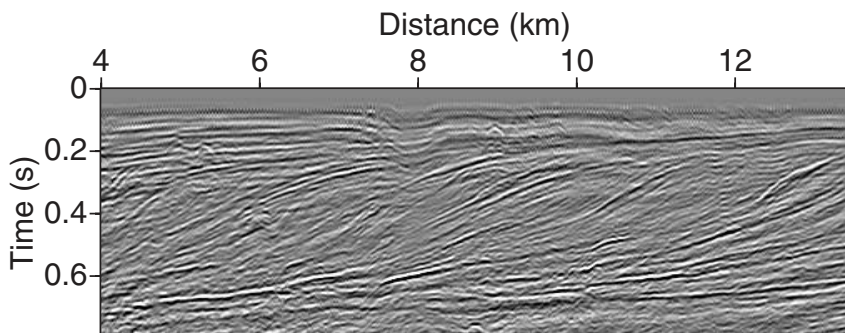


Fig. 24.6 Common stratigraphic truncations associated with lower boundary (arrow) of a sediment package. All data from SE Asia. (A) Concordance of the upper or lower boundary means strata do not truncate against the boundary. (B) Onlap is a situation where strata terminate against an originally dipping surface. (C) In Downlap the beds terminate down onto an originally horizontal surface, indicating the edge of sediment transport.

**A. West Africa systems tract****B. West Africa systems tract (detail)**

*Fig. 24.7 Systems tracts seen in offshore data from West Africa. (A) This long 2D line shows a classic prograding delta depositional sequence composed of systems tracts. The sigmoidal sequence boundaries are also called clinoforms. (B) Detail view.*

In a 3D horizontal section (time or horizon slice), the spatial extent of the amplitude anomaly can be recognized by its shape and analyzed for reservoir property variations. However, we should always be aware of acquisition footprint and discount any amplitude or waveform features that parallel the acquisition grid.

It is essential that a proper bin size be used in the hunt for stratigraphic targets. Figure 24.8 shows the blurring effect that is caused by using too large a bin size. Actual shooting parameters for this data result in a 17 m natural bin size; the other resolutions were simulated by nearest neighbor decimation and bilinear interpolation.

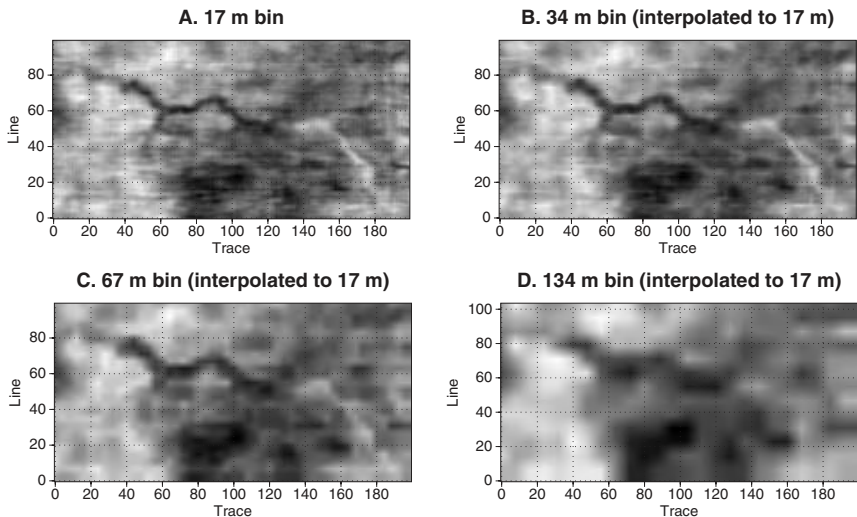


*Fig. 24.8 A buried channel system as seen in a time slice with various bin sizes. Note the blurring effect of using too large a bin size. Shooting larger bins saves money, but can seriously degrade interpretability of the data.*

If structure is negligible, the primary stratigraphic tool is the time slice. Lateral amplitude variation within the time slice must be understood to be a composite of  $(x,y)$  changes in reflection coefficient, gentle dip effects, tuning, noise, and acquisition or processing footprint. If the stratigraphic feature has a weak amplitude signature, it is often useful to sum two or more consecutive time slices together. This tends to enhance the stratigraphic feature, but only if the structural component across the feature is less than one-half of a period.

A single time slice is influenced by a slab of sediment with finite thickness. For this reason, multiple channels of slightly different depths may be contained in a single time slice (Figure 24.9). It is tempting to think that the slab thickness of a time slice is determined by the time sample rate  $dt$  through  $dz=v_{int} dt/2$ . But the depth interval associated with a time slice is determined by wavelet interference not time sample rate.

Specifically, if we accept that ultimate vertical resolution is one-quarter wavelength, then  $dz=v_{int}/(4f_{dom})$ . Taking Figure 24.9 as an example, the time sample rate is 4 ms, interval velocity is 2350 m/s, and dominant frequency is 50 Hz. How thick is the slab of sediment influencing this time slice? Using the time sample rate criteria, the thickness is 5 m but the more realistic interference criterion is 12 m.

## Time slices

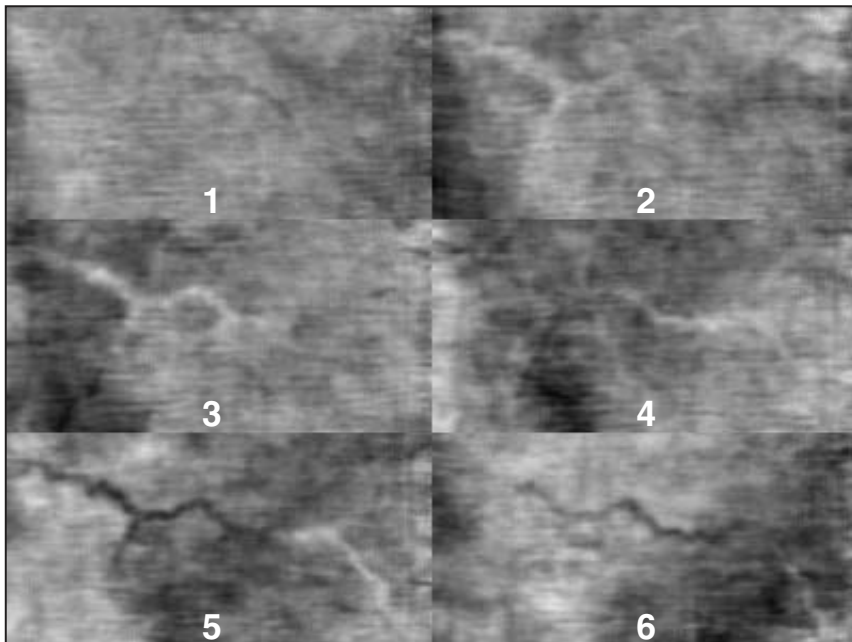


*Fig. 24.9 Time slice montage showing Eocene channels in the Stratton field of south Texas. Slice 1 is 824 ms and time sample rate is 4 ms. Each time slice consists of 100 lines and 200 traces with a bin size of 17 m. Channels are subtle features and thick ones persist from one time slice to the next.*

### 24.3 Case history: stacked sand channel systems

Stacked channel systems can be interpreted on 3D seismic data to simultaneously show channels of various ages. This is illustrated in Figure 24.10 for Eocene channels in the Stratton field of South Texas. Details of the 3D survey include

Bin size: 17 m x 17 m

Image area: 5.2 square km

Time sample rate: 4 ms (resampled from 2 ms)

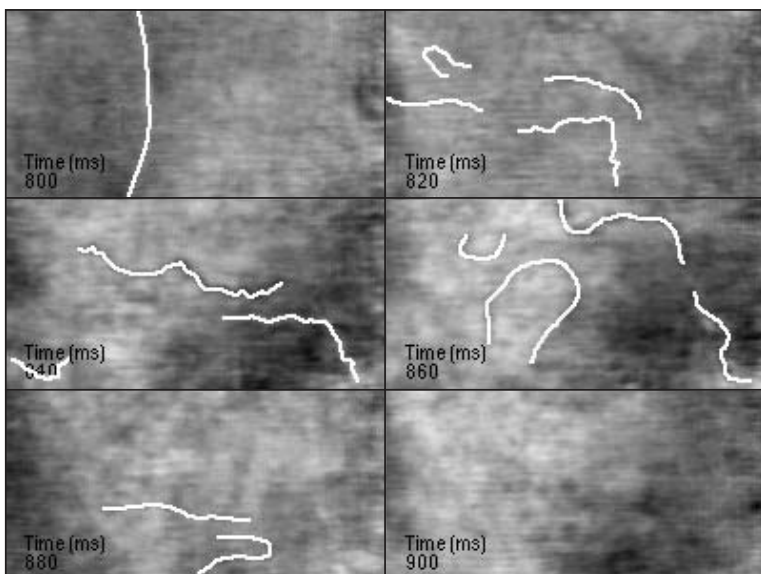
Frequency content: 10-90 Hz

Interval velocity: 2350 m/s

Channel max width: 137 m

Channel max area: 21 hectares (52 acres)

## A. Time slices (channels marked)



## B. Channel hit map

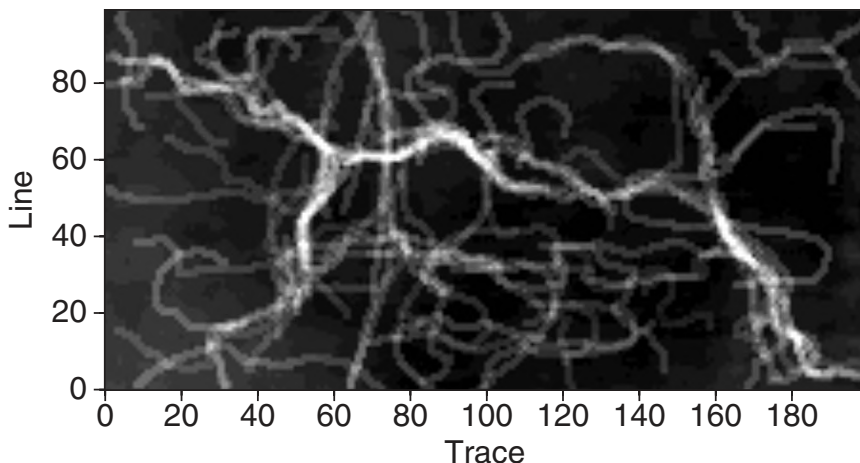


Fig. 24.10 (A) Selected time slices from Stratton field 3D data showing marked Eocene channels. The channels have been marked in a total of 34 time slices (a time interval of 136 ms). (B) Channel hit map. By averaging amplitudes in the entire stack of slices, the channels are all seen simultaneously. Brightness is proportional to the number of marked channels at each bin location.

## Elements of 3D Seismology

The design bin size was calculated for a deeper target than our channels. The recommended bin size at the channel level would be about 14 m. The 17 m bin size actually used is consistent with minor amplitude striping observed at the channel level. This is due to a combination of spatial aliasing and acquisition footprint.

It is clear that several vintages of channels exist in this interval of data. The complete interval over which one can map this stacked channel system is 800–936 ms corresponding approximately to depths 832–997 m.

Once the channel system is recognized by animating through the time slices, it is easy to imagine what kind of map we want to produce. From a production point of view, we want to encounter as many potential reservoirs as possible. We need some kind of a hit map indicating how many channels would be encountered by a well in any given bin. This can be created by marking the channels in each slice and projecting these marks through the stack of time slices to make the hit map.

Imagine that we intend to drill a well somewhere in the image area of this 3D survey. There are 20,000 bins. What are the chances that we will encounter thick or multiple channels over this interval? Table 24.1 gives some statistics.

There is roughly a 2% probability of hitting more than three channels in a random drilling location. But with the hit map in hand, we can greatly improve these odds.

Channel hits	Number of bins	% of total bins
0	12 704	63.5
1	4638	23
2	1564	8
3	594	3
4	272	1.4
5	99	0.5
6	71	0.35
7	35	0.18
8	15	0.075
9	7	0.035
10	1	0.005

Table 24.1 Probability of encountering multiple Eocene channels in the Stratton data set.

## 24.4 Stratigraphy and structure: a case history

The channels mapped in the previous section occur in an area with little structural dip. It is for this reason that time slices show the channels so clearly. If there were significant structural features such as folds, faults, and dip, then time slices would primarily show intersection bands where the time slice cuts across steep events.

To extract stratigraphic information in structurally complex areas, the primary tool is the tracked horizon slice. It is unlikely that autopicking will be possible, but the interpreter can manually pick any number of seed points, and interpolation can extract the horizon amplitude and time structure.

We illustrate this concept by considering part of an excellent case history by Abriel et al [1]. Bay Marchand is a giant oil field in the Gulf of Mexico about 70 miles south of New Orleans. Discovered in 1949, production is from Pleistocene-to Miocene-age sands ranging in depth 300–4000 m. There are about 60 productive sands segmented into nearly 600 individual reservoirs. The dominant structural feature of the field is a salt dome, and much of the production is associated with sand bodies terminated by the sediment-salt interface. The Bay Marchand 3D seismic survey has a bin size of 17 m. At the time of interpretation (1991), the field consisted of 800 drilled wells, of which 165 were active.

Plate 12A shows a time slice at about 2150 m subsea depth. Clearly visible are the salt-sediment interface, intersection bands associated with many steeply dipping seismic events, and faulting evidenced by discontinuities of these bands. Labels indicate the top and base of a particular sand named CP-7. Note this sand is clearly terminated to the southeast by a fault, but the northeast termination appears stratigraphic.

Through interactive interpretation, it is possible to extract horizon information for the CP-7. This horizon amplitude map is shown in Plate 12B, again clearly demonstrating fault termination to the southeast. It is believed that CP-7 amplitude is primarily related to sand quality with very little contribution from pore fluid. Sand thickness variations will have a strong influence on amplitude through the tuning effect, but there is sufficient well control in the field to detune horizon slices effectively removing this phenomena. The amplitudes in Plate 12B have a striking pattern, similar to river meanders, that requires further investigation.

An arbitrary vertical seismic section was extracted across the feature along the west-to-east line B-B'. This line is shown in Plate 13A. The top and base of CP-7 are labeled and are seen to terminate without offset across the line. This is

## **Elements of 3D Seismology**

further evidence of stratigraphic termination on the west and east edges of the feature. This line also demonstrates the difficulty of mapping channel-like features from 2D seismic data.

Amplitude fluctuations form the entire body of evidence that a channel is intersected by this line. It seems compelling in conjunction with the 3D horizon slice, but taken by itself we understand that such 2D amplitude variation can have many causes. Seismic sections are full of discontinuous amplitude features, and without the map view afforded by 3D seismic, there is no reason to interpret them solely as channels.

The final step in verifying the amplitude anomaly is a channel system is given in Plate 13B. Here we see log curves for five CP-7 well penetrations. Those in the high amplitude feature show well developed channel sand intervals, while outside the fairway the same stratigraphic unit is dominated by shale and thin, discontinuous sands.

## **24.5 Carbonates**

For many reasons the dominant application of seismic and sequence stratigraphy to date has been in clastic rocks. Clastics tend to have lower P-wave speed and therefore higher seismic resolution. Industry trends over the last decade have moved toward exploiting deep water clastics, such as turbidites and basin floor fans. Carbonate rocks do not have an accepted rock physics model analogous to the Gassmann theory universally used in clastics, and many carbonate reservoirs are in land or shallow marine areas, which present challenging acquisition and data quality problems.

Carbonates are much more prone to dissolution than clastics. Subaerial erosion at sea level lowstands is often expressed as rugose or karst topography surfaces. Also, carbonate deposition is largely due to *in situ* production of sediment or reef facies rather than transport of eroded sediments. Transgressive systems tracts may become very thick if carbonate production (up to 7 m per thousand years) keeps pace with sea level rise. Conversely, highstand system tracts tend to be thin, the carbonate factory only filling the available accommodation space and then shutting down until subsidence or sea level rise produces more space. This is quite unlike clastic highstand systems tracts that grow continuously by progradation as transported sediment comes from adjacent continental erosion. While recognizing these differences, we can apply the methods of seismic sequence stratigraphy in carbonate settings [186].

Figure 24.11 shows some common carbonate sequence geometries [160] and many of these are evident in the interpreted seismic line of Plate 14.

## DEPOSITIONAL SLOPE ANGLE AND CARBONATE SEQUENCES

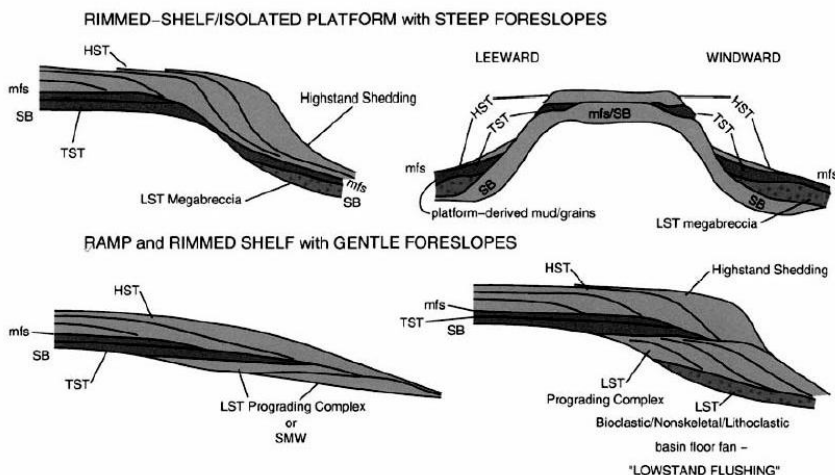


*Fig. 24.11 Relationship of depositional slope angle to systems tract development. (LST=lowstand, SMW=shelf margin wedge, TST=transgressive, HST=highstand in carbonate sequences). Low-to-gentle highstand slopes can develop bypass and in-situ lowstand carbonate banks or platforms (i.e., "lowstand refugios"). Highstand platforms having high foreslope angles are characterized by erosion and bypass at sea level lowstand times. The degree of progradation and aggradation is controlled, in part by the space that the carbonate factory is trying to fill. Aggradation is dominant where the carbonate platform faces a deep basin, and progradation results when the basin is sufficiently shallow that the carbonate platform is able to rapidly fill the accommodation. (Figure and caption from [160]).*

Carbonates can develop much steeper depositional slopes (up to 85 degrees on cemented margins) than clastics (generally less than 5 degrees). Where clastic deposition can occur at any latitude and in any water depth, carbonate generation is limited to plus or minus 30 degrees latitude and water depths of 100 m or less.

More than half of the world petroleum reserves reside in carbonate reservoirs, and there is an accelerating publication trend in the area of carbonate seismic stratigraphy. Even so, on a worldwide basis the actual seismic effort related to clastic reservoirs far exceeds that of carbonates.

# 25

## Seismic Attributes

### 25.1 Definition and history

When seismic processing is complete, we are left with a dense 3D matrix of numbers representing the migrated data volume. This is the amplitude data that primary interpretation deals with to extract structural and stratigraphic information as outlined in earlier chapters. But there are infinitely many ways to derive secondary quantities from the primary data cube. We could take, for instance, the signed logarithm of every sample value, or the cosine, or some signed fractional power. Or we could do a root-mean-square windowed average throughout the data, or the cross correlation of every trace with its neighbors, and so on. Each operation derives a new volume as large as the amplitude volume. All of these examples would be termed attributes.

As a working definition, we can say that seismic attributes are specific quantities of geometric, kinematic, dynamic, or statistical features derived from seismic data. Such attributes are used to visually enhance or isolate features of interest. They may also be calibrated to well control for reservoir property prediction. Note that attributes can lead to reservoir property estimates, but these properties are not themselves considered attributes.

Attributes are a relative new-comer in seismic data analysis, arriving only in the early 1970s in the form of complex trace analysis [173]. But this was arrival in name only. A vast array of procedures had been developed in data processing that could, and would, later be applied to interpretation problems. These included cross correlation, convolution, semblance, coherency, and many other operations.

In 1986 the first published steps were taken to extract 3D horizon information, such as dip and azimuth, using a dense grid of 2D lines [69]. By 1991 dip, azimuth, and artificial illumination attributes were routinely applied to 3D data volumes in major E&P companies [153]. The slow ramp of increased

attribute development was thrown into high gear in 1995 with publication of the coherence cube [8].

One class of seismic attributes could properly be called image processing products. These are items like edge detection, gradient images, texture segmentation, etc. Often such tools are developed in fields as diverse as medical imaging, digital photography, scientific visualization, etc. In this development, the boundary between seismic attributes and visualization is a blurred and moving target.

The proliferation of attributes is such that by 1997 Chen and Sidney [45] were able to categorize 224 of them. Making use of such a vast universe of attributes presents challenges of classification, physical interpretation, and use in reservoir prediction.

## 25.2 Classification schemes

With so many attributes available, and the number growing every day, there is a strong tendency to form classification schemes. Some of the more useful ones are discussed below.

**25.2.1 General and special.** Some attributes have a solid basis in physics or geometry, and we can term these general attributes. They are robust and can be expected to perform predictably from basin to basin around the world. Of course, like any seismic process, they can be rendered useless by severe random or coherent noise, or inappropriate geologic setting. General attributes include horizon peak amplitude and time structure, complex amplitude and frequency, generalized Hilbert attributes, horizon dip and azimuth, illumination, edge-preserved smoothing, edge detection, AVO, coherence, and spectral decomposition.

This is not a comprehensive list but should illustrate the class of general attributes. AVO is a good case in point. It is solidly based on the physics of angular elastic reflection coefficients. As workers have applied AVO worldwide, they have learned the geologic situations where it is useful and where it is not. This accretion of knowledge is possible because AVO is a robust, physically-based attribute.

The great majority of attributes are special rather than general. By *special*, we mean they only have significance through statistically meaningful well correlation and confirmation through seismic modeling. These attributes or attribute combinations only have local validity. Correlations between special attributes and reservoir properties do not persist from one field to another, although they may persist from one reservoir to another inside the same field. When a special attribute has a strong correlation with reservoir properties, it should always be possible to determine the physical meaning through seismic modeling studies. This takes time and effort but can lead to a deeper understanding of where the attribute is likely to be successful again. There is no

point listing special attributes since they form the broad collection left behind when the few general attributes are withdrawn.

The vast number and local validity of special attributes means that when a new one is developed, it does not attract much attention. On the other hand, a new general attribute is a major contribution if it delivers fundamentally new information about the subsurface.

**25.2.2 Dimensional.** Another way to divide up the universe of attributes is to consider whether the actual calculation operates on one trace, a 2D panel of traces, or a 3D subvolume of traces. This scheme is an analogous to seismic data processing where the distinction between single channel and multichannel is important. A weakness of this classification is that it deals only with volume attributes (the entire volume is processed) and does not accommodate horizon and interval attributes discussed below.

Table 25.1 indicates how some 1D attributes are related to geological subsurface features [175]. A selection of 2D and 3D attributes are listed in Table 25.2. Neither of these is a complete list of attributes but only some of the more common ones.

Dim	Name	Interpretation Applications
1D	Instantaneous amplitude	Lithology changes, unconformities, gas accumulation
1D	Derivative of envelope	Absorption, event sharpness, event correlation
1D	Instantaneous phase	Event continuity, structural and stratigraphic config
1D	Instantaneous frequency	Signature of events, thickness, Absorption and fracturing
1D	Instantaneous acceleration	Thin bed effects, possibly porosity
1D	Dominant frequency	Similar to inst freq, correlation tool
1D	Instantaneous bandwidth	Absorption effects, correlation tool
1D	Instantaneous Q	Direct estimate of absorption, fracture, Gas zone, possible permeability indicator
1D	Apparent polarity	Discriminate bright spots, data polarity indicator
1D	Normalized amplitude	Event correlation and event tracking, Event termination indicator
1D	Spectral decomposition	AVO, tuning, attenuation

*Table 25.1 Some 1D attributes and their uses (modified from [175]). All but the last can be collectively referred to as complex trace or Hilbert attributes. These can be more robustly computed in the presence of noise using the generalized Hilbert transform [122]. Spectral decomposition holds out the potential to be an important new general attribute [38].*

## Elements of 3D Seismology

Dim	Name	Interpretation Applications
2D	Edge detection	Channel and fault detection
2D	Directional gradient	Fault mapping, channels, acquisition footprint
2D	illumination	Similar to gradient
2D	Dip	Structure mapping
2D	Azimuth	Structure mapping
2D	Edge-preserved smoothing [123]	Reduce noise without blurring
3D	Coherency	Fault mapping, channel and texture detection, stratigraphy mapping, chaotic zone indicator

Table 25.2 Some 2D and 3D attributes with their uses

**25.2.3 Reflection characteristic.** A widely published third classification scheme is due to Brown [29, 30]. This divides the attribute universe into four groups: time, amplitude, frequency, and attenuation. Each of these in turn can be prestack or poststack, as well as window or horizon-based. The Brown classification tree is shown in Figure 25.1.

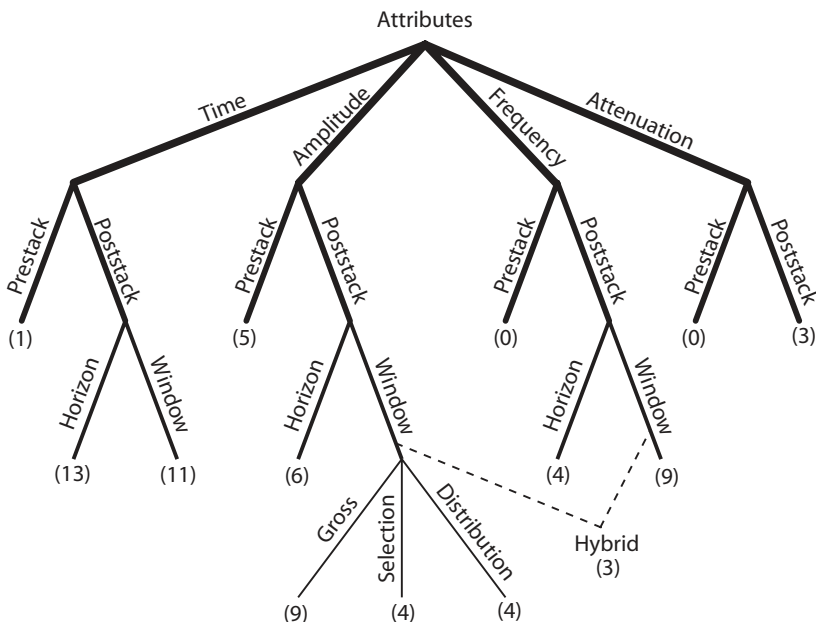


Fig. 25.1 Brown's seismic attribute classification tree based on reflection characteristics. The numbers in parentheses are the number of attributes in each category. For the name of individual attributes (see [30] or [165]).

The primary distinctions in Brown's system are characteristics of seismic reflection events, but a general attribute like coherence pertains to both time (structure) and amplitude (stratigraphy). Similarly, spectral decomposition has prestack application to AVO and poststack use for frequency, amplitude, and attenuation. While no classification scheme is perfect, Brown's is very useful in a rapidly changing landscape.

A similar but more elaborate classification scheme by Chen and Sidney [45] extends the first-order grouping to include waveshape, phase, correlation, energy, and ratios. They offer another version in the same paper with categories based on reservoir features—bright and dim spot, unconformity, etc.

**25.2.4 Procedural.** The final attribute classification scheme we will consider represents a processing perspective [45]. It is centered on the mechanics of how a given attribute is calculated, specifically if it relates to a horizon or the entire data volume.

Horizon attributes are extracted from a seismic data volume along the trajectory of a seismic event. The extraction can be instantaneous, or point-wise, with the attribute extracted at a single time point. The time slice is a special case. Complex trace attributes, and combinations thereof, are typically used in this way. Single trace windowing [130] is another possibility as shown in Figure 25.2. In this situation, several data values on the same trace are used to compute a single attribute value associated with the interval between two seismic horizons or other features. Multitrace windowing extends this idea to include nearby traces in some kind of selection pattern.

Volume attributes are computed without reference to any interpreted horizons. These can be single trace or multitrace computations. Examples of single trace volume attributes include complex trace quantities such as envelope, frequency, and phase. Coherence is a multitrace volume attribute.

## 25.3 Prediction of reservoir properties

Now that we have some idea (perhaps too many ideas) about how to classify attributes, the next question is how do we use them? Here we consider the general method of estimating reservoir properties using attributes and well control.

**25.3.1 Procedure.** The use of seismic attributes to predict reservoir properties involves four major components [93]:

1. tie and calibrate wells and seismic
2. identify seismic attribute to use as predictor of reservoir properties
3. predict reservoir properties between wells using seismic attribute
4. make reservoir management decisions based on predictions

## Elements of 3D Seismology

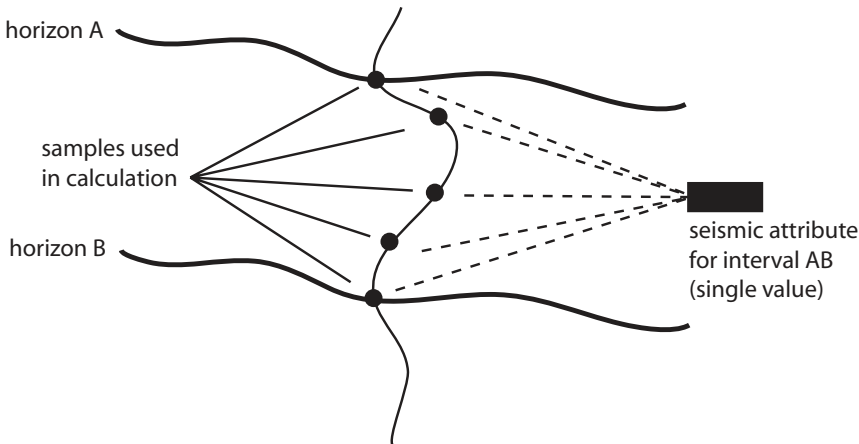


Fig. 25.2 Single trace windowing to create a seismic attribute associated with the interval between horizons A and B (redrawn from [130]).

There are a variety of computational tools available for accomplishing the prediction step 3, including linear or nonlinear regression, geostatistics, and neural networks.

Compared to sparse well control, 3D seismic data forms a dense grid with a seismic trace every 25 m or so. The distance between wells varies greatly. In a mature oil field, the interwell distance might be a few hundred meters, perhaps 1500 m for a gas field, and several kilometers for wildcat wells. Well log information is hard data, extremely high resolution and reliable, while the seismic data is laterally continuous but subject to bandwidth and interference effects causing it to be low resolution. Much like depth conversion, the role of seismic data in reservoir property prediction is to serve as a physics-based interpolator carrying log information into areas between and beyond well control points.

Behind any successful project of this type lie certain assumptions [82], including

- the well ties are correct
- the seismic data is properly interpreted
- the attribute-to-well connection is statistically significant
- there must be a plausible link between the attributes and the reservoir physical properties being predicted

**25.3.2 Case history.** The prediction aspect of seismic attributes benefited from the application of geostatistics in the 1990s. As an example, we consider the set of maps shown in Plate 15. These come from a case history in the Peciko field, Indonesia [76].

The reservoirs in this case are Miocene distributary mouth bars at about 3000 m depth. The individual sandstone bodies are 1–4 m thick and cover 60 square kilometers. Over time many such bars stacked to form thick sand-rich units of exploration interest. The data set consists of 18 wells, a 350 square kilometer 3D seismic data set, and a conceptual geological model of distributary mouth bars.

A 550 m interval was mapped for net sand using well control. The interval net sand thickness interpreted from well logs varied between 2.1 and 20.1 meters. Net sand mapping from well control was done using geostatistics. For an overview of this very powerful mapping and data integration technique see the excellent two-part article by Chambers et al. [43, 44].

The variogram for net sand thickness in the Peciko field showed clear anisotropy (not to be confused with seismic wave anisotropy) trending N135E. This is consistent with the geological model that indicates a sediment supply from the northwest. The observed maximum correlation distance along this preferred correlation is 8 km compared to 32 km in the orthogonal direction, again consistent with the geological model. The net sand map generated by kriging well control only is shown in Plate 15A. This map has a high level of uncertainty due to the sparse well control points.

The 3D seismic data can be used to constrain the net sand map if an attribute can be identified which correlates with known net sand values from well control. A series of horizon and interval attributes were computed related to amplitude, time, and complex trace values. An amplitude-related attribute was found to have a strong correlation coefficient (0.81) with net sand. The physical basis of this correlation is that amplitude is a linear function of bed thickness when the bed is below tuning thickness (see Fig. 20.17). This physical connection was born out by synthetic studies in the Peciko field wells.

The net sand map estimated using wells and the seismic attribute is shown in Plate 15B. The geostatistical technique used here is collocated kriging that honored the variogram anisotropy. Additional detail in the combined net sand map is obvious, but it is also more accurate. This can be proven by a geostatistical technique called crossvalidation, in which a new map is computed while ignoring one well and the predicted versus observed net sand at this well location is noted. The procedure is repeated for all wells and results are displayed as a cross plot of predicted versus observed net sand and a linear regression is done. Perfect prediction would result in a crossvalidation correlation coefficient of one. By integrating the seismic attribute with well data, the error defined in this way was reduced 46% compared to kriging with well control only.

## Elements of 3D Seismology

Attributes and well control can be combined through geostatistics to quantify probabilities as well as actual reservoir physical parameters. Using Bayesian sequential simulations, it is possible to produce a probability map of a location being “in the gas,” shown in Plate 15C. A common quantity for reservoir property prediction is hydrocarbon pore thickness (HPT), which is the product of net sand, porosity, and hydrocarbon saturation.

Through the Gassmann rock model discussed in chapter 6.7, all of these quantities have a physical relationship to the zero-offset reflection coefficient. For the Peciko field, HPT based on well data ranges 0.28–1.73 meters. Plate 15D is a map showing the probability of encountering  $HPT > 1.7$  meters. Underlying this result is the correlation coefficient (CC) between the seismic attribute and HPT, 0.73 in this case. Thus we would have more confidence in net sand prediction ( $CC=0.81$ ) than HPT prediction ( $CC=0.73$ )

It is worth noting that the reservoir property estimation procedure outlined here is a vertical ray procedure in the sense of vertical ray depth conversion discussed in section 23.3. In other words, it is assumed that seismic information resides directly beneath the bin location, an assumption that is valid only for mild lateral velocity variations.

**25.3.3 Multiattribute analysis.** In the previous section, we considered a case history that used one seismic attribute in conjunction with control from 18 wells to predict reservoir properties. Even though a single attribute contributed to the geostatistical mapping, several attributes were computed. Each attribute was correlated to reservoir property values from well control and the best one selected on the basis of correlation coefficient.

For a small number of data points, there is significant uncertainty in the correlation coefficient itself. For example, if a data set consisting of 10 points is found to have a CC of 0.8, the 95% confidence interval of the true correlation is  $CC=(0.34\text{--}0.95)$ . This only allows us to say the true correlation has 95% probability of being between these bounds [93]. Correlation coefficient inaccuracy for a small number of calibration points (i.e., wells) is a limiting factor for reservoir property mapping using seismic attributes.

Another pitfall is spurious correlation [93], which is a strong correlation that occurs purely by chance. The probability of observing a spurious correlation depends on the number of wells, the number of attributes, and the observed correlation coefficient. Figure 25.3 is a probability table based on ten seismic attributes. Assume we have five wells with reservoir property values that we correlate against the ten seismic attributes, and we observe one attribute has  $CC=0.7$ , which we interpret as a strong correlation. The probability of this being a spurious correlation, even though the true correlation is zero, is found to be 0.88 from the table (shaded column and row). In other words there is an 88%

		Number of wells								
		5	10	15	20	25	35	50	75	100
False corr. coefficient	0.1	1.00	1.00	1.00	1.00	1.00	1.00	1.00	0.99	0.98
	0.2	1.00	1.00	1.00	0.99	0.98	0.94	0.83	0.59	0.38
	0.3	1.00	0.99	0.96	0.89	0.79	0.57	0.29	0.09	0.02
	0.4	1.00	0.95	0.78	0.57	0.39	0.16	0.04	0.00	0.00
	0.5	0.99	0.78	0.45	0.22	0.10	0.02	0.00	0.00	0.00
	0.6	0.96	0.50	0.17	0.05	0.02	0.00	0.00	0.00	0.00
	0.7	0.88	0.22	0.04	0.01	0.00	0.00	0.00	0.00	0.00
	0.8	0.67	0.05	0.00	0.00	0.00	0.00	0.00	0.00	0.00
	0.9	0.32	0.00	0.00	0.00	0.00	0.00	0.00	0.00	0.00

(number of attributes = 10)

Fig. 25.3 Probability of a spurious correlation between at least one seismic attribute and a reservoir property of interest. The values are based on testing 10 seismic attributes against various numbers of wells. The shaded case says that there is an 88% probability of observing at least one 0.7 false correlation (true correlation is zero), using 10 attributes and five wells. (modified from [93])

probability of finding at least one false correlation of CC=0.7 when testing 10 attributes against five wells.

There are two risks associated with this situation. Type I risk is that a seismic attribute is selected as a predictor of a reservoir property, even though the attribute and reservoir property are truly uncorrelated. This leads to inaccurate, yet confident, predictions based on the attribute. Type II risk occurs when a seismic attribute is truly correlated with a reservoir property, yet the attribute is rejected because a larger, spurious correlation is found. This leads to inaccurate predictions based on the chosen attribute and therefore larger prediction errors. The economic consequences of Type II errors are thought to be more severe than Type I errors [93].

The moral of this story is that when dealing with a small number of wells, a correspondingly small number of attributes should be considered as predictor candidates. A good way to identify good candidates from the universe of attributes is to identify those that have a justifiable physical relationship to the reservoir property under consideration.

## 25.4 Selected general attributes

**25.4.1 Complex trace.** Complex trace attributes are based on the Hilbert transform which is used to create a complex trace from a real seismic trace. Mathematically, the relationships are [211]

$$p_c(t) = p_r(t) + i p_i(t) = A(t) e^{i\phi(t)} \quad (25.1)$$

where  $i = \sqrt{-1}$ ,  $p_c(t)$  is the complex seismic trace,  $p_r(t)$  is the observed real trace,  $p_i(t)$  is the imaginary or quadrature trace, and  $(A, \phi)$  are the amplitude and phase as described in appendix A. The imaginary part of the complex trace is the Hilbert transform of the real trace, which can be computed from

$$p_i(t) = \frac{i}{\pi t} * p_r(t) \quad (25.2)$$

where the asterisk denotes convolution. The complex amplitude is also called the envelope. Both an envelope and phase value are known for every time point, so these are called instantaneous attributes. The instantaneous frequency is related to the time derivative of the phase function

$$f(t) = \frac{1}{2\pi} \frac{d\phi(t)}{dt} \quad (25.3)$$

Plate 16 gives an example of these attributes in the context of a Jurassic carbonate buildup in the Smackover Formation of southern Alabama [82]. Each plot in the left column is field data, and the right column is model data. The top row shows seismic amplitude, the second row instantaneous frequency, and the bottom row instantaneous amplitude. Although clutter and noise are present in the field data, many of the model data features are seen. Complex amplitude and phase were found to be key attributes for porosity prediction.

Complex trace attributes were an important advance in the early 1970s. Prior to this, it was possible to calculate the amplitude and phase spectra for a whole trace or a time window. But as the window becomes shorter, Fourier theory tells us that frequency resolution becomes worse because the frequency sampling rate becomes larger (see appendix A.6 for details). In the limit of a one point window, there is no resolution in the frequency domain. The ability to compute point-wise complex amplitude, phase, and frequency was something new. Furthermore, from an understanding of Fourier theory, these attributes had clear physical interpretations.

With the seismic application of time-frequency transforms (i.e., spectral decomposition) developed over the last two decades, we can now associate a complete spectrum with each time point. Instantaneous frequency and phase are then understood to be merely average point-wise properties [11].

Complex trace attributes are easy to calculate, manage, and interpret, so they will remain useful. There is little proliferation of data, meaning that a seismic amplitude volume gives rise to a small number of attribute volumes (envelope, phase, frequency). But for advanced analysis, they are likely to be superseded by spectral decomposition attributes.

**25.4.2 Dip, azimuth, curvature, and gradient.** Dip, dip-azimuth, and curvature are familiar concepts from structural geology. Attributes of the same name and meaning can be calculated from horizon time structure maps [153] or as volume attributes [125].

Figure 25.4 shows a time slice at 1200 ms (A) and vertical seismic section (B) from the Gulf of Mexico [125]. Arrows on the vertical section highlight a subtle flexural feature that is difficult to interpret on the time slice data. Figure 25.4D is a dip slice at 1200 ms, calculated for a dip direction of N60E. White corresponds to positive downward dip. This image is a horizontal slice through an entire N60E dip volume. The proliferation of data in this kind of attribute work is obvious; a seismic amplitude cube can spawn any number of secondary dip, azimuth, and curvature attribute volumes.

The horizontal gradient is another general analysis tool. Figure 25.5 shows two gradient images computed from the same Gulf of Mexico data volume. The complex trace amplitude volume was computed, then sliced at 1200 ms, and that slice differentiated in two directions, North-South (A) and East-West (B). Subtle fault features can be seen in these images, and others would appear if the gradients were computed in different directions. The east-west gradient clearly shows vertical amplitude striping associated with weak acquisition footprint artifacts.

These attributes are powerful tools for delineating faults, folds, and other structural features.

**25.4.3 Coherence.** Adjacent traces in a seismic data volume can differ because of structure, stratigraphy, lithology, pore fluids, etc. Coherence [8] is a volume attribute that displays such discontinuities. The original algorithm was based on a normalized three-trace crosscorrelation (C1 algorithm). Further developments have included 3D semblance search over dip-azimuth pairs (C2), multitrace time-domain eigenstructure (C3), and a hybrid method that computes semblance along smoothed dip directions (C3.6).

## Elements of 3D Seismology

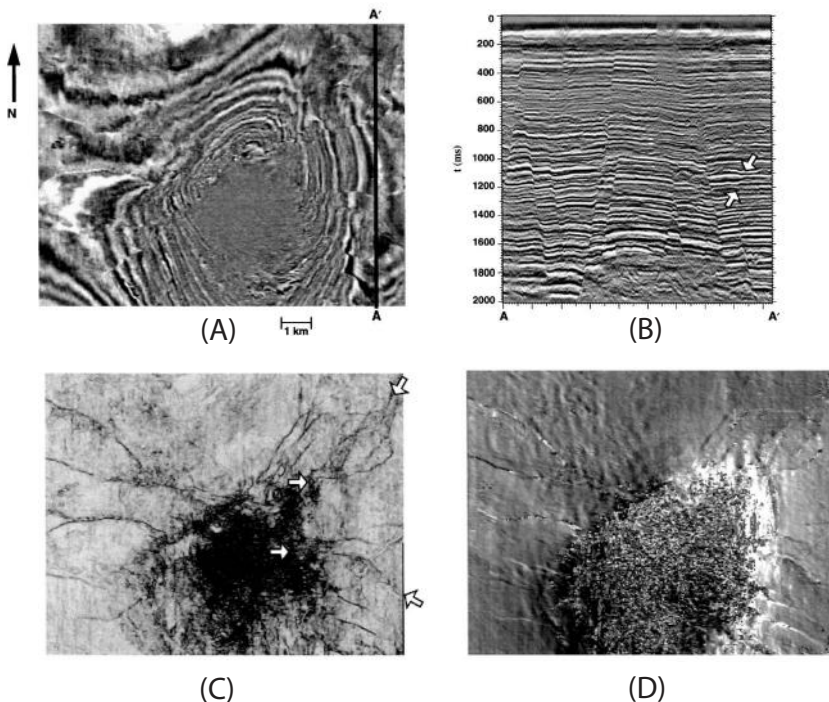
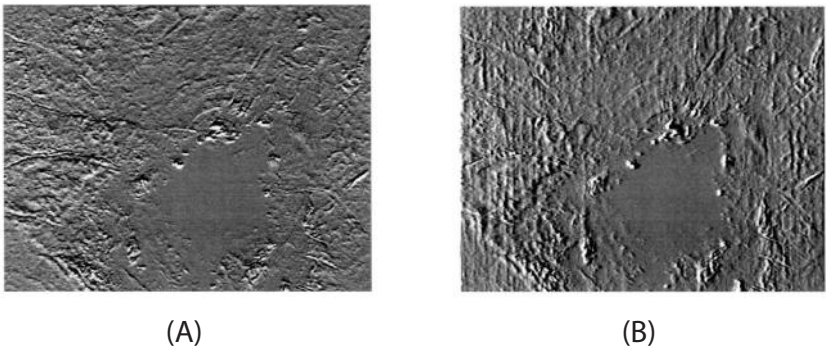


Fig. 25.4 Coherence and dip attributes. (From [125]) (A) Seismic amplitude time slice at 1200 ms in the Gulf of Mexico across a salt dome. (B) Seismic section along line A-A'. Arrows indicate subtle flexural feature difficult to see in the time slice data. (C) 1200 ms time slice through a coherence (C3.6 algorithm) volume generated from the seismic data volume. Note increased clarity of fault patterns compared to the amplitude time slice data. (D) 1200 ms time slice through a N60E dip volume. White indicates positive downward dip.

Even in its earliest form, coherence offered a remarkable new tool for analyzing the subsurface. Stratigraphic, structural, and reservoir features were visible in a way not possible before. Today coherence is an indispensable tool used routinely in 3D seismic work around the world.

Figure 25.4C illustrates the role of coherence in fault mapping. Comparison with the corresponding time slice reveals the difficulty in fault mapping from seismic amplitude data. Particularly notorious are faults parallel to strike, yet coherence localizes faults independent of local bedding dip.



*Fig. 25.5 Complex amplitude gradient attributes. (From [125]) (A) North-South gradient of a 1200 ms slice through a complex amplitude volume derived from data in Figure 25.4A-B. Subtle faults are seen as narrow features throughout the image. (B) East-West gradient showing vertical amplitude striping associated with acquisition footprint.*

The stratigraphic imaging power of coherence is evident in Figure 25.6. Image (A) is a horizon amplitude slice extracted from a 3D Gulf of Mexico data set and (B) is coherence along this same horizon. Such results are truly remarkable images of stratigraphy, and they have direct use in reservoir delineation and drilling.

**25.4.4 Spectral decomposition.** Spectral decomposition (SD) is a collective name for a class of methods that decomposes a 1D time series into a 2D time-frequency spectrum. This allows us to see inside a seismic trace in very powerful way.

The earliest form of SD was the short time Fourier Transform (STFT) defined as

$$g(f, \tau) = \int g(t) h(t - \tau) e^{i2\pi ft} dt \quad (25.4)$$

where  $g(f, \tau)$  is the time-frequency spectrum,  $g(t)$  is the time series,  $h(t-\tau)$  is a tapered window centered on the time point  $t=\tau$ , the spectral time variable is  $\tau$ , and  $f$  is frequency in Hz. The only difference between the STFT and the ordinary FT described in appendix A is the window function.

Since the late 1980s, a series of general time-frequency decomposition methods have been developed under the name of wavelet transform (WT). These have found application to 1D signal processing (1989), time-scale representations

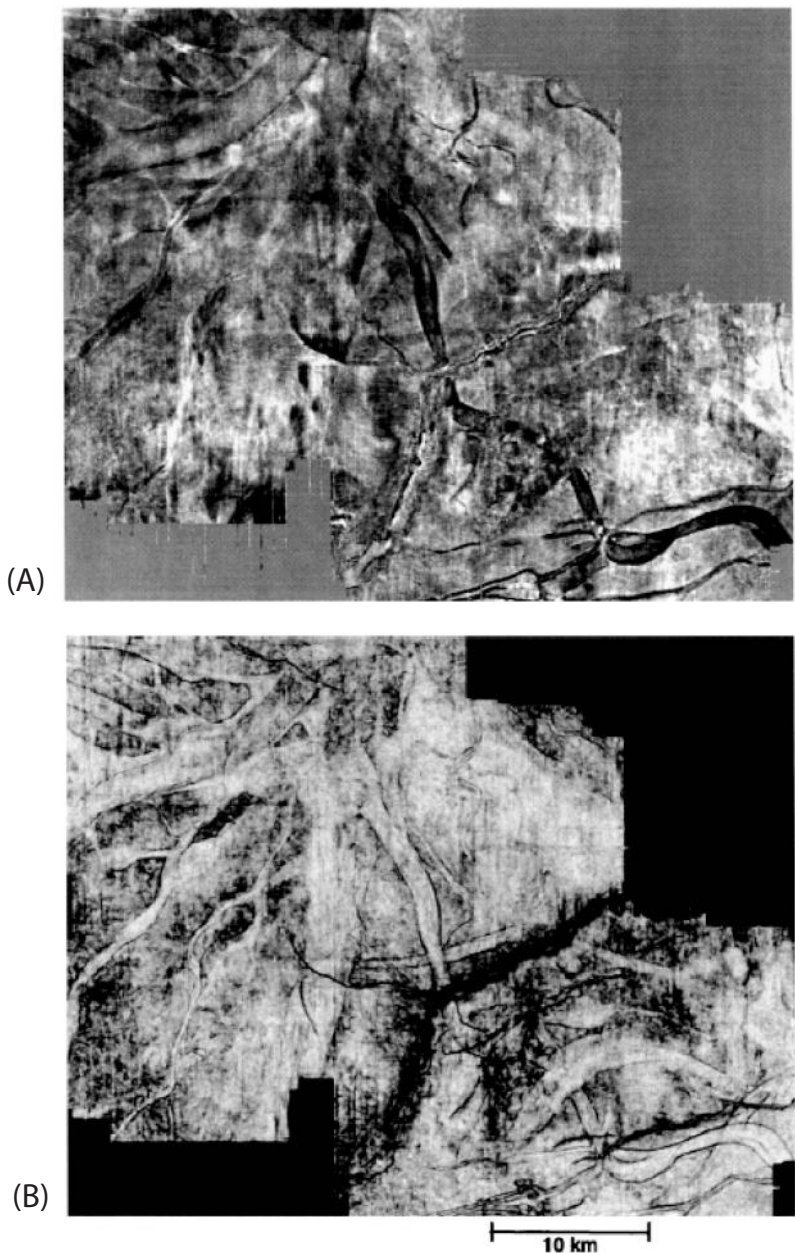


Fig. 25.6 Coherence and stratigraphy. (From [125]) (A) Gulf of Mexico horizon amplitude data. (B) Coherence image of the same horizon demonstrating the kind of remarkable stratigraphic detail of submarine sand channels available from this attribute.

(1989), filter bank theory (1992), 2D digital image processing (1992), as well as seismic data analysis (1994). Here the word *wavelet* does not mean a seismic wavelet, but a primitive waveform used to probe the time series and build the time-frequency spectrum.

Current wavelet transform applications range from voice recognition and cardiology to astrophysics and internet security. Available decomposition techniques include STFT, continuous and discrete wavelet transforms (CWT, DWT), wavelet packet decomposition (WPD), matching pursuit decomposition (MPD), and others in development.

The continuous wavelet transform is at the heart of these methods. Its mathematical definition is

$$g(a, \tau) = \frac{1}{\sqrt{a}} \int g(t) w^* \left( \frac{t - \tau}{a} \right) dt \quad (25.5)$$

where  $w()$  is the analyzing wavelet,  $*$  denotes complex conjugation,  $a$  is the scale (an inverse frequency parameter), and symbols in common with the STFT definition have the same meaning. Like the STFT, the CWT is windowed. But, importantly, the window is not of fixed time duration but has variable length. This is an essential difference and it is what allows wavelet-based methods to achieve time-frequency localization far superior to the STFT.

Plate 17 illustrates some time-frequency concepts on a simple seismic trace. The trace consists of three separated events; an isolated reflection, a tuning wavelet pair, and a wavelet pair representing the seismic resolution limit (onset of peak separation). The trace also contains a weak 60 Hz sinusoid, simulating power line hum on land seismic data.

The time-frequency representation generated by STFT is shown in Plate 17B. The STFT suffers from a trade-off in localizing energy in the time domain and frequency domain; it can do one or the other, but not both. Thus we see the isolated wavelet as a fat blob smeared across time-frequency space. The 60 Hz signal is easily seen, but there is little discrimination between events 1 and 2. It should be remembered, however, that even this fuzzy view of the time-frequency space provides significant information not available from a Fourier transform of the entire trace.

Matching pursuit decomposition, Plate 17C, gives a sharp spectral image. The isolated wavelet is localized in time and seen to have bandwidth 10–140 Hz in the MPD spectrum. The tuning case is clearly distinguishable from an isolated wavelet, and would be even if the wavelet had a 90-degree phase shift to mimic a

## Elements of 3D Seismology

tuning effect. In fact, the whole idea of tuning needs rethinking in light of spectral decomposition [38]. Recall the tuning condition is given by

$$z = v/(4f) \quad (25.6)$$

where  $z$  is the bed thickness,  $v$  is the bed interval velocity, and  $f$  is the frequency. In our earlier discussion of tuning, chapter 20.2, we identified  $f$  with the dominant frequency and used this equation to calculate tuning thickness of the bed. This is the broadband tuning condition and it allows us to scan a 3D survey area seeking tuning conditions of high amplitude (about 20% stronger than the actual reflection coefficient) and apparent 90-degree phase shift. But in light of spectral decomposition, this equation speaks differently. For a wide range of bed thicknesses, we can look into the time-frequency space and find a tuning frequency. This has clear application to mapping beds below broadband tuning thickness.

The matching pursuit decomposition image of event 3 is very interesting. At the onset of broadband vertical resolution, MPD shows two distinct frequencies. One relates to dominant frequency of the individual wavelets, and the other is associated with the lower-frequency composite waveform. Again, there is information beyond broadband resolution limits.

The final time-frequency spectrum in Plate 17D comes from the continuous wavelet transform. The vertical axis here is scale, a quantity inversely related to frequency. The CWT spectrum is less intuitive than STFT or MPD, but the three events are clearly distinguishable. The CWT is often used for categorizing jumps in otherwise continuous data. An example is Internet traffic, which in general varies smoothly with time. But occasionally an external event occurs such as a natural disaster or economic news, and the Internet load jumps. CWT analysis allows the jumps to be automatically identified and classified for further analysis. A seismic application of CWT is data compression [23].

Spectral decomposition has direct application to seismic interpretation [38, 144, 148], but it also suffers from data proliferation. Consider a migrated 3D seismic data cube. Spectral decomposition of each trace in the cube will generate a 2D spectrum panel, consisting of dozens of new traces, each one associated with a single frequency. The input data cube becomes dozens of output common frequency cubes, the total size approximating the prestack data that went into making the stack data cube.

Regardless of data proliferation, spectral decomposition promises to be an important part of future seismic interpretation. An example is shown in Plates 18 and 19. This case history [148] uses spectral decomposition to interpret incised valley stratigraphic features from a target 3 km deep in the U.S. midcontinent. The interval of interest is the Pennsylvanian Red Fork sandstone with a thickness

of 50 ms (90 m). Spectral decomposition allowed extraction of fixed-frequency horizon slices. A 36 Hz horizon slice was found to illuminate stratigraphic features identified from well control.

**25.4.5 Impedance.** One of the most heavily used volume attributes in reservoir analysis is impedance. Recall that acoustic impedance is the product of P-wave speed and density, both of which are influenced by important rock properties such as mineralogy, porosity, and pore fluids. Consequently, impedance inherits these dependencies.

The physical basis of impedance estimation is connected to synthetic seismogram generation. We found in chapter 20 that sonic and density measurements can be combined to form an impedance profile at a well location. If we let  $I_j$  be impedance of the  $j$ th layer in the earth model of Figure 20.1A, then the zero offset reflection coefficient (RC) for any given interface is

$$R_j = \frac{I_{j+1} - I_j}{I_{j+1} + I_j} \quad (25.7)$$

which can be rewritten as

$$I_{j+1} = I_j \left( \frac{1 + R_j}{1 - R_j} \right) \quad (25.8)$$

This relationship allows reconstruction of the impedance log from the reflection coefficient series [109]. It is a recursive integration of the type we encountered computing synthetic seismogram traveltimes in chapter 20.1.2. There are many issues complicating this theoretical result when applied to real data. These include error propagation from bad RCs, data processing problems in recovering the RC series, and loss of low-frequency trends in the impedance result due to bandlimiting of seismic data.

The first versions of impedance in the late 1970s were direct inversion methods in the sense that the recursion relation was actually used to invert for impedance from an approximate RC series [109].

Later indirect methods take a different approach [167]. Starting with an initial impedance model, a simulation operator creates a synthetic seismic section using the convolutional model. The synthetic section is then compared to the observed seismic section, the misfit is used to update the impedance model, and the process is repeated until the modeled and observed data match. This is a classic optimization scheme of the type seen earlier in Figure 11.1. This kind of impedance estimation [10] can simultaneously perform wavelet estimation and was first described in 1982. Continued development in this direction has lead to

## Elements of 3D Seismology

an arsenal of impedance methods including constrained sparse-spike inversion, stochastic inversion, and geostatistical inversion [183, 90].

To illustrate the nature of impedance results, we consider parts of a case history in the Northwest Java Basin of Indonesia [2]. A 2D migrated line from the study is shown in Plate 20. Processing of this data included NMO velocity analysis, CMP stack, and poststack time migration. Geometric spreading and trace balancing were used for display, but no gain was actually applied to the data prior to impedance inversion. The reservoir in this area is gas-bearing Miocene Cibulakan formation, composed of thin sandstone and limestone units at about 1500 m depth. Boxes highlight reservoir bright spots.

The impedance estimation method used in this case is constrained sparse-spike inversion (CSSI). At each iteration, a synthetic seismic line is generated from the impedance model. As the solution converges, the difference between synthetic and observed data becomes smaller. The final situation is shown in Plate 21. The observed data (A) is virtually identical to the synthetic data (B) as clearly shown by the difference plot (C).

The result in Plate 22 is a color display of the estimated impedance across the entire line. If the input were 3D migrated data, the process would deliver an impedance volume. Hot colors (red-yellow) on Plate 22 represent low impedance intervals, and cool colors (green-blue) are high values. The detail section (B) is labeled with reservoir intervals. Levels 1 and 5 are limestone units and appear as high impedance features. Sandstone reservoirs (2,3,4) have low impedance with local development of very low impedance due to gas effects. Low-impedance features 6 and 7 are probable sand units that are not seen in logs because the well is situated a short distance from the line. A nice feature of impedance for thin bed work is that tuning effects are minimized by the inversion process.

Impedance is considered an attribute even though it is actually a rock property. But it is not a property of primary interest in the same sense as porosity or fluid saturation. The main quantitative use of impedance is in reservoir property prediction. The approach is a familiar one. Impedance and reservoir properties are crossplotted using log data. If a robust statistical relationship is found, it can be used to calibrate the impedance image or volume to predict reservoir properties.

**25.4.6 Spice.** As a final example, consider the attribute called spice [104]. Imagine a well with sonic and density logs from which we can construct an acoustic impedance (AI) curve. From this we can construct a reflection coefficient (RC) series, and then convolve with a seismic wavelet to form a synthetic seismogram (SYN). Spice has the following remarkable property—spice curves generated from AI, RC, and SYN have the same shape. This is true for different seismic wavelets.

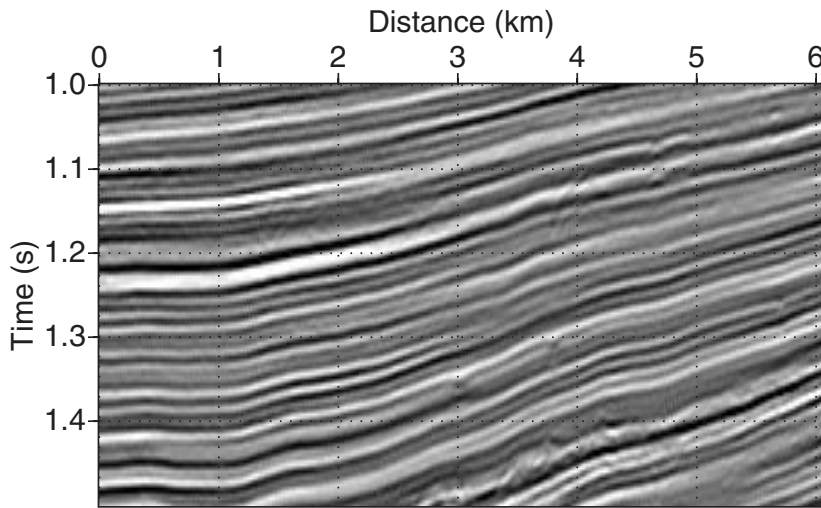
In a sense, spice looks through the wavelet and reflection coefficient series to form a shadow image of the underlying structure and stratigraphy. A distant cousin of spectral decomposition, the physical basis of spice relates to spectral shaping during the reflection process [205] and local transmission losses of the kind seen in Figure 20.14. Unlike spectral decomposition, there is no data proliferation in spice. It operates in such a way that one trace in gives one trace out, the migrated data cube generates a spice cube of the same dimensions.

Figure 25.7 shows a panel of migrated data from a 2D seismic line and the spice section computed from it. Intriguing stratigraphic relationships can be seen throughout the spice result. These correspond to exceedingly subtle features in the original data. As an example, consider the small region between 3–4 km and 1.2–1.3 seconds.

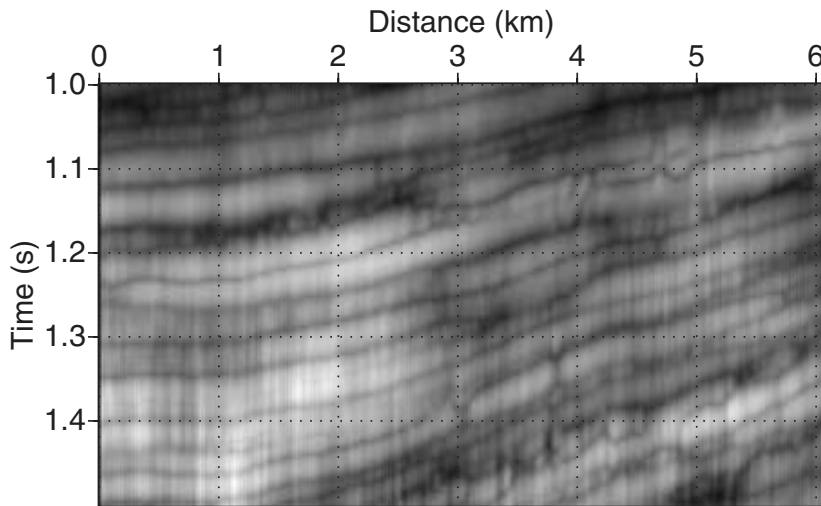
In the migration data, we see amplitude fluctuations and a bed termination (onlap) up and to the right. The spice image localizes the terminating bed and additionally shows the unit above downcutting to form the termination. Interestingly, stratigraphic intervals are often seen on spice images to have a bias that associate with interpreted sequence boundaries. This effect is seen as net brightening or darkening of different stratigraphic intervals in Figure 25.7B.

Figure 25.7 is a small part of one 2D seismic line. Imagine the vast amount of stratigraphic information this attribute could pull from a 3D data set. An obvious comparison is the stratigraphic detail seen in coherence time or horizon slices. But coherence does not deliver the kind of vertical stratigraphic image seen in spice. Spice also offers a different kind of detail complimentary to state-of-the-art impedance inversion as seen earlier in Plate 22.

Basin floor fans, turbidite deposits, fluvial systems, carbonate buildups , and other depositional systems are of increasing interest in the global seismic search for petroleum. Perhaps spice, and other attributes as yet unknown, will play a role in this search.



**A. Migration section**



**B. Spice section**

*Fig. 25.7 The spice attribute. (A) Southeast Asia 2D migrated seismic data showing stratigraphic features such as thinning, bed terminations, and an unconformity. (B) Spice attribute section generated from the migrated data revealing a shadow image of the geology. Note the subtle downcutting relationship between 3–4 km and 1.2–1.3 seconds. Many other stratigraphic features can be seen that are far from obvious on the migrated section.*

# 26

## Amplitude in Space, Time, and Offset

### 26.1 Prestack amplitude factors

In this chapter, we highlight those reservoir properties that affect amplitude as observed on seismic data. As a seismic ray progresses from source to receiver, many factors influence the amplitude. There is a source radiation pattern determined by source type, array, and coupling (see chapter 1.10). As the ray travels, there is continuous amplitude loss due to geometric spreading (see chapter 1.16.2). There is further continuous loss due to absorption (see chapter 6.8). Each time the ray passes through an impedance contrast interface, the amplitude is scaled by a transmission coefficient leading to cumulative transmission losses (see chapter 20.1.7).

In the reflection process, the amplitude is scaled by an angular reflection coefficient (see chapters 3.2.2, 5.9, 5.10). As the ray passes back up toward the acquisition surface, the amplitude is further reduced by more geometric spreading, absorption, and transmission loss. Finally, the amplitude measured by the receiver is a function of the returned amplitude, receiver coupling, and array directivity.

This seismic ray amplitude history can be summarized in the relationship

$$A(t, x, y, h, T) = A_0 \frac{S D_S D_R R}{G} \left( \prod_j T_j e^{-\alpha_j l_j} \right) R_{pp}(\theta, T) \quad (26.1)$$

where the symbols are defined in Table 26.1.

Symbol	Definition
$A$	observed amplitude
$A_0$	amplitude emitted by source
$\alpha_j$	absorption factor of layer $j$
$D_s, D_g$	source and receiver directivity functions
$G$	geometric spreading function
$\Pi$	product symbol
$R_{pp}(\theta, T)$	elastic P-P reflection coefficient
$t$	reflection time
$T$	acquisition date (vintage)
$T_j$	transmission coefficient of interface $j$
$\theta$	reflection incidence angle
$x, y$	midpoint (bin) coordinate
$x_o$	offset

Table 26.1 Definition of symbols.

Factors not included in the amplitude equation include

1. tuning
2. interference from multiple reflections
3. reflector curvature
4. surface waves, head waves, and other forms of shot-generated noise
5. random noise
6. recording system accuracy [206]
7. data processing artifacts [24]

## 26.2 Stack amplitude and $R_0$

As discussed in chapter 20.1.3, the acoustic and elastic P-P reflection coefficients at normal incidence are equal and given by

$$R_0 = \frac{\rho_2 v_2 - \rho_1 v_1}{\rho_2 v_2 + \rho_1 v_1} \quad (26.2)$$

$$= \frac{I_2 - I_1}{I_2 + I_1} \quad (26.3)$$

where layer 1 is the incident (upper) medium,  $v$  is P-wave speed,  $\rho$  is density, and  $I$  is impedance. This is the reflection coefficient that forms the basis of 3D

horizon amplitude interpretation and time-lapse studies. The critical assumption in both is that observed peak amplitude variations are proportional to underlying  $R_0$  changes. But how accurate is this assumption?

Real seismic data is shot with a range of offsets and collapsed back to zero offset through CMP stacking. If we consider an isolated, isotropic, elastic interface in the earth, its reflection amplitude as a function of incidence angle is given approximately by

$$R(\theta) \approx R_0 \cos^2\theta + .5 \Delta\sigma \sin^2\theta \quad (26.4)$$

where  $\theta$  is the incidence angle and  $\Delta\sigma$  is the Poisson ratio contrast across the interface. Modern marine shooting will give an incidence angle range of about 0–30°. The stacking process acts like a summation of all amplitudes in this range,

$$R_{stack} = \int_0^{30} R(\theta) d\theta \approx 0.5 R_0 + 0.067 \Delta\sigma \quad (26.5)$$

We see that stack amplitude is proportional to  $R_0$  and Poisson ratio contrast. Using parameters typical of shale and gas sand in the Gulf of Mexico [190] we have

$$R_0 = -.04 \quad (26.6)$$

$$\Delta\sigma = -.37 \quad (26.7)$$

and a top-of-sand stack amplitude of

$$R_{stack} = -0.02 - 0.025 = -0.045 \quad (26.8)$$

In this case, the stack amplitude is composed of 44% normal incidence reflection coefficient and 56% Poisson ratio contrast. So the assumption that stack amplitude is proportional to  $R_0$  has an error bar in this case of something more than 50%. A gas sand has extreme Poisson ratio properties, so this result can be taken as a cautionary tale and an upper limit.

### 26.3 Predictive rock model

With all these caveats understood, we can proceed to ask the following question. What are the reservoir property changes that best explain observed seismic amplitude variations observed in the interpreted 3D data volume?

We have seen one answer to this question in the form of reservoir property prediction using seismic attributes. That procedure statistically associates composite reservoir properties to seismic attributes. For example, hydrocarbon pore thickness (net pay, times porosity, times hydrocarbon saturation) might be associated with a windowed root mean square (RMS) amplitude attribute.

Another approach is to use a physics-based rock model. The general procedure is illustrated in Figure 26.1. Proceeding from top down, we begin with parameters describing the porous fluid-saturated rock. These include environment, fluid, and frame parameters from well log or laboratory measurements. This information is used in a rock model theory to calculate P-wave velocity, density, and other properties from the input parameters. The rock model theory also involves one or more free parameters used to localize the model, and make it specific to the reservoir under study.

Log or core measurements of seismic P-wave velocity are adjusted using an appropriate upscaling theory and used for calibration procedure. The upscaling methods discussed earlier include Backus averaging in chapter 2.7 and velocity dispersion correction in chapter 6.8. The actual calibration is often based on a crossplot of log/core velocity and porosity.

Regression on these data points allows determination of the free parameters, and the result is a predictive rock model. The rock model can be used to compute velocity, density, impedance, interval transit time, and reflection coefficients in response to changes in one or more frame, fluid, or environment parameters. Along with our assumption that seismic amplitude and reflection coefficients are proportional, the rock model forms the core of quantitative seismic interpretation.

We take the physical basis of amplitude variation in response to rock property changes to be the Gassmann theory as presented in chapter 6.7. These general results are seen in seismic data as amplitude changes with respect to lateral position, offset, or acquisition time. These variations are the foundation of amplitude interpretation, attribute analysis, and reservoir property prediction. The Gassmann model is well-suited to sandstones and less so to carbonates, but we will use it uniformly in the present discussion.

Can seismic data be interpreted without a calibrated rock model? Certainly. Structure can be completely characterized, stratigraphic elements based on reflector geometry and robust amplitude effects can be mapped. But the rock model becomes supremely important when interpretation is pressed into the regime of reservoir property prediction.

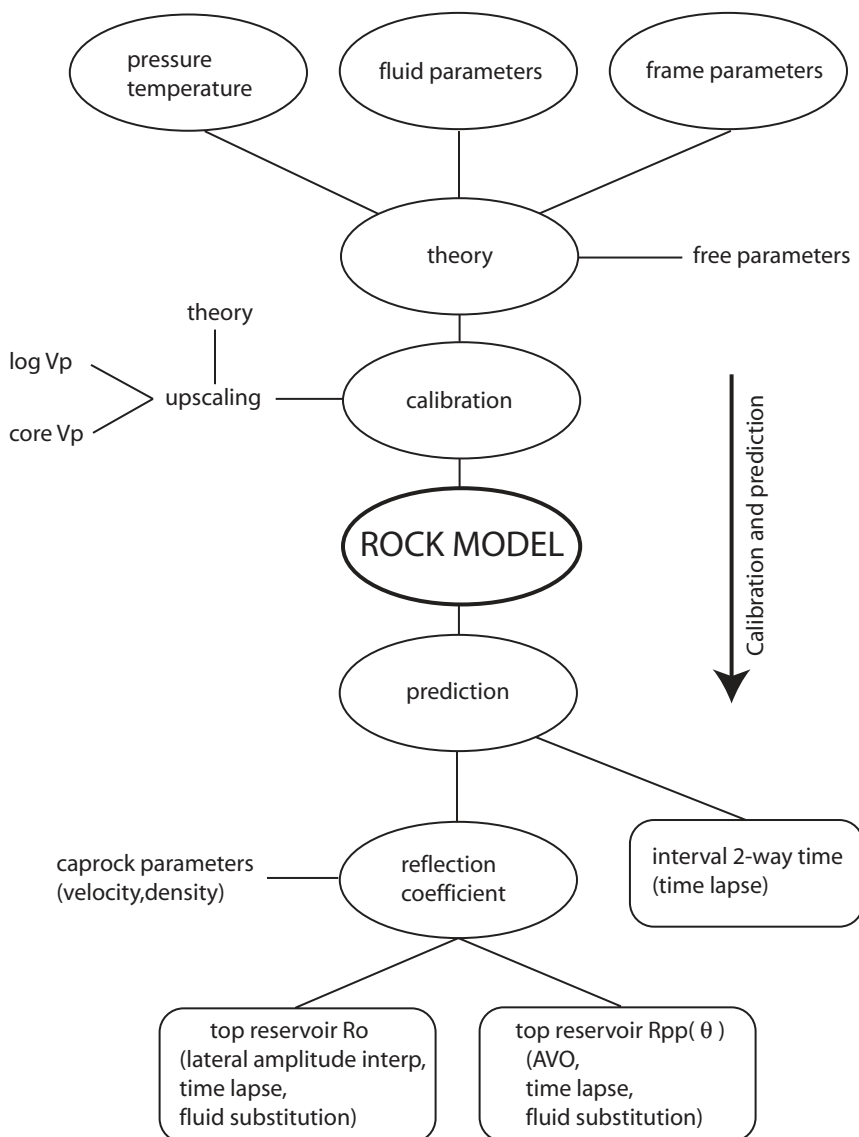


Fig. 26.1 Procedure for building a predictive rock model that can be used to link seismic measurements to reservoir property changes.

## 26.4 Calibrated rock model for Glenn sandstone

From the Gassmann theory in chapter 6.7 and the properties of reservoir fluids in chapter 4, we know the parameters that determine velocity and density in a porous fluid-saturated rock. These are listed in Table 26.2.

To show how changes in rock properties affect seismic amplitude, we will use a specific rock model for the Glenn sandstone in the Glenpool field of Northeastern Oklahoma. Figure 6.2 in chapter 6.7 shows the velocity-porosity relationship for the Glenn that allows us to calibrate the theory. Recall the Gassmann free parameters ( $a, b, c$ ) relate the mineral P-wave modulus,  $m_m$ , to the dry frame modulus,  $m_d$

$$m_d \approx m_m (a + b \phi^c) \quad (26.9)$$

The last column in Table 26.2 lists the in-situ reservoir properties of this formation and calibration parameters found by nonlinear regression on the data points in Figure 6.2. Figure 26.2 shows the calculated velocity and density curves.

Quantity	Units	Definition	Glenn sandstone
$k_m$	MPa	mineral bulk modulus	37 900
$\mu_m$	MPa	mineral shear modulus	44 300
$\rho_m$	g/cc	mineral mass density	2.65
$\phi$		porosity	.24
$(a, b, c)$		calibration parameters	(1,15,1)
°API	cc/g	API oil gravity	45
G		gas specific gravity	.56
S	ppm/(1 000 000)	salinity	.25
$S_o$		oil saturation	0
$S_g$		gas saturation	0
T	°C	temperature	120
P	MPa	pore pressure	10

Table 26.2 Parameters required by the Gassmann theory to calculate velocity and density for a porous fluid-saturated rock. Glenn sandstone parameters are shown in the last column.

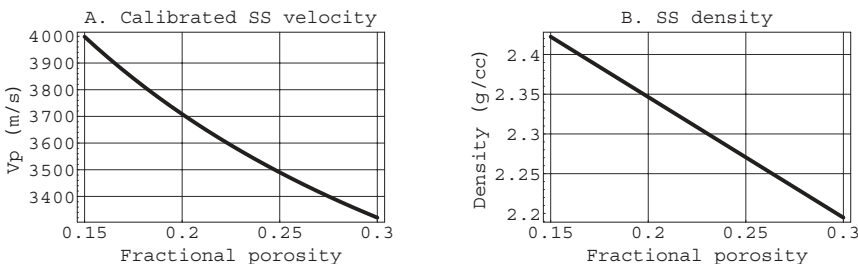


Fig. 26.2 Rock model P-Wave velocity and density plots for the Glenn sandstone. The calibration is based on nonlinear regression of the data in Figure 6.2.

## 26.5 Lateral and time-lapse effects

The Glenn sand calibrated rock model will illustrate a hierarchy of amplitude effects related to reservoir property changes. However, care must be taken in drawing general conclusions from these results. The Glenn is a Pennsylvanian-age midcontinent sandstone. It is representative of stiff, high velocity, paleozoic continental sandstones. The rock stiffness is captured by the calibration parameters  $(a,b,c)=(1,15,1)$ , which would be very different in soft, young rock. In a stiff formation like the Glenn, pore fluid changes do not influence impedance of the rock nearly as much as they would in rocks from a soft-rock basin like the Gulf of Mexico. To be of any real use for another reservoir, the results here need to be recomputed based on a calibrated rock model for that reservoir.

Figure 26.3 shows the impedance and reflection coefficient effect of changes in porosity, gas saturation, and oil saturation for the Glenn sandstone. The vertical axis for each impedance plot is the ratio of reservoir and caprock impedance,  $I_2/I_1$ . Caprock properties used in all plots are  $v_1=3800$  m/s and  $\rho_1=2.5$  g/cc. Thus the baseline case has an impedance drop across the interface of 15% (i.e., the reservoir has lower impedance). For each reflection coefficient plot the vertical axis is  $R_0$  normalized by  $R_0$  for the baseline case in Table 26.2. By using this normalized  $R_0$ , we can quickly determine which reservoir property changes have the strongest influence on the reflection coefficient.

The curves in Figure 26.3 look relatively simple. But it is important to realize that computation of each one involves every equation in chapter 4, the Gassmann equations in chapter 6, and sixteen rock property parameters.

**26.5.1 Gas.** The baseline Glenn parameters are a brine-saturated case, and the strongest amplitude effect we find is related to gas saturation, Figure 26.3A-B. As gas saturation goes from zero to 10%, there is a dramatic drop in impedance and this, in turn, causes a robust amplitude increase of about 90%. The amplitude

## Elements of 3D Seismology

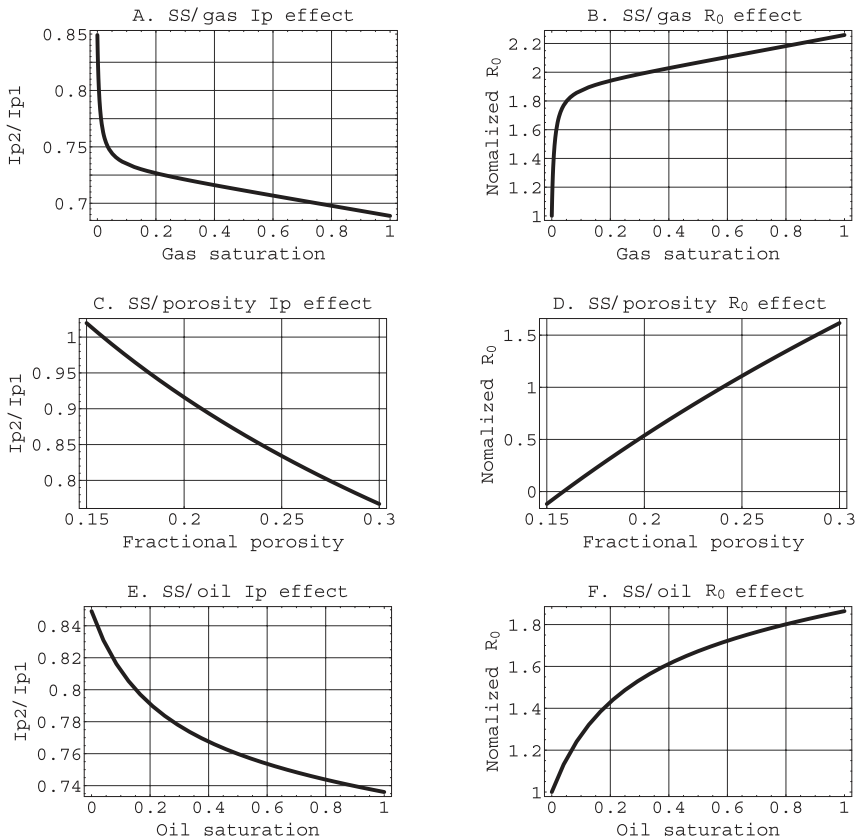


Fig. 26.3 Reservoir properties and seismic amplitude. These plots show the effect of reservoir property changes on acoustic impedance and  $R_0$  (normalized to the baseline case in Table 26.2). These curves are based on the Glenn sandstone calibrated rock model discussed in the text. (A)-(B) Impedance and  $R_0$  changes in response to changes in gas saturation. (C)-(D) Porosity effect. (E)-(F) Oil saturation effect.

grows further with increasing gas saturation, but the incremental gain is smaller. Across the total range of 0–100% gas saturation, the  $R_0$  impact is a 125% boost.

This is the well-known gas bright spot effect, which is used as a direct hydrocarbon indicator (DHI) in many young clastic basins around the world. A problem with this DHI is that non-commercial gas saturation gives nearly full bright spot effect. People therefore talk about using a bright spot to indicate gas and something else to estimate gas saturation. AVO has had some success as a gas saturation indicator [92].

**26.5.2 Porosity.** Average porosity of the Glenn is 24% and it ranges 15–30%. Holding all other reservoir properties constant, the effect of porosity variation is shown in Figure 26.3C-D. In the low porosity range, the effect is to increase impedance until at about 16% porosity the caprock and reservoir impedances are equal. This is an impedance match, and the result is a reflection coefficient of zero. Even though there is a shale-sandstone lithology contact at the top of the Glenn, it is seismically invisible at this magic porosity value. Above average porosity decreases impedance, generating a reflection coefficient up to 50% stronger. The maximum absolute  $R_0$  change due to porosity is 100%.

**26.5.3 Oil saturation.** The baseline Glenn sandstone model is 100% brine saturated. Introduction of oil into the pore fluid has the effect of lowering the impedance and therefore boosting the reflection coefficient. This is shown in Figure 26.3E-F. The reflection coefficient increase of more than 80% is surprising but consistent with the very different bulk moduli of oil and brine (see Figures 4.5 and 4.7).

Oil saturation varies laterally throughout a reservoir, in fact defining the field extent by the oil-water contact. Thus oil saturation is a target for reservoir property mapping from a 3D seismic survey. This lateral distribution and contact change over time as the field is produced, so oil saturation is a primary target in many time-lapse seismic studies.

**26.5.4 Lithology: sandstone-limestone.** The Glenn reservoir is clean sandstone, but we might wonder how lithology changes would influence seismic amplitude. Specifically we take the second lithology to be limestone composed of the mineral calcite. As the calcite fraction increases from zero, we pass through a spectrum of lithologies: clean sand, calcareous sand, sandy limestone, limestone.

To predict this effect, we need to consider a rock frame composed of quartz and calcite. The pertinent physical properties of these two minerals are

$$\text{Quartz } k_q = 37\ 900 \text{ MPa} \quad \mu_q = 44\ 300 \text{ MPa} \quad \rho_q = 2.65 \text{ g/cc}$$

$$\text{Calcite } k_c = 76\ 800 \text{ MPa} \quad \mu_c = 32\ 000 \text{ MPa} \quad \rho_c = 2.71 \text{ g/cc.}$$

The Gassmann theory requires us to supply the composite frame properties when more than one constituent is present. The composite mineral density is simply

$$\rho_m = c_f \rho_c + (1 - c_f) \rho_q \quad (26.10)$$

where  $c_f$  is the carbonate fraction. But how do we combine the moduli? There are ongoing theoretical issues related to this seemingly simple question [195].

## Elements of 3D Seismology

We will follow the mathematical form of both the Gassmann and fluid mixture theories to combine moduli by inverse proportion,

$$\begin{aligned} k_m &= \left( \frac{c_f}{k_c} + \frac{(1 - c_f)}{k_q} \right)^{-1} \\ \mu_m &= \left( \frac{\mu_f}{\mu_c} + \frac{(1 - \mu_f)}{\mu_q} \right)^{-1} \end{aligned} \quad (26.11)$$

In rock physics literature, this is termed the Reuss model and is known to be a lower bound on the actual value of  $(k_m \mu_m)$ .

Figure 26.4A-B shows the impedance and reflection coefficient impact of carbonate fraction for the Glenn formation. Increasing carbonate translates into increasing impedance. This moves the reservoir impedance closer to the caprock value and therefore reduces the reflection coefficient. The net effect is a 55% drop in  $R_0$  at the limestone end member. This result has application to seismic mapping of lateral lithology changes within the reservoir.

**26.5.5 Temperature (steamflood).** The baseline temperature for the Glenn is 120°C, and there is no natural phenomena that will induce a significant lateral change in this temperature over the area of a 3D seismic survey. However, an enhanced oil recovery project using steam injection could raise formation temperature dramatically. The effect of such a temperature change is shown in Figure 26.4C-D. From the Gassmann theory, we know the role of temperature is to change only the pore fluid properties not the mineral properties making up the frame. As temperature increases, we see the impedance falling and therefore the reflection coefficient increasing to a maximum boost of about 50%. Since the baseline pore fluid is brine, this effect follows directly from brine modulus and density variations with temperature as seen earlier in chapter 4.4. The effect on oil is even more pronounced.

This temperature effect can be the target of both lateral (extent of the steam front) and time-lapse studies (time evolution of the steam front).

**26.5.6 Lithology: sandstone-clay.** A second lithology change we will consider for the Glenn is clay content. The elastic properties of solid clay have recently been subjected to comprehensive study [195]. To investigate the order of magnitude influence we can expect from clay, we will use the properties of Illite, a clay mineral common in sandstones.

$$\text{Illite clay} \quad k_c = 56\ 200 \text{ MPa} \quad \mu_c = 28\ 500 \text{ MPa} \quad \rho_c = 2.75 \text{ g/cc} .$$

Measuring the elastic properties of clay minerals is not an easy undertaking and each method introduces different kinds of uncertainty. The values listed here are average Illite properties given in Table 5 of Wang et al. [195]. To find composite frame mineral moduli for use in the Gassmann theory we again accept

$$\begin{aligned} k_m &= \left( \frac{c_f}{k_c} + \frac{(1 - c_f)}{k_q} \right)^{-1} \\ \mu_m &= \left( \frac{c_f}{\mu_c} + \frac{(1 - c_f)}{\mu_q} \right)^{-1} \end{aligned} \quad (26.12)$$

where  $c_f$  now represents clay fraction and subscripted  $c$  denotes a clay quantity.

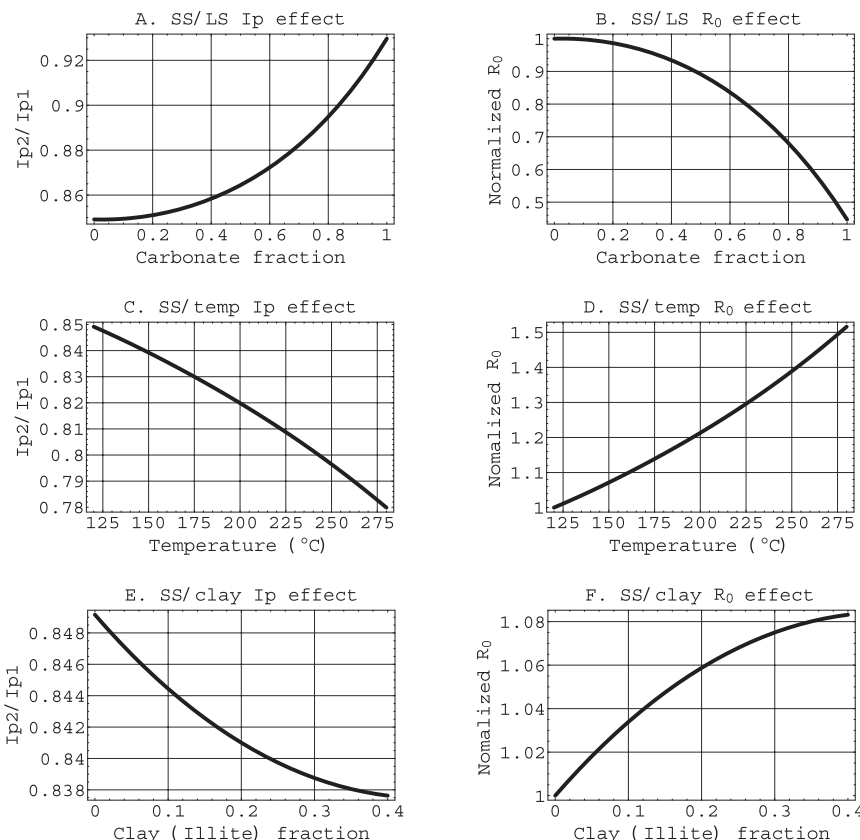


Fig. 26.4 Reservoir properties and seismic amplitude (continued). (A)-(B) Carbonate fraction effect. (C)-(D) Steamflood temperature effect. (E)-(F) Clay fraction effect.

## Elements of 3D Seismology

The effect of clay is shown in Figure 26.4E-F. The clay fraction ranges from zero (clean sand) to 30%, which is as high we are likely to encounter in a petroleum sandstone reservoir. Increasing clay content induces a slight drop in acoustic impedance and increase in  $R_0$ , with a maximum boost of 8%. This is by far the weakest amplitude effect we have encountered, and it would take unusual circumstances of data quality and reservoir uniformity to be seismically observable.

**26.5.7 Permeability.** The Biot-Gassmann theory assures us that permeability has no direct influence on seismic velocity until the wave frequencies are orders of magnitude higher than those available in petroleum seismic data. However, in many sandstones, there is a strong correlation between porosity or clay fraction and permeability. Porosity in particular is a robust impedance and amplitude factor. This means that if permeability is strongly correlated to porosity, that impedance volumes and porosity maps can be recast as permeability volumes and maps. The validity of these permeability products is determined by the reliability of the statistical permeability connection.

**26.5.8 Summary and discussion.** We have now itemized six reservoir property changes and their influence on the normal incidence reflection coefficient. The logical use of these results involves a horizon amplitude map for the Glenn such as the Wilcox map in Plate 7. How could we best explain such amplitude variations for the Glenn sandstone?

Gas is the strongest effect, but there is no evidence of a gas cap or even significant gas-oil-ratio in this field, so we eliminate gas as a candidate. Porosity is known to vary from an interval average of 15–30%, and this is a strong amplitude effect, so we hold on to this possibility.

After primary, secondary, and tertiary oil production, the residual oil saturation is still more than 70% in the Glenpool field. From Figure 26.3F, as oil saturation ranges between 100% and 70%, there is an amplitude change of about 12%, a small but possible effect. There is no actual lateral change in carbonate fraction for the Glenn formation, so we can eliminate this as a factor. The same is true of the temperature effect because the field is not under steam flood (which is primarily used in heavy oil reservoirs). Clay content is known to vary in the Glenn, so this effect is a valid candidate.

In summary, the most likely reservoir properties that can be predicted by seismic amplitude for the Glenn sandstone reservoir are porosity, oil saturation, and clay content, listed in order of decreasing influence. Knowing this, it is highly probable that a suitable amplitude-based seismic attribute would correlate strongly to a composite reservoir parameter formed by combining these three properties.

This exercise with the Glenn sandstone cannot provide general results applicable to all other reservoirs, but it does offer the procedure for linking reservoir rock properties to seismic quantities in poststack 3D and time-lapse seismic data.

## 26.6 Time-lapse 3D seismic

Time-lapse seismic has been mentioned several times, but what is it? Time-lapse 3D seismic (TL3D), also referred to as 4D seismic, is the process of shooting, processing, and interpreting multiple 3D surveys over a field. Each 3D survey has a different vintage (acquisition date), and by comparing the data volumes as the reservoir is produced over time it may be possible to map changes due to fluid movement. The concept is that as hydrocarbons are displaced from the reservoir, the rock properties change, which in turn influences the seismic amplitudes (and, to a lesser degree, traveltimes). By interpreting difference volumes, fluid flow in the reservoir can be estimated and worked into reservoir management plans.

A typical time interval between individual 3D surveys might be 4–7 years. No special acquisition methods are required for TL3D seismic, but it is very important that the survey be repeatable. Marine fixed-receiver acquisition systems are ideally suited to TL3D work because of perfect source-receiver coupling and the possibility of permanent receiver installation.

The first published accounts of TL3D seismic were towed acquisition projects from the North Sea and single-component work in the U.S. transition zone (both 1996), followed by four-component (4C) marine work and land TL3D (both 1998). Applications widened to include steamflood monitoring (1999), 4C amplitude-versus-offset, production history matching, elastic inversion, and application to carbonate reservoirs (all 2001). A good conceptual account of TL3D is found in Fanchi [65] and a comprehensive survey of historical and technical progress can be found in Lumley [120].

Fundamental to TL3D seismic is the interpretation of difference volumes in light of a predictive rock model. What kind of differences are there? We can think of three kinds:

- **Amplitude.** Amplitude differences proportional to zero offset reflection coefficient variations are the usual target of TL3D seismic interpretation. We attempt to say how the reflection coefficient,  $R_0$ , at the top of the reservoir will change as hydrocarbons are removed.
- **Travelttime.** If P-wave speed in the reservoir changes over time, then travelttime difference mapping may be possible. When present, a travelttime effect is much more robust and easily detected than

## Elements of 3D Seismology

amplitude effects. For some thick heavy oil reservoirs, traveltime effects may be observable and used as the primary indicator. Traveltime differences will probably not occur for gas because the rock velocity is nearly constant for any saturation more than 10%.

- **Waveform.** Waveform differences are the most difficult. They involve traveltime changes, reflection coefficient changes, and thin bed interference effects. For example, it might be easy to demonstrate in real data that over time the wavelet phase is changing in certain parts of a reservoir. But understanding the physical basis of this change could be a major project.

From earlier discussions in this chapter, it should be clear that TL3D reflection coefficient behavior is a complicated function of frame, fluid, and environmental parameters.

As an example, consider the time-lapse reservoir behavior in Figure 26.5. This synthetic result represents a sandstone gas reservoir with a mixed water and pressure depletion drive mechanism. This means that as gas is produced, there is both a drop in pressure and a drop in gas saturation. In Figure 26.5A the  $R_0$  surface is shown for a stiff sandstone similar to the Glenn. Being so stiff, the

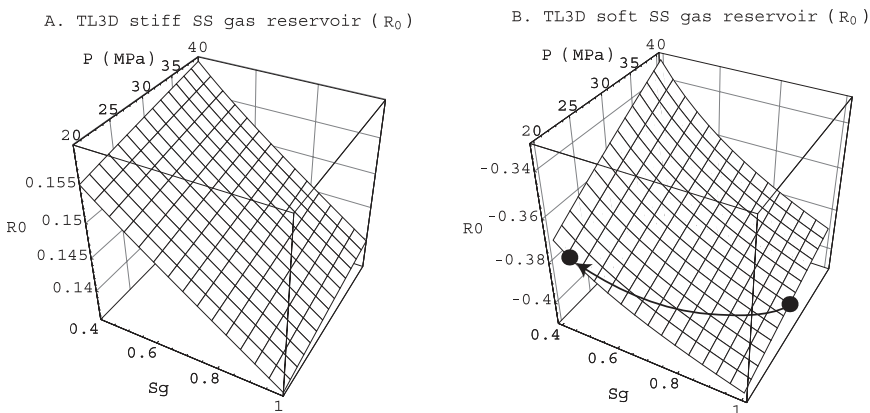


Fig. 26.5 Theoretical time-lapse behavior of  $R_0$  for two sandstone gas reservoirs. (A) Stiff reservoir rock is affected by gas but shows little change in reflection coefficient with pressure drop. (B) A soft reservoir is more strongly influenced by pressure changes. The dots represent conditions before and after production. The line is one possible production path between them. The maximum predicted amplitude change during production is 5.8%. Observation of such an amplitude change on marine 3D time-lapse data is within the limit of current technology.

pressure drop has little effect on the rock impedance and therefore little effect on the reflection coefficient.

By contrast, Figure 26.5B represents a soft sandstone reservoir that might be found in the Gulf of Mexico. As expected, pressure drop now has a stronger influence. The two points indicate conditions before production and some years later after production. These two points on the  $R_0$  production surface are connected by a directed line representing the transition from the initial to final state. It is only one possibility. The reflection coefficient change in this example is 5.8% from initial to final state.

Under good conditions, amplitude changes as small as 3–5% can be detected so the simulation in Figure 26.5 would represent a marginal candidate for time-lapse seismic analysis. Time-lapse 3D seismic projects are expensive and long-term. Even if we predict an observable amplitude effect, many other factors must be taken into account. This is the subject of technical risk assessment.

There are many factors which determine if a TL3D project is likely to succeed. The major ones are itemized in a TL3D fact sheet [121] as shown in Table 26.3. Representative values are given for the ideal case and three important petroleum regions.

A useful scoring system can also be set up involving key parameters of the problem [121]. The seismic related parameters are image quality, resolution, fluid contact visibility, and repeatability. For each category given next, a true statement earns one point, so the maximum is five points per category.

### **Image quality:**

1. good signal-to-noise ratio of migrated stack
2. clear image of reservoir reflection
3. reliable and meaningful amplitudes
4. no multiples or coherent noise problems
5. no shallow gas, statics, or velocity problems

**Resolution:** (1)  $RT > RL/2$ , (2)  $RT > RL$ , (3)  $RT > 2 \times RL$ , (4)  $RT > 3 \times RL$ , (5)  $RT > 4 \times RL$ , where RT is reservoir thickness and RL is vertical resolution limit.

### **Fluid contact (FC) visibility**

1. at least one FC visible in cross-section
2. several FCs visible in cross-section
3. one FC mappable aerially
4. several FCs are mappable aerially
5. all fluid contacts are mappable aerially

## Elements of 3D Seismology

Item	Ideal	Indonesia	Gulf of Mex	North Sea
<b>Reservoir</b>				
Depth (m)	shallow	200	2100-2450	2800-3200
Overburden pressure (psi)	low	530	7000-8000	7500-7500
Pore pressure (psi)	high	100-350	3100-3300	6500→5250
Net pressure (psi)	high	430-180	3900-4700	0→2250
Bubble point (psi)	low	110	3100	1250
Temperature (°F)	—	100-430	176-180	215
Unit thickness (m)	high	30	30-45	5-12
<b> Rocks</b>				
Dry bulk modulus (GPa)	low	2-3	3.0-5.8	10-30
Dry density (g/cc)	low	1.54-1.67	1.7-2.1	2.07-2.23
Porosity (%)	high	30-38	21-34	16-23
<b> Oil</b>				
Solution GOR (scf/stb)	high	0	250-350	>300
Gravity (°API)	high	22	25	36
Density (g/cc)	low	0.9	0.85	0.75
Bulk modulus (GPa)	low	1.5	1.2-1.5	0.92
<b> Water</b>				
Salinity (ppm)	high	40 000	190 000	200 000
Density (g/cc)	high	1.0	1.1	1.08
Bulk modulus (GPa)	high	2.25	3.35	3.0
<b> Gas</b>				
Density (g/cc)	low	0.1	0.1	0.12
Bulk modulus (GPa)	low	0.1	0.1	0.23
<b> Time-lapse fluids</b>				
Fluid saturation change (%)	high	5	90→10	90→10
Fluid compressibility contrast (%)	high	>1000	150-200	200
<b> Seismic</b>				
Dominant frequency (Hz)	high	125	50	25
Average resolution (m)	low	5	15	30
Image quality (1-5)	5	4	5	3
Repeatability (1-5)	5	5	4	2
Fluid contact visibility (1-5)	2	4	4	2
Pred. traveltime change (samples)	>4	20	0	0
Predicted impedance change (%)	>4	55	8-10	3-7

Table 26.3 Time-Lapse 3D fact sheet used to assess the technical risk of a time-lapse 3D (TL3D) project (modified from [121]).

### Repeatability

1. same acquisition method used for each survey,
2. permanent source and receiver installation used,
3. source and receiver repositioning verified for each survey,
4. same shooting direction used for each survey,
5. same bin size and offset/azimuth distribution for each survey.

Further scores are associated with important reservoir properties, as shown in Table 26.4, and the total reservoir and seismic score enter into a TL3D technical risk sheet, Table 26.5.

The goal of TL3D technical risk assessment is to ascertain if a particular field or reservoir is a likely candidate. The risk assessment does not replace rock model prediction of seismic response to reservoir changes. Rather, it offers an early inexpensive screen to identify likely candidates for further work.

The reservoir and seismic scores are collected in a TL3D technical risk sheet as shown in Table 26.5, where the results for each region are compared to an ideal case. A reasonable passing score for the reservoir total is 18 of 30 (60%), and 12 of 20 (60%) for the seismic total. They each have veto power, so they must independently

Item	5	4	3	2	1	0
Dry rock bulk modulus (GPa)	<3	3-5	5-10	10-20	20-30	30+
Fluid compress. contrast(% change)	250+	150-250	100-150	50-100	25-50	0-25
Fluid saturation change (% change)	50+	40-50	30-40	20-30	10-20	0-10
Porosity (%)	35+	25-35	15-25	10-15	5-10	0-5
Impedance change (% change)	12+	8-12	4-8	2-4	1-2	0
Traveltme change (samples)	10+	6-10	4-6	2-4	1-2	0

Table 26.4 Reservoir scorecard for key parameters are allocated scores from 5 (best) to 0 (worst) (modified from [121]).

Item	Ideal	Indonesia	Gulf of Mexico	North Sea
<b>Reservoir</b>				
Dry rock bulk modulus	5	5	4	2
Fluid compress. contrast	5	5	4	4
Fluid saturation change	5	5	5	3
Porosity	5	5	4	3
Predicted impedance change	5	5	4	3
Predicted travel time change	5	5	0	0
Reservoir total	30	30	21	15
<b>Seismic</b>				
Image quality	5	4	5	3
Resolution	5	5	4	1
Fluid contacts	5	4	4	2
Repeatability	5	5	4	2
Seismic total	20	18	17	8
<b>Total Score</b>	<b>50</b>	<b>48</b>	<b>38</b>	<b>23</b>

Table 26.5 Time-Lapse 3D technical risk scores for an ideal candidate and three cases from around the world (modified from [121]).

meet the 60% criteria. Technical feasibility is a necessary, but not a sufficient condition for a successful TL3D project. Economic feasibility is also required.

### 26.7 Offset effects (AVO)

Currently most amplitude interpretation is done on poststack migrated 3D data. This means that offsets originally in the data have been lost through stacking. However the prestack data contains additional information in the form of amplitude variation with offset (AVO). In many areas of the world, this can be extracted and used for reservoir analysis.

The physical basis of AVO is some form of elastic P-P reflection coefficient approximation as a function of incident angle ( $\theta$ )

$$R_{pp}(\theta) \approx A + B \sin^2\theta \quad (26.13)$$

where  $(A,B)$  are called the intercept and gradient. They are functions of elastic property contrasts across the interface as defined in chapter 5.10. Various approximations of this type have been developed since the 1960s, but the form published by Shuey [166] in 1985 is probably the most common used today. To use this relationship, it is necessary to transform the offset axis in CMP gathers to sine-squared of the incidence angle. This requires velocity information which can be estimated from the data itself.

An early application of AVO analysis in the mid-1980s was screening to distinguish productive and nonproductive bright spots in the Gulf of Mexico. Since that time, the number of AVO applications can be judged by the fact that more than 600 papers have been published or presented. Rutherford and Williams [158] published an AVO classification scheme in 1989 that persists in slightly modified form today.

To isolate the angular reflection coefficient, prestack data must be specially processed for AVO [63]. The major steps are

1. amplitude corrections including geometrical spreading, attenuation, surface consistent scaling
2. waveform corrections including source/receiver directivity compensation, and surface consistent deconvolution
3. traveltime corrections of NMO and residual NMO, multiple suppression, DMO, migration without stack, and sort to CMP gathers (a popular alternative is prestack time migration)

At this point the CMP gathers (or common image gathers from prestack migration) are ready for the AVO process. This consists of four steps:

1. each CMP is transformed from offset to  $\sin^2\theta$
2. for each time level of interest the amplitude data points are fit with a line characterized by the intercept, A, and gradient, B
3. repeating for all time levels yields A and B traces for each CMP
4. repeating for all CMPs yields A and B sections or data volumes.

Figure 26.6 shows a synthetic CMP gather along with the intercept and gradient trace computed from the gather. After NMO correction has flattened all events at all times, the CMP gather shows various kinds of AVO behavior. Some events have uniform strength across all offsets, some decay with offset, some grow

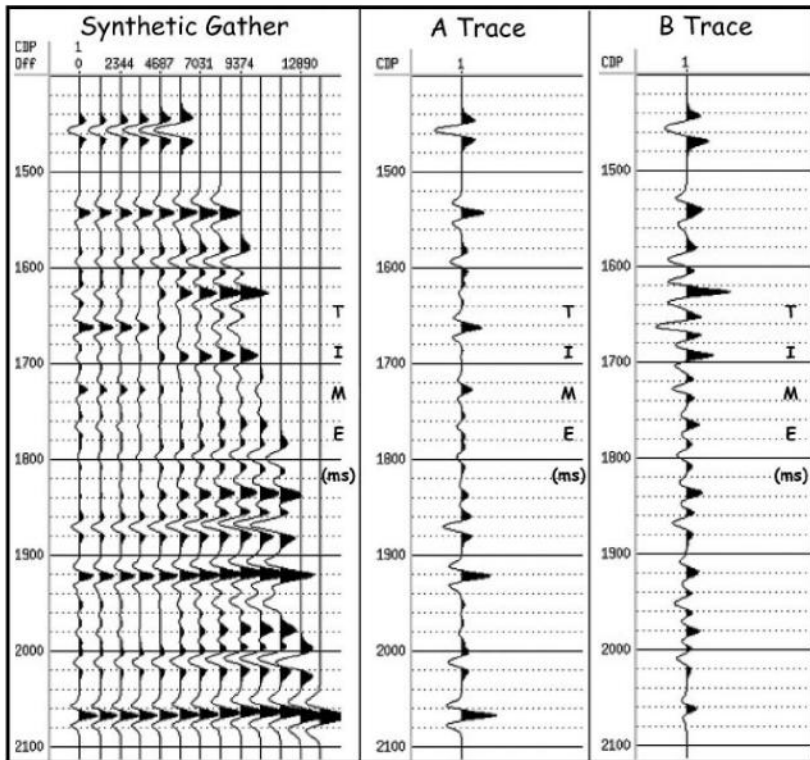
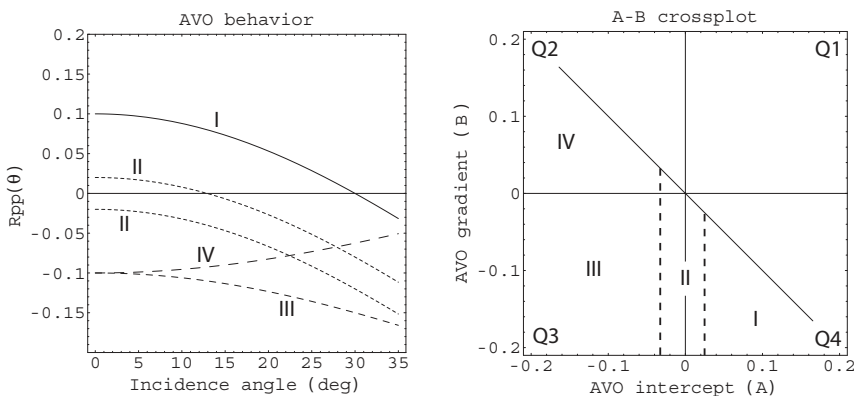


Fig. 26.6 Amplitude versus offset. The synthetic CMP gather shows various kinds of amplitude versus offset behavior. Using velocity information, the offset can be recast in terms of the incidence angle,  $\Theta$ . At each time level of interest, the amplitude data points are then fit with a line of the form  $A+B \sin^2\theta$ . The zero offset intercept values form a trace of A values, and the slope values form a B trace. These traces can be used directly to scan large data sets for AVO features or windowed and cross plotted for detailed reservoir analysis. (From [132]).

## Elements of 3D Seismology

stronger with offset, and others change polarity as offset increases. The basic observation leading to AVO is that some reservoir reflectors, chiefly gas sands, show an increase in amplitude with offset while non-gas reflectors show little increase or even a sharp decrease in amplitude with offset.

The traditional AVO model assumes sandstone overlain by shale. As mentioned earlier, a classification scheme has evolved to describe AVO behavior [158, 39, 72]. Figure 26.7 is an overview of AVO behavior and classification. Figure 26.7A shows variation of reflection coefficient with incidence angle not sine-squared of the incidence angle. The reflection coefficient is linear with respect to  $\sin^2\theta$  and therefore nonlinear with respect to  $\theta$ .



*Fig. 26.7 AVO classification scheme based on A-B crossplotting. (Redrawn from [6]). (A) Reflection coefficients as a function of incidence angle showing sandstone Classes I–IV. Type III is the classic response associated with a gas sand in the Gulf of Mexico. (B) AVO crossplot of intercept against gradient. The four AVO classes plot to separate areas on this diagram making it a useful tool for discriminating sandstone targets. Quadrants of the plot are labeled Q1–Q4.*

There are four classes of AVO behavior labeled I–IV. Class III is the classic gas effect AVO anomaly of a relatively strong intercept and increasing amplitude with offset (in an absolute sense). In Figure 26.7B, this information is given in terms of an intercept-gradient, or A-B, crossplot. The classes map to different areas in this plot. The physical basis of A-B cross plotting with respect to elastic wave theory is described in detail by Castagna et al. [40]. Table 26.6 gives the interpretation of AVO classes in terms of impedance contrast [39].

Class	Relative Impedance	Quadrant	A	B	AVO
I	Higher than overlying unit	Q4	+	-	Decreases
II	About the same as the overlying unit	Q2, Q3, or Q4	+ or -	-	Increase or decrease may change sign
III	Lower than overlying unit	Q3	-	-	Increases
IV	Lower than overlying unit	Q2	-	+	Decreases

Table 26.6 Summary of the connection between impedance contrast and AVO behavior. (From [39]). The quadrants refer to Figure 26.7B.

As the applications of AVO have moved beyond sandstone gas reservoirs, the relevance of this classification scheme has diminished. The use of A-B cross plotting, however, is still at the heart of AVO work. Figure 26.8A is an example A-B cross plot for a turbidite reservoir in the North Sea [6]. The closed lines represent isoprobability contours related to identification of three key facies as labeled. The contours enclose probabilities of 50% and greater. The value of AVO cross plotting is this kind of separation between reservoir and non-reservoir rocks in the A-B plane. The general idea is to identify a background non-reservoir trend, then seek out relatively rare anomalous trends representing reservoir rocks (Fig. 26.8B).

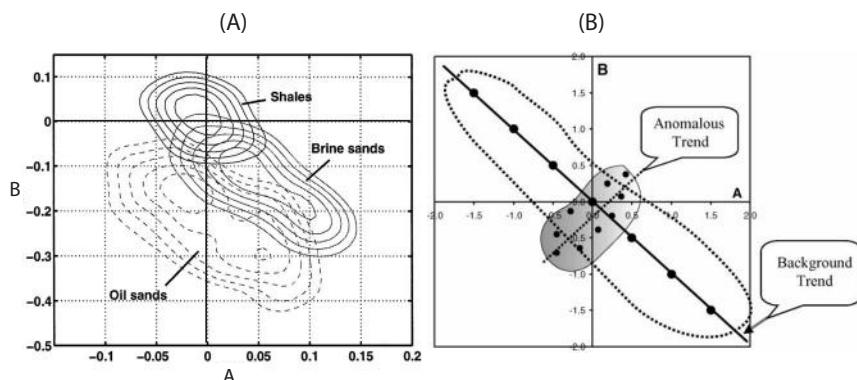


Fig. 26.8 A-B cross plotting is fundamental to AVO interpretation even when gas sand is not the target. (A) Probability contours in A-B space show partial separation of three key facies in North Sea turbidite reservoirs. (From [6]) (B) The general idea of A-B cross plotting is to establish a background non-reservoir trend and look for anomalous trends associated with reservoir rocks. (From [132]).

## **Elements of 3D Seismology**

The utility and understanding of AVO analysis continues to grow. Recent AVO literature relates to inversion, fluid property discrimination, fractures, uncertainty, land multicomponent 3D data, anisotropy, velocity analysis, porosity prediction, source rock identification, converted waves, thin beds, and gas hydrate analysis, to name a few.

It would be a mistake to think that every interpretation project involves AVO. It is routinely used in some high-profile areas like the Gulf of Mexico and North Sea, but AVO has had limited success in hard rock basins and with land data in general. Much like time-lapse 3D seismic, AVO is an important tool in those geological settings where it works well.

## Acknowledgments

First and foremost, I offer my sincere appreciation to Maria Dolores Proubasta. Her boundless enthusiasm and optimism have moved me forward many times when confidence waned and the task seemed endless. Furthermore, Maria Dolores was unacknowledged in the first edition despite spending many long hours as unofficial copy editor. I hasten to add that the many errors found in the first edition were incurred after her careful correction of the manuscript. For her contribution to both editions, I am deeply indebted.

My PennWell editor, Marla Patterson, has been a joy to work with, and largely through her promotional efforts, the first edition sold out to warrant a second edition.

Most of the material in the book was debugged in teaching a rotation of four classes in petroleum seismology at The University of Tulsa. I thank the many students in those classes, particularly Gary Bratcher who contributed *Mathematica*<sup>TM</sup> code for the Zoeppritz equations. I am grateful to The University of Tulsa for fostering an environment of scholarship that encourages faculty to undertake long-term writing projects such as this book and for granting a sabbatical leave in spring 2003 to compose this second edition.

Among professional colleagues, I had noteworthy discussions with Leon Thomsen on Backus averaging; Mike Batzle on the equations for brine modulus and density; James Berryman on Biot-Gassmann theory; John Scales on a closed form expression for the count of primary reflections in layered elastic media; Gijs Vermeer, Steve Roche, and Bill Dragoset on seismic acquisition; and Stan Laster on anisotropy.

### **Seismic data and software**

Seismic data that appears in this book is courtesy of Unocal (West Texas line header); Burlington Resources (3D fold and acquisition shot geometry), ExxonMobil (SE Asia 2D), Fairfield Industries (Gulf of Mexico 3D), Ralph Gobeli (West Africa 2D, Stratton reprocessing, Glennpool 3D processing) and Opseis (Glennpool 3D acquisition). The Stratton 3D seismic data set is available for a nominal fee from the Texas Bureau of Economic Geology. The Self-82 log suite is a product of DOE funding under contract number DE-FC22-93BC14951.

Public domain software used in creation of this book includes SeismicUn\*x (SU) from the Center for Wave Phenomena at the Colorado School of Mines masterfully maintained by John Stockwell, ObjectImage originally written by Wayne Rasband of the U.S. National Institutes of Health and now maintained by Norbert Visher of the University of Amsterdam, ImageJ by Wayne Rasband, and LastWave by Emmanuel Bacry of the Centre de Mathématiques Appliquées at the École Polytechnique in France.

This book benefited greatly from the use of *Textures*<sup>TM</sup> from Blue Sky TeX Systems and *Mathematica*<sup>TM</sup> from Wolfram Research.

### **Changes from the first edition**

This is more new book than second edition, not only 50% longer but perhaps 70% new or revised material throughout.

The scope of the book has been much broadened particularly in the areas of wave propagation, processing, thin layer phenomena, and attributes. An attempt has been made to organize wave propagation effects into those that occur in acoustic media (perhaps 85% of all seismic phenomena), solids (another 10%), and porous solids (the final 5%). The concept of a physically based, predictive rock model has been promoted to a central theme of seismic amplitude interpretation.

All units are now metric with the exception of a few credited figures. Mathematical symbols are more standardized and defined at the point of use rather than defined in a detached, unwieldy appendix.

The exercises have been deleted. This was a difficult decision but one that seemed necessary to move the work toward reference book status. Also, those inclined to teach from the book invariably generated exercises to reflect their own interests.

## **Figures and references**

All credited figures are courtesy of the Society of Exploration Geophysicists, except color Plate 4, which is courtesy of Landmark Graphics, a Halliburton Company.

I am particularly grateful to the efforts of Ted Bakamjian, publications manager of the SEG. He had vision and persistence that convinced the SEG to create an online archive of all *Geophysics* and *Leading Edge* contributions reaching back to the beginnings of both publications. He furthermore wisely advised the SEG to host this important function through the American Physical Society. The result has been an indispensable resource in writing this second edition, allowing many important concepts to be referenced back to primary source material.

Concerning the relative quality of references, first preference is given to peer-reviewed journals, then major reference books, then panel-reviewed publications (such as *Leading Edge*), and finally presented material such as SEG national meeting abstracts. The abstracts form an important body of rapid-publication material but are of uneven quality and accuracy. Nonetheless, some important advances appeared first, or solely, in the abstracts literature.

## **Errata**

The responsibility for any errors in this book reside solely with the author. Readers are encouraged to email any typographical errors or errors of fact to [cll@utulsa.edu](mailto:cll@utulsa.edu).

Should the need arise, an errata Web site will be maintained on the author's home page. This may be located via any standard Internet search engine using the key words "chris liner home page."

The following individuals are gratefully acknowledged as having contributed errata items on the first edition: Andreas Cordsen, Bryant Reasoner, Chun-Feng Li, Grant Byerly, Hamed El-Mowafy, I. H. Kartootmodjo ("Bimo"), Ian Harris, Robert Wilson, Ramin Nawab, and Youshun Sun.

# Contents of CD-ROM

## SeisCom

SeisCom (Seismic Companion) is an Excel workbook designed to perform many common calculations related to petroleum seismology. It is included here (SeisCom.xls) without warranty and it is strongly recommended that any critical calculations be independently confirmed. Use of SeisCom is unrestricted, except that the author's name cannot be removed and that the workbook, or any parts of it, cannot be sold.

Excel power users are encouraged to add functions to SeisCom and offer these back to the author to be considered for future versions. The added functionality can take the form of additional items on an existing sheet, or a new sheet for significant additions. For serious consideration, the new functions must adhere to the style of existing functions.

Movies

[Click here to download Quicktime movies](#)

## **Part IV**

*Color Plates*

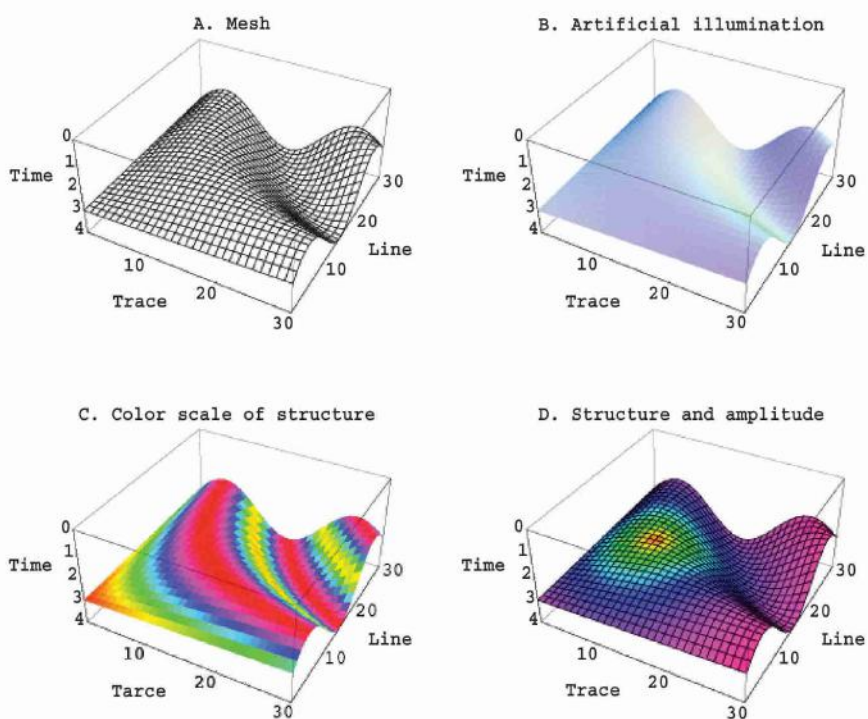


Plate 1. The horizon slice is a time structure surface generated by automatic event picking in the seismic data volume. Shown here are various perspective plots of time structure associated with a 3D horizon slice. (A) Simple time structure mesh. (B) Artificial illumination used to bring out subtle features in complex surfaces. (C) Color scale of time structure draped over the time structure surface. (D) Combined time structure (mesh) and horizon amplitude (color) display.

## Elements of 3D Seismology

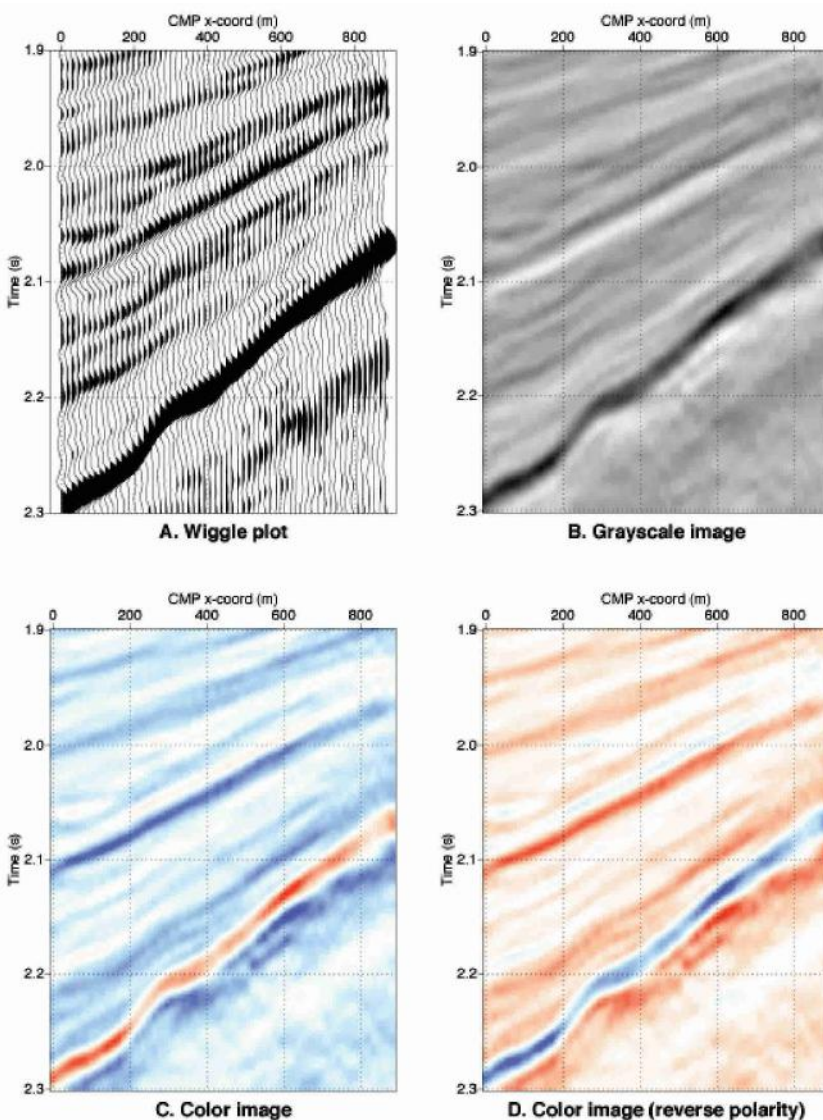


Plate 2. Display of seismic data composed of 60 traces and 101 time samples. (A) Wiggle trace display with variable area, meaning that deflections to the right are filled in with black. (B) Grayscale image of the same data. (C) Color image with red representing positive amplitudes. (D) Reverse polarity color image. Blue now represents positive amplitudes.

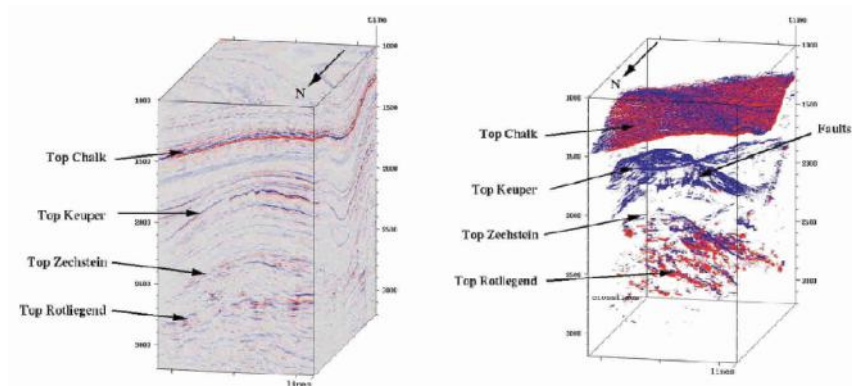


Plate 3. In volume visualization the data is mapped onto a 3D array of voxel graphic elements. Each voxel has a color representing seismic amplitude at that location and a variable transparency level. This allows creation of a semi-transparent data volume, in which certain amplitude ranges are opaque and all others are transparent. This example is from the southern North Sea Basin (From [62]).

## Elements of 3D Seismology

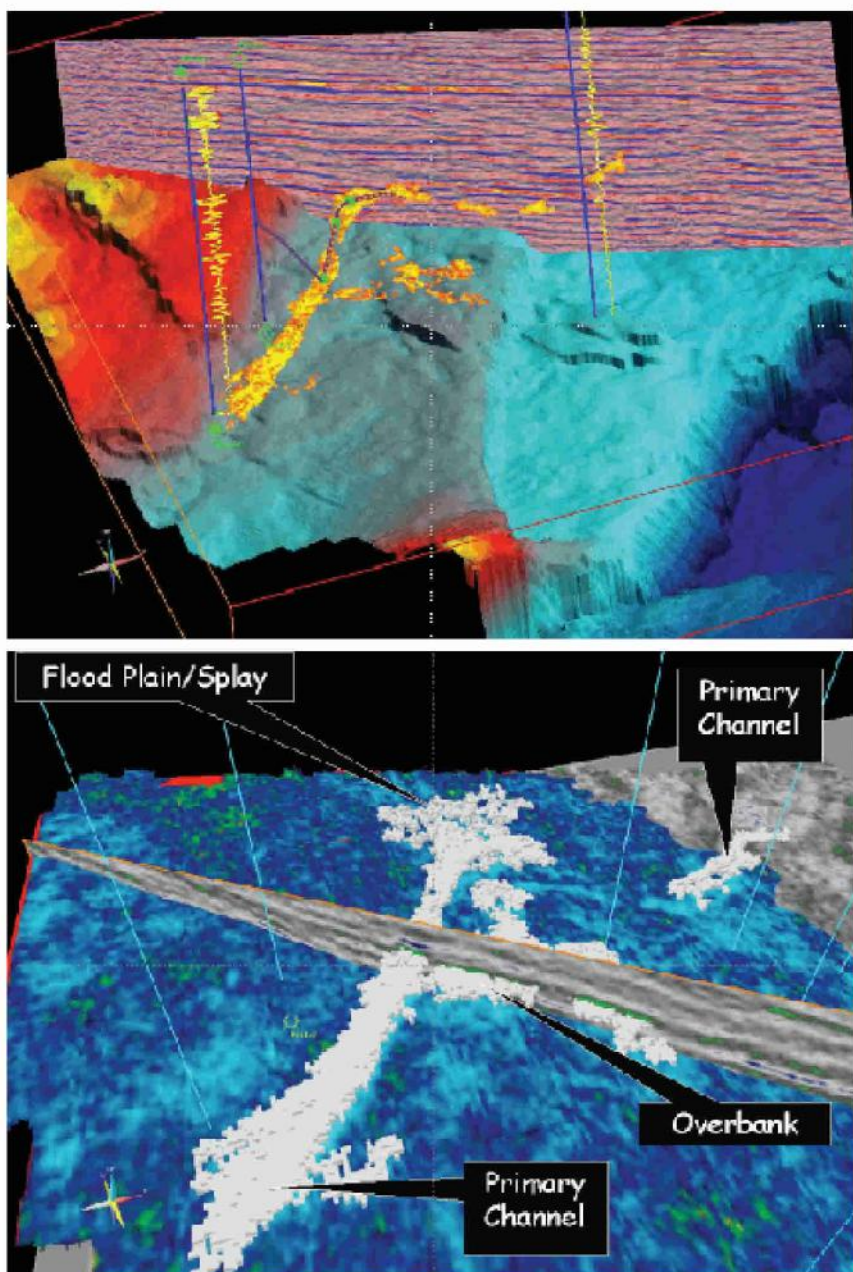
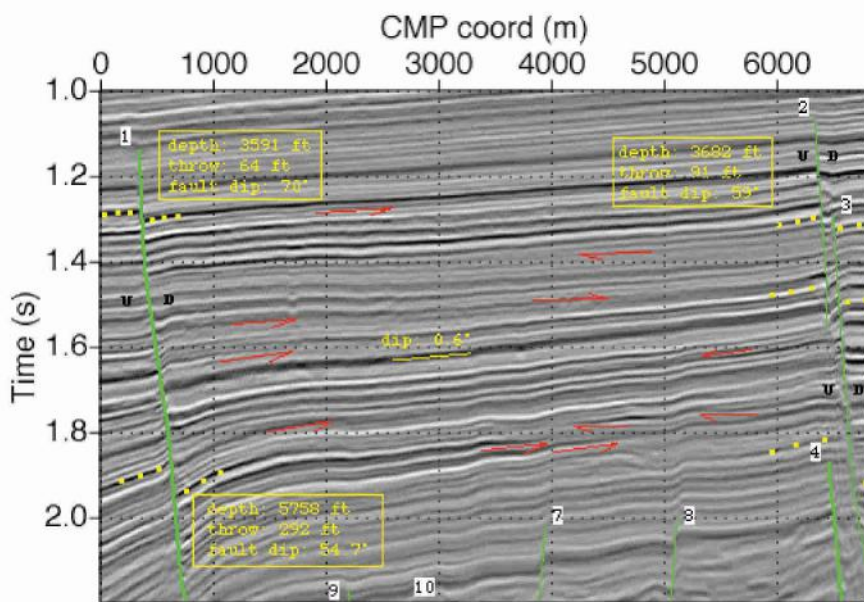


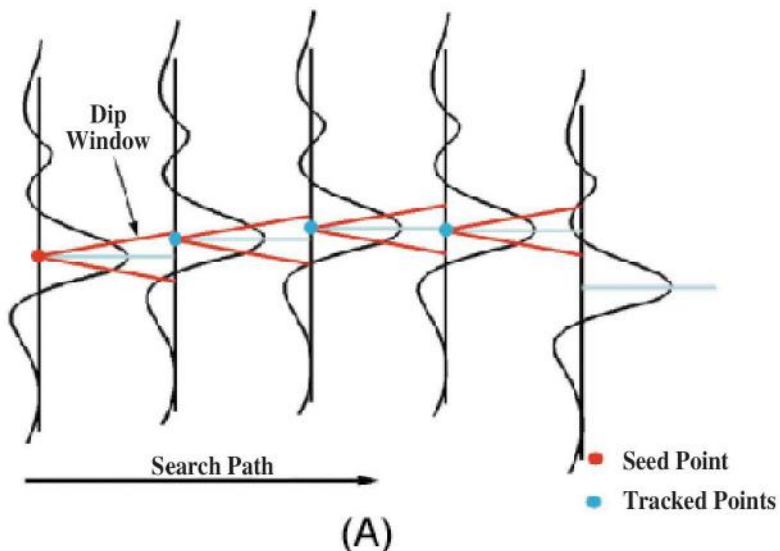
Plate 4. Immersive volume interpretation of 3D seismic data can include arbitrary 2D subsets, well tracks with log information and trajectory, rendered geologic surfaces, voxel tracking, and innumerable other features. These examples are from the Earthcube interpretation system (Courtesy Landmark Graphics, a Halliburton Company).



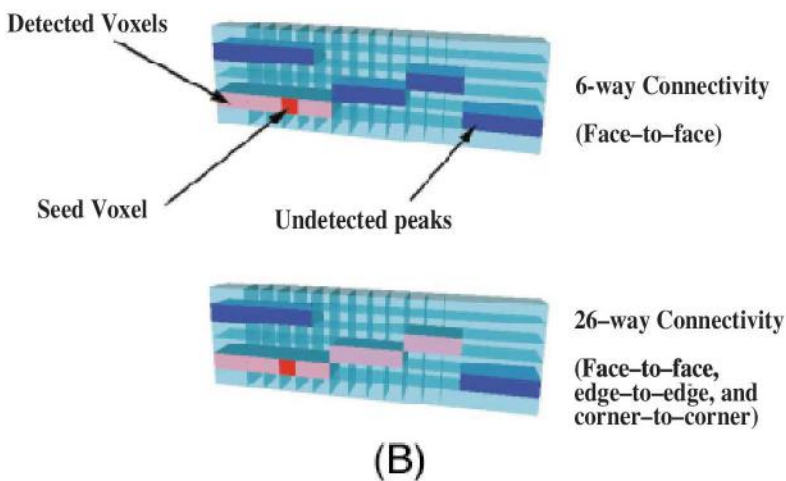
## 2D Migrated data

Plate 5. Part of a 2D seismic line marked up for interpretation. Faults are marked in green with line width denoting relative importance. Sense of throw is indicated as up fault throw (U) or down (D). Yellow dots indicate events used to calculate depth and fault throw, while yellow lines are events used for dip calculations. Fault numbers indicate relative age (1=most recently active, etc.). Red arrows show stratigraphic bed terminations. The arrowhead indicates if termination is from above or below.

## Elements of 3D Seismology



(A)



(B)

Plate 6. Automatic picking of seismic events (From [62]). (A) Tracking in a slice-based 3D interpretation system. A seed point and dip window are specified by the user, and the data is scanned trace-by-trace to follow the event of interest. The tracking then jumps to the next slice and proceeds. Any feature of the event may be tracked such as a peak, trough, or zero crossing. It is also possible in advanced systems to perform a short window cross correlation that follows waveforms that vary across the survey area. (B) In a volume interpretation system tracking can proceed along the faces and edges of each voxel.

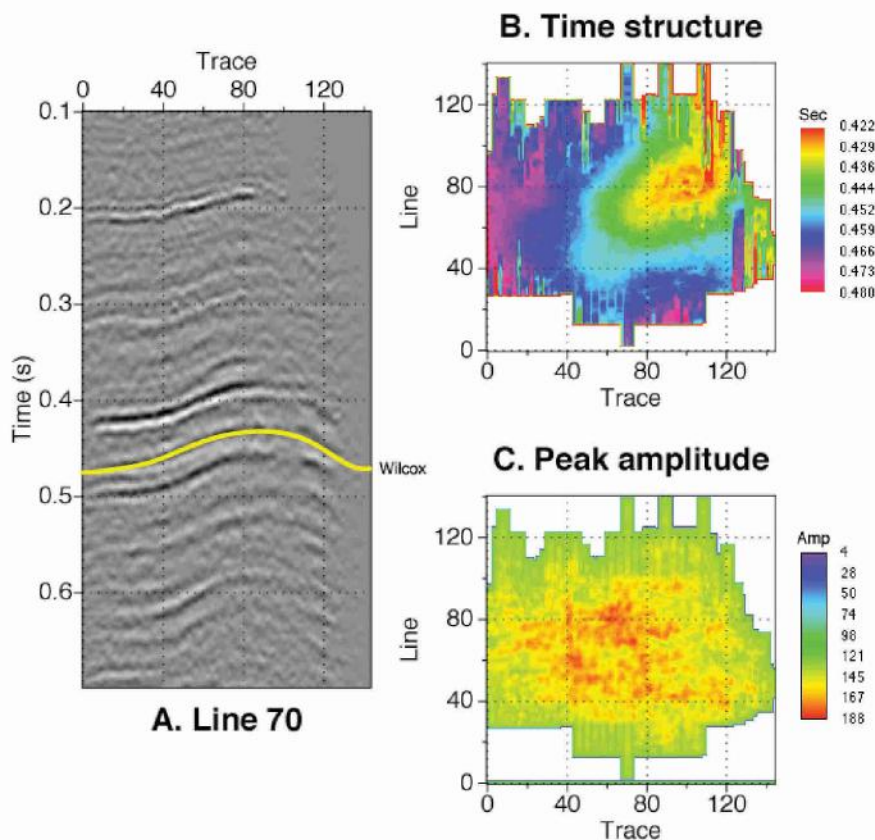


Plate 7. Tracking results for Devonian Wilcox in the Glenpool field of Northeast Oklahoma. A representative line is shown with top of Wilcox highlighted. Two maps are created by the tracking process—a time structure map and an amplitude map.

## Elements of 3D Seismology

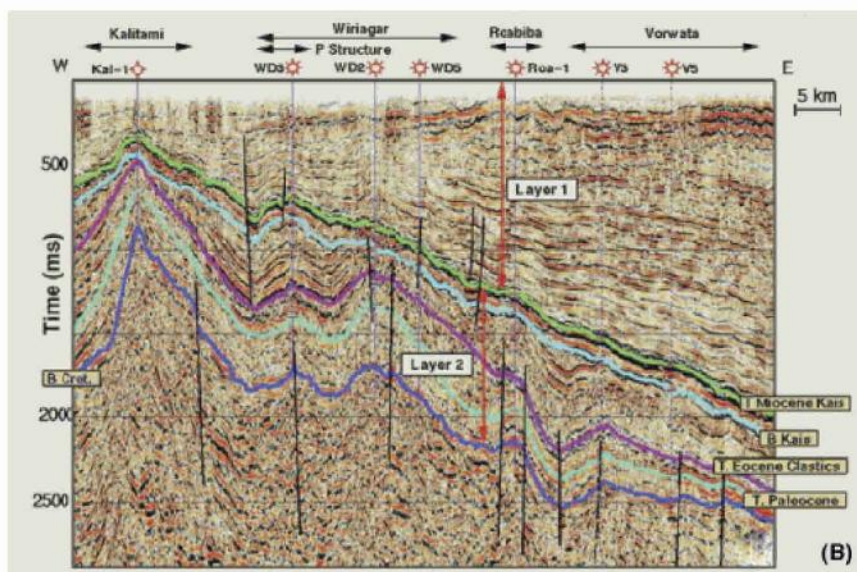
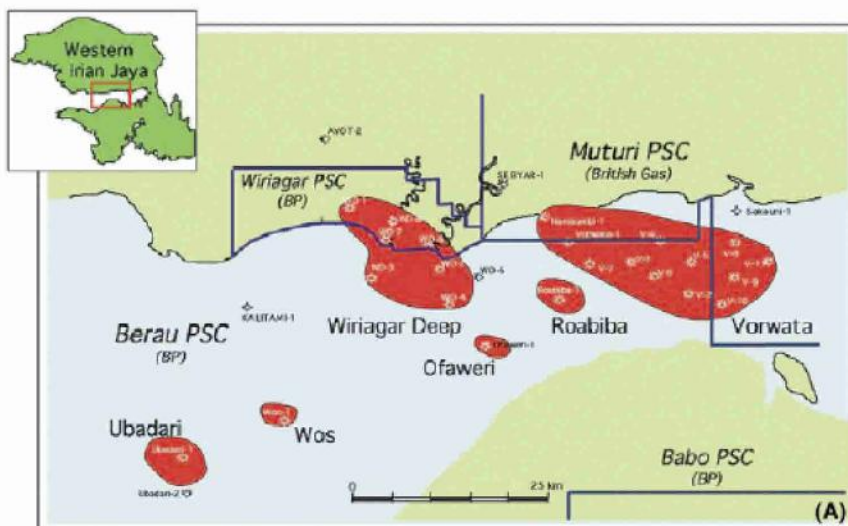


Plate 8. Depth conversion case history. (From [95]) (A) Area map including the Vorwata structure, in which additional drilling was done based on depth map results. (B) Regional interpreted seismic section. Target formation in the Vorwata area is Jurassic Sand which has a weak, erratic reflection. Therefore depth mapping proceeds by dividing the subsurface into two layers, which are described using linear velocity functions. The base Cretaceous map is combined with a well-derived Jurassic shale map to create a final Jurassic sand map.

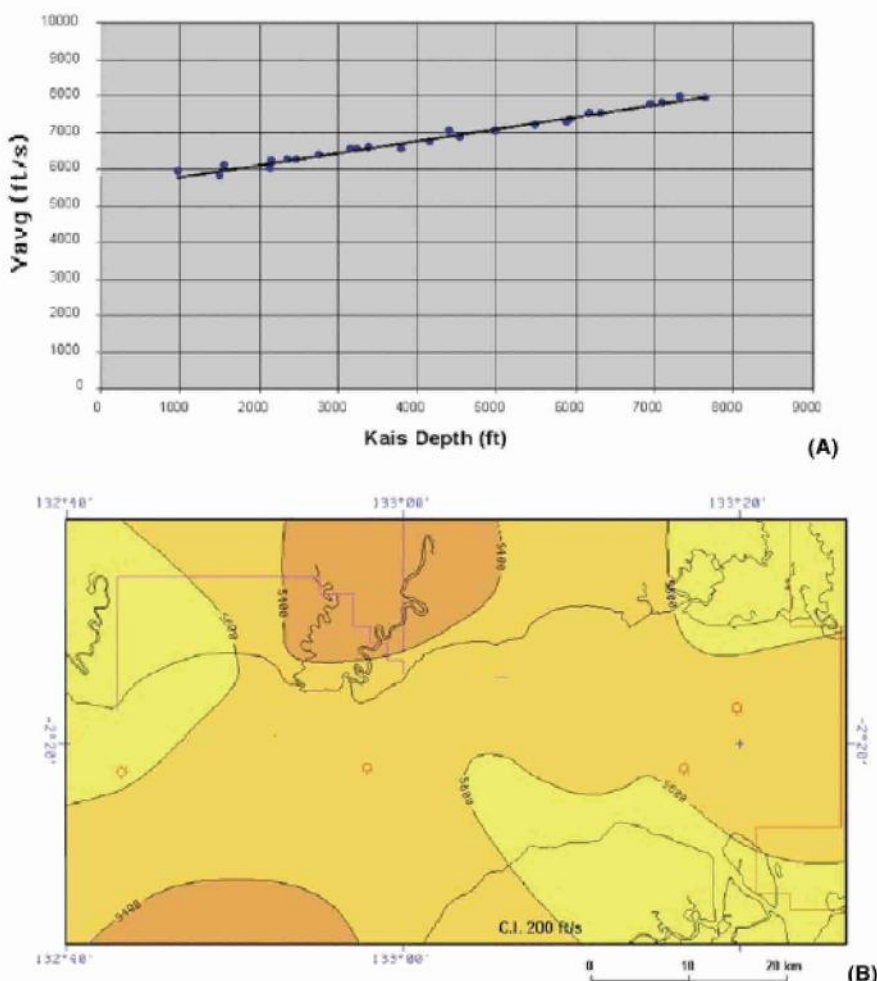


Plate 9. Depth conversion case history, continued. (From [95]) (A) Accuracy of the linear velocity model in layer one is indicated by the excellent correlation of top Kais average velocity and depth. Slope of this line is the velocity gradient. (B) Surface velocity map for layer one showing little variation. If the linear velocity model represented the subsurface perfectly, the surface velocity would be constant.

## Elements of 3D Seismology

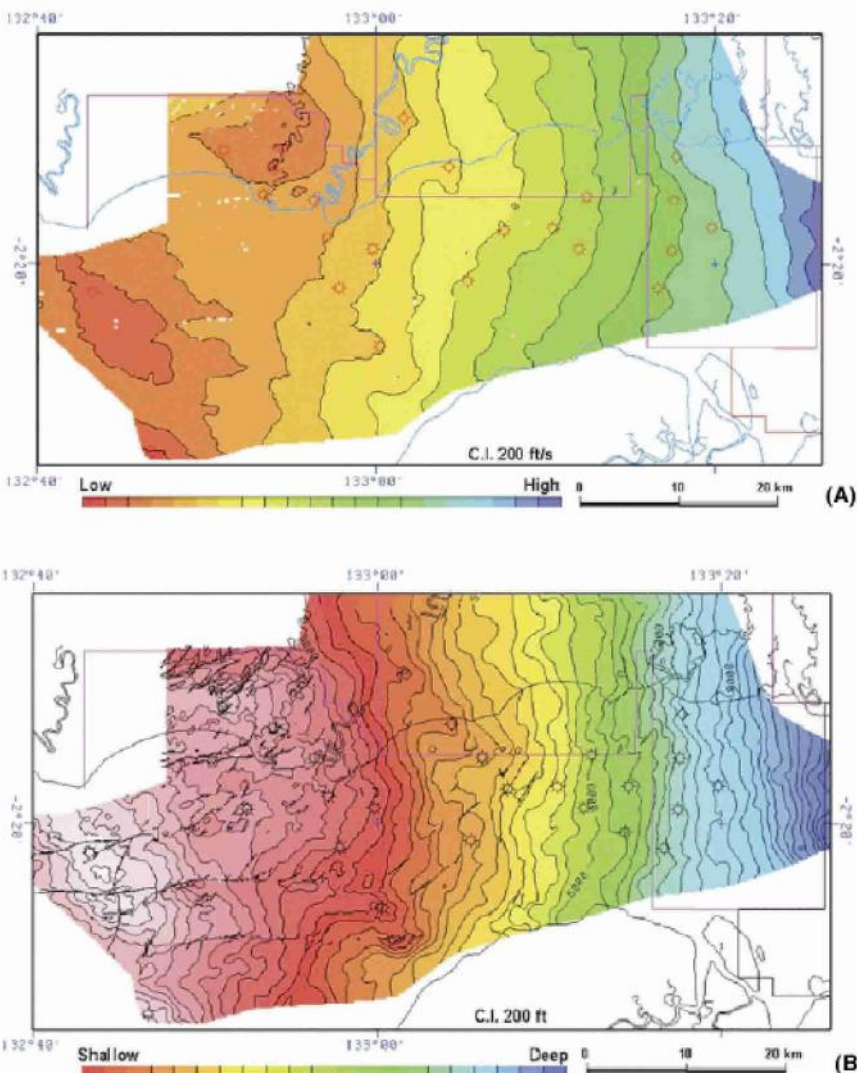


Plate 10. Depth conversion case history, continued. (From [95]) (A) Top Kais average velocity map. This is generated from a contoured surface velocity map, the known velocity gradient, and a gridded time structure map. (B) Top Kais gridded depth map produced by grid multiplication of the average velocity map and the time structure map. Since the linear velocity function is a good model for this horizon, the time structure (not shown) and depth structure are very similar.

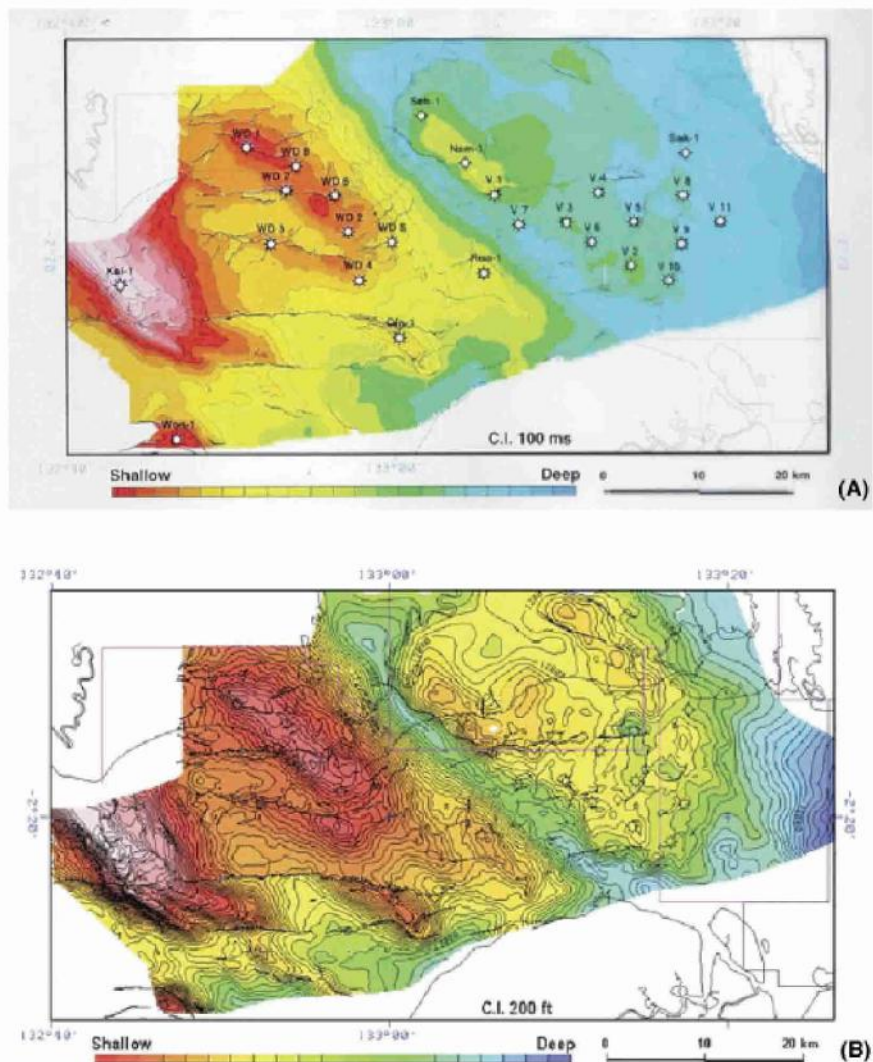


Plate 11. Depth conversion case history, continued. (From [95]) (A) Base Cretaceous time structure map and key wells. The complicated form of this map indicates lateral structural and lithologic variations. (B) Base of Cretaceous depth map. This is based on a linear model for the average interval velocity in layer two, conversion of layer two isochron times to thickness, and summation with the top Kais depth map. Eleven locations were planned and drilled using this map. The mean observed depth error for the new wells was less than 1%.

## Elements of 3D Seismology

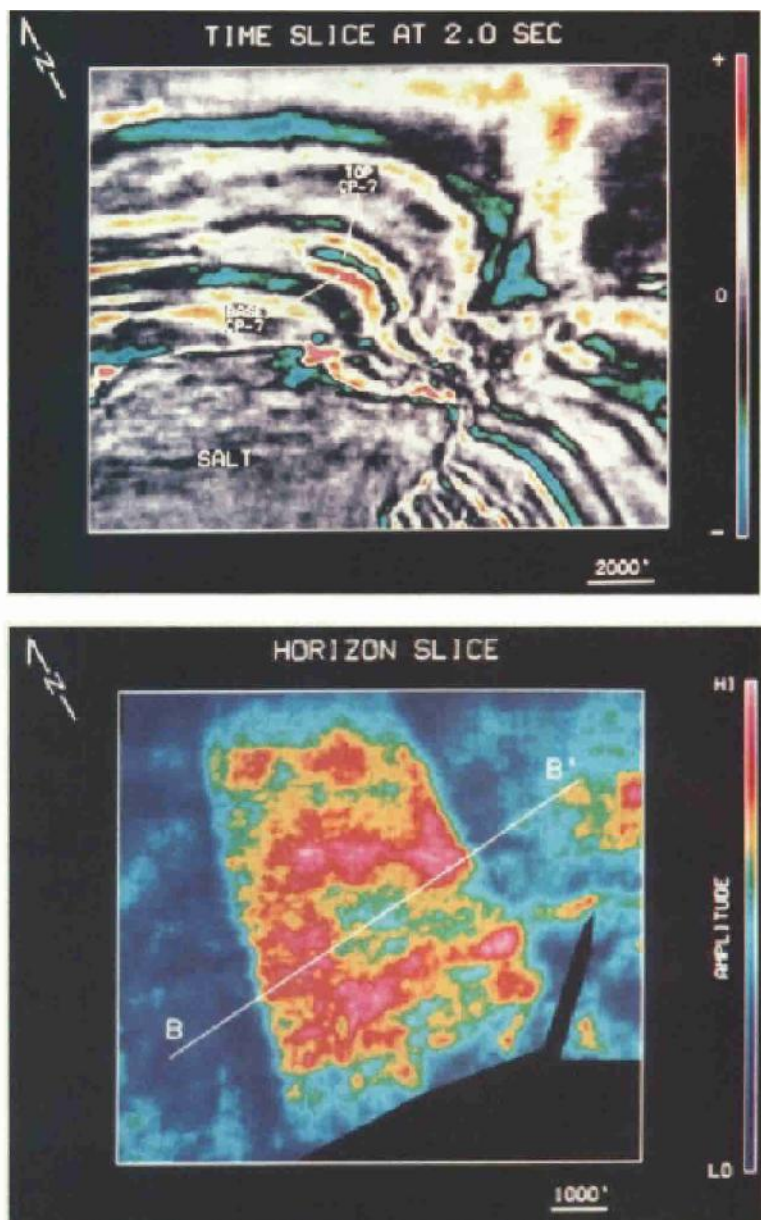


Plate 12. Stratigraphic case history in the Bay Marchand field of the Gulf of Mexico. (From [1]) (A) Time slice at about 2150 m subsea showing salt-sediment interface, faults, and steeply dipping CP-7 sand reflection events. (B) Horizon amplitude slice for the CP-7. Note meandering high amplitude feature and fault termination to the southeast. An arbitrary 2D section extracted along B-B' is shown in Plate 13.

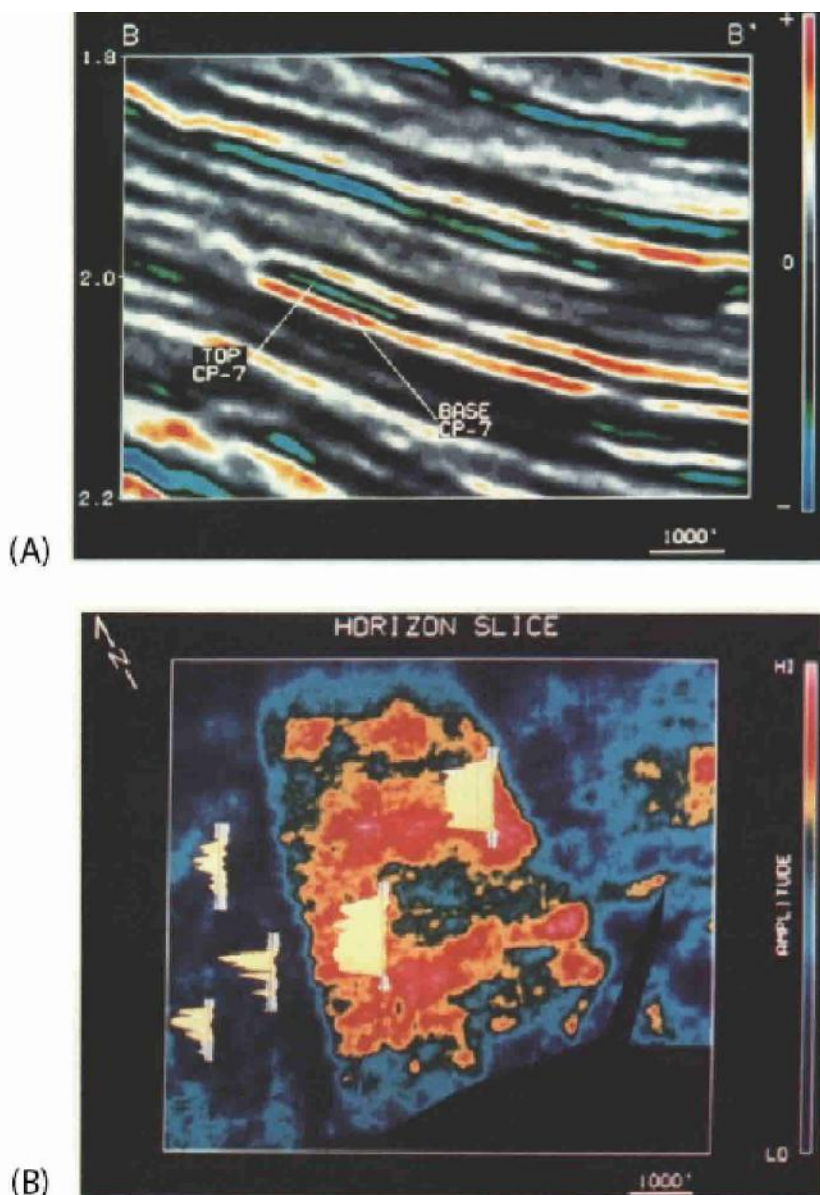


Plate 13. Stratigraphic case history in the Bay Marchand field of the Gulf of Mexico, continued. (From [1]). (A) Arbitrary vertical section along line B-B' of Plate 12B. Terminations without offset are evident at both ends of the high-amplitude feature confirming stratigraphic boundaries. (B) Horizon amplitude map with well log overlays. Penetrations in the high-amplitude area are associated with thick, high-quality sand while those outside the fairway are dominated by shale and thin sands.

## Elements of 3D Seismology

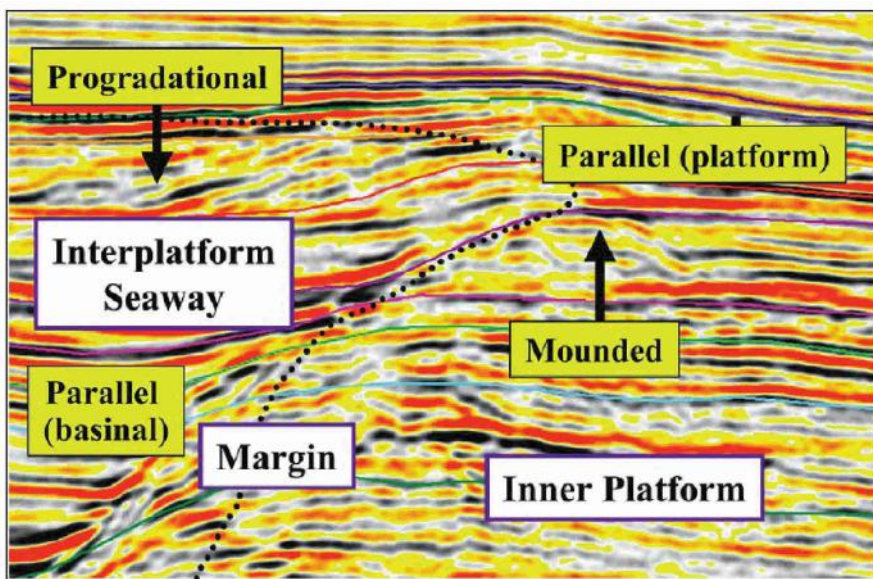


Plate 14. Five kilometer seismic profile across Neogene carbonate platform showing sequence stratigraphic interpretation. Dotted line indicates location of the platform margin through time. (From [160])

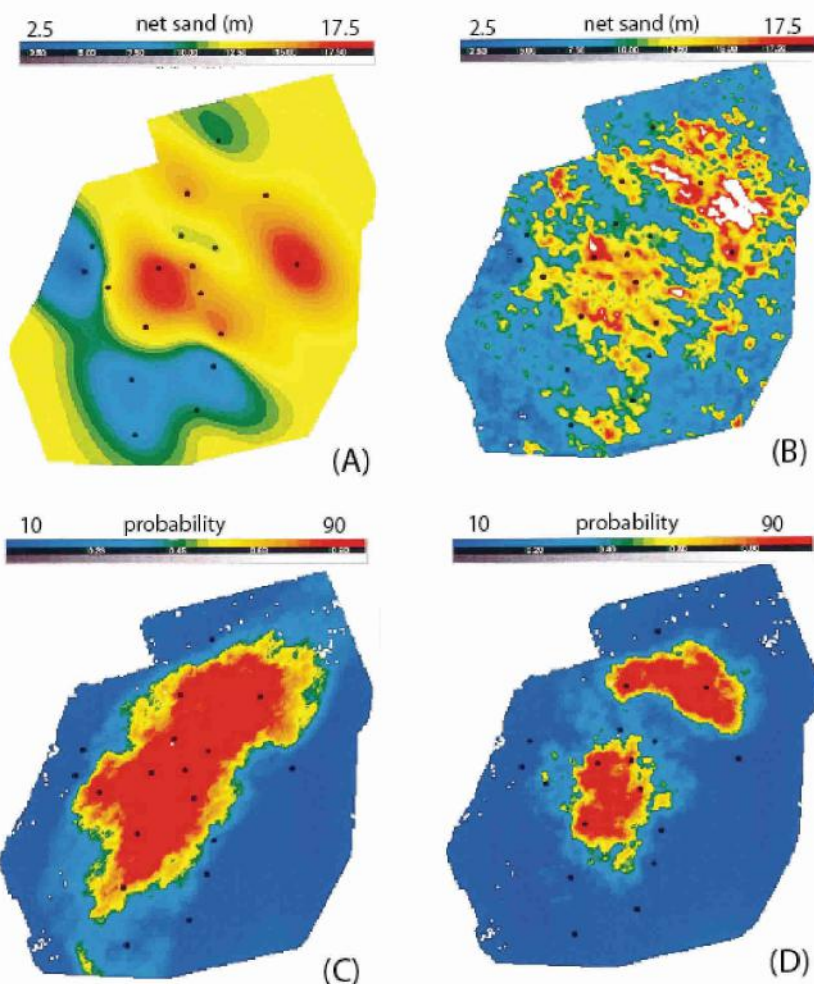


Plate 15. Case history of reservoir prediction using seismic attributes. (From [76]) □The study area is the Peciko field of Indonesia. (A) Kriged net sand map for a 550 m Miocene interval at about 3000 m depth. This was generated using only well control. The 18 well locations are shown as dots. (B) Net sand map generated by collocated kriging of wells and an amplitude-related seismic attribute. (C) Probability map of being in the closure. (D) Probability map of encountering hydrocarbon pore thickness (HPT) greater than 1.7 meters.

## Elements of 3D Seismology

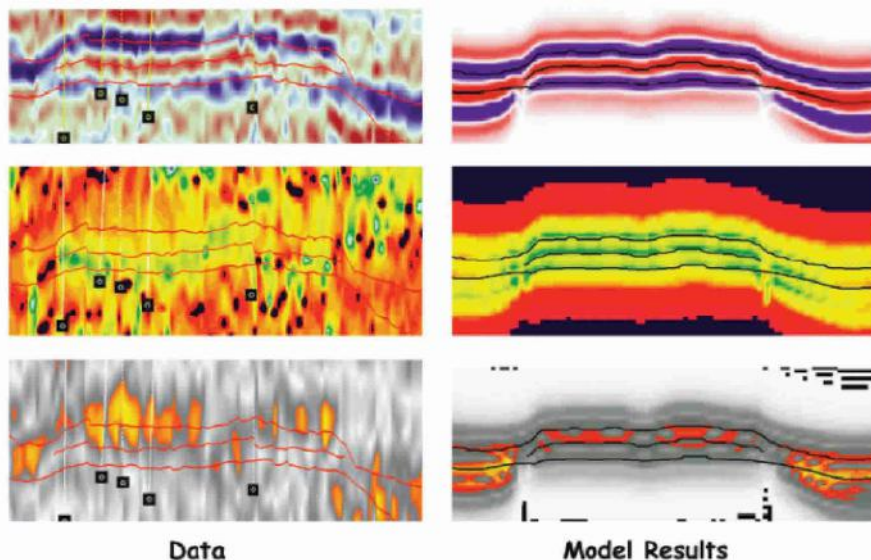


Plate 16. Complex trace attributes applied to field and model data for a carbonate buildup in the Jurassic Smackover formation of southern Alabama. (From [82]) Top row is seismic amplitude, middle row is instantaneous frequency, and bottom row is instantaneous phase. These instantaneous attributes were found useful in estimating porosity for the carbonate feature.

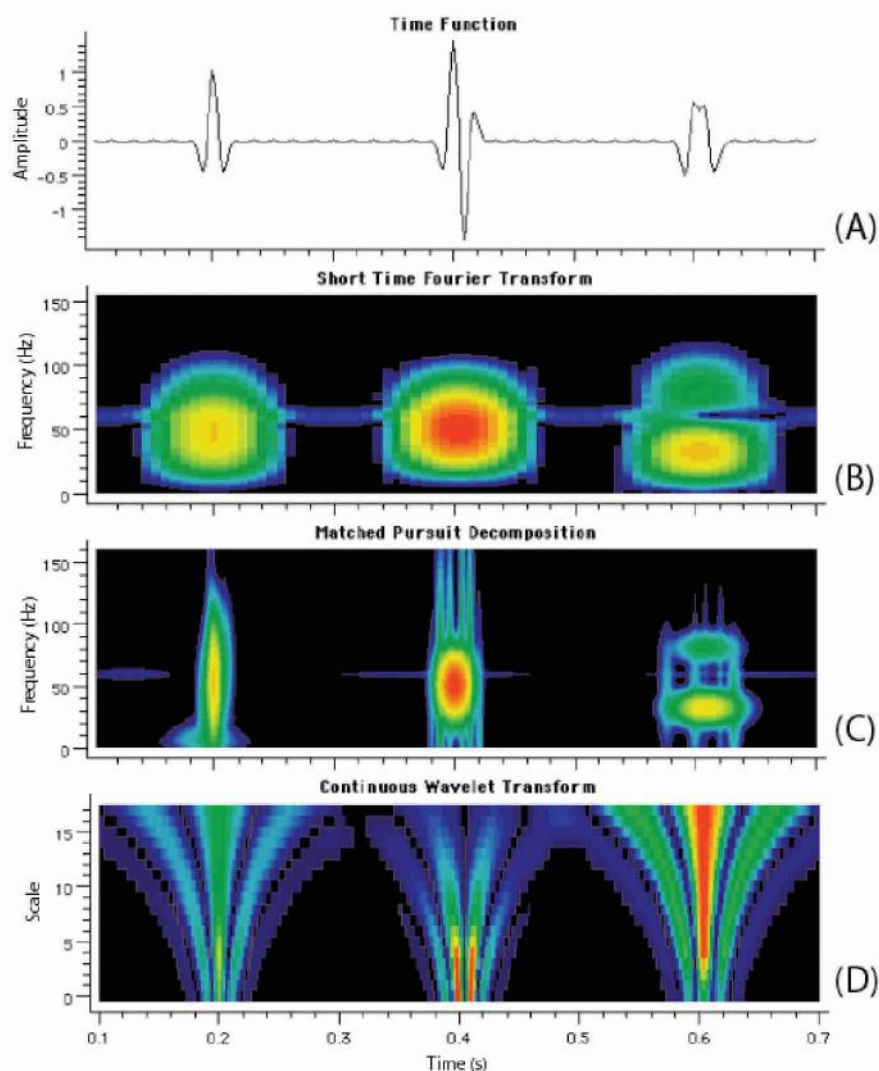
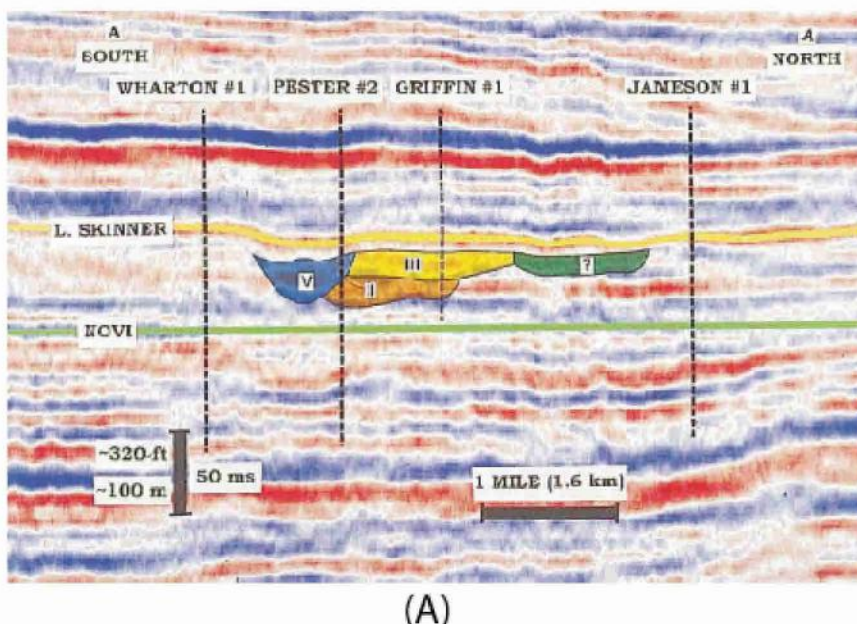
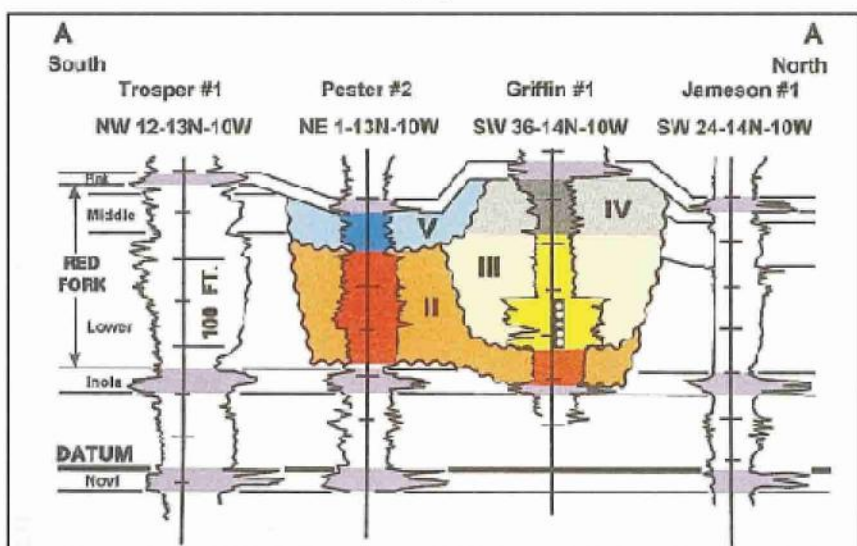


Plate 17. Time-frequency methods. (A) Synthetic trace containing three events: an isolated reflection, a tuning event, and an event at the onset of vertical resolution. (B) Time-frequency spectrum calculated using short time Fourier transform. (C) Spectrum computed by matched pursuit decomposition. (D) Continuous wavelet transform spectrum.

## Elements of 3D Seismology



(A)



(B)

Plate 18. Spectral decomposition case history. (From [148]) The target horizon is Pennsylvanian Red Fork Sandstone in the U.S. Midcontinent. (A) Interpreted seismic section with interpretation overlay showing incised valley features identified from well control. (B) Geologic model coincident with seismic line.

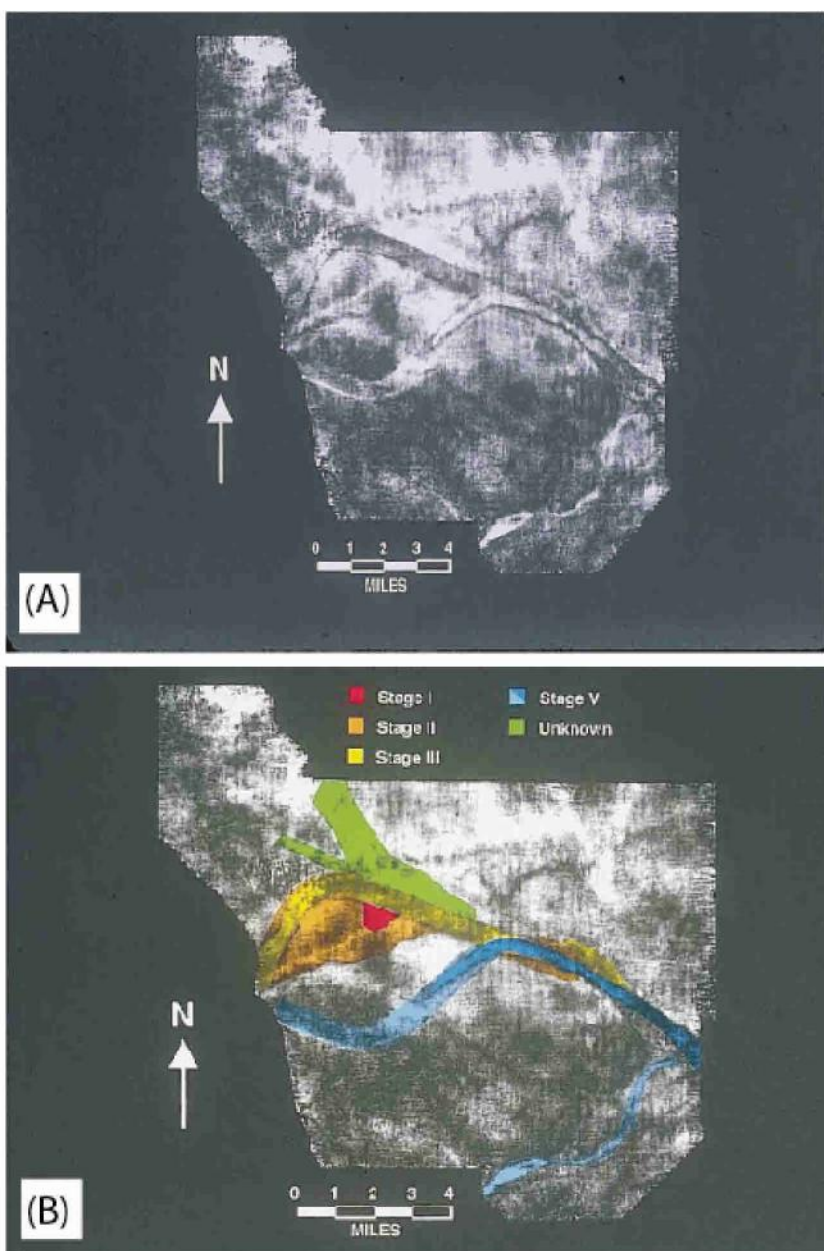


Plate 19. Spectral decomposition case history, continued. (From [148]) (A) Uninterpreted spectral decomposition 36 Hz horizon slice extracted 50 ms below the lower Skinner horizon. (B) Interpreted 36 Hz horizon slice.

## Elements of 3D Seismology

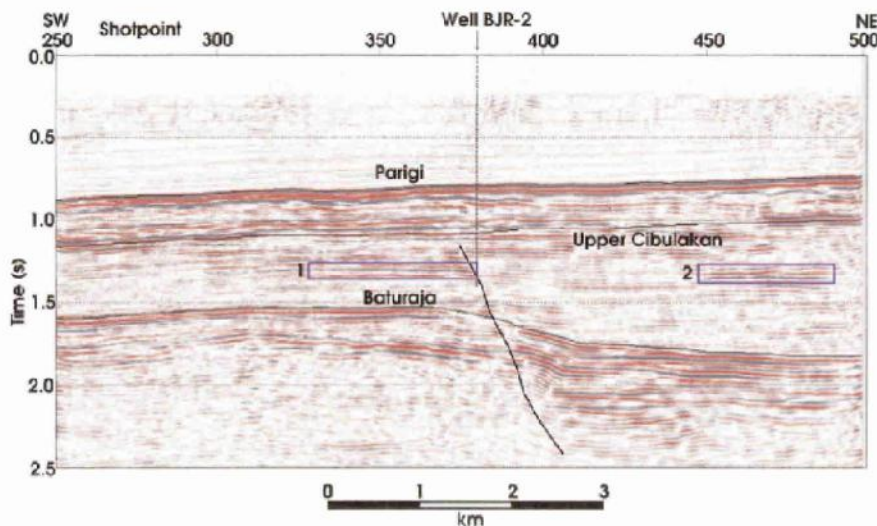


Plate 20. Impedance estimation case history. The input data is a migrated seismic section from the Northwest Java Basin of Indonesia. Boxes indicate reservoir bright spots in the Miocene Cibulakan Formation. (From [2])

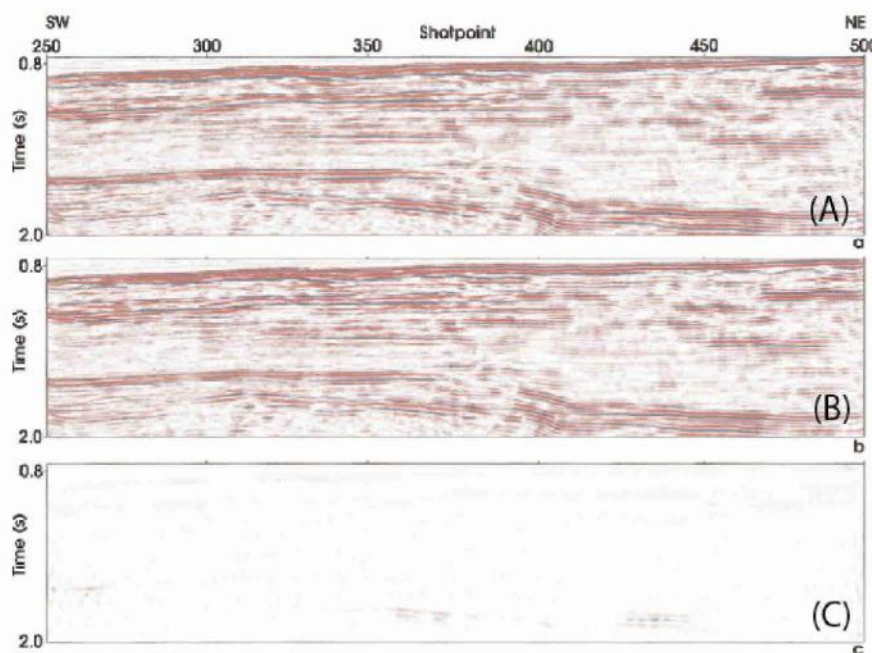


Plate 21. Impedance estimation case history, continued. (From [2]) (A) Observed migration data. (B) Synthetic data generated from the final impedance model. (C) The difference plot indicates a high-quality impedance result.

## Elements of 3D Seismology

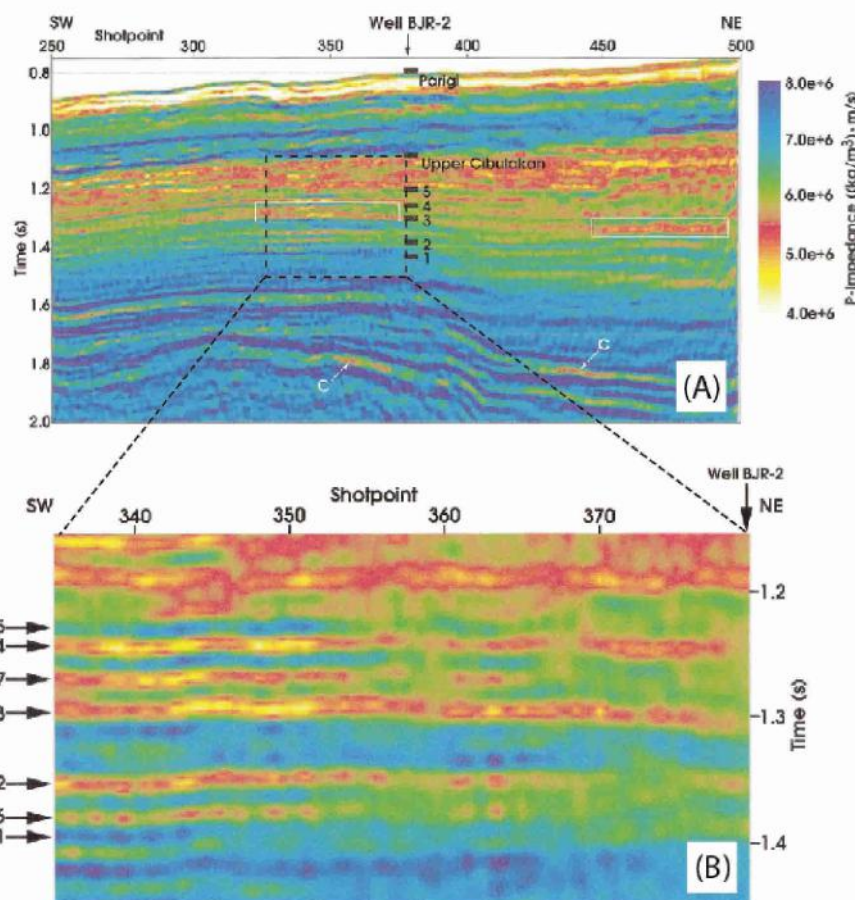


Plate 22. Impedance estimation case history, continued. (From [2]) (A) Impedance section showing low values in hot colors and high values in cool colors. (B) Detail of the impedance section with reservoirs labeled 1–5 and untested intervals 6–7. Low impedance in sandstone reservoirs 3 and 4 are probably gas-related.

# Copyrighted Materials

Copyright © 2004 PennWell Retrieved from www.knovel.com

For David and Samantha

And to the memory of Ruben Liner, Sr.

June 18, 1909–August 8, 2003

# Contents

Acknowledgments .....	.xv
-----------------------	-----

Introduction .....	.xix
--------------------	------

I. Waves: The Foundation of Seismology .....	.1
--	----

1 General Properties of Waves .....	.3
1.1 Mechanical waves .....	.3
1.2 Particle motion .....	.4
1.3 Polarization .....	.5
1.4 Elastic properties .....	.6
1.5 Wavespeed .....	.7
1.6 Display of wavefield data .....	.8
1.7 Waveform .....	.9
1.8 Impulse response .....	.15
1.9 Reciprocity .....	.17
1.10 Source and receiver directivity .....	.17
1.11 Wavefront and rays .....	.18
1.12 Huygens' principle .....	.20
1.13 Fermat's principle .....	.22
1.14 Snell's law .....	.23
1.15 Critical angle .....	.26
1.16 Dimensional effects .....	.26
1.16.1 Waveform .....	.26
1.16.2 Energy density and geometric spreading .....	.27
2 Waves in Fluids .....	.33
2.1 Why fluids? .....	.33
2.2 Parameters .....	.34
2.3 Equation of motion .....	.36
2.4 The big picture .....	.41
2.5 Velocity variation .....	.42
2.6 What about density? .....	.45
2.7 Fine layering .....	.45
3 Understanding Seismic Events .....	.51
3.1 Half space .....	.51
3.1.1 Uncertainty analysis applied to direct waves .....	.54
3.2 Reflection .....	.56
3.2.1 Traveltime .....	.56
3.2.2 Reflection coefficient .....	.62
3.2.3 Normal incidence .....	.63

## **Elements of 3D Seismology**

3.2.4	Angular reflection coefficient .....	.68
3.2.5	Postcritical reflection .....	.69
3.2.6	Fresnel zone .....	.71
3.3	Head wave .....	.78
3.4	The point source: Tying it all together .....	.81
3.5	Diffraction .....	.84
3.6	Ghost .....	.89
3.7	Velocity layering .....	.92
3.7.1	More events .....	.92
3.7.2	Multiples .....	.93
3.8	Classification .....	.96
<b>4</b>	<b>Reservoir Fluid Properties .....</b>	<b>.99</b>
4.1	Pressure and temperature range .....	.99
4.2	Gas .....	.100
4.2.1	Gas density .....	.100
4.2.2	Gas modules and velocity .....	.101
4.3	Oil .....	.102
4.3.1	Oil density .....	.104
4.3.2	Oil modules and velocity .....	.104
4.4	Brine .....	.106
4.4.1	Brine density .....	.107
4.4.2	Brine modules and velocity .....	.108
4.5	Fluid mixture .....	.108
4.5.1	Fluid density .....	.109
4.5.2	Fluid modules and velocity .....	.110
<b>5</b>	<b>Waves in Solids .....</b>	<b>.113</b>
5.1	Strain .....	.113
5.2	Stress .....	.115
5.3	Hooke's law and elastic parameters .....	.116
5.4	Equations of motion .....	.118
5.5	Wave types and speeds .....	.120
5.6	Mode conversion .....	.123
5.7	Snell's law and critical angles .....	.125
5.8	Velocity layering .....	.127
5.9	Elastic reflection coefficient .....	.127
5.10	Reflection coefficient approximations .....	.130
5.11	Anisotropy .....	.131
<b>6</b>	<b>Waves in Porous Solids .....</b>	<b>.135</b>
6.1	Rock as a porous solid .....	.135
6.2	Empirical relationships .....	.136
6.3	Parameters .....	.138
6.4	Equation of motion .....	.139
6.5	Wave types .....	.140
6.6	Rock density .....	.140
6.7	Gassmann theory and wavespeeds .....	.141

6.8 Attenuation and dispersion .....	144
6.9 Rock velocity ranges .....	150
<b>II. Acquisition: Gathering Seismic Data . . . . .</b>	<b>153</b>
<b>7 2D Land Acquisition . . . . .</b>	<b>155</b>
7.1 Historical summary .....	155
7.2 Hardware .....	156
7.2.1 Source .....	156
7.2.2 Receiver .....	160
7.2.3 Recording system .....	163
7.3 Field procedure .....	163
7.3.1 Vertical stack .....	164
7.3.2 Roll and cabling .....	164
7.4 SEGY headers and sorting .....	168
<b>8 Financial Aspects of 3D Seismic . . . . .</b>	<b>171</b>
8.1 The big picture: stock price .....	171
8.2 Economics .....	173
8.3 The exploration process .....	173
8.4 A savings/gain model .....	174
8.4.1 Savings .....	175
8.4.2 Gains .....	176
8.4.3 Net value, profit, and rate of return .....	176
8.5 Some industry trends .....	180
<b>9 Survey Predesign . . . . .</b>	<b>185</b>
9.1 Acquisition parameters .....	185
9.2 Time sample rate .....	187
9.3 Offset range .....	188
9.4 Listen time .....	189
9.5 Spatial sampling and aliasing .....	191
9.6 Total signal-to-noise improvement .....	196
<b>10 Land Shooting Geometry . . . . .</b>	<b>201</b>
10.1 Coordinates and related quantities .....	201
10.2 Cross spread method .....	204
10.3 Swath method .....	208
10.4 Fringe .....	210
10.5 Perimeter or loop method .....	212
10.6 Cabling, template shooting, and fold .....	215
10.7 Crooked line 2D .....	219
<b>11 Land 3D Design Optimization . . . . .</b>	<b>223</b>
11.1 Optimization and inversion .....	223
11.2 Assumptions, target variables, and constraints .....	226
11.3 A direct method .....	228
11.4 Method 2 .....	229
11.5 Examples .....	230

## **Elements of 3D Seismology**

<b>12 Marine Acquisition Methods .....</b>	<b>.235</b>
12.1 Towed receiver systems .....	.235
12.1.1 Receiver cable .....	.235
12.1.2 Source array .....	.239
12.1.3 Acquisition geometry .....	.242
12.1.4 Flip-flop shooting .....	.245
12.1.5 Positioning .....	.245
12.1.6 Cable feathering .....	.247
12.2 Fixed receiver systems .....	.248
12.3 Marine acquisition and the environment .....	.251
<b>13 Data Dimensionality and Components .....</b>	<b>.253</b>
<b>III. Data Processing: Creating the Seismic Image . . .</b>	<b>.259</b>
<b>14 Processing and Binning Overview .....</b>	<b>.261</b>
14.1 Why do we need to process seismic data? .....	.261
14.2 Filtering and noise removal .....	.264
14.3 Processing flow .....	.266
14.4 Bins .....	.270
14.4.1 Bin size calculation .....	.272
14.4.2 Effects of fold and offset variation .....	.275
14.4.3 Anatomy of a bin .....	.276
<b>15 Computing .....</b>	<b>.283</b>
15.1 RAM and disk storage .....	.283
15.2 The 2D survey size .....	.286
15.3 The 3D survey size .....	.286
15.4 Processing speed .....	.286
15.5 Speed and 3D migration .....	.289
<b>16 Creating the CMP Stack .....</b>	<b>.291</b>
16.1 Gain .....	.291
16.2 Deconvolution .....	.292
16.3 Sorting .....	.298
16.4 Normal moveout .....	.301
16.5 Dip moveout .....	.309
16.6 Common midpoint stacking .....	.312
16.7 Statics .....	.316
<b>17 Migration I: Concepts .....</b>	<b>.321</b>
17.1 Constant velocity migration and modeling pairs .....	.322
17.2 Dip from seismic slope .....	.326
17.3 Migration distance .....	.327
17.4 Variable velocity migration and modeling pairs .....	.327
17.5 3D migration .....	.327
17.6 Lateral resolution in 2D and 3D data .....	.333
17.7 Survey design for linear $v(z)$ .....	.337

<b>18</b>	<b>Migration II: Classification and Velocity Analysis .....</b>	<b>343</b>
18.1	Kinds of migration .....	343
18.2	Stolt migration theory .....	348
18.3	Overview of algorithms .....	349
18.4	Kirchhoff depth migration methodology .....	351
18.5	Migration velocity analysis .....	356
<b>19</b>	<b>Historical Perspective .....</b>	<b>361</b>
19.1	Progress in seismic processing .....	361
19.1.1	Dip moveout .....	361
19.1.2	Anisotropy .....	362
19.1.3	3D processes .....	363
19.1.4	Depth migration .....	364
19.2	A brief account of dip moveout .....	365
19.2.1	Dip moveout just isn't normal .....	365
19.2.2	Velocity variation .....	372
19.2.3	Anisotropy .....	374
<b>IV.</b>	<b>Color Plates .....</b>	<b>377</b>
<b>V.</b>	<b>Interpretation: Extracting Geologic Information from Seismic Data .....</b>	<b>401</b>
<b>20</b>	<b>Synthetic Seismogram, Tuning, and Resolution .....</b>	<b>403</b>
20.1	Creating the synthetic seismogram .....	403
20.1.1	Earth model .....	404
20.1.2	Traveltimes .....	406
20.1.3	Reflection coefficients .....	407
20.1.4	Wavelet .....	408
20.1.5	Convolutional model .....	411
20.1.6	Examples .....	412
20.1.7	Transmission loss .....	419
20.2	Tuning .....	423
20.3	Resolution .....	427
<b>21</b>	<b>Introduction to Interpretation .....</b>	<b>433</b>
21.1	What does it mean to interpret seismic data? .....	433
21.2	Background information .....	433
21.3	Interactive interpretation systems .....	438
21.4	Interactive interpretation project components .....	439
<b>22</b>	<b>Data Volume .....</b>	<b>443</b>
22.1	Data 2D subsets .....	444
22.2	Display of seismic data .....	447
22.3	Interpretation products .....	448

## **Elements of 3D Seismology**

<b>23 Structure .....</b>	<b>.451</b>
23.1 Fault detection and mapping .....	.452
23.2 Time structure and horizon tracking .....	.456
23.3 Time-to-depth conversion methods .....	.459
23.4 A vertical ray case history .....	.462
23.5 Structural uncertainty .....	.464
23.6 Extreme velocity variation .....	.467
<b>24 Stratigraphy .....</b>	<b>.469</b>
24.1 Stratigraphy and 2D seismic data .....	.469
24.2 Stratigraphy and 3D seismic data .....	.473
24.3 Case history: Stacked sand channel systems .....	.478
24.4 Stratigraphy and structure: A case history .....	.481
24.5 Carbonates .....	.482
<b>25 Seismic attributes .....</b>	<b>.485</b>
25.1 Definition and history .....	.485
25.2 Classification schemes .....	.486
25.2.1 General and special .....	.486
25.2.2 Dimensional .....	.487
25.2.3 Reflection characteristic .....	.488
25.2.4 Procedural .....	.489
25.3 Prediction of reservoir properties .....	.489
25.3.1 Procedure .....	.489
25.3.2 Case history .....	.491
25.3.3 Multiattribute analysis .....	.492
25.4 Selected general attributes .....	.494
25.4.1 Complex trace .....	.494
25.4.2 Dip, azimuth, curvature, and gradient .....	.495
25.4.3 Coherence .....	.495
25.4.4 Spectral decomposition .....	.497
25.4.5 Impedance .....	.501
25.4.6 Spice .....	.502
<b>26 Amplitude in Space, Time, and Offset .....</b>	<b>.505</b>
26.1 Prestack amplitude factors .....	.505
26.2 Stack amplitude and $R_0$ .....	.506
26.3 Predictive rock model .....	.508
26.4 Calibrated rock model for Glenn sandstone .....	.510
26.5 Lateral and time-lapse effects .....	.511
26.5.1 Gas .....	.511
26.5.2 Porosity .....	.513
26.5.3 Oil saturation .....	.513
26.5.4 Lithology: Sandstone-limestone .....	.513
26.5.5 Temperature (steamflood) .....	.514
26.5.6 Lithology: Sandstone-clay .....	.514
26.5.7 Permeability .....	.516
26.5.8 Summary and discussion .....	.516

26.6 Time-lapse 3D seismic .....	517
26.7 Offset effects (AVO) .....	522
<b>Appendix A Fourier Transform .....</b>	<b>527</b>
A.1 Definitions .....	527
A.2 Frequency domain .....	529
A.3 Spike input .....	533
A.4 Properties of the Fourier transform .....	534
A.5 Two spikes .....	538
A.6 The discrete case .....	539
A.7 Detection of periodic signals .....	540
A.8 2D Fourier transform .....	541
<b>Appendix B Glossary of Terms .....</b>	<b>545</b>
<b>Appendix C Conversion Factors .....</b>	<b>557</b>
<b>Appendix D Bibliography .....</b>	<b>559</b>
<b>Index .....</b>	<b>577</b>

# Appendix A

## Fourier Transform

The Fourier transform is of central importance in virtually all aspects of petroleum seismology. It is a method of analysis that detects periodicity in signals, a mathematical tool for solving partial differential equations, and a fertile domain for implementing processing algorithms. It is the mechanism for understanding the properties of waves including bandwidth, amplitude spectrum, phase spectrum, and stability with respect to inversion.

It is said of the ancient mathematician Euclid (circa 300 BCE) author of *The Elements of Geometry*: ...that Ptolemy once asked him if there was in geometry any shorter way than that of *the Elements*, and he replied that there was no royal road to geometry.

In a distant echo of that thought, there is no non-mathematical shortcut to understanding the Fourier transform and its uses. For a brief, but intensely detailed, account of the Fourier transform see Press et al. [149].

### A.1 Definitions

Consider a time function,  $g(t)$ , which is the measured output of some kind of experiment. An example would be pressure measured during the passage of a sound wave. This function is said to be in the time domain and the Fourier transform (FT) casts it into the frequency domain. Since the FT moves us from the physical domain (time) to the alternate domain (frequency), it is termed the *forward transform*. The definition of the forward FT is

$$g(\omega) = \int_{-\infty}^{\infty} g(t) e^{i\omega t} dt \quad (\text{A.1})$$

where  $i=\sqrt{-1}$ , and  $\omega$  is angular frequency.

## Elements of 3D Seismology

The notation  $g(\omega)$  denoting the transformed function uses the argument list to signify the domain. That is to say,  $g(t)$  and  $g(\omega)$  are entirely different functions, not simply the same function with  $\omega$  replacing  $t$  or vice versa. This can be confusing at first and for the one-dimensional FT we are discussing here, it would be just as convenient to denote the original time function as  $g(t)$  and the transform as  $G(\omega)$ , or some similar convention. In fact, this notation is common in time series analysis literature where multidimensional transforms are not encountered. But anticipating a 2D or 3D function that can be transformed with respect to one or more of its variables, the argument list notation is much more straightforward and will be used uniformly here.

The Fourier transform is an example of an integral transform and there are many others, including Laplace, Legendre, Radon, Hilbert, etc. The FT formula exhibits the common elements of such integral transforms; an original variable,  $t$ , the original space,  $g(t)$ , a transform variable,  $\omega$ , the transform space,  $g(\omega)$ , and the transform kernel  $e^{i\omega t}$ . Note the kernel is a function of both original and transform variables, as will always be the case with integral transforms.

The FT given above in terms of angular frequency is the most useful form when dealing with analytic problems, such as differential equations. The actual meaning of  $\omega$ , however, is cycles per radian, which is not a particularly intuitive quantity. For signal analysis and discrete problems, it is more straightforward to work with the usual concept of frequency as cycles per second using the relationship

$$\omega = 2\pi f \quad (\text{A.2})$$

where  $f$  is the frequency in Hertz having units of 1/sec and being the inverse of the period. For example, a 20 Hz wave has a period of 1/20 sec or 50 ms. Using this version of frequency the forward FT is

$$g(f) = \int_{-\infty}^{\infty} g(t) e^{i2\pi ft} dt \quad (\text{A.3})$$

Without further comment we will use either the  $\omega$  or  $f$  form as convenient for a particular application. Also, a useful shorthand notation for the Fourier transform is

$$g(f) = FT\{g(t)\} \quad (\text{A.4})$$

The inverse FT as defined by

$$g(t) = \int_{-\infty}^{\infty} g(\omega) e^{-i\omega t} d\omega \quad (\text{A.5})$$

operates on the frequency domain function to recover the time domain function. An important property of any useful integral transform is that of invertibility—a forward transform followed by an inverse transform should recover the original function

$$\mathcal{F}T^{-1}\{ \mathcal{F}T\{ g(t) \} \} = \mathcal{F}T^{-1}\{ g(f) \} = g(t) \quad (\text{A.6})$$

The FT has this property, but a word of caution is necessary. Throughout this discussion, we will ignore constant scaling factors. For example, one standard scaling of the forward FT has a multiplying factor of  $1/\sqrt{2\pi}$  and the same factor on the inverse transform. These are necessary in numerical implementations to preserve the invertibility of the FT. In other words, if the scale factors are not taken into account, then a forward and inverse FT applied in succession will not recover the original function, but the original function multiplied by some constant. While acknowledging this fact, the functional discussion given here is clarified by dropping the constant scale factors. Also, in what follows, all integrals will be assumed to have infinite limits unless otherwise indicated.

## A.2 Frequency domain

It is instructive to consider carefully the meaning of the forward FT. Consider a time function  $g(t)$ , where both  $t$  and  $g(t)$  are real. A FT of this function generates the frequency domain function  $g(f)$  where the frequency  $f$  is a real number (10 Hz, for example) but the function  $g(f)$  is complex. This means that for any frequency the function  $g(f)$  is a complex number. Following standard practice, we call this number  $z$  and write it as

$$z = x + iy \quad (\text{A.7})$$

where  $x$  is the real part of  $z$  and  $y$  is the imaginary part. Figure A.1 illustrates this concept. Fourier transform of a real function generates a complex number associated with each frequency, which the figure shows split into real and imaginary parts.

## Elements of 3D Seismology

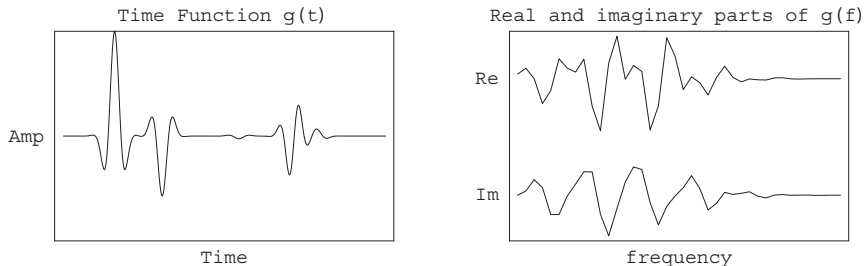


Fig. A.1 Applying a fourier transform to the time function  $g(t)$  generates a complex function  $g(f)$ , which is shown here split into real and imaginary parts.

This is called the Cartesian representation of the complex number, because  $(x,y)$  can be thought of as a two-dimensional coordinate system. To be specific, Figure A.2 shows  $z=4+3i$  as a point in the complex plane. Also shown in this figure are the amplitude,  $A$ , and phase,  $\theta$ , given by

$$\begin{aligned} A &= \sqrt{x^2 + y^2} \\ \theta &= \tan^{-1}(y/x) \end{aligned} \quad (\text{A.8})$$

which allow us to write

$$z = Ae^{i\theta} \quad (\text{A.9})$$

The amplitude is also called the radius, modulus, or absolute value. The expression  $A e^{i\theta}$  is the polar form of the complex number, so called because  $(A,\theta)$  can be considered as the radius and angle of polar coordinate system. For the example shown in Figure A.2 we have

$$\begin{aligned} A &= \sqrt{4^2 + 3^2} = 5 \\ \theta &= \tan^{-1}(4/3) = 0.64 \text{ radians} = 36.9^\circ \end{aligned} \quad (\text{A.10})$$

and we would say this complex number has an amplitude of 5 and phase of 36.9 degrees.

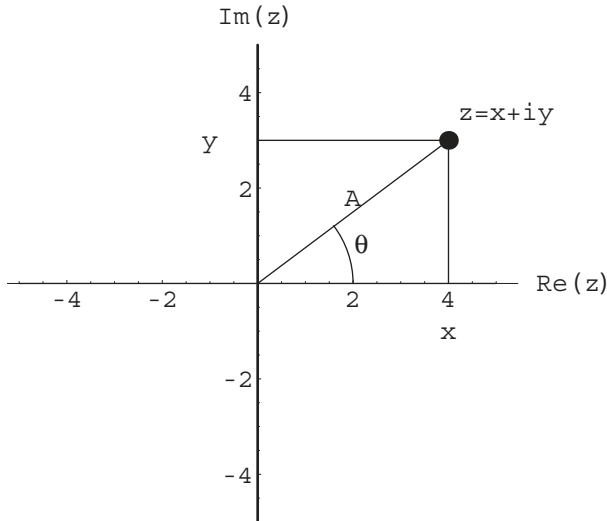


Fig. A.2 A Point in the complex plane,  $z=4+3i$ .

Writing a complex number in polar form leads to a deep association with trigonometric functions through Euler's formula

$$A e^{\pm i\theta} = A \cos\theta \pm A i \sin\theta \quad (\text{A.11})$$

An immediate consequence of this formula is a recipe for finding the real and imaginary parts of a complex number if we are given the amplitude and phase,

$$\begin{aligned} x &= A \cos\theta \\ y &= A \sin\theta \end{aligned} \quad (\text{A.12})$$

Since the sine and cosine functions are periodic, any number of phase values can give identical real and imaginary parts. Consider the case  $(A, \theta)=(1,0)$ , which leads to  $(x,y)=(1,0)$ , and another case  $(A, \theta)=(1,2\pi)$  that gives the same result. In general,  $(A, \theta + 2\pi)$  will always have the same real and imaginary parts as  $(A, \theta)$ .

## Elements of 3D Seismology

The real difficulty began when we computed the phase since the arctangent function is periodic

$$\frac{-\pi}{2} < \tan^{-1} \left( \frac{y}{x} \right) < \frac{\pi}{2} \quad , \quad -\infty < \frac{y}{x} < \infty \quad (\text{A.13})$$

It follows that recovering the real and imaginary parts from knowledge of the phase is non-unique. In practice, when people work with the phase of real data, it is necessary to “unwrap” the phase, which is a non-trivial problem.

Figure A.3A shows an example time function  $g(t)$ . When this is Fourier transformed to  $g(f)$ , a list of complex numbers is generated, each one associated with a different frequency. Figure A.3B shows the real and imaginary parts of  $g(f)$ . An amplitude and phase value can be calculated at each frequency, as shown in Figure A.3C and D. These are called amplitude and phase spectra.

The amplitude spectrum is particularly useful as it shows which frequency components reside in the signal and in what proportion. One way to think of the amplitude spectrum is that the FT decomposes the time domain signal into sine

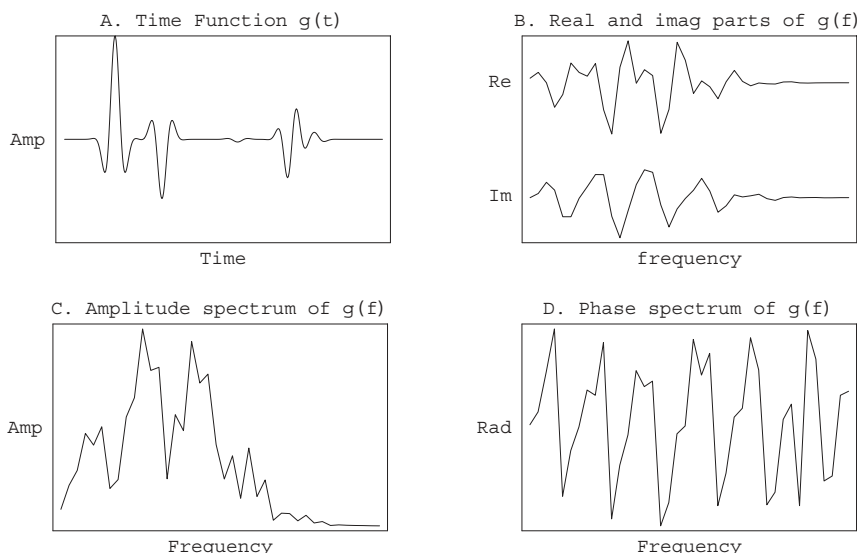


Fig. A.3 (A) The Time Function of Figure A.1. (B) Real and imaginary parts of the Fourier transform, (C) amplitude spectrum, and (D) phase spectrum.

and cosine waves with different frequencies, then figures out how much of each is in the signal. This information is displayed in the amplitude spectrum. But to actually reconstruct the original signal, each sine and cosine wave must have a time shift, otherwise all the cosine waves would peak at zero time and all the sine waves at  $\pi/2$ . The phase spectrum represents this time shift information.

### A.3 Spike input

One very simple kind of time function is the Dirac delta function,  $\delta(t-t_0)$ , which is a unit spike at time  $t=t_0$  and zero everywhere else

$$\delta(t - t_0) = \begin{cases} 1, & t = t_0 \\ 0, & t \neq t_0 \end{cases} \quad (\text{A.14})$$

This strange function is not really a function in the usual sense of the word, but something called a distribution. It has the interesting property that when integrated against another function, it pulls out a single value,

$$\int \delta(t - t_0) g(t) dt = g(t_0) \quad (\text{A.15})$$

where it is assumed that the point  $t_0$  is in the range of integration. This is called the sifting property and is very useful since it makes evaluating even nasty integrals a trivial exercise. For example,

$$\int \delta(t - 0.5) \cos(t) e^{-t^4} dt = \cos(0.5) e^{-(0.5)^4} = 0.824 \quad (\text{A.16})$$

To understand this result, think of the delta function as a pure spike (i.e., it has value 1.0 at a single point and is zero everywhere else). Multiply this in your mind by any function you can imagine. The only value to survive the multiplication is the value at the spike location.

We introduce something as arcane as the delta function because it allows us to analyze and understand the Fourier transform of the simplest possible time function, a unit spike. Consider the input time function to be a spike at time zero,  $g(t)=\delta(t)$ . How does this function look in the frequency domain? To find out we do the FT,

$$\begin{aligned} g(f) &= \int g(t) e^{i2\pi ft} dt \\ &= \int \delta(t) e^{i2\pi ft} dt \\ &= e^{i2\pi f(t=0)} \\ &= e^0 \\ &= 1 \end{aligned} \quad (\text{A.17})$$

## Elements of 3D Seismology

A time-zero spike has the following characteristics in the frequency domain: for all frequencies—the real part is one, the imaginary part is zero, the amplitude spectrum is one, and the phase spectrum is zero. Thus a spike at time zero has a flat spectrum (contains all frequencies) and zero phase (phase is zero at all frequencies). Turning this around, we conclude that building a spike in the time domain requires full bandwidth data.

What about a spike not at time zero? In this case, the time function is  $g(t)=\delta(t-t_0)$  and, by the same analysis, the FT gives a frequency domain representation as

$$g(f) = e^{i2\pi f t_0} \quad (\text{A.18})$$

As this result is in polar form, we can immediately conclude that again the amplitude spectrum is flat. The phase is not zero as before, but  $\theta=2\pi f t_0$ . Since the phase spectrum is nothing more than a plot of phase versus frequency, the spectrum in this case must be a straight line passing through the origin ( $f=0$ ) with slope  $2\pi t_0$ . These comments are verified by a numerical example in Figure A.4.

A consequence of this result is another useful definition of the Dirac delta function

$$\delta(t - t_0) = \int e^{i2\pi f t_0} e^{-i2\pi f t} df = FT^{-1}\{e^{i2\pi f t_0}\} \quad (\text{A.19})$$

showing its intimate connection with the Fourier transform.

### A.4 Properties of the Fourier transform

The Fourier transform has several interesting and useful properties [142]. One is linearity

$$FT\{g_1(t) + g_2(t)\} = FT\{g_1(t)\} + FT\{g_2(t)\} = g_1(f) + g_2(f) \quad (\text{A.20})$$

which says that if we add two time functions together and take the FT, this will give the same result as transforming each function individually and adding in the frequency domain.

Other elementary operations are a time or frequency shift

$$\begin{aligned} FT\{g(t - t_0)\} &= e^{i2\pi f t_0} g(f) \\ FT^{-1}\{g(f - f_0)\} &= e^{-i2\pi f_0 t} g(t) \end{aligned} \quad (\text{A.21})$$

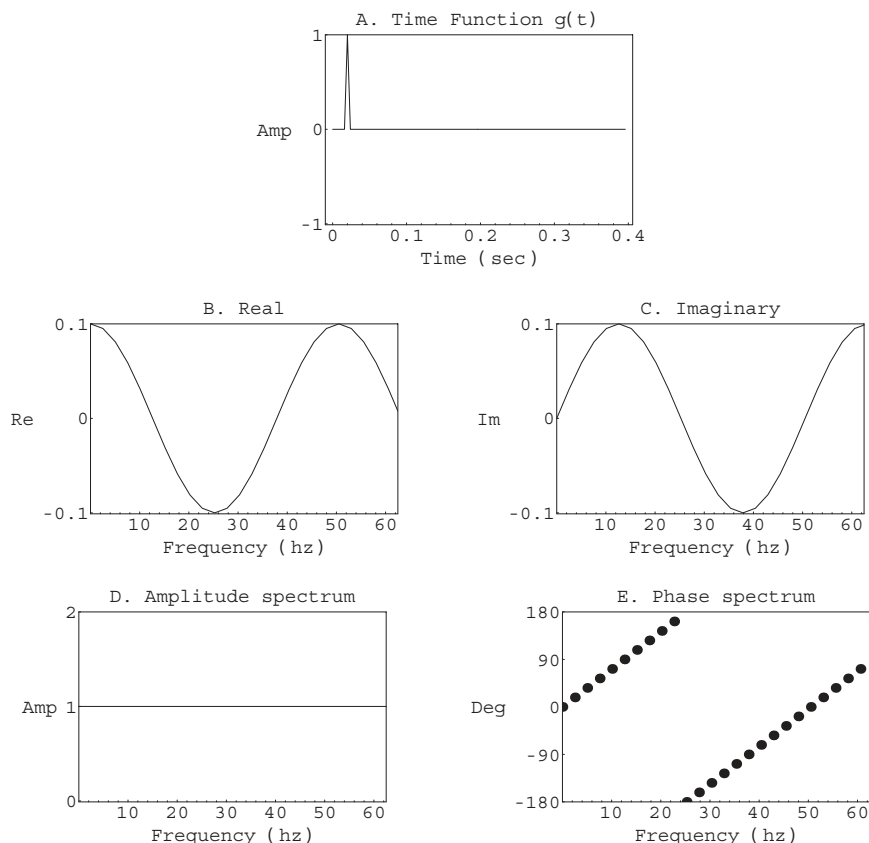


Fig. A.4 Fourier Transform a spike located at  $t=t_o$ . The amplitude spectrum is flat, as it would be for any spike, but the phase spectrum has a constant slope containing information about the time domain location of the spike. The phase spectrum slope is  $2\pi t_o$ . Phase wrapping is evident.

and the scaling property ( $a$  is a real constant)

$$\begin{aligned} FT\{g(at)\} &= \frac{1}{a} g(f/a) \\ FT^{-1}\{g(af)\} &= \frac{1}{a} g(t/a) \end{aligned} \quad (\text{A.22})$$

## Elements of 3D Seismology

Differentiation and integration properties are of particular importance for the solution of partial differential equations (such as the wave equation)

$$\begin{aligned} FT \left\{ \frac{d^\alpha g(t)}{dt^\alpha} \right\} &= (-i\omega)^\alpha g(\omega) \\ FT^{-1} \left\{ \frac{d^\alpha g(\omega)}{d\omega^\alpha} \right\} &= (it)^\alpha g(t) \\ FT \left\{ \int^\alpha g(t) dt \right\} &= \frac{g(\omega)}{(-i\omega)^\alpha} \\ FT^{-1} \left\{ \int^\alpha g(\omega) d\omega \right\} &= \frac{g(t)}{(it)^\alpha} \end{aligned} \quad (\text{A.23})$$

where the parameter  $\alpha$  represents the order of the derivative or integral. For example  $\alpha=2$  is the second derivative or second integral. A compact way to write down the effect of multiplication by  $(-i\omega)^\alpha$  in the frequency domain is

$$(-i\omega)^\alpha g(\omega) = \begin{cases} \frac{d^\alpha g(t)}{dt^\alpha}, & \alpha > 0 \\ g(t), & \alpha = 0 \\ \int^\alpha g(t) dt, & \alpha < 0 \end{cases} \quad (\text{A.24})$$

The parameter  $\alpha$  need not be an integer. In dip moveout theory, a “half derivative” operator arises, which is difficult to understand from a time domain perspective. However, applying this operator in the frequency domain is straightforward since

$$FT \left\{ \frac{\partial^{1/2}}{\partial t^{1/2}} g(t, \underline{x}) \right\} = (-i\omega)^{1/2} g(\omega, \underline{x}) \quad (\text{A.25})$$

This line of thought leads to a fractional calculus that is finding an increasing number of applications in physics, including charge transport in amorphous semiconductors, spread of contaminants in groundwater, and stress moduli of polymers [169].

A process central to seismology is convolution, defined in the time domain as

$$g_1(t) * g_2(t) = \int_{-\infty}^{\infty} g_1(\tau) g_2(t - \tau) d\tau \quad (\text{A.26})$$

but simply as multiplication in the frequency domain

$$FT \{g_1(t) * g_2(t)\} = g_1(f) g_2(f) \quad (\text{A.27})$$

In terms of amplitude and phase spectra it follows that

$$g_1(f) g_2(f) = A_1 A_2 e^{i(\theta_1 + \theta_2)} \quad (\text{A.28})$$

which says that when two time functions are convolved it has the effect of multiplying the amplitude spectra and adding the phase spectra.

Deconvolution, denoted here by the symbol  $*^{-1}$ , is easy enough to understand in the frequency domain

$$FT \left\{ g_1(t) *^{-1} g_2(t) \right\} = \frac{g_1(f)}{g_2(f)} = \frac{A_1}{A_2} e^{i(\theta_1 - \theta_2)} \quad (\text{A.29})$$

Closely related to convolution is the process of correlation

$$g_1(t) * g_2(t) = \int_{-\infty}^{\infty} g_1(\tau + t) g_2(\tau) d\tau \quad (\text{A.30})$$

whose frequency domain equivalent is multiplication by the complex conjugate

$$FT \{g_1(t) * g_2(t)\} = g_1(f) g_2^*(f) \quad (\text{A.31})$$

where the superscripted \* should not be confused with the convolution symbol. The relationship above leads to the result

$$g_1(f) g_2^*(f) = A_1 A_2 e^{i(\theta_1 - \theta_2)} \quad (\text{A.32})$$

showing that correlation of two time functions has the effect of multiplying the amplitude spectra and subtracting the phase spectra.

### A.5 Two spikes

Earlier results allow us to quickly consider the case of an input time function with two spikes at times ( $t_1, t_2$ ). This is the sum of two functions, each containing a single spike, and the linearity property of the FT allows us to immediately write

$$g(f) = FT\{ \delta(t - t_1) + \delta(t - t_2) \} = e^{i2\pi f t_1} + e^{i2\pi f t_2} \quad (\text{A.33})$$

Despite the simplicity of this expression, the amplitude and phase spectra are complicated. Figure A.5 is an example of two spikes separated by 16 ms (0.016 s). It shows the amplitude spectrum has developed a notch at

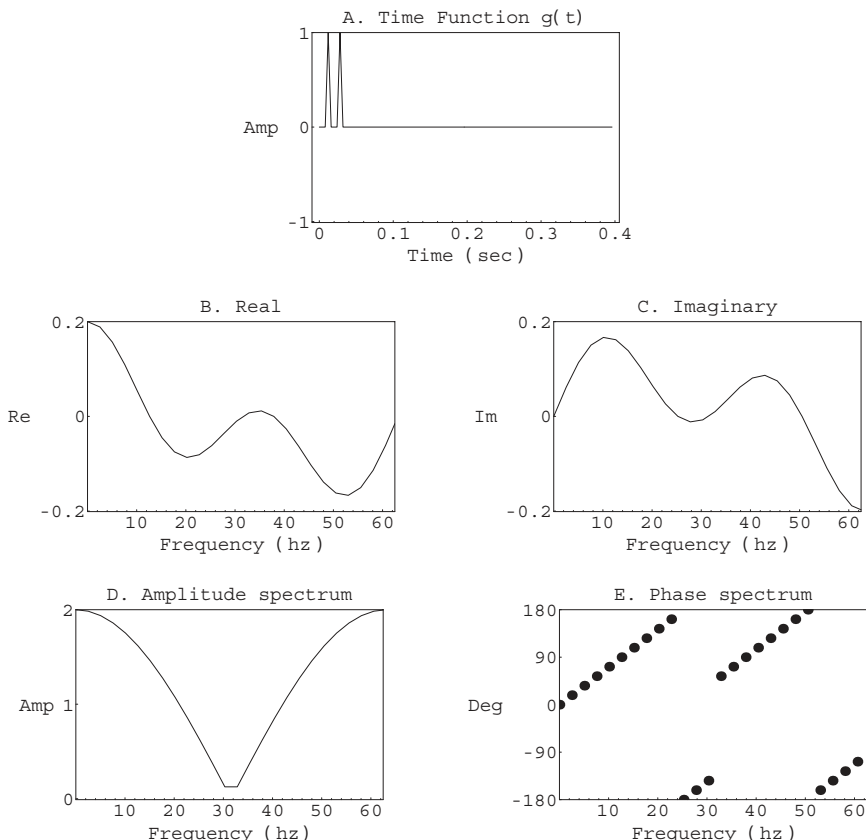


Fig. A.5 Fourier Transform of Two Spikes. Note notch in the amplitude spectrum at about 30 Hz and phase discontinuity at this frequency.

$$f_{notch} = \frac{1}{2(t_2 - t_1)} = 31.25 \text{ Hz} \quad (\text{A.34})$$

and the phase, while still linear in segments, is discontinuous at the notch. Clearly we could expand these results to ten or one hundred spikes, and things would only get more complicated. But the general lesson to be learned is that the amplitude spectrum associated with two or more time-domain spikes contains all frequencies but is not flat, and the phase is not continuous (for more than two spikes it will not be linear, either).

## A.6 The discrete case

To this point, we have considered the function  $g(t)$  to be a continuous function. In any computer application however, the time function will be sampled at regular time intervals. Such a function is a time series and can be represented as a list of numbers

$$g(t) = \{g_1, g_2, g_3, \dots, g_{nt}\} \quad (\text{A.35})$$

where successive values are understood to be separated by a constant interval of time called the time sample rate,  $dt$ , the total number of samples is  $nt$  and the maximum time contained in the series is

$$t_{max} = (nt - 1) dt \quad (\text{A.36})$$

If the time domain is characterized by a sample rate, number of samples, and maximum time, then symmetry of the FT requires that the frequency domain be characterized by corresponding quantities. Table A.1 shows the discrete quantities in each domain. The concept of Nyquist frequency is particularly important, as it is the highest frequency that can be reliably measured by a given time sample rate. This leads to the concept of aliasing.

Time domain		Frequency domain	
$dt$	sample rate	$df = 1/(2 t_{max})$	sample rate
$nt$	number of samples	$nf = nt$	number of samples
$t_{max} = (nt - 1) dt$	max time	$f_N = 1/(2 dt)$	Nyquist (max) frequency

Table A.1 Correspondence of Time and Frequency Domain Quantities

## Elements of 3D Seismology

The forward Fourier transform involves an integral, and the discrete transform approximates that integral by a summation,

$$g(f_m) = \sum_{n=1}^{nt} g(t_n) e^{i2\pi f_m t_n} \quad (\text{A.37})$$

A simple example helps to understand the discrete FT. Consider a time series consisting of four points  $g(t)=\{0,1,0,0\}$  and a time sample rate of 2 ms (0.002 seconds). The time associated with the first sample is zero, 2 ms for the second, 4 ms for the third, and 6 ms for the last. Since  $t_{max}=0.006$  sec, the frequency sampling is  $df=1/(0.012)=83.3$  Hz. The results of computing the FT are, as usual, complex numbers or amplitude and phase.

$$\begin{aligned} \text{Amplitude Spectrum} &= \{1, 1, 1, 1\} \\ \text{Phase Spectrum} &= \{0, 60, 120, 180\} \end{aligned}$$

Degrees

A brute force numerical FT of an  $n$ -point time series will take  $n^2$  computer operations. However, owing to the many symmetries of this transform [149], it is possible to do it in  $n \log_2 n$  operations. (The modern history of this fact dates from 1965, but the concept was apparently known to the great mathematician Gauss (1777–1855) and several later authors.)

Such an algorithm of  $n \log_2 n$  operations is called a fast Fourier transform, or FFT. To understand the implications of this, consider a 3D seismic survey consisting of one million traces, each one containing one thousand time samples. This is not a particularly big data set by today's standards. The total number of data samples in this case is  $10^9$ . A brute force FT would involve  $1 \times 10^{18}$  operations compared to  $3 \times 10^{10}$  for the FFT. How long would these computations take? The fastest generally available supercomputer in the world today is a teraflop machine capable of performing  $10^{12}$  operations per second. On such a machine, the slow transform method would take about eleven and one-half days, whereas the FFT would be done in three one hundredths of a second (0.03 sec).

### A.7 Detection of periodic signals

As an example of the power of the FFT for decomposition of complex signals, consider Figure A.6. The upper plot is a time series that appears to have no structure, although on close inspection it seems to nearly, but not quite, have mirror symmetry about 0.5 sec. The lower plot shows the amplitude spectrum of this time series is composed of essentially five frequencies: 12, 15, 20, 30, and 60 Hz. In addition, the amplitude spectrum tells us that the 12 Hz component is stronger than the 15, which is stronger than the 20, and so on. The FT has the ability to extract this information because the periodic components persist for

the entire time series. If they changed over time in some way, then time-frequency spectrum analysis would be required.

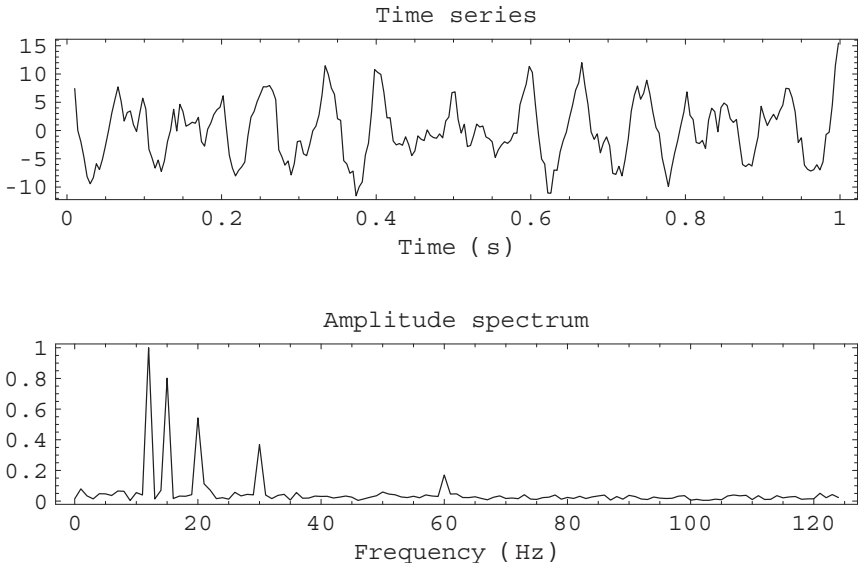


Fig. A.6 Detection of Periodicity in a Signal

## A.8 2D Fourier transform.

It is possible to extend the Fourier transform to any number of dimensions. While there are some applications for 3D FT (3D Stolt migration is one), by far the most common uses are for 1D and 2D. In the usual seismic case, a panel of data will have a vertical time axis (increasing down) and a horizontal space axis. Denoting such a panel of data  $g(t,x)$ , its 2D FT is defined by

$$g(f,k) = \int \int g(t,x) e^{i2\pi ft} e^{-i2\pi kx} dt dx = \int \int g(t,x) e^{i2\pi(ft-kx)} dt dx \quad (\text{A.38})$$

where  $k$  is the wavenumber, or spatial frequency in units of cycles per unit length. Note the forward FT for  $x$  has the exponent sign flipped in the kernel. This convention arises because of certain symmetry properties of the wave equation to

## Elements of 3D Seismology

which the 2D transform is often applied. In fields other than geophysics, image processing for example, this sign convention is not used.

The inverse 2D FT is

$$g(t, x) = \int \int g(f, k) e^{-i2\pi(ft-kx)} df dk \quad (\text{A.39})$$

Just as frequency is 1/period, wavenumber is 1/wavelength. That is, a wavelength of 100 m would have a wavenumber value of 0.01 cycles per meter.

Table A.2 itemizes the limits and sampling for the spatial part of the 2D FT, note the complete symmetry with Table A.1.

Space domain		Wavenumber domain	
$dx$	sample rate	$dk = 1/(2 x_{max})$	sample rate
$nx$	number of samples	$nk = nx$	number of samples
$x_{max} = (nx - 1) dx$	max distance	$k_N = 1/(2 dx)$	Nyquist (max) wavenumber

Table A.2 Correspondence of Space and Wavenumber Domain Quantities

An important property of the 2D FT is the fact that a linear feature in one domain is linear in the other domain. The delta function can be used to describe a linear feature

$$g(t, x) = \delta(t - x/v) \quad (\text{A.40})$$

which we can think of as the disturbance from a wave moving across a collection of receivers with speed  $v$ . Figure A.7A shows a data panel of this type. From the properties discussed above, 2D Fourier transform of this delta function gives

$$\begin{aligned} g(f, k) &= \int \int \delta(t - x/v) e^{i2\pi(ft-kx)} dt dx \\ &= \int e^{i2\pi(fx/v - kx)} dx \\ &= \int e^{i2\pi(f/v - k)x} dx \\ &= \delta(f/v - k) \end{aligned} \quad (\text{A.41})$$

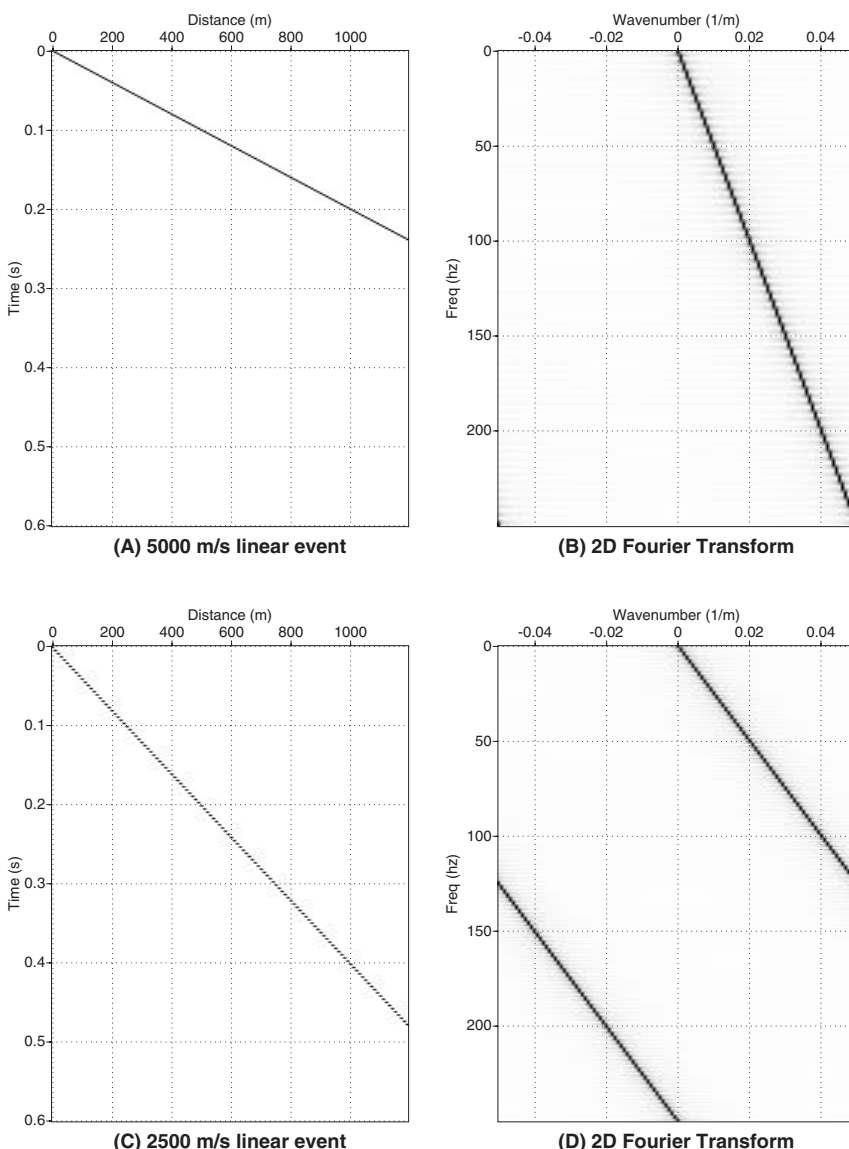


Fig. A.7 Examples of the 2D Fourier transform. Note that a linear event in physical ( $t, x$ ) space maps to a linear event in Fourier ( $f, k$ ) space.

## Elements of 3D Seismology

The last result draws in a previous definition of the delta function, while allowing for the flipped sign in the space transform. In  $(f,k)$  space, the function  $\delta(f/v-k)$  is only nonzero along the line defined by  $f/v-k=0$ . This means we can find the velocity from

$$v = \frac{f}{k} \quad (\text{A.42})$$

or, conversely, the slowness,  $s$ , which is the inverse velocity

$$s = \frac{1}{v} = \frac{k}{f} \quad (\text{A.43})$$

This is confirmed by the numerical example in Figure A.7. The parameters for this example are

$$\begin{aligned} (dt, nt, t_{max}) &= (2 \text{ ms}, 600, 1.2 \text{ s}) \\ (dx, nx, x_{max}) &= (10 \text{ m}, 120, 1200 \text{ m}) \\ (df, nf, f_N) &= (0.42 \text{ hz}, 600, 250 \text{ hz}) \\ (dk, nk, k_N) &= (0.00042 \text{ 1/m}, 120, 0.05 \text{ 1/m}) \end{aligned} \quad (\text{A.44})$$

Panel A is the  $(t,x)$  domain image of a single linear event passing through the origin. As this event arrives at 0.2 sec at a distance of 1000 m, it corresponds to a velocity of 5000 m/s. A 2D FT maps this into  $(f,k)$  space as shown in B, which uses the traditional seismic view of showing both positive and negative wavenumbers, but only positive frequencies along an axis increasing downward. As expected, the event is still linear. Furthermore, it passes through the  $(f,k)$  point  $(100 \text{ Hz}, 0.02 \text{ 1/m})$ , which associates with a velocity of  $100/0.02=5000 \text{ m/s}$ .

Panels C and D show the same example for a lower velocity event (2500 m/s). In Fourier space, the event slopes such that it intersects the positive Nyquist wavenumber at about 125 Hz, then reappears at negative Nyquist wavenumber and continues with the same slope till it goes off the bottom of the plot, which corresponds to the Nyquist frequency. If negative frequencies were displayed, the event would be seen again coming in from negative Nyquist frequency and so on. This effect is called spatial aliasing, and it can occur with respect to the frequency axis (termed aliasing or temporal aliasing) or the wavenumber axis (spatial aliasing).

This discussion of the 2D Fourier transform merely touches on the subject. Yilmaz [212] gives a clear and detailed account of the 2D transform and its applications to seismic filtering, analysis and imaging.

# Appendix B

## Glossary of Terms

This glossary is merely a starting point for the technical language of petroleum seismology. The standard reference for all geophysical terms is Sheriff's Dictionary [165].

**3D seismic** The process of shooting and processing seismic data in such a way that a volume of data is produced and interpreted for geologic meaning.

**4D seismic** The process of shooting, processing, and interpreting multiple 3D surveys over a field. Each 3D survey has a different vintage (acquisition date). Also called time-lapse 3D (TL3D).

**Acoustic impedance** The product of P-wave velocity and bulk modulus. Changes in acoustic impedance give rise to reflection coefficients.

**Acoustic medium** A material characterized by bulk modulus and mass density. A fluid, which can support one mechanical wave type—sound.

**Acoustic reflection coefficient** Reflection coefficient for a wave striking the interface between two acoustic layers.

**Acquisition area** Contains all source and receiver locations in a 3D seismic survey. See Figure 10.9.

**Acquisition footprint** Any map view regularity or pattern in seismic data which is not of geological origin. Can be due to acquisition or processing problems.

**Acquisition fringe** Area between image area and acquisition area. See Figure 10.9.

**Aliasing** The process of sampling a continuous function using too large a sample interval. If a time function is involved, it is termed temporal aliasing or simply aliasing. When a wavefield (a function of space and time) is improperly sampled along a space axis, it is called spatial aliasing.

## **Elements of 3D Seismology**

**Amplitude map** A map, generated by tracking, which displays seismic amplitude associated with a horizon of interest. See Plate 7.

**Amplitude versus offset** Prestack interpretation technique that analyzes variations in amplitude as a function of offset or incident angle. Is often used to discriminate gas from non-gas bright spots.

**Angular reflection coefficient** Reflection coefficient which is a function of the incidence angle of the wave. See Figures 3.11–3.13.

**Array** A collection of sources or receivers acting as one unit.

**Array directivity** See radiation pattern.

**Attenuation** For a seismic wave traveling through the earth, amplitude loss due to several physical processes, including gradual conversion of wave energy into heat absorption.

**AVO** See amplitude versus offset.

**Azimuth** Angle measured counterclockwise from north to a line pointing at the receiver location as seen from the source (or midpoint). This is a common definition, but others are in use. See Figure 10.1.

**Bin** Area on earth surface which captures any trace whose midpoint falls in the bin area. All the traces in a bin form a 3D CMP gather. See Figures 14.7 and 14.8.

**Biot theory** Rock physics theory for calculating velocity and density of a porous fluid-saturated rock at seismic and higher frequencies. Gassman theory is a special case valid at low frequencies encountered in seismic data.

**Bright spot** High amplitude seismic reflection commonly due to presence of gas.

**BSR** Acronym for bottom simulating reflector. In many offshore areas in the world, a gas hydrate (clathrate) layer develops in the shallow subsurface. This solid-phase gas typically generates a reflection event (BSR) parallel to the sea floor reflection.

**Cabled static** Cabling term implying that all receivers were live for all shots. Common in small land surveys and marine streamer surveys.

**Cabling** Details of which receiver groups are live for which shots in land and fixed receiver marine seismic acquisition.

**Checkshot** A direct traveltime measurement between the earth surface and a geologic horizon in the earth.

**Checkshot survey** Several checkshots in a well. Used to correct traveltimes calculated from sonic logs. Related to synthetic seismogram.

**Common “XYZ” gather** A collection of seismic traces which have one fixed, or common, characteristic “XYZ”. For example, a common shot gather is all traces which were generated by the same shot. Other standard gathers include common offset (COS), common receiver, common midpoint (CMP), and common azimuth.

**Component** Orientation of a source or receiver. Standard seismic data involves a vertical (or explosive) source shooting into vertical receivers.

**CMP** (1) Literally, common midpoint. The point halfway between source and receiver. (2) Universal seismic acquisition technique that yields many prestack traces at each midpoint location.

**CMP fold** Number of traces in a CMP gather that are summed through stacking to make one poststack trace.

**CMP gather** Gather of all traces in a seismic survey having the same midpoint (2D) or bin (3D).

**CMP stack** A stack of all prestack traces associated with the same midpoint or bin.

**Common midpoint** See CMP.

**Common offset** See COS.

**Confining pressure** Pressure at depth in the earth due to the overlying column of rock. Also called lithostatic pressure.

**COS** A section or gather of all traces that have the same offset.

**Dead oil** Crude oil containing no dissolved gas.

**Depth migration** A migration algorithm which correctly handles any kind of velocity variation.

**Depth slice** Horizontal slice of a 3D seismic depth cube.

**Difference volume** Seismic data volume created by subtracting two coincident 3D seismic surveys of different vintage.

## **Elements of 3D Seismology**

**Dip moveout** A seismic process, which removes traveltime effects due to offset while honoring all possible dips. See Figure 19.3.

**Direct wave** A seismic or sound wave which directly, without reflection, travels from the source to the receiver. For constant velocity, appears as a linear event on 2D shot records. See Figures 3.2 and 3.3.

**Earth model** A numerical representation of some section of the earth. Usually involves P-wave velocity, and perhaps density, associated with each grid point or layer. An earth model can be 1D, 2D, or 3D. See Figure 1.3.

**Elastic medium** A material characterized by three or more stiffness coefficients. A solid that can support P- and S-waves.

**Far offset** Distance from source to farthest receiver.

**Fermat's principle** Basic law of physics, which says that in a variable velocity medium, seismic rays will take that path which involves the least possible traveltime.

**Flat fold** Constant fold throughout the sweet spot in a 3D survey.

**Fluid replacement** A kind of calculation that predicts how rock velocity and density will change as pore fluid changes.

**Fold** Generic term to describe how many seismic traces are summed through stacking.

**Fold/migration fringe** That part of the image area which is unreliable due to build-up of CMP fold, or reflections are lost to migration distance. See Figure 10.9.

**Fold striping** Variation of CMP fold parallel to the acquisition grid in a 3D seismic survey. This can affect amplitude and signal-to-noise ratio to form an example of acquisition footprint. Fold striping can occur from improper survey design (3D fold not an integer) or execution.

**Gassman theory** Rock physics theory for calculating velocity and density of a porous fluid-saturated rock at seismic frequencies. Special case of the Biot theory.

**Gather** See common “XYZ” gather.

**Geophone** A receiver for measuring seismic wave motions at the earth surface, on the seafloor, etc. Usually measures vertical component of particle velocity. See Figure 7.5.

**Geometric spreading** For a seismic wave traveling through the earth, amplitude loss due to 3D spreading of the wavefront.

**Ground roll** Generic term for seismic waves which only exist near the earth's surface. Considered to be noise.

**Group** A receiver array.

**Group interval** Distance between receiver groups.

**Half-offset** One-half source-receiver distance.

**Head wave** A seismic wave that can exist when a low velocity layer (LVL) overlies a high velocity layer (HVL). It is neither a direct arrival nor a reflection. See Figure 3.19.

**Homogeneous** A material with physical parameters that do not change from one  $(x,y,z)$  location to another.

Also called inhomogeneous.

**Horizon slice** See amplitude map.

**Hydrophone** A receiver for measuring sound waves in water. A pressure sensor.

**Image area** Contains all midpoint locations in a 3D seismic survey. See Figure 10.9.

**Image** The product of seismic data processing that shows locations in the subsurface where parameters of the medium change.

**Imaging** Processing for the purpose of creating a subsurface image from seismic data.

**Incident wave** During the reflection process, the wave that comes in to strike the interface. See Figure 1.17.

**Inhomogeneous** A material with physical parameters that change from one  $(x,y,z)$  location to another.

Also called heterogeneous.

**Interface** A surface in the earth where velocity, density, or other seismic parameters are discontinuous, or change abruptly. Often, but not necessarily, coincident with change of rock type.

**Interpretation** Analysis of seismic data for the purpose of extracting geologic or reservoir engineering information.

**Inversion** (1) The estimation of medium parameters given observed wavefield values. (2) Processing for the purpose of accurately estimating subsurface parameters (velocity, density, etc.) from seismic data. (3) A situation where a low-velocity layer underlies a high-velocity layer.

## **Elements of 3D Seismology**

**Lateral resolution** The ability to see fine-scale features in map view, such as small reefs and channel features.

**Live oil** Crude oil containing saturation levels of dissolved gas.

**Love wave** A kind of ground roll made up of *SH*-waves trapped in a low-velocity surface layer.

**Medium** Term designating particular layer or section of an earth model. Plural is media.

**Midpoint** Point on the earth surface half-way between source and receiver. See Figure 10.1.

**Migration** The seismic process which provides a final image of the subsurface in terms of vertical reflection time or depth.

**Migration aperture** See migration distance.

**Migration distance** Before and after migration, the distance a reflection segment appears to have moved horizontally.

**Migration impulse response** The subsurface image created by migration when the input data consists of one spike of amplitude on one trace. See Figures 17.2 and 17.7–17.10.

**Mode** Term applied to a seismic wave indicating whether it is a P-wave, SV-wave or *SH*-wave.

**Mode conversion** The process whereby one kind of seismic wave generates another kind during the reflection process. See Figure 5.4.

**Multichannel process** A seismic process that operates on several traces simultaneously and tends to be expensive, particularly for 3D data.

**Multioffset VSP** A VSP that has several sources at various distances from the wellhead.

**Multiple reflection** A seismic event which has undergone reflection more than once. There are several terms used to describe different kinds of multiples, including water bottom, interbed, pegleg, etc.  
See Figure 3.31.

**Near offset** Distance from source to nearest receiver.

**Normal moveout** A seismic process which removes reflection traveltime effects due to offset, zero or constant dip. See Figures 16.7–16.12.

**Offset** Distance between the source and receiver associated with a trace. For 2D data, offset can be signed or unsigned. See Figure 10.1.

**Offset clustering** A common effect in land data where traces in a 3D CMP gather are strongly grouped at a few offsets. This effect arises from orthogonal shooting geometries.

**Orthogonal shooting** The use of perpendicular shot and receiver lines in land 3D acquisition.

**P-wave** A kind of seismic wave whose particle motion is parallel to the direction of wave travel. The main wave type used in seismic exploration. This wave can exist in solids and fluids, and can partially mode convert to SV-waves.

**Parameter** A quantity in a wave equation that is not a coordinate or a wavefield quantity. Examples are mass density, wave speeds, and elastic coefficients.

**Parameter coupling** The common situation where two or more parameters can have offsetting effects on the computed wavefield. A classic example is P-wave velocity and density, which may individually change, yet leave the acoustic impedance unchanged and thus do not affect reflection coefficients.

**Particle motion** The movement of individual particles during the passage of a wave. For example, the particle motion is vertical for a horizontally traveling surface water wave. Special cases are particle displacement, velocity, and acceleration.

**Pore pressure** Pressure at depth in the earth due to the overlying column of fluid. Also called hydrostatic pressure.

**Poststack** An object or process related to seismic data after CMP stacking.

**Poststack migration** A migration algorithm which operates after CMP stacking.

**Prestack** An object or process related to seismic data before CMP stacking.

**Prestack migration** A migration algorithm which operates on prestack traces.

**Processing** See seismic processing.

**Radiation pattern** Angular function for an array describing relative strength of seismic waves emitted or received in various directions. Both source and receiver arrays have radiation patterns.

**Rayleigh wave** A kind of ground roll made up of P- and SV-waves.

## **Elements of 3D Seismology**

**Receiver** A device for measuring seismic or sound waves. The output of a receiver is a seismic trace.

**Receiver array** A collection of receivers laid out in a specific pattern and electrically connected to give a single output trace. The purpose of the receiver array is to suppress ground roll in the output.

**Reflected wave** During the reflection process, the wave that goes out from the interface on the same side as the incident wave. See Figure 1.17.

**Reflection** (1) The process whereby a seismic wave strikes and partially bounces off an interface. See Figure 1.17. (2) An event on a seismic section associated with reflection from an interface in the earth. See Figure 1.4.

**Reflection coefficient** Function describing the amount of amplitude (or energy) reflected when a wave strikes an interface.

**Reflector** Interface in the earth associated with a particular reflection event.

**Refracted wave** Same as head wave.

**Refraction** Same as head wave.

**S-wave** A kind of seismic wave whose particle motion is perpendicular to the direction of wave travel. This wave can exist in solids, but not in fluids.

**SH-wave** A kind of S-wave with horizontal particle motion. This wave cannot mode convert.

**SV-wave** A kind of S-wave with vertical particle motion. This wave can partially mode-convert to P-waves.

**Scattered wave** A reflected or transmitted wave. See Figure 1.17.

**Section** (1) A side-by-side display of many seismic traces. (2) A vertical slice through a poststack 3D seismic data volume.

**Seismic event** Any locally continuous object on a seismic display, for example a reflection event curve (2D) or surface (3D).

**Seismic processing** The computer manipulation of field data to produce a final subsurface image.

**Seismic trace** A time series generated by a receiver or receiver array.  
The response of the earth to a seismic source.

**Seismic wave** A mechanical wave which propagates in a solid material due to its stiffness, or elasticity. Seismic P-waves can also exist as sound waves in fluids. S-waves cannot exist in fluids.

**Shot** A seismic energy source.

**Shotpoint interval** Distance between adjacent sources.

**Shot record** A common shot gather. See Figures 14.6 and 16.6.

**Signal-to-noise ratio** Ratio of peak signal amplitude to average noise amplitude. See Figure 9.8.

**Simulation** The mathematical or computational process of computing a wavefield from a wave equation given a knowledge of the parameters of the medium.

**Single channel process** A seismic process that operates on one trace at a time and is therefore inexpensive.

**Snell's law** Basic law of physics describing how seismic rays bend when passing through an interface between materials of different velocity. Snell's law can be derived from Fermat's principle.

**Sort** The process of rearranging traces in a seismic survey to form common "XYZ" gathers. For example, a 2D seismic line may be sorted into common offset gathers, common shot gathers, etc.

**Sound wave** A mechanical wave which propagates in a fluid due to the fluid's compressibility. A sound wave in a solid is a seismic P-wave.

**Source** An object or process that generates seismic waves.

**Stack** Process of summing two or more traces to create one output trace.

**Streamer** A receiver cable for marine acquisition. See Figure 12.1.

**Sweet spot** Reliable part of a 3D image area inside the fold/migration fringe. See Figure 10.9.

**Sweep** Signal generated by a vibroseis source.

**Synthetic data** Seismic data created numerically in a computer, usually for the purpose of testing processing algorithms or validating interpretation details.

## **Elements of 3D Seismology**

**Synthetic seismogram** Simulated seismic trace at a well location based on sonic and density logs (plus checkshots, if available). Used to associate seismic reflection events to geologic horizons. See Figures 20.7–20.11.

**Time migration** A migration algorithm which correctly handles vertical velocity variation, but not lateral velocity variation.

**Time slice** Horizontal slice of a 3D seismic time cube.

**Time structure map** A map, generated by tracking, which displays vertical reflection time to a horizon of interest. See Plates 7 and 11A.

**Trace** A one-dimensional graph of some quantity as a function of time or depth. Plotted with time or depth increasing downward. Without a qualifier, assume “seismic trace” is intended.

**Tracking** The interpretation process of following a reflection surface throughout a data cube and extracting its time structure and amplitude information. See Plates 6 and 7.

**Transmitted wave** During the reflection process, the wave that goes out from the interface on the side opposite the incident wave. See Figure 1.17.

**Transmission loss** For a seismic wave traveling through the earth, the cumulative amplitude loss due to transmission across many interfaces. See Figure 20.14.

**Turning wave** A downgoing seismic wave which bends continuously according to Snell’s law, ultimately traveling along an arc and turning toward the earth’s surface. Turning waves have only been observed in young, clastic basins such as the Gulf of Mexico. See Figure 9.3.

**Velocity** Speed at which a seismic wave travels.

**Vertical fold** Number of repeated shot records that are summed through vertical stacking.

**Vertical resolution** The ability to identify individual peaks on a seismic trace with the top and base of geologic unit or bed. See Figures 20.18–20.20.

**Vertical seismic profile** A seismic acquisition technique where a surface source shoots into a series of receivers located down a well. A full seismic trace is recorded from each receiver.

**Vertical stack** A field procedure where traces from repeated shots are stacked. This is aimed at reducing random noise.

**Vibroseis** Mechanical source for land seismic acquisition consisting of a truck with a vibrating metal plate in contact with the earth.

**VSP** See vertical seismic profile.

**Zoeppritz equations** System of four equations that describe the amplitude of all reflected and transmitted waves in elastic reflection.

**Zero offset VSP** A VSP that has one source which is located at or near the wellhead.

# Appendix C

## Conversion Factors

To convert	Into	Multiply by	To convert	Into	Multiply by
psi	GPa	$6.895 \times 10^{-5}$	ft	meter	0.3048
psi	MPa	0.006895	mile	kilometer	1.6093
psi	KPa	6.895	ft/s	m/s	0.3048
GPa	psi	147,000	$mi^2$	$km^2$	2.587
MPa	psi	147	$mi^2$	acres	640
KPa	psi	0.147	$mi^2$	hectares	258.7
MPa	atm	10.14	$mi^2$	GOM blocks	0.1111
atm	psi	14.7	$km^2$	$mi^2$	2.587
atm	MPa	0.1014	acre	$km^2$	0.004042
			acre	hectare	0.4042
			acre	GOM block	$1.736 \times 10^{-4}$
			GOM block	sq mile	9
			GOM block	sq km	23.28
			GOM block	hectare	23280
			g/cc	$kg/m^3$	1000

Table 29.1 (Left) Pressure Unit Relationships. The same units are also used for modulus, stress and elastic constants. (Right) Commonly used conversion factors. Abbreviations are for giga-Pascals (gPa), mega-Pascals (mPa), kilo-Pascals (kPa), pounds per square inch (psi), standard atmospheres (atm), and Gulf of Mexico (GOM).

# Appendix D

## Bibliography

- [1] Abriel, W. L., Neale, P. S., Tissue, J. S., and Wright, R. M., 1991, "Modern technology in an old area: Bay Marchand revisited," *Geophysics*: The leading edge of exploration (June), 21–35.
- [2] Adriansyah, A. and McMechan, G. A., 2002, "Analysis and interpretation of seismic data from thin reservoirs: Northwest Java Basin, Indonesia," *Geophysics*, Soc. of Expl. Geophys., 67, 14–26.
- [3] Aki, K. and Richards, P. G., 1980, *Quantitative Seismology: Theory and Methods*, W. H. Freeman, San Francisco.
- [4] Arfken, G., 1970, *Mathematical Methods for Physicists*, 2nd edition, Academic Press.
- [5] Arntsen, B. and Carcione, J. M., 2000, "A new insight into the reciprocity principle," *Geophysics*, Soc. of Expl. Geophys., 65, 1604–1612.
- [6] Avseth, P., Mukerji, T., Jorstad, A., Mavko, G. and Veggeland, T., 2001, "Seismic reservoir mapping from 3-D AVO in a North Sea turbidite system," *Geophysics*, Soc. of Expl. Geophys., 66, 1157–1176.
- [7] Backus, M., 1962, "Long-wave elastic anisotropy produced by horizontal layering," *J. Geoph. Res.*, 67, 4427.
- [8] Bahorich, M. and Farmer, S., 1995, "3-D seismic discontinuity for faults and stratigraphic features: The coherence cube," *The Leading Edge*, 14, no. 10, 1053–1058.
- [9] Baker, B. B., and Copson, E. T., 1939, *The mathematical theory of Huygen's Principle*, Oxford U. Press
- [10] Bamberger, A., Chavent, G., Hemon, C. and Lailly, P., 1982, "Inversion of normal incidence seismograms," *Geophysics*, Soc. of Expl. Geophys., 47, 757–770.

## **Elements of 3-D Seismology**

- [11] Barnes, A. E., 1993, “When the concepts of spectral frequency and instantaneous frequency converge,” *The Leading Edge*, 12, no. 10, 1020–1023.
- [12] Barr, F. J., Wright, R. M., Abriel, W. L., Sanders, J. I., Obkirchner, S., and Womack, B. A., 1990, A Dual-sensor bottom-cable 3-D survey in the Gulf of Mexico, SEG national meeting abstracts, 855–858.
- [13] Batzle, M. and Wang, Z., 1992, “Seismic properties of pore fluids,” *Geophysics*, vol. 57, no. 11, 1396–1408.
- [14] Beyer, R. T., 1974, “Nonlinear Acoustics,” reprint 1997, Acoustical Society of America.
- [15] Bee, M. F., Bearden, J. M., Herkenhoff, E. F., Supiyanto, H., and Koestner, B., 1994, “Efficient 3D seismic surveys in a jungle environment,” *First Break*, vol. 12, no. 5, 253–259.
- [16] Berryman, J. G., and Thigpen, L., 1985, “Nonlinear and semilinear dynamic poroelasticity with microstructure,” *J. Mech. Phys. Solids*, Vol. 33, No. 2, pp. 97–116.
- [17] Biondi, B., 2001, “Kirchhoff imaging beyond aliasing,” *Geophysics*, Soc. of Expl. Geophys., 66, 654–666
- [18] Bleistein, N., 1984, “Mathematical methods for wave phenomena”: Academic Press.
- [19] Biot, M. A., 1956a, “Theory of propagation of elastic waves in a fluid-saturated porous solid, I: Low frequency range,” *J. Acoust. Soc. Am.*, 28, 168–178.
- [20] Biot, M. A., 1956b, “Theory of propagation of elastic waves in a fluid-saturated porous solid, II: Higher frequency range,” *J. Acoust. Soc. Am.*, 28, 179–181.
- [21] Born, M., and Wolf, E., 1959, “Principles of optics, electromagnetic theory of propagation, interference and diffraction of light”: Sixth edition, Pergamon Press.
- [22] Bortfeld, R., 1961, “Approximations to the reflection and transmission coefficients of plane longitudinal and transverse waves”: *Geophys. Prosp., Eur. Assn. Geosci. Eng.*, 09, 485–502.
- [23] Bosman, C. L. and Reiter, E., 1993, “Seismic data compression using wavelet transforms,” 63rd Ann. Internat. Mtg: Soc. of Expl. Geophys., 1261–1264
- [24] Bouska, J., 1998, “Interpreter’s Corner—Double vision for interpreters: Case histories showing the value of dual processing for 3-D surveys”: *The Leading Edge*, 17, no. 11, 1520–1540.

- [25] Bourbie, T., Coussy, O., and Zinszner, B., 1987, "Acoustics of porous media": Gulf Publishing Company.
- [26] Box, R. and Lowrey, P., 2003, "Reconciling sonic logs with check-shot surveys: Stretching synthetic seismograms," *The Leading Edge*, 22, no. 6, 510–517.
- [27] Brink, M., Andreassen, P., Ursin-Holm, B., Key, S., Luheshi, M. N., and Buddery, D., 1991, "Cost-effective 3-D surveying by cooperation between three oil companies," SEG national meeting abstracts, 789–791.
- [28] Brown, A. R., 1991, "Interpretation of three-dimensional seismic data," 3rd edition, AAPG Memoir 42.
- [29] Brown, A. R., 1996, "Interpreter's corner—Seismic attributes and their classification": *The Leading Edge*, 15, no. 10, 1090.
- [30] Brown, A. R., 1999, "Interpretation of three-dimensional seismic data," 5th Ed.: AAPG Memoir 42.
- [31] Brown, D., 2000, "Bad News: Last Year Was 'Dastardly' Good News: It'll Be a Better Year": *AAPG Explorer*, 21(2).
- [32] Bruhl, M., Vermeer, G. J. O. and Kiehn, M., 1996, "Short note—Fresnel zones for broadband data": *Geophysics*, Soc. of Expl. Geophys., 61, 600–604.
- [33] Brune, R. H., O'Sullivan, B., Lu, L., 1994, "Comprehensive analysis of marine 3-D bin coverage," *Geophysics*: The leading edge of exploration (July), 757–762.
- [34] Cagniard, L., 1939, Réflexion et Réfraction des ondes Sismique Progressives: Gauthiers-Villars, Paris. (English translation, 1962, Reflection and Refraction of Progressive Seismic Waves: Trans. by E. A. Flinn and C. H. Dix, McGraw-Hill, New York.)
- [35] Caldwell, J., 2002, "Does air-gun noise harm marine mammals?": *The Leading Edge*, 21, no. 1, 75–78.
- [36] Caldwell, J., 1999, "Marine multicomponent seismology": *The Leading Edge*, 18, no. 11, 1274–1282.
- [37] Castagna, J. P., Batzle, M. L. and Eastwood, R. L., 1985, "Relationships between compressional-wave and shear-wave velocities in clastic silicate rocks": *Geophysics*, Soc. of Expl. Geophys., 50, 571–581.
- [38] Castagna, J. P., Sun, S. and Siegfried, R. W., 2003, "Instantaneous spectral analysis: Detection of low-frequency shadows associated with hydrocarbons": *The Leading Edge*, 22, no. 2, 120–127.
- [39] Castagna, J. P. and Swan, H. W., 1997, "Principles of AVO crossplotting": *The Leading Edge*, 16, no. 04, 337–342.

## **Elements of 3-D Seismology**

- [40] Castagna, J. P., Swan, H. W. and Foster, D. J., 1998, “Framework for AVO gradient and intercept interpretation”: *Geophysics*, Soc. of Expl. Geophys., 63, 948–956.
- [41] Chakraborty, A. and Okaya, D., 1994, “Application of wavelet transform to seismic data,” 64th Ann. Internat. Mtg: Soc. of Expl. Geophys., 725–728.
- [42] Chakraborty, A. and Okaya, D., 1995, “Frequency-time decomposition of seismic data using wavelet-based methods”: *Geophysics*, Soc. of Expl. Geophys., 60, 1906–1916.
- [43] Chambers, R. L., Yarus, J. M. and Hird, K. B., 2000, “Petroleum geostatistics for nongeostatisticians: Part 1”: *The Leading Edge*, 19, no. 05, 474–479.
- [44] Chambers, R. L., Yarus, J. M. and Hird, K. B., 2000, “Petroleum geostatistics for nongeostatisticians”: Part 2: *The Leading Edge*, 19, no. 06, 592–599.
- [45] Chen, Q. and Sidney, S., 1997, Seismic attribute technology for reservoir forecasting and monitoring: *The Leading Edge*, 16, no. 05, 445–456.
- [46] Cheng, N., 1996, “Nonlinear wave propagation in sandstone: A numerical study”: *Geophysics*, Soc. of Expl. Geophys., 61, 1935–1938.
- [47] Chun, J. H. and Jacewitz, C. A., 1981, “Fundamentals of frequency-domain migration”: *Geophysics*, Soc. of Expl. Geophys., 46, 717–733.
- [48] Claerbout, J. F., 1985, *Imagining the Earth’s Interior*, Blackwell Scientific Publications, London.
- [49] Clay, C. S., and Medwin, H., 1977, *Acoustical oceanography Principles & Applications*: John Wiley & Sons Inc.
- [50] Coperude, S. P., 2002, “Effect of the Endangered Species Act on geophysical exploration in the United States”: *The Leading Edge*, 21, no. 1, 70–71.
- [51] Cox, M., 2002, “Static corrections for seismic reflection surveys”: Society of Exploration Geophysicists, Tulsa, OK.
- [52] Crampin, S., 1985, “Evaluation of anisotropy by shear-wave splitting”: *Geophysics*, Soc. of Expl. Geophys., 50, 142–152.
- [53] Crawford, J. M., Doty, W. E. N. and Lee, M. R., 1960, “Continuous signal seismograph”: *Geophysics*, Soc. of Expl. Geophys., 25, 95–105.
- [54] Crews, G. A., Musser, J. A., and Phillips, H. F., 1991, “Economical high-resolution 3-D seismic survey technique without interpolation,” SEG national meeting abstracts, 754–756.
- [55] Dai, N., Vafidis, A. and Kanasewich, E. R., 1995, “Wave propagation in heterogeneous, porous media: A velocity-stress, finite-difference method”: *Geophysics*, Soc. of Expl. Geophys., 60, 327–340

- [56] Davidson, D. S., and Bandell, A., 1990, "A novel 3-D marine acquisition technique," SEG national meeting abstracts, 863–866.
- [57] De Buyl, M., 1989, "Optimum field development with seismic reflection data," *Geophysics: The leading edge of exploration* (April), 14–20.
- [58] Dellinger, J., Murphy, G., Etgen, J. and Gray, S., 1999, "Efficient 2.5-D true-amplitude migration": *The Leading Edge*, 18, no. 8, 946–949.
- [59] Dellinger, J.A., Nolte, B. and Etgen, J.T., 2001, "Alford rotation, ray theory, and crossed-dipole geometry": *Geophysics*, Soc. of Expl. Geophys., 66, 637–647.
- [60] Dix, C. H., 1952, *Seismic prospecting for oil*: Harper & Brothers, NY.
- [61] Djikpesse, H. A. and Tarantola, A., 1999, "Multiparameter + L 1 norm waveform fitting: Interpretation of Gulf of Mexico reflection seismograms": *Geophysics*, Soc. of Expl. Geophys., 64, 1023–1035.
- [62] Dorn, G. A., 1998, "Modern 3-D seismic interpretation," *The Leading Edge*, 17, no. 09, 1262–1272.
- [63] Doyle, F. F., 1990, "Principles of AVO processing," SEG national meeting abstracts, 1486.
- [64] Elrod, D. and Walker, R., 2000, "Myriad facets of the nonexclusive data business," *The Leading Edge*, 19, no. 06, 640–647.
- [65] Fanchi, J. R., 2001, "Time-lapse seismic monitoring in reservoir management," *The Leading Edge*, 20, no. 10, 1140–1147.
- [66] Faust, L. Y., 1951, "Seismic velocity as a function of depth and geologic time," *Geophysics*, Soc. of Expl. Geophys., 16, 192–206.
- [67] Faust, L. Y., 1953, "A velocity function including lithologic variation," *Geophysics*, Soc. of Expl. Geophys., 18, 271–288
- [68] Fei, T., and Larner, K., 1995, "Elimination of numerical dispersion in finite-difference modeling and migration by flux-corrected transport," *Geophysics*, Soc. of Expl. Geophys., 60, 1830–1842.
- [69] Finn, C. J., 1986, "Estimation of three dimensional dip and curvature from reflection seismic data," M.S thesis, Univ. of Texas at Austin.
- [70] Fliedner, M. M., Crawley, S., Bevc, D., and Popovici, A. M., 2002, "Velocity model building by wavefield-continuation imaging in the deepwater Gulf of Mexico," *Geophysics: The leading edge of exploration* (December), 1232–1236.
- [71] Fokkema, J. T. and van den Berg, P. M., 1993, "Seismic applications of reciprocity," Elsevier Science Publishers.

## **Elements of 3-D Seismology**

- [72] Foster, D. J., Keys, R. G. and Reilly, J. M., 1997, "Another perspective on AVO crossplotting," *The Leading Edge*, 16, no. 09, 1233–1237.
- [73] Foster, M. S., Nunn, K. R., Lewis, S. A. and Reynolds, D. J., 1997, "Zero-phasing seismic data without wells in offshore West Africa: Reducing uncertainty and variability of the wavelet," *Geophysics*, Soc. of Expl. Geophys., 62, 352–361.
- [74] French, W. S., 1990, "Practical seismic imaging," *Geophysics*: The leading edge of exploration (August), 13–20.
- [75] Gassmann, F., 1951, "Elastic waves through a packing of spheres," *Geophysics*, 16, 673–685.
- [76] Gastaldi, C., Biguenet, J. P. and de Pazzis, L., 1997, "Reservoir characterization from seismic attributes: An example from the Peciko field (Indonesia)," *The Leading Edge*, 16, no. 03, 263–266.
- [77] Garotta, R., 2000, "Shear waves from acquisition to interpretation," Distinguished Instructor Course Notes, Soc. of Expl. Geophys.
- [78] Gibson, R. L., Jr. and Tzimeas, C., 2002, "Quantitative measures of image resolution for seismic survey design," *Geophysics*, Soc. of Expl. Geophys., 67, 1844–1852.
- [79] Gikas, V. Cross, P. A., and Ridyard, D., 1999, "Reliability analysis in dynamic systems: Implications for positioning marine seismic networks," *Geophysics*, Soc. of Expl. Geophys., 64, 1014–1022.
- [80] Godley, A. D., 1931, "Herodotus with an English translation," 4 vol., Harvard University Press, Cambridge, Massachusetts.
- [81] Gray, S., 1997, "Seismic imaging: Use the right tool for the job," *Geophysics*: The leading edge of exploration (November), 1585–1588.
- [82] Hart, B. S., 2002, "Validating seismic attribute studies: Beyond statistics," *The Leading Edge*, 21, no. 10, 1016–1021.
- [83] Hickey, C.J. and Sabatier, J.M. , 1995, "Measurements of Biot Type I and Type II Waves in an Air-Filled Packing of Sand," Paper 5aPA14, ASA Meeting, Washington, DC.
- [84] Hill, S., Shultz, M. and Brewer, J., 1999, "Acquisition footprint and fold-of-stack plots," *The Leading Edge*, 18, no. 6, 686–695.
- [85] Hilterman, F., 1990, "Is AVO the seismic signature of lithology? A case history of Ship Shoal-south addition," *The Leading Edge*, 09, no. 06, 15–22.
- [86] Huygens, C., 1690, "Treatise on light in which are explained the causes of that which occurs in reflexion, \$ refraction and particularly in the strange refraction of iceland crystal," Reprint 1912, University of Chicago Press.

- [87] Greenlee, S. M., Gaskins, G. M., and Johnson, M. G., 1994, “3-D seismic benefits from exploration through development: An Exxon perspective,” *Geophysics: The leading edge of exploration* (July), 730–734.
- [88] Hale, D., 1991, “Course notes: Dip moveout processing,” *Soc. Expl. Geophys.*
- [89] Hatton, L., and Haddow, K, 1991, “The effects of source array crossline directivity on 3D migration,” *First Break*, vol. 9, no.9 , 427–431.
- [90] Helgesen, J., Magnus, I., Prosser, S., Saigal, G., Aamodt, G., Dolberg, D. and Busman, S., 2000, “Comparison of constrained sparse spike and stochastic inversion for porosity prediction at Kristin Field,” *The Leading Edge*, 19, no. 04, 400–407.
- [91] Henry, S., 2000, “Pitfalls in synthetics,” *The Leading Edge*, 19, no. 06, 604–606.
- [92] Kabir, N., Lavaud, B. and Chavent, G., 2000, “Estimation of density contrast by AVO inversion beyond the linearized approximation: An indicator of gas saturation,” 70th Ann. Internat. Mtg: Soc. of Expl. Geophys., 243–246.
- [93] Kalkomey, C. T., 1997, “Potential risks when using seismic attributes as predictors of reservoir properties,” *The Leading Edge*, 16, no. 03, 247–251.
- [94] Kao, J. C., Schneider, W. A. and Whitman, W. W., 1990, “Automated interpolation of two-dimensional seismic grids into three-dimensional data volume,” *Geophysics*, Soc. of Expl. Geophys., 55, 433–442.
- [95] Keho, T., and Samsu, S., 2002, “Depth conversion of Tangguh gas fields,” *The Leading Edge*, 21, no. 10, 1214–1219.
- [96] Kelkar, M., Liner, C., and Kerr, D., 1999, *Integrated Approach Towards the Application of Horizontal Wells to Improve Waterflooding Performance*: USDOE Office of Fossil Energy, Report number DOE/BC/14951-26.
- [97] Kerr, D., Ye, L., Hahar, A., Kelkar, M. and Montgomery, S., 1999, “Glenn Pool Field, Oklahoma: A Case of Improved Production from a Mature Reservoir,” AAPG Bulletin, Vol. 83, No 1, p. 1–18.
- [98] Knight, W. V., 1989, “Estimating the value of a geophysical survey,” *Soc. of Expl. Geophys.*, (October), 46–48.
- [99] Krail, P. M., and Shin, Y., 1990, “Deconvolution of a directional marine source,” *Soc. of Expl. Geophys.*, vol. 55, no. 12, 1542–1548.
- [100] Laster, S. J., 1985, “The present state of seismic data acquisition—One view,” *Soc. of Expl. Geophys.*, 50, 2443–2451.

## **Elements of 3-D Seismology**

- [101] Lawyer, L. C., Bates, C. C. and Rice, R. B., 2001, *Geophysics in the affairs of mankind*, 429.
- [102] Leavey, R. A., Hardage, B. A. and Finley, R. J., 1994, "An integrated approach to identifying natural gas reservoir compartment using 3-D seismic depositional facies analysis and production tests," Examples from middle frio fluvial reservoir, Stratton field, south Texas, 64th Ann. Internat. Mtg. Soc. of Expl. Geophys., 802.
- [103] Levin, F. K., 1971, "Apparent velocity from dipping interface reflections," *Geophysics*, Soc. of Expl. Geophys., 36, 510–516.
- [104] Li, C-F., 2003, Personal communication.
- [105] Li, X.-Y., Dai, H., Mueller, M. C. and Barkved, O. I., 2001, "Compensating for the effects of gas clouds on C-wave imaging: A case study from Valhall," *The Leading Edge*, 20, no. 9, 1022–1028.
- [106] Lindsey, J. P., 1989, "The Fresnel zone and its interpretive significance," *Geophysics: The leading edge of exploration* (October), 33–39.
- [107] Lindsay, R. B., 1960, *Mechanical Radiation*, 4th edition, McGraw-Hill.
- [108] Lindsay, R. and Van Koughnet, R., 2001, "Sequential Backus averaging: Upscaling well logs to seismic wavelengths," *The Leading Edge*, 20, no. 02, 188–191.
- [109] Lindseth, R. O., 1979, "Synthetic sonic logs—a process for stratigraphic interpretation," *Geophysics*, Soc. of Expl. Geophys., 44, 3–26.
- [110] Liner, C. L., 1991, "Theory of a 2.5-D acoustic wave equation for constant density media (short note)," *Geophysics*, Soc. of Expl. Geophys., 56, 2114–2117.
- [111] Liner, C. L., 1994, "Rayleigh wave approximations," *Journal of Seismic Exploration*, 3, 273–281.
- [112] Liner, C. L., 1995, "Some analytic aspects of a 2.5-D wave equation," *Geophysics*, Soc. of Expl. Geophys., 60, 1536–1540.
- [113] Liner, C. L., 1992–2002, "Seismos," *Geophysics: The leading edge of exploration*.
- [114] Liner, C. L., 1997, "Greek seismology: Being an annotated sourcebook of earthquake theories and concepts in classical antiquity," Samizdat Press, <http://samizdat.mines.edu/>
- [115] Liner, C. L., and Gobeli, R., 1996, "Bin size and linear  $\nu(z)$ ," 66th Ann. Internat. Mtg., Soc. Expl. Geophys, Expanded Abstracts, 47–50.

- [116] Liner, C. L., and Gobeli, R., 1997, “3-D seismic survey design and linear  $v(z)$ ,” 67th Ann. Internat. Mtg., Soc. Expl. Geophys, Expanded Abstracts, 43–46.
- [117] Liner, C. L., Underwood, W. D. and Gobeli, R., 1999, “Poster Paper—3-D seismic survey design as an optimization problem,” *The Leading Edge*, 18, no. 9, 1054–1060.
- [118] Liner, C. L., Gobeli, R., and Underwood, W. D., 1998, “3-D Seismic survey design as an optimization problem,” 68th Ann. Internat. Mtg., Soc. Expl. Geophys, Expanded Abstracts, 117–120.
- [119] Linpack, 2003, <http://www.netlib.org/lapack/>
- [120] Lumley, D., 2001, “Time-lapse seismic reservoir monitoring,” *Geophysics*, Soc. of Expl. Geophys., 66, 50–53.
- [121] Lumley, D. E., Behrens, R. A., and Wang, Z., 1997, “Assessing the technical risk of a 4-D seismic project,” *Geophysics: The leading edge of exploration* (September), 1287–1291.
- [122] Luo, Y., Al-Dossary, S., Marhoon, M. and Alfaraj, M., 2003, “Generalized Hilbert transform and its applications in geophysics,” *The Leading Edge*, 22, no. 3, 198–202.
- [123] Luo, Y., Marhoon, M., Al Dossary, S. and Alfaraj, M., 2002, “Edge-preserving smoothing and applications,” *The Leading Edge*, 21, no. 2, 136–142.
- [124] Mackay, S., Fried, J., and Carvill, C., 2003, “The impact of water-velocity variations on deepwater seismic data,” *The Leading Edge*, 22, no. 4, 344–350.
- [125] Marfurt, K. J. and Kirlin, R. L., 2000, “3-D broad-band estimates of reflector dip and amplitude,” *Geophysics*, Soc. of Expl. Geophys., 65, 304–320.
- [126] Marfurt, K. J. and Kirlin, R. L., 2001, “Narrow-band spectral analysis and thin-bed tuning,” *Geophysics*, Soc. of Expl. Geophys., 66, 1274–1283.
- [127] Marsden, D., Bush, M. D. and Johng, D. S., 1995, “Analytic velocity functions,” *The Leading Edge*, 14, no. 07, 775–782.
- [128] Mavko, G., Chan, C., and Mukerji, T., 1995, “Fluid substitution: Estimating changes in  $V_p$  without knowing  $V_s$ ,” *Geophysics*, vol. 60, no. 6, 1750–55.
- [129] Meinardus, H. A. and Schleicher, K. L., 1993, “3-D time-variant dip moveout by the f-k method,” *Geophysics*, Soc. of Expl. Geophys., 58, 1030–1041.

## **Elements of 3-D Seismology**

- [130] Michelena, R. J., Gonzales, E. and Capello de P., M., 1998, "Similarity analysis: A new tool to summarize seismic attributes information," *The Leading Edge*, 17, no. 04, 545–548.
- [131] Mittet, R., 2002, "Free-surface boundary conditions for elastic staggered-grid modeling schemes," *Geophysics*, Soc. of Expl. Geophys., 67, 1616–1623.
- [132] Mahob, P.N. and Castagna, J. P., 2003, "AVO polarization and hodograms: AVO strength and polarization product," *Geophysics*, Soc. of Expl. Geophys., 68, 849–862.
- [133] Morrice, D. J., Kenyon, A. S. and Beckett, C. J., 2001, "Optimizing operations in 3-D land seismic surveys," *Geophysics*, Soc. of Expl. Geophys., 66, 1818–1826.
- [134] Morse, P. M., and Feshbach, H., 1953, *Methods of Theoretical Physics*, McGraw-Hill.
- [135] Nedimović, M. R. and West, G. F., 2003, "Crooked-line 2D seismic reflection imaging in crystalline terrains: Part 1, data processing," *Geophysics*, Soc. of Expl. Geophys., 68, 274–285.
- [136] Nedimović, M. R. and West, G. F., 2003, "Crooked-line 2D seismic reflection imaging in crystalline terrains: Part 2, migration," *Geophysics*, Soc. of Expl. Geophys., 68, 286–296.
- [137] O'Doherty, R. G., and Anstey, A. N., 1971, "Reflections on amplitudes," *Geoph. Prosp.*, 19, 430.
- [138] Officer, C. B., 1958, *Introduction to the Theory of Wound Transmission with Application to the Ocean*, McGraw-Hill.
- [139] Operto, S., Xu, S. and Lambare, G., 2000, "Can we quantitatively image complex structures with rays?" *Geophysics*, Soc. of Expl. Geophys., 65, 1223–1238.
- [140] Osen, A., Amundsen, L. and Reitan, A., 1999, "Removal of water-layer multiples from multicomponent sea-bottom data," *Geophysics*, Soc. of Expl. Geophys., 64, 838–851.
- [141] Packwood, J., and Mukerji, T., 1998, "Short Course notes: Introduction to Rock Physics," Geophysical Society of Tulsa, Tulsa, OK.
- [142] Page, C. H., 1955, *Physical Mathematics*, D. Van Nostrand Company, Princeton, New Jersey.
- [143] Pan, J. and Moldoveanu, N., 2001, "Single-sensor towed streamer acquisition: a case study from the Gulf of Mexico," 71st Ann. Internat. Mtg, Soc. of Expl. Geophys., 33–36.

- [144] Partyka, G., Gridley, J. and Lopez, J., 1999, "Interpretational applications of spectral decomposition in reservoir characterization," *The Leading Edge*, 18, no. 3, 353–360.
- [145] Pearce, J., and Mittleman, D., 2002, "Defining the Fresnel zone for broadband radiation," *Physical Review E* 66, 056602
- [146] Peterson, R. A., Fillippone, W. R. and Coker, F. B., 1955, "The synthesis of seismograms from well-log data," *Geophysics*, Soc. of Expl. Geophys., 20, 516–538.
- [147] Petroleum Geo-Services, 2003,  
<http://www.pgs.com/geophysical/marine/resources/dbaFile7280.html>
- [148] Peyton, L., Bottjer, R. and Partyka, G., 1998, "Interpretation of incised valleys using new 3-D seismic techniques: A case history using spectral decomposition and coherency," *The Leading Edge*, 17, no. 09, 1294–1298
- [149] Press, W. H., Flannery, B. P., Teukolosky, S. A., Vetterling, W. T., 1989, *Numerical Recipes The Art of Scientific Computing*, Cambridge University Press.
- [150] Ramos, A. C. B. and Castagna, J. P., 2001, "Useful approximations for converted-wave AVO," *Geophysics*, Soc. of Expl. Geophys., 66, 1721–1734.
- [151] Reblin, M. T., Chapel, G. G., Roche, S. L., and Keller , C., 1991, "A 3-D reflection seismic survey over the Dollarhide field, Andrews County, Texas," *Geophysics: The leading edge of exploration* (August), 11–15.
- [152] Ricker, N., 1940, "The form and nature of seismic waves and the structure of seismograms," *Geophysics*, Soc. of Expl. Geophys., 05, 348–366.
- [153] Rijks, E. J. H. and Jauffred, J. C. E. M, 1991, "Attribute extraction: An important application in any detailed 3-D interpretation study," *The Leading Edge*, 10, no. 09, 11–19.
- [154] Ritchie, W., 1991, "Onshore 3-D acquisition techniques: A retrospective, SEG national meeting abstracts," 750–753.
- [155] Robinson, E. A., 1957, "Predictive decomposition of seismic traces," *Geophysics*, Soc. of Expl. Geophys., 22, 767–778.
- [156] Ronen, S. and Liner, C. L., 2000, "Least-squares DMO and migration," *Geophysics*, Soc. of Expl. Geophys., 65, 1364–1371.
- [157] Roy, J. P., 1996, "Cost effective interpretation workstations," *Hart's Petro Systems World* (Jan/Feb), 21.
- [158] Rutherford, S. R. and Williams, R. H., 1989, "Amplitude-versus-offset variations in gas sands," *Geophysics*, Soc. of Expl. Geophys., 54, 680–688.

## **Elements of 3-D Seismology**

- [159] Saito, H., 1989, “Traveltimes and raypaths of first arrival seismic waves: Computation method based on Huygen’s principle,” 59th Ann. Internat. Mtg: Soc. of Expl. Geophys., 244.
- [160] Sarg, J. F. and Schuelke, J. S., 2003, “Integrated seismic analysis of carbonate reservoirs: From the framework to the volume attributes,” *The Leading Edge*, 22, no. 7, 640–645.
- [161] Scales, J. A. and Snieder, R., 2000, “The Anatomy of Inverse Problems,” *Geophysics*, Soc. of Expl. Geophys., 65, 1708–1710.
- [162] Schneider, W. A., 1998, “3-D Seismic: A historical note,” *Geophysics*: The leading edge of exploration (March) , 375–380.
- [163] Seattle Times, 1998, “Factors that affect stock performance;” Week of June 14, 1998.
- [164] Shen, F., Zhu, X. and Toksoz, M. N., 2002, “Effects of fractures on NMO velocities and P-wave azimuthal AVO response,” *Geophysics*, Soc. of Expl. Geophys., 67, 711–726.
- [165] Sheriff, R. E., 2002, *Encyclopedic Dictionary of Exploration Geophysics*, 4th edition, Society of Exploration Geophysicists, Tulsa, OK.
- [166] Shuey, R. T., 1985, “A simplification of the Zoeppritz-equations,” *Geophysics*, Soc. of Expl. Geophys., 50, 609–614.
- [167] Simmons, J. L., Jr. and Backus, M. M., 1996, “A matched-filter approach to impedance estimation,” *Geophysics*, Soc. of Expl. Geophys., 61, 484–495.
- [168] Simmons, J. A., Ferragamo, M. J., Moss, C. F., 1998, “Echo-delay resolution in sonar images of the big brown bat, *Eptesicus fuscus*,” *Proc. Natl. Acad. Sci.* Vol. 95, pp. 12647D12652,
- [169] Sokolov, I. M., Klafter, J., and Blumen, A., 2002, “Fractional kinetics,” *Physics Today*, vol. 55, no. 11, pp.48–54.
- [170] Sollid, A., and Ursin, B., 2003, “Scattering-angle migration of ocean-bottom seismic data in weakly anisotropic media,” *Geophysics*, Soc. of Expl. Geophys., 68, 641–655.
- [171] Stolt, R. H., 1978, “Migration by Fourier transform,” *Geophysics*, Soc. of Expl. Geophys., 43, 23–48.
- [172] Swan, H. W., 1993, “Properties of direct AVO hydrocarbon indicators, in Backus, M. M., Ed., Offset-dependent reflectivity—theory and practice of AVO analysis,” Soc. of Expl. Geophys., 78–92.
- [173] Taner, M. T., Koehler, F. and Sheriff, R. E., 1979, “Complex seismic trace analysis,” *Geophysics*, Soc. of Expl. Geophys., 44, 1041–1063

- [174] Taner, M. T., and Koehler, F., 1969, "Velocity spectra derivation and applications of velocity functions," *Geophysics*, 34, 859D881.
- [175] Taner, M. T., Schuelke, J. S., O'Doherty, R., and Baysal, E., 1994, "Seismic attributes revisited," SEG national meeting abstracts, 1104–1106.
- [176] TGS NOPEC, 2003,  
[http://www.tgsnopec.com/gulf\\_of\\_mexico/3d\\_data\\_library.htm](http://www.tgsnopec.com/gulf_of_mexico/3d_data_library.htm)
- [177] Telford, W. M., Geldart, L. P., Sheriff, R. E., and Keys, D. A., 1976, *Applied Geophysics*, Cambridge University Press.
- [178] Thomsen, L., 2002, "Understanding seismic anisotropy in exploration and exploitation," Distinguished Instructor Course Notes, Soc. of Expl. Geophys.
- [179] Thomsen, L., 1986, "Weak elastic anisotropy," *Geophysics*, Soc. of Expl. Geophys., 51, 1954–1966.
- [180] Thore, P., Shtuka, A., Lecour, M. A., Ait-Ettajer, T. and Cognot, R., 2002, "Structural uncertainties: Determination, management, and applications," *Geophysics*, Soc. of Expl. Geophys., 67, 840–852.
- [181] Tolstoy, I., 1973, *Wave Propagation*, McGraw-Hill.
- [182] Top 500 Supercomputer Sites, 2002, <http://www.top500.org/>
- [183] Torres-Verdin, C., Victoria, M., Merletti, G. and Pendrel, J., 1999, "Trace-based and geostatistical inversion of 3-D seismic data for thin-sand delineation: An application in San Jorge Basin, Argentina," *The Leading Edge*, 18, no. 9, 1070–1077.
- [184] Treitel, S., 1970, "Principles of digital multichannel filtering," *Geophysics*, Soc. of Expl. Geophys., 35, 785–811.
- [185] Turnbull, H. W., 1939, *The Great Mathematicians*, Reprinted 1993, Barnes and Noble Books.
- [186] University of Georgia Sedimentation Lab, 2000,  
<http://www.uga.edu/~strata/sequence/seqStrat.html>
- [187] U.S. Department of Energy, 2003, World Oil Market and Oil Price Chronologies: <http://www.eia.doe.gov/cabs/chron.html>
- [188] Vail, P. R., Mitchum, R. M., and Thompson, S., 1977, "Changes of sea level from coastal onlap: in Payton, C. E., Ed., Seismic Stratigraphy Applications to hydrocarbon exploration," AAPG Memoir 26, 63D81.

## **Elements of 3-D Seismology**

- [189] Van Wagoner, J. C., H. W. Posamentier, R. M. Mitchum, P. R. Vail, J. F. Sarg, T. S. Loutit, and J. Hardenbol, 1988, "An overview of the fundamentals of sequence stratigraphy and key definitions." In C. K. Wilgus, B. S. Hastings, C. G. St. C. Kendall, H. W. Posamentier, C. A. Ross, J. C. Van Wagoner, eds., *Sea-level changes: an integrated approach*. Society of Economic Paleontologists and Mineralogists Special Publication No. 42, p. 39–45.
- [190] Verm, R., and Hilterman, F., 1995, "Lithology color-coded seismic sections: The calibration of AVO crossplotting to rock properties," *Geophysics: The leading edge of exploration* (August), 848.
- [191] Vermeer, G., 2002, "3-D Seismic survey design," Society of Exploration Geophysicists, Tulsa, OK.
- [192] Versteeg, R., 1994, "The Marmousi experience: Velocity model determination on a synthetic complex data set," *The Leading Edge*, 13, no. 09, 927–936.
- [193] Vortman, L. J., 1963, "Cratering experiments with large high-explosive charges," *Geophysics*, Soc. of Expl. Geophys., 28, 351–368.
- [194] Walton, G. G., 1972, "Three-dimensional seismic method," *Geophysics*, Soc. of Expl. Geophys., 37, 417–430.
- [195] Wang, Z., Wang, H. and Cates, M., 2001, "Effective elastic properties of solid clays," *Geophysics*, Soc. of Expl. Geophys., 66, 428–440.
- [196] Weatherby, B. B., 1940, "The history and development of seismic prospecting," *Geophysics*, Soc. of Expl. Geophys., 05, 215–230.
- [197] Weinstock, R., 1952, "Calculus of Variations with Applications to Physics and Engineering," (Reprint 1972), Dover Publications, NY.
- [198] Weisstein, E. W., 2003, Eric Weisstein's world of physics:  
<http://scienceworld.wolfram.com/physics/>
- [199] Whitcombe, D. N., 1994, "Fast model building using demigration and single-step ray migration," *Geophysics*, Soc. of Expl. Geophys., 59, 439–449.
- [200] White, J. E., 1983, "Underground sound, Application of seismic waves," Elsivier.
- [201] Widess, M. B., 1973, "How thin is a thin bed" *Geophysics*, Soc. of Expl. Geophys., 38, 1176–1254.
- [202] Widess, M. B., 1982, "Quantifying resolving power of seismic systems," *Geophysics*, Soc. of Expl. Geophys., 47, 1160–1173.
- [203] Winkler, K. W., and Murphy, W. F. III, 1995, "Acoustic velocity and attenuation in porous rocks: in Rock Physics and Phase Relations," *A Handbook of Physical Constants*, American Geophysical Union.

- [204] Winterstein, D. F. and De, G. S., 2001, "Case History VTI documented," *Geophysics*, Soc. of Expl. Geophys., 66, 237–245.
- [205] Wolf, A., 1937, "The reflection of elastic waves from transition layers of variable velocity," *Geophysics*, Soc. of Expl. Geophys., 02, 357–363.
- [206] Wood, G. W. and Badger, A. S., 1991, "Total recording system accuracy," SEG national meeting abstracts, 757–760.
- [207] Woods Hole Oceanographic Institution, 2003,  
<http://woodshole.er.usgs.gov/operations/sfmapping/seismicsources.htm>
- [208] Wright, D.G., 2002, "Proposed guidelines to assist the geophysical exploration industry in meeting the requirements of Canadas Fisheries Act," *The Leading Edge*, 21, no. 1, 72–74.
- [209] Wuenschel, P. C., 1960, "Seismogram synthesis including multiples and transmission coefficients," *Geophysics*, Soc. of Expl. Geophys., 25, 106–129.
- [210] Wyllie, M. R. J., Gregory, A. R. and Gardner, L. W., 1956, "Elastic wave velocities in heterogeneous and porous media," *Geophysics*, Soc. of Expl. Geophys., 21, 41–70.
- [211] Yilmaz, O., 2002, "Seismic data analysis: Processing, inversion, and interpretation of seismic sdata," Society of Exploration Geophysicists, Tulsa, OK.
- [212] Yilmaz, O., 1987, "Seismic processing," Society of Exploration Geophysicists, Tulsa, OK.
- [213] Zhu, J., Lines, L. and Gray, S., 1998, "Smiles and frowns in migration/velocity analysis," *Geophysics*, Soc. of Expl. Geophys., 63, 1200–1209.

# INDEX

---

## Index Terms

## Links

1D attributes	487			
1D Fourier transform	266	528		
1D seismic	403	405		
seismic source	403			
1D signal processing	497			
2D acoustic wave simulation	16			
2D amplitude variation	482			
2D attributes	487			
2D data	53	155	298	307
	315	444	470	
data subsets	444			
data volume	444			
land acquisition	155			
marine acquisition	298	307	315	
2D digital image processing	499			
2D dipping interface	60			
2D fold	165	227	229	231
common midpoint fold	165			
2D Fourier transform	264	541		
2D image	254			
2D impulse response	325			
2D interpretation (interactive interpretation project)	441			

## Index Terms

## Links

2D land acquisition (seismic data)	155
field procedure	163
hardware	156
historical summary	155
lines grid	173
shooting geometry	160
Society of Exploration Geophysicists headers and sorting	168
2D land shooting geometry	160
2D lines grid	173
2D marine seismic	298     307     315
common midpoint gather	307
2D migration	335     343     383
migrated data	343     383
migrated image	443
2D offset	202
2D point source	26
2D prestack	
data	332     443
migration	332
2D section	262
2D seismic line	156     169     383     451
grid	503
451	
2D seismic survey	xxii     53     56     155
286     298     307     315	
383     403     444     451	
469     503	
data	53     155     288     307
315     444     470	

This page has been reformatted by Knovel to provide easier navigation.

## Index Terms

## Links

2D seismic survey ( <i>Cont.</i> )				
line	156	169	383	451
	503			
shot profile	56			
stack section	168			
stratigraphy	469			
survey size	286			
2D velocity model	8			
2D wavefronts	29			
2D/3D				
attribute analysis (interactive interpretation)	441			
combined interpretation (interactive)	441			
mapping (interactive interpretation)	441			
structural analysis (interactive interpretation)	441			
2.5D wave equation modeling	27			
3D attributes	487			
3D				
bin	272	277		
common midpoint gather	271			
3D coverage	242			
3D data processing	266	363	438	
before interpretation	438			
3D dip moveout saddle	373			
3D dipping reflector	60			
3D elastic waves	120			
3D fold	216	227	232	
tolerance	227			
3D image volume	444			
3D interpretation (interactive interpretation project)	384	441		
interpretation system	384			

This page has been reformatted by Knovel to provide easier navigation.

<u>Index Terms</u>	<u>Links</u>
3D line source	26
3D midpoint interval	204
3D migration	289    327    330    336
computing speed	342    344
migration concepts	289
3D normal moveout	327
3D offset	363
3D prestack data	202
3D prestack depth migration	444
3D prestack migration	289
3D receiver array	332
3D seismic data financial aspects	163
economics	171
exploration process	173
industry trends	173
savings/gain model	180
3D seismic data	174
financial aspects	266
processing	363
stratigraphy	336
3D seismic design optimization	438
assumptions	473
constraints	476
direct method	223
examples	226
inversion	230
method 2	223
target variables	229

This page has been reformatted by Knovel to provide easier navigation.

## Index Terms

## Links

3D seismic sequence stratigraphy	473			
3D seismic survey	xxii	88	155	163
	168	171	202	214
	223	238	262	276
	286	363	428	473
	476	517	540	
Advantages	xxii			
Computer	xxiii			
cost	174			
data	155	171	266	363
	438	444	473	476
design/design optimization	223			
echo	xxiii			
edges	xxiii			
financial aspects	171			
information	xxiii			
layers	xxiii			
offset	202			
onion	xxii			
prestack migration	289	332		
processes	363			
quality	xxii			
receiver array	163			
risk	xxiii			
shot record	88	214		
size (computing)	262	286		
stack volume	xxiii	168		
shooting parameters	235			
shooting geometry	364			
stratigraphy	473	476		

This page has been reformatted by Knovel to provide easier navigation.

## Index Terms

## Links

3D shooting geometry	364	
3D shot record	88	214
3D Stolt migration	541	
3D visualization (interactive interpretation project)	441	
3D volume	262	286
4C amplitude versus offset	517	
4C ocean bottom cable data	345	
4D		
data	255	345
object	254	
seismic	253	517
5D		
object	255	
volume	255	
90-degree phase shift	426	499
90-degree wavelet	426	
100% coverage	156	

## **A**

A-B crossplotting	524	
Abriel,W.et al.	481	
Abrupt dip changes	452	
Absolute amplitude	452	
Absolute value	530	
Absorbing medium	146	
Absorption coefficient	147	423
Absorption loss	148	

## Index Terms

## Links

Absorption	8	144	146	423
	505			
absorbing medium	146			
coefficient	147	423		
loss	148			
Accommodation space equation	469			
Accurate amplitude information	18			
Acoustic:				
half-space	52			
impedance	xxiii	45	62	64
	407	420	501	
medium	34	65	127	
modeling	123			
ranging	246			
reflection coefficient	129			
velocity model	44			
wave equation	40			
wave phenomena	3			
waves	xxiii	3	12	15
	33	40	44	52
	62	64	67	123
	127	129	246	407
	420	501		
wave simulation	16			
Acquisition (gathering seismic data)	90	153	261	275
	293	298	307	315
	323	338	340	363
	365	438	452	460
	462	476	480	495
	497	505	517	

This page has been reformatted by Knovel to provide easier navigation.

## Index Terms

## Links

Acquisition (gathering seismic data) ( <i>Cont.</i> )					
2D land	155				
acreage	173				
area	185	210			
cost	164	174	192	275	
	340				
data dimensionality and components	253				
date	517				
datum	460				
depth	90				
financial aspects of 3D seismic	171				
footprint	216	227	275	452	
	476	480	495	497	
fringe	210	214			
geometry	155	242	261	293	
grid	452	476			
land 3D design optimization	223				
land shooting geometry	201				
marine acquisition methods	235	298	307	315	
parameters	185	223			
problems	438				
surface	316	323	338	460	
	462	505			
survey predesign	185				
time	164	199	216		
towed receiver systems	242				
Action integral	38	120			
Aggradation	483				
Air bubble	239				

## Index Terms

## Links

Air guns	17	51	124	239
	248	252		
array	124	240	248	
wavelet	240			
Air waves	122			
Aki, K. and Richards, P.	113	122	130	144
Alabama	394	494		
Algorithms	17	289	349	349
	351	394	495	527
	540			
migration	349	351		
Aliasing	187	191	338	437
	480	539	544	
survey predesign	191			
Aligned bed terminations	452			
Aligning	417			
Ambient noise	264			
American Petroleum Institute gravity	102			
Amplitude	14	28	33	65
	76	91	99	121
	130	148	187	227
	238	261	291	301
	346	351	361	385
	409	412	430	447
	449	452	454	482
	486	489	497	505
	530	532	534	537
accuracy	447			
anomaly	452	482		
balancing	291			

This page has been reformatted by Knovel to provide easier navigation.

## Index Terms

## Links

Amplitude ( <i>Cont.</i> )				
bands	452			
calibrated rock model for Glenn sandstone	510			
classes	524			
control	187			
corrections (seismic data processing)	261			
cross plotting	525			
decay	29	121	292	
differences	517			
displacement	454			
effects (Glenn sandstone rock model)	511			
errors	227			
factor	409			
gradient	131	522		
in space, time, and offset (seismic data interpretation)	65	505		
intercept	131	522		
interpretation	525			
lateral and time-lapse effects	511			
map	385	447		
offset effects (amplitude versus offset)	522			
predictive rock model	508			
prestack amplitude factors	505			
ratio	28			
reflection coefficients	506			
resolution	447			
spectrum	14	76	148	238
	261	291	301	409
	412	430	527	532
	534	537		
spectrum notch	538			

This page has been reformatted by Knovel to provide easier navigation.

## Index Terms

## Links

Amplitude ( <i>Cont.</i> )				
stack amplitude reflection coefficients	506			
striping	497			
time-lapse 3D seismic	517			
variation	449			
versus offset (AVO) analysis	33	91	99	130
	187	346	351	361
	449	486	489	512
	522			
versus offset behavior	449	523		
versus offset classification	522	524		
versus offset model	524			
volume	517			
Analog cables	236			
Analog-to-digital conversion	160	163	197	236
converter	160			
Analogy	324			
Analyzing wavelet	499			
Anatomy				
(bin)	276			
of seismic trace	411			
Angular				
acoustic reflection coefficient	69			
coverage	276			
frequency	527			
reflection	xxii	68	505	
reflection coefficient	68	505		
unconformity	474			
Anhydrite	435			
Animated feature film	448			

This page has been reformatted by Knovel to provide easier navigation.

## Index Terms

## Links

Animating	480
Anisotropic	
dip moveout	374
layer	127
medium	8      20      46
P-waves	5
rock	6      17
solid	4      120
Anisotropy	
4	17      20      33
46	93      120      127
131	304      308      351
362	364      374      362
374	417      437      491
	526
dip moveout	374
sonic logging	417
thickness variogram	491
waves in solids	131
Annualized rate of return	177
Antialiasing condition	272
Anticlines	326
Aperture	242      322
limited	322
Apex	56      60
°API gravity	102
Apparent dip	456
Apparent structural closure	467
Apparent velocity	309

## Index Terms

## Links

Appendices	527
bibliography	559
conversion factors	557
Fourier transform	527
glossary of terms	545
Appraisal	173
Aransas National Wildlife Refuge	251
Arbitrary	
2D section	390
line	445
vertical lines	473
vertical section	481
Argument list notation	528
Aristotle	24
Array	241    423    505
directivity	423
505	
Art museum	160
Artificial illumination	452    485
Artists	448
Artley, C.	373
ASCII format	168
Assets	171
Assumptions (land 3D design optimization)	226
Astrophysics	499
Asymptotic	58
Attenuation	3    46    63    144
	261    273    291    322
	362    364    417    419
dispersion	144

This page has been reformatted by Knovel to provide easier navigation.

## Index Terms

## Links

Attenuation ( <i>Cont.</i> )					
processes		144			
waves in porous solids		144			
Attorney		449			
Attribute volume		495			
Attributes		264	361	393	411
		441	449	485	488
		491	495	498	502
		508	516		
analysis		361	508		
classification		488			
Autocorrelation		294	298		
Automatic					
gain control		261	292		
inversion		225			
picking/autopicking (seismic events)		384	456	459	481
tracking/autotracking		441	458		
Average					
dip		462			
interval velocity		454	464		
velocity		46	387	454	462
Azimuth		xxii	58	132	170
		173	203	205	209
		212	227	242	244
		247	250	276	281
		363	454	485	495
		520			
angles		206			
coverage		173	250	281	

## Index Terms

## Links

Azimuth ( <i>Cont.</i> )				
distribution	205	212	227	242
	244	247	520	
histograms	242			
range	278			
seismic attributes	495			
Azimuthal anisotropy	132			

## **B**

Back-dragging	248			
Background information (seismic data interpretation)	433			
3D production	437			
data before interpretation	438			
literature and legends	437			
lithology	434			
other data	437			
seismic velocity	436			
stratigraphy	435			
structure	434			
well control	435			
Background non-reservoir trend	525			
Backus, M	46			
Backus average/averaging	45	49	417	419
	508			
Bad traces	167			
Balloon	29			
Bandlimiting (seismic data)	322	501		
Bandpass frequency filter	266			

## Index Terms

## Links

Bandwidth	14	149	301	437
	469	490	527	534
Bandwidth octaves	15			
base of weathering	316			
Basement features	437			
Basement rock	420			
Basin floor fans	472	482	503	
Bat	15			
Batzle, M. and Wang, Z.	99	108		
Bay Marchand field	390	481		
Bayesian sequential simulation	492			
Beach ball	71			
Bed				
aligned	452			
bedset	472			
classification	470			
interval velocity	500			
terminations	9	383	391	452
	469	472	503	
thickness	430	500		
Bee	15			
Beowulf cluster	287			
Bibliography	559			
Big brown bat	15			
Big picture (waves in fluids)	41			
Bilinear interpolation	476			
Bin				
area	271			
anatomy (seismic data processing)	276			
calculation	272			

This page has been reformatted by Knovel to provide easier navigation.

## Index Terms

## Links

Bin ( <i>Cont.</i> )				
center	271	276		
size	196	206	227	231
	235	272	337	339
	476	480	520	
Binning process	272			
Bins (seismic data processing)	xxii	170	196	206
	210	213	227	231
	235	270	337	339
	459	463	476	480
	492	520		
anatomy	276			
area	271			
center	271	276		
fold and offset variation effects	275			
process	272			
size	196	206	227	231
	235	272	337	339
	476	480	520	
Biological assessment	251			
Biot, M.	41			
Biot				
assumptions	139			
Biot-Gassmann theory	516			
theory	141			
Birds				
biology	251			
depth controllers	236			
Birefringence	132			
Blurring effect	476			

This page has been reformatted by Knovel to provide easier navigation.

## Index Terms

## Links

Boat movement	445			
Body waves	4	34		
Book value	172			
Boomer	239			
Borehole	42	417	448	
data	448			
problems (sonic logging)	417			
Born, M.and Wolf, E.	21			
Bortfeld,R.	130			
Bottom cable acquisition	363			
Boulders	146			
Boundary conditions	63	68	128	
Bright spot	111	292	398	449
	489	449	502	522
Brightness	479			
Brine	99	106	135	138
	140	511	513	
brine-gas mixture	111			
brine-oil mixture	111			
brine-saturated case	511			
bulk modulus	513			
density	106	109	514	
modulus and velocity	106	108	514	
reservoir fluid properties	106			
velocity	106	108		
Broadband	74	76	500	
radiation	74			
tuning	500			
Brown, A.	488			
Brown classification tree	488			

This page has been reformatted by Knovel to provide easier navigation.

## Index Terms

## Links

Bubble				
cancellation	240			
pulse	239			
Budget	173	185		
Bulk modulus	7	34	37	117
	139	141	513	
Buoy system	248			
Buried focus	326			
Buried static problems	434			

## C

Cable	164	215	235	238
	242	246	270	
curvature	247			
depth	238			
feathering (towed receiver systems)	247	270		
Cabling (land shooting geometry)	215			
Cabling information	164			
Cagniard, L.	80			
Calcite	132	140	143	513
fraction	513			
Calculus of variations	39			
Calibrated rock model (Glenn sandstone)	510			
Calibration	136	142	144	508
	510			
constant	136	142	144	
Cambrian age	420			
Canadian Department of Fisheries and Oceans	251			
Candidate solutions	231			
Canyon walls	156			

This page has been reformatted by Knovel to provide easier navigation.

## Index Terms

## Links

Capital investment	173	179	182	
trends	183			
Caprock	511	513		
impedance	511			
Carbonate				
buildups	503			
fraction	464	513	515	
fraction map	464			
geometry	482			
generation	483			
reservoir	482	517		
rock dissolution	146			
rock	135	143	146	240
	394	434	464	469
	482	494	503	508
	513	515		
sequence	482			
stratigraphy	482			
Cardiology	499			
Cartesian				
coordinates	40			
representation	530			
Case history	386	393	396	462
	478	491	500	502
depth conversion	386			
impedance estimation	398			
reservoir prediction	393	491		
spectral decomposition	396			
stacked sand channel system	478			

## Index Terms

## Links

Case history ( <i>Cont.</i> )				
stratigraphy	390			
structure	481			
vertical ray	462			
Castagna, J., et al.	524			
Catalog inversion	225			
Cementation	137	150	462	
Cement-forming minerals	135			
Center for Wave Phenomena	352			
Central peak	14			
Chalk	133			
Chambers, R., et al.	491			
Channels	273	324	333	423
	431	435	477	482
channel systems	477			
hit map	479			
sand intervals	482			
Checkshots	404	417	436	441
Earth model	404			
with sonic log	404			
without sonic log	404			
Chen, Q. and Sidney, S.	486	489		
Chirp	157			
Cibulakan formation	398	502		
Claerbout, J.	88	321	364	
Classification				
bed terminations	470			
dimensional	487			
general and special	486			
noise	196			

This page has been reformatted by Knovel to provide easier navigation.

## Index Terms

## Links

Classification ( <i>Cont.</i> )					
procedural	489				
reflection characteristic	488				
schemes (seismic attributes)	486				
tree (seismic event)	96				
velocity layering	96				
Clastic					
basin (salt)	191	467			
rock	191	420	434	462	
	464	469	482		
Clay	140	514			
content	514	516			
effect	515				
fraction	515				
lithology	514				
minerals	140	515			
Clean sand	516				
Cliniform	463	476			
Closure	188				
Cluster					
of midpoints	276				
of offsets	276				
Clustering of wells	459				
Coda	46				
Coherence (seismic attributes)	486	489	495	503	
cube	486				
Coherency	264	361	452	485	
coherence cube	486				
Coherent noise	264	519			
Collocated kriging	393	491			

This page has been reformatted by Knovel to provide easier navigation.

## Index Terms

## Links

Color conventions	447				
Color image	380	447			
Color plates	377				
Colorado School of Mines,The	352				
Combinatorial analysis	228				
Commercial synthetic seismogram	418				
Common depth point	xx	168			
Common image gathers	166	298	351	357	
	359	522			
domain	359				
flattening	359				
Common midpoint (CMP) stack creation (seismic data processing)	197	254	261	269	
	271	291	346	364	
	423	502	507		
approach	291				
common midpoint stacking	312				
deconvolution	292	294			
dip moveout	309	311			
gain	291				
normal moveout	301				
sorting	298	300			
stacking	197	254	271	291	
	364	423	507		
statics	316				
Common midpoint fold	165	169	197	208	
	210	213	276	438	
gathers	270	301	304	333	
	357	522			

This page has been reformatted by Knovel to provide easier navigation.

## Index Terms

## Links

Common midpoint ( <i>Cont.</i> )				
interval	194	196		
shooting	156	165	167	
stacking	197	254	271	291
	364	423	507	
tracks	242			
Common offset	166	190	254	371
	443			
section	166	190	254	371
Common receiver gathers	166	298		
Common reflection point	168			
Common shot gather	53	166		
Compaction	274	462		
Complex				
amplitude gradient	497			
conjugate	537			
function	530			
number	69	529	540	
plane	530			
reflection coefficient	71			
seismic attributes	494			
terrain	361			
trace analysis	485			
trace attributes	394	485	487	489
	494			
Compliance tensor	117			
Component economics	174			
Composite frame properties	513			
Compound fault zone	453			
Compressional waves	34	140		

This page has been reformatted by Knovel to provide easier navigation.

## Index Terms

## Links

Computational fluid dynamics	253			
Computationally intensive programs	287			
Computer interpretation systems	438			
Computer	xxiii	168	188	232
	257	261	269	283
	363	433	438	448
computer power xxiii	283	363	448	
interpretation systems	438			
Computer power	xxiii	269	283	363
	448			
2D survey size	286			
3D seismic data	xxiii			
3D survey size	286			
computationally intensive programs	287			
computing effort	269			
computing time	269			
processing speed	286	363		
RAM and disk storage	283			
speed and 3D migration	289			
Computing (seismic data processing)	xxiii	168	188	232
	257	261	269	283
	363	433	438	448
2D survey size	286			
3D survey size	286			
computing time	269			
processing speed	286			
RAM and disk storage	283			
speed and 3D migration	289			
Concordance	475			
Condensed section	472			

This page has been reformatted by Knovel to provide easier navigation.

## Index Terms

## Links

Confidence interval	492
Confining pressure	99
Conglomerate	135
Conical waves	78
Conjugate gradient	228
Conjugation	499
Connectivity analysis	451
Conservation of energy	64
Constant	
fold	276
scaling factors	529
velocity medium	19
velocity migration and modeling pairs	322     328
Constrained sparse-spike inversion	502
Constraints (land 3D design optimization)	226
Constructive interference	321
Continental weathering	471
Continuity of pressure	64
Continuous	
function	539
wavelet transform	395     499
Contouring	440     459     463
Controlled source	156
Conversion factors	557
Converted waves	526
Convolution	xxii     282     411     485
	494     501     536
model	411     501
Convolutional model	411     501
synthetic seismogram	411

This page has been reformatted by Knovel to provide easier navigation.

<u>Index Terms</u>	<u>Links</u>			
Coordinates/related quantities (land shooting geometry)	201			
Core measurements	4	135	143	
Correlation	451	489	491	516
	537			
across faults	451			
coefficient	491			
coefficient inaccuracy	492			
distance	491			
false correlation	493			
Cost function	225	228	231	
Cost per trace	248			
Costs (land 3D acquisition)	181			
Coupling	235	248	505	
Cox, M.	316			
Crash resistance	288			
Crawford, J. and Doty, W.	156			
Cretaceous				
age	386	389	463	
depth map	389			
map	386	389	464	
structure map	464			
time structure map	389			
Critical				
angle (waves)	26	69	78	125
	129			
distance	79			
frequency	140			
offset	79			
reflection	79			

## Index Terms

## Links

Crooked line 2D (land shooting geometry)	219			
Cross				
correlation	384	459	485	495
dipole sonic log	437			
spread (array)	204			
spread geometry	204			
spread method (land shooting)	204			
Crossed array	204			
Crossline direction	205			
Crossline Fresnel zone	343			
Crossline sections	445			
Crossover offset	79			
Crossplotted properties	502			
Crossplotting	491	502	524	
crossplotted properties	502			
Crossvalidation correlation coefficient	491			
Crosswell acquisition	363			
Crosswell data	472			
Crude oil. <i>See</i> Oil.				
Crystal symmetry	132			
Cultural interference	185	264		
Currents (water)	276			
Curvature (seismic attributes)	495			
Curve of maximum convexity	88			
Curved ray effects	189			

## Index Terms

## Links

### D

Damping factor	146		
Data			
3D seismic	xxii		
acquisition	322		
aliasing	193		
binning	261		
bins	270		
components	254		
compression	500		
computing	283		
creating common midpoint stack	291		
creating seismic image	259		
data 2D subsets	444		
density	9		
dependency	255		
dimensionality and components (seismic filtering and			
noise removal	264		
gathering/acquisition)	253		
historical perspective	361		
interpretation products	448		
migration classification and velocity analysis	343		
migration concepts	321		
need to process seismic data	261		
processing	17	42	259
processing (binning overview)	261		
processing (creating seismic image)	259		
processing flow	266	268	
proliferation	495	500	503

This page has been reformatted by Knovel to provide easier navigation.

## Index Terms

## Links

Data ( <i>Cont.</i> )				
quality	xxii	167	185	191
	197	447	467	516
seismic data display	447			
storage	283			
tail	168			
visualization	448			
volume (seismic data interpretation)	xxii	443		
Datum plane	202	262	316	
Dead traces	444			
Decibel	30			
Decision diagram migration	347			
Decision makers	448			
Decomposition	395			
Deconvolution	261	266	292	294
	363	537		
common midpoint stack creation	292	294		
example	297			
gap	296	299		
spike	294	297		
Dedicated machine	289			
Deep water	249	364	435	474
	482			
multiples	249			
shale	474			
Definition and history (seismic attributes)	485			
Definitions (glossary)	545			
Deformation	113	139	451	
Delay	192			
Delta function	15	533	542	

This page has been reformatted by Knovel to provide easier navigation.

## Index Terms

## Links

Densely drilled shallow horizon	460			
Density	33	37	45	47
	49	62	81	101
	118	139	142	150
	152	407	412	420
	501			
fluctuation	37	139		
log	47	420		
measurement units	101			
model	412			
range	150			
waves in fluids	45			
Depositional				
environment	435	473		
sequence	470	472		
slope angle	483			
system	469			
Depth	44	46	168	236
	304	344	351	359
	364	386	403	407
	435	445	456	459
	464	467	490	
axis	345			
case history	386			
controllers (bird)	236			
conversion	44	46	304	386
	403	436	459	464
	490			
cube	460			
domain	407			

This page has been reformatted by Knovel to provide easier navigation.

## Index Terms

## Links

Depth ( <i>Cont.</i> )				
error	359	389	464	
grid	464			
map	386	462	467	
migration	304	344	351	364
	435	467		
points	168			
predictions	462			
slice	445			
structure	388	459	468	
techniques	460			
Depth-to-time conversion	468			
Design				
example (land 3D seismic)	230			
optimization (seismic survey)	223			
parameters (template shooting)	217			
Desktop computers	283			
Detection				
of periodicity	541			
of periodic signals (Fourier transform)	540			
Detune	481			
Deviated well	466			
DEVILISH (dipping event velocity inequality licked)	365			
Devonian age	385	459		
Diagenesis	137			
Difference volumes (time-lapse 3D seismic)	517			
amplitude	517			
traveltime	517			
waveform	518			
Differential equations	528			

This page has been reformatted by Knovel to provide easier navigation.

## Index Terms

## Links

Differential global positioning system (DGPS)	246			
Diffraction	84	87	189	192
	273	309	322	434
curve	309			
diffractor	322			
fault	273	434		
limbs	192			
rays	189			
seismic events	84	87		
traveltime	88			
Diffractor	322			
Digital				
cables	236			
computers	261			
logs	137	448		
photography	486			
Dilatation	115			
Dim spot	489			
Dimensional				
classification (seismic attributes)	487			
effects (waves)	26			
energy density and geometric spreading	27			
waveform	26			
Dimensions (data)	254			
Dimensionless quantity	65			
Dim-out	452			
Dip (seismic attributes)	326	329	495	

## Index Terms

## Links

Dip (structural)	xxii	57	60	167
	189	192	309	261
	269	298	309	326
	329	337	340	343
	346	361	364	383
	404	451	456	463
	477	481	485	495
		536		
angle		192		
azimuth	456	495		
calculations		383		
changes		452		
effects		477		
estimates		456		
filter		313		
moveout	193	261	269	298
		309		
line	343	346	361	364
	452	463	536	
seismic slope	326	329	495	
slice		495		
volume		495		
window		384		
Dip from seismic slope (migration concepts)	326	329	495	
Dip moveout (DMO)	193	261	269	298
	309	346	361	364
	452	463	536	
anisotropy		374		
common midpoint stack creation	309	311		
ellipse		371		

This page has been reformatted by Knovel to provide easier navigation.

## Index Terms

## Links

Dip moveout (DMO) ( <i>Cont.</i> )					
impulse response	368	372	374		
offset	365				
operator	373				
saddle	373				
smile	369	371			
stack	452				
theory	536				
velocity variation	372				
Dipole sonic logs	436				
Dipping interface	57	60			
Dipping reflections	189				
Dipping reflector	60	312			
Dirac delta function	533				
Direct arrival raypaths	19				
Direct arrival	19	53	241	270	
raypaths	19				
Direct hydrocarbon indicator	512				
Direct inversion methods	501				
Direct method (land 3D design optimization)	228				
Direct waves	19	51	54	79	
	122	271			
Directional acceleration	236				
Directivity (wave)	17	22	241	291	
control	241				
patterns	22				
source	17				
Discontinuities	42	495			

## Index Terms

## Links

Discontinuous	
amplitude	482
reflection	462
sands	482
Discrete case (Fourier transform)	539
Discrete wavelet transform	499
Disk reflection energy peaking	78
Disk storage (computing)	283
Disk thrashing	289
Dispersion	46     144     419
attenuation	144
waves in porous solids	144
Dispersive medium	8
Displacement	36     114     118     120
Display gain	81
Dissipation (wave energy)	139
Dissolution	146     482
carbonate rock	146
Dissolved gas	103     108
methane	108
Distance between wells	490
Distortion	316     467
Distributary mouth bars	491
Distribution	533
Divergence operator	40
Dividends	171
Dix, C.	113
Dolomite	135     140     435     469

## Index Terms

## Links

Dominant				
frequency	12	14	73	78
	240	273	337	408
	410	426	477	
period	12	238	301	
wavelength	12			
Double refraction	132			
Double square-root equation	84	88	322	
Down dip survey	340			
Downcutting	503			
Downgoing reflection	19			
Downhole sensors	251			
Downlap	475			
Downslope zero crossing	12			
Downsweep	157			
Downthrown block	454			
Drilling	xxii	171	173	179
	451	480	497	
activities	173			
costs	171			
drilling risk	xxii	173	175	451
	480			
dry holes	xxiii	173	175	
risk	173			
Dual cable shooting	242			
Duality	324			
DVD quality video	284			
Dynamic travelttime corrections	262			

## Index Terms

## Links

### **E**

Earnings	171			
Earth image	322			
Earth model	42	87	120	190
	319	403		
checkshots	405			
processing velocities	405			
sonic log	404			
synthetic seismogram	404			
vertical seismic profile	404			
Earth Simulator	285	288		
Earth surface	4	42		
EarthCube	382	439		
Earthquakes	xix	120	161	
theories	xix			
Echo	xxiiii	156	407	
3D seismic data	xxiiii	156		
echolocation technique	xxiii	156		
Ecology	251			
Economic				
consequences	493			
evaluation	437			
factor	192			
parameter	275			
Economics (3D seismic data)	171	173	192	275
	433	437	493	
Edge detection	xxiiii	210	264	266
	486			
Edge diffraction	326			

## Index Terms

## Links

Edge effects	210				
Edge-preserved smoothing	486				
Efficiency	156				
Eigenstructure	495				
Eight-fold vertical stack	164				
Eikonal equation	356				
Elastic					
behavior	33				
constants	117				
earth	403				
effect	51	113	362		
half-space	122				
inversion	517				
medium	65	121	139		
migration	256				
parameters	6	116	120		
phenomena	99	123	160		
potential energy	119				
P-P reflection coefficient	522				
processes	345				
property	3	6	35	515	
waves	6				
reflection angles	126				
reflection behavior	128				
reflection coefficient	xx	127	411	486	
	506				
solids	38				
wave phenomena	364				
wave propagation	3				

## Index Terms

## Links

Elastic ( <i>Cont.</i> )				
waves	xx	3	113	120
	123	364		
wave simulation	123			
waves in solids	xx	127		
Electrical				
circuit	63			
current	160			
properties	38			
resistivity	137			
Electromagnetic waves	38			
Electronic dock	248			
Elephant	15			
Elevation	202	262		
Ellipse	367	371		
Empirical relationships (waves in porous solids)	136			
wavespeed	136			
Empirical wavespeed	136			
Endangered Species Act (ESA)	251			
Energy				
density	27			
geometric spreading	27			
functions	41			
transport	3			
English units	155			
Enhanced recovery	451	514		
project	514			
Entertainment application	448			
Envelope	489	494		
Environment parameters	508			

This page has been reformatted by Knovel to provide easier navigation.

## Index Terms

## Links

Environmental				
damage	156	251		
impact (marine acquisition)	251			
Eocene				
age	478			
channels	478			
Equations of motion		xx	36	43
				118
	139			
waves in fluids	36			
waves in porous solids	139			
waves in solids	118			
Erosion	459	469	482	
Error	501	507		
propagation	501			
Euclid	527			
Euler's formula	531			
Euler-Lagrange equation	39	120	139	
Eustatic sea level	470			
change	470			
rise	470			
Event				
curvature	351			
flattening	304	441		
numbers (velocity layering)	92			
picking	379			
tracking	xxiii			
Evidence of faulting	453			
Exabyte	284			
Exaflop	287			

<u>Index Terms</u>	<u>Links</u>
Examples	157      230      412      414
land 3D design optimization	230
sweeps	157
synthetic seismogram	412      414
Exhaustive search	225
Expense factor	177
Exploding reflector model	327
Exploration	173      435      491
concept	435
process	173
Explosives	51      156      159      239
explosive source	51      157
Extended binary-coded decimal interchange code (EBCDIC)	168
External costs	174
Extreme	
distortion	467
lateral velocity variation	467
subweathering topography	262
topography	202      262      345      364
velocity variation (seismic data interpretation)	467
<b>F</b>	
Facies	525
False	
correlation	493
dip	194
structures	316      318      357      435
Fanchi, T.	517
Far offset	164      227      278

This page has been reformatted by Knovel to provide easier navigation.

## Index Terms

## Links

Farings	236			
Fast Fourier transform	540			
Fault connectivity	451			
Fault detection	452	496		
mapping	452	496		
Fault plane	309	445	452	
reflection	309	452		
Faults/faulting	xxii	9	88	273
	309	362	383	390
	434	437	441	445
	449	451	481	495
detection	452			
diffraction	273	434		
location	451			
mapping	452	496		
parallel to strike	496			
patterns	451	456	496	
plane	309	445	452	
shadow	452			
seismic data interpretation	452			
slices	449			
termination	362	481		
throw	383	452	455	
types	451			
zones	452			
Fermat's principle	22			
Fessenden reflection seismic experiments	xx			
patent	xx	155		
Feynman, R.	438			

<u>Index Terms</u>	<u>Links</u>
Field procedures (2D land data acquisition)	163
roll and cabling	164
vertical stack	164
Field procedures	155     163
2D land data acquisition	163
Field variables	37     119
Filling of ocean basins	471
Filter bank theory	499
Filtered amplitude	267
Filtered Lena	267
Filtering process/operation	261     264     544
noise removal	264
Finance factor	275
Financial aspects (3D seismic data)	171
Fine layering	8       45
waves in fluids	45
Fine-scale features	273
Finite-amplitude waves	40
Finite difference	364
First arrival	79
First critical angle	125     129
First Fresnel zone	74
Fish/fishery (habitat)	251
Fixed receiver systems (marine acquisition methods)	248
Fixed-frequency horizon slice	501
F-K migration	348     364
(f,k) space	544
Flag parameter	230
Flat spectrum	534
Flattening	304     441

This page has been reformatted by Knovel to provide easier navigation.

## Index Terms

## Links

Flexural feature	495
Flip-flop shooting (towed receiver systems)	245
Floating point operator/operations	287      289
Flow barriers	452
Fluid	
brine	106
contact	445      519
contact visibility (time-lapse 3D seismic)	519
density	34      109      140
factor images	264
flow	517
gas	100
mixture (reservoir fluid properties)	108      140
mixture density	109      140
mixture theories	514
model (waves)	33
modulus and velocity	110
movement	517
oil	102
pressure and temperature range	99
properties	34      65      99      139
	526
property discrimination	526
reservoir	99
saturation	502
substitution	99
viscosity	139
visibility	519
Fluid-fluid angular reflection coefficient	68
Fluid-fluid contact	34

This page has been reformatted by Knovel to provide easier navigation.

## Index Terms

## Links

Fluids (waves in)	33		
big picture	41		
equation of motion	36		
density	45		
fine layering	45		
fluid model	33		
parameters	34		
velocity variation	42		
Flutter noise	236		
Fluvial systems	503		
Focus			
analysis	357		
locations	356		
Fold			
164	197	208	210
215	227	275	313
453	481	495	
build-up	211		
folded rocks	453		
land shooting geometry	215		
map	211		
migration fringe	210		
offset variation effects	275		
of stack	208	313	
striping	217	227	276
two	212		
Footstep	161		
Forces			
distribution	120		
orientation	116		
Fort Bend County, Texas	155		

This page has been reformatted by Knovel to provide easier navigation.

## Index Terms

## Links

Formation microscanner	472				
Forward Fourier transform	527	540			
Fourier					
2D Fourier transform	541				
amplitude spectrum	76	157	159		
definitions	527				
detection of periodic signals	540				
discrete case	539				
domain	349	364	430		
fast Fourier transform	540				
forward Fourier transform	527	540			
frequency domain	529				
methods	351				
properties	534				
space	544				
spike input	533				
theory	494				
transform	265	301	348	395	
	397	499	527		
transform properties	534				
two spikes	538				
Fourth-order moveout	309				
Fourth-order traveltime	93				
Four-way closure	449				
Fractional calculus	536				
Fractures	7	33	132	134	
	139	251	437	452	
	526				
fracturing	437	452			
mapping	134				

This page has been reformatted by Knovel to provide easier navigation.

## Index Terms

## Links

Fractures ( <i>Cont.</i> )				
mechanics	251			
porosity	139			
Free parameters	142	508	510	
Free surface	4	34	96	
multiples	96			
Frequency				
content	241			
domain	349	412	494	499
	527	529	537	539
Fourier transform	529			
filtering	264	266		
range (sonic logging)	417			
resolution	494			
sampling rate	494			
shift	534			
Fresnel zone	71	73	333	343
diameter	73			
geometry	73			
Friendly multiples	46			
Fringe (land shooting geometry)	210			
Frown	359			
Full azimuth data	278			
Full cycle economics	174			
Full fold	438			
Full-waveform sonic log	143			
Fundamental experiment	51			
Future value	177			

## Index Terms

## Links

### G

Gains (3D seismic data)	176	261	266	291
	423	502		
common midpoint stack creation	291			
Gap deconvolution	296	299		
Gas	99	108	111	135
	138	239	248	400
	452	490	502	511
	516	518	524	
amplitude	511			
bubble	239			
bulk modulus	100			
cap	516			
clouds	248			
density	100			
effect	502	511	516	524
field	490			
hydrate	526			
indicator (saturation)	512			
in solution	104			
intake	104			
methane	108			
migration	452			
modulus and velocity	100			
reservoir	518	525		
reservoir fluid properties	99	135	138	
sand	524			
saturation	108	111	511	
shallow	519			

This page has been reformatted by Knovel to provide easier navigation.

## Index Terms

## Links

Gas ( <i>Cont.</i> )				
sound speed	102			
time-lapse effects	511			
velocity	100			
Gas-free brine	108			
Gas-oil ratio	104	516		
Gas-related impedance	400			
Gassmann, F.	141			
Gassmann				
equation	143	145	511	
model	492	508		
theory	141	482	508	510
	513			
wavespeeds	141			
Gauss	540			
Gaussian beams	364			
Gaussian cosine wavelet	78			
Gaussian-tapered cosine wavelet	77			
Gazdag migration	349	351	364	
General attributes	486			
General classification (seismic attributes)	486			
General inverse problem	224			
Generalized Hilbert transform	487			
Gentle structure	460			
Geologic				
age	136			
amplitude in space, time, and offset	505			
data volume	443			
extreme velocity variation	467			
fault detection and mapping	452	496		

This page has been reformatted by Knovel to provide easier navigation.

## Index Terms

## Links

Geologic ( <i>Cont.</i> )				
features	xxiii	9	423	
horizons	404	412	417	419
	436	445		
information extraction (seismic data)	45	96	175	254
	262	264	273	276
	294	362	383	386
	392	396	401	
interpretation	45	96	175	254
	262	264	273	276
	294	362	383	386
	392	396	401	
introduction	433			
model	396	491		
seismic attributes	485			
setting	486			
stratigraphy	469			
structure (seismic data interpretation)	451	496		
structural uncertainty	464			
subcrop map	451			
surfaces	382			
synthetic seismogram,tuning, and resolution	403			
time structure and horizon tracking	456	458		
time-to-depth conversion methods	459			
unit	423			
vertical ray case history	462			

<u>Index Terms</u>	<u>Links</u>			
Geology	xxiii	9	45	96
	136	175	254	262
	264	273	276	294
	362	382	386	392
	396	401		
information extraction from seismic data	45	96	175	254
	262	264	273	276
	294	362	383	386
	392	396	401	
Geometric spreading	3	27	27	63
	144	148	261	292
	502	505	522	
Geophone	160	197	199	236
array	161	199		
group		197		
model		162		
Geophysical Research Corporation		155		
Geophysical Service Incorporated		201		
Geophysicist		283		
Geophysics	283	361		
Geoquest		439		
Geostatistical/geostatistics				
mapping		492		
inversion		502		
Geothermal gradient		99		
Ghost/ghosting (seismic events)	89	93	123	238
	235	238	248	
delay	91	238	248	
delay time		91		
frequency		238		

This page has been reformatted by Knovel to provide easier navigation.

## Index Terms

## Links

Ghost/ghosting (seismic events) ( <i>Cont.</i> )					
geometry		91			
ghosting		238			
notches		238			
reflection		89			
Glacial rebound	470	473			
Glacial terrain	146				
Glaciation	146	470	473		
Glenn sandstone	137	144	510		
amplitude effects		511			
rock model		510			
Glenpool field	46	137	145	385	
	420	436	459	510	
Global					
minimization method		225			
minimum		228			
positioning system (GPS)	163	246			
sea level change		470			
sea level curve		473			
Golf ball		71			
Government regulations		251			
Gradient (seismic attributes)		495			
Gradient images		486			
Gradient operator		40			
Grain size distribution		135			
Grain size	135	469			
distribution		135			
Gravitational					
field		37			
potential energy		38			

This page has been reformatted by Knovel to provide easier navigation.

<u>Index Terms</u>	<u>Links</u>			
Gravity	37	139	437	
data	437			
Grayscale image	10	380	447	
Grazing incidence	129			
Green's function	411			
Grid operations/gridding	173	287	388	388
computing	440	451	459	463
multiplication		287		
of 2D lines		388		
Gridded depth map	173	388		
Ground motion	51	160	235	
measurements		235		
Groundwater	471	536		
Group coordinate	201			
Group interval	163	353		
Group velocity	8	133		
Growth fault	434			
Gulf of Mexico	44	66	185	191
	235	252	273	275
	312	337	339	341
	346	390	422	428
	445	452	458	460
	467	481	495	507
	511	519	522	524
		526		

## Index Terms

## Links

### **H**

Hagadoorn,J.	364
Hale, D.	365
Half derivative operator	536
Half-space (seismic events)	51      123
uncertainty analysis (direct waves)	54
Half-wavelength interference condition	73
Hamilton, W.	39
Hard interface	70      130
Hard rock basins	526
Hard seafloor	65      67      435
Hardware (2D land data acquisition)	155
receiver	160
recording system	163
source	156
Headers and sorting (SEGY)	168
Headwaves	78      84      127      189
amplitude	264      270      506
seismic events	80
traveltime	78
Heavy gas	270
Heavy oil reservoir	102
Hero of Alexandria	516      518
Herodotus	39
Heterogeneous material	xx
High frequency	7
loss	8      71      148
missing	266

## Index Terms

## Links

High quality data	447				
High velocity wedge	460				
Highstand					
platforms	483				
tract	470	472	482		
Hilbert	528				
Hilbert attributes	264	486			
Hilbert transform	494				
Hilterman, F.	130				
Histograms	205	242			
Historical perspective (seismic data processing)	361				
dip moveout	365				
progress	361				
History matching	517				
History	xix	155	361	485	
2D land data acquisition	155				
reflection seismology	xix	155			
seismic attributes	485				
seismic data processing	361				
Hit map	479				
Hole problems	404				
Hooke's law	37	116			
elastic parameters	116				
Horizon					
amplitude	xxiii	275	379	390	
	431	450	473	481	
	497	507	516		
amplitude map	275	391	431	459	
	481				
amplitude slice	390	497			

This page has been reformatted by Knovel to provide easier navigation.

## Index Terms

## Links

Horizon ( <i>Cont.</i> )					
attributes	487	489			
depth maps	451				
dip	486				
peak amplitude	486				
slice	379	397	449	452	
	481	501			
time structure map	495				
tracking (seismic data interpretation)	447	452	456	458	
	467				
Horizontal coordinates	445				
gradient	452	495			
interface	56	325			
map	452				
reflectors	465				
resolution	451				
HTI anisotropy	132				
Human					
brain	288				
ear/hearing	14				
eye/visual system	264	266	447		
Huygens' principle	20	75			
Huygens-Fresnel principle	22				
Hydrocarbon(s)	393	451	492	508	
	517				
accumulations	451				
pore thickness	393	492	508		
saturation	492				
Hydrophone	236	250			
pressure sensor	250				

This page has been reformatted by Knovel to provide easier navigation.

## Index Terms

## Links

Hydrostatic pressure	99	110
Hyperbolic		
curve	56	84
moveout	56	94
reflection	93	
Hypervolume	444	

## I

Identification	403			
Igneous rock	66			
Illite clay	514			
Illumination	452	485		
Image	9	120	124	193
	204	210	434	444
	447	452	460	467
	486	519	544	
area	204	210	444	
depth	447			
depth conversion	460			
display	9			
enhancement	452			
processing	264	486		
quality	193	452	519	
ray depth conversion	460			
rays	460	467		
time-lapse 3D seismic	519			
volume	278	444		
Imaginary trace	494			

## Index Terms

## Links

Imaging (seismic data processing)	xxiii	7	9	17
	42	120	124	193
	204	210	259	434
	444	447	452	460
	467	486	519	544
computing	283			
creating common midpoint stack	291			
data processing and binning overview	261			
historical perspective	361			
image quality	519			
migration classification and velocity analysis	343			
migration concepts	321			
Immersive				
environment	448			
volume interpretation	382			
Impedance	45	62	64	68
	264	291	322	398
	403	407	412	420
	423	441	447	501
	505	511	513	516
	524			
estimation	398	501		
inversion	264	503		
log	423	501		
method	502			
model	399			
ratio	421			
section	400			
seismic attributes	501			
volume	502			

This page has been reformatted by Knovel to provide easier navigation.

## Index Terms

## Links

Implied summation	117			
Importance of migration	333			
Impulse response (waves)	6	15	328	332
dip moveout (DMO)	368	372	374	
migration	321	325	333	351
Incidence angle	24	56	68	188
	507	522		
Incident				
medium	64	506		
wave	75			
Incised valley	396	473	500	
fill	573			
stratigraphy	500			
Incoherent noise	197	199		
Incompressibility	34			
Incompressible fluid	35			
Incorrect position	461			
Index notation	114			
Indirect inversion methods	501			
Indonesia	393	398	462	491
	502			
Industry trends (3D seismic data)	180			
Inertial				
effects	139			
property	35			
Information (3D seismic data)	xxiii	401		
amplitude in space,time, and offset	505			
data volume	443			
introduction	433			
resolution	403			

This page has been reformatted by Knovel to provide easier navigation.

## Index Terms

## Links

Information (3D seismic data) ( <i>Cont.</i> )	
seismic attributes	485
stratigraphy	469
synthetic seismogram, tuning, and structure	451
Initial discovery	173
Inline direction	202     206
sections	445
Input channels (traces/record)	163
Instantaneous	
amplitude	494
attributes	394     494
extraction	489
frequency	394     494
interval velocity	464
phase	394
Instrumented oil field	251
Integer 2D fold	229
Integral transform	528
Integrated depth map	464
Interactive interpretation project components	439
2D interpretation	441
2D/3D attribute analysis	441
2D/3D combined interpretation	441
2D/3D mapping	441
2D/3D structural analysis	441
3D visualization	441
interactive 2D/3D interpretation	441
logs	440
seismic/well volume loading	441
synthetics	441

This page has been reformatted by Knovel to provide easier navigation.

## Index Terms

## Links

Interactive interpretation	438	481		
2D/3D interpretation	441			
project components	439			
systems	438			
Intercept-gradient crossplot	524			
Interchangeable sections	236			
Interface	34	42	56	60
	127	266	406	
Interference	185	419	423	431
	477	490		
other survey	185			
patterns	419			
phenomena	423			
Interior least tern	251			
Internal costs	174			
Internal multiple	95			
Internet				
security	499			
traffic	500			
Interpolation	431			
Interpretation (extracting geologic information from				
seismic data)	45	96	175	254
	262	264	273	276
	294	362	383	386
	392	396	401	
amplitude in space, time, and offset	505			
costs	175			
data volume	443			
introduction	433			
products	448			

This page has been reformatted by Knovel to provide easier navigation.

## Index Terms

## Links

Interpretation (extracting geologic information from seismic data) ( <i>Cont.</i> )	
seismic attributes	485
seismic section	386
stratigraphy	469
structure	451
synthetic seismogram, tuning, and resolution	403
systems	438
Interpretation of seismic data (introduction)	433
background information	433
interactive interpretation project components	439
interactive interpretation systems	438
purpose	433
Interpretation	
products (data volume)	448
systems	438
Interpreted seismic line	482
Interpreted seismic section	386
Intersection bands	481
Interval	
attributes	487
transit time	508
velocity	46    272    274    304
Intervals	
	46    227    272    274
	304    487    508
Intrinsic	
absorption	144
anisotropy	134

## Index Terms

## Links

Inverse				
filter	294			
normal moveout	312			
problem	120	224		
transform	529			
velocity	544			
Inversion		17	42	45
		223	526	529
invertibility	529			
methods	17	42	45	
optimization	223			
problem	120	224		
Invertibility		529		
Invest/Investment		173	179	182
capital	173			
trends	183			
Irian Jaya		462		
Irregular surveys		444		
Isochron (time interval)		389	464	
Isopach map		463		
Isoprobability contours		525		
Isotropic elastic				
case	4	118	120	127
solid	4			
Isotropic velocity		308		
scan	309			
Iterations		225		

## Index Terms

## Links

### **J**

Jump correlation	456				
Jungle environment	181				
Jurassic					
age	386	394	462	494	
sand	386	462			
sand map	386				
shale	386	462			
shale map	386				

### **K**

Kais formation	387	462			
average velocity and depth	387				
average velocity map	388				
depth map	389				
Karst					
features	146				
topography	482				
Keho, T., and Samsu, S.	462				
Kernel	541				
Kinetic energy	36	41	118	139	
Kirchhoff					
2D prestack depth migration	352				
depth migration methodology	351	364			
diffraction integral	75				
migration	351	353	364		
theory	75				
Knott elastic wave theory	xx				
Kriging	393	459	491		

This page has been reformatted by Knovel to provide easier navigation.

## Index Terms

## Links

### L

Laboratory measurements	143	508		
core	143			
Lagrangian				
function	38	40	119	139
mechanics	38			
Lamb elastic wave theory	xx			
Lamb, H.	80			
Lamb's problem	80			
Lamé parameter	118			
Lamina set	472			
Land 3D seismic design optimization (seismic data gathering/acquisition)	223			
assumptions	226			
constraints	226			
direct method	228			
examples	230			
method 2	229			
optimization and inversion	223			
target variables	226			
Land seismic data	81	155	181	223
	240	242	266	270
	499	526		
3D seismic	181	223		
acquisition costs	181			
multicomponent 3D	526			
Land seismic survey	81	155	181	201
	223	240	242	266
	270	445	499	526

This page has been reformatted by Knovel to provide easier navigation.

## Index Terms

## Links

Land seismic survey ( <i>Cont.</i> )				
data	81	155	181	223
	240	242	266	270
	499	526		
design optimization	223			
shooting geometry	201			
Land shooting geometry (seismic data				
gathering/acquisition)	201			
cabling	215			
coordinates and related quantities	201			
crooked line 2D	219			
cross spread method	204			
fold	215			
fringe	210			
perimeter/loop method	212			
swath method	208			
template shooting	215			
Land shot record	270			
Landmark Graphics, a Halliburton Company	382	439		
Land-sea transition zones	249			
Laplace	528			
Laplacian operator	4			
Large 3D surveys	286			
Large offset	58			
Laser ranging	246			
Laster, S.	157			
Lateral				
2D/3D data migration concepts	333			
amplitude variation	477			
gradient operations	264			

This page has been reformatted by Knovel to provide easier navigation.

## Index Terms

## Links

Lateral ( <i>Cont.</i> )	
limit	71
lithology changes	464
positioning errors	364
resolution	71     333     346     423
	428
strike-slip faults	452
velocity gradient	460     467
velocity variation	93     134     262     309
	345     356     361     363
	460     465     467
waves	84
Lateral and time-lapse effects (amplitude)	511
gas	511
lithology (sandstone-clay)	514
lithology (sandstone-limestone)	513
oil saturation	513
permeability	516
porosity	513
summary	516
temperature (steamflood)	514
Latitude	483
Layer-based velocity model	42
Layered medium	92
Layered solid	127
Layers (3D seismic data)	xxiii
Layer thickness	464
Lead-in cable	236
Leaky faults	437
Lease map	449

This page has been reformatted by Knovel to provide easier navigation.

## Index Terms

## Links

Leasehold information	448
Leasing situations	171
Least time principle	23
Legendre	528
Legends and literature (seismic data interpretation)	437
Lena image	264      266
Life cycle	180
Lifetime rate of return	177
Light	132
Limestone	xxiii      66      135      140
	435      469      502      513
lithology	513
Line header	156      285
Line response	326      329
Linear	
events	53
fit	462
function	386      388      454      462
model	387      429      455      462
motion	39
moveout	79
profile	191
regression	491
sweeps	158
velocity	191      386      429      454
	462
$v(x,z)$ effects	417
$v(z)$ function	275
$v(z)$ medium	337
$v(z)$ survey design	337

This page has been reformatted by Knovel to provide easier navigation.

## Index Terms

## Links

Linearity	534
Lines (vertical cuts)	445
Linpack benchmark	288
Linux operating system	287
Lisbon earthquake (1755)	xix
Listen time	164      189
survey predesign	189
Literature and legends (seismic data interpretation)	437
Litharenite sandstone	135
Lithification	274
Lithologic variability	389      464
Lithology	33      42      135      274
	389      405      434      464
	495      513
lithification	274
sandstone-clay	514
sandstone-limestone	513
seismic data interpretation	434
variations	389      464
Lithostatic pressure	99
Live oil	103
Local minimization method	225
Local minimum	228
Logistics	185
Log/logging	4      45      135      137
	143      147      354      391
	403      412      417      436
	440      448      454      502
	508
correlation	440

This page has been reformatted by Knovel to provide easier navigation.

## Index Terms

## Links

Log/logging ( <i>Cont.</i> )				
data	135	417	502	
digital logging	137	448		
interactive interpretation	440			
neutron density logging	405			
neutron porosity logging	137			
sonic logging	4	45	137	143
	147	354	403	417
	436	448	454	
Long 2D seismic lines	473			
Long period multiples	96	435		
Long wavelength statics	435			
Longitudinal wave	4	34		
Loop/perimeter method (land shooting geometry)	212			
Loss curve	423			
Lossless medium	147			
Low energy events	127			
Low frequency	71	266		
missing	266			
Low impedance	400			
Low porosity	150			
Low slope events	266			
Low velocity layer	150	316		
Lowstand				
refugios	483			
tract	470	472	482	
wedge	472			
Lumley, D .	517			
Lurching	236			

## Index Terms

## Links

### M

Magnetic properties	38			
Magnetics	437			
Mammals	251			
Manual inversion	225			
Manual warping	460			
Map migration	460			
Map view geometry	202			
Map/mapping	134	202	275	386
	391	393	431	441
	447	449	451	463
	480	492	495	
2D/3D	441			
amplitude	275	385	391	431
	447	459	481	
carbonate fraction	464			
channel hit	479			
Cretaceous	386	389	451	464
Cretaceous depth	389			
Cretaceous geologic subcrop	451			
Cretaceous structure	464			
depth	386	388	451	459
	462	464	467	
fault	452	496		
fold	211			
fracture	134			
geologic subcrop	451			
geostatistical	492			
hit	479			

This page has been reformatted by Knovel to provide easier navigation.

## Index Terms

## Links

Map/mapping ( <i>Cont.</i> )				
horizon amplitude	275	391	431	459
	481			
horizon depth	451			
horizontal gradient	452			
horizon time structure	495			
isopach	463			
Jurassic sand	386			
Jurassic shale	386			
lease	449			
mappable features	447			
map view geometry	202			
migration	460			
net sand	393			
non-unique	459			
probability	393	492		
reflectivity	322			
structure	385	388	458	464
	467	495		
surface velocity	388			
thickness	430			
time structure	385	388	458	464
	467	495		
velocity	388	463		
wells-only depth	459			
Mappable features	447			
Marginal wells/producers	xxiii	175		
Marine 3D seismic survey	67	89	185	223
	235	270	275	423
	455	460	517	

This page has been reformatted by Knovel to provide easier navigation.

## Index Terms

## Links

Marine 3D seismic survey ( <i>Cont.</i> )				
data	67	235	270	275
	455	460	507	
acquisition methods	89	235	423	507
		517		
Marine acquisition methods (seismic data gathering/acquisition)	89	235	423	507
		517		
environmental effect	251			
fixed receiver systems	248	517		
source	239	423		
source array	242			
towed receiver systems	235			
Marine				
air gun	17			
cable	237			
ecology	251			
fixed-receiver acquisition systems	248	517		
mammals	251			
seismology	124			
towed-receiver acquisition systems	235			
Marine seismic data	67	235	270	275
	455	460	507	
Marine seismic source	239	242		
array	242			
Marine seismic surveys	65	67	89	124
	148	155	185	223
	235	270	275	423
	460	507		

## Index Terms

## Links

Marine seismic surveys ( <i>Cont.</i> )				
acquisition methods	89	235	423	507
	517			
data	67	235	270	275
	455	460	507	
source	239	423		
source array	242			
Marked-up section	456			
Market prices	171			
Marmousi velocity model	19	21		
Marsh habitat	251			
Mass density	6	403		
Massively parallel architecture/configuration	287	364		
Matched impedance	65	513		
Matched pursuit decomposition	395	499		
Matrix velocity	138			
Maximum				
convexity curve	88			
flooding surface	472			
fold	212	313		
near offset	216	227	231	
offset	188			
recording time	189			
uncertainty direction	466			
Maxwell's equation	xx			
Mayne, W.	156			
Meander channels	435			
Meandering feature	390			
Mechanical waves	3	33	38	118
	132	138		

This page has been reformatted by Knovel to provide easier navigation.

## Index Terms

## Links

Medical imaging	253	255	322	448
	486	499		
applications	253			
Megabyte	287			
Megaflop	287			
Megapascal (mPa)	35			
Methane	108			
Method 2 (land 3D design optimization)	229			
Method and Apparatus for Locating Ore Bodies (1917)	xx			
Metric system	155			
Metrodorus of Chios	xix			
Midpoint	56	60	164	166
	191	201	203	209
	215	221	242	244
	248	250	270	276
	279	327	330	353
	366	369	443	
bin	270			
cluster	271	276		
coordinate	201	203		
coverage	210	248	250	327
	330	353		
footprint	216			
gathers	166			
geometry (2D crooked line)	221			
interval	191	204		
lines	209			
plot	215			
scatter	279			
tracks	244			

This page has been reformatted by Knovel to provide easier navigation.

## Index Terms

## Links

Mie scattering	146				
Migrated					
3D data	445				
data	322	404	443	445	
	455	485	503		
depth volume	467				
image	322				
seismic section	398				
section	455				
time	349				
volume	443	485			
Migration	88	189	193	195	
	261	269	278	321	
	370	398	404	417	
	423	433	437	443	
	445	455	460	464	
	467	485	503		
3D data	445				
action	350				
algorithm	349				
amplitude behavior	346				
aperture	327				
classification and velocity analysis	343				
concepts	321				
data section	455				
data volume	443	485			
decision diagram	347				
depth accuracy	346				
distance	326	330	333	340	
importance	333				

This page has been reformatted by Knovel to provide easier navigation.

## Index Terms

## Links

Migration ( <i>Cont.</i> )				
impulse response	321	325	333	351
topography	262			
types	343	437	460	
velocity	189	343	438	465
velocity analysis	356	344	438	
Migration classification and velocity algorithms				
overview	349	351		
analysis	343			
Kirchhoff depth migration methodology	351			
migration types	343			
migration velocity analysis	356			
Stolt migration theory	348			
Migration concepts (seismic data processing)	321			
3D migration	327	330		
constant velocity migration and modeling pairs	322	328		
dip from seismic slope	326	329		
lateral resolution in 2D and 3D data	333			
migration distance	327	330		
survey design for linear $v(z)$	337			
variable velocity migration and modeling pairs	327	330		
Migration decision diagram	347			
Migration depth accuracy	346			
Migration distance	326	330	333	340
migration concepts	327	330		
Migration from topography	262			
Migration importance	333			
Migration impulse response	321	325	333	351
geometry	333			

## Index Terms

## Links

Migration types (seismic data processing)	343	437	460	
2D migration	343			
3D migration	344			
depth migration	344			
poststack migration	344			
prestack migration	344			
time migration	344			
Migration velocity	189	343	356	438
	465			
analysis	343	356	438	
uncertainty	465			
Milne seismograph	xx			
Mineral density	140			
Mineralogy	7	33	135	137
	140	501		
Minerals Management Service	252			
Minimization problem	24			
Minimum phase	298			
Minimum travelt ime	84			
Miocene				
age	393	398	462	481
	491	502		
interval	393			
Misfit	225	501		
function	225			
Missing				
far offsets	278			
high frequencies	266			
log intervals	404			

## Index Terms

## Links

Missing ( <i>Cont.</i> )	
low frequency data	266
near offsets	278
Mississippi Canyon	185
Mixing law	109     140
Mode conversion	33     113     123     127
	144     248     250     362
cases	124
imaging	124
waves in solids	123
Mode-converted imaging	124
Mode-converted waves	113     248     250
Modeling	7     17     42     322
	330
<i>See also</i> specific model type.	
Modeling/migration pairs	322     330
constant velocity migration	322     328
variable velocity migration	327     330
Modern analog	435
Modulus (amplitude)	530
Monochromatic field	74
Monochromatic wave	12
Moore's law	363
Moveout (time delay)	56     95.
<i>See also</i> Dip moveout and Normal moveout.	
Movie loop	449
Mudstone	135
Multiattribute analysis (reservoir properties)	492
Multiazimuth vertical seismic profile	404
Multichannel process/processing	268     363     480     487

This page has been reformatted by Knovel to provide easier navigation.

## Index Terms

## Links

Multicomponent					
bottom cable	248				
geophone	160	163			
receivers	17	203			
seismic data	123	256	345	526	
Multidimensional transform	528				
Multioffset vertical seismic profile	404				
Multipathing	364				
Multiphysics	37				
Multiple					
reflection interference	506				
sources	159				
steamer acquisition	237				
suppression	17	261	269	363	
Multiples (velocity layering)	46	67	93	95	
	127	144	235	264	
	276	294	296	304	
	419	434	438	519	
Multitrace windowing	489				
Mute	189	261	264	303	
	313	438	444		
cut	313	438			
zone	438	444			

## **N**

Naming conventions	257				
Nanoscale technology	284				
National Marine Fisheries Service	252				
Natural bin size	207				
Natural gas. <i>See</i> Gas.					

This page has been reformatted by Knovel to provide easier navigation.

## Index Terms

## Links

Navigation	246			
Near offset	164	167	278	
section	167			
Nearest neighbor decimation	476			
Near-field elastic waves	5			
Near-field region	122			
Near-surface materials	150	152		
Near-surface velocities	270			
Need to process (seismic data)	261			
amplitude corrections	261			
noise reduction	261			
travelttime corrections	261			
wavelet adjustments	261			
Neogene carbonate	392			
Nesting	251			
Net sand	393	491		
map	393			
thickness	491			
Net value (3D seismic data)	176			
Neural networks	490			
Neurons	288			
Neutron density log	405			
Neutron porosity logging	137			
New Orleans	481			
Newton's law	37			
Nine-component case	256			

## Index Terms

## Links

Noise	31	96	142	185
	196	236	248	261
	264	301	313	337
	361	412	431	458
	477	486	494	506
amplitude	198			
classification	196			
incoherent	197	199		
reduction	261			
removal/filtering	264			
Nomenclature	444			
Non-acoustic reflection amplitude	113			
Non-commercial gas saturation	512			
Non-geologic variations	227			
Nonhyperbolic curves	317			
Non-hyperbolic moveout	93	133	309	
curves	133			
Nonlinear				
equations	40			
medium	8			
regression	137	510		
sweeps	157			
theories	139			
waves	40			
Non-normal incidence	68			
Non-reservoir rocks	525			
Nonspecular rays	71			
Non-square bin	273			
Non-unique answer	120	532		
Non-unique map	459			

This page has been reformatted by Knovel to provide easier navigation.

## Index Terms

## Links

Normal distance	60				
Normal incidence	63	125	262	407	
	460				
coefficient	65				
reflection	63	125	407		
Normal moveout (NMO)	56	189	261	266	
	269	276	298	301	
	346	361	363	365	
	367	369	374	502	
application	266				
common midpoint stack creation	301				
correction	301	313			
flattening	304				
process	301				
programs	298				
stretch	302				
stretch mute	303				
time	367	369			
velocity	189	269	276	298	
	304	310	363	502	
Normal moveout velocity	189	269	276	298	
	304	310	363	502	
analysis	269	276	298	304	
	306	310	363	502	
errors	304				
function	304				
Normal to the interface	24				
Normal vector	465				
Normalization	228	261			
North Sea	238	517	525		

This page has been reformatted by Knovel to provide easier navigation.

## Index Terms

## Links

North Sea Basin	381	448		
Northwest Java Basin	398	502		
Notch (amplitude spectrum)	538			
Number of units	157			
Numerical modeling	448			
Numerical Recipes (1989)	137			
Nylon rope	236			
Nyquist frequency	157	187	238	539
Nyquist wavenumber	544			

## O

Objective function	225			
Observational seismology	xx			
Observer notes	159			
Ocean	4	9	37	42
	51	66	248	345
	363	471		
floor	9	66	248	250
surface	42			
temperature	471			
Ocean-air interface	4			
Ocean basin filling	471			
Ocean bottom cable (OBC)	248	345		
4C data	345			
Ocean bottom seismometer (OBS)	249	363		
acquisition	250			
Octaves	14			
bandwidth	15			
Off-end shot profile	53			
Office of Naval Research	252			

This page has been reformatted by Knovel to provide easier navigation.

## Index Terms

## Links

Offset	xxii	53	58	164
	188	201	205	212
	254	275	280	365
	443	520	522	
amplitude effects		522		
clustering	205	276		
dip moveout		365		
disribution	277	280	520	
range		188		
summation		443		
variation effects		275		
vector		201		
Offset (dip moveout)		365		
Offset effects (amplitude)		522		
Offset/fold variation effects (bins)		275		
Offset range (survey predesign)		188		
Oil	99	102	111	135
	138	140	171	451
	490	513	516	
bright spot		111		
density		103		
enhanced recovery	451	514		
modulus	103	513		
reservoir fluid properties		102		
saturation	108	111	511	516
sound speed		106		
velocity		103		
Oil (reservoir fluid properties)	102	513		
density		103		
modulus and velocity	103	513		

This page has been reformatted by Knovel to provide easier navigation.

## Index Terms

## Links

Oil bulk modulus	513				
Oil field	490				
Oil price	171				
Oil saturation	108	111	511	516	
time lapse effects (amplitude)	513				
Oil-water contact	513				
Oklahoma	46	137	385	420	
	436	510			
Onboard seismic processing	237				
One-pass migration	344				
Onion concept (3D seismic data)	xxii				
Onlap	475	503			
Operating system	438				
Operational issues	185				
Operations per data sample	289				
Operator aliasing	193	351			
Optimization	137	223	228	230	
	238	417	465	501	
3D survey design	223				
examples	230				
inversion (land 3D design)	223				
methods	225				
problem	137	223			
results	233				
theory	223				
weights	230				
well trajectories	465				

## Index Terms

## Links

Optimum				
cable depth	238			
design	226	228	230	
examples	230			
shooting	223			
well trajectories	465			
Orchard field	155			
Orientation	444			
Other survey interference	185			
Over-migrated result	357			
Overpressure	100	251		
Overthrust areas	364			
 <b>P</b>				
Parallel line method	242			
Parameters	34	120	138	
coupling	120			
waves in fluids	34			
waves in porous solids	138			
Parasequence set	472			
Partial differential equations	527	536		
Particle motion (waves)	4	34	121	133
	236			
Particle velocity	160	248	251	
Pattern recognition	157			
Peak	12	251	384	410
	447	459	507	
amplitude	410	459	507	
particle velocity	251			
Peciko field	393	491		

This page has been reformatted by Knovel to provide easier navigation.

## Index Terms

## Links

Pegleg multiple	95				
Pennsylvanian age	137	396	500	511	
Perimeter/loop method (land shooting geometry)	212				
Perimeter survey	212				
Periodic components	540				
Periodicity	527				
Periodic signals detection (Fourier transform)	540				
Permanent receiver installation	517				
Permanent seismic installation	251				
Permeability	33	139	141	516	
effects on amplitude	516				
Permian age	420				
Persian siege of Barce	xx				
Personal computer	284	448			
Petabyte	284				
Petaflop	287				
Petroleum reserves	483				
Petroleum seismology	xxi	270			
advances	xxi				
Petroleum traps	452				
Petrologist	135				
Phase	xxii	7	70	76	
	129	133	189	261	
	348	351	364	409	
	426	434	441	473	
	489	494	499	527	
	530	532	535	537	
change	72	129	189		
discontinuity	538				
factor	409				

This page has been reformatted by Knovel to provide easier navigation.

## Index Terms

## Links

Phase ( <i>Cont.</i> )				
match	441			
rotation	261	441		
shift	71	77	348	351
	364	426	499	
shift migration	348	351	364	
shift plus interpolation	351			
spectrum	76	410	412	527
	532	535	537	
unwrapping	532			
velocity	7	133		
wrapping	535			
unwrapping	532			
Physical domain	349			
Physically-based attribute	486			
Physics	113	120	275	344
	347	349	351	433
	447	459	486	490
	508	536		
Physics-based interpolator	490			
Physics-based rock model	508			
Piecewise continuous velocity model	42			
Piezoelectric ceramic crystal	236			
Pinchout	449			
Pinnacle reefs	435	473		
Pitching	236			
Pitfalls	433			
Pixels	447			
Plates (color)	377			
Platform margin	392			

This page has been reformatted by Knovel to provide easier navigation.

## Index Terms

## Links

Play generation	173			
Pleistocene age	481			
Point diffractor	84	87	322	327
model	88			
Point response	330	332		
Point source (seismic events)	16	81	83	133
	242			
Point-wise extraction	489			
Poisson ratio	118	507		
Polar coordinate system	530			
Polar form	530	534		
Polarity/polarization (wave)	5	84	132	410
	414	424	427	435
	524			
direction	132			
reflections	424			
reversal	410			
SEG convention	414			
Polarization direction	132			
Polymers	536			
Poor data areas	459			
Pore fluid	xxii	7	33	65
	110	138	481	495
	501	511	514	
changes	xxii	511		
density	140			
mixture	110	140		
properties	514			
space	135			
viscosity	139	141		

This page has been reformatted by Knovel to provide easier navigation.

## Index Terms

## Links

Pores in rock	146			
Poroelastic medium	113			
Poroelastic property	3			
Porosity	3	7	33	38
	41	46	65	113
	135	146	150	394
	492	494	501	510
	513	516	526	
amplitude effects	513			
prediction	494	526		
Porous elastic solids	38			
Porous fluid-saturated rock	510			
Porous frame moduli	142			
Porous rock velocity	150			
Porous solids (waves in)	41	46	135	
attenuation and dispersion	144			
elastic solids	38			
empirical relationships	136			
equation of motion	139			
frame moduli	142			
Gassmann theory and wavespeeds	141			
parameters	138			
rock	135	150		
rock density	140			
rock velocity ranges	150	152		
wave types	140			
Position uncertainty	465			
Position vectors	201			

## Index Terms

## Links

Positioning	155	235	245	
issues	235			
equipment	236	245		
towed receiver systems	245			
error	246			
Postcritical incidence angle	70			
Postcritical reflection	69	79	130	189
reservoir	130			
Poststack				
data (3D seismic)	xxiii			
depth migration	346			
dimensions	254			
migration	269	328	344	346
	358	361	364	366
	369	443	502	
time migration	269	502		
traces	269			
Potential energy	36	38	41	119
	139			
Potential reservoirs	480			
Power line hum	499			
Power transformers	15			
Precritical incidence angle	70			
Precritical reflection	79			
Precursor noise	292			
Predicted amplitude change	518			
Predictive deconvolution	296			
Predictive rock model	508	517		
Predictor	493			
Preference weights	226			

This page has been reformatted by Knovel to provide easier navigation.

## Index Terms

## Links

Present value	177			
Press, F., et al.	527			
Pressure	7	34	40	42
	99	110	115	137
	235	274	437	518
condition	42			
data	437			
measurements	235			
increase	7			
definition	40			
depletion drive mechanism	518			
drop	519			
gradient	99	110		
reservoir fluid properties	99			
Pressure/temperature range (reservoir fluid properties)	99			
Prestack				
ellipse	368	372		
focus	367			
impulse response	331	371		
migration	88	202	269	286
	291	298	309	331
	344	346	351	354
	359	361	364	367
	374	434	443	460
		522		
multiples	296			
partial migration	365			
process/processing	269	272		
seismic data	xxiii	131	354	
seismic line	354			

This page has been reformatted by Knovel to provide easier navigation.

## Index Terms

## Links

Prestack ( <i>Cont.</i> )					
theory		88			
time migration		346			
trace basis		181			
traces	168	181	266	269	
	275	365			
Prestack amplitude factors		505			
Prestack data	253	292	367	433	
	452	505	522		
2D data		253			
3D data		253			
amplitude factors		505			
Prestack depth migration	298	346	351	355	
	359	364	374	434	
	460				
velocity analysis		359			
Prestack interpolation		207			
Prestack interpretation		91			
Price-earnings ratio		172			
Pricing trends		181			
Primary					
arrival		238			
event		95			
pulse	90	240			
reflection	89	127	420		
Primary-to-bubble amplitude ratio		239			
Principle of least time		23			
Probability	383	393	466	480	
	492				
map	393	492			

This page has been reformatted by Knovel to provide easier navigation.

## Index Terms

## Links

Probability ( <i>Cont.</i> )	
table	492
Procedural classification (seismic attributes)	489
Processing	
algorithms	527
costs	174      188
example	268
flow (seismic data processing)	266      268
footprint	477
problems	438
report	444
speed (computing)	286
times	269
velocities (Earth model)	405
Production	
251	435      448      517
519	
data	448
history matching	517
problems	436
seismic data interpretation	437
surface	519
technology	251
Profit (3D seismic data)	176
Progradation	482
Prograding delta	
depositional sequence	476
Progress in seismic data processing	361
3D processes	363
anisotropy	362
depth migration	364

This page has been reformatted by Knovel to provide easier navigation.

## Index Terms

## Links

Progress in seismic data processing ( <i>Cont.</i> )	
dip moveout	361
Proliferation of data	495
Propagation angle	131
Proposed locations	449
Prospect definition	173
Prospect key feature	449
PS imaging	248
Pseudocode	229
Public land	251
Pulse	161
Pure mode transverse waves	6
Purpose (seismic data interpretation)	433
P-wave	4      34      118      120
	122
modulus	118

## **Q**

Quadrature trace	494
Quality control (3D seismic data)	xxii      146      150      313
	419      441      463
quality factor	146      150      419
Quantitative seismic interpretation	508
Quartz	132      135      140      142
	513
arenite sandstone	135
Quasi P-wave	4
Quasi S-wave one	4
Quasi S-wave two	4

## Index Terms

## Links

### R

Radar technique	xxiii			
Radiation pattern	17	91	121	123
	242	364	505	
Radiation pressure	40			
Radio-positioning	246			
Radius	530			
Radon	528			
RAM and disk storage (computing)	283			
Ramform ships	238			
Random noise	164	198	276	313
	506			
Rate of return (3D seismic data)	176			
Rate of sedimentation	470			
Rate of water depth increase	470			
Raw seismic data	261			
Raw time	369			
Raw traveltime	263			
Ray				
bending	24	327	344	435
	460			
depth conversion	460			
equations	23			
fan	21	354		
theory	19			
tracing	127	364		
Rayleigh wave	xx	5	121	146
scattering	146			
speed	121			

## Index Terms

## Links

		19	23	58	97
Raypath					
geometry		23			
Rays		xx	5	18	23
		51	58	61	87
		89	97	121	146
		166	189	205	327
		344	354	364	404
		435	460		
raypath		19	23	58	97
		205			
Real-time transmission			248		
Rebinning			276		
Receiver					
array		162			
balancing		291			
cable (towed receiver systems)		235			
density		216	227	232	
directivity		17	291		
footprint		244			
geometry		213			
ghost		90	240		
group		192	216		
hardware		160			
intervals		192	218	227	236
patch		213			
spacing		53			
spread		223			
template		216			

## Index Terms

## Links

Receivers	53	90	155	160
	192	213	216	218
	223	227	232	235
	244	291		
Reciprocity (waves)	17	203		
principle	17			
Recording system	53	90	155	160
	192	213	215	218
	223	227	232	235
	244	248	291	403
channels	163	227		
geometry	53	403		
hardware	163			
receiver	53	90	155	160
	192	213	216	218
	223	227	232	235
	244	291		
unit	248			
Recursion	406			
Recursive integration	501			
Red Fork sandstone	396	500		
Red-green-blue color code	447			
Reefs	273	333	423	435
	482			
Reference frequency	148			
Refining	179			
Reflecting interface	273			

## Index Terms

## Links

Reflection (seismic events)	xx	xxii	42	51
	56	84	128	156
	164	166	190	241
	262	270	273	291
	294	407	411	424
	433	447	459	477
	488	492	501	506
	511	516	519	524
angular reflection coefficient		68		
change		519		
characteristic (seismic attributes)		488		
coefficient	xxii	62	68	84
	128	141	155	291
	294	301	406	411
	424	447	459	477
	492	501	505	511
	516	519	524	
coefficient approximations (waves in solids)		130		
coefficient change		519		
coefficient phase		413		
coefficient series	294	407	411	501
dispersal		167		
events		42	241	
Fresnel zone		71	73	
geometry		56		
hyperbola		79	270	
normal incidence		63		
phase		413		
physics	433	459		
point dispersal		167		

This page has been reformatted by Knovel to provide easier navigation.

## Index Terms

## Links

Reflection (seismic events) ( <i>Cont.</i> )				
points	56	156	164	166
	190	262		
postcritical reflection	69			
process	503	505		
seismology	xx	51	141	155
reflecting interface	273			
seafloor	67			
series	294	407	411	501
synthetic seismogram	407			
time	301	406		
traveltime	56			
Reflectivity				
image	257	322		
map	322			
Reflector				
depth	56	190	262	336
	338	473	524	
dip	336			
geometry	262			
reservoir	473			
terminations	524			
	190			
Refraction				
statics	78	241	270	316
	435			
survey	270	316	435	
	316			
<i>See also</i> Headsaves				
Regional stress fields	8			
Regional stress orientation	132			
Regression	142	490	508	

This page has been reformatted by Knovel to provide easier navigation.

## Index Terms

## Links

Regulations	251				
Repeatability	xxii	247	517	519	
time-lapse 3D seismic	xxii	520			
Repeated index summation	117				
Repositioning	520				
Reserves estimate	xxiii				
Reservoir	xxii	139	187	251	
	333	400	417	437	
	473	476	481	485	
	489	501	505	508	
	512	515	519	521	
	524				
delineation	497				
decisions	489				
engineering	451				
features	489				
fluid mixture	108				
fluid ranges	111				
intervals	502				
management	489	517			
prediction case history	393				
pressure	139				
reflector	524				
rocks	473	525			
scorecard	521				
temperature	139				
thickness	519				
Reservoir fluid properties (waves)	99				
pressure and temperature range	99				
brine	106				

This page has been reformatted by Knovel to provide easier navigation.

## Index Terms

## Links

Reservoir fluid properties (waves) ( <i>Cont.</i> )				
dependencies	111			
fluid mixture	108			
gas	100			
oil	102			
parameters	111			
ranges	111			
Reservoir properties prediction (seismic attributes)	187	393	485	489
	502	508		
case history	491			
multiattribute analysis	492			
procedure	489			
Residual				
curvature	359			
diffraction	357			
multiples	438			
oil saturation	516			
statics	318			
Resolution	xxii	78	207	298
	301	337	362	410
	423	427	453	482
	490	494	499	519
lateral	xxii			
limit	430	499		
synthetic seismogram	427			
thickness	428			
time-lapse 3D seismic	519			
Resolving power	429			
Resonant frequency	162			
Restart capability	288			

This page has been reformatted by Knovel to provide easier navigation.

## Index Terms

## Links

Result values	230			
Reuss model	514			
Reverse polarity	67	380		
color image	380			
Reverse time	351	364		
migration	351			
Ricker wavelet	76	424		
Right depth	362			
Right lateral location	362			
Rigid displacement	114			
Rigidity	118			
Ringy appearance	437			
Risk/risk assessment	xxiii	173	193	431
	434	493	519	
assessment	520			
RMS amplitude	459			
Roabiba sand	462			
Rock				
as porous solid (waves)	135			
calibrated	510			
density (waves in porous solids)	140			
fabric	134			
failure	451			
fragment inclusions	146			
model	482	508		
physics	482	514		
physics model	482			
predictive	508			
stiffness	511			
theory	508			

This page has been reformatted by Knovel to provide easier navigation.

## Index Terms

## Links

Rock ( <i>Cont.</i> )				
units	xxiii			
velocity ranges (waves in porous solids)	150	152		
Rock properties	xxiii	7	27	65
	113	134	140	433
	482	501	511	514
		517		
density	140			
fabric	134			
physics	482	514		
porosity	113			
porous solid	135			
stiffness	511			
units	xxiii			
Roll-along procedure	216			
Roll and cabling (field procedure)	164			
Root mean square	304	508		
average velocities	304			
Rope	114			
Rotation	114			
Rough surface scattering	474			
Rugose topography	482			
Rutherford, S.and Williams, R.	522			

## **S**

Safety	156			
Salinity	106			
Salt	44	106	312	364
	390	434	437	446
	458	467	481	496

This page has been reformatted by Knovel to provide easier navigation.

## Index Terms

## Links

Salt ( <i>Cont.</i> )					
body	44	437			
dome	446	458	481	496	
face	312				
formations	434				
velocity	468				
Salt-sediment interface	390	458			
Sand	66	386	390	435	
	473	478	498	507	
bodies	435	481			
channel	473	478	498		
map	386				
quality	481				
reflection events	390				
thickness	481				
Sand-rich sediments	473				
Sandstone	xxiii	135	140	143	
	400	424	469	491	
	502	511	513	518	
	524				
bodies	491				
gas reservoir	518	525			
lithology	513				
reservoir	400	491	516	518	
	524				
targets	524				
Sandstone-clay lithology	514				
Sandstone-limestone lithology	513				

## Index Terms

## Links

Saturated rock	
density	140
moduli	141
P-wave modulus	143
Savings/gain model (3D seismic data)	174
gains	176
net value	176
profit	176
rate of return	176
savings	175     179
Scalar migration	345
Scalar quantity	119     236
Scaling property	535
Scattered waves	24       64       124
Scatterer	322
Scattering	24       64       124       128
angles	125     128
fault zones	452
regimes	146
rough surface	474
waves	24       64       124
Schneider, W.	364
Scientific programming	288
Scientific visualization	486
Screen propagator	364
Seafloor	9       42       65       124
	248     273     298     434
	471
multiples	248     298

This page has been reformatted by Knovel to provide easier navigation.

## Index Terms

## Links

Seafloor ( <i>Cont.</i> )				
reflection	67			
spreading	471			
topography	434			
Sea level change	470	472	482	
global	470			
rise	482			
Search method	459			
Seasonal changes	460			
Second critical angle	125	130		
Second Fresnel zone	78			
Secondary source	22	75		
Section migration	460			
Sections (vertical cuts)	445			
Security system	161			
Sediment	135	148	469	473
supply	481	491		
Sedimentary rock	135	148		
Sedimentary systems	469			
Sedimentation	469			
rate	470			
Sedimentologist	135			
Sediment-salt interface	481			
Seed point	384	459	481	
SEGY format	168	285	414	
headers and sorting	168			
Seismic acquisition	251			
Seismic amplitude	512	515	517	

## Index Terms

## Links

Seismic attributes (seismic data interpretation)	485
classification schemes	486
definition and history	485
reservoir properties prediction	489
selected general attributes	494
Seismic contractor	251
Seismic crew costs	66
Seismic data characteristics	407     413     444
volume	444
Seismic data display	380     447
data volume	447
Seismic data gathering/acquisition	xxii     42     153     407
2D land acquisition	155
data dimensionality and components	253
financial aspects of 3D seismic	171
land 3D design optimization	223
land shooting geometry	201
marine acquisition methods	235
survey predesign	185
volume	443
Seismic data interpretation	xxii     401
amplitude in space, time, and offset	505
analysis	489
data volume	443
introduction	433
seismic attributes	485
stratigraphy	469
structure	451
synthetic seismogram,tuning, and resolution	403

This page has been reformatted by Knovel to provide easier navigation.

## Index Terms

## Links

Seismic data processing history	361				
progress	361				
Seismic data processing	xvi	xxii	245	261	
	361	407	443		
bins	270				
filtering and noise removal	264				
history	361				
need to process data	261				
processing flow	266	268			
volume	443				
Seismic data volume	xxii	443			
3D seismic	xxii				
data 2D subsets	444				
interpretation products	448				
seismic data display	447				
Seismic depth migration	365				
Seismic events (waves)	51	96	384	403	
classification tree	96				
diffraction	84	87			
ghost	89				
half space	51				
headwave	78				
point source	81	83			
reflection	56				
velocity layering	92				
Seismic experiment	256				
Seismic image/imaging (data processing)	17	189	251	259	
computing	283				
creating common midpoint stack	291				
data processing and binning overview	261				

This page has been reformatted by Knovel to provide easier navigation.

## Index Terms

## Links

Seismic image/imaging (data processing) ( <i>Cont.</i> )				
historical perspective	361			
migration classification and velocity analysis	343			
migration concepts	321			
Seismic interpretation	45	96	175	254
	262	264	273	276
	294	362	383	386
	392	396	401	
project	439			
systems	438			
Seismic inversion	225	361		
Seismic jump correlation	456			
Seismic modeling	26	403	486	
Seismic patterns	472			
Seismic processing programs	261			
Seismic processing	261	264		
programs	261			
Seismic profile/profiling	156	392		
Seismic quality factor	146	150	419	
Seismic rays	3	505		
amplitude	505			
Seismic response	xxii	403		
Seismic sequence stratigraphy	473			
Seismic simulation	407			
Seismic slopes	329			
Seismic stratigraphy	xxii	27	33	273
	343	390	433	435
	437	449	469	489
	495	497	503	508
Seismic survey design	337			

This page has been reformatted by Knovel to provide easier navigation.

## Index Terms

## Links

Seismic trace	51	168	170	266
headers	168	170		
structure	168			
Seismic velocity (seismic data interpretation)	436			
Seismic waves	28			
Seismic/well volume loading (interactive interpretation project)	441			
Seismically observable	516			
SeismicUn*x	261			
Selected general attributes (seismic data interpretation)	494			
azimuth	495			
coherence	495			
complex trace	494			
curvature	495			
dip	495			
gradient	495			
impedance	501			
spectral decomposition	497	499		
spice	502			
Semblance	459	485	495	
estimate	459			
Semiconductors	536			
Semi-exhaustive search	229			
Semi-transparent	381			
Sensitivity	304	358		
Sequence boundary	472			
Sequence stratigraphy	392	469	472	482
interpretation	392			
Series	74			

This page has been reformatted by Knovel to provide easier navigation.

## Index Terms

## Links

Seven-layer model	416			
Shadow processing	264			
Shale	xxiii	8	132	135
	140	386	435	462
	469	482	507	524
map	386			
Shallow events	304			
Shallow gas	519			
Shallow section	93			
Shallow water	249	435		
Shear				
deformation	118			
modulus	118	141		
splitting	8	132		
strain	115			
waves	6	8	123	132
	160	248		
Shelf-margin tract	472			
Ship				
lurch	236			
track	242			
vibration	248			
Shock waves	40			
Shooting				
between the flags	205			
direction	520			
geometry	157	160		
logistics	251			
pattern	248			
problems	276			

This page has been reformatted by Knovel to provide easier navigation.

## Index Terms

## Links

Shoreline proximity	469			
Short time Fourier transform	395	497	499	
Short-period multiples	96	144		
Shot				
and group density	227			
balancing	291			
coordinate	201			
density	216	227	230	
gather	166			
intervals	192	218	227	286
	353			
profiles	53	58	61	165
	275			
records	51	53	58	166
	169	269	292	353
spacing	235			
Shot-centered template shooting	217	226		
Shot-generated noise	199			
Shot-receiver density flag	226			
Shuey approximation	131			
Shuey, R.	130	522		
Sidelobes	14			
Sifting property	533			
Signal				
amplitude	198			
analysis	528			
and noise overlap	264			
events	264			
power	240			
quality	431			

This page has been reformatted by Knovel to provide easier navigation.

## Index Terms

## Links

Signal-to-noise ratio	196	276	313	519
improvement	196			
variations	276			
Siliciclastic rock	135			
Silt	66	135		
Simulated data	224			
Simulation	42	83	85	120
	224	322	403	407
	492	501		
operator	501			
Simultaneous sources	157			
Sinc wavelet	12	14	414	425
Single-channel process	266	373	487	
Single-component receiver	160			
Single-fold geometry	208			
Single-trace windowing	489			
Six-cable acquisition	244			
Skinner horizon	397			
Sky color	146			
Slalom line	219			
Sleeve gun	239			
Slice-based interpretation	384	438	448	
system	384	438		
Slices (horizontal/subhorizontal cuts)	384	438	445	448
Slope fan	472			
Slope filtering	264			
Slowness	53	406	544	
Slow P-wave	140			
Smackover formation	394	494		
Small deformation	139			

This page has been reformatted by Knovel to provide easier navigation.

## Index Terms

## Links

Smile	359	369	371	
Smoothing	264			
Snell path	71			
Snell's law	3	23	56	68
	71	125	327	344
	411	460		
critical angles	125			
Society of Exploration Geophysicists format Y (SEGY)	168	285	414	
headers and sorting	168			
Sodium chloride	106			
Soft reservoir	518			
Soft seafloor	65			
Soft sediment	422			
Software	xvi	236	261	284
	287	365	433	438
Solids (waves in)	113			
anisotropy	131			
elastic reflection coefficient	127			
equations of motion	118			
Hooke's law and elastic parameters	116			
mode conversion	123			
reflection coefficient approximations	130			
Snell's law and critical angles	125			
strain	113			
stress	115			
velocity layering	127			
wave types and speeds	120			
Solid-solid interface	127			
Sonar technique	xxiii			
Sonic frequencies	8			

This page has been reformatted by Knovel to provide easier navigation.

## Index Terms

## Links

Sonic log (Earth model)	404			
with checkshots	404			
without checkshots	404			
Sonic logging	4	45	137	143
	147	354	403	417
	436	454		
anisotropy	417			
borehole problems	417			
data	417			
Earth model	404			
frequency range	417			
Sonic velocity	48	435		
Sort/sorting	166	168	298	300
SEGY format	168			
common midpoint stack creation	298	300		
Sound radiation	242			
Sound speed	10	246	403	
in air	10			
in water	246			
Sound waves	4	13	28	34
	36	51	236	241
Sound with sound interaction	40			
Source				
ghost	90	240		
hardware	156	403		
point	19			
power	156			
radiation pattern	121			
rocks	473	526		
rocks identification	526			

This page has been reformatted by Knovel to provide easier navigation.

## Index Terms

## Links

Source ( <i>Cont.</i> )					
spectral content	156				
waveform	27				
wavelet	75	240			
Source array	155	157	159	239	
	245				
geometry	240				
towed receiver systems	239				
Source directivity (waves)	17				
Source-receiver distance	53				
Source (seismic)	17	27	75	90	
	121	156	239	245	
	403				
South Africa	15				
Southeast Asia	10	453	474	504	
South Texas	478				
Space domain	542				
Sparkers	239				
Sparse well control	491				
Spatial aliasing	191	273	276	338	
	404	437	480	544	
condition	192				
geometry	339				
sampling	191				
Spatial frequency	541				
Spatial sampling	191	298			
survey predesign	191				
Special attributes	486				
Special classification (seismic attributes)	486				
Specific gravity	100				

This page has been reformatted by Knovel to provide easier navigation.

<u>Index Terms</u>	<u>Links</u>			
Spectral decomposition (seismic attributes)	396	497	499	
case history	396			
Spectral decomposition	396	426	486	489
	495	497	499	503
seismic attributes	396	497	499	
case history	396			
Spectral shaping	503			
Spectroscopy	74			
Speed and 3D migration (computing)	289			
Sperm whales	252			
Spherical				
divergence	29			
spreading	29			
Spherical waves	75			
Spice	502			
curves	502			
image	503			
seismic attributes	502			
Spike	15	294	297	430
	533			
deconvolution	294	297		
input (Fourier transform)	533			
Spiking deconvolution	294	297		
Split-spread shot profile	53			
Spreading losses	31			
Spring	36			
Spurious correlation	492			
Square template	227			
Square-root-t tail	27			
Squeezed dip moveout ellipse	372			

This page has been reformatted by Knovel to provide easier navigation.

## Index Terms

## Links

Stack				
(3D seismic data)	xxiii			
amplitude reflection coefficient	506			
bandwidth	301			
in	312			
response	316			
section	313	366		
Stacked sand channel systems (stratigraphy)	478			
case history	478			
Stacking	xxiii	168	197	254
	301	312	316	366
	464	478	506	522
Standing's volume factor	104			
Static(s)	93	150	202	227
	261	266	276	278
	309	316	357	363
	451	519		
common midpoint stack creation	316			
corrections	150	202	262	276
	278	316	318	
static shifts	150			
processing	227			
Station intervals	227			
Statistics	480	490	502	
inversion	502			
mapping	492			
Steam				
monitoring	517			
steamflood	514	517		
steam front	514			

This page has been reformatted by Knovel to provide easier navigation.

## Index Terms

## Links

Steam ( <i>Cont.</i> )		
steam injection	514	
temperature effects	514	
Steel	35	
Steep dips	191	273
Steep slopes	266	
Steepest descent	228	
Steeply dipping information	266	
Stiffness coefficient	117	139
Stiff reservoir rock	518	
Stochastic inversion	502	
Stock performance	171	
Stock price/big picture (3D seismic data)	171	
Stokes' theory of diffraction	xx	
Stolt migration	348	364
theory	348	
Stopping criteria	225	
Strain	113	118
energy function	119	451
waves in solids	113	
Strategic planning	173	
Stratigraphic		
analysis	473	
bed terminations	469	482
bed truncations	473	
case history	390	
detail	498	
imaging	497	
intervals	503	
modeling	27	

This page has been reformatted by Knovel to provide easier navigation.

## Index Terms

## Links

Stratigraphic ( <i>Cont.</i> )				
targets	343	476		
Stratigraphy (seismic data interpretation)	xxii	27	33	273
	343	390	433	435
	437	449	469	489
	495	497	503	508
2D seismic data	469			
3D seismic data	473	476		
analysis	473			
carbonates	482			
case history	390			
imaging	497			
modeling	27			
stacked sand channel systems case history	478			
structure case history	481			
targets	343	476		
Stratton field	454	478		
Streamers	223	235	247	276
marine data	276			
Streaming cavitation	40			
Stress	115	236	451	
component	117			
waves in solids	115			
Stretch	236	301		
mute	301			
section	236			
Strike	433	451	454	456
and dip relationships	457			
lines	433	452		
orientation	456			

This page has been reformatted by Knovel to provide easier navigation.

## Index Terms

## Links

Strike ( <i>Cont.</i> )					
strike-slip faults		452			
Strong aliasing		192			
Strong correlation		492			
Strong lateral velocity					
gradient		467			
variation		468			
Structural geology		451	495		
Structurally complex areas		481			
Structure (seismic data interpretation)		33	188	292	346
		356	404	433	437
		441	449	451	481
		489	495	503	508
analysis		441	451		
case history		481			
closure		436			
complexity		346	452	481	
extreme velocity variation		467			
fault detection and mapping		452			
features		356	495		
framework		451			
geology		451	495		
imaging		292			
interpretation		452	456		
map		464			
resolution		188			
setting		449			
structural uncertainty		464			
style		434	451		
time structure and horizon tracking		456	458		

This page has been reformatted by Knovel to provide easier navigation.

## Index Terms

## Links

Structure (seismic data interpretation) ( <i>Cont.</i> )				
time-to-depth conversion methods	459			
uplift	464			
vertical ray case history	462			
Strum noise	236			
Subaeriel erosion	482			
Subarkose sandstone	135			
Subarrays	240			
Subresolution thickness	430			
bed detection	431			
mapping	430			
Subsalt	345	351	364	434
	460	467		
amplitude versus offset analysis	351			
area	345			
imaging	434	460		
Subsidence	482			
Subthrust area	345	467		
Subtle				
fault features	495			
flexural feature	496			
structural interpretation	47			
structure	188			
Subvertical faulting	452			
Subvertical information	266			
Subweathering	262	316		
layer	262			
velocity	317			
Supercomputer	283	289	344	540
Superposition	321	326		

This page has been reformatted by Knovel to provide easier navigation.

## Index Terms

## Links

Surface geology	437			
Surface gravity waves	5	34		
Surface layer multiple	95			
Surface velocity	43	387	462	
map	388			
Surface waves	4	31	34	159
	163	199	264	506
energy	159			
Survey area	456	462		
Survey design	xxii	185	337	
linear $v(z)$	337			
predesign	185			
Survey party	163			
Survey predesign (seismic data acquisition parameters	185			
gathering/acquisition)	185			
listen time	189			
offset range	188			
spatial sampling and aliasing	191			
time sample rate	187			
total signal-to-noise improvement	196			
Swamp habitat	251			
Swan, H.	130			
Swath method (land shooting)	208			
geometry	208			
S-wave	4	121		
Sweep(s)	157	159	164	
length	159			
per unit	164			
technology	157			
time	164			

## Index Terms

## Links

Sweet spot	210	276		
Symmetric-split-spread	164			
Symmetric strain	115			
Symmetry	115	117	539	
Synapses	288			
Synclines	326			
Synthetic				
3D bin	279			
common midpoint gather	523			
convolutional model	411			
data	399			
Earth model	404			
examples	412	414		
migration	193			
reflection coefficients	407			
seismic section	501			
seismogram creation	403			
transmission loss	419			
traveltimes	406			
wavelet	408			
Synthetic seismogram	65	403	435	501
creation	403			
resolution	427			
tuning	423			
Synthetic to seismic phase match	441			
Synthetics (interactive interpretation project)	441	452		
Systems tract	472	476	483	
development	483			

## Index Terms

## Links

### T

Tagging studies	252			
Tail buoy	236	246		
Takeoff angle	56	91		
Tangent plane	24			
Target depth	274			
Targeted prestack depth migration	351			
Target parameters	233			
Targets	210	226	230	233
	272	343	476	524
depth	274			
parameters	233			
variables (land 3D design optimization)	226	230		
Technical risk	59	520		
assessment	59			
feasibility	522			
Technology stretch	448			
Tectonic				
movements	470			
setting	434			
stress	8			
subsidence	470			
Telemetry				
acquisition	363			
system	248			
Telford, W., et al.	30			

## Index Terms

## Links

Temperature	7	34	42	99
	137	274	514	
condition	7	34	42	99
		514		
effects (steamflood)		514		
increase		7		
range		99		
steamflood		514		
Temperature/pressure range (reservoir fluid properties)		99		
Template aspect ratio	216	227	229	
Template shooting	215	225	232	
land shooting geometry		215		
Temporal aliasing	187	544		
Tensor	114	116	119	
notation		117		
quantity		114		
Teraflop	288			
Terminations (bed)	9	383	391	452
	469	472	503	
classification		470		
Terminology (glossary)		545		
Test function		142		
Texas	155	454	478	
Texture segmentation		486		
The Colorado School of Mines		352		
Theoretical resolution		337		
Thermal gradient		99		
Thickness	431	477	491	
mapping		431		

This page has been reformatted by Knovel to provide easier navigation.

## Index Terms

## Links

Thin beds	410	415	423	427
	431	502	518	526
cases	424			
interference	518			
Thin layering	134	304	417	
effects	417			
media	304			
Thinly layered media	304			
Thomsen anisotropy parameters	132	362		
Thomsen, L.	362			
Three-layer model	415			
Throw	383	452	454	
<i>See also</i> Faults/Faulting				
Tides	276			
Time and effort (man days)	440			
Time average equation	137			
Time axis	345			
Time domain	407	499	527	534
	539			
Time-frequency				
analysis	541			
decomposition	497			
localization	499			
methods	395			
plots	157			
representation	499			
space	499			
spectrum	497	499	541	
transform	495			
Time function	530	532	538	

This page has been reformatted by Knovel to provide easier navigation.

## Index Terms

## Links

Time lapse					
3C3D (TL3C3D)	256				
5D data	256				
9C3D (TL9C3D)	256				
Time-lapse 3D seismic		xxii	99	247	255
		507	513	517	526
amplitude	xxii	517			
difference volumes	517				
fluid contact visibility	519				
image quality	519				
repeatability	520				
resolution	519				
TL3D	255	520			
TL3D fact sheet	520				
Time-lapse behavior		518			
Time-lapse effects (amplitude)		511			
gas	511				
lithology (sandstone-clay)	514				
lithology (sandstone-limestone)	513				
oil saturation	513				
permeability	516				
porosity	513				
summary	516				
temperature (steamflood)	514				
Time-lapse reservoir behavior		518			
Time map		467			
Time migration		304	344	349	460
data	460				
methods	349				
Time of flight		324			

This page has been reformatted by Knovel to provide easier navigation.

<u>Index Terms</u>	<u>Links</u>
Time sample rate	9      169      187      477 539
survey predesign	187
Time series	8      497      541
Time shift	534
Time slice	275      390      431      445 449      452      454      458 473      477      481      489 495
thickness	477
Time slope	53      326
Time structure	xxiii      379      385      388 447      451      456      458 467      481      486
contours	451      458
map	385      388      458
horizon tracking	456      458
seismic data interpretation	456      458
Time throw	454
Time trace	13
Time-scale representations	497      499
Time-to-depth conversion	441      452      459
seismic data interpretation methods	459
Time-velocity pairs	304
Time-zero spike	534
Top500 Internet website	288
Toplap	474
Topographic statics	316

<u>Index Terms</u>	<u>Links</u>
Topography	202      262      316      345
	364      482
extreme	202      262      345      364
statics	316
Total cost (3D seismic survey)	174
Total count of primary reflections	127
Total differential	55
Total energy	27
Total internal reflection	70
Total reflection energy	77
Total signal-to-noise improvement (survey predesign)	196
Towed acquisition	235      517
receiver systems	235      517
Towed receiver systems (marine acquisition methods)	235      517
acquisition geometry	242
cable feathering	247
flip-flop shooting	245
positioning	245
receiver cable	235
source array	239
streamers	248
Trace(s)	164      168      170      191
	285      445      502
balancing	502
header	168      170      285
length	164
spacing	191
Tracking (event)	xxiii      384      445
results	385
surfaces	445

This page has been reformatted by Knovel to provide easier navigation.

## Index Terms

## Links

Transform					
kernel	528				
space	528				
variable	528				
Transgressive systems tracts	472	482			
Transition zone	155	216	248	251	
area	248				
Translation	114				
Transmission angle	24				
Transmission coefficient	420	423	505		
Transmission effects	435				
Transmission loss	144	419	503	505	
synthetic seismogram	419				
Transmission medium	64				
Transmitted ray	24				
Transmitted wave angle	125				
Transparency	381	448			
Transverse waves	4				
Traveltime	51	53	56	84	
	88	92	261	270	
	324	352	364	404	
	406	417	460	517	
characteristics	51				
computation	364				
corrections	261				
curves	56	88			
difference	517				
geometry	53				
minimum	60				
reflection	56				

This page has been reformatted by Knovel to provide easier navigation.

## Index Terms

## Links

Traveltime ( <i>Cont.</i> )				
synthetic seismogram	406			
tables	352	365		
Triplication	326			
Trough	12	384	447	
True correlation	492			
True dip	456			
Truncations (stratigraphic bed)	473			
Tuning	423	430	477	481
	491	499	502	506
condition	500			
curve	425	430		
synthetic seismogram	423			
thickness	426	500		
wavelet pair	499			
Tunnel detection	xx			
Turbidites	473	482	503	525
Turnbull, H.	39			
Turning waves	44	189	191	349
	351			
Two spikes (Fourier transform)	538			
Two strings (array/group)	162			
Two-layer model	414			
Two-pass migration	344			
Two-way transmission coefficient	421	423		
Type II P-wave	4			
Type II wave	140			

## Index Terms

## Links

### **U**

U.S. Midcontinent	396	500		
U.S. National Center for Atmospheric Research (NCAR)	284			
U.S. transition zone	517			
Ultimate seismic experiment	256			
Ultrasonic				
core study	140			
measurements	147			
Ultrasound technique	xxiii	140	147	
core study	140			
measurements	147			
Unaliased data	195			
Unaliased image	273			
Unbalanced force	239			
Uncertainty	54	138	142	465
	491	526		
analysis	54			
position	165			
Uncertainty analysis (direct waves)	54			
method	55			
Unconformity	9	146	473	489
	504			
surfaces	9	146		
Uncorrelated	493			
Under-migrated result	357			
Undershooting	214			
Unit spacing	157			
Unit vector	7			

This page has been reformatted by Knovel to provide easier navigation.

## Index Terms

## Links

United States	251	396	500	517
Units				
of measurement	155			
of pressure	115			
of stress	115			
UNIX	284	439		
Unmigrated data	71	433		
Unocal	155			
Untested intervals	400			
Unwrap the phase	532			
Upscaling	419	436	454	508
theory	508			
Upsweep	157			
Up-to-the-basin faults	435			

## **V**

Vacuum-fluid contact	34			
Vanilla ice cream	xxiii			
Variable area	447			
Variable velocity migration	327	330		
modeling pairs	327	330		
Variational approach	41			
Variations in water velocity	460			
Variogram	491			
Vector	119	123	236	250
	256	345		
migration	345			
offset	201			
quantity	236			
seismic data	256			

This page has been reformatted by Knovel to provide easier navigation.

## Index Terms

## Links

Vector ( <i>Cont.</i> )				
seismic response	250			
seismology	123			
Vehicle traffic	264			
Velocity	7	15	15	42
	62	91	127	150
	261	273	278	304
	306	317	337	344
	351	354	363	372
	387	412	417	441
	454	460	462	465
	467	508	519	522
	526			
analysis	261	278	304	306
	317	344	351	356
	363	441	526	
dispersion correction	508			
error	357			
function	273			
gradient	42	45	337	387
	454	462	467	
information	522			
layering (classification)	96			
layering (more events)	92			
layering (multiples)	93	95		
migration analysis	356			
model	8	15	42	44
	354	412	417	455
	462	467		
panel	304			

This page has been reformatted by Knovel to provide easier navigation.

## Index Terms

## Links

Velocity ( <i>Cont.</i> )					
problems	519				
range	150				
resolution	304				
uncertainty	465				
variation	42	372	460	465	
	467				
variation (dip moveout)	372				
variation (waves in fluids)	42				
Vermeer, G.	216	298			
Vertical cable	249	363			
Vertical cuts	445				
Vertical fractures	132				
Vertical ground motion	160				
Vertical rays	460	462	467	492	
case history	462				
depth conversion	460	463			
Vertical reflection time	454				
Vertical resolution	395	416	423	427	
	431	477	519		
limit	416	427	519		
Vertical seismic profile (VSP)	173	354	403	420	
	436	448	452	472	
analysis	420				
data	472				
Earth model	404				
Vertical seismic sections	449	495			
Vertical stack	159	164	197	199	
	261				
field procedure	164				

This page has been reformatted by Knovel to provide easier navigation.

## Index Terms

## Links

Vertical stacking	159	197		
Vertical traveltime	417			
Vertical velocity variation	372			
Vibration	5	236	248	
patterns	5			
Vibroseis	156	164	197	261
	266			
correlation	157	164	197	261
sweeps	158			
Vintage	255	517		
axis	256			
dimension	255	257		
Visual attributes	264			
Visualization	448	486		
methods	448			
Voice recognition	499			
Voltaire	448			
Volume (3D seismic data)	xxii	34		
Volume attributes	487	489	501	
Volume interpretation	382	384	438	448
system	438			
Volume visualization	381			
Volumetric density model	45			
Volumetric depth conversion	460			
Volumetric display	447			
Vorwata structure	386	462		
Voxel	381	384	447	
graphic elements	381			
tracking	382			
VTI anisotropy	132			

This page has been reformatted by Knovel to provide easier navigation.

## Index Terms

## Links

Vugular porosity	146		
<b>W</b>			
Wang,Z., et al.	515		
Washouts	417		
Water	99		
Water depth	248      470      483		
increase rate	470		
Water gun	239		
Water saturation	108		
Water turbulence	236		
Water velocity	249      460		
variations	460		
Wave action	264		
Wave amplitude	7		
Wave base	248		
Wave energy dissipation	139		
Wave equation	19      33      120      202		
datuming	202		
methods	19		
modeling	225		
redatuming	262		
Wavefield	8      16      18      20		
28	81      83      85		
193	349      403		
data	8      349		
data display	8		
evolution	86		
sampling	193		

This page has been reformatted by Knovel to provide easier navigation.

## Index Terms

## Links

Wavefield ( <i>Cont.</i> )				
snapshot	16	18	20	81
	83	85		
Waveform	7	9	12	26
	71	276	384	430
	447	473	499	518
differences	518			
dimensional effects	26			
inconsistencies	276			
Wavefront	18	26	28	51
	71	133		
rays	18			
Waveguide	435			
Wave-induced flow	139			
Wavelength	7	12	241	273
Wavelet	xxii	12	76	93
	96	238	261	266
	294	298	395	408
	416	423	425	431
	434	441	477	497
	499			
adjustments, (seismic data processing)	261			
design	441			
dominant period	238			
estimation	418	501		
interference	76	417	477	
packet decomposition	499			
pair	499			
phase	435			
processing	266			

This page has been reformatted by Knovel to provide easier navigation.

## Index Terms

## Links

Wavelet ( <i>Cont.</i> )				
specification	418			
synthetic seismogram	408			
transform	395	497	499	
waveform	499			
Wave frequency	12			
Wavenumber	322	348	541	
aperture	322			
domain	542			
Wave period	12	528		
Wave phase	413			
Wave propagation	5	33	113	138
direction	5			
Wave pulse	12			
Waves (general properties)	3			
critical angle	26			
dimensional effects	26			
elastic properties	6			
Fermat's principle	22			
Huygens' principle	20			
impulse response	15			
mechanical waves	3			
particle motion	4			
polarization	5			
reciprocity	17			
Snell's law	23			
source and receiver directivity	17			
wavefield data display	8			
waveform	9	12		

This page has been reformatted by Knovel to provide easier navigation.

## Index Terms

## Links

Waves (general properties) ( <i>Cont.</i> )	
wavespeed	7
wavefront and rays	18
Waves in fluids	33
big picture	41
density	45
equation of motion	36
fine layering	45
fluid model	33
parameters	34
velocity variation	42
Waves in porous solids	135
attenuation and dispersion	144
empirical relationships	136
equation of motion	139
Gassmann theory and wavespeeds	141
parameters	138
rock as a porous solid	135
rock density	140
rock velocity ranges	150      152
wave types	140
Waves in solids	113
anisotropy	131
elastic reflection coefficient	127
equations of motion	118
Hooke's law and elastic parameters	116
mode conversion	123
reflection coefficient approximations	130
Snell's law and critical angles	125
strain	113

This page has been reformatted by Knovel to provide easier navigation.

## Index Terms

## Links

Waves in solids ( <i>Cont.</i> )				
stress	115			
velocity layering	127			
wave types and speeds	120			
Wave scattering	64	146		
Waveshape	489			
Wavespeed	7	34	121	136
	141			
ratio	121			
relationships	136			
waves in porous solids	141			
Wave speeds (in solids)	120			
Waves (seismology)	1			
general properties	3			
in fluids	33			
in porous solids	135			
in solids	113			
reservoir fluid properties	99			
seismic events	51			
Wave types	120	133	140	
porous solids	140			
solids	120			
Wave velocity	35			
Weak lateral velocity variation	460			
Weathering layer	89	150	235	262
	362	270	316	435
	460			
Wedge model	428			
Well clustering	459			

## Index Terms

## Links

Well control	42	396	417	431
	435	448	459	473
	481	485	490	501
seismic data interpretation	435			
Well location	463			
Well log/logging	4	45	135	137
	143	147	354	391
	403	412	417	436
	440	448	454	502
	508			
correlation	440	486		
data	135	417	502	
digital logging	137	448		
interactive interpretation	440			
neutron density logging	405			
neutron porosity logging	137			
sonic logging	4	45	137	143
	147	354	403	417
	436	454		
Well trajectories	465			
Wells-only depth map	459			
West Africa	66	473	476	
West Texas	155			
Wetlands	251			
Whale	15	252		
White, J.	121			
Whooping crane	251			
Wide angle reflection	70	79		
Wide line shooting	208			
Wiggle plot	9	11	447	

This page has been reformatted by Knovel to provide easier navigation.

## Index Terms

## Links

Wiggle trace display	9	380		
Wilcox formation	385	436	459	516
Wildcat wells	490			
Wind	264			
Windows	284			
Window/windowing	459	489		
Work effort (man days)	439			
Workstation	283			
World petroleum reserves	483			
World's fastest computer	289			
World War II	235			
Wyllie equation	137	144		
Wyllie, M.	137			

## **X**

x-bin	445
-------	-----

## **Y**

y-bin	445			
Yilmaz, O.	93	157	261	321
	544			

## **Z**

Zero crossing	384	459		
Zero dip	270	273		

## Index Terms

## Links

Zero offset				
action	369			
offset	56	92	168	195
	295	297	301	317
	325	330	336	349
	366	369	403	422
	460	492	501	517
reflection time	92	336		
offset data	317	460		
offset reflection coefficient	501	517		
offset seismic trace	403			
offset time	301			
offset transmission loss	422			
offset vertical seismic profile	404			
Zero phase	410	424	426	534
wavelet	410	426		
Zero porosity limit	142			
Zoeppritz elastic wave theory		xx		
Zoeppritz equations	128	130		